

# **Crystallography and Surface Structure**

An Introduction for Surface Scientists and Nanoscientists

2<sup>nd</sup> Edition

**Klaus Hermann**

Fritz-Haber-Institut der Max-Planck-Gesellschaft, Faradayweg 4-6, D-14195 Berlin, Germany

Book cover text:

“The book cover includes a scanning electron microscopy picture of a stepped Cu<sub>2</sub>O surface (large circular area) kindly provided by Marc Willinger, Fritz-Haber Institute Berlin.”

## PREFACE TO THE SECOND EDITION

As a result of feedback from readers of the first edition of this book and from colleagues, this second edition is a major revision which goes beyond mere error correction and minor clarification. While the book has been modified and extended greatly, the initial concept of a combined tutorial introduction into surface crystallography, with bulk crystallography as a basis, and an overview of modern subjects for the advanced researcher is still conserved. Many sections have been updated for completeness and extended to include recent developments due to the advent of new and more refined measuring techniques.

The second edition is also targeted at researchers working on graphene and other weakly adsorbing overlayers which form large size moiré patterns observed by scanning tunneling and electron microscopy. They might appreciate the new section on moiré lattice formation which until now has not been available in textbook format. Nanoparticle physicists and materials scientists who are interested in structure information of very small particles and seek to connect e.g. electronic and magnetic properties with structural data, may benefit from the sections about nanoparticles, crystal spheres, nanotubes, as well as faceting. This might also interest catalytic chemists trying to interpret chemical behavior such as reactivity by structural information of small particles.

Specific items which have been newly added or revised include

- nanoclusters and crystallites, giving a basic overview on structure details,
- incommensurate and quasicrystals, being treated on a common basis,
- basics of epitaxy and crystal growth,
- further details on chiral surfaces and adsorbates,
- the theoretical treatment of high-order commensurate (HOC) overlayers,
- the theory of interference lattices and moiré patterns,
- the geometric structure of high-symmetry adsorbate sites,
- more detailed computational algorithms in the appendices,
- structure database formats, documenting measured surface structures.

Furthermore, the list of references to original publications and books on specific subjects has been revised and extended to account for more recent experimental and theoretical developments. The set of exercises concluding each section has been substantially enlarged following suggestions by readers of the first book edition. All structure graphics in this book have been created using the interac-

tive software *Balsac* (Build and Analyze Lattices, Surfaces, And Clusters) developed by the author ((C) K. Hermann, Fritz-Haber Institut, Berlin, 1990-2015).

Michel A. Van Hove and Wolfgang Moritz have once again lent invaluable support through constructive criticism and detailed suggestions. I am particularly indebted to Michel for our fruitful discussions during various extended research visits to the Institute of Computational and Theoretical Studies (ICTS) at Hong Kong Baptist University, which helped to improve the revised text in innumerable ways. Advice from other colleagues on subjects specific to the second edition has likewise been instrumental to the improvement of this edition, including suggestions on interference lattices by Michael S. Altman, on growth mechanisms by Ernst G. Bauer, on quasicrystals by Renee D. Diehl, and on chirality by Andrew J. Gellman and Rasmita Raval. Critical reading of the final manuscript by Travis Jones and color design advice on figures by Liudmyla Masliuk are greatly acknowledged.

Finally, unsurpassed support and overwhelming patience by my wife Hanna has again proven essential for the completion of this book project.

Fritz-Haber-Institut, Berlin  
Autumn 2015

Klaus Hermann

## **PREFACE TO THE FIRST EDITION**

The objective of this book is to provide students and researchers with the crystallographic foundations necessary to understand structure and symmetry of surfaces and interfaces of crystalline materials. This includes macroscopic single crystals as well as crystalline nanoparticles. Knowledge of their geometric properties is a prerequisite for the interpretation of corresponding experimental and theoretical results, which explain both their physical and chemical behavior. In particular, surface and interface structure is of vital importance for studies of properties near single crystal surfaces, but also for research on thin films at solid substrates. Here technological applications range from semiconductor devices and magnetic storage disks to heterogeneous catalysts.

Crystalline nanoparticles, such as nanotubes, nanowires, or compact particles of finite size have recently attracted considerable interest due to their novel chemical and physical properties. Examples are carbon nanotubes, silicon nanowires, nanosize quantum dots at semiconductor surfaces, or catalytically active crystallites. These particles are of finite size in one or more dimensions, but their local atom arrangement can still be close to that of extended bulk crystals. In addition, their surfaces and interfaces with other material can be described analogously to those found for single crystal surfaces. Thus, surface crystallography, covered in this book, can also be applied to analyze structural properties of nanoparticle surfaces.

While treatises on three-dimensional crystallography are abundant, there are only few chapters on surface crystallography available in specialized surface science reviews. In particular, comprehensive textbooks on surface structure have not yet been published. Nevertheless, students and researchers entering the field need to obtain a thorough overview of surface structure and geometry, which includes all relevant basic crystallographic methods required for theoretical and experimental analyses. This book tries to serve this purpose. It is primarily meant for graduate and PhD students in physics, chemistry, and crystallography, but will also help researchers who want to learn more details about geometric structure at surfaces of single crystals or nanoparticles.

The book is written by a theoretical surface scientist. Therefore, the discussion of methods and approaches in the text is frequently adapted to surfaces and differs in some places from traditional crystallographic treatment. As an example, number theoretical methods are used to derive appropriate transformations between equivalent lattice descriptions. Further, some of the conventional surface structure concepts are looked at from a different view point and go beyond the standard treat-

ment known inside the surface science community. Examples are the introduction of Miller indices based on netplane-adapted lattices and a thorough mathematical treatment of symmetry, which results in the seventeen two-dimensional space groups. Therefore, the text can also be used as a resource complementary to the standard surface science literature.

This book project started as a manuscript of a series of lectures on surface crystallography, given by the author at several international workshops and in universities as well as research institutions where surface science and catalysis groups were engaged in research on structural properties of surfaces. Questions and discussions during the lectures were often the source of more detailed work on different sections of the manuscript and thus helped to improve its presentation. Furthermore, research visits to various surface science groups raised the author's awareness of new or incompletely treated issues to be dealt with. The author is indebted to all those who contributed with their scientific curiosity and criticism. The text has benefited from numerous discussions with surface scientists, crystallographers, and mathematicians of whom only a few are mentioned in alphabetic order: Gerhard Ertl, Klaus Heinz, Bernhard Hornfeck, Klaus Müller, John B. Pendry, Gabor A. Somorjai, D. Phil Woodruff. Wolfgang Moritz served as an extremely valuable sparring partner in the world of crystallography. Very special thanks go to Michel A. Van Hove whose constructive criticism, rich ideas, and continuous support during the writing phase were unmatched. Without him the book would not exist in its present form.

Finally, I am greatly indebted to my wife Hanna for her patience and loving care throughout the time it took to finish this book and beyond.

Fritz-Haber-Institut, Berlin  
Summer 2010

Klaus Hermann

## CONTENTS

<b>Preface to the Second Edition</b> .....	p
<b>Preface to the First Edition</b> .....	p
<b>1 Introduction</b> .....	p
<b>2 Bulk Crystals: Three-Dimensional Lattices</b> .....	p
2.1 Basic Definition .....	p
2.2 Representation of Bulk Crystals .....	p
2.2.1 Alternative Descriptions Conserving the Lattice Representation .....	p
2.2.2 Alternative Descriptions Affecting the Lattice Representation .....	p
2.2.2.1 Cubic, Hexagonal, and Trigonal Lattices .....	p
2.2.2.2 Superlattices .....	p
2.2.2.3 Linear Transformations of Lattice Vectors .....	p
2.2.3 Centered Lattices .....	p
2.3 Periodicity Cells of Lattices .....	p
2.4 Lattice Symmetry .....	p
2.5 Reciprocal Lattice .....	p
2.6 Neighbor Shells .....	p
2.7 Nanoparticles and Crystallites .....	p
2.8 Incommensurate Crystals and Quasicrystals .....	p
2.8.1 Modulated Structures .....	p
2.8.2 Incommensurate composite crystals .....	p
2.8.3 Quasicrystals .....	p
2.9 Exercises .....	p
<b>3 Crystal Layers: Two-Dimensional Lattices</b> .....	p
3.1 Basic Definition, Miller Indices .....	p
3.2 Netplane-Adapted Lattice Vectors .....	p

3.3	Symmetrically Appropriate Lattice Vectors: Minkowski Reduction .....	p
3.4	Miller Indices for Cubic and Trigonal Lattices .....	p
3.5	Alternative Definition of Miller Indices, Miller-Bravais Indices .....	p
3.6	Symmetry Properties of Netplanes .....	p
3.6.1	Centered Netplanes .....	p
3.6.2	Inversion .....	p
3.6.3	Rotation .....	p
3.6.4	Mirror Operation .....	p
3.6.5	Glide Reflection .....	p
3.6.6	Symmetry Groups .....	p
3.7	Crystal Systems and Bravais Lattices in Two Dimensions .....	p
3.8	Crystallographic Classification of Netplanes and Monolayers .....	p
3.8.1	Oblique Netplanes .....	p
3.8.2	Primitive Rectangular Netplanes .....	p
3.8.3	Centered Rectangular Netplanes .....	p
3.8.4	Square Netplanes .....	p
3.8.5	Hexagonal Netplanes .....	p
3.8.6	Classification Overview .....	p
3.9	Exercises .....	p
<b>4</b>	<b>Ideal Single Crystal Surfaces .....</b>	<b>p</b>
4.1	Basic Definition, Termination .....	p
4.2	Morphology of Surfaces, Stepped and Kinked Surfaces .....	p
4.3	Miller Index Decomposition .....	p
4.4	Chiral and Achiral Surfaces .....	p
4.5	Exercises .....	p
<b>5</b>	<b>Real Crystal Surfaces .....</b>	<b>p</b>

5.1	Surface Relaxation .....	p
5.2	Surface Reconstruction .....	p
5.3	Growth Processes .....	p
5.4	Facetting .....	p
5.5	Exercises .....	p
<b>6</b>	<b>Adsorbate layers .....</b>	<b>p</b>
6.1	Definition and Classification .....	p
6.2	Adsorbate Sites .....	p
6.3	Wood Notation of Surface Structure .....	p
6.4	High-Order Commensurate (HOC) Overlayers .....	p
6.5	Interference Lattices .....	p
6.5.1	Basic formalism .....	p
6.5.2	Interference and Wood Notation .....	p
6.5.3	Anisotropic Scaling, Stretching and Shifting .....	p
6.6	Symmetry and Domain Formation .....	p
6.7	Adsorption at Surfaces and Chirality .....	p
6.8	Exercises .....	p
<b>7</b>	<b>Experimental Analysis of Real Crystal Surfaces .....</b>	<b>p</b>
7.1	Experimental Methods .....	p
7.2	Surface Structure Compilations .....	p
7.3	Database Formats for Surface and Nanostructures .....	p
7.4	Exercises .....	p
<b>8</b>	<b>Nanotubes .....</b>	<b>p</b>
8.1	Basic Definition .....	p
8.2	Nanotubes and Symmetry .....	p
8.3	Complex Nanotubes .....	p



8.4 Exercises .....	p
<b>Appendices</b> .....	p
A Sketches of High-Symmetry Adsorbate Sites .....	p
B Parameter Tables of Crystals.....	p
C Mathematics of the Wood Notation .....	p
C.1 Basic Formalism and Examples .....	p
C.2 Wood-Representability .....	p
D Mathematics of the Minkowski Reduction .....	p
E Details of Number Theory .....	p
E.1 Basic Definitions and Functions .....	p
E.2 Euclid's Algorithm .....	p
E.3 Linear Diophantine Equations .....	p
E.4 Quadratic Diophantine Equations .....	p
E.5 Number Theory and $2 \times 2$ Matrices .....	p
F Details of Vector Calculus and Linear Algebra .....	p
G Details of Fourier Theory .....	p
H List of Surface Web Sites .....	p
I List of Surface Structures .....	p
<b>References</b> .....	p
<b>Glossary and Abbreviations</b> .....	p
<b>Index</b> .....	p

## 1 INTRODUCTION

Research in many areas of materials science requires detailed knowledge about crystalline solids on an atomic scale. These systems may represent real materials such as complex semiconductors, or may act as meaningful models, for example, simulating reactive sites of catalysts. Here physical and chemical insight depends very much on details of the geometric structure of local environments near atoms and of possible periodic atom arrangements inside the crystal as well as at its surface. As examples we mention that

- **chemical binding** between atoms inside a crystal but also at its surfaces depends, apart from atomic parameters, strongly on local geometry [1], [2]. This is very often expressed by local **coordination** describing the number and arrangement of nearest neighbor atoms with respect to the binding atom. As an example, metal atoms inside a bulk metal crystal are usually characterized by a large number of nearest neighbors, eight or twelve, yielding metallic binding. At surfaces, the change in chemical binding due to different coordination, compared with that inside the bulk, is tightly connected with local structure which can be expressed by relaxation and reconstruction. Further, atoms or molecules can adsorb at specific sites of crystalline substrates, where the adsorption geometry is essential for an understanding of local binding behavior.
- **electronic properties** at surfaces of single crystals can differ substantially from those of the corresponding bulk. For example, the existence of a surface can induce additional electronic states, surface states, that have been found in experiments and studied theoretically for some time [3]. Here the detailed surface structure determines the existence as well as the energetic behavior of the states. Further, electronic interband transitions in silicon nanowires and nanodots are found to cause photoluminescence which does not occur in silicon bulk crystals [4]. The difference is explained by both the spatial confinement of the nanoparticles and also by changes in geometric properties of their atom arrangement. Finally, it has been claimed from experiment that semiconducting bulk silicon shows metallicity at its  $(7 \times 7)$  reconstructed  $(1\ 1\ 1)$  surface [5], and metallicity is also found in theoretical studies on silicon nanowires [6].
- **magnetism** of crystalline bulk material as well as of its surfaces depends on the crystal structure and local coordination. For example, vanadium sesquioxide,  $V_2O_3$ , in its monoclinic crystal structure is anti-ferromagnetic at low temperatures, whereas its high-temperature

phase, described by a trigonal corundum lattice, is paramagnetic [7]. Vanadium crystals with a body-centered cubic lattice are found to be paramagnetic in their bulk volume but ferromagnetic at their surfaces [8]. Other examples are thin iron films grown on top of copper single crystal surfaces where, as a function of film thickness, their crystal structure changes and, as a consequence, their magnetic properties [9].

- **anisotropic electrical conductivity** is often connected with dense atom packing along specific directions inside a crystal. An example is given by trigonal  $\text{LiCoO}_2$  crystals which form the most common lithium storage material for rechargeable batteries. Here the electrical conductivity is greatly enhanced along densely packed Co and Li planes while it is much smaller perpendicular to the planes [10].
- **catalytic surface reactions** depend crucially on structural properties of the surfaces of crystalline catalyst materials at an atomic scale [11], [12]. The atomic surface structure determines possible adsorption and reaction sites for molecules, which can support specific catalytic reactions but can also exclude others, also known as structure-reactivity relationships [11]. For example catalytic CO oxidation happens at single crystal surfaces of platinum with different efficiency depending on the surface orientation [13], where the surface structure determines the type and density of reactive sites.

In addition to bulk crystals and their surfaces, studies on crystalline **nanoparticles** [14], [15] have become an exciting field of research. This includes nanotubes [16], nanowires [14], or compact particles of finite size, such as atom clusters [17], fullerenes [18], or quantum dots [19], which show novel physical and chemical properties deviating from those of the corresponding bulk material. Examples are carbon nanotubes providing substrate material to yield new active catalysts [20] or silicon nanowires whose visible photoluminescence is determined by their size [21]. Further, nanosize quantum dots at semiconductor surfaces are found to yield quite powerful light emitting diodes (LED) of technological relevance [19].

These nanoparticle systems are described as **atom aggregates** of finite size in one or more dimensions, where their local geometric arrangement can still be close to that of extended bulk crystals. Likewise, their spatial confinement with corresponding surfaces and interfaces can be considered analogous to that appearing at bulk crystal surfaces. Therefore, surface crystallography, initially developed to describe structural properties at single crystal surfaces, also forms a sound basis to

characterize the structure of nanoparticle surfaces. This is particularly interesting since the relative number of atoms positioned at nanoparticle surfaces compared with those of their inner volume is always larger than that of extended macroscopic single crystals. Thus, the relative importance of atoms at **nanoparticle surfaces** in determining physical properties is expected to be larger than that of atoms at single crystal surfaces. In addition, nanoparticles can possess symmetry and geometric properties which do not appear in single crystals or at their surfaces. Examples are icosahedral clusters or curved nanoparticle surfaces which originate from bending single crystal sections, where in this book **nanotubes** will be discussed as examples.

In many experimental and theoretical studies real crystalline systems are, for the sake of simplicity, approximately described as **ideal single crystals** with a well defined atomic composition and an unperturbed three-dimensional periodicity. In addition, planar surfaces of the single crystals are often assumed to be bulk-terminated and of unperturbed two-dimensional periodicity. With this approximation in mind a rigorous mathematical description of all structural parameters becomes possible and is one of the basic subjects of classical crystallography. As an illustration, Fig. 1.1 shows the structure of a section of an ideal single crystal of magnesium oxide, MgO, with its perfect

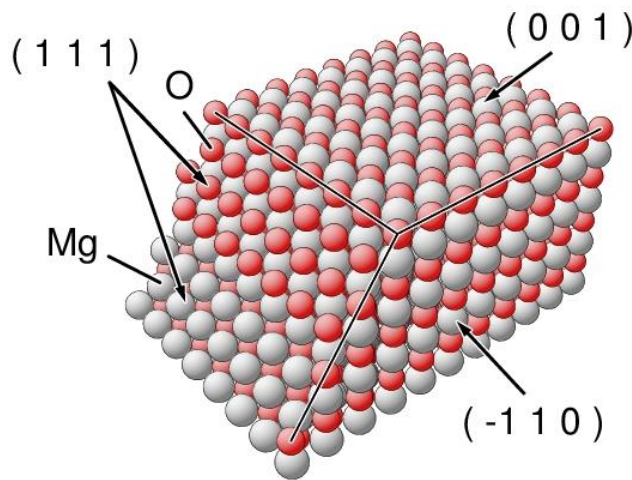


Fig. 1.1. Section of an MgO crystal (NaCl lattice). The atoms are shown as shaded balls of different color and labeled accordingly. The section is enclosed by non-polar (0 0 1), (-1 1 0) and by polar (1 1 1) oriented surfaces.

three-dimensional periodic arrangement of atoms. Here sections of ideal planar surfaces, originating from bulk truncation, become visible and demonstrate the variety of surface types for the same crystal depending on the crystal cut.

In the following sections of this book we will discuss basic elements and **mathematical methods** used in crystallography to evaluate structural parameters of single crystals with particular emphasis on their surfaces. We start with ideal bulk crystals of three-dimensional periodicity, where classical bulk crystallography provides a quantitative description. Then we introduce ideal two-dimensional surfaces as a result of bulk truncation along specific directions including high density, vicinal, stepped, kinked, and chiral surfaces. We give a detailed account of their two-dimensional symmetry behavior following the crystallographic classification scheme of Bravais lattices and two-dimensional space groups. Next, we discuss details of the deviation of atomic structure at surfaces due to changes in surface binding compared with the bulk. This is usually described by surface relaxation and reconstruction, where we consider different schemes. In addition, structural behavior during growth processes is discussed. Then we deal with crystallographic aspects of commensurate, high-order commensurate, and incommensurate adsorbate systems as special cases of surface reconstruction. Here also the different structure notations used in the literature will be described. The discussion of surface structure will be completed by an overview of the surfaces that have been analyzed quantitatively at an atomic level in scattering, diffraction, imaging, or spectroscopic experiments. Further, formal requirements of complete quantitative surface structure databases will be considered. Finally, we describe theoretical aspects and structural details of nanotubes of different element composition as special cases of rolled sections of crystal monolayers. These nanotubes are examples of a larger class of crystalline materials, nanoparticles mentioned above, and demonstrate that crystallographic methods can also be applied to these systems in order to account for their structural properties. Finally, the book concludes with appendices spelling out further details of the mathematical methods used in the different sections, with tabulations of typical surface sites, and with compilations of structural parameters of crystals.

The theoretical concepts treated in this book will be illustrated by example applications for further understanding which includes results from **measured** real single crystal surfaces documented in the Surface Structure Database (**SSD**) [22], [23], [24] or its earlier version **SCIS** (Surface Crystallographic Information Service) [25]. In addition, each section of the book concludes with a set of **exercises**. These exercises are of varying difficulty, ranging from simple questions to small research projects, and are meant to stimulate the discussion about the different subjects and to contribute to their clarification. Some of the exercises may require **visualization tools** for crystals, such as **Balsac** [26], or **Survis**, the visualization part of the SSDIN package [27] or the like.

In the theoretical treatment of some structural properties of ideal single crystals we will apply **number theoretical methods**, dealing with relations between integers. While this approach is not commonly used in textbooks on surface science or crystallography it can simplify the formal treatment considerably. Examples are solutions of linear and quadratic Diophantine equations which facilitate the discussion of monolayers or of atom neighbor shells in crystals. Therefore, number theoretical methods will be introduced briefly as required and further details are found in Appendix E.

A few illustrations are included as **stereo pictures** for an enhanced three-dimensional impression. These pictures may be viewed by either using optical stereo glasses (available separately) or by cross-eyed viewing without glasses. In the latter case, viewing for an extended time may overstrain the eyes and should be avoided.

Clearly, the present book cannot cover all aspects of the field and may, in some cases, be quite brief. Further, the selection of topics as well as their presentation is, to some degree, determined by the author's personal preferences. However, the interested reader is referred to the extensive crystallographic literature, see e.g. Refs. [28], [29], [30], [31], [32], [33], to the surface science literature, see e.g. [34], [35], [36], [37], [38], [39], or to the solid state physics literature, see e.g. Refs. [1], [2], [40], to explore additional details.

## 2 BULK CRYSTALS: THREE-DIMENSIONAL LATTICES

This section deals with geometric properties of three-dimensional **bulk crystals**, which are described, in their perfect structure, by atom arrangements that are periodic in three dimensions. As an example, Fig. 2.1 shows a section of a tetragonal  $\text{YBa}_2\text{Cu}_3\text{O}_7$  crystal, where vectors  $\underline{R}_1$ ,  $\underline{R}_2$ ,  $\underline{R}_3$  (lattice vectors) indicate the mutually perpendicular directions of periodicity. Further, the basis of the crystal structure consists of 13 atoms (1  $\times$  yttrium, 2  $\times$  barium, 3  $\times$  copper, 7  $\times$  oxygen) inside a rectangular block (unit cell) which is repeated periodically inside the crystal. The building unit is shown to the left of the figure.

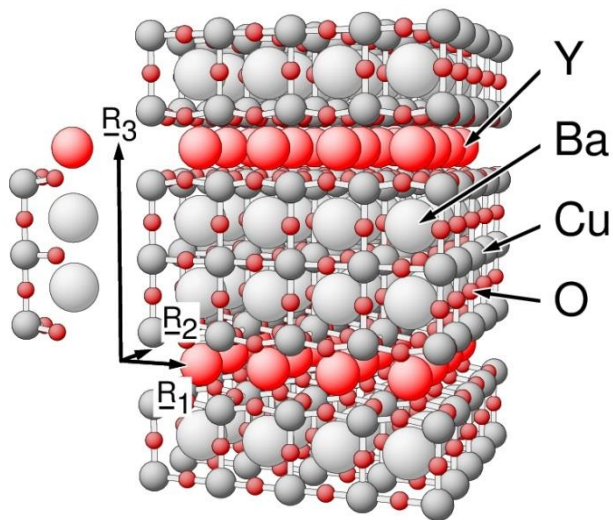


Fig. 2.1. Section of a tetragonal  $\text{YBa}_2\text{Cu}_3\text{O}_7$  crystal. The atoms are labeled accordingly. In addition, the basis of 13 atoms inside a rectangular cell and lattice vectors  $\underline{R}_1$ ,  $\underline{R}_2$ ,  $\underline{R}_3$  are included to the left.

In this section, all **basic definitions** used for a quantitative description of structural properties of perfect three-dimensionally periodic crystals will be provided. Here the crystals are considered in terms of their translational symmetry, i.e. periodicity, but also by their different point symmetry elements, such as inversion points, mirror planes or rotation axes, which characterize the positions of all atoms inside a crystal. While the definitions and general properties are rather abstract and **mathematical**, they can become quite relevant for theoretical studies of real three-dimensional crystals. As an example, lattice representations of crystals are required as input to any electronic structure calculation for solid crystalline material. Further, the theoretical treatment of three-dimensional crystals serves as a foundation to study surfaces of single crystals, as will be discussed in Secs. 4, 5, and 6.

## 2.1 Basic Definition

The basic definition of a perfect three-dimensional bulk crystal becomes quite clear by considering a simple example. Fig. 2.2a shows a section of the cubic CsCl crystal, which is periodic in three perpendicular directions. Thus, its periodicity can be described by orthogonal vectors  $\underline{R}_1$ ,  $\underline{R}_2$ ,  $\underline{R}_3$  (**lattice vectors**), indicated in Fig. 2.2b, whose lengths define corresponding periodicity lengths. The lattice vectors span a cubic cell (**morphological unit cell**) which contains one cesium and chlorine atom each at positions given by vectors  $\underline{r}_1$  (Cs) and  $\underline{r}_2$  (Cl) (**lattice basis vectors**), see Fig. 2.2b. A periodic repetition of the unit cell along  $\underline{R}_1$ ,  $\underline{R}_2$ ,  $\underline{R}_3$  can then be used to build the complete infinite crystal.

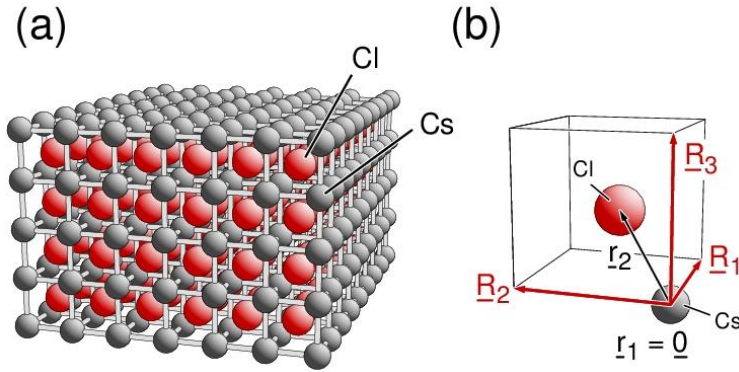


Fig. 2.2. (a) Section of a cubic CsCl crystal. Sticks connect neighboring Cs atoms to indicate the crystal structure. (b) Primitive morphological unit cell with two atoms, Cs and Cl, inside. The lattice vectors  $\underline{R}_1$ ,  $\underline{R}_2$ ,  $\underline{R}_3$  as well as lattice basis vectors,  $\underline{r}_1 = \underline{0}$  for Cs and  $\underline{r}_2$  for Cl, are shown and labeled accordingly.

In the general case, the formal definition of a perfect three-dimensional bulk **crystal** starts from a three-dimensionally periodic arrangement of atoms. Here the crystal periodicity is described by a **lattice** with **lattice vectors**  $\underline{R}_1$ ,  $\underline{R}_2$ ,  $\underline{R}_3$ . Thus, the lattice forms an infinite and periodic array of **lattice points** reached from a common origin by vectors  $\underline{R}$  with

$$\underline{R} = n_1 \underline{R}_1 + n_2 \underline{R}_2 + n_3 \underline{R}_3 \quad (2.1)$$

where the coefficients  $n_1$ ,  $n_2$ ,  $n_3$  can assume any integer value. This means, in particular, that each lattice point experiences the same environment created by all other points.

The lattice vectors can be given in different ways, where the choice depends on the type of application. While for numerical calculations it may be preferable to define  $\underline{R}_1$ ,  $\underline{R}_2$ ,  $\underline{R}_3$  with respect to an absolute **Cartesian coordinate system** as



$$\underline{\mathbf{R}}_i = (x_i, y_i, z_i), \quad i = 1, 2, 3 \quad (2.2)$$

it is common in the crystallographic literature to define these vectors by **lattice parameters** describing their lengths (**lattice constants**)  $a, b, c$  and by their mutual **angles**  $\alpha, \beta, \gamma$ , as sketched in Fig. 2.3, where

$$\begin{aligned} a &= |\underline{\mathbf{R}}_1|, \quad b = |\underline{\mathbf{R}}_2|, \quad c = |\underline{\mathbf{R}}_3| \\ \underline{\mathbf{R}}_1 \cdot \underline{\mathbf{R}}_2 &= a b \cos(\gamma), \quad \underline{\mathbf{R}}_1 \cdot \underline{\mathbf{R}}_3 = a c \cos(\beta), \quad \underline{\mathbf{R}}_2 \cdot \underline{\mathbf{R}}_3 = b c \cos(\alpha) \end{aligned} \quad (2.3)$$

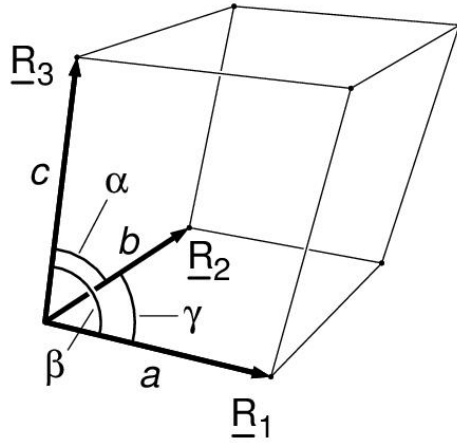


Fig. 2.3. Definition of crystallographic lattice parameters  $a, b, c, \alpha, \beta, \gamma$  in a perspective view, see text.

Examples are given by lattices denoted as

$$\text{simple cubic} \quad \text{where} \quad a = b = c, \quad \alpha = \beta = \gamma = 90^\circ \quad (2.4)$$

$$\text{hexagonal} \quad \text{where} \quad a = b \neq c, \quad \alpha = \beta = 90^\circ, \quad \gamma = 120^\circ \quad (2.5)$$

Relations (2.3) can be **converted** to yield lattice vectors in Cartesian coordinates starting from the six parameters,  $a, b, c$ , and  $\alpha, \beta, \gamma$ , given in (2.3), where one possible conversion is

$$\begin{aligned} \underline{\mathbf{R}}_1 &= a (1, 0, 0), \quad \underline{\mathbf{R}}_2 = b (\cos(\gamma), \sin(\gamma), 0) \\ \underline{\mathbf{R}}_3 &= c (\cos(\beta), (\cos(\alpha) - \cos(\beta) \cos(\gamma)) / \sin(\gamma), v_3 / \sin(\gamma)) \end{aligned} \quad (2.6a)$$

with

$$v_3 = \{ (\cos(\beta - \gamma) - \cos(\alpha)) (\cos(\alpha) - \cos(\beta + \gamma)) \}^{1/2} \quad (2.6b)$$

This yields for simple cubic lattices with (2.4)

$$\underline{\mathbf{R}}_1 = a (1, 0, 0), \quad \underline{\mathbf{R}}_2 = a (0, 1, 0), \quad \underline{\mathbf{R}}_3 = a (0, 0, 1) \quad (2.7)$$

and for hexagonal lattices with (2.5)

$$\underline{\mathbf{R}}_1 = a ( 1, 0, 0 ), \quad \underline{\mathbf{R}}_2 = a ( -1/2, \sqrt{3}/2, 0 ), \quad \underline{\mathbf{R}}_3 = c ( 0, 0, 1 ) \quad (2.8)$$

The lattice vectors  $\underline{\mathbf{R}}_1, \underline{\mathbf{R}}_2, \underline{\mathbf{R}}_3$  span a six-faced polyhedron (so-called parallelepiped), defining the **morphological unit cell**, often referred to as the **unit cell**, whose edges are parallel to  $\underline{\mathbf{R}}_1, \underline{\mathbf{R}}_2, \underline{\mathbf{R}}_3$  and whose volume  $V_{el}$  is given by

$$V_{el} = | ( \underline{\mathbf{R}}_1 \times \underline{\mathbf{R}}_2 ) \cdot \underline{\mathbf{R}}_3 | \quad (2.9)$$

The unit cell is called a **primitive unit cell** if its volume is the smallest of all possible unit cells in the crystal. This is equivalent to requiring that there is no additional lattice point, described by vector  $\underline{\mathbf{R}}'$  with

$$\underline{\mathbf{R}}' = \kappa_1 \underline{\mathbf{R}}_1 + \kappa_2 \underline{\mathbf{R}}_2 + \kappa_3 \underline{\mathbf{R}}_3, \quad 0 \leq \kappa_i < 1 \quad (2.10)$$

inside the morphological unit cell of the lattice. Otherwise, the cell is **non-primitive** and there must be one or more additional lattice points  $\underline{\mathbf{R}}'$  inside the unit cell. Analogously, lattice vectors  $\underline{\mathbf{R}}_1, \underline{\mathbf{R}}_2, \underline{\mathbf{R}}_3$  whose morphological unit cell is primitive are called **primitive lattice vectors**, otherwise **non-primitive**. As an example, the cubic unit cell of CsCl as well the corresponding lattice vectors, shown in Fig. 2.2, are primitive. On the other hand, replacing all cesium and chlorine atoms in Fig. 2.2 by one atom type, for example iron, yields a body-centered cubic crystal. Here the lattice vectors  $\underline{\mathbf{R}}_1, \underline{\mathbf{R}}_2, \underline{\mathbf{R}}_3$ , shown in the figure, are non-primitive, since vector  $\underline{\mathbf{r}}_2$  now becomes a lattice vector inside the morphological unit cell.

In a crystal, the morphological unit cell contains in general  $p$  atoms at positions given by vectors  $\underline{\mathbf{r}}_1 \dots \underline{\mathbf{r}}_p$  (**lattice basis vectors**) which form the **basis** of the crystal structure (the basis is sometimes also called the **structure**). Each atom at  $\underline{\mathbf{r}}_i$  carries a **label** characterizing its properties, such as its nuclear charge or element name. These labels, usually omitted in the following, will be attached to each lattice basis vector if needed. For example, a definition  $\underline{\mathbf{r}}_3^{\text{Cl}}$  would refer to a chlorine atom placed at a position given by the third lattice basis vector. All lattice basis vectors  $\underline{\mathbf{r}}_i$  inside the morphological unit cell can be written as **linear combinations** of the lattice vectors  $\underline{\mathbf{R}}_1, \underline{\mathbf{R}}_2, \underline{\mathbf{R}}_3$  according to

$$\underline{\mathbf{r}}_i = x_i \underline{\mathbf{R}}_1 + y_i \underline{\mathbf{R}}_2 + z_i \underline{\mathbf{R}}_3, \quad i = 1 \dots p \quad (2.11)$$

where  $x_i, y_i,$  and  $z_i$  are real-valued coefficients with  $|x_i| < 1, |y_i| < 1, |z_i| < 1$ . This use of **relative coordinates**  $x_i, y_i, z_i$  to describe atoms inside the unit cell is common practice in the crystallographic literature [28], [29], [30], [31], [32], [33]. Note that according to definition (2.11), the coeffi-

cients  $x_i, y_i, z_i$  are in general not connected with the Cartesian coordinate system but with coordinate axes given by the lattice vectors  $\underline{\mathbf{R}}_1, \underline{\mathbf{R}}_2, \underline{\mathbf{R}}_3$ .

The **origin** of the morphological unit cell inside a crystal can always be chosen freely since the complete infinite crystal consists of a periodic arrangement of unit cells in three dimensions. In particular, the origin does not need to coincide with a specific atom position, as considered in the example of CsCl mentioned above. However, it is usually chosen to coincide with the location of the largest number of point symmetry elements, such as inversion points or origins of mirror planes and rotation axes, which are given by the lattice vectors  $\underline{\mathbf{R}}_1, \underline{\mathbf{R}}_2, \underline{\mathbf{R}}_3$  together with the lattice basis vectors  $\underline{\mathbf{r}}_1 \dots \underline{\mathbf{r}}_p$ . This will be discussed in greater detail in Sec. 2.4.

Altogether, a **crystal** is characterized uniquely by its **lattice** defined by lattice vectors  $\underline{\mathbf{R}}_1, \underline{\mathbf{R}}_2, \underline{\mathbf{R}}_3$  and its **basis** defined by lattice basis vectors  $\underline{\mathbf{r}}_1 \dots \underline{\mathbf{r}}_p$ . Thus, general atom positions inside the crystal can be given by

$$\underline{\mathbf{r}} = n_1 \underline{\mathbf{R}}_1 + n_2 \underline{\mathbf{R}}_2 + n_3 \underline{\mathbf{R}}_3 + \underline{\mathbf{r}}_i \quad (2.12)$$

where the coefficients  $n_1, n_2, n_3$  can assume any integer value and index  $i = 1 \dots p$  counts the number of atoms in the unit cell. Here the lattice and the basis can be treated as **separate** elements of a crystal structure (which are only connected by the symmetry elements as will be discussed in Sec. 2.4).

## 2.2 Representation of Bulk Crystals

There is one important aspect that characterizes all formal descriptions of crystal structures, the fact that mathematical descriptions of crystals are **not unique**. This means that, for a given definition of a crystal, one can always find an infinite number of alternatives which describe the same crystal. While this ambiguity may be considered a drawback at first glance, it allows choosing crystal representations according to additional constraints, e.g. those given by symmetry, physical or chemical properties. Here one can distinguish between alternative descriptions which affect the crystal basis but not its lattice representation and those where both the lattice representation and the basis are affected.

### 2.2.1 Alternative Descriptions Conserving the Lattice Representation

Examples of alternative crystal descriptions which do not affect the crystal lattice are given by elemental or compound **decompositions** of a crystal. Here the basic idea is to decompose the basis inside the unit cell of a complex crystal into components and consider (fictitious) crystals of these components with the same periodicity as that of the initial crystal, given by its lattice. This decomposition is of didactic value but may also help to understand details of chemical binding inside the crystal, for example, discriminating between intra- and inter-molecular binding in molecular crystals. In the simplest case, a crystal with  $p$  atoms in its primitive unit cell can be considered alternatively as a combination of  $p$  crystals with the same lattice but with only one atom in their primitive unit cells. The origins of the corresponding  $p$  crystals can be set at positions given by the lattice basis vectors  $\underline{r}_i$  of the complete non-primitive crystal.

As a very simple example, the cubic **cesium chloride**, CsCl, crystal, shown in Fig. 2.2, is defined by a simple cubic lattice with lattice vectors  $\underline{R}_1, \underline{R}_2, \underline{R}_3$  given by (2.7). Further, its basis includes two atoms, Cs and Cl, which can be positioned at

$$\underline{r}_1 = a ( 0, 0, 0 ) \text{ for Cs } , \quad \underline{r}_2 = a ( 1/2, 1/2, 1/2 ) \text{ for Cl} \quad (2.13)$$

with  $a$  denoting the lattice constant of CsCl. Thus, the crystal can be considered as a combination of two simple cubic monoatomic crystals, one for cesium and one for chlorine, where their origins are shifted by  $\underline{r}_0 = \underline{r}_2 - \underline{r}_1 = a ( 1/2, 1/2, 1/2 )$  with respect to each other.

A more complex example is the tetragonal **YBa<sub>2</sub>Cu<sub>3</sub>O<sub>7</sub>** crystal, shown in Fig. 2.1. Here the lattice vectors can be written in Cartesian coordinates as

$$\underline{R}_1 = a ( 1, 0, 0 ) , \quad \underline{R}_2 = a ( 0, 1, 0 ) , \quad \underline{R}_3 = c ( 0, 0, 1 ) \quad (2.14a)$$

and the morphological unit cell contains 13 atoms resulting in 13 lattice basis vectors  $\underline{r}_i$  with

$$\begin{aligned} \text{Y atom :} & \quad \underline{r}_1 = (1/2, 1/2, 5/6) \\ \text{Ba atoms :} & \quad \underline{r}_2 = (1/2, 1/2, 1/6) , \quad \underline{r}_3 = (1/2, 1/2, 1/2) \\ \text{Cu atoms :} & \quad \underline{r}_4 = (0, 0, 0) , \quad \underline{r}_5 = (0, 0, 1/3) , \quad \underline{r}_6 = (0, 0, 2/3) \\ \text{O atoms :} & \quad \underline{r}_7 = (1/2, 0, -\epsilon) , \quad \underline{r}_8 = (0, 1/2, -\epsilon) , \quad \underline{r}_9 = (0, 0, 1/6) \\ & \quad \underline{r}_{10} = (0, 1/2, 1/3) , \quad \underline{r}_{11} = (0, 0, 1/2) \\ & \quad \underline{r}_{12} = (1/2, 0, 2/3+\epsilon) , \quad \underline{r}_{13} = (0, 1/2, 2/3+\epsilon) \end{aligned} \quad (2.14b)$$

using relative coordinates (2.11) where experiments yield a relative position shift  $\varepsilon = 0.026$  of four oxygen atoms. This crystal can be decomposed conceptually into 13 monoatomic (tetragonal) crystals, one yttrium, two barium, three copper, and seven oxygen crystals.

Alternatively, one can decompose the  $\text{YBa}_2\text{Cu}_3\text{O}_7$  crystal into physically more meaningful subunits which include **several** of the atoms of the initial unit cell. As an example, Fig. 2.4 illustrates a decomposition of the  $\text{YBa}_2\text{Cu}_3\text{O}_7$  crystal into its copper oxide and its heavy metal components, denoted  $\text{Cu}_3\text{O}_7$  and  $\text{YBa}_2$ , respectively, in Fig. 2.4. Here the unit cells of the component crystals contain ten and three atoms each, where the  $\text{Cu}_3\text{O}_7$  component is believed to contribute to the high-temperature superconductivity of  $\text{YBa}_2\text{Cu}_3\text{O}_7$ .

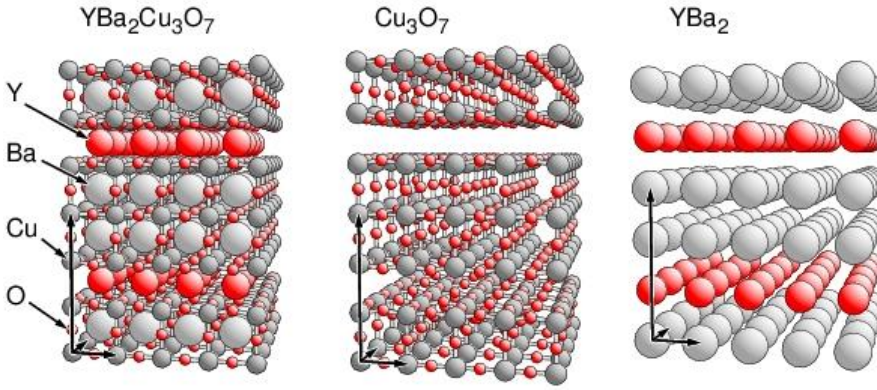


Fig. 2.4. Decomposition of the  $\text{YBa}_2\text{Cu}_3\text{O}_7$  crystal, left, into its copper oxide,  $\text{Cu}_3\text{O}_7$ , (center) and heavy metal,  $\text{YBa}_2$ , components (right). Atoms are shown as colored balls and labeled accordingly. In addition, the lattice vectors  $\underline{R}_1$ ,  $\underline{R}_2$ ,  $\underline{R}_3$  are indicated by arrows.

A very illustrative example of crystal decomposition is given by the **diamond** crystal, shown in Fig. 2.5. Its lattice can be defined as a cubic lattice where the lattice vectors are given by (2.7). The basis of the crystal includes eight carbon atoms in tetrahedral arrangements resulting in eight lattice basis vectors  $\underline{r}_i$  with

$$\begin{aligned}
 \underline{r}_1 &= (0, 0, 0), & \underline{r}_2 &= (0, 1/2, 1/2), & \underline{r}_3 &= (1/2, 0, 1/2) \\
 \underline{r}_4 &= (1/2, 1/2, 0), & \underline{r}_5 &= (1/4, 1/4, 1/4), & \underline{r}_6 &= (1/4, 3/4, 3/4) \\
 \underline{r}_7 &= (3/4, 1/4, 3/4), & \underline{r}_8 &= (3/4, 3/4, 1/4)
 \end{aligned} \tag{2.15}$$

in relative coordinates (2.11). This shows, first, that the diamond crystal can be decomposed into eight simple cubic (sc) crystals, each with one carbon in the primitive unit cell. Further, the lattice basis vectors  $\underline{r}_5$ ,  $\underline{r}_6$ ,  $\underline{r}_7$ ,  $\underline{r}_8$  arise from  $\underline{r}_1$ ,  $\underline{r}_2$ ,  $\underline{r}_3$ ,  $\underline{r}_4$  by identical shifts with

$$\underline{r}_{i+4} = \underline{r}_i + 1/4 (1, 1, 1), \quad i = 1, 2, 3, 4 \quad (2.16)$$

This suggests that the diamond crystal can also be decomposed into two identical cubic crystals with four atoms in their unit cells each, where the origins of the two crystals are shifted by a vector  $a/4 (1, 1, 1)$  with respect to each other. The lattices of the two component crystals will be shown in Sec. 2.2.2.1 to be identical to face-centered cubic (fcc) lattices. Thus, the diamond crystal can be alternatively described by a superposition of two fcc crystals which becomes clear by an inspection of Fig. 2.5.

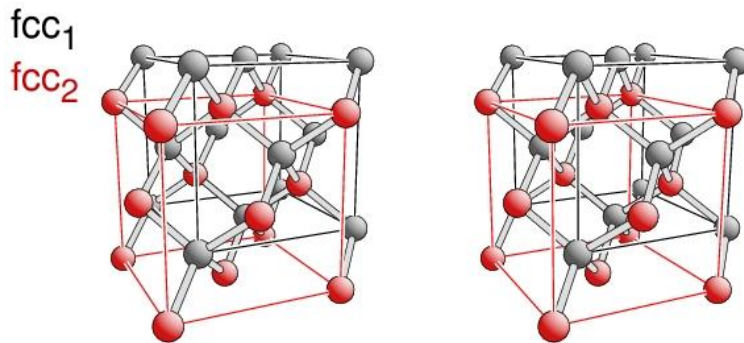


Fig. 2.5. Decomposition of the diamond crystal into two (shifted) face-centered cubic crystals, denoted  $fcc_1$  (gray balls, black lines) and  $fcc_2$  (red balls and red lines). The crystal is shown in a stereo view where the visual three-dimensional impression is obtained by cross-eyed viewing.

## 2.2.2 Alternative Descriptions Affecting the Lattice Representation

There are many possibilities of alternative descriptions of crystals where their lattices are represented differently. These alternatives may be preferred because of **conceptual** convenience but may also be required due to **computational** necessity. Examples are symmetry adapted lattices combining translational with point symmetry properties or surface adapted lattices facilitating the definition of atom coordinates in surface studies.

Crystallographers have defined a set of constraints on lattice vectors  $\underline{R}_1$ ,  $\underline{R}_2$ ,  $\underline{R}_3$  to yield a unique description of a lattice according to Niggli [41] which allows an easy distinction between the different types of three-dimensional Bravais lattices discussed in Sec. 2.4. First, the lattice vectors are chosen such that they form a right-handed vector triplet, which can be expressed mathematically by the constraint

$$(\underline{R}_1 \times \underline{R}_2) \cdot \underline{R}_3 > 0 \quad (2.17)$$

Further, they are assumed to reflect three smallest periodicity lengths along different directions in the crystal and are arranged such that

$$|\underline{\mathbf{R}}_1| \leq |\underline{\mathbf{R}}_2| \leq |\underline{\mathbf{R}}_3| \quad (2.18)$$

In addition, all lattices are grouped according to their scalar products  $s_{ij} = \underline{\mathbf{R}}_i \cdot \underline{\mathbf{R}}_j$  into two classes,

$$s_{12} \geq 0, \quad s_{13} \geq 0, \quad s_{23} \geq 0 \quad (\text{type 1, **acute**}) \quad (2.19a)$$

$$s_{12} \leq 0, \quad s_{13} \leq 0, \quad s_{23} \leq 0, \quad \text{with at least one } s_{ij} < 0 \quad (\text{type 2, **obtuse**}) \quad (2.19b)$$

where lattices with other  $s_{ij}$  combinations can be easily converted to one of the two classes by inverting two of the lattice vectors  $\underline{\mathbf{R}}_i, \underline{\mathbf{R}}_j$  to yield  $-\underline{\mathbf{R}}_i, -\underline{\mathbf{R}}_j$ . Further, simple iterative algorithms have been developed [42], [43] to reduce a general vector set  $\underline{\mathbf{R}}_1, \underline{\mathbf{R}}_2, \underline{\mathbf{R}}_3$  of type 1 or 2 to a unique description with  $\underline{\mathbf{R}}_1, \underline{\mathbf{R}}_2, \underline{\mathbf{R}}_3$  referring to vectors of smallest length in the lattice. This **reduced lattice vector set** fulfills, apart from (2.17) and (2.18), the inequalities

$$-\min(\underline{\mathbf{R}}_i^2, \underline{\mathbf{R}}_j^2) \leq 2|\underline{\mathbf{R}}_i \cdot \underline{\mathbf{R}}_j| < \min(\underline{\mathbf{R}}_i^2, \underline{\mathbf{R}}_j^2), \quad i \neq j, \quad i, j = 1, 3 \quad (2.20)$$

which can be used to identify and classify reduced unique vector sets  $\underline{\mathbf{R}}_1, \underline{\mathbf{R}}_2, \underline{\mathbf{R}}_3$ . Type 2 lattices require an additional constraint which reads

$$2(|\underline{\mathbf{R}}_1 \cdot \underline{\mathbf{R}}_2| + |\underline{\mathbf{R}}_1 \cdot \underline{\mathbf{R}}_3| + |\underline{\mathbf{R}}_2 \cdot \underline{\mathbf{R}}_3|) \leq \underline{\mathbf{R}}_1^2 + \underline{\mathbf{R}}_2^2 \quad (2.21)$$

to yield a unique description [42].

The application of the above constraints to two-dimensional lattices described by lattice vectors  $\underline{\mathbf{R}}_1, \underline{\mathbf{R}}_2$  is straightforward. Here the two vectors are required to yield the smallest periodicity lengths along different directions in the lattice and are ordered according to

$$|\underline{\mathbf{R}}_1| \leq |\underline{\mathbf{R}}_2| \quad (2.22)$$

This allows, as in the three-dimensional case, two lattice classes differing by the scalar product  $s_{12} = \underline{\mathbf{R}}_1 \cdot \underline{\mathbf{R}}_2$ ,

$$s_{12} \geq 0 \quad (\text{type 1, **acute**}) \quad \text{and} \quad s_{12} < 0 \quad (\text{type 2, **obtuse**}) \quad (2.23)$$

The Minkowski reduction, see Sec. 3.3 and Appendix D, can be used to reduce a general vector set  $\underline{\mathbf{R}}_1, \underline{\mathbf{R}}_2$  of type 1 or 2 to a unique description referring to vectors of smallest length in the lattice.

This reduced vector set fulfills, apart from (2.22), the inequality

$$-\min(\underline{\mathbf{R}}_1^2, \underline{\mathbf{R}}_2^2) \leq 2(\underline{\mathbf{R}}_1 \cdot \underline{\mathbf{R}}_2) < \min(\underline{\mathbf{R}}_1^2, \underline{\mathbf{R}}_2^2) \quad (2.24)$$

which can be used to test whether a vector set  $\underline{R}_1, \underline{R}_2$  is reduced or not. The constraints (2.22) and (2.23) yield a unique description which allows a simple distinction between the different types of two-dimensional Bravais lattices discussed in Sec. 3.7. They can also serve as a basis for a more general classification scheme proposed in the literature [44]. In two dimensions obtuse lattice descriptions can always be converted to acute descriptions, preferred by many surface scientists, by swapping the lattice vectors and replacing one of the two, e.g.  $\underline{R}_1$ , by its negative,  $-\underline{R}_1$ , where, however, one of the two representations may violate constraint (2.22).

Many researchers in the surface science community (and not only there) find it convenient to think in Cartesian coordinates, using orthogonal unit vectors in three-dimensional space. Therefore, they prefer to characterize lattices, if possible, by orthogonal lattice vectors  $\underline{R}_1, \underline{R}_2, \underline{R}_3$  even at the expense of having to consider corresponding crystal bases with a larger number of atoms. This will be discussed for face- and body-centered cubic lattices in Sec. 2.2.2.1.

Theoretical studies on extended geometric perturbations inside a crystal, such as those originating from periodic imperfections or distortions, require often considering unit cells with lattice vectors  $\underline{R}_1', \underline{R}_2', \underline{R}_3'$  which are larger than those given by  $\underline{R}_1, \underline{R}_2, \underline{R}_3$  of the unperturbed crystal. Here a direct computational comparison of results for the perturbed crystal with those for the unperturbed crystal is often facilitated by applying the same (enlarged) lattice vectors  $\underline{R}_1', \underline{R}_2', \underline{R}_3'$  to both systems. As a result, the unperturbed crystal is described by a lattice with a larger than primitive unit cell and an appropriately increased number of atoms. This is the basic idea behind so-called **superlattice** methods which will be discussed in Sec. 2.2.2.2.

Ideal single crystal surfaces, which originate from bulk truncation yielding two-dimensional periodicity at the surface, will be treated in great detail in Sec. 4. Here the analysis of structural properties at the surface can be facilitated greatly by using so-called **netplane-adapted** lattice vectors  $\underline{R}_1', \underline{R}_2', \underline{R}_3'$ . These are given by linear transformations of the initial bulk lattice vectors, where the shape of the morphological unit cell may change but not its volume nor the number of atoms inside the cell. Differently oriented surfaces require different sets of netplane-adapted lattice vectors leading to many alternative descriptions of the bulk lattice, as discussed in Sec. 2.2.2.3.



### 2.2.2.1 Cubic, Hexagonal, and Trigonal Lattices

The family of cubic lattices, simple, body-centered, and face-centered cubic, are closely connected with each other, which is why many scientists use the simplest of the three, the **simple cubic** lattice as their reference. This lattice, also called **cubic-P** and often abbreviated by **sc** is described in Cartesian coordinates by lattice vectors

$$\underline{R}_1^{\text{sc}} = a(1, 0, 0), \quad \underline{R}_2^{\text{sc}} = a(0, 1, 0), \quad \underline{R}_3^{\text{sc}} = a(0, 0, 1) \quad (2.25)$$

which are three mutually orthogonal vectors of equal length, given by the lattice constant  $a$ .

The **body-centered cubic** lattice, also called **I-centered** or **cubic-I** and often abbreviated by **bcc**, see Fig. 2.6, can be defined in Cartesian coordinates by lattice vectors

$$\underline{R}_1 = a/2(-1, 1, 1), \quad \underline{R}_2 = a/2(1, -1, 1), \quad \underline{R}_3 = a/2(1, 1, -1) \quad (2.26)$$

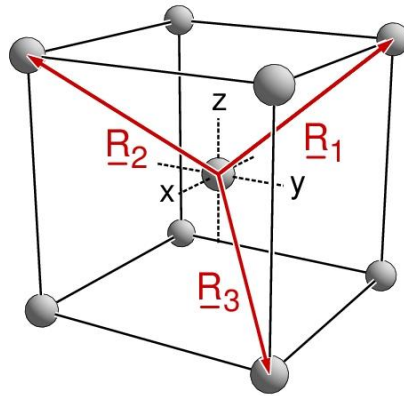


Fig. 2.6. Lattice vectors  $\underline{R}_1$ ,  $\underline{R}_2$ ,  $\underline{R}_3$  of the body-centered cubic (bcc) lattice sketched inside a cubic frame with Cartesian coordinates,  $x$ ,  $y$ , and  $z$ , indicated. Atoms of the corresponding bcc crystal are shown as balls.

Here the three vectors are of the same length

$$|\underline{R}_1| = |\underline{R}_2| = |\underline{R}_3| = (\sqrt{3}/2)a \quad (2.27)$$

but they are not orthogonal to each other, forming angles  $\alpha = \beta = \gamma = 109.47^\circ$  ( $\cos \alpha = -1/3$ ) according to (2.3). **General lattice points** of the bcc lattice are given in Cartesian coordinates by vectors

$$\begin{aligned} \underline{R} &= n_1 \underline{R}_1 + n_2 \underline{R}_2 + n_3 \underline{R}_3 = a/2(-n_1 + n_2 + n_3, n_1 - n_2 + n_3, n_1 + n_2 - n_3) = \\ &= a/2(N_1, N_2, N_3), \quad n_1, n_2, n_3, N_1, N_2, N_3 \text{ integer} \end{aligned} \quad (2.28)$$

where the integers  $n_1$ ,  $n_2$ ,  $n_3$  and  $N_1$ ,  $N_2$ ,  $N_3$  are connected by

$$N_1 = -n_1 + n_2 + n_3, \quad N_2 = n_1 - n_2 + n_3, \quad N_3 = n_1 + n_2 - n_3 \quad (2.29)$$

Relation (2.28) together with the definition of the simple cubic lattice vectors can be written as

$$\underline{\mathbf{R}} = n_1 \underline{\mathbf{R}}_1 + n_2 \underline{\mathbf{R}}_2 + n_3 \underline{\mathbf{R}}_3 = 1/2 (N_1 \underline{\mathbf{R}}_1^{\text{sc}} + N_2 \underline{\mathbf{R}}_2^{\text{sc}} + N_3 \underline{\mathbf{R}}_3^{\text{sc}}) \quad (2.30)$$

which demonstrates the connection between the body-centered and the simple cubic lattices. While the integer coefficients  $n_1, n_2, n_3$  can be chosen freely the integer coefficients  $N_1, N_2, N_3$  are not independent. Relations (2.29) yield

$$N_2 = N_1 + 2(n_1 - n_2), \quad N_3 = N_1 + 2(n_1 - n_3) \quad (2.31)$$

Hence, the integers  $N_1, N_2, N_3$  can only be all odd or all even for any choice of  $n_1, n_2, n_3$ .

If  $N_1, N_2, N_3$  in (2.28) are **all even**, i.e. they can be represented by

$$N_i = 2 m_i, \quad i=1, 2, 3 \quad \text{for any integer } m_i \quad (2.32)$$

then relation (2.30) together with (2.32) leads to

$$\underline{\mathbf{R}} = m_1 \underline{\mathbf{R}}_1^{\text{sc}} + m_2 \underline{\mathbf{R}}_2^{\text{sc}} + m_3 \underline{\mathbf{R}}_3^{\text{sc}} \quad m_1, m_2, m_3 \text{ integer} \quad (2.33)$$

which describes a simple cubic lattice as one subset of the bcc lattice.

If, on the other hand,  $N_1, N_2, N_3$  in (2.28) are **all odd**, i.e. they can be represented by

$$N_i = 2m_i + 1, \quad i=1, 2, 3 \quad \text{for any integer } m_i \quad (2.34)$$

then relation (2.30) together with (2.34) leads to

$$\underline{\mathbf{R}} = m_1 \underline{\mathbf{R}}_1^{\text{sc}} + m_2 \underline{\mathbf{R}}_2^{\text{sc}} + m_3 \underline{\mathbf{R}}_3^{\text{sc}} + \underline{\mathbf{v}} \quad m_1, m_2, m_3 \text{ integer} \quad (2.35)$$

with

$$\underline{\mathbf{v}} = 1/2 (\underline{\mathbf{R}}_1^{\text{sc}} + \underline{\mathbf{R}}_2^{\text{sc}} + \underline{\mathbf{R}}_3^{\text{sc}}) \quad (2.36)$$

This also describes a simple cubic lattice as the second subset of the bcc lattice, where the second sc lattice is, however, shifted by a vector  $\underline{\mathbf{v}}$  with respect to the first. Thus, the constraints for  $N_1, N_2, N_3$  in (2.29) yield a decomposition of the bcc lattice into **two** identical sc lattices which are shifted with respect to each other by vector  $\underline{\mathbf{v}}$  given by (2.36). The two sc lattices are sketched in Fig. 2.7 and denoted 'sc<sub>1</sub>', 'sc<sub>2</sub>' in the figure.

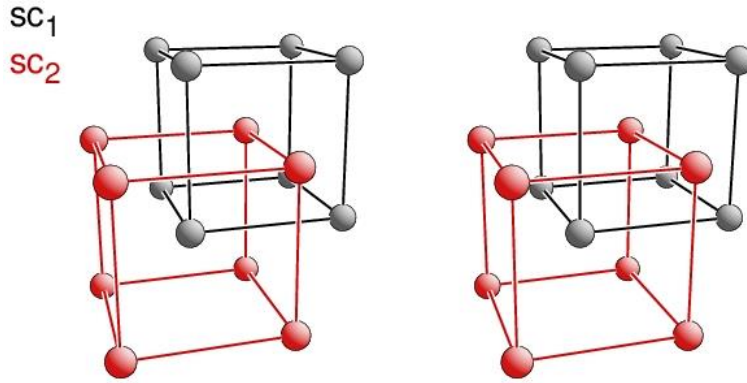


Fig. 2.7. Visual decomposition of the body-centered cubic crystal into two (shifted) simple cubic crystals, denoted  $sc_1$  (gray balls, black lines) and  $sc_2$  (red balls and red lines). The crystal is shown in a stereo view where the visual three-dimensional impression is obtained by cross-eyed viewing.

As a consequence, any crystal with a bcc lattice given by lattice vectors (2.26) can be alternatively described by a crystal with a simple cubic lattice with lattice vectors (2.25), where the unit cell of the sc lattice contains twice as many atoms with atom pairs separated by vector  $\underline{y}$ . Further, the lattice vectors  $\underline{R}_1^{sc}$ ,  $\underline{R}_2^{sc}$ ,  $\underline{R}_3^{sc}$  of the sc lattice representation are **non-primitive** since vector

$$\underline{y} = 1/2 (\underline{R}_1^{sc} + \underline{R}_2^{sc} + \underline{R}_3^{sc}) = \underline{R}_1 + \underline{R}_2 + \underline{R}_3 \quad (2.37)$$

according to (2.26) is a true lattice vector.

The **face-centered cubic** lattice, also called **F-centered** or **cubic-F** and often abbreviated by **fcc**, see Fig. 2.8, can be defined in Cartesian coordinates by lattice vectors

$$\underline{R}_1 = a/2 (0, 1, 1), \quad \underline{R}_2 = a/2 (1, 0, 1), \quad \underline{R}_3 = a/2 (1, 1, 0) \quad (2.38)$$

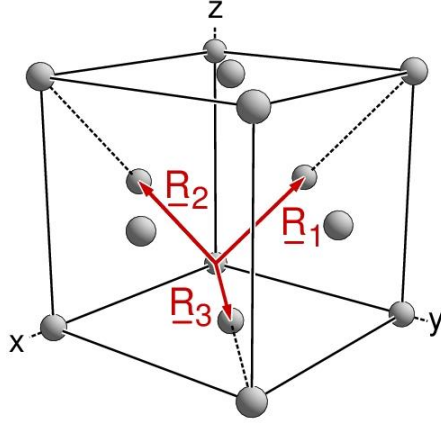


Fig. 2.8. Lattice vectors  $\underline{R}_1$ ,  $\underline{R}_2$ ,  $\underline{R}_3$  of the face-centered cubic (fcc) lattice sketched inside a cubic frame and labeled accordingly. Atoms of the corresponding fcc crystal are shown as balls. The dashed lines are meant to assist the visual orientation inside the figure.

As for the bcc lattice, the three vectors are of the same length

$$|\underline{R}_1| = |\underline{R}_2| = |\underline{R}_3| = a/\sqrt{2} \quad (2.39)$$

but not orthogonal to each other, forming angles  $\alpha = \beta = \gamma = 60^\circ$  ( $\cos \alpha = 1/2$ ) according to (2.3).

**General lattice points** of the fcc lattice are given in Cartesian coordinates by vectors

$$\begin{aligned} \underline{R} &= n_1 \underline{R}_1 + n_2 \underline{R}_2 + n_3 \underline{R}_3 = a/2 (n_2 + n_3, n_1 + n_3, n_1 + n_2) = \\ &= a/2 (N_1, N_2, N_3), \quad n_1, n_2, n_3, N_1, N_2, N_3 \text{ integer} \end{aligned} \quad (2.40)$$

where the integers  $n_1, n_2, n_3$  and  $N_1, N_2, N_3$  are connected by

$$N_1 = n_2 + n_3, \quad N_2 = n_1 + n_3, \quad N_3 = n_1 + n_2 \quad (2.41)$$

Relation (2.40) together with the definition of the simple cubic lattice vectors can be written as

$$\underline{R} = n_1 \underline{R}_1 + n_2 \underline{R}_2 + n_3 \underline{R}_3 = 1/2 (N_1 \underline{R}_1^{\text{sc}} + N_2 \underline{R}_2^{\text{sc}} + N_3 \underline{R}_3^{\text{sc}}) \quad (2.42)$$

which shows the connection between the face-centered and the simple cubic lattice. As in the bcc case, the integer coefficients  $N_1, N_2, N_3$  are not independent. Even and odd valued combinations of the initial coefficients  $n_1, n_2, n_3$  yield eight cases as shown in Table 2.1.

Table 2.1. List of all possible even/odd integer combinations  $N_1, N_2, N_3$  following from even/odd integer combinations  $n_1, n_2, n_3$  according to equation (2.41). Characters 'e' and 'o' stand for even and odd integers, respectively.

case	$n_1$	$n_2$	$n_3$	$N_1$	$N_2$	$N_3$
1	e	e	e	e	e	e
2	o	o	o	e	e	e
3	o	e	e	e	o	o
4	e	o	o	e	o	o
5	e	o	e	o	e	o
6	o	e	o	o	e	o
7	e	e	o	o	o	e
8	o	o	e	o	o	e

As a result, integers  $N_1, N_2, N_3$  reduce to **four** different types of **even/odd combinations**,

- (a)  $N_i = 2 m_i$ ,  $i=1, 2, 3$ , (cases 1, 2 in Table 2.1) which results, according to (2.42), in

$$\underline{\mathbf{R}} = a/2 (N_1, N_2, N_3) = a (m_1, m_2, m_3), \quad m_1, m_2, m_3 \text{ integer} \quad (2.43a)$$

describing the simple cubic lattice given by (2.25) with its origin coinciding with that of the fcc lattice, corresponding to an origin shift  $\underline{v}_1 = \underline{0}$ , see below.

- (b)  $N_1 = 2 m_1$ ,  $N_2 = 2m_2 + 1$ ,  $N_3 = 2 m_3 + 1$ , (cases 3, 4) resulting in

$$\begin{aligned} \underline{\mathbf{R}} &= a/2 (N_1, N_2, N_3) = a (m_1, m_2, m_3) + \underline{v}_2 \\ \underline{v}_2 &= 1/2 (\underline{\mathbf{R}}_2^{\text{sc}} + \underline{\mathbf{R}}_3^{\text{sc}}) \end{aligned} \quad (2.43b)$$

describing the sc lattice with an origin shift  $\underline{v}_2$ .

- (c)  $N_1 = 2 m_1 + 1$ ,  $N_2 = 2m_2$ ,  $N_3 = 2 m_3 + 1$ , (cases 5, 6) resulting in

$$\begin{aligned} \underline{\mathbf{R}} &= a/2 (N_1, N_2, N_3) = a (m_1, m_2, m_3) + \underline{v}_3 \\ \underline{v}_3 &= 1/2 (\underline{\mathbf{R}}_1^{\text{sc}} + \underline{\mathbf{R}}_3^{\text{sc}}) \end{aligned} \quad (2.43c)$$

describing the sc lattice with an origin shift  $\underline{v}_3$ .

(d)  $N_1 = 2m_1 + 1$ ,  $N_2 = 2m_2 + 1$ ,  $N_3 = 2m_3$ , (cases 7, 8) resulting in

$$\begin{aligned}\underline{\mathbf{R}} &= a/2 (N_1, N_2, N_3) = a (m_1, m_2, m_3) + \underline{\mathbf{v}}_4 \\ \underline{\mathbf{v}}_4 &= 1/2 (\underline{\mathbf{R}}_1^{\text{sc}} + \underline{\mathbf{R}}_2^{\text{sc}})\end{aligned}\quad (2.43d)$$

describing the sc lattice with an origin shift  $\underline{\mathbf{v}}_4$ .

Therefore, the constraints for  $N_1, N_2, N_3$  in (2.41) yield a decomposition of the fcc lattice into **four** identical sc lattices which are shifted with respect to each other according to their origins at  $\underline{\mathbf{v}}_1, \underline{\mathbf{v}}_2, \underline{\mathbf{v}}_3, \underline{\mathbf{v}}_4$ , given by (2.43a-d). The four sc lattices are sketched in Fig. 2.9 and denoted ‘sc<sub>1</sub>’ to ‘sc<sub>4</sub>’ in the figure.

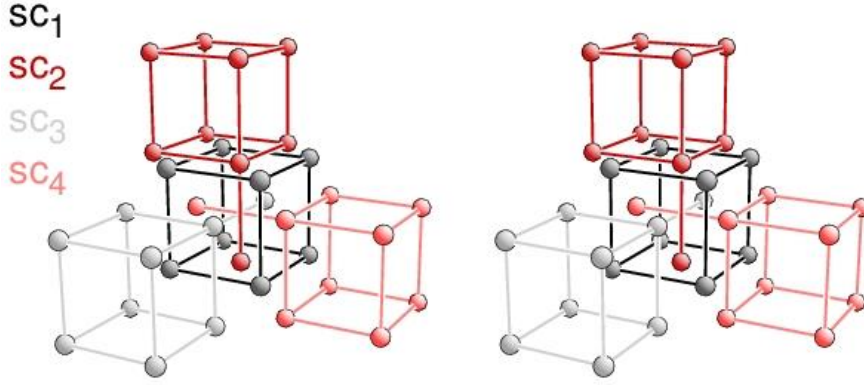


Fig. 2.9. Visual decomposition of the fcc crystal into four (shifted) simple cubic crystals, denoted sc<sub>1</sub> (dark gray balls, black lines), sc<sub>2</sub> (dark red balls and lines), sc<sub>3</sub> (light gray balls and lines), and sc<sub>4</sub> (light red balls and lines). The crystal is shown in a stereo view where the visual three-dimensional impression is obtained by cross-eyed viewing.

As a consequence, any crystal with an fcc lattice given by lattice vectors (2.38) can be alternatively described by a crystal with an sc lattice with lattice vectors (2.25), where the unit cell of the sc lattice contains four times as many atoms with atom pairs separated by vectors  $\underline{\mathbf{v}}_i - \underline{\mathbf{v}}_j$ ,  $i, j = 1 \dots 4$ .

Further, the lattice vectors  $\underline{\mathbf{R}}_1^{\text{sc}}, \underline{\mathbf{R}}_2^{\text{sc}}, \underline{\mathbf{R}}_3^{\text{sc}}$  of the sc lattice representation are **non-primitive** since the four vectors  $\underline{\mathbf{v}}_i$

$$\begin{aligned}\underline{\mathbf{v}}_1 &= \underline{\mathbf{0}} & \underline{\mathbf{v}}_2 &= 1/2 (\underline{\mathbf{R}}_2^{\text{sc}} + \underline{\mathbf{R}}_3^{\text{sc}}) = \underline{\mathbf{R}}_1 \\ \underline{\mathbf{v}}_3 &= 1/2 (\underline{\mathbf{R}}_1^{\text{sc}} + \underline{\mathbf{R}}_3^{\text{sc}}) = \underline{\mathbf{R}}_2 & \underline{\mathbf{v}}_4 &= 1/2 (\underline{\mathbf{R}}_1^{\text{sc}} + \underline{\mathbf{R}}_2^{\text{sc}}) = \underline{\mathbf{R}}_3\end{aligned}\quad (2.44)$$

according to (2.38) are true lattice vectors.

The **hexagonal** lattice, also called **hexagonal-P** and often abbreviated by **hex**, is described by two lattice vectors  $\underline{\mathbf{R}}_1^{\text{hex}}, \underline{\mathbf{R}}_2^{\text{hex}}$  of equal length  $a$ , forming an angle of either  $120^\circ$  (**obtuse represen-**

**tation**) or  $60^\circ$  (**acute representation**) between them. A third lattice vector  $\underline{\mathbf{R}}_3^{\text{hex}}$  of length  $c$ , is perpendicular to both  $\underline{\mathbf{R}}_1^{\text{hex}}$  and  $\underline{\mathbf{R}}_2^{\text{hex}}$ . Thus, the vectors of the obtuse representation can be described in Cartesian coordinates by

$$\underline{\mathbf{R}}_1^{\text{hex}} = a (1, 0, 0), \quad \underline{\mathbf{R}}_2^{\text{hex}} = a (-1/2, \sqrt{3}/2, 0), \quad \underline{\mathbf{R}}_3^{\text{hex}} = c (0, 0, 1) \quad (2.45a)$$

and those of the acute representation by

$$\underline{\mathbf{R}}_1^{\text{hex}} = a (1, 0, 0), \quad \underline{\mathbf{R}}_2^{\text{hex}} = a (1/2, \sqrt{3}/2, 0), \quad \underline{\mathbf{R}}_3^{\text{hex}} = c (0, 0, 1) \quad (2.45b)$$

where  $a, c$  are the lattice constants of the hexagonal lattice. While the two representations are equivalent, the **obtuse** representation of crystal lattices is often **preferred** over the acute one and will be used in the following.

There is a special type of crystal structure with hexagonal lattice, the so-called **hexagonal close-packed (hcp)** crystal structure, illustrated by Fig. 2.10 and called **hex (hcp)** in the following. It is defined by a hexagonal lattice, given in obtuse representation by (2.45a) with a lattice constant ratio  $c/a$  of  $\sqrt{8/3} = 1.63299$ . Further, the hexagonal unit cell contains two identical atoms at positions

$$\underline{\mathbf{r}}_1^{\text{hcp}} = a (0, 0, 0), \quad \underline{\mathbf{r}}_2^{\text{hcp}} = (a/2, a/\sqrt{12}, c/2) = a (1/2, 1/\sqrt{12}, \sqrt{2/3}) \quad (2.45c)$$

see Fig. 2.10b. The  $c/a$  ratio and the atom positions are chosen such that each atom is surrounded by 12 nearest neighbor atoms at equal distance (equal to lattice constant  $a$ ), achieving the same atom density as crystals with a corresponding fcc lattice. While hcp crystals in their rigorous mathematical definition do not exist in nature they occur, to a good approximation, i.e. with ratios  $c/a$  close to  $\sqrt{8/3}$ , for many single crystals of metals, such as beryllium, magnesium, titanium, cobalt, ruthenium, and cadmium, see Table B.3 of Appendix B.

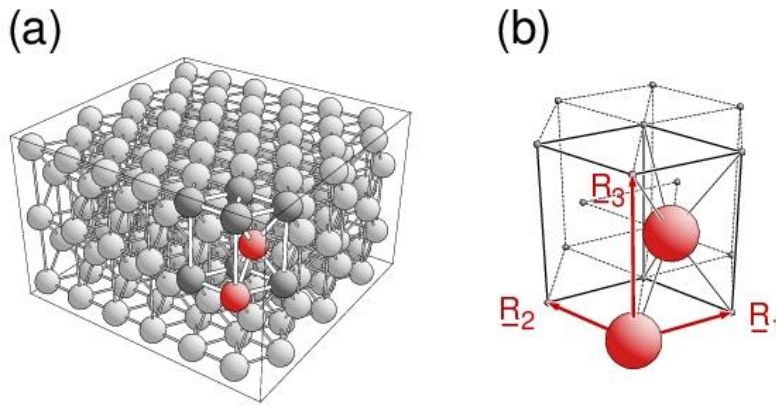


Fig. 2.10. (a) Section of a hexagonal crystal with close-packed geometry (hcp). Sticks connect atoms with nearest and second nearest neighbors to indicate the crystal structure. (b) Primitive morphological unit cell with two atoms inside. The lattice vectors  $\underline{R}_1$ ,  $\underline{R}_2$ ,  $\underline{R}_3$  (obtuse representation) are labeled accordingly. The unit cell is embedded in a hexagonal environment (dashed lines) to indicate its symmetry.

Analogous to the family of cubic lattices, there is also a close connection between trigonal and hexagonal lattices, where scientists often prefer hexagonal over trigonal lattice descriptions. The **trigonal** lattice, also called **trigonal-R** or **rhombohedral**, is described by three lattice vectors  $\underline{R}_1$ ,  $\underline{R}_2$ ,  $\underline{R}_3$  of equal length  $a$ , which form identical angles  $\alpha = \beta = \gamma$ . Thus, the lattice vectors can be thought of as arising from each other by a  $120^\circ$  rotation about a common axis given by  $(\underline{R}_1 + \underline{R}_2 + \underline{R}_3)$ , see Fig. 2.11a. Assuming the rotation axis as the  $z$  axis of a Cartesian coordinate system, the vectors can be described in Cartesian coordinates by

$$\begin{aligned} \underline{R}_1 &= a (c_1, 0, c_2), \quad \underline{R}_2 = a (-1/2 c_1, \sqrt{3}/2 c_1, c_2), \quad \underline{R}_3 = a (-1/2 c_1, -\sqrt{3}/2 c_1, c_2), \\ c_1 &= \cos(\varphi), \quad c_2 = \sin(\varphi) \end{aligned} \quad (2.46)$$

where  $\varphi$  denotes the angle between each of the three lattice vectors and the  $xy$  plane, see Fig. 2.11a, and is determined by

$$\cos(\alpha) = \cos(\beta) = \cos(\gamma) = 1/4 \{ 1 - 3 \cos(2\varphi) \} \quad (2.47)$$



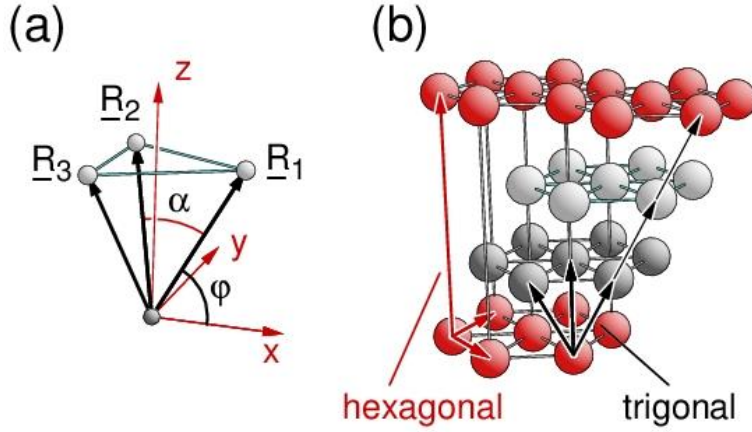


Fig. 2.11. (a) Lattice vectors  $\underline{R}_1$ ,  $\underline{R}_2$ ,  $\underline{R}_3$  of the trigonal (rhombohedral) lattice with definitions of the Cartesian coordinate system and of angles  $\varphi$ ,  $\alpha$ , see text. (b) Three trigonal lattices combining to form a non-primitive hexagonal lattice. Lattice vectors are shown by arrows, black for trigonal and red for hexagonal. The visual correlation between the two lattices is indicated by thin gray sticks connecting hexagonal lattice points.

Thus, the three vectors  $\underline{R}_1'$ ,  $\underline{R}_2'$ ,  $\underline{R}_3'$  with

$$\begin{aligned}\underline{R}_1' &= \underline{R}_1 - \underline{R}_2 = \sqrt{3} c_1 a (\sqrt{3}/2, -1/2, 0) \\ \underline{R}_2' &= \underline{R}_2 - \underline{R}_3 = \sqrt{3} c_1 a (0, 1, 0) \\ \underline{R}_3' &= \underline{R}_1 + \underline{R}_2 + \underline{R}_3 = 3 c_2 a (0, 0, 1)\end{aligned}\quad (2.48)$$

form a **hexagonal sublattice (obtuse representation)** of the trigonal lattice since

$$\begin{aligned}|\underline{R}_1'|^2 &= |\underline{R}_2'|^2 = 3 a^2 \cos(\varphi)^2, \quad |\underline{R}_3'|^2 = 9 a^2 \sin(\varphi)^2 \\ \angle(\underline{R}_1', \underline{R}_2') &= 120^\circ, \quad \angle(\underline{R}_1', \underline{R}_3') = \angle(\underline{R}_2', \underline{R}_3') = 90^\circ\end{aligned}\quad (2.49)$$

(Actually, lattice vectors (2.48) can be easily shown to coincide with definition (2.45a) of a hexagonal lattice by applying a rotation by  $30^\circ$  about the axis through  $\underline{R}_3'$  and a scaling of the lattice constants where constants  $a$  and  $c$  in (2.45a) correspond to  $(\sqrt{3} c_1 a)$  and  $(3 c_2 a)$  in (2.48).)

**General lattice points** of the hexagonal sublattice are given according to (2.46), (2.48) by vectors

$$\begin{aligned}\underline{R} &= n_1 \underline{R}_1' + n_2 \underline{R}_2' + n_3 \underline{R}_3' = \\ &= (n_1 + n_3) \underline{R}_1 + (n_2 - n_1 + n_3) \underline{R}_2 + (n_3 - n_2) \underline{R}_3 = \\ &= m_1 \underline{R}_1 + m_2 \underline{R}_2 + m_3 \underline{R}_3\end{aligned}\quad (2.50)$$

where the coefficients  $m_i$  and  $n_i$  are connected by linear transformations written in matrix form as

$$\begin{pmatrix} m_1 \\ m_2 \\ m_3 \end{pmatrix} = \begin{pmatrix} 1 & 0 & 1 \\ -1 & 1 & 1 \\ 0 & -1 & 1 \end{pmatrix} \cdot \begin{pmatrix} n_1 \\ n_2 \\ n_3 \end{pmatrix} \quad \text{and} \quad \begin{pmatrix} n_1 \\ n_2 \\ n_3 \end{pmatrix} = \frac{1}{3} \begin{pmatrix} 2 & -1 & -1 \\ 1 & 1 & -2 \\ 1 & 1 & 1 \end{pmatrix} \cdot \begin{pmatrix} m_1 \\ m_2 \\ m_3 \end{pmatrix} \quad (2.51a,b)$$

According to (2.51b) the hexagonal sublattice is described by integer values  $n_1, n_2, n_3$  only if the corresponding trigonal coefficients  $m_1, m_2, m_3$  fulfill the **three** conditions

$$2 m_1 - m_2 - m_3 = 3 g, \quad m_1 + m_2 - 2 m_3 = 3 g', \quad m_1 + m_2 + m_3 = 3 g'' \quad (2.52)$$

where  $g, g', g''$  are integers. Since

$$m_1 + m_2 + m_3 = (m_1 + m_2 - 2 m_3) + 3 m_3 = -(2 m_1 - m_2 - m_3) + 3 m_1 \quad (2.53)$$

fulfilling one of the three conditions (2.52) will automatically satisfy the other two. Considering the complete trigonal lattice, all sets of coefficients  $m_1, m_2, m_3$  can be grouped according to one of the three categories,

$$m_1 + m_2 + m_3 = 3 g \quad (2.54a)$$

$$m_1 + m_2 + m_3 = 3 g + 1 \quad \text{or} \quad (m_1 - 1) + m_2 + m_3 = 3 g \quad (2.54b)$$

$$m_1 + m_2 + m_3 = 3 g + 2 \quad \text{or} \quad (m_1 - 2) + m_2 + m_3 = 3 g \quad (2.54c)$$

Here the condition (2.54a) was shown to result in a hexagonal lattice whose origin coincides with that of the trigonal lattice. The conditions of (2.54b) also lead to a hexagonal lattice. However, its origin is shifted with respect to that of the trigonal lattice by a trigonal lattice vector  $\underline{R}_1$  (or  $\underline{R}_2$  or  $\underline{R}_3$ ). Analogously, the conditions of (2.54c) lead to an identical hexagonal lattice with its origin shifted by a trigonal lattice vector  $2 \underline{R}_1$  (or any combination of two trigonal lattice vectors). Since all lattice points of the trigonal lattice satisfy one of the three conditions (2.54) the **trigonal** lattice can be decomposed into **three** identical **hexagonal** lattices which are shifted with respect to each other as sketched by the thinner arrows in Fig. 2.11b.

Altogether, any crystal with a trigonal lattice, given by lattice vectors (2.46), can be alternatively described by a crystal with a non-primitive hexagonal lattice, with lattice vectors (2.48), where the unit cell of the hexagonal lattice contains three times as many atoms compared with that of the trigonal lattice. Further, the lattice vectors  $\underline{R}_1^{\text{hex}}, \underline{R}_2^{\text{hex}}, \underline{R}_3^{\text{hex}}$  of the hexagonal lattice representation are **non-primitive**.

### 2.2.2.2 Superlattices and Repeated Slabs

As mentioned earlier, theoretical studies on physical or chemical parameters inside a crystal require often considering a unit cell with lattice vectors  $\underline{\mathbf{R}}_1, \underline{\mathbf{R}}_2, \underline{\mathbf{R}}_3$  which is larger than the primitive cell of the lattice given by  $\underline{\mathbf{R}}_{o1}, \underline{\mathbf{R}}_{o2}, \underline{\mathbf{R}}_{o3}$ . Examples of this so-called **supercell** or **superlattice** concept include spin alignment in anti-ferromagnetic crystals [45], where the magnetic lattice, defined by positions of the different spins, differs from the geometric lattice of the crystal. In addition, local perturbations, such as vacancies, added atoms, or substituted atoms in alloy formation [46], of otherwise perfect crystals have been examined theoretically [47] applying supercell concepts. Here single perturbations are simulated by those in an artificial crystal with large supercells such that distances between periodic copies of the perturbations are large enough to avoid physical coupling. Further, small distortions of lattice positions which can result in periodicity with large supercells have been considered in so-called frozen phonon calculations [48]. Finally, we mention the use of supercell geometry in calculations of physical and chemical properties of single crystal surfaces. These calculations are often based on the so-called **repeated slab geometry** [48], where the surface region is approximated by a slab of finite thickness and a vacuum gap repeated periodically such that overall a three-dimensional periodicity with a large supercell is achieved.

The basic **mathematical** idea behind **conventional** supercell descriptions relies on the fact that any crystal with a lattice described by primitive lattice vectors  $\underline{\mathbf{R}}_{o1}, \underline{\mathbf{R}}_{o2}, \underline{\mathbf{R}}_{o3}$  and an atom basis can be represented by an alternative (non-primitive) lattice with (larger) lattice vectors  $\underline{\mathbf{R}}_1, \underline{\mathbf{R}}_2, \underline{\mathbf{R}}_3$  and an appropriately modified basis. The alternative vectors are connected with those of the initial lattice by a linear transformation which must be integer-valued if the global three-dimensional periodicity is to be conserved. This can be expressed mathematically by a **transformation matrix**  $\underline{\mathbf{T}}$  with

$$\begin{pmatrix} \underline{\mathbf{R}}_1 \\ \underline{\mathbf{R}}_2 \\ \underline{\mathbf{R}}_3 \end{pmatrix} = \begin{pmatrix} t_{11} & t_{12} & t_{13} \\ t_{21} & t_{22} & t_{23} \\ t_{31} & t_{32} & t_{33} \end{pmatrix} \cdot \begin{pmatrix} \underline{\mathbf{R}}_{o1} \\ \underline{\mathbf{R}}_{o2} \\ \underline{\mathbf{R}}_{o3} \end{pmatrix} = \underline{\mathbf{T}} \cdot \begin{pmatrix} \underline{\mathbf{R}}_{o1} \\ \underline{\mathbf{R}}_{o2} \\ \underline{\mathbf{R}}_{o3} \end{pmatrix} \quad (2.55)$$

where the elements  $t_{ij}$  of matrix  $\underline{\mathbf{T}}$  are integers. As a consequence, the volumes  $V_{el}$  and  $V_{el}^o$  of the unit cells of the two lattices, defined by (2.9), are connected by

$$V_{el} = |(\underline{\mathbf{R}}_1 \times \underline{\mathbf{R}}_2) \cdot \underline{\mathbf{R}}_3| = |\det(\underline{\mathbf{T}})| |(\underline{\mathbf{R}}_{o1} \times \underline{\mathbf{R}}_{o2}) \cdot \underline{\mathbf{R}}_{o3}| = |\det(\underline{\mathbf{T}})| V_{el}^o \quad (2.56)$$

where (2.55) together with vector relation (F.9) of Appendix F is applied. This means, in particular, that the volume  $V_{el}$  of the supercell must be an integer multiple of volume  $V_{el}^0$  of the initial unit cell.

In the simplest case, the superlattice description results from simple **scaling** of the initial lattice vectors, corresponding to a transformation

$$\underline{\mathbf{R}}_1 = m_1 \underline{\mathbf{R}}_{01}, \quad \underline{\mathbf{R}}_2 = m_2 \underline{\mathbf{R}}_{02}, \quad \underline{\mathbf{R}}_3 = m_3 \underline{\mathbf{R}}_{03} \quad (2.57)$$

with integer-valued  $m_1, m_2, m_3$ . Thus, the transformation matrix  $\underline{\mathbf{T}}$  becomes diagonal, i.e.

$$\underline{\mathbf{T}} = \begin{pmatrix} m_1 & 0 & 0 \\ 0 & m_2 & 0 \\ 0 & 0 & m_3 \end{pmatrix} \quad (2.58)$$

As an **illustration**, we consider a fictitious simple cubic crystal with ferromagnetic and anti-ferromagnetic ordering of its atoms, where the anti-ferromagnetism introduces a doubling of the lattice vectors in two dimensions, as sketched in Fig. 2.12. Thus, the lattice vectors of the anti-ferromagnetic crystal,  $\underline{\mathbf{R}}_1, \underline{\mathbf{R}}_2, \underline{\mathbf{R}}_3$ , can be connected with those of the ferromagnetic crystal,  $\underline{\mathbf{R}}_{01}, \underline{\mathbf{R}}_{02}, \underline{\mathbf{R}}_{03}$ , by

$$\underline{\mathbf{R}}_1 = 2 \underline{\mathbf{R}}_{01}, \quad \underline{\mathbf{R}}_2 = 2 \underline{\mathbf{R}}_{02}, \quad \underline{\mathbf{R}}_3 = \underline{\mathbf{R}}_{03} \quad (2.59)$$

Theoretical studies of the anti-ferromagnetic crystal must be based on a lattice description given by  $\underline{\mathbf{R}}_1, \underline{\mathbf{R}}_2, \underline{\mathbf{R}}_3$  while those of the ferromagnetic crystal allow the use of the smaller lattice vectors  $\underline{\mathbf{R}}_{01}, \underline{\mathbf{R}}_{02}, \underline{\mathbf{R}}_{03}$ . However, a direct comparison of physical properties of the two crystals with different spin alignments can be simplified by using identical lattice parameters which suggests applying the superlattice vectors  $\underline{\mathbf{R}}_1, \underline{\mathbf{R}}_2, \underline{\mathbf{R}}_3$  also for the ferromagnetic crystal.

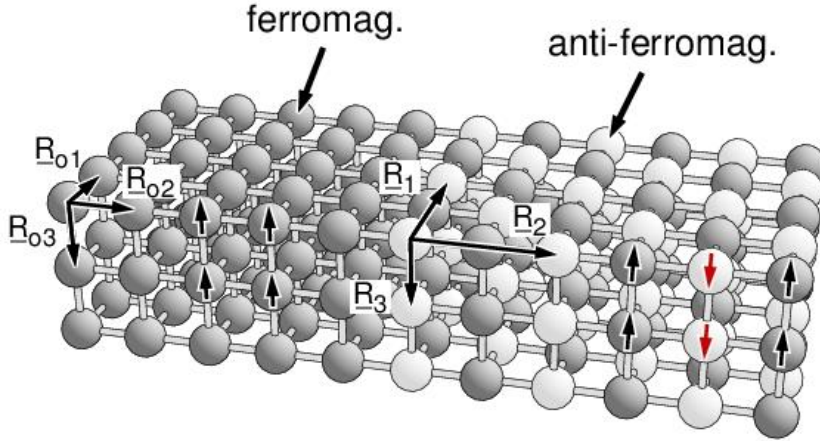


Fig. 2.12. Fictitious simple cubic crystal with ferromagnetic (left) and anti-ferromagnetic ordering (right). Atoms are shown as dark (spin up) and light (spin down) balls with their spin orientation indicated by black and red arrows. The superlattice vectors  $\underline{R}_1$ ,  $\underline{R}_2$ ,  $\underline{R}_3$  and primitive lattice vectors  $\underline{R}_{01}$ ,  $\underline{R}_{02}$ ,  $\underline{R}_{03}$  are labeled accordingly.

Incidentally, Fig. 2.12 shows that, for the present simple cubic crystal with its anti-ferromagnetic spin alignment, alternative lattice vectors  $\underline{R}_1'$ ,  $\underline{R}_2'$ ,  $\underline{R}_3'$  with

$$\underline{R}_1' = 1/2 (\underline{R}_{01} + \underline{R}_{02}), \quad \underline{R}_2' = 1/2 (\underline{R}_{02} - \underline{R}_{01}), \quad \underline{R}_3' = \underline{R}_{03} \quad (2.60)$$

could also be chosen, yielding a smaller morphological unit cell than that given by (2.59). This vector set can also be used to describe a superlattice of the ferromagnetic crystal.

As mentioned above, computational studies of physical and chemical properties of single crystal surfaces are often based on the so-called **repeated slab geometry** [48] which can be considered a **modified** supercell concept. Within this concept a single crystal with a confining planar surface of given orientation and periodicity is described approximately by a two-dimensionally periodic solid layer (**slab**) of finite thickness cut out of the bulk crystal. Here two bulk lattice vectors,  $\underline{R}_1$  and  $\underline{R}_2$ , characterize the two-dimensional periodicity of the surface (and that of the slab). In addition, the slab is repeated periodically along the direction of its surface normal with a vacuum gap between adjacent slabs where the periodicity vector  $\underline{R}_3$  is chosen appropriately. This procedure creates an altogether three-dimensionally periodic crystal system with a **fictitious** superlattice  $\underline{R}_1$ ,  $\underline{R}_2$ ,  $\underline{R}_3$  which is connected with the initial crystal lattice only by vectors  $\underline{R}_1$  and  $\underline{R}_2$ . As a result, matrix  $\underline{T}$  of (2.55) contains integer-valued elements in its first and second rows while its third row may be real-valued. Within the **repeated slab** concept physical and chemical parameters of crystalline surfaces can be evaluated by well established computational methods developed a long time ago for

three-dimensionally periodic bulk crystals in solid state physics. For this approach to be meaningful the slabs must be sufficiently thick so that the surfaces of their upper and lower sides are electronically decoupled. Further, the vacuum distance between neighboring slabs must be sufficiently large such that they do not influence each other electronically.

As an illustration, Fig. 2.13 shows three slabs of a magnesium oxide crystal confined by  $(1\ 0\ 0)$  and  $(-1\ 0\ 0)$  oriented surfaces at their tops and bottoms consisting of four MgO layers each with a vacuum separation of about three times the slab thickness. The appropriate superlattice vectors  $\underline{R}_1$ ,  $\underline{R}_2$ ,  $\underline{R}_3$ , referring to a  $2 \times 2$  supercell laterally, i.e. along  $\underline{R}_1$  and  $\underline{R}_2$ , are sketched and labeled accordingly. The size of the supercell is much larger than that of the bulk crystal and the number of atoms in the cell,  $4 \times 8 = 32$  in the present model structure, is rather large compared with that of the primitive bulk containing 2 atoms. Therefore, computational studies applying the repeated slab geometry are usually much more demanding than those of the corresponding bulk crystal.

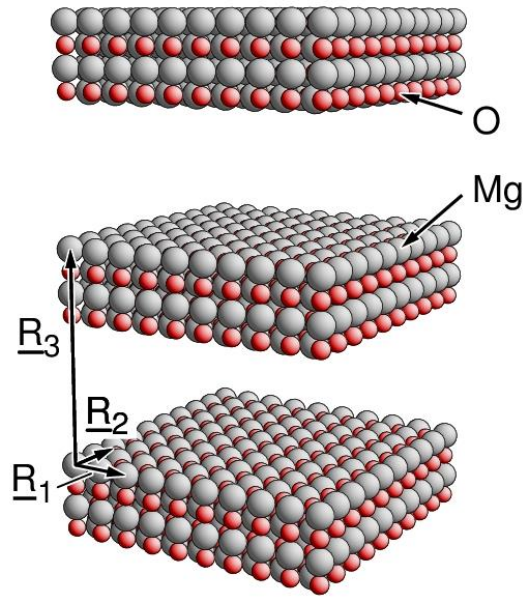


Fig. 2.13. Structure of MgO substrate confined by  $(1\ 0\ 0)$  and  $(-1\ 0\ 0)$  oriented surfaces in repeated slab geometry (three slabs). The superlattice vectors  $\underline{R}_1$ ,  $\underline{R}_2$ ,  $\underline{R}_3$  are labeled accordingly.

As another illustration, Fig. 2.14 shows a more complicated structure of three slabs of a face-centered cubic silver crystal confined by kinked surfaces (denoted  $(12\ 11\ 7)$  and  $(-12\ -11\ -7)$ , respectively) at their tops and bottoms with a vacuum separation corresponding to four times the slab thickness. Again, the appropriate superlattice vectors  $\underline{R}_1$ ,  $\underline{R}_2$ ,  $\underline{R}_3$  show that the size of the supercell with 25 atoms is much larger than the primitive cell of the bulk crystal with one atom only, demon-

strating the difference in computational effort between slab and bulk calculations.

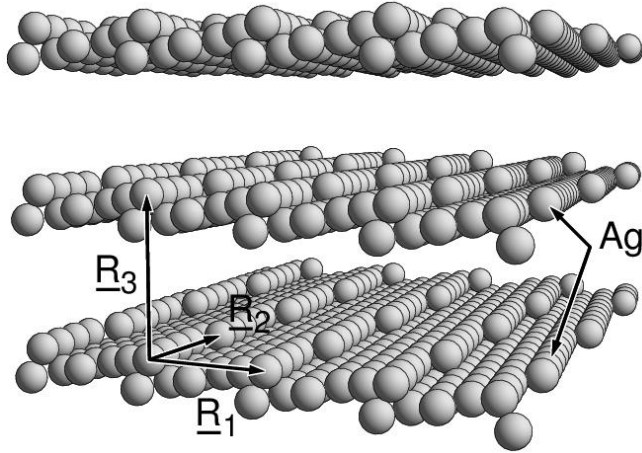


Fig. 2.14. Structure of silver substrate confined by  $(12\ 11\ 7)$  and  $(-12\ -11\ -7)$  oriented surfaces in repeated slab geometry (three slabs). The superlattice vectors  $\underline{R}_1$ ,  $\underline{R}_2$ ,  $\underline{R}_3$  are labeled accordingly.

### 2.2.2.3 Linear Transformations of Lattice Vectors

One group of alternative descriptions of crystal lattices is given by those where the alternative lattice vectors  $\underline{R}_1$ ,  $\underline{R}_2$ ,  $\underline{R}_3$  are **linear combinations** of their initial counterparts  $\underline{R}_{o1}$ ,  $\underline{R}_{o2}$ ,  $\underline{R}_{o3}$  with integer coefficients. This was already discussed in connection with the superlattice concept, and the basic linear transformation was defined by (2.55). Amongst these alternatives, there are lattice descriptions, whose morphological unit cells change their shape but not their volume, when compared with those of the initial lattice.

The latter alternatives can be used in practical cases to **adapt** the lattice description of a single crystal to additional **geometric constraints**, in particular those introduced by the existence of a single crystal surface. Therefore, these alternative descriptions are important for a crystallographic characterization of single crystal surfaces, as will become more evident in Secs. 4 and 5. In addition, they can be used to adapt lattice descriptions such that symmetry elements of the lattice become easily visible. As a simple example in two dimensions, Fig. 2.15 shows two alternative descriptions of the square lattice by lattice vectors  $\underline{R}_{o1}$ ,  $\underline{R}_{o2}$  and  $\underline{R}_1$ ,  $\underline{R}_2$ , respectively, where the two sets are connected by a linear transformation

$$\underline{R}_1 = -\underline{R}_{o1} - \underline{R}_{o2}, \quad \underline{R}_2 = 2\underline{R}_{o1} + \underline{R}_{o2} \quad (2.61)$$

Both vector sets,  $\underline{R}_{o1}$ ,  $\underline{R}_{o2}$  and  $\underline{R}_1$ ,  $\underline{R}_2$ , provide mathematically exact descriptions of the square lattice

and form morphological unit cells of the same volume. However, lattice vectors  $\underline{\mathbf{R}}_{o1}$ ,  $\underline{\mathbf{R}}_{o2}$  are of the same length and perpendicular with respect to each other. Thus, their unit cell reveals additional symmetry properties of the lattice, such as mirror and rotational symmetry.

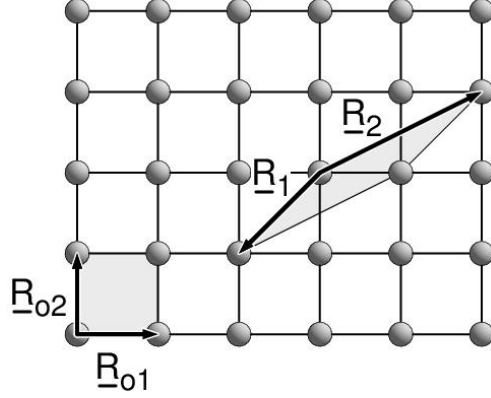


Fig. 2.15. Alternative description of the square lattice by lattice vectors  $\underline{\mathbf{R}}_{o1}$ ,  $\underline{\mathbf{R}}_{o2}$  and  $\underline{\mathbf{R}}_1$ ,  $\underline{\mathbf{R}}_2$ , respectively. The morphological unit cells of the two descriptions are emphasized by gray painting.

In the **general case**, we consider lattice vectors  $\underline{\mathbf{R}}_1$ ,  $\underline{\mathbf{R}}_2$ ,  $\underline{\mathbf{R}}_3$  of an alternative lattice description as a result of a linear transformation applied to an initial set of lattice vectors  $\underline{\mathbf{R}}_{o1}$ ,  $\underline{\mathbf{R}}_{o2}$ ,  $\underline{\mathbf{R}}_{o3}$ , which according to (2.55) can be written in matrix form as

$$\begin{pmatrix} \underline{\mathbf{R}}_1 \\ \underline{\mathbf{R}}_2 \\ \underline{\mathbf{R}}_3 \end{pmatrix} = \begin{pmatrix} t_{11} & t_{12} & t_{13} \\ t_{21} & t_{22} & t_{23} \\ t_{31} & t_{32} & t_{33} \end{pmatrix} \cdot \begin{pmatrix} \underline{\mathbf{R}}_{o1} \\ \underline{\mathbf{R}}_{o2} \\ \underline{\mathbf{R}}_{o3} \end{pmatrix} = \underline{\underline{\mathbf{T}}} \cdot \begin{pmatrix} \underline{\mathbf{R}}_{o1} \\ \underline{\mathbf{R}}_{o2} \\ \underline{\mathbf{R}}_{o3} \end{pmatrix} \quad (2.62)$$

If the lattice vectors  $\underline{\mathbf{R}}_1$ ,  $\underline{\mathbf{R}}_2$ ,  $\underline{\mathbf{R}}_3$  are to describe the same set of lattice points as vectors  $\underline{\mathbf{R}}_{o1}$ ,  $\underline{\mathbf{R}}_{o2}$ ,  $\underline{\mathbf{R}}_{o3}$ , then a general lattice point at  $\underline{\mathbf{R}}$  must be representable by an integer-valued linear combination of both sets of lattice vectors, i.e.

$$\underline{\mathbf{R}} = n_{o1} \underline{\mathbf{R}}_{o1} + n_{o2} \underline{\mathbf{R}}_{o2} + n_{o3} \underline{\mathbf{R}}_{o3} = n_1 \underline{\mathbf{R}}_1 + n_2 \underline{\mathbf{R}}_2 + n_3 \underline{\mathbf{R}}_3, \quad n_{oi}, n_i \text{ integer} \quad (2.63)$$

Thus, any triplet of integers  $n_1$ ,  $n_2$ ,  $n_3$  corresponds to another integer triplet  $n_{o1}$ ,  $n_{o2}$ ,  $n_{o3}$  and vice versa. This means, in particular, that the transformation matrix  $\underline{\underline{\mathbf{T}}} = (t_{ij})$  in (2.62) must be **integer-valued**. Further, transformation (2.62) can be inverted to yield

$$\begin{pmatrix} \underline{\mathbf{R}}_{o1} \\ \underline{\mathbf{R}}_{o2} \\ \underline{\mathbf{R}}_{o3} \end{pmatrix} = \begin{pmatrix} t_{11}' & t_{12}' & t_{13}' \\ t_{21}' & t_{22}' & t_{23}' \\ t_{31}' & t_{32}' & t_{33}' \end{pmatrix} \cdot \begin{pmatrix} \underline{\mathbf{R}}_1 \\ \underline{\mathbf{R}}_2 \\ \underline{\mathbf{R}}_3 \end{pmatrix} = \underline{\underline{\mathbf{T}}}^{-1} \cdot \begin{pmatrix} \underline{\mathbf{R}}_1 \\ \underline{\mathbf{R}}_2 \\ \underline{\mathbf{R}}_3 \end{pmatrix} \quad (2.64)$$



where the matrix elements  $t_{ij}'$  of the inverse matrix  $\underline{\underline{T}}^{-1}$  also must be integers. Since all elements of  $\underline{\underline{T}}$  are integers the determinant of matrix  $\underline{\underline{T}}$ , given by

$$\det(\underline{\underline{T}}) = t_{11} (t_{22} t_{33} - t_{23} t_{32}) + t_{12} (t_{23} t_{31} - t_{21} t_{33}) + t_{13} (t_{21} t_{32} - t_{22} t_{31}) \quad (2.65)$$

must be integer-valued. The same must be true for the inverse matrix  $\underline{\underline{T}}^{-1}$ . From linear algebra we know that

$$\det(\underline{\underline{T}}^{-1}) = 1 / \det(\underline{\underline{T}}) \quad (2.66)$$

Thus, both determinant values must be non-zero integers, i.e.  $|\det(\underline{\underline{T}})| \geq 1$  and  $|\det(\underline{\underline{T}}^{-1})| \geq 1$ , which according to (2.66) can only be possible if

$$\det(\underline{\underline{T}}) = \det(\underline{\underline{T}}^{-1}) = \pm 1 \quad (2.67)$$

Here the determinant value -1 can be safely ignored since it affects only the sequence in which the lattice vectors appear in the transformation (connected with handedness of the vector set). Any transformation (2.62) with  $\det(\underline{\underline{T}}) = -1$  can be modified to yield  $\det(\underline{\underline{T}}) = 1$  by exchanging one vector pair  $\underline{\underline{R}}_i, \underline{\underline{R}}_j$  in the transformation.

Relation (2.67) imposes a **constraint** to possible transformation matrices  $\underline{\underline{T}}$ . Combining (2.67) with (2.65) one can write

$$\det(\underline{\underline{T}}) = a_1 t_{11} + a_2 t_{12} + a_3 t_{13} = 1 \quad (2.68)$$

with integer-valued coefficients  $a_i$  where

$$\begin{aligned} a_1 &= t_{22} t_{33} - t_{23} t_{32} \\ a_2 &= t_{23} t_{31} - t_{21} t_{33} \\ a_3 &= t_{21} t_{32} - t_{22} t_{31} \end{aligned} \quad (2.69)$$

Equation (2.68) represents a linear Diophantine equation containing only integers as parameters and variables. As shown in Appendix E.3, this equation has integer solutions  $a_1, a_2, a_3$  for given  $t_{11}, t_{12}, t_{13}$  only if the latter three numbers have no common divisor greater than 1. Thus, the transformed lattice vector

$$\underline{\underline{R}}_1 = t_{11} \underline{\underline{R}}_{01} + t_{12} \underline{\underline{R}}_{02} + t_{13} \underline{\underline{R}}_{03} \quad (2.70)$$

is of **smallest length** along its direction in the lattice. Rearranging the components in the determinant (2.65) we can easily derive analogous relations

$$\det(\underline{\underline{T}}) = b_1 t_{21} + b_2 t_{22} + b_3 t_{23} = 1 \quad (2.71)$$

$$\det(\underline{T}) = c_1 t_{31} + c_2 t_{32} + c_3 t_{33} = 1 \quad (2.72)$$

with integer-valued coefficients  $b_i, c_i$ , where

$$\begin{aligned} b_1 &= t_{32} t_{13} - t_{12} t_{33} , & c_1 &= t_{12} t_{23} - t_{13} t_{22} \\ b_2 &= t_{33} t_{11} - t_{13} t_{31} , & c_2 &= t_{13} t_{21} - t_{11} t_{23} \\ b_3 &= t_{31} t_{12} - t_{11} t_{32} , & c_3 &= t_{11} t_{22} - t_{12} t_{21} \end{aligned} \quad (2.73)$$

Then the corresponding linear Diophantine equations (2.71), (2.72) have integer solutions  $b_1, b_2, b_3$  for given  $t_{21}, t_{22}, t_{23}$  (and  $c_1, c_2, c_3$  for given  $t_{31}, t_{32}, t_{33}$ ) only if the latter three numbers have no common divisor greater than 1. Thus, the transformed lattice vectors

$$\underline{R}_2 = t_{21} \underline{R}_{o1} + t_{22} \underline{R}_{o2} + t_{23} \underline{R}_{o3} \quad (2.74)$$

$$\underline{R}_3 = t_{31} \underline{R}_{o1} + t_{32} \underline{R}_{o2} + t_{33} \underline{R}_{o3} \quad (2.75)$$

are also of **smallest length** along their direction in the lattice.

### 2.2.3 Centered Lattices

In Sec. 2.2.2.1 it was shown that the bcc lattice, characterizing, for example, iron single crystals, see Fig. 2.16a, can be described by non-primitive lattice vectors  $\underline{R}_1, \underline{R}_2, \underline{R}_3$  which form a simple cubic lattice. However, there is an additional lattice vector  $\underline{R}'$  inside the morphological unit cell, spanned by  $\underline{R}_1, \underline{R}_2, \underline{R}_3$ , which points to the center of the cubic unit cell, as illustrated in Fig. 2.16b. This is an example of a more general property of non-primitive lattice representation, commonly denoted as **centering** and discussed in the following.

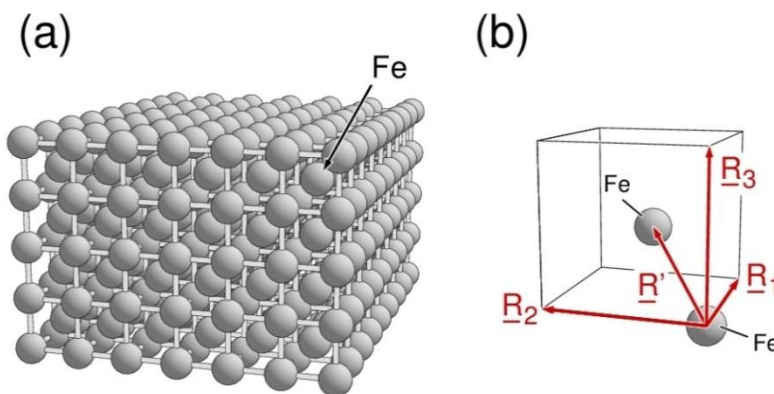


Fig. 2.16. (a) Section of a body-centered cubic iron (Fe) crystal. Sticks between atom balls indicate the crystal structure. (b) Non-primitive simple cubic morphological unit cell with two iron atoms inside. Lattice vectors  $\underline{R}_1, \underline{R}_2, \underline{R}_3$ , and  $\underline{R}'$  are labeled accordingly.

First, we consider possible **lattice vectors**  $\underline{\mathbf{R}}'$  at the **faces** of the morphological unit cell of a lattice represented by **non-primitive** lattice vectors  $\underline{\mathbf{R}}_1, \underline{\mathbf{R}}_2, \underline{\mathbf{R}}_3$ . For this we assume that each of the vectors  $\underline{\mathbf{R}}_1, \underline{\mathbf{R}}_2, \underline{\mathbf{R}}_3$  is of smallest length compared with all general lattice vectors along the same direction. Then an additional lattice point at a face of the morphological unit cell (excluding cell edges) can be described by a vector  $\underline{\mathbf{R}}'$  given by

$$\underline{\mathbf{R}}' = \kappa_i \underline{\mathbf{R}}_i + \kappa_j \underline{\mathbf{R}}_j, \quad 0 < \kappa_i, \kappa_j < 1, \quad (i, j) = (1, 2), (1, 3), (2, 3) \quad (2.76)$$

and for general values  $\kappa_i, \kappa_j$  there is always a second lattice point at the face of the cell with vector  $\underline{\mathbf{R}}''$  given by

$$\underline{\mathbf{R}}'' = \underline{\mathbf{R}}_i + \underline{\mathbf{R}}_j - \underline{\mathbf{R}}' = (1 - \kappa_i) \underline{\mathbf{R}}_i + (1 - \kappa_j) \underline{\mathbf{R}}_j \quad (2.77)$$

If, however, the face is assumed to contain **only one** additional lattice point then the vectors  $\underline{\mathbf{R}}'$  and  $\underline{\mathbf{R}}''$  must coincide, i.e.

$$\underline{\mathbf{R}}'' - \underline{\mathbf{R}}' = (1 - 2\kappa_i) \underline{\mathbf{R}}_i + (1 - 2\kappa_j) \underline{\mathbf{R}}_j = 0 \quad (2.78)$$

Here the expressions in brackets must both be zero since the vectors  $\underline{\mathbf{R}}_i, \underline{\mathbf{R}}_j$  are linearly independent. This leads to

$$\kappa_i = \kappa_j = 1/2, \quad \underline{\mathbf{R}}' = 1/2 (\underline{\mathbf{R}}_i + \underline{\mathbf{R}}_j) \quad (2.79)$$

yielding a lattice vector  $\underline{\mathbf{R}}'$  in the center of the cell face spanned by  $\underline{\mathbf{R}}_i, \underline{\mathbf{R}}_j$  (**face centering**). Relation (2.79) written as

$$\underline{\mathbf{R}}_i = 2 \underline{\mathbf{R}}' - \underline{\mathbf{R}}_j, \quad \underline{\mathbf{R}}_j = 2 \underline{\mathbf{R}}' - \underline{\mathbf{R}}_i \quad (2.80)$$

means in particular that  $(\underline{\mathbf{R}}', \underline{\mathbf{R}}_j)$  and  $(\underline{\mathbf{R}}_i, \underline{\mathbf{R}}')$  can be used as alternative lattice vector sets to represent the set  $(\underline{\mathbf{R}}_i, \underline{\mathbf{R}}_j)$ .

Next, we consider possible **lattice vectors**  $\underline{\mathbf{R}}'$  **inside** the morphological unit cell defined by lattice vectors  $\underline{\mathbf{R}}_1, \underline{\mathbf{R}}_2, \underline{\mathbf{R}}_3$ . An additional lattice point inside the cell (excluding cell faces and edges) can be described by a vector  $\underline{\mathbf{R}}'$  given by

$$\underline{\mathbf{R}}' = \kappa_1 \underline{\mathbf{R}}_1 + \kappa_2 \underline{\mathbf{R}}_2 + \kappa_3 \underline{\mathbf{R}}_3, \quad 0 < \kappa_i < 1, \quad i = 1, 2, 3 \quad (2.81)$$

and for general values  $\kappa_1, \kappa_2, \kappa_3$  there is always a second lattice point at the face of the cell with vector  $\underline{\mathbf{R}}''$  given by

$$\underline{\mathbf{R}}'' = \underline{\mathbf{R}}_1 + \underline{\mathbf{R}}_2 + \underline{\mathbf{R}}_3 - \underline{\mathbf{R}}' = (1 - \kappa_1) \underline{\mathbf{R}}_1 + (1 - \kappa_2) \underline{\mathbf{R}}_2 + (1 - \kappa_3) \underline{\mathbf{R}}_3 \quad (2.82)$$

If, however, the cell is assumed to contain **only one** additional lattice point then the vectors  $\underline{\mathbf{R}}'$  and  $\underline{\mathbf{R}}''$  must coincide, i.e.

$$\underline{\mathbf{R}}'' - \underline{\mathbf{R}}' = (1 - 2\kappa_1) \underline{\mathbf{R}}_1 + (1 - 2\kappa_2) \underline{\mathbf{R}}_2 + (1 - 2\kappa_3) \underline{\mathbf{R}}_3 = 0 \quad (2.83)$$

Again the expressions in brackets must all be zero since the vectors  $\underline{\mathbf{R}}_1, \underline{\mathbf{R}}_2, \underline{\mathbf{R}}_3$  are linearly independent. This leads to

$$\kappa_1 = \kappa_2 = \kappa_3 = 1/2 \quad , \quad \underline{\mathbf{R}}' = 1/2 (\underline{\mathbf{R}}_1 + \underline{\mathbf{R}}_2 + \underline{\mathbf{R}}_3) \quad (2.84)$$

yielding a lattice vector  $\underline{\mathbf{R}}'$  in the center of the cell spanned by  $\underline{\mathbf{R}}_1, \underline{\mathbf{R}}_2, \underline{\mathbf{R}}_3$  (**body centering**). Relation (2.84) written as

$$\underline{\mathbf{R}}_i = 2 \underline{\mathbf{R}}' - \underline{\mathbf{R}}_j - \underline{\mathbf{R}}_k \quad , \quad (i, j, k) = (1, 2, 3), (2, 3, 1), (3, 1, 2) \quad (2.85)$$

means in particular that  $(\underline{\mathbf{R}}', \underline{\mathbf{R}}_2, \underline{\mathbf{R}}_3)$ ,  $(\underline{\mathbf{R}}_1, \underline{\mathbf{R}}', \underline{\mathbf{R}}_3)$ , and  $(\underline{\mathbf{R}}_1, \underline{\mathbf{R}}_2, \underline{\mathbf{R}}')$  can be used as alternative lattice vector sets to represent the set  $(\underline{\mathbf{R}}_1, \underline{\mathbf{R}}_2, \underline{\mathbf{R}}_3)$ .

Altogether, additional lattice vectors  $\underline{\mathbf{R}}' = \kappa_1 \underline{\mathbf{R}}_1 + \kappa_2 \underline{\mathbf{R}}_2 + \kappa_3 \underline{\mathbf{R}}_3$  inside the morphological unit cell of a lattice, represented by non-primitive lattice vectors  $\underline{\mathbf{R}}_1, \underline{\mathbf{R}}_2, \underline{\mathbf{R}}_3$ , allow **four** choices of centering

$$\begin{aligned} \text{(a) body centering} \quad & \kappa_1 = \kappa_2 = \kappa_3 = 1/2 \quad , \quad \underline{\mathbf{R}}_a = 1/2 (\underline{\mathbf{R}}_1 + \underline{\mathbf{R}}_2 + \underline{\mathbf{R}}_3) \\ \text{(b) face centering} \quad & \kappa_2 = \kappa_3 = 1/2, \kappa_1 = 0 \quad , \quad \underline{\mathbf{R}}_b = 1/2 (\underline{\mathbf{R}}_2 + \underline{\mathbf{R}}_3) \\ \text{(c) face centering} \quad & \kappa_1 = \kappa_3 = 1/2, \kappa_2 = 0 \quad , \quad \underline{\mathbf{R}}_c = 1/2 (\underline{\mathbf{R}}_1 + \underline{\mathbf{R}}_3) \\ \text{(d) face centering} \quad & \kappa_1 = \kappa_2 = 1/2, \kappa_3 = 0 \quad , \quad \underline{\mathbf{R}}_d = 1/2 (\underline{\mathbf{R}}_1 + \underline{\mathbf{R}}_2) \end{aligned} \quad (2.86)$$

As an illustration Fig. 2.17 shows the lattice vectors  $\underline{\mathbf{R}}_a, \underline{\mathbf{R}}_b, \underline{\mathbf{R}}_c, \underline{\mathbf{R}}_d$ , referring to the four choices.

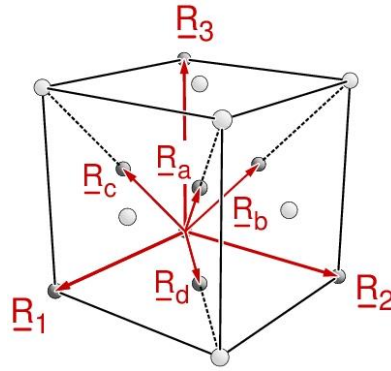


Fig. 2.17. Non-primitive morphological unit cell with choices (a) to (d) for possible lattice vectors inside the cell. The possible lattice vectors  $\underline{R}_a$ ,  $\underline{R}_b$ ,  $\underline{R}_c$ ,  $\underline{R}_d$ , as well as the lattice vectors  $\underline{R}_1$ ,  $\underline{R}_2$ ,  $\underline{R}_3$  defining the morphological unit cell are labeled accordingly. The dashed lines are meant to assist the visual orientation inside the figure.

If several of the vector choices (a) to (d) for  $\underline{R}'$  in (2.86) appear simultaneously in the unit cell there are additional **compatibility restrictions**. First, a lattice point (a) in the center of the unit cell excludes the appearance of any of the additional lattice points (b) to (d), and vice versa, since this would also result in additional lattice points  $\underline{R}' = 1/2 \underline{R}_i$  at the edges of the cell, which contradicts the assumption of vectors  $\underline{R}_i$  being of smallest length along their direction. Thus, lattices with non-primitive lattice vectors and additional lattice points (a) form a separate group of lattices, called **I-centered lattices** ('I' = 'Inner', preferred by crystallographers) or **body-centered (bcc) lattices**. Examples of this lattice type are the bcc lattices describing many metal crystal structures, such as Cr, V, Mo, W, and Fe, the latter shown in Fig. 2.16.

Second, lattices with only additional lattice points (b) form their own group, called **A-centered lattices** ('A' refers to the first lattice vector  $\underline{R}_1$ , determining the stacking of the additional lattice points). Those with only additional lattice points (c) form a group, called **B-centered lattices** ('B' refers to the second lattice vector  $\underline{R}_2$ ), and those with only additional lattice points (d) form a group, called **C-centered lattices** ('C' refers to the third lattice vector  $\underline{R}_3$ ). The appearance of two additional lattice points of choices (b) to (d) in (2.86) leads immediately to the appearance of a third lattice point as can be shown quite easily. As an example, the existence of lattice vectors  $\underline{R}_b$  and  $\underline{R}_c$  implies a lattice vector  $\underline{R} = \underline{R}_b + \underline{R}_c - \underline{R}_3$  which equals  $\underline{R}_d$ . Thus, the existence of more than one additional lattice point of choices (b) to (d) in (2.86) is only possible if all three types of lattice points exist at the same time. This group of lattices is called **F-centered lattices** ('F' = 'Face', preferred by crystallographers) or **face-centered (fcc) lattices**. Examples of this lattice type are the fcc lattices describing many metal crystal structures, such as Ni, Cu, Pt, and Ag.

Altogether, additional lattice points inside the morphological unit cell of a lattice with non-primitive lattice vectors, resulting in a centered unit cell, allow **five choices** as shown in Fig. 2.18. An additional lattice point in the cell center defines **I-centered** lattices. Further, additional points in the centers of the cell faces parallel to  $\underline{R}_2$  and  $\underline{R}_3$  (with no other additional lattice points) define **A-centered** lattices. Analogously, centering of cell faces parallel to  $\underline{R}_1$  and  $\underline{R}_3$  defines **B-centered** lattices, and centering of cell faces parallel to  $\underline{R}_1$  and  $\underline{R}_2$  defines **C-centered** lattices. Finally, **F-centered** lattices have additional lattice points at centers of all six faces of the unit cell.

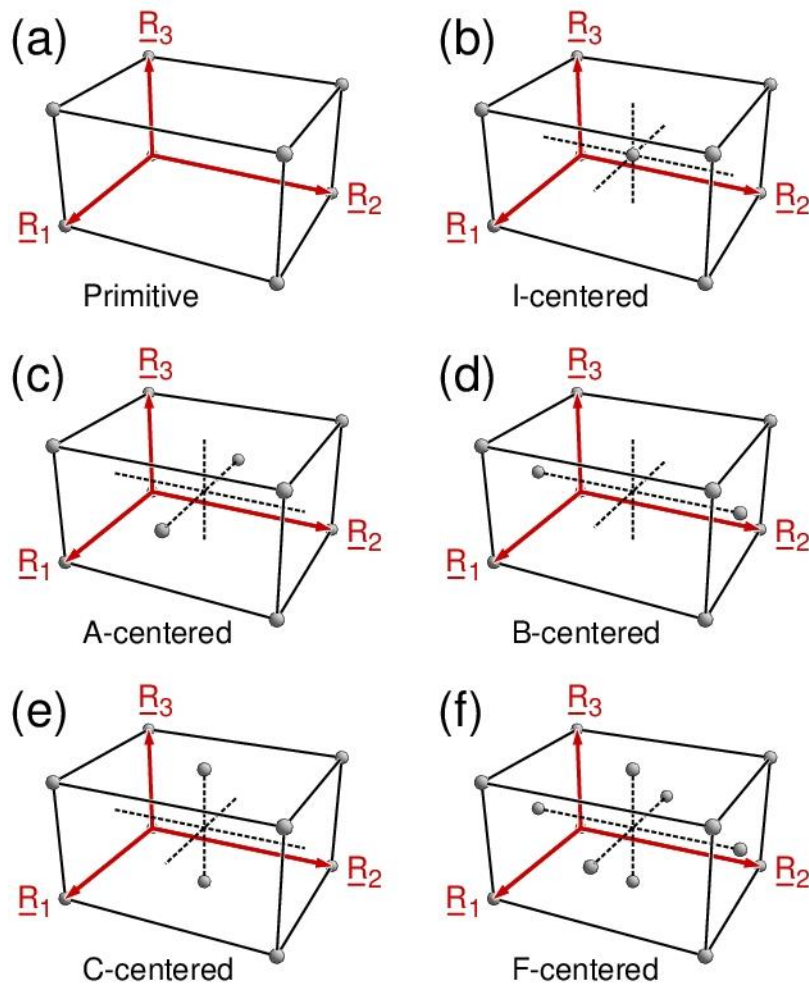


Fig. 2.18. Different centering of morphological unit cells. (a) Primitive, (b) I-centered, (c) A-centered, (d) B-centered, (e) C-centered, and (f) F-centered cell. The lattice vectors  $\underline{R}_1$ ,  $\underline{R}_2$ ,  $\underline{R}_3$  defining the morphological unit cell are labeled accordingly. The dashed lines are meant to assist the visual orientation inside the cells.

### 2.3 Periodicity Cells of Lattices

In Sec. 2.1, the **morphological unit cell** of a lattice with lattice vectors  $\underline{R}_1$ ,  $\underline{R}_2$ ,  $\underline{R}_3$  was defined as a six-faced polyhedron spanned by  $\underline{R}_1$ ,  $\underline{R}_2$ ,  $\underline{R}_3$  with its edges parallel to the lattice vectors and a volume  $V_{el}$  given by (2.9). If the lattice vectors are of smallest length in the lattice the corresponding polyhedral unit cells are also called **Buerger cells** [49]. If, in addition, the lattice vectors result from a reduction according to Niggli [41], providing a unique description in a crystallographical sense, see Sec. 2.2.2, then the unit cells are referred to as **Niggli cells**. As examples, the three **cubic** lattices discussed in Sec. 2.2.2.1 with lattice vectors defined by (2.25), (2.26), and (2.38) yield cell volumes according to (2.9)

$$\begin{aligned} V_{el} &= a^3 && \text{for sc lattices} \\ V_{el} &= 1/2 a^3 && \text{for bcc lattices} \\ V_{el} &= 1/4 a^3 && \text{for fcc lattices} \end{aligned} \quad (2.87)$$

In general, the morphological unit cell contains all  $p$  atoms which form the basis of a crystal structure. A continued repetition of the cell in the three directions along  $\underline{R}_1$ ,  $\underline{R}_2$ ,  $\underline{R}_3$  fills the complete three-dimensional space and describes the complete infinite crystal.

Assuming primitive lattice vectors  $\underline{R}_1$ ,  $\underline{R}_2$ ,  $\underline{R}_3$ , the **volume** of the morphological unit cell, given by (2.9) and connected with the atom density of the crystal, is unique whereas the cell **shape** is not. The shape is only determined by the requirement that a continued repetition of the cell in the three directions along  $\underline{R}_1$ ,  $\underline{R}_2$ ,  $\underline{R}_3$  fills the complete three-dimensional space without holes and overlaps. This can be achieved by very differently shaped **alternative unit cells**. As an illustration in two dimensions, Fig. 2.19 shows a section of the square lattice, where, apart from the square shaped morphological unit cell, spanned by lattice vectors  $\underline{R}_1$  and  $\underline{R}_2$  (bottom left), two alternative (polygonal) unit cells are included.

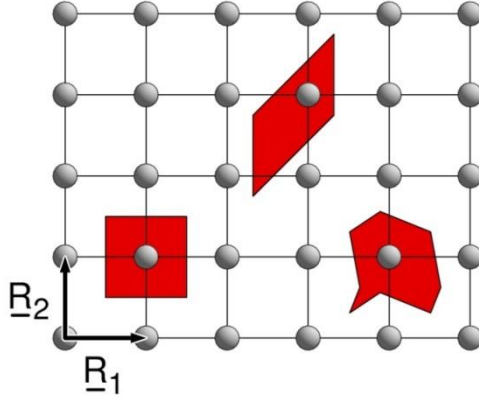


Fig. 2.19. Alternative unit cells of the square lattice, see text. The different unit cells are emphasized by red filling. The lattice vectors  $\underline{R}_1$  and  $\underline{R}_2$  are sketched at lower left corner.

The arbitrariness in the shape of alternative unit cells can be removed by additional constraints such as symmetry requirements, where the unit cell is assumed to reflect all point symmetry elements of the lattice. An additional constraint is compactness where all points inside the unit cell are assumed to be as close as possible to a lattice point. This leads to the definition of **Voronoi** or **Wigner-Seitz cells** which are commonly known in solid state physics [1], [2].

The **formal definition** of Wigner-Seitz cells considers for each point at position  $\underline{r}$  its distances  $d = |\underline{r} - \underline{R}|$  with respect to any lattice point  $\underline{R} = n_1 \underline{R}_1 + n_2 \underline{R}_2 + n_3 \underline{R}_3$ . Then position  $\underline{r}$  can be assigned to a lattice point  $\underline{R}$  by requiring that its distance  $d$  with respect to this lattice point is the smallest of all possible distances. The collection of all points  $\underline{r}$  assigned to a given lattice point defines its Wigner-Seitz cell. There will always be points  $\underline{r}$  whose distances with respect to two (or more, up to four [50]) lattice points are identical. These points define the **boundaries** separating Wigner-Seitz cells of adjacent lattice points. More precisely, if  $\underline{R}_a$  and  $\underline{R}_b$  denote two adjacent lattice points, then points  $\underline{r}$  of equal distance with respect to  $\underline{R}_a$  and  $\underline{R}_b$  satisfy relation

$$|\underline{r} - \underline{R}_a|^2 = r^2 - 2 \underline{r} \underline{R}_a + R_a^2 = |\underline{r} - \underline{R}_b|^2 = r^2 - 2 \underline{r} \underline{R}_b + R_b^2 \quad (2.88)$$

leading to

$$\begin{aligned} (\underline{R}_a - \underline{R}_b) \underline{r} &= 1/2 (R_a^2 - R_b^2) = 1/2 (\underline{R}_a - \underline{R}_b) (\underline{R}_a + \underline{R}_b) \\ (\underline{R}_a - \underline{R}_b) [\underline{r} - 1/2 (\underline{R}_a + \underline{R}_b)] &= 0 \end{aligned} \quad (2.89)$$

Equation (2.89) defines all points  $\underline{r}$  on a plane perpendicular to  $(\underline{R}_a - \underline{R}_b)$  and bisecting the line connecting  $\underline{R}_a$  with  $\underline{R}_b$ . Thus, boundaries separating adjacent Wigner-Seitz cells must be sections of planes and Wigner-Seitz cells must be **polyhedral** in shape. As an illustration, Figs. 2.20 and 2.21 compare morphological unit cells (Niggli cells) with Wigner-Seitz cells for the body- and face-



centered cubic lattices. Both polygonal Wigner-Seitz cells are highly symmetric which reflects the large number of point symmetry elements of the cubic lattice. This applies also to the Wigner-Seitz cell of the simple cubic lattice which forms a cube and is identical in shape with the morphological unit cell. A complete set of Wigner-Seitz cells for all 14 Bravais lattices can be found in Refs. [32] and [50].

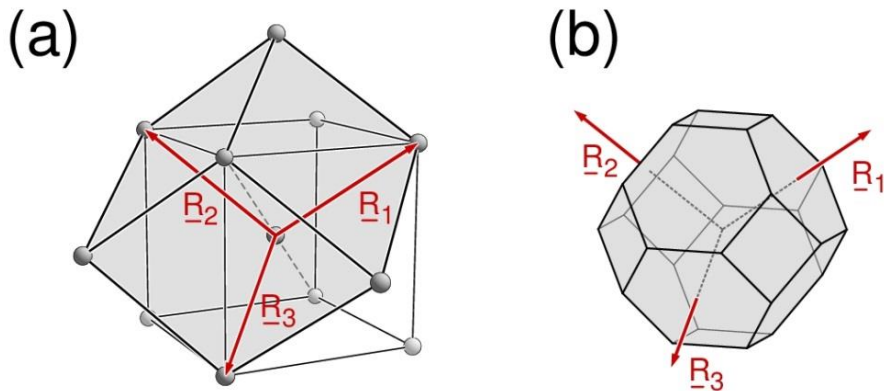


Fig. 2.20. (a) Morphological unit cell (Niggli cell) and (b) Wigner-Seitz cell of the bcc lattice. The polygonal cells are shaded in gray with lattice vectors labeled accordingly. The dashed lines are meant to assist the visual orientation inside the figures.

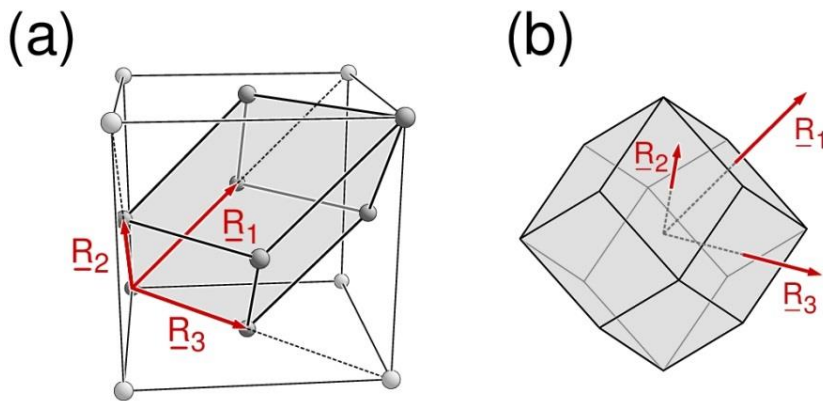


Fig. 2.21. (a) Morphological unit cell (Niggli cell) and (b) Wigner-Seitz cell of the fcc lattice. The polygonal cells are shaded in gray with lattice vectors labeled accordingly. The dashed lines are meant to assist the visual orientation inside the figures.

It is interesting to note that there is a continuous transition, the so-called **Bain path** [51], from bcc to fcc lattices, where the intermediate lattice type is centered tetragonal (ct) characterized by lattice vectors

$$\underline{R}_1 = (a, 0, 0), \quad \underline{R}_2 = (0, a, 0), \quad \underline{R}_3 = 1/2 (a, a, c) \quad (2.90)$$

The ratio  $q = c/a$  of the two lattice constants determines the actual lattice type, where  $q = 1$  reflects the bcc and  $q = \sqrt{2}$  yields the fcc lattice. The Wigner-Seitz cells must also transform continuously along the Bain path. This is illustrated in Fig. 2.22, where Wigner-Seitz cells of the ct lattice are shown for different ratios  $q$  between 0.8 and 1.6.

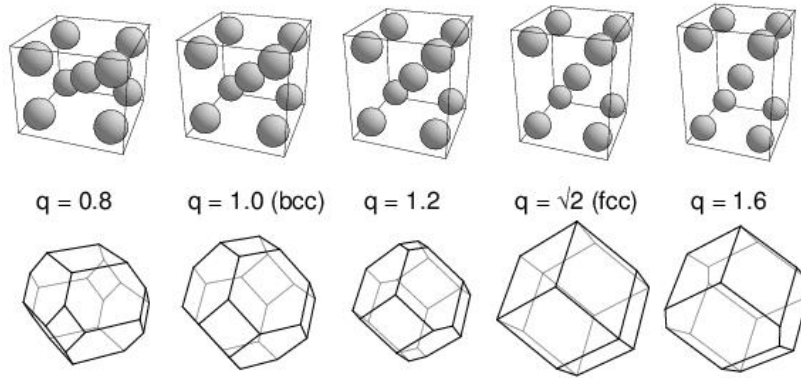


Fig. 2.22. Shape of Wigner-Seitz cells of the centered tetragonal (ct) lattice for different ratios  $q = c/a$ . Here  $q = 1$  and  $q = \sqrt{2}$  represent the bcc and fcc lattice, respectively. The top figures refer to rectangular blocks of a fictitious monoatomic ct crystal illustrating the lattice structure for corresponding ratios  $q$ .

## 2.4 Lattice Symmetry

A wide area of crystallography concerns the **classification** of all possible types of crystal structure based on their symmetry behavior. This subject will be discussed extensively for two-dimensional lattices (netplanes) in Secs. 3.7 and 3.8, due to its importance for the characterization of single crystal surfaces. The present section deals with symmetry of crystal structures in three dimensions. However, only **basic results** will be briefly discussed and the reader is referred to the literature [28], [29], [30], [31], [32], [33] for more detailed information.

Based on its initial definition, every lattice, given by lattice vectors  $\underline{R}_1, \underline{R}_2, \underline{R}_3$ , has **translational symmetry** along any direction described by **general lattice vectors**

$$\underline{R} = n_1 \underline{R}_1 + n_2 \underline{R}_2 + n_3 \underline{R}_3 \quad , \quad n_i \text{ integer} \quad (2.91)$$

Thus, a lattice viewed from two points  $\underline{r}$  and  $\underline{r}'$ , which are separated by  $\underline{R}$ , looks identical. This can be expressed mathematically using a **translation operation**  $t(\underline{R})$  which acts on vector  $\underline{r}$  to yield a shifted vector  $\underline{r}'$  with

$$\underline{r}' = t(\underline{R}) \underline{r} = \underline{r} + \underline{R} \quad (2.92)$$

Then translational symmetry of the lattice means that the lattice does not change geometrically when a translation operation (2.92) is applied.

In addition, lattices may exhibit **point symmetry** with respect to given points  $\underline{r}_0$  of the lattice space (symmetry origins), which do not need to coincide with general lattice points defined by vectors (2.91). A lattice is considered symmetric with respect to a point symmetry operation  $\mathbf{P}$  if it does not change geometrically when the operation is applied. A **point symmetry operation** can be written formally as

$$\underline{r} \rightarrow \underline{r}' = \mathbf{P} \underline{r} \quad (2.93)$$

where in three dimensions five different types of operations  $\mathbf{P}$  are generally available. These are

- $\mathbf{i}(\underline{r}_0)$       **inversion** with respect to symmetry origin  $\underline{r}_0$ ,
- $\mathbf{C}_\varphi(\underline{r}_0, \underline{e})$       **rotation** by an angle  $\varphi$  about an axis along vector  $\underline{e}$  through symmetry origin  $\underline{r}_0$ ,
- $\mathbf{\sigma}(\underline{r}_0, \underline{e})$       **mirroring (reflection)** with respect to a plane with normal vector  $\underline{e}$  through symmetry origin  $\underline{r}_0$ ,
- $\mathbf{S}_\varphi(\underline{r}_0, \underline{e})$       **rotoinversion** by an angle  $\varphi$  about an axis along  $\underline{e}$  through  $\underline{r}_0$ . This combines a rotation  $\mathbf{C}_\varphi(\underline{r}_0, \underline{e})$  with an inversion  $\mathbf{i}(\underline{r}_0)$ ,
- $\mathbf{S}'_\varphi(\underline{r}_0, \underline{e})$       **rotoreflexion** by an angle  $\varphi$  about an axis along  $\underline{e}$  through  $\underline{r}_0$ . This combines a rotation  $\mathbf{C}_\varphi(\underline{r}_0, \underline{e})$  with a mirror operation  $\mathbf{\sigma}(\underline{r}_0, \underline{e})$ , where direction vector  $\underline{e}$  of the rotation axis coincides with the normal vector of the mirror plane.

The latter two symmetry operations combine two of the other operations, a rotation with inversion or with reflection. This means, in particular, that a lattice may be symmetric with respect to one of the two combined symmetry operations but may not exhibit the symmetry of the two component operations. Rotoinversion and rotoreflexion are connected with each other by a rotation by  $180^\circ$  which can be formally written as

$$\mathbf{S}'_\varphi(\underline{r}_0, \underline{e}) = \mathbf{S}_\varphi(\underline{r}_0, \underline{e}) \mathbf{C}_{180}(\underline{r}_0, \underline{e}) = \mathbf{C}_{180}(\underline{r}_0, \underline{e}) \mathbf{S}_\varphi(\underline{r}_0, \underline{e}) \quad (2.94)$$

Thus, the two symmetry operations can be used equivalently in a symmetry classification of three-dimensional crystal lattices. Here the **Hermann-Mauguin** or **international notation**, which forms the basis of the International Tables of Crystallography [33] and is by now the standard approach

amongst crystallographers, considers rotoinversion as the standard symmetry operation while the **Schönflies notation**, practiced by many physicists, uses roto-reflection.

There are two additional symmetry operations which can appear in three-dimensional crystal lattices, namely

- $T_{\varphi}(\underline{r}_0, \underline{e}, t)$  **rototranslation (screw operation)** by an angle  $\varphi$  about an axis along  $\underline{e}$  through  $\underline{r}_0$  and subsequent translation by vector  $t \cdot \underline{e}$ .
- $g(\underline{r}_0, \underline{e}, \underline{g})$  **glide reflection**, combining a reflection  $\sigma(\underline{r}_0, \underline{e})$  with a translation by vector  $\underline{g}$ , where vectors  $\underline{g}$  and  $\underline{e}$  are perpendicular to each other.

Both operations are not true point symmetry operation since they contain a translational component. However, rototranslations are required to describe the symmetry of crystals which contain screw axes. Glide reflections appear as symmetry elements in centered three-dimensional crystal lattices.

Translational and point symmetry elements of a lattice are subject to **compatibility constraints**. These constraints limit the number of possible point symmetry operations available for a characterization of different types of lattices. Examples are constraints on possible angles  $\varphi$  of rotation operations and of the direction  $\underline{e}$  of their axes, of mirror plane orientations, or positions of inversion centers. These constraints for three-dimensional lattices will not be detailed in this book. However, they will be discussed extensively for the case of two-dimensional lattices (netplanes) in Sec. 3.6. Using these constraints together with group theoretical methods provides the basis of a **general classification scheme** of all crystal lattices which is documented in the International Tables of Crystallography [33]. As an illustration of the compatibility constraints, possible rotation axes inside lattices will be considered. This can already serve for a rough classification of all possible lattice types into seven **crystal systems** and 14 different types of lattices, the so-called **three-dimensional Bravais lattices**.

In Sec. 3.6.3 it will be shown that the compatibility of rotational and translational symmetry in two-dimensional lattices restricts rotation angles  $\varphi$  to integer multiples of  $(360^\circ/n)$ , where only values  $n = 2, 3, 4, 6$  are allowed. The corresponding mathematical proof is also valid for three-dimensional lattices. If a lattice transforms into itself by a rotation by  $\varphi = (360^\circ/n)$ , it will also do so for all rotations by  $\varphi' = p(360^\circ/n)$ ,  $p = 1, \dots, n$ . This property can be used to characterize rotation axes by their ‘foldedness’  $n$ . An **n-fold rotation axis** in a lattice allows rotations by all integer mul-

tuples of the angle  $360^\circ/n$  about its axis, where the rotated images coincide with the initial lattice. Thus, lattices allow only 2-, 3-, 4-, and 6-fold rotation axes as rotational point symmetry elements. There are two different naming conventions for rotation axes in crystal lattices. The so-called **Hermann-Mauguin** or **International notation**, is preferred by crystallographers and used in the International Tables of Crystallography [33]. In this notation an n-fold rotation axis is denoted by its foldedness as **n**. In contrast, the so-called **Schönflies** notation uses the symbol **C<sub>n</sub>** for an n-fold rotation axis. Table 2.2 lists all possible n-fold rotation axes of three-dimensional lattices together with their Hermann-Mauguin and Schönflies names. (It also includes the corresponding names for mirror symmetry planes and inversion centers.)

Table 2.2. Naming conventions (Hermann-Mauguin, Schönflies) for the simple point symmetry elements of three-dimensional lattices, see text.

Symmetry	Hermann-Mauguin	Schönflies
2-fold rotation axis	<b>2</b>	<b>C<sub>2</sub></b>
3-fold rotation axis	<b>3</b>	<b>C<sub>3</sub></b>
4-fold rotation axis	<b>4</b>	<b>C<sub>4</sub></b>
6-fold rotation axis	<b>6</b>	<b>C<sub>6</sub></b>
Mirror plane	<b>m</b>	<b>σ</b>
Inversion	<b><math>\bar{1}</math> or -1</b>	<b>i</b>

The four different rotation axes can **distinguish** between the different types of three-dimensional lattices. First, there are lattices which do not possess any rotational axis. They form the most general type of **Bravais lattices** and will be called **triclinic-P**. Any centering of a triclinic-P lattice according to Sec. 2.2.3 will lead to another triclinic-P lattice, i.e. will not create any new lattice type. Thus, the triclinic-P lattice, shown in Fig. 2.23, is the only member of the **triclinic crystal system**.

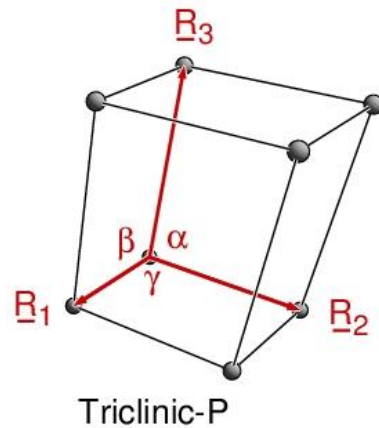


Fig. 2.23. Morphological unit cell of the triclinic-P lattice with lattice vectors  $\underline{R}_1$ ,  $\underline{R}_2$ ,  $\underline{R}_3$  and angles  $\alpha$ ,  $\beta$ ,  $\gamma$  labeled accordingly.

Next, we assume that a lattice possesses a **2-fold rotation axis**, where the origin of the lattice can always be set to lie on the axis. Then, we consider two lattice points, given by a general lattice vector  $\underline{R}^{(0)}$  (not on the axis), and its image  $\underline{R}^{(1)}$ , which arises from rotating  $\underline{R}^{(0)}$  about the axis by  $180^\circ$ . The sum of the two general lattice vectors,  $\underline{R}^c = (\underline{R}^{(0)} + \underline{R}^{(1)})$ , is a general lattice vector pointing along the rotation axis. Therefore, as a result of translational symmetry, there are an infinite number of lattice points on the rotation axis. Of these lattice points, the one nearest to the origin can be used to define lattice vector  $\underline{R}_3$  of the lattice. On the other hand, the difference vector  $\underline{R}^a = (\underline{R}^{(1)} - \underline{R}^{(0)})$  is a general lattice vector perpendicular to the rotation axis suggesting infinitely many lattice points along its direction. Of these, again the one nearest to the origin can be used to define lattice vector  $\underline{R}_1$  of the lattice. The same procedure can be applied to a different general lattice vector  $\underline{R}^{(2)}$  and its rotational image  $\underline{R}^{(3)}$ , where the difference vector  $\underline{R}^b = (\underline{R}^{(3)} - \underline{R}^{(2)})$  is also perpendicular to the rotation axis. Then the smallest lattice vector along  $\underline{R}^b$  can be used to define lattice vector  $\underline{R}_2$  of the lattice. Vectors  $\underline{R}_1$  and  $\underline{R}_2$  may have to be exchanged to guarantee a right-handed system, but, altogether, the vector triplet  $\underline{R}_1$ ,  $\underline{R}_2$ ,  $\underline{R}_3$  provides an appropriate set of lattice vectors describing the lattice with its 2-fold rotation axis. For the following discussion, these lattice vectors will be described by their lengths  $a$ ,  $b$ ,  $c$  (lattice constants) and mutual angles  $\alpha$ ,  $\beta$ ,  $\gamma$ , according to (2.3) and sketched in Fig. 2.3. This means, in particular, for the present symmetry and choice of lattice vectors that  $\alpha = \beta = 90^\circ$ .

The lattice vectors  $\underline{R}_1$ ,  $\underline{R}_2$ ,  $\underline{R}_3$  where the angle  $\gamma$  assumes any value different from  $60^\circ$ ,  $90^\circ$ , and  $120^\circ$  define the **monoclinic crystal system**. If the morphological unit cell of  $\underline{R}_1$ ,  $\underline{R}_2$ ,  $\underline{R}_3$  is primitive the corresponding Bravais lattice will be called **monoclinic-P**. Centering a monoclinic-P lattice ac-

cording to Sec. 2.2.3 can create different lattices depending on the type of centering. Here C-centering will only modify the lattice vectors  $\underline{R}_1$  and  $\underline{R}_2$  but will keep the monoclinic-P lattice. In contrast, A-centering leads to a new lattice type, **monoclinic-A**, which cannot be described by a monoclinic-P lattice. Likewise, B-centering, creates a new lattice type, **monoclinic-B**, different from monoclinic-P. However, monoclinic-A and monoclinic-B lattices are morphologically equivalent since they differ only by an interchange of lattice vectors  $\underline{R}_1$  and  $\underline{R}_2$ . Thus, it is sufficient to consider one of the two lattice types, where crystallographers prefer **monoclinic-B** over monoclinic-A. Further, F- and I-centering can be shown to also be equivalent to B-centering by appropriate origin shifts and lattice vector modifications. Thus, the monoclinic crystal system can be represented by **two** unique Bravais lattices, monoclinic-P and monoclinic-B, shown in Fig. 2.24.

It should be noted that crystallographers often describe the monoclinic crystal system by using lattice vector  $\underline{R}_2$  (**B axis**) to define the direction of the 2-fold rotation axis of a crystal. This geometry, referred to in the International Tables of Crystallography [33] as the ‘**first setting**’ (as opposed to the ‘second setting’ discussed above), corresponds to lattice vector angles  $\alpha = \gamma = 90^\circ$ ,  $\beta \neq 60^\circ, \neq 90^\circ, \neq 120^\circ$ . The interchange of crystal axes between the two settings does not affect the discussion of possible crystal types, except that the first setting considers **monoclinic-P** and centered **monoclinic-C** as the unique monoclinic lattices.

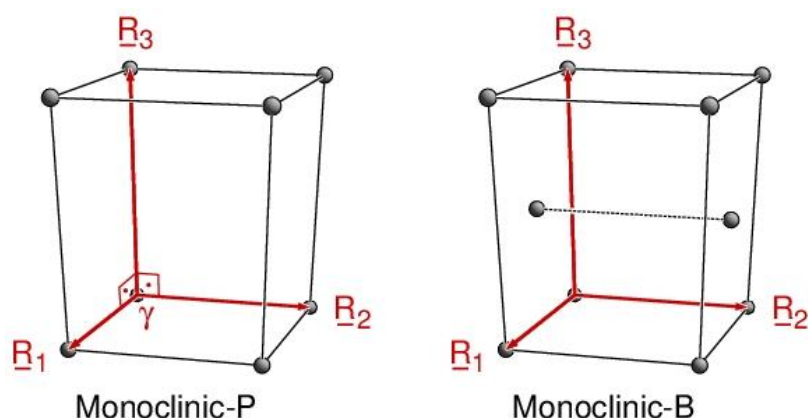


Fig. 2.24. Morphological unit cells of the monoclinic crystal system, monoclinic-P and monoclinic-B lattices with lattice vectors  $\underline{R}_1$ ,  $\underline{R}_2$ ,  $\underline{R}_3$  and angles  $\alpha = \beta = 90^\circ$ ,  $\gamma$  labeled accordingly (angles only for monoclinic-P). Angles of  $90^\circ$  are indicated by small rectangles filled with a dot. The dashed line connecting opposing lattice points is meant to guide the eye.

Lattice vectors  $\underline{R}_1$ ,  $\underline{R}_2$ ,  $\underline{R}_3$  with the angle  $\gamma = 90^\circ$ , i.e. for  $\alpha = \beta = \gamma = 90^\circ$ , but with different vector lengths,  $a \neq b$ ,  $a \neq c$ ,  $b \neq c$ , define the **orthorhombic crystal system**. If the morphological unit

cell of  $\underline{R}_1$ ,  $\underline{R}_2$ ,  $\underline{R}_3$  is primitive the corresponding Bravais lattice will be called **orthorhombic-P**. Centering an orthorhombic-P lattice according to Sec. 2.2.3 will always create different lattices. Here A-, B-, and C-centerings lead to new lattice types, **orthorhombic-A, -B, and -C**, respectively, which cannot be described by an orthorhombic-P lattice. However, these three centered lattices are morphologically equivalent and differ only by an interchange of corresponding lattice vectors. Thus, only one of these lattice types needs to be considered, where crystallographers often prefer **orthorhombic-C** over the other two. In addition, I- and F-centerings yield new lattice types, **orthorhombic-I** and **orthorhombic-F**. Therefore, the orthorhombic crystal system can be represented by **four** unique Bravais lattices, orthorhombic-P, orthorhombic-C, orthorhombic-I, and orthorhombic-F, shown in Fig. 2.25.

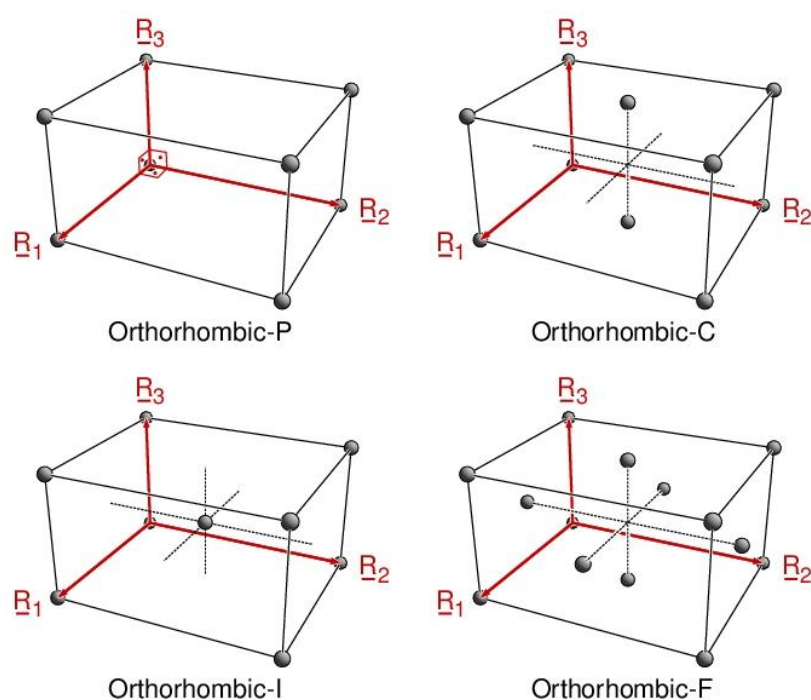


Fig. 2.25. Morphological unit cells of the orthorhombic crystal system, orthorhombic-P, orthorhombic-C, orthorhombic-I, and orthorhombic-F, lattices with lattice vectors  $\underline{R}_1$ ,  $\underline{R}_2$ ,  $\underline{R}_3$  and angles  $\alpha = \beta = \gamma = 90^\circ$  labeled accordingly (angles only for orthorhombic -P indicated by small rectangles filled with a dot). The dashed lines connecting lattice points are meant to guide the eye.

Lattice vectors  $\underline{R}_1$ ,  $\underline{R}_2$ ,  $\underline{R}_3$  with angles  $\alpha = \beta = \gamma = 90^\circ$  but with vector lengths,  $a = b \neq c$ , define the **tetragonal crystal system**. If the morphological unit cell of  $\underline{R}_1$ ,  $\underline{R}_2$ ,  $\underline{R}_3$  is primitive the corresponding Bravais lattice will be called **tetragonal-P**. Here the two constraints,  $a = b$  and  $\gamma = 90^\circ$  mean, in particular, that the 2-fold rotation axis along  $\underline{R}_3$  is also a **4-fold** rotation axis. Therefore, A- and B-centering of a tetragonal-P lattice is not possible. Further, C-centering will on-



ly modify the lattice vectors  $\underline{R}_1$  and  $\underline{R}_2$  but will keep the tetragonal-P lattice. However, I-centering results in a new lattice type, **tetragonal-I**, which cannot be represented by a tetragonal-P lattice. In addition, F-centering can be shown to result in a tetragonal-I lattice by appropriate origin shifts and lattice vector modifications. Thus, the tetragonal crystal system can be represented by **two** unique Bravais lattices, tetragonal-P and tetragonal-I, shown in Fig. 2.26.

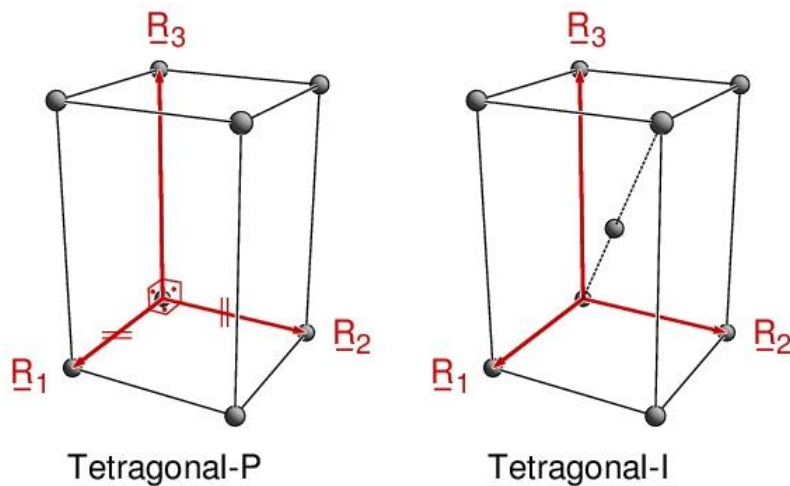


Fig. 2.26. Morphological unit cells of the tetragonal crystal system, tetragonal-P and tetragonal-I lattices with lattice vectors  $\underline{R}_1$ ,  $\underline{R}_2$ ,  $\underline{R}_3$  and angles  $\alpha = \beta = \gamma = 90^\circ$  labeled accordingly (angles only for tetragonal -P indicated by small rectangles filled with a dot). Parallel pairs of short lines indicate vectors of equal length. The dashed line connecting opposing lattice points is meant to guide the eye.

Lattice vectors  $\underline{R}_1$ ,  $\underline{R}_2$ ,  $\underline{R}_3$  with angles  $\alpha = \beta = \gamma = 90^\circ$  but with three equal vector lengths,  $a = b = c$ , define the **cubic crystal system**. If the morphological unit cell of  $\underline{R}_1$ ,  $\underline{R}_2$ ,  $\underline{R}_3$  is primitive the corresponding Bravais lattice will be called **cubic-P** or **simple cubic (sc)**. For this crystal system the 2-fold rotation axis along  $\underline{R}_3$  is also a **4-fold** rotation axis, analogous to the tetragonal case. In addition, there are 4-fold rotation axes along  $\underline{R}_1$  and  $\underline{R}_2$ . As a consequence, neither A- nor B- nor C-centering of a cubic-P lattice is possible. However, I- and F-centerings yield new lattice types, **cubic-I** or **body-centered cubic (bcc)**, and **cubic-F** or **face-centered cubic (fcc)**. As a consequence, the cubic crystal system includes **three** unique Bravais lattices, cubic-P, cubic-I, and cubic-F, shown in Fig. 2.27.

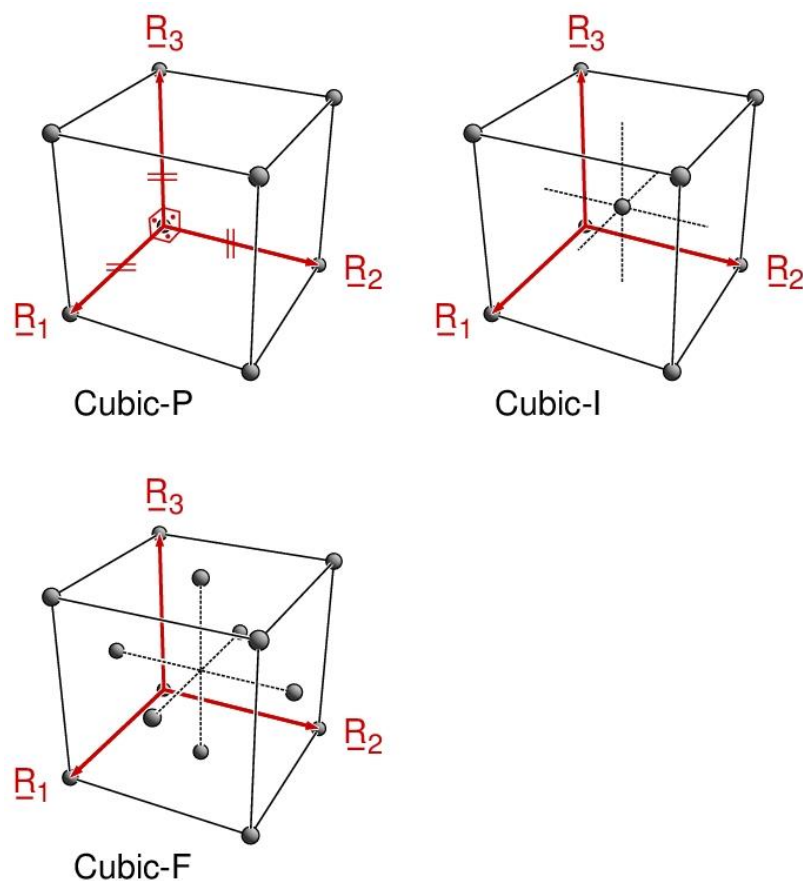


Fig. 2.27. Morphological unit cells of the cubic crystal system, cubic-P, cubic-I, and cubic-F, lattices with lattice vectors  $\underline{R}_1$ ,  $\underline{R}_2$ ,  $\underline{R}_3$  and angles  $\alpha = \beta = \gamma = 90^\circ$  labeled accordingly (angles only for cubic-P indicated by small rectangles filled with a dot). Parallel pairs of short lines indicate vectors of equal length. The dashed lines connecting opposing lattice points are meant to guide the eye.

So far, all lattice vector sets  $\underline{R}_1$ ,  $\underline{R}_2$ ,  $\underline{R}_3$  with vector  $\underline{R}_3$  pointing along a 2- and 4-fold rotation axis have been considered. In addition,  $\underline{R}_3$  can define the direction of a **6-fold** rotation axis. This corresponds to  $\alpha = \beta = 90^\circ$ ,  $\gamma = 60^\circ$ ,  $a = b$ , and defines the **hexagonal crystal system**. In this system, the lattice vectors  $\underline{R}_1$  and  $\underline{R}_2$  can be represented in two ways. The initial definition is based on the 6-fold rotation axis and uses an angle  $\gamma = 60^\circ$  between  $\underline{R}_1$  and  $\underline{R}_2$  (**acute representation**). The alternative definition uses an angle  $\gamma = 120^\circ$  between  $\underline{R}_1$  and  $\underline{R}_2$ , (**obtuse representation**) and is often preferred by crystallographers. The latter representation emphasizes the 3-fold rotation axis along  $\underline{R}_3$ , which is, however, combined with a 2-fold axis to form the 6-fold rotation axis. If the morphological unit cell of the hexagonal lattice is primitive the corresponding Bravais lattice will be called **hexagonal-P**. Any centering of a hexagonal-P lattice according to Sec. 2.2.3 will destroy the hexagonal symmetry. Thus, the hexagonal crystal system includes only the hexagonal-P Bravais lattice, shown in Fig. 2.28.

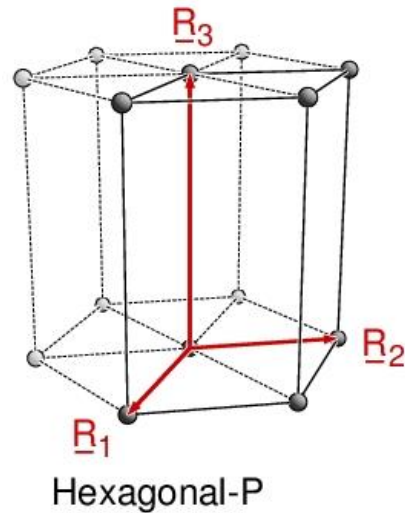


Fig. 2.28. Morphological unit cell of the hexagonal-P lattice with lattice vectors  $\underline{R}_1$ ,  $\underline{R}_2$ ,  $\underline{R}_3$  labeled accordingly. The dashed lines connecting lattice points in hexagonal arrangements at top and bottom planes are meant to guide the eye.

The present lattice classification is based on lattices where lattice vector  $\underline{R}_3$  points along a 2-fold rotation axis. Therefore, it cannot immediately be used to describe lattices with a pure 3-fold rotation axis along  $\underline{R}_3$  since the combination of coinciding 2- and 3- fold rotation axes leads to a 6-fold rotation axis and, thus, to the hexagonal crystal system discussed previously. However, we can start from a 3-fold rotation axis through a lattice point and consider three other lattice points. These are given by a general lattice vector  $\underline{R}^{(0)}$  from the lattice point and its two images  $\underline{R}^{(1)}$ ,  $\underline{R}^{(2)}$ , which arise from rotating  $\underline{R}^{(0)}$  about the axis by  $120^\circ$  and  $240^\circ$ , respectively. If these vectors are of the smallest length along their direction they can be used as lattice vectors  $\underline{R}_1$ ,  $\underline{R}_2$ ,  $\underline{R}_3$ . By construction these lattice vectors are of identical length and form identical angles with each other, i.e.  $a = b = c$  and  $\alpha = \beta = \gamma$ , which defines the **trigonal** or **rhombohedral crystal system**. This crystal system also includes only one Bravais lattice, the **trigonal-R** lattice ('R' = 'Rhomboidal' reminds of the alternative name), shown in Fig. 2.29. The trigonal and hexagonal lattices are closely connected with each other. As an example, Sec. 2.2.2.1 shows that a trigonal-R lattice can be alternatively described by a hexagonal lattice with non-primitive lattice vectors. Further, the trigonal-R lattice yields for  $\alpha = \beta = \gamma = 90^\circ$  a cubic-P lattice, for  $\alpha = \beta = \gamma = 60^\circ$  a cubic-F lattice, and for  $\alpha = \beta = \gamma = 109.47^\circ$  ( $\cos(\alpha) = -1/3$ ) a cubic-I lattice. Thus, the cubic lattices may also be defined by their (four different) 3-fold rotation axes rather than by 2- and 4-fold rotation axes.

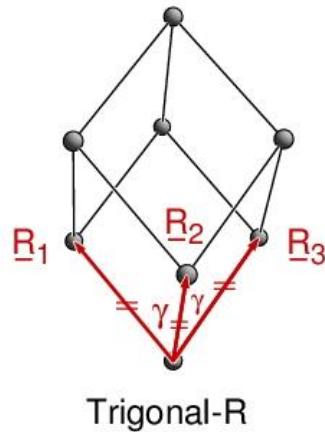


Fig. 2.29. Morphological unit cell of the trigonal-R (rhombohedral) lattice with lattice vectors  $\underline{R}_1$ ,  $\underline{R}_2$ ,  $\underline{R}_3$  and angles  $\gamma$  (given for the two front sides) labeled accordingly. Parallel pairs of short lines indicate vectors of equal length.

Altogether, the existence of rotation axes inside lattices allows a first classification of all lattice types yielding the **seven crystal systems** and **14 different Bravais lattices** listed in Table 2.3 and sketched in Fig. 2.30.

Table 2.3. List of the seven crystal systems with their Bravais lattice members described by lattice constants  $a$ ,  $b$ ,  $c$ , and angles  $\alpha$ ,  $\beta$ ,  $\gamma$ . Angles quoted without specific values are assumed to differ from  $60^\circ$ ,  $90^\circ$ , and  $120^\circ$ . For each crystal system, the corresponding Bravais lattices with crystallographic labels as well as with the highest point symmetry group in Schoenflies notation are included.

Crystal system	Lattice constants	Bravais lattices	Symmetry
Triclinic	$a \neq b \neq c$ , $\alpha, \beta, \gamma$	-P	$C_i$
Monoclinic	$a \neq b \neq c$ , $\alpha = 90^\circ, \beta = 90^\circ, \gamma$	-P, -B	$C_{2h}$
Orthorhombic	$a \neq b \neq c$ , $\alpha = \beta = \gamma = 90^\circ$	-P, -C, -I, -F	$D_{2h}$
Tetragonal	$a = b \neq c$ , $\alpha = \beta = \gamma = 90^\circ$	-P, -I	$D_{4h}$
Hexagonal	$a = b \neq c$ , $\alpha = \beta = 90^\circ$ , $\gamma = 60^\circ$ (acute), $120^\circ$ (obtuse)	-P	$D_{6h}$
Trigonal, Rhombohedral	$a = b = c$ , $\alpha = \beta = \gamma$	-R	$D_{3d}$
Cubic	$a = b = c$ , $\alpha = \beta = \gamma = 90^\circ$	-P, -I, -F	$O_h$

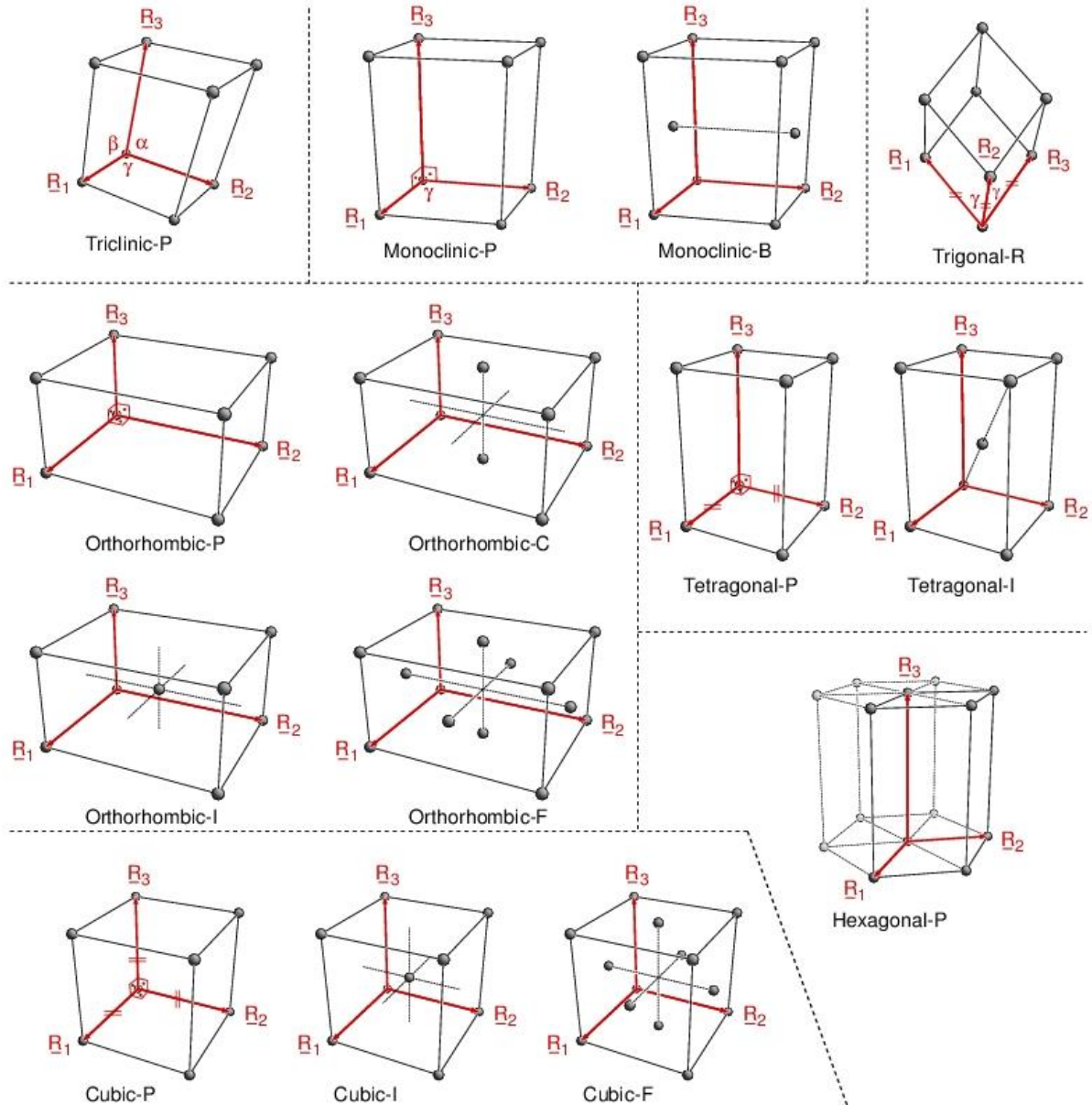


Fig. 2.30. Morphological unit cells the 14 three-dimensional Bravais lattices, described in Table 2.3, with lattice vectors  $\underline{R}_1$ ,  $\underline{R}_2$ ,  $\underline{R}_3$  and angles  $\alpha$ ,  $\beta$ ,  $\gamma$  labeled accordingly. Angles of  $90^\circ$  are indicated by small rectangles filled with a dot. Parallel pairs of short lines indicate vectors of equal length. The dashed lines connecting opposing lattice points are meant to guide the eye.

A complete classification of all possible lattice types must also take into account point symmetry elements other than rotations. However, this will not affect the basic family of crystal systems and Bravais lattices obtained so far. In fact, Bravais lattices and their morphological unit cells are always found to exhibit the largest number of symmetry elements of all lattices of a given crystal system. Atom positions, defining the basis inside the morphological unit cell of a crystal, may result in lower symmetry than suggested by the shape of the unit cell (given by the crystal system

and the corresponding Bravais lattice). This allows for lattices with identical lattice vectors but different point symmetry properties. Applying group theoretical methods, it can be shown that, altogether, there are 230 different ways to combine symmetry with lattices, described by the **230** different **three-dimensional space groups**, tabulated in the International Tables of Crystallography [33]. For a full discussion see [32] and references therein.

## 2.5 Reciprocal Lattice

In addition to the initial lattice vectors  $\underline{R}_1, \underline{R}_2, \underline{R}_3$  describing a lattice in real space the definition of a second set of vectors,  $\underline{G}_1, \underline{G}_2, \underline{G}_3$ , given by vector products

$$\begin{aligned}\underline{G}_1 &= \beta (\underline{R}_2 \times \underline{R}_3), \quad \underline{G}_2 = \beta (\underline{R}_3 \times \underline{R}_1), \quad \underline{G}_3 = \beta (\underline{R}_1 \times \underline{R}_2) \\ \beta &= (2\pi) / [(\underline{R}_1 \times \underline{R}_2) \cdot \underline{R}_3] = (2\pi) / V_{el}\end{aligned}\quad (2.95)$$

has proven to be quite useful for various applications discussed in this book. Examples are the calculation of distances between adjacent monolayers or of atom densities of monolayers described in Sec. 3.1. The reciprocal lattice defined by (2.95) is also central to wave diffraction by lattices and to electronic band structure theory of crystals. Since the scaling factor  $\beta$  in (2.95) is of dimension  $[\text{length}^{-3}]$  vectors  $\underline{G}_i$  are of dimension  $[\text{length}^{-1}]$ . They are closely related to the initial lattice vectors and can be used to define a complementary lattice in reciprocal space, the **reciprocal lattice**. Therefore, these vectors are called **reciprocal lattice vectors**. They have a number of interesting properties of which we mention only a few in the following.

- (a) The reciprocal lattice vectors  $\underline{G}_i$  fulfill **orthogonality relations**

$$\underline{G}_i \cdot \underline{R}_i = 2\pi \quad \text{for } i = 1, 2, 3; \quad \underline{G}_i \cdot \underline{R}_j = 0 \quad \text{for } i \neq j \quad (2.96)$$

which is clear from definitions (2.95) and basic properties of vector products.

- (b) The **volume** of the **unit cell** of the reciprocal lattice is **inverse** to that of the real space lattice. According to definition (2.9) and using a property of the vector product of three vectors  $\underline{a}, \underline{b}, \underline{c}$

$$\underline{a} \times (\underline{b} \times \underline{c}) = (\underline{a} \cdot \underline{c}) \underline{b} - (\underline{a} \cdot \underline{b}) \underline{c} \quad (2.97)$$

we obtain

$$\begin{aligned}
V_G &= (\underline{G}_1 \times \underline{G}_2) \cdot \underline{G}_3 = \beta^3 \{(\underline{R}_2 \times \underline{R}_3) \times (\underline{R}_3 \times \underline{R}_1)\} \cdot (\underline{R}_1 \times \underline{R}_2) = \\
&= \beta^3 \{((\underline{R}_2 \times \underline{R}_3) \cdot \underline{R}_1) \underline{R}_3 - ((\underline{R}_2 \times \underline{R}_3) \cdot \underline{R}_3) \underline{R}_1\} \cdot (\underline{R}_1 \times \underline{R}_2) = \\
&= \beta^3 \{((\underline{R}_2 \times \underline{R}_3) \cdot \underline{R}_1) \underline{R}_3\} \cdot (\underline{R}_1 \times \underline{R}_2) = \\
&= \beta^3 \{\underline{R}_3 (\underline{R}_1 \times \underline{R}_2)\}^2 = (2\pi)^3 / [(\underline{R}_1 \times \underline{R}_2) \cdot \underline{R}_3] = (2\pi)^3 / V_{el} \quad (2.98)
\end{aligned}$$

and, thus,

$$V_G V_{el} = (2\pi)^3 \quad (2.99)$$

- (c) The **reciprocal** lattice of the **reciprocal** lattice of a real space lattice is identical to the **real** space lattice. This can be proven by simple vector calculus using relations (2.95) and (2.97) as discussed in Appendix F. Thus, we can write formally

$$\{\underline{R}_1, \underline{R}_2, \underline{R}_3\}^{-1} = \{\underline{G}_1, \underline{G}_2, \underline{G}_3\}, \quad \{\underline{G}_1, \underline{G}_2, \underline{G}_3\}^{-1} = \{\underline{R}_1, \underline{R}_2, \underline{R}_3\} \quad (2.100)$$

Explicit examples of reciprocal lattices are

- the **sc lattice** whose reciprocal lattice also defines an **sc** lattice, i.e.

$$\begin{aligned}
\underline{R}_1^{sc} &= a(1, 0, 0) & \underline{G}_1^{sc} &= 2\pi/a(1, 0, 0) \\
\underline{R}_2^{sc} &= a(0, 1, 0) & \underline{G}_2^{sc} &= 2\pi/a(0, 1, 0) \\
\underline{R}_3^{sc} &= a(0, 0, 1) & \underline{G}_3^{sc} &= 2\pi/a(0, 0, 1)
\end{aligned} \quad (2.101)$$

- the **fcc lattice** whose reciprocal lattice defines a **bcc** lattice, i.e.

$$\begin{aligned}
\underline{R}_1^{fcc} &= a/2(0, 1, 1) & \underline{G}_1^{fcc} &= 2\pi/a(-1, 1, 1) \\
\underline{R}_2^{fcc} &= a/2(1, 0, 1) & \underline{G}_2^{fcc} &= 2\pi/a(1, -1, 1) \\
\underline{R}_3^{fcc} &= a/2(1, 1, 0) & \underline{G}_3^{fcc} &= 2\pi/a(1, 1, -1)
\end{aligned} \quad (2.102)$$

- the **bcc lattice** whose reciprocal lattice defines an **fcc** lattice, i.e.

$$\begin{aligned}
\underline{R}_1^{bcc} &= a/2(-1, 1, 1) & \underline{G}_1^{bcc} &= 2\pi/a(0, 1, 1) \\
\underline{R}_2^{bcc} &= a/2(1, -1, 1) & \underline{G}_2^{bcc} &= 2\pi/a(1, 0, 1) \\
\underline{R}_3^{bcc} &= a/2(1, 1, -1) & \underline{G}_3^{bcc} &= 2\pi/a(1, 1, 0)
\end{aligned} \quad (2.103)$$

In general, lattice types and their symmetry properties in reciprocal space, defined by reciprocal lattice vectors  $\underline{G}_1, \underline{G}_2, \underline{G}_3$ , can be related with those of the corresponding real space lattices, lattice vectors  $\underline{R}_1, \underline{R}_2, \underline{R}_3$ . This is clear from Table 2.4 which lists for each of the 14 three-dimensional Bravais lattices discussed in Sec. 2.4 the corresponding reciprocal Bravais lattice.

Table 2.4. List of real and corresponding reciprocal Bravais lattices.

	<b>Real space lattice</b>	<b>Reciprocal space lattice</b>
1	Triclinic-P	Triclinic-P
2	Monoclinic-P	Monoclinic-P
3	Monoclinic-A, -B	Monoclinic-A, -B
4	Orthorhombic-P	Orthorhombic-P
5	Orthorhombic-A, -B, -C	Orthorhombic-A, -B, -C
6	Orthorhombic-I	Orthorhombic-F
7	Orthorhombic-F	Orthorhombic-I
8	Tetragonal-P	Tetragonal-P
9	Tetragonal-I	Tetragonal-I
10	Hexagonal-P	Hexagonal-P
11	Trigonal-R	Trigonal-R
12	Cubic-P (sc)	Cubic-P (sc)
13	Cubic-I (bcc)	Cubic-F (fcc)
14	Cubic-F (fcc)	Cubic-I (bcc)

Reciprocal lattice vectors are also useful for the decomposition of real space coordinates  $\underline{r}$  into multiples of lattice vectors  $\underline{R}_1, \underline{R}_2, \underline{R}_3$ . If a spatial coordinate  $\underline{r}$  is written as

$$\underline{r} = x_1 \underline{R}_1 + x_2 \underline{R}_2 + x_3 \underline{R}_3, \quad x_i \text{ real} \quad (2.104)$$

then the orthogonality theorem (2.96) yields for  $i = 1, 2, 3$

$$\underline{G}_i \underline{r} = x_1 (\underline{G}_i \underline{R}_1) + x_2 (\underline{G}_i \underline{R}_2) + x_3 (\underline{G}_i \underline{R}_3) = 2\pi x_i \quad (2.105)$$

Thus, the mixing coefficients  $x_i$  can be calculated as scalar products involving reciprocal lattice vectors.

Many physical properties of a perfect three-dimensional bulk crystal with its periodicity described by lattice vectors  $\underline{R}_1, \underline{R}_2, \underline{R}_3$  are characterized by functions  $f(\underline{r})$  which are periodic in space where the periodicity coincides with that of the crystal lattice, i.e.

$$f(\underline{r} + \underline{R}) = f(\underline{r}) \quad \text{with} \quad \underline{R} = n_1 \underline{R}_1 + n_2 \underline{R}_2 + n_3 \underline{R}_3, \quad n_i \text{ integer} \quad (2.106)$$

Examples are the electron density  $\rho(\underline{r})$  or the electrostatic potential  $V(\underline{r})$  in a perfect crystal. In a harmonic analysis (**Fourier analysis**) these periodic functions  $f(\underline{r})$  are represented by a (generally



infinite) series of harmonic functions written as exponentials  $\exp(i \underline{G} \underline{r})$  of imaginary argument ( $i$  being the imaginary unit number), i.e.

$$f(\underline{r}) = \sum_{\underline{G}} c_{\underline{G}} \exp(i \underline{G} \underline{r}) \quad \text{with} \quad \underline{G} = k_1 \underline{G}_1 + k_2 \underline{G}_2 + k_3 \underline{G}_3, \quad k_i \text{ integer} \quad (2.107)$$

Vectors  $\underline{G}$  in this expansion are linear combinations of reciprocal lattice vectors with integer-valued mixing coefficients  $k_i$  and  $c_{\underline{G}}$  are expansion coefficients of the series determined by integrals

$$c_{\underline{G}} = \frac{1}{V_{\text{el}}} \iiint_{V_{\text{el}}} f(\underline{r}) \exp(-i \underline{G} \underline{r}) d^3 r \quad (2.108)$$

where the three-dimensional integration is carried out over the elementary cell  $V_{\text{el}}$  of the real space lattice, for further mathematical details see Appendix G. Thus, the Fourier expansion (2.107) is based on a summation of terms which are determined by reciprocal lattice vectors. This is justified by real and reciprocal lattice vectors obeying the orthogonality theorem (2.96). According to

$$\begin{aligned} \underline{G} \underline{R} &= (k_1 \underline{G}_1 + k_2 \underline{G}_2 + k_3 \underline{G}_3) (n_1 \underline{R}_1 + n_2 \underline{R}_2 + n_3 \underline{R}_3) \\ &= 2\pi (k_1 n_1 + k_2 n_2 + k_3 n_3) = 2\pi N \end{aligned} \quad (2.109)$$

and

$$\exp(i 2\pi N) = 1, \quad N \text{ integer} \quad (2.110)$$

we obtain with (2.107)

$$f(\underline{r} + \underline{R}) = \sum_{\underline{G}} c_{\underline{G}} \exp(i \underline{G}(\underline{r} + \underline{R})) = \sum_{\underline{G}} c_{\underline{G}} \exp(i \underline{G} \underline{r}) \exp(i \underline{G} \underline{R}) = f(\underline{r}) \quad (2.111)$$

Thus, the Fourier series reproduces the periodicity (2.106).

## 2.6 Neighbor Shells

Geometric parameters of periodic crystals are fully described by their translational and point symmetries. However, in some cases physical and chemical properties may be represented more appropriately by considering local atom neighborhoods and relationships between atoms in spherical environments. This leads to the concept of **neighbor shells**. Neighbor shells start from an atom of the crystal and characterize its environment by surrounding atoms. Here, all atoms at a given **distance** or distance **range** with respect to the central atom and irrespective of their direction are collected to form a **shell**. The neighbor shells are ordered according to their **shell radii** (given by the

interatomic distances) where the closest shell with the smallest radius is sometimes called the (first) **coordination shell**. Then the atoms of the different shells span the complete crystal, if all radii up to infinity are considered.

Physical applications of the neighbor shell concept include shell models to describe lattice vibrations (balls-and-springs approach to phonons [52]), tight-binding methods [53] to describe electronic properties of crystals, or electrostatic potential calculations based on point charges in ionic crystals [54]. Fig. 2.31 illustrates the neighbor shell concept by sketching the six smallest shells

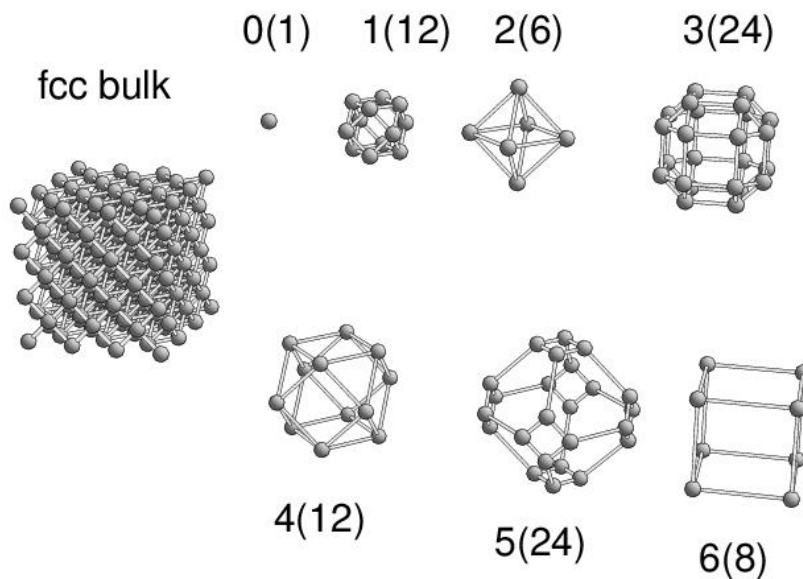


Fig. 2.31. Neighbor shells of a crystal with an fcc lattice. The labels ' $i(M_i)$ ' combine the shell index  $i$  (0 for central atom, 1 to 6) with the corresponding shell multiplicity  $M_i$  (1 to 24). A section of the fcc bulk crystal (labeled 'fcc bulk') is included to the left.

in a crystal with an fcc lattice. Further, Table 2.5 lists radii and numbers of atom members  $M_i$  (**shell multiplicities**) of the smallest six neighbor shells of crystals with cubic (sc, bcc, fcc) and hexagonal close-packed (hcp) lattices. Sometimes, the multiplicity of the smallest neighbor shell is also called the **coordination number** denoting the number of closest atom neighbors which can form direct bonds with the central atom.

Table 2.5. Radii  $D_i$  and shell multiplicities  $M_i$  of the smallest six neighbor shells of crystals with (a) simple (sc), (b) body-centered cubic (bcc), (c) face-centered (fcc), and (d) hexagonal close-packed (hcp) lattice, see text. The radii  $D_i$  are given with respect to the corresponding lattice constant  $a$  (with  $c/a = \sqrt{8/3}$  for hcp).

(a) sc			(b) bcc	
i	$M_i$	$D_i/a$	$M_i$	$D_i/a$
1	6	1 = 1.0000	8	$\sqrt{3/4} = 0.8660$
2	12	$\sqrt{2} = 1.4142$	6	1 = 1.0000
3	8	$\sqrt{3} = 1.7321$	12	$\sqrt{2} = 1.4142$
4	6	2 = 2.0000	24	$\sqrt{11/4} = 1.6583$
5	24	$\sqrt{5} = 2.2361$	8	$\sqrt{3} = 1.7321$
6	24	$\sqrt{6} = 2.4495$	6	2 = 2.0000

(c) fcc			(d) hcp	
i	$M_i$	$D_i/a$	$M_i$	$D_i/a$
1	12	$1/\sqrt{2} = 0.7071$	12	1 = 1.0000
2	6	1 = 1.0000	6	$\sqrt{2} = 1.4142$
3	24	$\sqrt{3/2} = 1.2247$	2	$\sqrt{8/3} = 1.6330$
4	12	$\sqrt{2} = 1.4142$	18	$\sqrt{3} = 1.7321$
5	24	$\sqrt{5/2} = 1.5811$	12	$\sqrt{11/3} = 1.9149$
6	8	$\sqrt{3} = 1.7321$	6	2 = 2.0000

The **formal definition** of a neighbor shell starts from a crystal with lattice vectors  $\underline{R}_1, \underline{R}_2, \underline{R}_3$  and a basis, given by atom positions  $r_1, \dots, r_p$ . Then the  $i^{\text{th}}$  neighbor shell  $S_i(\underline{R}_c, D_i, \varepsilon_i)$  inside a crystal is defined as a collection of crystal atoms surrounding a **shell center**  $\underline{R}_c$ , which may or may not coincide with the position of a crystal atom. The shell includes all atoms, at general positions  $\underline{R} = n_1 \underline{R}_1 + n_2 \underline{R}_2 + n_3 \underline{R}_3 + \underline{r}_i$ , whose distances  $D = |\underline{R} - \underline{R}_c|$  lie within the **shell range**,

$$(D_i - \varepsilon_i/2) \leq D \leq (D_i + \varepsilon_i/2) \quad (2.112)$$

where  $D_i$  defines the **shell radius** and  $\varepsilon_i$  the **shell thickness**. The number  $M_i$  of atoms belonging to a neighbor shell, also called the **shell multiplicity**, is determined by the position of the shell center  $\underline{R}_c$  in the crystal, the geometry of the crystal lattice, and its basis. Here monoatomic crystals with lattices of high symmetry, providing many atom pairs of identical distance, are expected to result in shells with large shell multiplicities  $M_i$  even for vanishing  $\varepsilon_i$ . On the other hand, crystals with lattices of low symmetry may lead to sets of shells, where, even for  $\varepsilon_i > 0$  ('fuzzy shells'), each shell

contains only few atoms such that the shell concept may not be useful. The determination of the **complete set of shells** for a perfect single crystal seems straightforward since all atom positions are defined mathematically. However, the actual computation can be quite tedious as will be illustrated in the following.

All atom positions inside a monoatomic crystal with a **simple cubic** (sc) lattice can be represented by vectors

$$\underline{\mathbf{R}} = n_1 \underline{\mathbf{R}}_1 + n_2 \underline{\mathbf{R}}_2 + n_3 \underline{\mathbf{R}}_3 = a (n_1, n_2, n_3) , \quad n_i \text{ integer} \quad (2.113)$$

in Cartesian coordinates with  $a$  denoting the lattice constant. Then, neighbor shells about the origin  $\underline{\mathbf{R}}_c = (0, 0, 0)$  with shell radius  $D_i$  and a range  $\varepsilon_i = 0$  can be defined, according to (2.112), by

$$D_i^2 = |\underline{\mathbf{R}} - \underline{\mathbf{R}}_c|^2 = R^2 = a^2 (n_1^2 + n_2^2 + n_3^2) \quad (2.114)$$

Thus, neighbor shells for radii  $D_i$  are determined by

$$D_i = a \sqrt{N_i} \quad (2.115)$$

where

$$N_i = n_1^2 + n_2^2 + n_3^2 \quad (2.116)$$

and  $N_i$ ,  $n_1$ ,  $n_2$ , and  $n_3$  are integer-valued. (**Shell indices**  $i$  count the shells according to the size of their radii.) Equation (2.116) forms a **quadratic Diophantine** equation for given  $N_i$  with possible solutions  $n_1$ ,  $n_2$ ,  $n_3$ . Depending on the specific values  $n_k$  of a solution, there are always alternative solutions and, thus, other shell members, which reflect the symmetry of the cubic lattice and determine the number of symmetry related shell members, also called the **symmetry related shell multiplicity**  $M_i^{\text{sym}}$ . Here we can distinguish six different cases, defined by constraints for the solutions  $n_i$ , as given in Table 2.6.

Table 2.6. Alternative solutions of Diophantine equation (2.116) and symmetry related shell multiplicities  $M_i^{\text{sym}}$ , see text.

Case	Constraints on $n_k$	Alternatives ( $n_1, n_2, n_3$ )	$M_i^{\text{sym}}$
1	$n_1 = n > 0,$ $n_2 = n_3 = 0$	$(\pm n, 0, 0), (0, \pm n, 0),$ $(0, 0, \pm n)$	6
2	$n_1 = n_2 = n > 0,$ $n_3 = 0$	$(\pm n, \pm n, 0), (\pm n, 0, \pm n),$ $(0, \pm n, \pm n)$	12
3	$n_1 = n_2 = n_3 = n > 0$	$(\pm n, \pm n, \pm n)$	8
4	$n_1 > 0, n_2 > 0,$ $n_1 \neq n_2, n_3 = 0$	$(\pm n_1, \pm n_2, 0), (\pm n_1, 0, \pm n_2),$ $(0, \pm n_1, \pm n_2), (\pm n_2, \pm n_1, 0),$ $(\pm n_2, 0, \pm n_1), (0, \pm n_2, \pm n_1)$	24
5	$n_1 > 0, n_1 \neq n,$ $n_2 = n_3 = n > 0$	$(\pm n_1, \pm n, \pm n), (\pm n, \pm n_1, \pm n),$ $(\pm n, \pm n, \pm n_1)$	24
6	$n_1 > 0, n_2 > 0,$ $n_3 > 0, n_1 \neq n_2,$ $n_1 \neq n_3, n_2 \neq n_3$	$(\pm n_1, \pm n_2, \pm n_3), (\pm n_1, \pm n_3, \pm n_2),$ $(\pm n_2, \pm n_1, \pm n_3), (\pm n_2, \pm n_3, \pm n_1),$ $(\pm n_3, \pm n_1, \pm n_2), (\pm n_3, \pm n_2, \pm n_1)$	48

In addition to the symmetry related shell multiplicities  $M_i^{\text{sym}}$  of the different shells there may be **accidental shell multiplicities**  $M_i^{\text{acc}}$ . They arise from the fact that equation (2.116) may have different solutions  $n_1, n_2, n_3$  where the actual absolute values  $n_k$  differ. This leads to neighbor shells with increased total shell multiplicity. Examples are listed in Table 2.7. In fact, accidental shell multiplicities  $M_i^{\text{acc}}$  of neighbor shells are responsible for the fact that

Table 2.7. Alternative solutions of Diophantine equation (2.116). Parameter  $M_i^{\text{tot}} = M_i^{\text{sym}} + M_i^{\text{acc}}$  denotes the total number of alternative solutions for each value of  $N_i$  including symmetry related and accidental shell multiplicities,

$N_i$	( $n_1, n_2, n_3$ )	$M_i^{\text{tot}}$
9	(3, 0, 0), (2, 2, 1)	$6 + 24 = 30$
25	(5, 0, 0), (4, 3, 0)	$6 + 24 = 30$
74	(8, 3, 1), (7, 5, 0), (7, 4, 3)	$48 + 24 + 48 = 120$
101	(10, 1, 0), (9, 4, 2), (8, 6, 1), (7, 6, 4)	$24 + 48 + 48 + 48 = 168$

**total shell multiplicities**  $M_i^{\text{tot}} = M_i^{\text{sym}} + M_i^{\text{acc}}$  do not have an upper limit when shell radii increase to an arbitrary size. In addition, total shell multiplicities  $M_i^{\text{tot}}$  depend on the shell radius in a chaotic fashion. While  $M_i^{\text{tot}}$  values increase on the average with shell radii there are always shells of very small total shell multiplicity. As examples we mention the 54<sup>th</sup> neighbor shell ( $N_i = 64, M_i^{\text{tot}} = 6$ ) and the 107<sup>th</sup> neighbor shell ( $N_i = 128, M_i^{\text{tot}} = 12$ ). Fig. 2.32a illustrates the chaotic behavior of  $M_i^{\text{tot}}$

with shell index for the first 100 neighbor shells of a crystal with a simple cubic lattice (shell no. 100 corresponds to a radius of 10.816 in units of the lattice constant  $a$ , see Fig. 2.33).

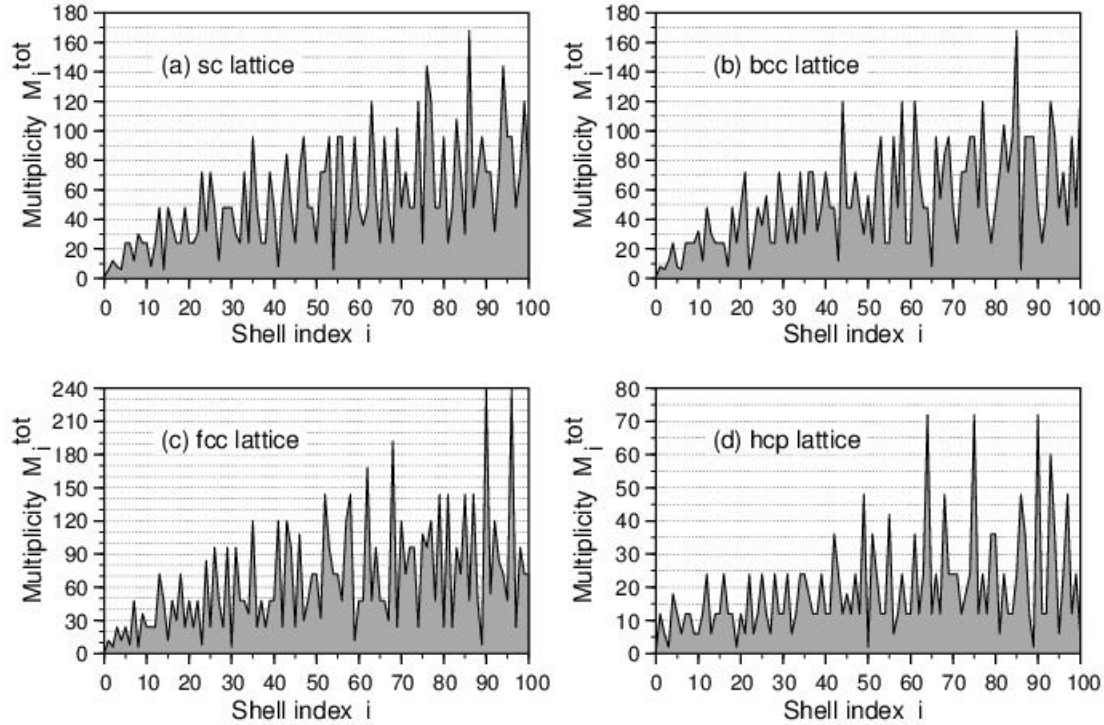


Fig. 2.32. Shell multiplicity  $M_i^{\text{tot}}$  as a function of the shell index  $i$  up to the 100<sup>th</sup> shell for crystals with an (a) sc, (b) bcc, (c) fcc, and (d) hexagonal close-packed (hcp) lattice. For the range of shell radii, see Fig. 2.33.

Note that equation (2.116) does not yield solutions for integer values  $N_i$  with  $N_i = 4^p (8q+7)$ , where  $p$  and  $q$  are positive integers as shown in Appendix E.4. This means, in particular, that  $N_i$  according to (2.116) is larger than  $i$  for  $i > 6$ . As a consequence, shell radii  $D_i$  of the sc lattice given by (2.115) do not scale with  $\sqrt{i}$ . This is also clear from Fig. 2.33 which shows the relative shell radii  $D_i/a$  as a function of the shell index  $i$  and demonstrates the deviation of  $D_i/a$  from the  $\sqrt{i}$  dependence for the sc lattice.

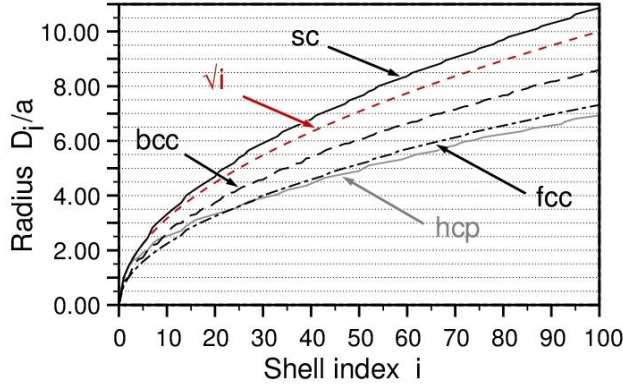


Fig. 2.33. Relative shell radii  $D_i/a$  as a function of the shell index  $i$  up to the 100<sup>th</sup> shell for crystals with an sc, bcc, fcc, and hexagonal close-packed (hcp) lattice, see text.

The results obtained for crystals with an sc lattice can be applied to crystals with **centered cubic** lattices. In Sec. 2.2.3 it was shown that the **bcc** lattice can be represented by non-primitive simple cubic lattice vectors  $\underline{R}_1$ ,  $\underline{R}_2$ ,  $\underline{R}_3$  with an additional lattice vector  $\underline{R}'$  pointing to the center of the morphological unit cell. Therefore, general lattice points can be described by **two sets** of lattice vectors, i.e. by

$$\underline{R} = n_1 \underline{R}_1 + n_2 \underline{R}_2 + n_3 \underline{R}_3 = a (n_1, n_2, n_3) , \quad n_i \text{ integer} \quad (2.117)$$

and by

$$\underline{R} = \underline{R}' + n_1 \underline{R}_1 + n_2 \underline{R}_2 + n_3 \underline{R}_3 = a (n_1 + 1/2, n_2 + 1/2, n_3 + 1/2) , \quad n_i \text{ integer} \quad (2.118)$$

in Cartesian coordinates. As a consequence, for a crystal with a bcc lattice, neighbor shells about the origin  $\underline{R}_c = (0, 0, 0)$  with shell radius  $D_i$  and a range  $\varepsilon_i = 0$  can be defined, according to (2.112), by two sets, by

$$D_i^2 = |\underline{R} - \underline{R}_c|^2 = a^2 (n_1^2 + n_2^2 + n_3^2) = a^2/4 ((2n_1)^2 + (2n_2)^2 + (2n_3)^2) \quad (2.119)$$

referring to vectors (2.117) and by

$$\begin{aligned} D_i^2 &= |\underline{R} - \underline{R}_c|^2 = a^2 ((n_1+1/2)^2 + (n_2+1/2)^2 + (n_3+1/2)^2) \\ &= a^2/4 ((2n_1+1)^2 + (2n_2+1)^2 + (2n_3+1)^2) \end{aligned} \quad (2.120)$$

referring to vectors (2.118). Thus, in both cases neighbor shells for shell radii  $D_i$  are determined by

$$D_i = a/2 \sqrt{N_i} \quad (2.121)$$

which agrees with the result for crystals with an sc lattice. However, the integers  $N_i$  are determined by **two** different quadratic Diophantine equations

$$N_i = (2n_1)^2 + (2n_2)^2 + (2n_3)^2 = 4 \{n_1^2 + n_2^2 + n_3^2\} \quad (2.122a)$$

and

$$N_i = (2n_1+1)^2 + (2n_2+1)^2 + (2n_3+1)^2 = 4 \{n_1^2 + n_2^2 + n_3^2 + n_1 + n_2 + n_3\} + 3 \quad (2.122b)$$

with possible solutions  $n_1, n_2, n_3$ . The  $N_i$  values of the two equations cannot coincide since  $N_i$  of equation (2.122a) must be even,  $N_i = 4P$  ( $P$  integer), to yield integers  $n_1, n_2, n_3$  while  $N_i$  of equation (2.122b) must be odd,  $N_i = 4P + 3$  ( $P$  integer). Further, equations (2.122a, b) can be understood as special cases of the quadratic Diophantine equation (2.116) defining neighbor shells of a crystal with a simple cubic lattice, however, with two separate sets of  $N_i$  values. Altogether, the complete set of neighbor shells of a crystal with a bcc lattice can be decomposed into **two disjoint sets**, corresponding to  $N_i = 4P$  and  $N_i = 4P + 3$ , which are each described by **selected shells** of a crystal with a simple cubic lattice and a lattice constant  $a/2$  according to (2.121).

As to the **symmetry related shell multiplicities**  $M_i^{\text{sym}}$  of the different shells, the first shell set, defined by equation (2.122a), allows all cases 1 to 6 of Table 2.6 while the second set, determined by equation (2.122b), is restricted to cases 3, 5, 6 (cases 1, 2, 4 apply to even numbers  $n_i$ ). Analogous to crystals with a simple cubic lattice, the **total shell multiplicities**  $M_i^{\text{tot}}$  of crystals with a bcc lattice depend on the shell radius in a chaotic fashion, with  $M_i^{\text{tot}}$  values increasing with shell radii on the average but also with shells of very small total shell multiplicity in between. As examples we mention the 65<sup>th</sup> neighbor shell ( $N_i = 48, M_i^{\text{tot}} = 8$ ) and the 86<sup>th</sup> neighbor shell ( $N_i = 64, M_i^{\text{tot}} = 6$ ). Fig. 2.32b shows the chaotic behavior of  $M_i^{\text{tot}}$  with shell index for the first 100 neighbor shells of a crystal with a bcc lattice (shell no. 100 corresponds to a radius of 8.602 in units of the lattice constant  $a$ , see Fig. 2.33).

The results for crystals with a bcc lattice can also be applied analogously the **cesium chloride** (CsCl) crystal. This crystal, shown in Fig. 2.2a, is described by an sc lattice and a basis of two atoms, Cs and Cl, where the primitive morphological unit cell contains Cs atoms at its corners and a Cl atom at its center (or vice versa), see Fig. 2.2b. Thus, if the element types were ignored, the lattice would be described as a bcc lattice. Therefore, according to (2.119), (2.120), (2.121), (2.122) the neighbor shell arrangement in the CsCl crystal is given by the **two sets** of shells found for crystals with a bcc lattice. Each set contains only one element type, **Cs** or **Cl**. This means, in particular, that for this ionic crystal neighbor shells contain ions of only one kind, of positive ( $\text{Cs}^+$ ) or of negative ( $\text{Cl}^-$ ) charge. However, the shells do not strictly alternate between positive and negative charge with increasing shell radius. As an illustration Table 2.8 lists the charge sequence for the first 20



neighbor shells starting at the center of a Cs atom (listed as shell no. 0).

Table 2.8. Charge sequence for the first 20 neighbor shells of the CsCl crystal starting at the center of a Cs atom (shell no. 0).

Shell no. (element)	0 (Cs)	1 (Cl)	2 (Cs)	3 (Cs)	4 (Cl)	5 (Cs)	6 (Cs)	7 (Cl)	8 (Cs)	9 (Cs)	10 (Cl)
Charge	+1	-8	+6	+12	-24	+8	+6	-24	+24	+24	-32

Shell no. (element)	11 (Cs)	12 (Cl)	13 (Cs)	14 (Cs)	15 (Cl)	16 (Cs)	17 (Cs)	18 (Cl)	19 (Cs)	20 (Cs)
Charge	+12	-48	+30	+24	-24	+24	+8	-48	+24	+48

The results obtained for crystals with an sc lattice can also be applied to crystals with an **fcc** lattice. In Sec. 2.2.3 it was shown that the fcc lattice can be represented by non-primitive simple cubic lattice vectors  $\underline{R}_1$ ,  $\underline{R}_2$ ,  $\underline{R}_3$  with three additional lattice vectors  $\underline{R}^{(1)}$ ,  $\underline{R}^{(2)}$ ,  $\underline{R}^{(3)}$ , pointing to the centers of the three unique faces of the morphological unit cell. Therefore, general lattice points can be described by **four sets** of lattice vectors, i.e. by

$$\underline{R} = \underline{r}_c + n_1 \underline{R}_1 + n_2 \underline{R}_2 + n_3 \underline{R}_3 \quad \text{with} \quad \underline{r}_c = \underline{R}^{(0)} = \underline{0}, = \underline{R}^{(1)}, = \underline{R}^{(2)}, = \underline{R}^{(3)} \quad (2.123)$$

yielding in Cartesian coordinates

$$\begin{aligned} \underline{R}^{(0)} &= (0, 0, 0) , \quad \underline{R} = a/2 ( 2n_1, 2n_2, 2n_3 ) , \\ \underline{R}^{(1)} &= a/2 ( 0, 1, 1 ) , \quad \underline{R} = a/2 ( 2n_1, 2n_2+1, 2n_3+1 ) , \\ \underline{R}^{(2)} &= a/2 ( 1, 0, 1 ) , \quad \underline{R} = a/2 ( 2n_1+1, 2n_2, 2n_3+1 ) , \\ \underline{R}^{(3)} &= a/2 ( 1, 1, 0 ) , \quad \underline{R} = a/2 ( 2n_1+1, 2n_2+1, 2n_3 ) , \quad n_i \text{ integer} \end{aligned} \quad (2.124)$$

As a consequence, for a crystal with an fcc lattice, neighbor shells about the origin  $\underline{R}_c = (0, 0, 0)$  with shell radius  $D_i$  and a range  $\varepsilon_i = 0$  can be defined, according to (2.112), by four sets, by

$$\begin{aligned} D_i^2 &= |\underline{R} - \underline{R}_c|^2 = a^2/4 \{ (2n_1)^2 + (2n_2)^2 + (2n_3)^2 \} , \\ D_i^2 &= |\underline{R} - \underline{R}_c|^2 = a^2/4 \{ (2n_1)^2 + (2n_2+1)^2 + (2n_3+1)^2 \} , \\ D_i^2 &= |\underline{R} - \underline{R}_c|^2 = a^2/4 \{ (2n_1+1)^2 + (2n_2)^2 + (2n_3+1)^2 \} , \\ D_i^2 &= |\underline{R} - \underline{R}_c|^2 = a^2/4 \{ (2n_1+1)^2 + (2n_2+1)^2 + (2n_3)^2 \} , \quad n_i \text{ integer} \end{aligned} \quad (2.125)$$

referring to vectors  $\underline{R}$  according to (2.124). Thus, in all four cases neighbor shells for shell radii  $D_i$

are determined by

$$D_i = a/2 \sqrt{N_i} \quad (2.126)$$

which agrees with the result for crystals with sc and bcc lattices. However, the integers  $N_i$  are now determined by **four** different quadratic Diophantine equations

$$N_i = (2n_1)^2 + (2n_2)^2 + (2n_3)^2 = 4 \{n_1^2 + n_2^2 + n_3^2\} \quad (2.127a)$$

$$N_i = (2n_1)^2 + (2n_2+1)^2 + (2n_3+1)^2 = 4 \{n_1^2 + n_2^2 + n_3^2 + n_2 + n_3\} + 2 \quad (2.127b)$$

$$N_i = (2n_1+1)^2 + (2n_2)^2 + (2n_3+1)^2 = 4 \{n_1^2 + n_2^2 + n_3^2 + n_1 + n_3\} + 2 \quad (2.127c)$$

$$N_i = (2n_1+1)^2 + (2n_2+1)^2 + (2n_3)^2 = 4 \{n_1^2 + n_2^2 + n_3^2 + n_1 + n_2\} + 2 \quad (2.127d)$$

with possible solutions  $n_1, n_2, n_3$ . Here equation (2.127a) yields integers  $n_1, n_2, n_3$  only for  $N_i = 4P$  ( $P$  integer), whereas equations (2.127b-d) yield integers  $n_1, n_2, n_3$  for  $N_i = 4P + 2$  ( $P$  integer). Thus,  $N_i$  values of the three equations (2.127b-d) can coincide whereas they cannot coincide with  $N_i$  values of equation (2.127a). Further, equations (2.127a-d) can be considered as special cases of the quadratic Diophantine equation (2.116) defining neighbor shells of a crystal with a simple cubic lattice, however, with two separate sets of  $N_i$  values. Altogether, the complete set of neighbor shells of a crystal with an fcc lattice can be decomposed into **two disjoint sets**, corresponding to  $N_i = 4P$  and  $N_i = 4P + 2$ , which are described each by **selected shells** of a crystal with a simple cubic lattice and a lattice constant  $a/2$  according to (2.121).

As to **symmetry related shell multiplicities**  $M_i^{\text{sym}}$  of the different shells, the first shell set, defined by equation (2.127a), refers to all cases 1 to 6 of Table 2.6. The second set, determined by equations (2.127b-d), is restricted to cases 2, 4, 5, 6 (cases 1, 3 do not allow one even and two odd numbers  $n_i$ ). Analogous to crystals with sc and bcc lattices, the **total shell multiplicities** of crystals with an fcc lattice depend on the shell radius in a chaotic fashion with  $M_i^{\text{tot}}$  values increasing with shell radii on the average but also with shells of very small total shell multiplicity in between. As examples we mention the 30<sup>th</sup> neighbor shell ( $N_i = 16, M_i^{\text{tot}} = 6$ ) and the 90<sup>th</sup> neighbor shell ( $N_i = 48, M_i^{\text{tot}} = 8$ ). Fig. 2.32c illustrates the chaotic behavior of  $M_i^{\text{tot}}$  with shell index for the first 100 neighbor shells of a crystal with an fcc lattice (shell no. 100 corresponds to a radius of 7.316 in units of the lattice constant  $a$ , see Fig. 2.33).

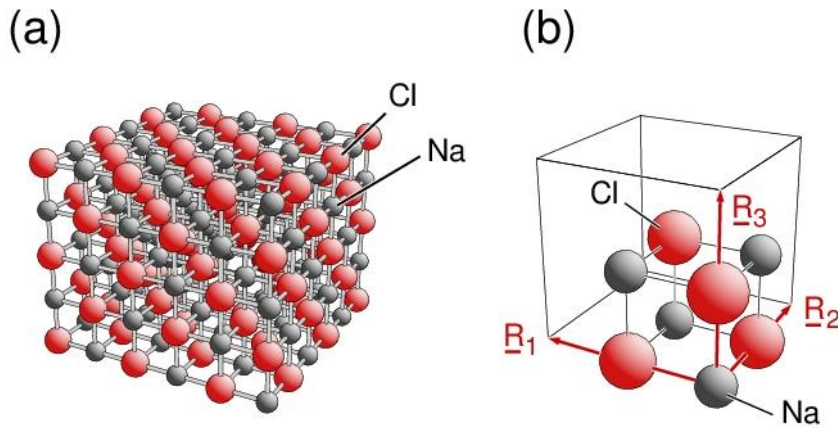


Fig. 2.34. (a) Section of a cubic NaCl crystal. Sticks connect Na with neighboring Cl atoms to indicate the crystal structure. (b) Primitive morphological unit cell with eight atoms,  $4 \times \text{Na}$  and  $4 \times \text{Cl}$ , inside. The lattice vectors  $\underline{R}_1$ ,  $\underline{R}_2$ ,  $\underline{R}_3$  are labeled accordingly

The results for crystals with sc and fcc lattices can also be applied to the **sodium chloride** (NaCl) crystal. This crystal, shown in Fig. 2.34a can be defined by a simple cubic lattice and a basis of eight atoms, four Na and Cl each. The primitive morphological unit cell contains Na atoms at its corners as well as at the centers of the three unique faces, while Cl atoms reside in the cell center and at midpoints of all unique edges, see Fig. 2.34b. (Na and Cl atoms can be interchanged in the definition.) In fact the two elemental parts of the crystal can both be characterized by fcc lattices shifted with respect to each other. Further, if the element types were ignored, the lattice would be described by a simple cubic lattice of lattice constant  $a/2$ . Therefore, according to the previous discussion, the neighbor shell arrangement of the NaCl crystal is given by the **two sets** of shells for the **Na** part, described by equations (2.127a-d) for a crystal with an fcc lattice, where  $N_i = 4P$  or  $N_i = 4P + 2$ . Further, the shells of the Cl part can be shown to be described by

$$\begin{aligned}
 N_i &= (2n_1+1)^2 + (2n_2+1)^2 + (2n_3+1)^2 = 4 \{n_1^2 + n_2^2 + n_3^2 + n_1 + n_2 + n_3\} + 3 \\
 N_i &= (2n_1+1)^2 + (2n_2)^2 + (2n_3)^2 = 4 \{n_1^2 + n_2^2 + n_3^2 + n_1\} + 1 \\
 N_i &= (2n_1)^2 + (2n_2+1)^2 + (2n_3)^2 = 4 \{n_1^2 + n_2^2 + n_3^2 + n_2\} + 1 \\
 N_i &= (2n_1)^2 + (2n_2)^2 + (2n_3+1)^2 = 4 \{n_1^2 + n_2^2 + n_3^2 + n_3\} + 1
 \end{aligned} \tag{2.128}$$

leading to  $N_i = 4P+1$  or  $N_i = 4P+3$ . This also defines **two sets** of shells of the **Cl** part. Thus, the shell arrangement in the NaCl lattice is given by **four sets** of shells, two for Na and Cl each, which are disjoint and contain only one element type. Therefore, neighbor shells of ionic crystals of the NaCl type contain ions of only one kind, of positive ( $\text{Na}^+$ ) or of negative ( $\text{Cl}^-$ ) charge, analogous to

CsCl discussed above. Further, the ionic  $\text{Na}^+$  and  $\text{Cl}^-$  shells do not strictly alternate with increasing shell radius, also in analogy with CsCl. As an illustration Table 2.9 lists the charge sequence for the first 20 neighbor shells starting at the center of a Na atom (listed as shell no. 0).

Table 2.9. Charge sequence for the first 20 neighbor shells of the NaCl lattice starting at the center of a Na atom (denoted as shell no. 0).

<b>Shell no.</b>	0	1	2	3	4	5	6	7	8	9	10
<b>(element)</b>	(Na)	(Cl)	(Na)	(Cl)	(Na)	(Cl)	(Na)	(Na)	(Cl)	(Na)	(Cl)
<b>Charge</b>	+1	-6	+12	-8	+6	-24	+24	+12	-30	+24	-24

<b>Shell no.</b>	11	12	13	14	15	16	17	18	19	20
<b>(element)</b>	(Na)	(Cl)	(Na)	(Na)	(Cl)	(Na)	(Cl)	(Na)	(Cl)	(Na)
<b>Charge</b>	+8	-24	+48	+6	-48	+36	-24	+24	-48	+24

Crystals with a **hexagonal** lattice and close-packed (**hcp**) structure (i.e. with  $c/a = \sqrt{8/3}$ ) and two identical atoms in the primitive unit cell, see Fig. 2.10) are described by neighbor shells surrounding atoms, which have, at larger distances, less atom members in each shell compared to the fcc lattice of equal atom density. This is confirmed by Fig. 2.32d, which shows the chaotic behavior of  $M_i^{\text{tot}}$  with increasing shell radius for the first 100 neighbor shells (shell no. 100 corresponds to a radius of  $6.931 a$ , where  $a$  is the lattice constant, see Fig. 2.33).

There are **no explicit** formulas to determine properties, such as radius or shell multiplicity, of the  $n^{\text{th}}$  neighbor shell of a given lattice. However there is a simple **strategy** to evaluate neighbor shells up to a maximum radius  $D_{\text{max}}$  in a crystal with its lattice described by any lattice vectors  $\underline{R}_1$ ,  $\underline{R}_2$ ,  $\underline{R}_3$  and with a corresponding basis. For the sake of simplicity, we confine ourselves to crystals with one atom in the primitive unit cell and primitive lattice vectors  $\underline{R}_1$ ,  $\underline{R}_2$ ,  $\underline{R}_3$ . Then, after selecting a shell center  $\underline{R}_c$  inside the morphological unit cell we build a polyhedral cell around  $\underline{R}_c$  including all atom positions  $\underline{R}$  with respect to the shell center, i.e.

$$\underline{R} = n_1 \underline{R}_1 + n_2 \underline{R}_2 + n_3 \underline{R}_3 - \underline{R}_c \quad \text{with} \quad -N_k \leq n_k \leq N_k, \quad k = 1, 2, 3 \quad (2.129)$$

The inscribed sphere of this polyhedral cell, centered at  $\underline{R}_c$ , has a radius  $D_{\text{max}}$  which is given by the smallest of three lengths, i.e. by

$$\begin{aligned}
D_{\max} &= \min \left( \left| N_1 \underline{\mathbf{R}}_1 \cdot \frac{(\underline{\mathbf{R}}_2 \times \underline{\mathbf{R}}_3)}{|\underline{\mathbf{R}}_2 \times \underline{\mathbf{R}}_3|} \right|, \left| N_2 \underline{\mathbf{R}}_2 \cdot \frac{(\underline{\mathbf{R}}_3 \times \underline{\mathbf{R}}_1)}{|\underline{\mathbf{R}}_3 \times \underline{\mathbf{R}}_1|} \right|, \left| N_3 \underline{\mathbf{R}}_3 \cdot \frac{(\underline{\mathbf{R}}_1 \times \underline{\mathbf{R}}_2)}{|\underline{\mathbf{R}}_1 \times \underline{\mathbf{R}}_2|} \right| \right) = \\
&= V_{\text{el}} \min \left( \frac{N_1}{|\underline{\mathbf{R}}_2 \times \underline{\mathbf{R}}_3|}, \frac{N_2}{|\underline{\mathbf{R}}_3 \times \underline{\mathbf{R}}_1|}, \frac{N_3}{|\underline{\mathbf{R}}_1 \times \underline{\mathbf{R}}_2|} \right) \quad (2.130)
\end{aligned}$$

Fig. 2.35 illustrates the inscribed sphere for a polyhedral cell of a crystal with triclinic-P lattice with  $N_1 = N_2 = N_3 = 2$ .

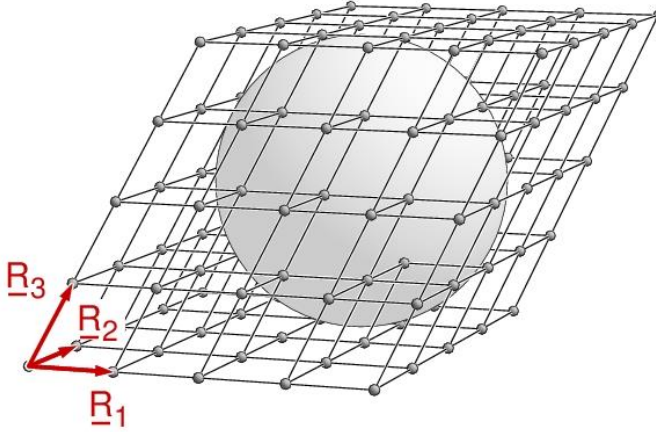


Fig. 2.35. Polyhedral cell of a crystal with triclinic-P lattice with inscribed sphere. The lattice vectors are labeled accordingly.

As a next step we evaluate all atom positions of the polyhedral cell according to (2.129) together with their distances  $D$  with respect to the center  $\underline{\mathbf{R}}_c$  given by

$$D = |\underline{\mathbf{R}}| = |n_1 \underline{\mathbf{R}}_1 + n_2 \underline{\mathbf{R}}_2 + n_3 \underline{\mathbf{R}}_3 - \underline{\mathbf{R}}_c| \quad (2.131)$$

Sorting these atom positions according to their  $D$  values in increasing order and grouping those with equal (or very similar) distances yields neighbor shells with respect to  $\underline{\mathbf{R}}_c$  where, however, only those shells with  $D \leq D_{\max}$  are guaranteed to be complete. Determining shells of radii larger than  $D_{\max}$  is achieved by increasing the ranges  $N_i$  in (2.130) and going through the same procedure.

The concept of neighbor shells also becomes important for bulk crystals with a **surface**. There the truncation of the perfect three-dimensional crystal, yielding the crystal substrate below and vacuum above, creates atom environments near the surface which are incomplete if compared with perfect bulk environments. This will be discussed in more detail in Sec. 4.1.

## 2.7 Nanoparticles and Crystallites

Finite size particles are characterized by aggregates of atoms which can be of the same element type but are exposed to different local environments depending on their location inside the particle or at its surface. Atoms close to the particle surface are coordinated with fewer atom neighbors compared to those near the particle center which influences their interatomic binding and affects the particle structure. This is different from the atom arrangement inside a perfect monoatomic crystal with its three-dimensional periodicity which results in equivalent atom centers and, thus, leads to identical binding environments and atom coordination. The inhomogeneity of atom environments in finite particles depends strongly on the particle size since the relative number of surface atoms compared with those of the inner particle core becomes smaller with increasing size. Thus, one might expect that deviations from a crystalline bulk structure become less important for most of the atoms as the particle size increases.

In many cases, structural properties of **clusters** with only a few atoms, typically 1 to 200, do not reflect those of corresponding bulk crystals. Here structural details depend on the specific cluster and there are no general guidelines as to interatomic distances or angles or as to symmetry. As an example, density-functional theory studies on silver clusters with up to 12 atoms,  $\text{Ag}_n$ ,  $n = 2, \dots, 12$ , [55] have identified equilibrium structures which differ substantially from those of sections of the face-centered cubic crystal found for bulk silver. This is illustrated by Fig. 2.36 which shows two energetically very close isomers of the  $\text{Ag}_7$  cluster, (a) a tricapped tetrahedron (also verified by experiment) and (b) a pentagonal bipyramid where in both isomers interatomic distances  $d_{\text{Ag-Ag}}$  close to  $2.7 \text{ \AA}$  on the average are obtained. This is considerably smaller than the nearest neighbor value  $d_{\text{Ag-Ag}} = 2.89 \text{ \AA}$  in the fcc silver crystal. Further, the isomer (b) includes a 5-fold rotation symmetry axis which is forbidden in bulk crystals as discussed in Sec. 2.4.

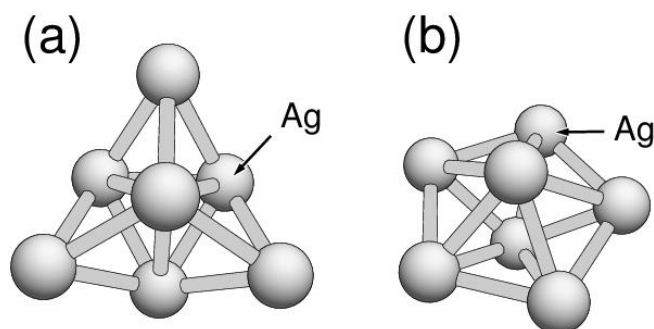


Fig. 2.36. Balls-and-sticks models of two isomers of the  $\text{Ag}_7$  cluster, (a) tricapped tetrahedron and (b) pentagonal bipyramid.

Larger metal clusters are also found to exhibit symmetry properties which are not compatible with those of bulk crystals. As examples, many alkaline earth (Be, Mg, Ca, Sr) and transition metal clusters (Ni, Co) in gas phase, the former with up to 5000 atoms [56], are believed to form compact particles with **icosahedral symmetry** for selected atom numbers  $N$ , so-called **magic numbers**, for which particles  $\text{Me}_N$  are found to occur in preferred abundance. However, icosahedral symmetry cannot appear in perfect bulk crystals since it includes 5-fold rotational axes.

The geometric definition of an icosahedral cluster is based on the concept of **polyhedral atom shells** of increasing size about a central atom where the shells are of icosahedral symmetry  $I_h$ . These compact closed shells consist of planar sections of triangular shape where the equilateral triangles are filled by close-packed (hexagonal) arrays of atoms with  $n$  atoms at each triangle side. Each triangle shares its three edges with adjacent triangles where five triangles meet at corners which are centers of 5-fold rotational axes. This yields, altogether, shells with 20 triangles sharing 30 identical edges and 12 corners. As an illustration, Fig. 2.37 shows icosahedral shells for  $n = 2, 4,$  and  $9$  atoms per edge which form the outer shells of icosahedral clusters of  $N = 13, 147,$  and  $2057$  atoms, respectively.

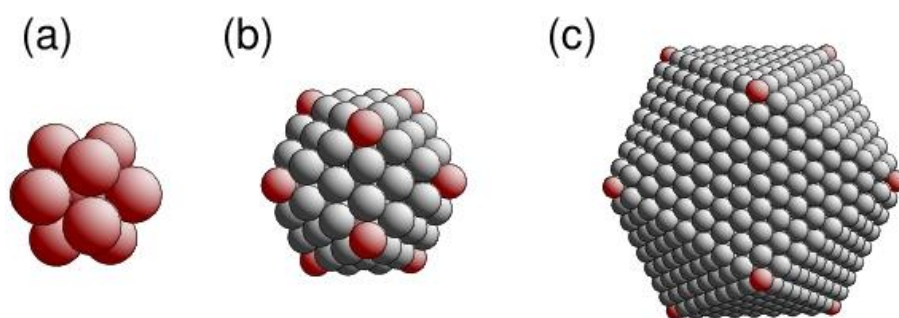


Fig. 2.37. Atom ball models of icosahedral shells for (a)  $n = 2,$  (b)  $n = 4,$  (c)  $n = 9,$  see text. Corner atoms are emphasized by red shading.

If the shell edges contain  $n$  atoms each, the total number of atoms  $n_s(n)$  of the  $n^{\text{th}}$  icosahedral shell ( $n > 1$ ) amounts to

$$n_s(n) = 20 \left( 3 \frac{1}{5} + 3(n-2) \frac{1}{2} + \frac{1}{2}(n-3)(n-2) \right) = 10(n-1)^2 + 2 \quad (2.132)$$

and the normalized distance  $r_a(n)$  of the corner atoms from the shell center (neglecting any surface relaxations of the atomic positions) is, after some trigonometric calculus, given by

$$r_a(n) = \frac{r(n)}{a} = \left( \frac{1}{2} \sqrt{1 + \frac{2}{3-\sqrt{5}}} \right) (n-1) = 0.95106 \cdot (n-1) \quad (2.133)$$

where  $a$  is the distance between neighboring atoms on the shell. Further, the combination of  $n$  concentric icosahedral shells to form an icosahedral cluster yields  $N(n)$  atoms where

$$N(n) = 1 + \sum_{i=2}^n n_s(i) = \frac{1}{3}(2n-1)[5n(n-1)+3] \quad (2.134)$$

Numbers  $N(n)$  are usually called **magic numbers** and have been discussed in mathematical detail in the literature [57]. In the larger icosahedral clusters,  $n > 4$ , one can distinguish between atoms inside the cluster ('bulk' atoms) which experience a full nearest neighbor environment of 12 atoms (6 at distances  $d = 0.951 a$  and 6 at  $d = a$ , respectively) and atoms of the outer shell ('surface' atoms) where the environment consists of 6 (1 at  $d = 0.951 a$  and 5 at  $d = a$ , corner), 8 (2 at  $d = 0.951 a$  and 6 at  $d = a$ , edge), or 9 (3 at  $d = 0.951 a$  and 6 at  $d = a$ , facet inside triangle) atoms. The ratio of the number of surface and bulk atoms  $\rho(n)$  given by

$$\rho(n) = \frac{n_s(n)}{(N(n) - n_s(n))} \quad (2.135)$$

decreases with increasing cluster size converging to  $\rho(n) \approx 3/n$  for  $n \gg 1$ . Table 2.10 lists shell and cluster sizes as well as relative radii of corner atoms for icosahedral clusters up to 3000 atoms.



Table 2.10. Shell sizes  $n_s(n)$ , cluster sizes  $N(n)$ , normalized radii  $r_a(n)$  of corner atoms, and ratio of surface to bulk atoms  $\rho(n)$  for icosahedral and cuboctahedral clusters with up to 3000 atoms. The values of  $n_s(n)$ ,  $N(n)$ , and  $\rho(n)$  are valid for both cluster types while  $r_a(n)$  values differ with the results for cuboctahedral clusters added in parentheses

<b>n</b>	<b><math>n_s(n)</math></b>	<b><math>N(n)</math></b>	<b><math>r_a(n)</math></b>	<b><math>\rho(n)</math></b>
1	1	1	---	---
2	12	13	0.951 (1.000)	12.000
3	42	55	1.902 (2.000)	3.231
4	92	147	2.853 (3.000)	1.673
5	162	309	3.804 (4.000)	1.102
6	252	561	4.755 (5.000)	0.816
7	362	923	5.706 (6.000)	0.645
8	492	1415	6.657 (7.000)	0.533
9	642	2057	7.609 (8.000)	0.454
10	812	2869	8.560 (9.000)	0.395

Large metal clusters have also been found to exhibit symmetry which can be associated with finite sections of cubic bulk crystal structures, both face- and body-centered cubic. Here examples are aluminum and indium clusters between 1000 and 10000 atoms in gas phase [56] which are suggested to form compact particles with **cubic symmetry**, reflecting sections of the fcc bulk crystal, where for selected atom numbers  $N$  (**magic numbers**) the metal clusters are found to occur in preferred abundance. Amongst these, **cuboctahedral** cluster shapes have been discussed [56].

As in the icosahedral case, a cuboctahedral cluster can be constructed by packing polyhedral atom shells of increasing size about a central atom where, however, the shells are of cubic symmetry  $O_h$ . They consist of planar sections of both triangular and square shape. The equilateral triangles are filled by close-packed (hexagonal) arrays of atoms with  $n$  atoms at each triangle side while the squares reflect  $n \times n$  square arrays of atoms where the nearest neighbor distances agree with those of the triangular sections. This yields a lower atom packing inside the squares compared with the triangles. Each triangle shares its three edges with adjacent squares and squares are connected only with triangles at their edges. Further, two triangles and two squares join at each corner of the cluster. This yields altogether shells with 8 triangles and 6 squares sharing 24 identical edges and 12

corners. Fig. 2.38 shows cuboctahedral shells for  $n = 2, 4,$  and  $9$  atoms per edge which form the outer shells of cuboctahedral clusters of  $N = 13, 147,$  and  $2057$  atoms, respectively.

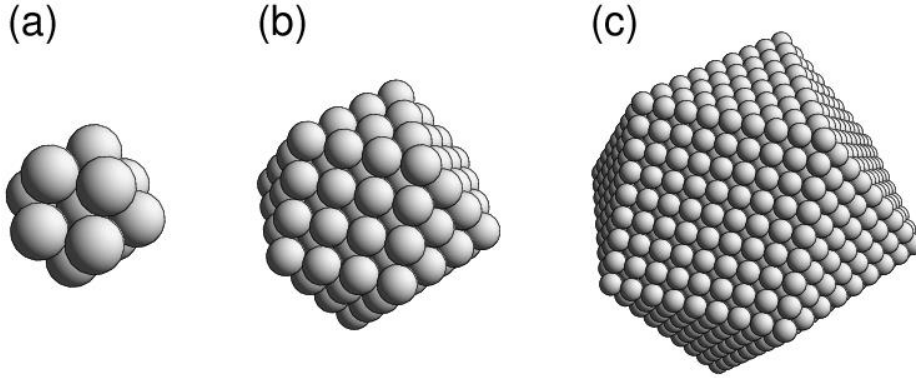


Fig. 2.38. Atom ball models of cuboctahedral shells for (a)  $n = 2,$  (b)  $n = 4,$  (c)  $n = 9,$  see text. Corner atoms are emphasized by red shading.

If the shell edges contain  $n$  atoms each, the 8 triangular sections account for

$$n_s^{\text{tria}}(n) = 8 \left( 3 \frac{1}{4} + 3(n-2) \frac{1}{2} + \frac{1}{2} (n-3)(n-2) \right) = 4(n-1)^2 + 2 \quad (2.136)$$

atoms and the 6 square sections for

$$n_s^{\text{sqr}}(n) = 6 \left( 4 \frac{1}{4} + 4(n-2) \frac{1}{2} + (n-2)^2 \right) = 6(n-1)^2 \quad (2.137)$$

atoms which yields a total number of atoms  $n_s(n)$  of the  $n^{\text{th}}$  cuboctahedral shell ( $n > 1$ ) with

$$n_s(n) = n_s^{\text{tria}}(n) + n_s^{\text{sqr}}(n) = 10(n-1)^2 + 2 \quad (2.138)$$

which, according to (2.132), agrees with the atom count of the  $n^{\text{th}}$  icosahedral shell. The normalized distance  $r_a(n)$  of the corner atoms from the shell center (shell radius) is given by

$$r_a(n) = \frac{r(n)}{a} = (n-1) \quad (2.139)$$

where  $a$  is the distance between neighboring atoms on the shell. Since the atom count of cuboctahedral shells (2.138) is identical to that of icosahedral shells the total numbers of atoms  $N(n)$  in a cuboctahedral cluster agrees with the corresponding icosahedral value and is given by (2.134). Thus, the magic numbers  $N(n)$  are identical for cuboctahedral and icosahedral clusters [57] while the atom packing differs between the two cluster types. The distinction between atoms inside the cluster ('bulk' atoms) and those of the outer shell ('surface' atoms) for larger cuboctahedral clusters,  $n > 3,$

is analogous to that for icosahedral clusters. Here bulk atoms experience the nearest neighbor environment of 12 atoms (at distances  $d = a$ ) which is identical to the geometry inside the fcc bulk crystal. In contrast, the environment of surface atoms consists of 5 (corner), 7 (edge), 8 (inside square), or 9 (inside triangle) atoms with identical distances  $d = a$ . In addition, the ratio of the number of surface and bulk atoms  $\rho(n)$  given by (2.135) yields values which agree for corresponding cuboctahedral and icosahedral clusters.

Clusters of cuboctahedral shape and moderate size, up to 1000 atoms, represent a fairly good approximation to spherical particles since the atoms of the different planar sections do not vary too much in their distance from the cluster center. This is illustrated in Fig. 2.39 which compares the cuboctahedral cluster for  $n = 4$  (147 atoms) with a ‘spherical’ cluster which contains all atoms inside a sphere whose radius is equal to the radius  $r_a$  of the corner atoms of the cuboctahedral cluster. The spherical cluster, containing 177 atoms, differs from the cuboctahedral cluster only by 5 additional atoms (painted red in Fig. 2.39b) sitting on top of each square section and roughening the cluster surface. Clearly, the difference between cuboctahedral and corresponding spherical clusters will become larger with increasing cluster size when more atoms can fill the void between the planar shell sections and the spherical boundary resulting in smooth transitions between planar shell sections of high packing density.

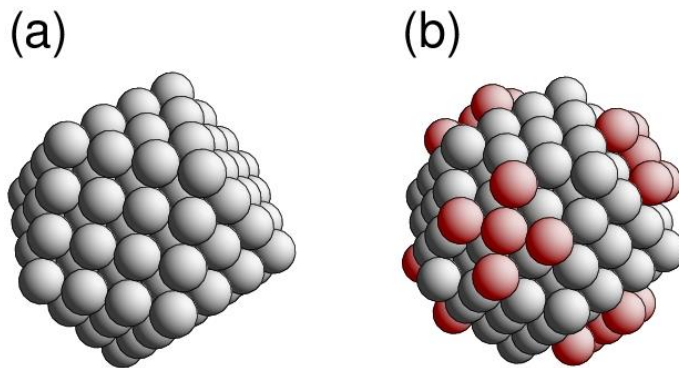


Fig. 2.39. Comparison of atom ball models of (a) the cuboctahedral cluster ( $n = 4$ , see Fig. 2.38b) with (b) a cluster of similar size with spherical constraints. Atom balls outside the cuboctahedron are emphasized by red shading.

Other high-symmetry sections of **face-centered cubic** bulk crystals have been suggested in the literature [56], [57] as possible structures of metal clusters where we mention only **simple octahedral** clusters whose closed shells consist of 8 planar sections of equilateral triangular shape filled by close-packed (hexagonal) arrays of atoms resulting in 12 identical edges with  $n$  atoms each and 6

corners. This leads to closed shell clusters with  $N(n)$  atoms (magic numbers),  $n_s(n)$  atoms per shell, and normalized shell radii  $r_a(n)$  given by

$$N(n) = \frac{1}{3}n(2n^2 + 1) \quad , \quad n_s(n) = 4(n-1)^2 + 2 \quad , \quad r_a(n) = \frac{1}{\sqrt{2}}(n-1) \quad (2.140)$$

where clusters with odd  $n$  contain an atom in the cluster center while for even  $n$  the cluster center is void. As an illustration, Fig. 2.40a shows a simple octahedral cluster for  $n = 7$  containing 231 atoms. Also more complex cubic cluster structures with polyhedral shells representing mixtures of square and hexagonal sections have been considered. Here we mention only the **truncated octahedral** type, shown with 201 atoms in Fig. 2.40b, which is obtained from a simple octahedral cluster by cutting off the 6 corners symmetrically. This cluster shape is reminiscent of the Wigner-Seitz cell of a body-centered cubic crystal, see Sec. 2.3. The corresponding clusters consist of 6 square and 8 hexagonal sections forming 36 identical edges with  $n$  atoms each and 24 corners. The closed shell clusters are characterized by

$$N(n) = 16n^3 - 33n^2 + 24n - 6 \quad ,$$

$$n_s(n) = 30(n-1)^2 + 2 \quad , \quad r_a(n) = \frac{\sqrt{10}}{2}(n-1) \quad (2.141)$$

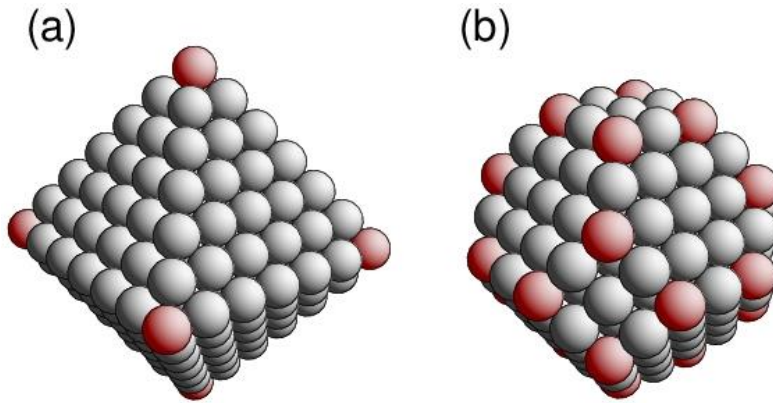


Fig. 2.40. Atom ball models of clusters (a) simple octahedral with  $n = 7$  (231 atoms), (b) truncated octahedral with  $n = 3$  (201 atoms). Corner atoms are emphasized by red shading.

Further, metal atom clusters of high-symmetry described by sections of **body-centered cubic** bulk crystals have been discussed in the literature [56] where we mention only **dodecahedral** and **truncated dodecahedral** clusters, shown in Fig. 2.41. The dodecahedral shells consist of 12 identical rhombohedral sections each which are filled with close-packed arrays of atoms (distorted hex-

agonal, reflecting the densest planar packing inside the bcc crystal). The cluster shape, see Fig. 2.41a, is reminiscent of the Wigner-Seitz cell of a face-centered cubic crystal, see Sec. 2.3. Truncated dodecahedral clusters, see Fig. 2.41b, are obtained from dodecahedral clusters by cutting off the 6 corners symmetrically. The resulting cluster shells contain 6 square and 12 distorted hexagonal sections each and are similar to the Wigner-Seitz cell of a body-centered cubic crystal, see Sec. 2.3.

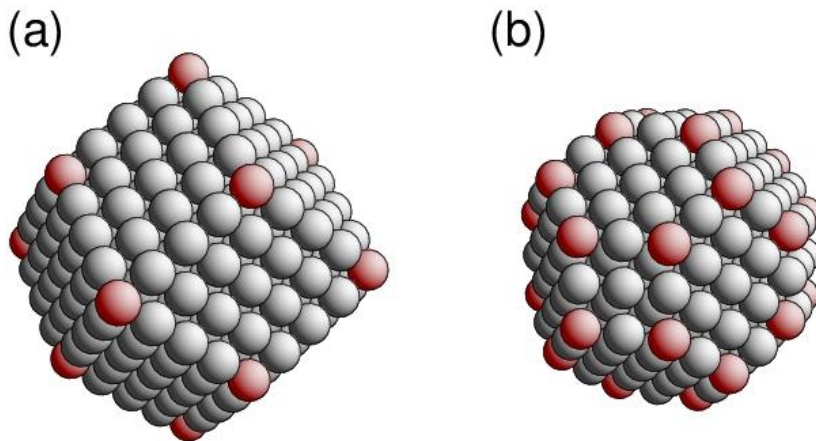


Fig. 2.41. Atom ball models of clusters (a) dodecahedral with  $n = 5$ , (b) truncated dodecahedral with  $n = 3$ . Corner atoms are emphasized by red shading.

Very large clusters above 100,000 atoms up to macroscopic sizes, usually referred to as **crystallites** or **grains**, can be assumed to form a crystalline structure inside their inner core with periodic arrangement of atoms within a finite volume. Under equilibrium conditions their exterior shape is often determined by planar surface sections (**facets**) of densely packed atom arrangements where there are transition regions between the facets. The geometric structure of the planar sections has been found to be very close to that of high-density crystal layers discussed in Sec. 4.2 with transitions involving more open layers with steps and kinks.

The global shape of crystallites has been discussed applying **quasi-continuum** models [58], [59] to polyhedral particles whose facets are considered as planar sections with normal directions along those of high-density crystal layers. In these models each polygonal facet is characterized by its size and a **surface free energy** per area where the latter depends on the atom density as well as on local binding properties of the facet layer. The size of the different facets can then be determined in an optimization of the total surface free energy of the particle for a given particle volume [60], [61] neglecting differences in binding energy at corners and edges. This yields the equilibrium

shape of the crystallite. The procedure based on the **Gibbs-Wulff theorem** [58], [59] is also known as Wulff construction.

In its simplest version the **Wulff construction** starts from a crystallite center and a continuous energy function  $\gamma(\underline{n})$  which depends only on the crystallographic direction vector  $\underline{n}$  from the center and defines the surface free energy per area of a crystal layer whose layer normal vector equals vector  $\underline{n}$ . Then the total surface free energy of the polyhedral crystallite with  $N$  surface facets is given by

$$\gamma_{\text{tot}} = \sum_{i=1}^N \gamma(\underline{n}_i) a_i \quad (2.142)$$

where  $\underline{n}_i$  denotes the normal vector of the  $i^{\text{th}}$  facet and  $a_i$  is the polygon area of the facet. To obtain the equilibrium shape of the crystallite for a given volume, function  $\gamma_{\text{tot}}$  needs to be minimized with respect to the number  $N$  of facets, the facet orientations  $\underline{n}_i$ , and their polygonal areas  $a_i$ . The Gibbs-Wulff theorem [58], [59], [60] states, in its simplest version, that the shape of a polyhedral crystallite in its thermodynamic equilibrium is achieved if all facets lie at distances  $d_i$  from the crystallite center which are proportional to the corresponding surface free energies per area  $\gamma(\underline{n}_i)$ . As a consequence, a polyhedral crystallite can be constructed from a surface free energy function  $\gamma(\underline{n})$  by considering a set of discrete planes  $S(\underline{n}_i)$  with normal vectors  $\underline{n}_i$  at distances  $d_i = \lambda \gamma(\underline{n}_i)$  from the crystallite center enclosing the center. (Here  $\lambda$  is a global scaling factor to be adjusted later.) Then the equilibrium surface of the crystallite is described by all points on the planes  $S(\underline{n}_i)$  which, for a given direction  $\underline{n}$ , are closest to the crystallite center. This yields polygonal areas (facets) forming the shape of the polyhedral crystallite where in a subsequent step the scaling constant  $\lambda$  is adjusted such that the required crystallite volume is obtained. In practical applications, the selection of planes  $S(\underline{n}_i)$  is restricted to sets of high-density crystal layers (perpendicular to  $\underline{n}_i$ ) and respective free energy values  $\gamma(\underline{n}_i)$  are taken from experimental data for the corresponding surfaces of high atom density or from theoretical surface energies.

As an illustration, Fig. 2.42 shows sketches of Wulff polyhedra of a cubic crystallite where 26 planes  $S(\underline{n}_i)$  perpendicular to high-symmetry directions ( $x$   $y$   $z$ ) are allowed to contribute to the shape of the crystallite. Further, free energy values  $\gamma(\underline{n}_i)$  are assumed to be equal for symmetry equivalent directions  $\underline{n}_i$  resulting in a parameter set

$$\begin{aligned}
 \mathbf{n}_i = (x, y, z) &= (\pm 1, \pm 1, \pm 1) \quad \text{with } \gamma_{(111)} \\
 &= (\pm 1, 0, 0), (0, \pm 1, 0), (0, 0, \pm 1) \quad \text{with } \gamma_{(001)} \\
 &= (\pm 1, \pm 1, 0), (\pm 1, 0, \pm 1), (0, \pm 1, \pm 1) \quad \text{with } \gamma_{(011)}
 \end{aligned}
 \tag{2.143}$$

Fig. 2.42a shows the Wulff polyhedron for surface free energy values  $\gamma_{(111)} = \gamma_{(001)} = \gamma_{(011)} = 1.0$  in relative units. If one of the three values, e.g.  $\gamma_{(001)}$ , is increased, the corresponding high-symmetry planes are less preferred and do not appear or contribute smaller polygon areas to the Wulff polyhedron which reflects the minimum energy shape. This is evident in Fig. 2.42b where  $\gamma_{(001)}$  is increased to  $\gamma_{(001)} = 1.5$  and high-symmetry planes corresponding to normal vectors  $(001)$  and their symmetry equivalents do not appear at the polygon surface. Figs. 2.42c and 2.42d show the analogous effect for increased values  $\gamma_{(111)} = 1.5$  and  $\gamma_{(011)} = 1.5$ , respectively.

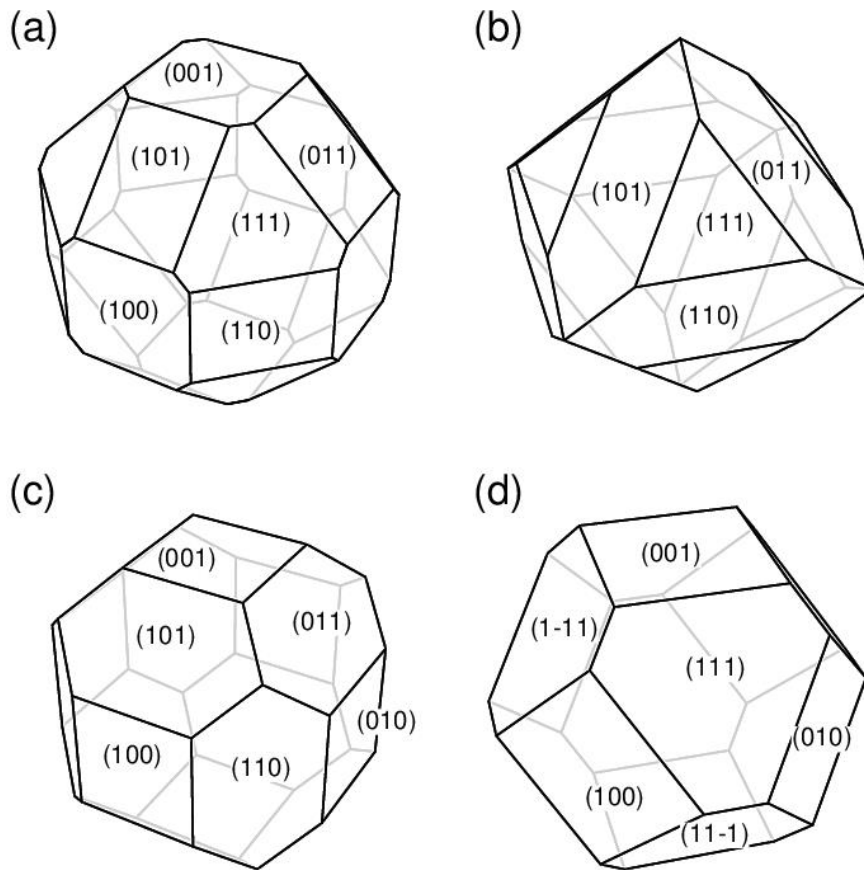


Fig. 2.42. Sketches of Wulff polyhedra of a cubic crystallite for different surface free energy scenarios, see text. (a)  $\gamma_{(111)} = \gamma_{(001)} = \gamma_{(011)} = 1.0$ ; (b)  $\gamma_{(111)} = \gamma_{(011)} = 1.0$ ,  $\gamma_{(001)} = 1.5$ ; (c)  $\gamma_{(001)} = \gamma_{(011)} = 1.0$ ,  $\gamma_{(111)} = 1.5$ ; (d)  $\gamma_{(111)} = \gamma_{(001)} = 1.0$ ,  $\gamma_{(011)} = 1.5$ . Directions of selected polygon surfaces,  $(x\ y\ z)$ , are labeled accordingly.

The Wulff construction can be generalized [61] formally to smoothed polygonal shapes of crystallites with continuous transitions between planar areas which, on an atomic scale, account for open atom arrangements with steps and kinks between high-density atom arrays. Even a formal treatment of particles with generally curved surfaces has been considered. These generalizations are achieved by replacing the summation in (2.142) by a surface integration which, however, complicates the optimization procedure considerably. Further details which go beyond the scope of this book can be found in Ref. [61]. Finally, it should be emphasized that the shape of real crystallites found in experiment is not exclusively determined by surface free energy considerations, which are the basis of the Wulff construction. Depending on preparation, kinetics, and local impurities, growth conditions of the different crystal planes can influence the shape of crystallites and may lead to metastable shapes which differ considerably from those of a Wulff construction.

## 2.8 Incommensurate Crystals and Quasicrystals

There are solid materials which exhibit **long-range atomic order** as well as **local symmetry** behavior. However, they are not periodic in three dimensions and are usually referred to as **aperiodic crystals**. They are different in their structural properties from amorphous materials, which show only some short-range order in their atom arrangement. As a result, the International Union of Crystallography extended its definition of a crystal to a solid producing discrete X-ray diffraction patterns where its ordering can be either periodic or aperiodic [62]. This includes three different groups of aperiodic crystals [63], those with modulated structures, incommensurate composite crystals, and quasicrystals which will be briefly discussed in the following.

### 2.8.1 Modulated structures

According to Sec. 2.1 ideal periodic crystals are defined by lattice vectors  $\underline{R}_{01}$ ,  $\underline{R}_{02}$ ,  $\underline{R}_{03}$  describing their basic periodicity where

$$\underline{R}_0 = n_1 \underline{R}_{01} + n_2 \underline{R}_{02} + n_3 \underline{R}_{03} \quad , \quad n_i \text{ integer} \quad (2.144)$$

denotes all lattice positions which, for primitive lattices, may be set to coincide with atom sites. In crystals with modulated structures the basic periodicity is modulated by adding a modulation vector



$\underline{u}(\underline{r})$  to each atom position where  $\underline{u}(\underline{r})$  is a periodic function in space with its periodicity described by a second lattice given by modulation vectors  $\underline{U}_1, \underline{U}_2, \underline{U}_3$  such that

$$\underline{u}(\underline{r} + m_1 \underline{U}_1 + m_2 \underline{U}_2 + m_3 \underline{U}_3) = \underline{u}(\underline{r}) , \quad m_i \text{ integer} \quad (2.145)$$

Thus, general atom positions  $\underline{R}$  in a crystal with a modulated structure are given by

$$\underline{R} = \underline{R}_o + \underline{u}(\underline{R}_o) \quad (2.146)$$

The basic and modulation lattices are connected by a linear transformation written as

$$\begin{pmatrix} \underline{U}_1 \\ \underline{U}_2 \\ \underline{U}_3 \end{pmatrix} = \begin{pmatrix} d_{11} & d_{12} & d_{13} \\ d_{21} & d_{22} & d_{23} \\ d_{31} & d_{32} & d_{33} \end{pmatrix} \cdot \begin{pmatrix} \underline{R}_{o1} \\ \underline{R}_{o2} \\ \underline{R}_{o3} \end{pmatrix} = \underline{\underline{D}} \cdot \begin{pmatrix} \underline{R}_{o1} \\ \underline{R}_{o2} \\ \underline{R}_{o3} \end{pmatrix} \quad (2.147)$$

where one can distinguish three cases,

- (a) matrix  $\underline{\underline{D}}$  or its inverse  $\underline{\underline{D}}^{-1}$  contain only integer-valued elements  $d_{ij}$ . Then the two lattices are commensurate with the joint periodicity determined by lattice vectors  $\underline{U}_1, \underline{U}_2, \underline{U}_3$  or  $\underline{R}_{o1}, \underline{R}_{o2}, \underline{R}_{o3}$ . Thus the modulated structure describes a strictly **periodic** atom arrangement. This is illustrated in Fig. 2.43a sketching a square lattice with lattice constant  $a$  modulated by a longitudinal wave displacement along vector  $\underline{L}_{\text{wave}}$  whose length (modulation wavelength) is equals  $4a$ .
- (b) matrix  $\underline{\underline{D}}$  contains a mixture of integer or fractional-valued elements  $d_{ij}$ . Then matrix  $\underline{\underline{D}}$  can be written as a product of two matrices,  $\underline{\underline{D}} = \underline{\underline{B}}^{-1} \underline{\underline{A}}$  where  $\underline{\underline{A}}, \underline{\underline{B}}$  are integer-valued such that there is also a joint periodicity. The lattices are high-order commensurate, as discussed in detail for two-dimensional periodicities at surfaces in Sec. 6.4, and the modulated structure describes again a strictly **periodic** atom arrangement.
- (c) matrix  $\underline{\underline{D}}$  contains real-valued elements  $d_{ij}$ . Then the two lattices are incommensurate and the resulting atom arrangement (2.146) is **aperiodic**.

Altogether, an aperiodic primitive crystal with a modulated structure is defined by atom positions (2.146) with a displacement function  $\underline{u}(\underline{r})$  whose periodicity is incommensurate with that of the basic lattice. This corresponds formally to the requirement that the transformation matrix  $\underline{\underline{D}}$  in (2.147) contains real-valued elements  $d_{ij}$ . Modulated crystal structures have been observed for example for monoclinic sodium carbonate,  $\gamma\text{-Na}_2\text{CO}_3$ , [64] or  $\text{KSm}(\text{MoO}_4)_2$  [65].

Modulation vectors  $\underline{u}(\underline{r})$  can also refer to one- and two-dimensionally periodic functions, re-

flecting crystals with preferred modulation directions. As an illustration, Fig. 2.43b shows a simple two-dimensional example of an aperiodic lattice. Here the square lattice with lattice constant  $a$  is modulated by a transverse wave displacement perpendicular to vector  $\underline{L}_{\text{wave}}$  whose length (modulation wavelength) is given by  $(3\sqrt{2})a$ .

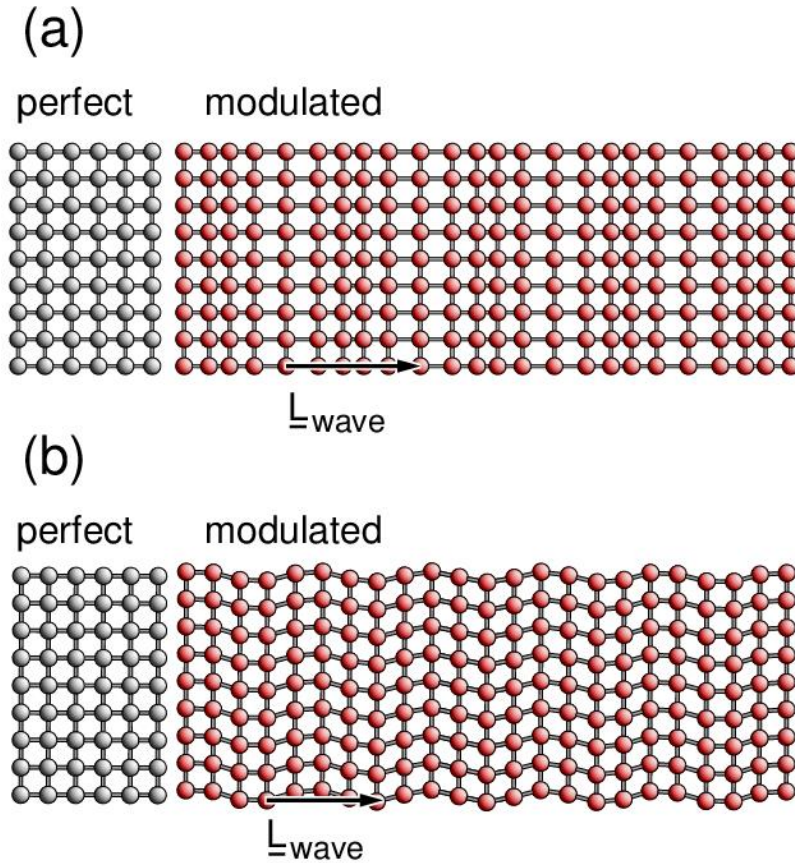


Fig. 2.43. Commensurate and incommensurate modulation of a square lattice; (a) periodic lattice with longitudinal wave modulation, (b) aperiodic lattice with transverse wave modulation. The left sections ('perfect') show the perfect square lattice with lattice constant  $a$ , while the modulated lattices ('modulated') are shown to the right. Vectors  $\underline{L}_{\text{wave}}$  denote the directions and wave lengths of the modulations with  $L_{\text{wave}} = 4a$  in (a),  $= (3\sqrt{2})a$  in (b).

## 2.8.2 Incommensurate composite crystals

These crystals consist, in the simplest case, of two crystal components,  $S_1$  and  $S_2$ , which themselves form periodic structures with lattice vectors  $\underline{R}_{11}$ ,  $\underline{R}_{12}$ ,  $\underline{R}_{13}$  and  $\underline{R}_{21}$ ,  $\underline{R}_{22}$ ,  $\underline{R}_{23}$ , respectively, where the two sublattices are mutually incommensurate yielding an altogether aperiodic crystal structure with long-range order. This requires the two sublattices to be sufficiently open such that

crystal component  $S_1$  can accommodate all atoms of component  $S_2$  or viceversa. Examples are layer type crystals where layers of atoms from component  $S_1$  alternate with those from component  $S_2$  yielding strict periodicity perpendicular to the layers. By contrast, the two-dimensional periodicity of the two components parallel to the layers is incommensurate. In general, this yields a linear transformation between the two sublattices where

$$\begin{pmatrix} \underline{\mathbf{R}}_{21} \\ \underline{\mathbf{R}}_{22} \\ \underline{\mathbf{R}}_{23} \end{pmatrix} = \begin{pmatrix} d_{11} & d_{12} & 0 \\ d_{21} & d_{22} & 0 \\ 0 & 0 & m \end{pmatrix} \cdot \begin{pmatrix} \underline{\mathbf{R}}_{11} \\ \underline{\mathbf{R}}_{12} \\ \underline{\mathbf{R}}_{13} \end{pmatrix} = \underline{\underline{\mathbf{D}}} \cdot \begin{pmatrix} \underline{\mathbf{R}}_{11} \\ \underline{\mathbf{R}}_{12} \\ \underline{\mathbf{R}}_{13} \end{pmatrix}, \quad d_{ij} \text{ real, } m \text{ integer or fractional} \quad (2.148)$$

assuming that the lattice vectors  $\underline{\mathbf{R}}_{1i}$ ,  $\underline{\mathbf{R}}_{2i}$ ,  $i = 1, 2$ , point parallel to the layers and  $\underline{\mathbf{R}}_{13}$ ,  $\underline{\mathbf{R}}_{23}$  connect between (e.g. are perpendicular to) adjacent layers. (If all elements  $d_{ij}$  in (2.148) would be integer- or fractional-valued the resulting lattice combination and thus the crystal would be strictly periodic in three dimensions.)

As an example, the crystal of the misfit layer compound  $(\text{LaS})_{1.13}\text{TaS}_2$  has been found [66] to form a layer type structure with alternating LaS and TaS<sub>2</sub> layers, see Fig. 2.44. Here the two lattice vectors perpendicular to the layers,  $\underline{\mathbf{R}}_{13}$  and  $\underline{\mathbf{R}}_{23}$ , as well as one pair,  $\underline{\mathbf{R}}_{12}$  and  $\underline{\mathbf{R}}_{22}$ , parallel to the layers coincide, while the lattice vectors  $\underline{\mathbf{R}}_{11}$  and  $\underline{\mathbf{R}}_{21}$  along the layers are different in length and incommensurate as indicated in Fig. 2.44. In experiment, the LaS layer is found to buckle and both layers also exhibit incommensurate modulations [66] which are ignored for the present purpose and not included in Fig. 2.44.

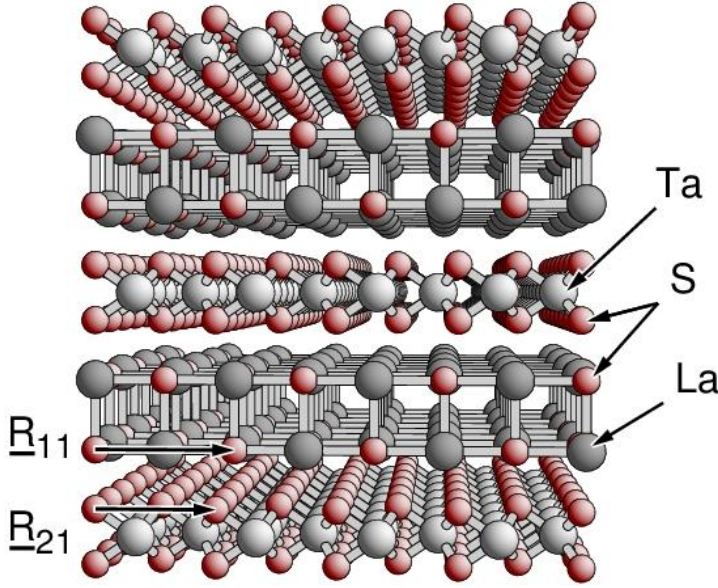


Fig. 2.44. (a) Schematic view of a section of the layer type  $(\text{LaS})_{1.13}\text{TaS}_2$  crystal. Sticks connect neighboring atoms of the LaS and  $\text{TaS}_2$  layers with atoms labeled accordingly. The incommensurate lattice vectors  $\underline{\mathbf{R}}_{11}$  (LaS layer) and  $\underline{\mathbf{R}}_{21}$  ( $\text{TaS}_2$  layer) are indicated by arrows connecting sulfur atoms.

The different periodicities of incommensurate composite layer crystals along their layers, expressed by transformation (2.148) between  $\underline{\mathbf{R}}_{11}$ ,  $\underline{\mathbf{R}}_{12}$  and  $\underline{\mathbf{R}}_{21}$ ,  $\underline{\mathbf{R}}_{22}$  are formally equivalent with the periodic arrangement of **incommensurate adsorbate overlayers** at single crystal surfaces, discussed Sec. 6.1. Therefore, the mathematical treatment of the two types of systems can be put on the same basis.

Other groups of incommensurate composite crystals include two-component materials where component  $S_1$  forms a framework with open channels. Then the atoms of component  $S_2$  arrange in 1-dimensionally periodic chains inside the channels where the chain periodicity is incommensurate with the periodicity of the host along the channels. This yields in general a linear transformation between the two sublattices where

$$\begin{pmatrix} \underline{\mathbf{R}}_{21} \\ \underline{\mathbf{R}}_{22} \\ \underline{\mathbf{R}}_{23} \end{pmatrix} = \begin{pmatrix} m_{11} & m_{12} & 0 \\ m_{21} & m_{22} & 0 \\ 0 & 0 & d \end{pmatrix} \cdot \begin{pmatrix} \underline{\mathbf{R}}_{11} \\ \underline{\mathbf{R}}_{12} \\ \underline{\mathbf{R}}_{13} \end{pmatrix} = \underline{\underline{\mathbf{D}}} \cdot \begin{pmatrix} \underline{\mathbf{R}}_{11} \\ \underline{\mathbf{R}}_{12} \\ \underline{\mathbf{R}}_{13} \end{pmatrix}, \quad m_{ij} \text{ integer or fractional, } d \text{ real} \quad (2.149)$$

assuming that the lattice vectors  $\underline{\mathbf{R}}_i$ ,  $\underline{\mathbf{R}}_{2i}$ ,  $i = 1, 2$ , define a common two-dimensional lattice of the crystal (e.g. perpendicular to the channels) and  $\underline{\mathbf{R}}_{13}$ ,  $\underline{\mathbf{R}}_{23}$  point along the channels.

An example, the compound  $\text{Rb}_{1.37}\text{MnO}_2$  (derived from  $\text{Rb}_{15}\text{Mn}_{11}\text{O}_{22}$ ) [67] has been found to

consist of an open hexagonal host lattice of rubidium atoms where chains of connected  $\text{MnO}_4$  tetrahedra form inside the hexagonal Rb channels. Here the two lattice vectors along the hexagonal channels,  $\underline{R}_{13}$  and  $\underline{R}_{23}$ , are incommensurate and the periodicity along the  $\text{MnO}_4$  chains is further perturbed by modulation. In contrast, the two components, Rb and  $\text{MnO}_4$ , share the two-dimensional periodicity perpendicular to the channels, as shown in Fig. 2.45. In experiment, the connected  $\text{MnO}_4$  units defining the inner chains are found to distort and form spiral columns [67] which are ignored for the present purpose and not shown in Fig. 2.45.

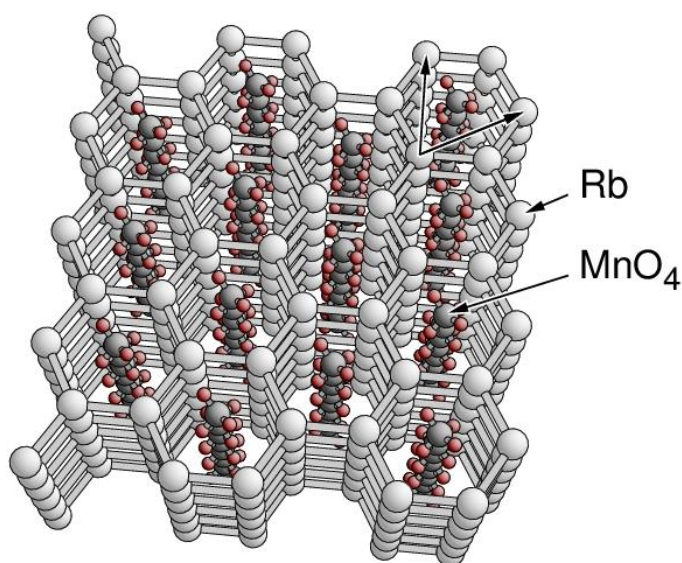


Fig. 2.45. Schematic view of a section of the  $\text{Rb}_{1.37}\text{MnO}_2$  crystal. Sticks connect neighboring atoms of the Rb host lattice and the  $\text{MnO}_4$  chains with atoms labeled accordingly. The periodicity perpendicular to the hexagonal channels is indicated by arrows connecting rubidium atoms.

### 2.8.3 Quasicrystals

There is a third class of crystals which exhibit long-range order but are not periodic in three dimensions. They were first suggested by experiment [68] and are referred to as quasiperiodic crystals or quasicrystals. These materials, consisting in many cases of aluminum-rich metal alloys, exhibit numerous exciting physical and chemical properties [69], [70], [71], [72], [73], [74], [75]. Examples are high mechanical hardness as well as relatively low electrical and thermal conductance which make quasicrystalline materials good candidates for surface coatings. Surfaces of quasicrystals are known for their low friction and adhesion, as well as for their good oxidation resistance [76], [77]. Aperiodic crystals including quasicrystals have become a common playground for math-

ematicians [70], [71], [78]. As a result, there is a wealth of publications and textbooks dealing with quasicrystals, going far beyond the scope of the present book. References [28], [69], [70], [71], [72], [73], [74], [78], [79] represent only a few examples. Here we confine ourselves to some aspects of structure and symmetry of quasicrystals by simple examples illustrating general issues.

As a first example of quasicrystalline order, a two dimensional model of a quasicrystal will be considered. This model is connected with the mathematical theory of **Penrose tiling** [78], [80]. The basic subject of this theory is to cover a plane completely without holes or overlaps using tiles of a finite set of different polygons, so-called **prototiles**. Here we consider only **rhombic** prototiles of two different shapes, a ‘**fat**’ rhombus with its smallest vertex angle at  $\alpha = 360^\circ/5 = 72^\circ$  and a ‘**thin**’ rhombus with its smallest vertex angle at  $\beta = 36^\circ$ , where both rhombuses have edges of the same length  $a$ , as shown in Fig. 2.46. As a consequence of the choice of angles (whose values will become more evident when rotational symmetry of the tiling pattern is considered), the long diagonal of the fat rhombus has a length of  $\tau a$ , while the short diagonal of the thin rhombus has a length of  $(1/\tau) a$  (diagonals as dashed lines in Fig. 2.46), where  $\tau = (1 + \sqrt{5}) / 2 = 1.618034$  denotes the **golden ratio** or **golden mean**.

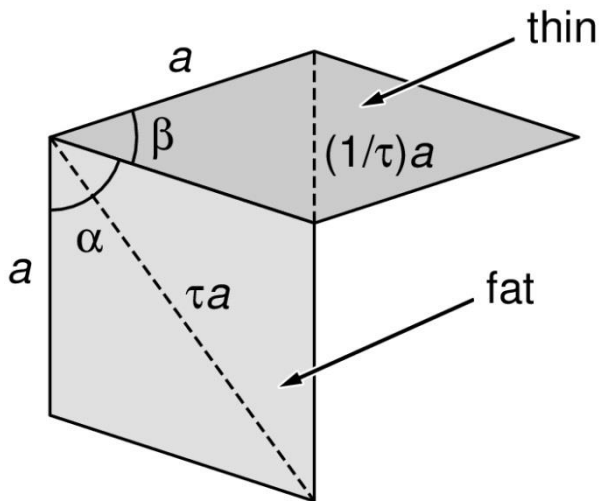


Fig. 2.46. Rhombic Penrose prototiles; fat (light gray) and thin (dark gray) tiles with edge lengths  $a$  and with smallest vertex angles of  $\alpha = 72^\circ$  and  $\beta = 36^\circ$ , respectively.

Sets of the two prototiles can be arranged such that they form a two-dimensionally **periodic pattern**, shown in Fig. 2.47. In this figure atoms are placed at the centers of all rhombuses, one large for each fat and one small for each thin rhombus. This leads to a planar atom arrangement which describes a two-dimensionally **periodic crystal** with primitive lattice vectors  $\underline{R}_1$  and  $\underline{R}_2$  and a

basis of three atoms, two large and one small, included in Fig. 2.47. The corresponding lattice is characterized as centered rectangular by its symmetry, see Sec. 3.8.6.

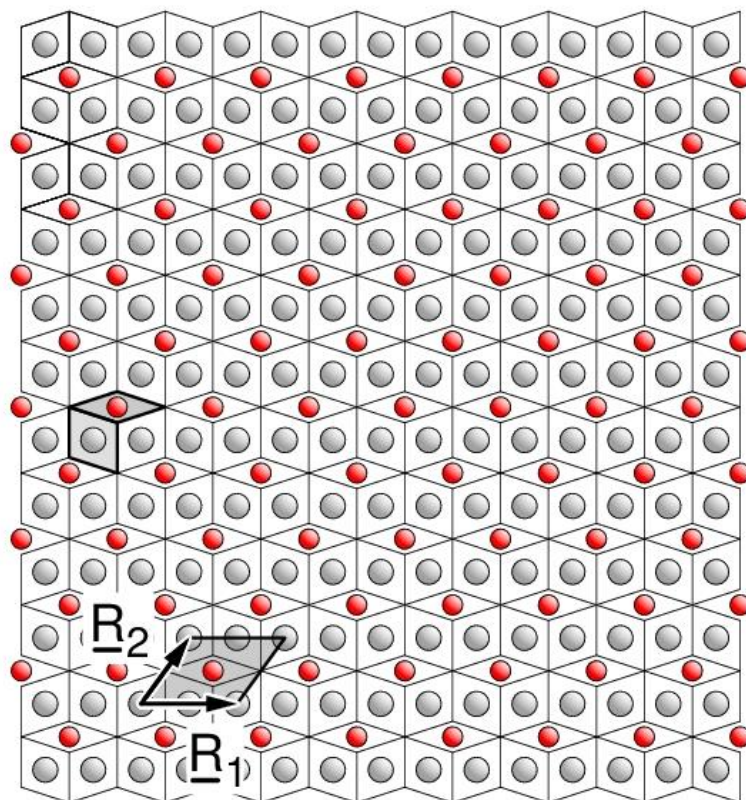


Fig. 2.47. Rhombic Penrose prototiles arranged to form a two-dimensionally periodic pattern. Two different prototiles are emphasized by light and dark background, respectively. Atoms are added at the centers of the tiles to form a two-dimensional crystal. Lattice vectors are labeled accordingly with the morphological unit cell emphasized by a gray background.

On the other hand, sets of the two rhombuses can also be positioned such that they cover the plane completely but do not exhibit periodicity in any direction as indicated in Fig. 2.48. A closer inspection of the tiling evidences **global 5-fold symmetry** for exactly one vertex at the center (labeled by a black dot in Fig. 2.48). In addition, there are many smaller regions (indicated by black sticks connecting thick neighbor atoms), which exhibit **local 5-fold symmetry** without being periodic repeat units. Global 5-fold symmetry is not compatible with translational symmetry as shown in Sec. 3.6.3. Thus, placing atoms at the centers of all rhombuses, as indicated in Fig. 2.48, does not yield a two-dimensionally periodic crystal. (Atomic positions in a real quasicrystal are slightly more complicated, as will be shown below.) However, the existence of local symmetry suggests some order which justifies calling the set of atoms a **quasicrystal**. There is an additional geometric aspect that becomes clear from an analysis of Fig. 2.48. The local regions with 5-fold symmetry are not

completely random in their distribution but follow the global 5-fold symmetry such that similar pentagonal regions with higher complexity are formed. This property is connected with **self-similarity** and is also encountered in models of three-dimensional quasicrystals.

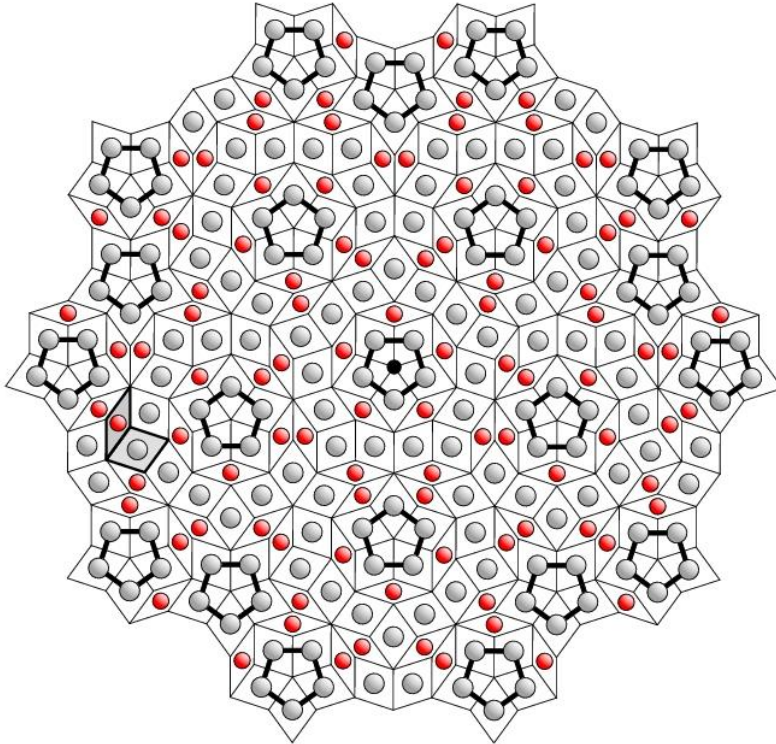


Fig. 2.48. Aperiodic (quasicrystal) arrangement of rhombic Penrose prototiles illustrating 5-fold symmetry. Two different prototiles are emphasized by light and dark background, respectively. Atoms are added at the centers of all tiles to form a two-dimensional quasicrystal.

Further, a detailed analysis of the atom arrangement in Fig. 2.48 evidences that many atoms are positioned along **(infinite) rows** which are **parallel** to each other and point in different directions. This becomes even clearer in Fig. 2.49, where some of these rows are emphasized by lines to guide the eye. The sequences of separations between specific parallel lines follow a pattern, where only two different distances appear, labeled L (large) and s (small) in Fig. 2.49. The distance sequence, indicated by 'sLLsLsL' from the top of the figure, seems to be random at first sight. However, it can be shown to be associated with sequences appearing in the mathematical theory of **Fibonacci numbers** [78] which will not be discussed further, see Exercise 2.32.



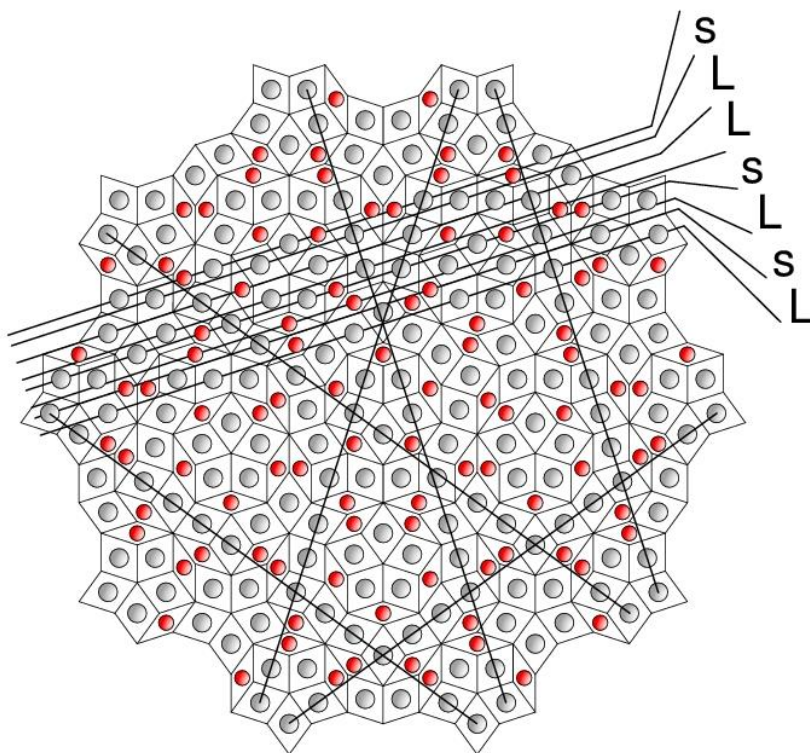


Fig. 2.49. Aperiodic (quasicrystal) arrangement of rhombic Penrose prototiles illustrating linear atom rows. The rows are emphasized by black lines. In addition, parallel atom rows, separated by two distinct distances, large (L) and small (s), are shown with their distances labeled accordingly, see text.

A more complex mathematical treatment of Penrose tiling [78] shows that its structural properties can be obtained by considering periodic lattices in **higher dimensions**, 5-dimensional in the case of two-dimensional Penrose tiling. Then, projections of an aperiodic section of the 5-dimensional lattice can provide the structure of the two-dimensional aperiodic quasicrystal. This result is more general and also applies to three-dimensional quasicrystals, where the corresponding higher dimensional lattices are 6-dimensional. In this approach, the atom composition of the aperiodic sections in six dimensions determines the composition of the three-dimensional quasicrystal. The approach leads to a classification of quasicrystals into **two types** [81]. First, **icosahedral** quasicrystals do not exhibit periodicity in any direction but allow one global and many local 5-fold rotation axes. Second, **polygonal (dihedral)** quasicrystals contain one global 8-, 10-, or 12-fold rotation axis (octagonal, decagonal and dodecagonal quasicrystals) and are periodic along this axis. However, these quasicrystals are aperiodic in planes perpendicular to the rotation axis (quasiperiodic ordering). Further details concerning the mathematics behind possible projections go far beyond the scope of this book and can be found in the literature cited above, see e.g. Ref. [78].

As an illustration of projecting a periodic lattice of higher dimension to yield a lower-dimensional aperiodic quasicrystal we consider the **cut-and-project** method applied to a two-dimensional square lattice of lattice constant  $a$  as shown in Fig. 2.50. The square unit cell of the lattice, outlined in red in the figure, serves as a starting point to construct a strip between two parallel lines through two diagonal corners where the lines form an angle  $\alpha = \arctan(1/\tau) = 31.717^\circ$  with the corresponding sides of the cell ( $\tau$  denoting the golden ratio) and are, thus, separated by a distance  $w = a \{ \cos(\alpha) + \sin(\alpha) \}$ , see Fig. 2.50. The area between the parallel lines includes atoms of the square lattice (painted red in the figure) whose coordinates are projected onto one of the parallel lines. This defines a linear string of locations where atoms are placed (the string is shifted upwards in the figure for better visibility). This array of atoms is **aperiodic** with two distinct interatomic distances, a long and a short distance,  $L$  and  $s$ , respectively. The ratio of the distances is given by  $L/s = \tau$  and the sequence of distances,  $LsLLsLsLLsLsLLsLsLL \dots$ , reflects the Fibonacci series which defines a 1-dimensional quasicrystal, also known as a **Fibonacci chain**. This sequence of long and short distances was discussed before for Penrose tiling, see Fig. 2.49.

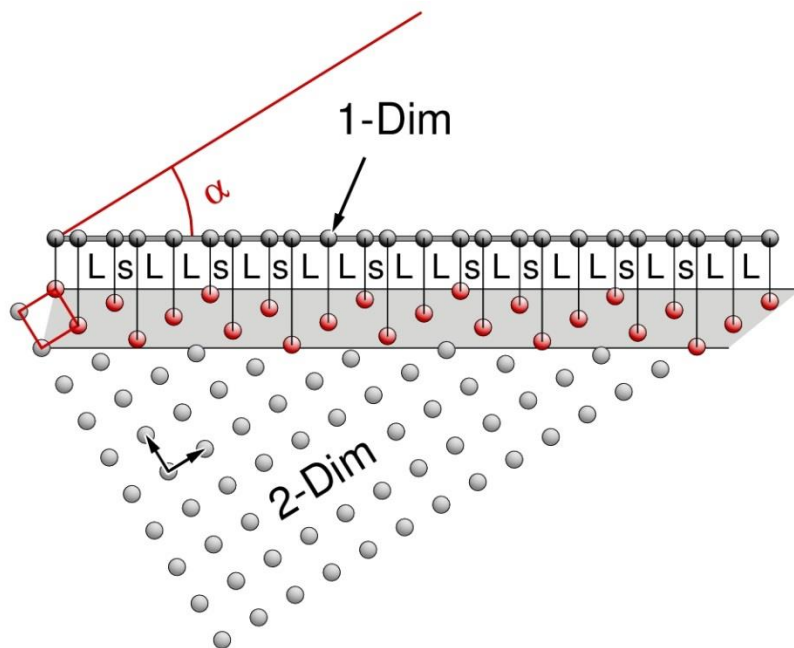


Fig. 2.50. Projection of a strip of finite width in a two-dimensional square lattice (cut-and-project procedure) to yield a Fibonacci chain. The atoms inside the strip are painted red and those of the Fibonacci chain are dark gray. Long and short distances between chain atoms are labeled  $L$  and  $s$ , respectively. The unit cell of the square lattice is outlined in red and lattice vectors indicated by arrows.

The structural features discussed for purely mathematical models, like Penrose quasicrystals,

and Fibonacci chains can be also found in real three-dimensional quasicrystals and at their surfaces. As an illustration, Figs. 2.51 and 2.52 show geometric models of the surface of an icosahedral *i*-AlCuFe quasicrystal (characterized in its chemical composition as  $\text{Al}_{65}\text{Cu}_{20}\text{Fe}_{15}$  [82]). This model was used to analyze the surface structure of *i*-AlCuFe by low-energy electron diffraction (LEED) [83].

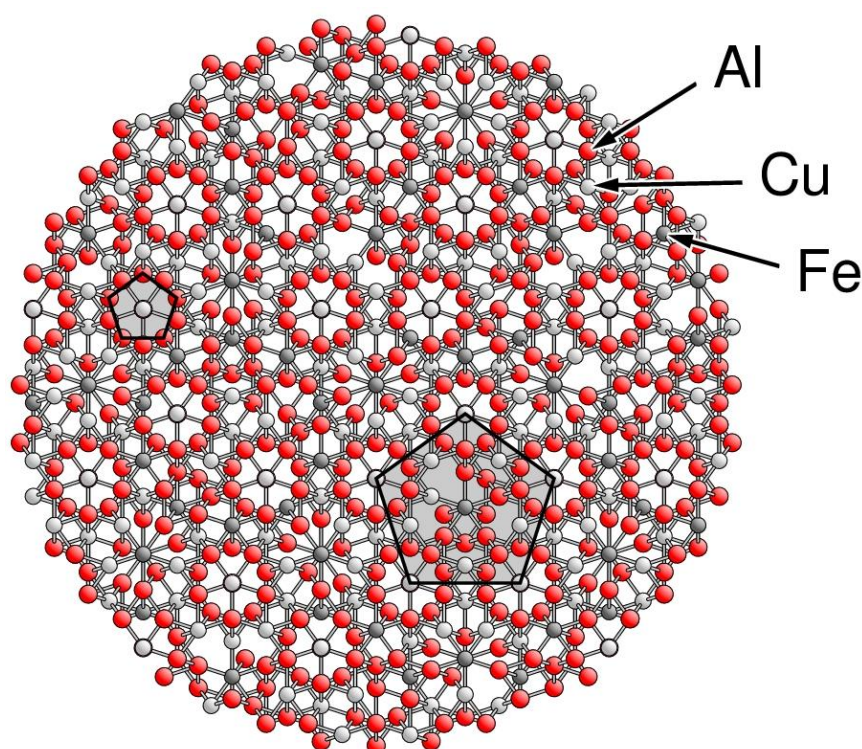


Fig. 2.51. Structural model of the surface of an icosahedral *i*-AlCuFe quasicrystal in a top view. The different atom types, Al, Cu, Fe, are labeled accordingly. Two local environments of different size with 5-fold symmetry are emphasized by gray background.

The top view, given in Fig. 2.51, appears less ordered than in Fig. 2.48 because it does not contain a global 5-fold axis. It has many rings of mostly 10 Al atoms, each of which form 2 pentagonal rings of 5 atoms in two different planes and, thus, have local 5-fold symmetry. Either a copper or an iron atom resides in the symmetry centers. In addition, there are larger atom environments of more complex structure, such as pentagons consisting of 5-rings of 10 Al atoms each, which also exhibit local 5-fold symmetry: see the larger pentagon emphasized in Fig. 2.51, which is blown up relative to the smaller emphasized pentagon. This can be taken as a first indication of self-similarity of the surface. Fig. 2.52 shows the same quasicrystal surface in a side view, i.e. along the surface. Here an additional structural feature becomes clear. The *i*-AlCuFe quasicrystal forms approximate layers parallel

to the surface, similar to those found for periodic crystals. This is emphasized in Fig. 2.52 by white horizontal lines with a similar distance with respect to each other. While there are few atoms between the layers, most of the atoms are positioned close to the planes indicated by the lines. (It should be noted that the structure shown in Figs. 2.51 and 2.52 is not an ‘open’ low-density network, but a nearly close-packed structure. The atoms spheres in the figures are reduced in size to help visibility.)

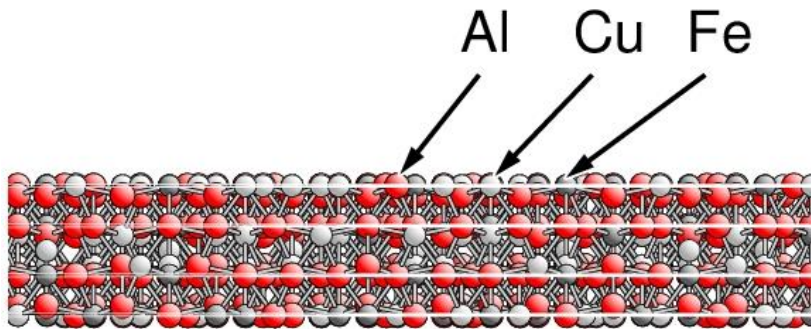


Fig. 2.52. Structural model of a surface of an icosahedral *i*-AlCuFe quasicrystal in a side view. The different atom types, Al, Cu, Fe, are labeled accordingly. The approximate layer structure is indicated by white horizontal lines.

## 2.9 Exercises

- 2.1. A crystal lattice is given by lattice vectors  $\underline{R}_1$ ,  $\underline{R}_2$ ,  $\underline{R}_3$  with lattice constants  $a$ ,  $b$ ,  $c$  and mutual angles  $\alpha$ ,  $\beta$ ,  $\gamma$  according to (2.3). Proof that the volume of the morphological unit cell is given by

$$V_{\text{el}} = a b c \{1 - \cos^2(\alpha) - \cos^2(\beta) - \cos^2(\gamma) + 2 \cos(\alpha) \cos(\beta) \cos(\gamma)\}^{1/2}$$

- 2.2. A crystal is described by lattice vectors  $\underline{R}_1$ ,  $\underline{R}_2$ ,  $\underline{R}_3$  and a monoatomic basis. Replacing the atoms by hard balls of equal radii such that the balls are the largest without overlapping fills the crystal space partly, leaving empty space in between. The volume ratio of the space filled by balls and that of the complete crystal defines the packing ratio  $q_{\text{pack}}$ . Determine the packing ratio  $q_{\text{pack}}$  for crystals with (a) sc, (b) fcc, (c) bcc, (d) hex (hcp) lattice.
- 2.3. Characterize visually and formally (primitive) sublattices of the ions inside the NaCl, CsCl, and diamond crystal. For lattice vectors, see (2.25), (2.26), (2.38), (2.13), (2.15).
- 2.4. Analyze the centered tetragonal (ct) lattice with

$$\underline{\mathbf{R}}_1 = (a, 0, 0), \quad \underline{\mathbf{R}}_2 = (0, a, 0), \quad \underline{\mathbf{R}}_3 = 1/2 (a, a, c)$$

and show that fcc- and bcc lattices are special cases. Determine the value of  $c/a$  for these cases.

- 2.5. Discuss the structural phase transition bcc  $\rightarrow$  ct  $\rightarrow$  fcc (Bain path) based on the lattice definition of Exercise 2.4 and visualize respective morphological and Wigner-Seitz unit cells.
- 2.6. Consider an alternative Bain path characterized by lattice vectors

$$\underline{\mathbf{R}}_1 = a (1, 0, 0), \quad \underline{\mathbf{R}}_2 = a (1/2, \sqrt{3}/2, 0), \quad \underline{\mathbf{R}}_3 = a (1/2, 1/\sqrt{12}, x)$$

for  $0.1 < x < 1.0$  and show that bcc, sc, and fcc lattices are special cases with  $x_{\text{bcc}} = 1/\sqrt{24}$ ,  $x_{\text{sc}} = 2/\sqrt{24}$ ,  $x_{\text{fcc}} = 4/\sqrt{24}$ . Which lattice symmetries appear along the continuous path  $0.1 < x < 1.0$ ? Visualize respective morphological unit and Wigner-Seitz cells.

- 2.7. The hexagonal graphite crystal can be defined by lattice vectors  $\underline{\mathbf{R}}_1, \underline{\mathbf{R}}_2, \underline{\mathbf{R}}_3$  and a basis of four C atoms where

$$\begin{aligned} \underline{\mathbf{R}}_1 &= a (1, 0, 0), & \underline{\mathbf{R}}_2 &= a (1/2, \sqrt{3}/2, 0), & \underline{\mathbf{R}}_3 &= c (0, 0, 1) \\ \underline{\mathbf{r}}_1 &= (0, 0, 0), & \underline{\mathbf{r}}_2 &= 1/3 (1, 1, 0), & \underline{\mathbf{r}}_3 &= 1/2 (0, 0, 1) \\ \underline{\mathbf{r}}_4 &= (2/3, 2/3, 1/2), & & & c/a &= 2.72 \end{aligned}$$

with  $\underline{\mathbf{R}}_i$ ,  $i = 1, 2, 3$ , in Cartesian coordinates and  $\underline{\mathbf{r}}_k$ ,  $k = 1, 2, 3, 4$ , in relative coordinates, see (2.11). Show that the crystal structure is hexagonal layer-type and can be built by stacking honeycomb-structured planes of atoms. What is the stacking direction?

- 2.8. The rhombohedral graphite crystal can be defined by lattice vectors  $\underline{\mathbf{R}}_1, \underline{\mathbf{R}}_2, \underline{\mathbf{R}}_3$  and a basis of two C atoms where

$$\begin{aligned} \underline{\mathbf{R}}_1 &= a (\sqrt{3}/2, -1/2, c/a), & \underline{\mathbf{R}}_2 &= a (0, 1, c/a), & \underline{\mathbf{R}}_3 &= a (-\sqrt{3}/2, -1/2, c/a) \\ \underline{\mathbf{r}}_1 &= (1/6, 1/6, 1/6), & \underline{\mathbf{r}}_2 &= (-1/6, -1/6, -1/6), & c/a &= 2.36 \end{aligned}$$

with  $\underline{\mathbf{R}}_i$ ,  $i = 1, 2, 3$ , given in Cartesian coordinates and  $\underline{\mathbf{r}}_k$ ,  $k = 1, 2$ , in relative coordinates, see (2.11). Show that this crystal structure is also hexagonal layer-type and can be built by stacking honeycomb-structured monolayers of atoms. Prove that the hexagonal structure description

$$\begin{aligned} \underline{\mathbf{R}}_1 &= a (1, 0, 0), & \underline{\mathbf{R}}_2 &= a (1/2, \sqrt{3}/2, 0), & \underline{\mathbf{R}}_3 &= c (0, 0, 1) \\ \underline{\mathbf{r}}_1 &= (0, 0, 0), & \underline{\mathbf{r}}_2 &= 1/3 (1, 1, 0), & \underline{\mathbf{r}}_3 &= 1/3 (1, 1, 1) \end{aligned}$$

$$\underline{r}_4 = 1/3 (2, 2, 1), \quad \underline{r}_5 = 1/3 (2, 2, 2), \quad \underline{r}_6 = 1/3 (0, 0, 2)$$

$$c/a = 4.08$$

is equivalent to the rhombohedral description above.

- 2.9. Compare the crystal structures of rhombohedral and hexagonal graphite. Show that hexagonal graphite results in stacking of honeycomb-structured planes of atoms according to ... A B A B ... as opposed to ... A B C A B C ... for rhombohedral graphite. Here A, B, C denotes the planes with those of the same label positioned directly above each other (shifted by  $\underline{R}_3$  of the hexagonal lattice).
- 2.10. Consider a hexagonal lattice with lattice vectors  $\underline{R}_{01}, \underline{R}_{02}, \underline{R}_{03}$  given in obtuse representation where  $a = |\underline{R}_{01}| = |\underline{R}_{02}|$  and  $\underline{R}_{01}\underline{R}_{02} = -1/2 a^2$ . Show that there are, altogether, 12 equivalent representations (6 obtuse and 6 acute) with vectors  $\underline{R}_1$  and  $\underline{R}_2$  of the same length as  $|\underline{R}_{01}|$  and identical  $\underline{R}_3 = \underline{R}_{03}$ .
- 2.11. Show that there is a continuous structural transition from rhombohedral graphite to diamond and discuss the structural elements.
- 2.12. Consider initial lattice vectors  $\underline{R}_{01}, \underline{R}_{02}, \underline{R}_{03}$  of a three-dimensional crystal and a corresponding superlattice representation by lattice vectors  $\underline{R}_1, \underline{R}_2, \underline{R}_3$  where

$$\underline{R}_1 = \kappa_{11} \underline{R}_{01} + \kappa_{12} \underline{R}_{02} + \underline{R}_{03}, \quad \underline{R}_2 = \kappa_{21} \underline{R}_{01} + \kappa_{22} \underline{R}_{02} + \underline{R}_{03}, \quad \underline{R}_3 = \underline{R}_{03}$$

Determine constraints on  $\kappa_{ij}$  such that the two representations result in identical volumes of their morphological unit cells.

- 2.13. Consider a three-dimensional crystal with non-primitive lattice vectors  $\underline{R}_1, \underline{R}_2, \underline{R}_3$  and a lattice point inside the morphological unit cell described by vector

$$\underline{R}' = \kappa_1 \underline{R}_1 + \kappa_2 \underline{R}_2 + \kappa_3 \underline{R}_3, \quad 0 \leq \kappa_i < 1$$

Which parameter combinations  $\kappa_1, \kappa_2, \kappa_3$  must be excluded and why?

- 2.14. Consider a three-dimensional crystal with non-primitive lattice vectors  $\underline{R}_1, \underline{R}_2, \underline{R}_3$  which are of smallest length compared with all general lattice vectors pointing along the same directions. Assume a lattice vector  $\underline{R}'$  inside the morphological unit cell, i.e.

$$\underline{R}' = \kappa_1 \underline{R}_1 + \kappa_2 \underline{R}_2 + \kappa_3 \underline{R}_3, \quad 0 < \kappa_i < 1$$

where  $(\underline{R}', \underline{R}_2, \underline{R}_3)$ ,  $(\underline{R}_1, \underline{R}', \underline{R}_3)$ , and  $(\underline{R}_1, \underline{R}_2, \underline{R}')$  form alternative lattice vector sets to describe the initial lattice. Show that this can be achieved only for

$$\underline{R}' = (\underline{R}_1 + \underline{R}_2 + \underline{R}_3) / p, \quad p \text{ integer}$$

- 2.15. Consider a two-dimensional set of non-primitive lattice vectors,  $\underline{R}_1$  and  $\underline{R}_2$ , which are of smallest length compared with all general lattice vectors pointing along the same directions. Assume a lattice vector  $\underline{R}'$  inside the morphological unit cell, i.e.

$$\underline{R}' = \kappa_1 \underline{R}_1 + \kappa_2 \underline{R}_2, \quad 0 < \kappa_i < 1$$

where  $(\underline{R}', \underline{R}_2)$  and  $(\underline{R}_1, \underline{R}')$  form alternative lattice vector sets to describe  $\underline{R}_1$  and  $\underline{R}_2$ . Show that this can be achieved only for

$$\underline{R}' = (\underline{R}_1 + \underline{R}_2) / p, \quad p \text{ integer}$$

- 2.16. Consider the Wigner-Seitz cells (WSC) of a (a) sc, (b) fcc, (c) bcc lattice with lattice constant  $a$ . Determine for each WSC the volume of the largest inscribed sphere  $V_{\text{sph}}$  and compare it with the WSC volume  $V_{\text{el}}$ . How do the ratios  $q_{\text{WSC}} = V_{\text{sph}} / V_{\text{el}}$  compare with the packing ratios  $q_{\text{pack}}$  determined in Exercise 2.2?
- 2.17. A crystal lattice is described by lattice vectors  $\underline{R}_1, \underline{R}_2, \underline{R}_3$  where the morphological unit cell contains 3-fold rotation axes along directions

$$\underline{e}_1 = (1, 1, 1), \quad \underline{e}_2 = (1, -1, 1), \quad \underline{e}_3 = (-1, 1, 1), \quad \underline{e}_4 = (-1, -1, 1)$$

in Cartesian coordinates.

- (a) Determine the  $3 \times 3$  matrices  $\underline{T}$  of Cartesian coordinate transformations

$$\begin{pmatrix} x' \\ y' \\ z' \end{pmatrix} = \begin{pmatrix} t_{11} & t_{12} & t_{13} \\ t_{21} & t_{22} & t_{23} \\ t_{31} & t_{32} & t_{33} \end{pmatrix} \cdot \begin{pmatrix} x \\ y \\ z \end{pmatrix} = \underline{T} \cdot \begin{pmatrix} x \\ y \\ z \end{pmatrix}$$

referring to the corresponding eight rotation operations.

- (b) Determine all point symmetry elements of the morphological unit cell given by  $\underline{R}_1, \underline{R}_2, \underline{R}_3$ .

- 2.18. The morphological unit cell of a crystal, described by orthogonal lattice vectors  $\underline{R}_1, \underline{R}_2, \underline{R}_3$ , contains three 2-fold rotation axes along directions

$$\underline{e}_1 = (1, 0, 0), \quad \underline{e}_2 = (0, 1, 0), \quad \underline{e}_3 = (0, 0, 1) \quad \text{in Cartesian coordinates.}$$

- (a) Determine all possible symmetry elements of the unit cell originating from the 2-fold rotation axes.
- (b) Fill the unit cell with atoms such that the cell allows only the symmetry elements found in (a).
- 2.19. A crystal is described by cubic lattice vectors  $\underline{R}_1, \underline{R}_2, \underline{R}_3$  and a basis of two different atoms A, B, located at

$$\underline{r}_1^A = (0, 0, 0), \quad \underline{r}_2^B = \kappa_1 \underline{R}_1 + \kappa_2 \underline{R}_2 + \kappa_3 \underline{R}_3, \quad |\kappa_i| < 1, \quad i = 1, 2, 3$$

in relative coordinates, see (2.11). Find values  $\kappa_1, \kappa_2, \kappa_3$  where neighbor shells with respect to atom A contain both types of atoms in the same shell.

- 2.20. Determine neighbor shells (distances, shell multiplicities) of monoatomic crystals with (a) fcc, (b) bcc, (c) hex (hcp), and (d) diamond lattice up to 5<sup>th</sup> nearest neighbors. Which shells are identical for these lattices assuming the same value of lattice constant  $a$ .
- 2.21. A crystal of the semiconductor Gallium arsenite, GaAs, can be described by an fcc lattice and a two-atom basis with

$$\begin{aligned} \underline{R}_1 &= a/2 (0, 1, 1), & \underline{R}_2 &= a/2 (1, 0, 1), & \underline{R}_3 &= a/2 (1, 1, 0) \\ \underline{r}_1 &= (0, 0, 0), & \underline{r}_2 &= 1/4 (1, 1, 1) \end{aligned}$$

with  $\underline{R}_i, i = 1, 2, 3$ , in Cartesian coordinates and  $\underline{r}_k, k = 1, 2$ , in relative coordinates, see (2.11). (This is also the crystal structure of cubic zincblende, ZnS.) Show that neighbor shells with respect to Ga or As centers contain only atoms of the same type.

- 2.22. Consider a monoatomic crystal described by simple cubic lattice vectors  $\underline{R}_1, \underline{R}_2, \underline{R}_3$  and determine neighbor shells with respect to the midpoint between two adjacent atoms in the crystal up to the 10<sup>th</sup> shell. Calculate the number of shell multiplicities  $M_i$  and corresponding cluster radii  $D_i$  as functions of the shell index  $i$ .
- 2.23. A crystal of titanium dioxide,  $\text{TiO}_2$ , with rutile structure can be described by a tetragonal lattice and a six-atom basis with

$$\begin{aligned} \underline{R}_1 &= a (1, 0, 0), & \underline{R}_2 &= a (0, 1, 0), & \underline{R}_3 &= c (0, 0, 1) \\ \underline{r}_1^{\text{Ti}} &= (0, 0, 0), & \underline{r}_2^{\text{Ti}} &= (1/2, 1/2, 1/2), & \underline{r}_3^{\text{O}} &= (x, x, 0) \\ \underline{r}_4^{\text{O}} &= (1-x, 1-x, 0), & \underline{r}_5^{\text{O}} &= (1/2+x, 1/2-x, 1/2), & \underline{r}_6^{\text{O}} &= (1/2-x, 1/2+x, 1/2) \\ a &= 4.593 \text{ \AA}, & c &= 2.958 \text{ \AA}, & x &= 0.3053 \end{aligned}$$



with  $\underline{R}_i$ ,  $i = 1, 2, 3$ , in Cartesian coordinates and  $\underline{r}_k$ ,  $k = 1, \dots, 6$ , in relative coordinates.

- (a) Show that each titanium atom has four oxygen atoms in its 1<sup>st</sup> and two in its 2<sup>nd</sup> neighbor shell. Determine Ti-O distances of the two oxygen shells with respect to the central titanium.
- (b) The six oxygen atoms of the two neighbor shells form edges of a polyhedron. Determine its shape.
- (c) Determine point symmetry elements of the crystal.
- 2.24. Consider atom clusters  $A_N$  with  $N$  atoms originating from a central atom  $A$  and its  $n$  neighbor shells in a crystal ( $n < 10$ ) with an (a) fcc, (b) bcc, (c) hex (hcp) lattice. Determine the total number of atoms  $N(n)$  and corresponding cluster radii  $R(n)$  as a function of the shell index  $n$ .
- 2.25. Build radially symmetric  $C_{60}$  ('Buckminster ball'),  $C_{24}$ , and  $C_{12}$  clusters. Here equilateral carbon hexagons join with each other and with pentagons, squares, and triangles, respectively to form a polyhedral structure of 'spherical' shape, i.e. all atom centers lie on a sphere with respect to a common center. Determine the sphere radius of each cluster as a function of the interatomic C-C distance  $d_{C-C}$  assuming equal distances in all cases ( $d_{C-C} = 1.4 \text{ \AA}$  in experiment). Hints:
- (a)  $C_{60}$  combines 20 hexagons with 12 pentagons. Each pentagon is adjacent only to hexagons. The cluster resembles a competition soccer ball.
- (b)  $C_{24}$  combines 8 hexagons with 6 squares. Each square is adjacent only to hexagons. The cluster resembles the Wigner-Seitz cell of a bcc crystal.
- (c)  $C_{12}$  combines 4 hexagons with 4 triangles. Each triangle is adjacent only to hexagons. The cluster resembles a tetrahedron with edges cut off symmetrically.
- 2.26. Determine orientations and areas of all surfaces of the Wulff polyhedra for the cubic crystallites shown in Fig. 2.42.
- 2.27. Consider a Wulff polyhedron of a cubic crystallite with low-energy planes perpendicular to  $(\pm 1, \pm 1, \pm 1)$  with surface energies  $\gamma_{(111)}$  and perpendicular to  $(\pm 1, 0, 0)$ ,  $(0, \pm 1, 0)$ ,  $(0, 0, \pm 1)$  with surface energies  $\gamma_{(001)}$  where  $(x, y, z)$  refers to vectors in Cartesian coordinates.
- (a) Determine the polyhedron volume and surface area as a function of  $q = \gamma_{(001)}/\gamma_{(111)}$ .

- (b) Assume surface energy ratios  $q = \gamma_{(001)}/\gamma_{(111)}$  and show that the Wulff polyhedra are cubes for  $q \geq \sqrt{3}$ , capped cubes for  $2/\sqrt{3} \leq q < \sqrt{3}$ , capped octahedra for  $1/\sqrt{3} \leq q < 2/\sqrt{3}$ , and octahedra for  $q < 1/\sqrt{3}$ .
- (c) Determine the volume of the sphere surrounding the Wulff polyhedron for given ratio  $q$  where the polyhedron edges lie on the sphere surface.
- 2.28. Consider a Wulff polyhedron with low-energy planes of equal surface energy  $\gamma$  and perpendicular to  $(1, 1, 1)$ ,  $(-1, -1, 1)$ ,  $(-1, 1, -1)$ ,  $(1, -1, -1)$  in Cartesian coordinates. Show that the shape is tetrahedral.
- 2.29. Consider a Wulff polyhedron to be defined by 12 planes through  $\underline{R}_i$  with normal vectors along  $\underline{R}_i$  in Cartesian coordinates where  $\underline{R}_i = (x, y, z) = (\pm 1, \pm 1, \pm \sqrt{2})$ ,  $(\pm 2, 0, 0)$ ,  $(0, \pm 2, 0)$ . Show that the shape of the polyhedron is that of a Wigner-Seitz cell of the face-centered cubic lattice. Determine the relative surface energies  $\gamma_{(x, y, z)}$  of the different planes.
- 2.30. Consider a Wulff polyhedron to be defined by 14 planes through  $\underline{R}_i$  with normal vectors along  $\underline{R}_i$  in Cartesian coordinates where  $\underline{R}_i = (x, y, z) = (\pm 1, \pm 1, \pm 1)$ ,  $(\pm 2, 0, 0)$ ,  $(0, \pm 2, 0)$ ,  $(0, 0, \pm 2)$ . Show that the shape of the polyhedron is that of a Wigner-Seitz cell of the body-centered cubic lattice. Determine the relative surface energies  $\gamma_{(x, y, z)}$  of the different planes.
- 2.31. Show that the Wulff polyhedron of a hexagonal crystal with its hexagonal axis along  $z$  in Cartesian coordinates and surface energies  $\gamma_{(x, y, 0)} = \gamma_a$ ,  $\gamma_{(0, 0, z)} = \gamma_c$  is a hexagonal prism independent of  $\gamma_a$  and  $\gamma_c$ .
- 2.32. The two-dimensional Penrose crystal, see Fig. 2.49, includes parallel atom rows where adjacent rows are separated by two distinct distances, a small and a large distance,  $s$  and  $L$ , respectively. The sequence of these distances can be generated iteratively by the following recipe
- start with a one-member sequence  $S_1$  of distance  $s$  or  $L$ ;
  - generate the next sequence  $S_{k+1}$  by replacing in the present sequence  $S_k$  all distances  $s$  by  $L$  and all  $L$  by two distances  $s, L$ .
- This generates sequences  $S_k$  with an increasing number  $N_k$  of distances, of which  $N_k^L$  counts large and  $N_k^s$  small distances. An example is the eight-distance sequence ‘ $L s L L s L s L$ ’.

- (a) Show that the number of distances  $N_k$  in sequence  $S_k$ , starting with sequences  $S_1 = s$ ,  $S_2 = L$ , can be determined iteratively by

$$N_k = N_{k-1} + N_{k-2} \quad , \quad N_1 = N_2 = 1$$

yielding the Fibonacci number series 1, 1, 2, 3, 5, 8, 13, ...

- (b) Show that the starting  $N_k$  members of distances in sequence  $S_{k+1}$  are identical to those of  $S_k$ .
- (c) Show that the ratio of the number of large distances,  $N_k^L$ , and that of small distances,  $N_k^s$ , of sequence  $S_k$  can be determined iteratively by

$$q_k = N_k^L / N_k^s : \quad q_k = 1 + 1/q_{k-1}$$

Show that ratio  $q_k$  converges for infinitely large sequences to the golden ratio

$$\tau = (1 + \sqrt{5}) / 2 = 1.618034 \quad .$$

- (d) Show that the ratio  $p_k = N_k / N_{k-1}$  of the number of distances  $N_k$  of two successive sequences converges for infinitely large sequences to the golden ratio  $\tau$ .

2.33. A Fibonacci chain is created by projecting atoms inside a strip cut from a square lattice of lattice constant  $c$  where the cutting angle  $\alpha$  is given by  $\tan(\alpha) = 1/\tau$ , see Fig. 2.50.

- (a) Show that the width  $w$  of the strip is given by  $w = c \frac{(\tau+1)}{\sqrt{\tau^2+1}}$ .

- (b) Assume that the two different interatomic distances along the chain are  $L$  (long) and  $s$  (short). Proof that  $L/s = \tau$  ,  $L = c \cos(\alpha) = c \tau (\tau^2+1)^{-1/2}$  ,  $s = c \sin(\alpha) = c (\tau^2+1)^{-1/2}$  with  $\tan(\alpha) = 1/\tau$  .

2.34. Cut-and-project (CAP) chains in general can be created by projecting atoms inside a strip cut from a square lattice of lattice constant  $c$  where the cutting angle is  $\alpha$  analogous to Fig. 2.50.

- (a) Show that CAP chains for  $\tan(\alpha) = n/m$  ( $n, m$  integer) are periodic. For other angles  $\alpha$  they are aperiodic with always only two different interatomic lengths  $L$  and  $s$ .
- (b) Show that the width  $w$  of the strips is given by  $w = c \{ \sin(\alpha) + \cos(\alpha) \}$ .
- (c) Proof that  $s/L = \tan(\alpha)$  ,  $L = c \cos(\alpha)$  ,  $s = c \sin(\alpha)$ .

2.35. Consider a monoatomic crystal with modulated lattice structure where atom positions are given by

$$\underline{\mathbf{R}}_o = n_1 \underline{\mathbf{R}}_{o1} + n_2 \underline{\mathbf{R}}_{o2} + n_3 \underline{\mathbf{R}}_{o3} + \underline{\mathbf{u}}(\underline{\mathbf{R}}_o), \quad n_i \text{ integer}$$

$$\underline{\mathbf{u}}(\underline{\mathbf{r}}) = \underline{\mathbf{u}}_o \sin(\underline{\mathbf{G}} \underline{\mathbf{r}}), \quad \underline{\mathbf{u}}_o, \underline{\mathbf{G}} \text{ fixed}$$

Determine vectors  $\underline{\mathbf{G}}$  which result in a truly periodic lattice.

### 3 CRYSTAL LAYERS: TWO-DIMENSIONAL LATTICES

#### 3.1 Basic Definition, Miller Indices

The concept of **monolayers** and **netplanes** in crystals is of central importance for the analysis of many structural properties of single crystals as well as of their surfaces. It can simplify conceptual thinking about crystal structure but is also essential for practical applications. For example, electron and photon diffraction from single crystal surfaces are often treated by theoretical methods that consider scattering from different crystal layers to build the complete diffraction image. Here the basic idea is that any three-dimensionally periodic crystal can be **decomposed** into planar two-dimensionally periodic monolayers, which are **stacked** along the third dimension. This is illustrated in the Fig. 3.1, which shows different two-dimensionally periodic monolayers inside a monoatomic crystal with an fcc lattice, where square, rectangular, and hexagonal layers are displayed. (The netplane nomenclature, used to label the monolayers in Fig. 3.1, refers to Miller indices which will be explained below.) Clearly, monolayers can assume quite different structure depending on how they are oriented in the crystal.

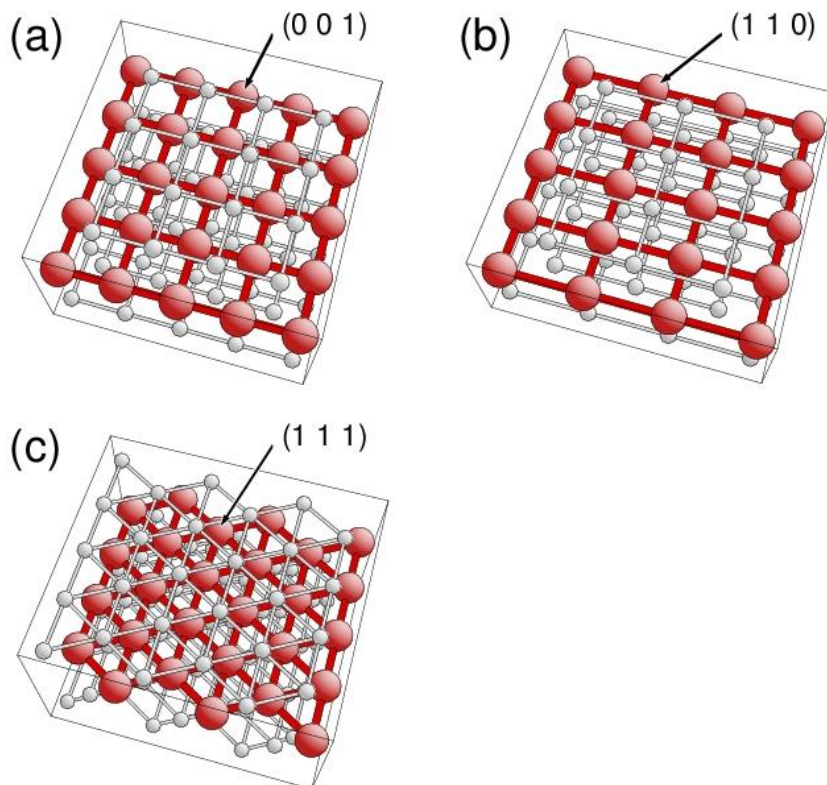


Fig. 3.1. Different monolayers of a crystal with an fcc lattice, (a) square  $(0\ 0\ 1)$  monolayer, (b) rectangular  $(1\ 1\ 0)$  monolayer, and (c) hexagonal  $(1\ 1\ 1)$  monolayer. In each case the second monolayer from the top is emphasized by large red balls.

The **formal definition** of a monolayer starts from a perfect bulk crystal with its periodicity defined by lattice vectors  $\underline{\mathbf{R}}_{o1}$ ,  $\underline{\mathbf{R}}_{o2}$ , and  $\underline{\mathbf{R}}_{o3}$  and its basis by lattice basis vectors  $\underline{\mathbf{r}}_{o1} \dots \underline{\mathbf{r}}_{op}$ , where we focus first on the lattice. **General lattice vectors**  $\underline{\mathbf{R}}$  of the lattice can always be described by linear combinations

$$\underline{\mathbf{R}} = n_{o1} \underline{\mathbf{R}}_{o1} + n_{o2} \underline{\mathbf{R}}_{o2} + n_{o3} \underline{\mathbf{R}}_{o3} , \quad n_{oi} \text{ integer} \quad (3.1)$$

However, according to Sec. 2.2.2.3, there are an infinite number of alternative descriptions of the same lattice by other vector sets  $\underline{\mathbf{R}}_1$ ,  $\underline{\mathbf{R}}_2$ ,  $\underline{\mathbf{R}}_3$ , where some may be more appropriate for describing specific monolayers. These alternative vector sets are connected with their initial counterparts,  $\underline{\mathbf{R}}_{o1}$ ,  $\underline{\mathbf{R}}_{o2}$ ,  $\underline{\mathbf{R}}_{o3}$ , by linear transformations according to (2.62) with integer-valued transformation matrices  $\underline{\mathbf{T}}$ , where  $\det(\underline{\mathbf{T}}) = 1$ . (Matrix  $\underline{\mathbf{T}}$  also transforms all lattice basis vectors  $\underline{\mathbf{r}}_{o1} \dots \underline{\mathbf{r}}_{op}$  to yield  $\underline{\mathbf{r}}_1 \dots \underline{\mathbf{r}}_p$ .) If we consider one of these **transformed lattice vector sets** defined by an appropriate matrix  $\underline{\mathbf{T}}$  then general lattice vectors  $\underline{\mathbf{R}}$  can be written, analogous to (3.1), as

$$\underline{\mathbf{R}} = ( n_1 \underline{\mathbf{R}}_1 + n_2 \underline{\mathbf{R}}_2 ) + n_3 \underline{\mathbf{R}}_3 , \quad n_i \text{ integer} \quad (3.2)$$

The parentheses in (3.2) emphasize that, for a fixed value  $n_3$ , the infinite set of vectors  $\underline{\mathbf{R}}$  for all integer values  $n_1, n_2$  forms a two-dimensional lattice with lattice vectors  $\underline{\mathbf{R}}_1$  and  $\underline{\mathbf{R}}_2$ . Thus, different values of  $n_3$  provide a collection of parallel two-dimensional lattices, which are identical in their periodicity defined by  $\underline{\mathbf{R}}_1$  and  $\underline{\mathbf{R}}_2$  and whose origins are separated from each other by vector  $\underline{\mathbf{R}}_3$ . These sublattices of the bulk lattice are called **netplanes**, sometimes also **crystallographic planes**, and the complete set of parallel netplanes spans the three-dimensional lattice. Further, the planar symmetry of the netplanes depends on the choice of the transformed lattice vectors  $\underline{\mathbf{R}}_1$ ,  $\underline{\mathbf{R}}_2$ , and, therefore, on the corresponding transformation matrix  $\underline{\mathbf{T}}$ . (Additional symmetry issues will be discussed in greater detail in Secs. 3.7 and 3.8.)

The concept of netplanes is intimately connected with the definition of monolayers. A **monolayer** describes a collection of atoms on a **plane** in a crystal. The atoms are located at **positions** given by a **lattice basis vector**  $\underline{\mathbf{r}}_i$ ,  $i = 1 \dots p$ , and its periodic equivalents where the periodicity is defined by vectors  $\underline{\mathbf{R}}_1$  and  $\underline{\mathbf{R}}_2$  of a **netplane**. Then the complete set of parallel monolayers is obtained by shifting each of the origins  $\underline{\mathbf{r}}_i$ ,  $i = 1 \dots p$ , by any integer multiple of lattice vector  $\underline{\mathbf{R}}_3$ . As examples, Fig. 3.1 shows three different monolayers for corresponding choices of lattice vectors  $\underline{\mathbf{R}}_1$  and  $\underline{\mathbf{R}}_2$ . The complete set of monolayers for all  $\underline{\mathbf{r}}_i$  fills the three-dimensional crystal. Further, depending on vectors  $\underline{\mathbf{R}}_1$  and  $\underline{\mathbf{R}}_2$ , monolayers originating from different positions  $\underline{\mathbf{r}}_i$  can lie on the same plane, which leads to polyatomic monolayers. This can be seen already in Fig. 1.1 for the MgO crystal

where monolayers denoted by (1 1 1) refer to planes of single Mg or O atoms while those labeled (0 0 1) contain both Mg and O atoms in the same plane.

It should be noted that the **definition** of a **monolayer** given in this book is rather general and **deviates** from definitions used in numerous surface science publications. In the latter, the term ‘monolayer’ often refers to adsorbate overlayers at single crystal bulk where the overlayer density corresponds to one adsorbate particle per substrate atom or unit cell (described as monolayer coverage). With the present definition this would be an adsorbate monolayer with a specific coverage while those of different coverage would also be called monolayers.

The relationship between netplanes and monolayers forms the two-dimensional **analogue** to that between lattices and crystals in the three-dimensional case. Thus, one can also consider a **morphological unit cell** of a netplane or monolayer, defined by the parallelogram spanned by lattice vectors  $\underline{\mathbf{R}}_1$  and  $\underline{\mathbf{R}}_2$  with cell area  $A_{el}$  given by

$$A_{el} = | \underline{\mathbf{R}}_1 \times \underline{\mathbf{R}}_2 | \quad (3.3)$$

The unit cell will be called **primitive** if it is of smallest possible area in the netplane. Further, a monolayer can be assigned a basis of atoms given by corresponding **lattice basis vectors**  $\underline{\mathbf{r}}_i$ . Thus, in the example of a (0 0 1) monolayer of MgO one could define two lattice basis vectors,  $\underline{\mathbf{r}}_1^{\text{Mg}}$ ,  $\underline{\mathbf{r}}_2^{\text{O}}$ , inside the corresponding morphological unit cell describing positions of the two unique atoms Mg and O. It should be noted that surface scientists often use the word ‘netplane’ to describe a monolayer. However, in a strict sense a **netplane** can be considered only a **mathematical construct** to characterize the two-dimensional periodicity and symmetry properties of a monolayer.

The definition of a netplane is based on **transformed** lattice vectors  $\underline{\mathbf{R}}_1$ ,  $\underline{\mathbf{R}}_2$ ,  $\underline{\mathbf{R}}_3$  of a three-dimensional lattice, where the two vectors  $\underline{\mathbf{R}}_1$  and  $\underline{\mathbf{R}}_2$  determine the periodicity of the netplane. Thus, vectors  $\underline{\mathbf{R}}_1$ ,  $\underline{\mathbf{R}}_2$ ,  $\underline{\mathbf{R}}_3$  and the corresponding transformation **matrix**  $\underline{\mathbf{T}}$  can be considered to be **netplane-adapted** and matrix  $\underline{\mathbf{T}}$  may be used to characterize netplanes. The **normal direction** of a netplane can be viewed as the normal component of the stacking direction of corresponding monolayers inside a crystal. It is given by a vector  $\underline{\mathbf{n}}$  where, using transformation  $\underline{\mathbf{T}}$  from (2.62),

$$\begin{aligned} \underline{\mathbf{n}} &= \alpha (\underline{\mathbf{R}}_1 \times \underline{\mathbf{R}}_2) = \alpha \sum_{i=1}^3 \sum_{j=1}^3 t_{1i} t_{2j} (\underline{\mathbf{R}}_{0i} \times \underline{\mathbf{R}}_{0j}) \\ &= \alpha \{ h (\underline{\mathbf{R}}_{02} \times \underline{\mathbf{R}}_{03}) + k (\underline{\mathbf{R}}_{03} \times \underline{\mathbf{R}}_{01}) + l (\underline{\mathbf{R}}_{01} \times \underline{\mathbf{R}}_{02}) \} \end{aligned} \quad (3.4)$$

with coefficients

$$\begin{aligned} h &= t_{12} t_{23} - t_{13} t_{22}, & k &= t_{13} t_{21} - t_{11} t_{23}, & l &= t_{11} t_{22} - t_{12} t_{21} \\ \alpha &= |\underline{\mathbf{R}}_1 \times \underline{\mathbf{R}}_2|^{-1}. \end{aligned} \quad (3.5)$$

Here  $\alpha$  is only a normalization constant to guarantee that  $|\underline{\mathbf{n}}| = 1$ . Since all elements of the transformation matrix  $\underline{\mathbf{T}}$  are integers the coefficients  $h$ ,  $k$ , and  $l$  must also be integer-valued and are commonly named (**generic**) **Miller indices**. This means in particular that, according to (3.4), normal directions of netplanes in a lattice are always discrete and generic Miller indices  $(h k l)$  can be used to **characterize** sets of netplanes for a given **direction**. In this spirit transformation matrices  $\underline{\mathbf{T}}$  which are connected with netplane stacking directions will be labeled  $\underline{\mathbf{T}}^{(h k l)}$  in the following.

Miller indices can assume both positive and negative integer values where in crystallography negative indices are often written with the minus sign above the number, such as  $(-4 \ 1 \ 2)$  being written as  $(\bar{4} \ 1 \ 2)$ , which saves a character space. However, in this book we do not adopt this notation and all negative indices will be given with a minus sign in front.

According to (3.4) netplane normal vectors  $\underline{\mathbf{n}}$  are given as linear combinations of three vectors  $(\underline{\mathbf{R}}_{oi} \times \underline{\mathbf{R}}_{oj})$  that arise from vector products of the initial lattice vectors. Thus, based on the definition (2.95) of reciprocal lattice vectors,  $\underline{\mathbf{G}}_{o1}$ ,  $\underline{\mathbf{G}}_{o2}$ ,  $\underline{\mathbf{G}}_{o3}$ , in Sec. 2.5 any normal vector  $\underline{\mathbf{n}}$  points along a vector  $\underline{\mathbf{G}}_{(h k l)}$ , where

$$\begin{aligned} \underline{\mathbf{G}}_{(h k l)} &= \beta (\underline{\mathbf{R}}_1 \times \underline{\mathbf{R}}_2) = h \underline{\mathbf{G}}_{o1} + k \underline{\mathbf{G}}_{o2} + l \underline{\mathbf{G}}_{o3} \\ \beta &= (2\pi) / [(\underline{\mathbf{R}}_1 \times \underline{\mathbf{R}}_2) \cdot \underline{\mathbf{R}}_3] = (2\pi) / [(\underline{\mathbf{R}}_{o1} \times \underline{\mathbf{R}}_{o2}) \cdot \underline{\mathbf{R}}_{o3}] = (2\pi) / V_{el} \end{aligned} \quad (3.6)$$

Thus,  $\underline{\mathbf{G}}_{(h k l)}$  is a **general reciprocal lattice** vector and is quite useful in describing numerous properties of netplanes and monolayers.

As an example, the **distance**  $d_{(h k l)}$  between two adjacent  $(h k l)$  netplanes or monolayers, which are connected by a lattice vector  $\underline{\mathbf{R}}_3$ , can be written as

$$\begin{aligned} d_{(h k l)} &= \underline{\mathbf{n}} \cdot \underline{\mathbf{R}}_3 = (\underline{\mathbf{G}}_{(h k l)} \cdot \underline{\mathbf{R}}_3) / |\underline{\mathbf{G}}_{(h k l)}| = (2\pi/V_{el}) (\underline{\mathbf{R}}_1 \times \underline{\mathbf{R}}_2) \cdot \underline{\mathbf{R}}_3 / |\underline{\mathbf{G}}_{(h k l)}| = \\ &= 2\pi / |\underline{\mathbf{G}}_{(h k l)}| \end{aligned} \quad (3.7)$$

Thus, if the length of  $\underline{\mathbf{G}}_{(h k l)}$ , determined by the size of the generic Miller indices, becomes large, the distance between adjacent netplanes becomes small. Netplanes belonging to large Miller indices lie close together.



Further, the average **atom density**  $\rho_{(hkl)}$  of a monolayer with an  $(hkl)$  netplane is, according to (3.6), (3.7), given by

$$\rho_{(hkl)} = n_{(hkl)} / |\underline{\mathbf{R}}_1 \times \underline{\mathbf{R}}_2| = n_{(hkl)} (2\pi/V_{el}) / |\underline{\mathbf{G}}_{(hkl)}| = n_{(hkl)} d_{(hkl)} / V_{el} \quad (3.8)$$

where  $n_{(hkl)}$  denotes the number of co-planar atoms in the unit cell of the monolayer. Thus, for large vectors  $\underline{\mathbf{G}}_{(hkl)}$  the atom density of corresponding monolayers becomes small while monolayers belonging to small Miller indices are the densest. As an illustration, Table 3.1 lists Miller indices  $(hkl)$  and densities  $\rho_{(hkl)}$  and of the ten densest monolayers with  $(hkl)$  netplanes of the sc, fcc, bcc, and hex (hcp) lattices calculated using (3.8). All Miller indices of the cubic lattices are given in sc notation by symmetry related families  $\{hkl\}$ ; (m), with m denoting the number of family members, see below. Miller indices of the hcp lattice refer to the obtuse representation

Table 3.1. Average atom densities  $\rho_{(hkl)}$  of the ten densest  $(hkl)$  monolayers ( $\{hkl\}$  monolayer families) of crystals with (a) sc, (b) fcc, (c) bcc, and (d) hcp lattice, see text. The densities  $\rho_{(hkl)}$  are defined with respect to the square of the corresponding lattice constant  $a$  (applying  $c/a = \sqrt[3]{8/3}$  for hcp).

	$\{hkl\}$ ; (m)	$\rho_{(hkl)}/a^2$		$\{hkl\}$ ; (m)	$\rho_{(hkl)}/a^2$
<b>(a) sc</b>					
1	{1 0 0}; (6)	1 = 1.000	6	{2 2 1}; (24)	$1/\sqrt{9} = 0.333$
2	{1 1 0}; (12)	$1/\sqrt{2} = 0.707$	7	{3 1 0}; (24)	$1/\sqrt{10} = 0.316$
3	{1 1 1}; (8)	$1/\sqrt{3} = 0.577$	8	{3 1 1}; (24)	$1/\sqrt{11} = 0.302$
4	{2 1 0}; (24)	$1/\sqrt{5} = 0.447$	9	{3 2 0}; (24)	$1/\sqrt{13} = 0.277$
5	{2 1 1}; (24)	$1/\sqrt{6} = 0.408$	10	{3 2 1}; (24)	$1/\sqrt{14} = 0.267$
<b>(b) fcc</b>					
1	{1 1 1}; (8)	$4/\sqrt{3} = 2.309$	6	{4 2 0}; (24)	$4/\sqrt{20} = 0.894$
2	{2 0 0}; (6)	$4/\sqrt{4} = 2.000$	7	{4 2 2}; (24)	$4/\sqrt{24} = 0.816$
3	{2 2 0}; (12)	$4/\sqrt{8} = 1.414$	8	{5 1 1}; (24)	$4/\sqrt{27} = 0.770$
4	{3 1 1}; (24)	$4/\sqrt{11} = 1.206$	9	{5 3 1}; (48)	$4/\sqrt{35} = 0.676$
5	{3 3 1}; (24)	$4/\sqrt{19} = 0.918$	10	{4 4 2}; (24)	$4/\sqrt{36} = 0.667$
<b>(c) bcc</b>					
1	{1 1 0}; (12)	$2/\sqrt{2} = 1.414$	6	{3 2 1}; (48)	$2/\sqrt{14} = 0.535$
2	{2 0 0}; (6)	$2/\sqrt{4} = 1.000$	7	{4 1 1}; (24)	$2/\sqrt{18} = 0.471$
3	{2 1 1}; (24)	$2/\sqrt{6} = 0.816$	8	{4 2 0}; (24)	$2/\sqrt{20} = 0.447$
4	{3 1 0}; (24)	$2/\sqrt{10} = 0.632$	9	{3 3 2}; (24)	$2/\sqrt{22} = 0.426$
5	{2 2 2}; (8)	$2/\sqrt{12} = 0.577$	10	{5 1 1}; (24)	$2/\sqrt{27} = 0.385$

(d) hcp	(h k l); (m)	$\rho_{(h k l)}/a^2$
1	(0 0 $\pm 1$ ); (2)	$2/\sqrt{3} = 1.155$
2*	$\pm(1 1 0)$ , $\pm(2 -1 0)$ , $\pm(1 -2 0)$ ; (6)	$1/\sqrt{2} = 0.707$
3	$\pm(1 0 0)$ , $\pm(0 1 0)$ , $\pm(1 -1 0)$ ; (6)	$\sqrt{(3/8)} = 0.612$
4*	$\pm(1 1 \pm 2)$ , $\pm(2 -1 \pm 2)$ , $\pm(1 -2 \pm 2)$ ; (12)	$2/\sqrt{11} = 0.603$
5	$\pm(1 0 \pm 1)$ , $\pm(0 1 \pm 1)$ , $\pm(1 -1 \pm 1)$ ; (12)	$\sqrt{(12/41)} = 0.541$
6	$\pm(1 0 \pm 2)$ , $\pm(0 1 \pm 2)$ , $\pm(1 -1 \pm 2)$ ; (12)	$\sqrt{(3/17)} = 0.420$
7*	$\pm(3 0 \pm 2)$ , $\pm(0 3 \pm 2)$ , $\pm(3 -3 \pm 2)$ ; (12)	$2/\sqrt{27} = 0.385$
8	$\pm(1 1 \pm 1)$ , $\pm(2 -1 \pm 1)$ , $\pm(1 -2 \pm 1)$ ; (12)	$2/\sqrt{35} = 0.338$
9	$\pm(2 0 \pm 1)$ , $\pm(0 2 \pm 1)$ , $\pm(1 -1 \pm 1)$ ; (12)	$\sqrt{(12/137)} = 0.296$
10	$\pm(2 1 0)$ , $\pm(1 2 0)$ , $\pm(-1 3 0)$ , $\pm(-2 3 0)$ , $\pm(3 -2 0)$ , $\pm(3 -1 0)$ ; (12)	$\sqrt{(3/56)} = 0.231$

(i.e.  $\angle(\mathbf{R}_{o1}, \mathbf{R}_{o2}) = 120^\circ$ , see Sec. 2.2.2.1) and are given in generic 3-index notation. Note that for the hex (hcp) lattice the 2<sup>nd</sup>, 4<sup>th</sup> and 7<sup>th</sup> densest monolayers, denoted by asterisks (\*) in Table 3.1, contain two atoms in their morphological unit cells, i.e.  $n_{(h k l)} = 2$  while for all others  $n_{(h k l)} = 1$ .

If a lattice exhibits, in addition to translation symmetry, also **point symmetry** then geometrically identical netplanes may appear for different Miller index values. These equivalent netplanes are often grouped into **families**, where each family is characterized by Miller indices  $\{h k l\}$  written inside **curly** brackets. An example is given by the simple cubic lattice with the six equivalent netplanes, denoted by Miller indices  $(\pm 1 0 0)$ ,  $(0 \pm 1 0)$ ,  $(0 0 \pm 1)$ , forming a family described as  $\{1 0 0\}$ . This notation is also used in Table 3.1 for monolayers of cubic lattices.

In a generalization of (3.4), directions inside a lattice may also be defined by Miller indices  $h, k, l$ , which are, in general, non-integer- or integer-valued. These directions are usually written as  $[h k l]$  inside **square** brackets. In addition, lattices with point symmetry allow symmetry equivalent directions where corresponding **direction families** are written as  $\langle h k l \rangle$  inside **pointed** brackets. As an example, the simple cubic lattice includes eight equivalent directions  $\pm[1 1 1]$ ,  $\pm[-1 1 1]$ ,  $\pm[1 -1 1]$ ,  $\pm[1 1 -1]$ , which form a direction family  $\langle 1 1 1 \rangle$ .

### 3.2 Netplane-Adapted Lattice Vectors

The discussion in Sec. 3.1 showed that  $(h k l)$  netplanes can be associated with linear transformations  $\underline{\mathbb{T}}^{(h k l)}$ , connecting the initial lattice vectors  $\underline{\mathbf{R}}_{01}$ ,  $\underline{\mathbf{R}}_{02}$ ,  $\underline{\mathbf{R}}_{03}$  with **netplane-adapted** lattice vectors  $\underline{\mathbf{R}}_1$ ,  $\underline{\mathbf{R}}_2$ ,  $\underline{\mathbf{R}}_3$  according to (2.62), where vectors  $\underline{\mathbf{R}}_1$  and  $\underline{\mathbf{R}}_2$  determine the netplane periodicity. Thus, transformations  $\underline{\mathbb{T}}^{(h k l)}$  are essential for any **computation** of crystal properties which requires quantitative information about netplanes by their explicit lattice vectors  $\underline{\mathbf{R}}_1$  and  $\underline{\mathbf{R}}_2$  derived from the initial lattice vectors  $\underline{\mathbf{R}}_{01}$ ,  $\underline{\mathbf{R}}_{02}$ ,  $\underline{\mathbf{R}}_{03}$ . As an example we mention theoretical evaluations of elastic moduli along specific crystal directions. Transformed lattice vectors are also an essential ingredient for any quantitative theoretical treatment of ideal single crystal surfaces as will be discussed in detail in Sec. 4.

The close relationship between transformation matrices  $\underline{\mathbb{T}}^{(h k l)}$  and Miller indices  $(h k l)$  becomes clear from the following relations obtained by using equations (2.62), (2.96), and (3.6)

$$\begin{aligned}\underline{\mathbf{G}}_{(h k l)} \underline{\mathbf{R}}_1 &= (h \underline{\mathbf{G}}_{01} + k \underline{\mathbf{G}}_{02} + l \underline{\mathbf{G}}_{03}) (t_{11} \underline{\mathbf{R}}_{01} + t_{12} \underline{\mathbf{R}}_{02} + t_{13} \underline{\mathbf{R}}_{03}) \\ &= 2\pi (t_{11} h + t_{12} k + t_{13} l) = 0 \\ \underline{\mathbf{G}}_{(h k l)} \underline{\mathbf{R}}_2 &= (h \underline{\mathbf{G}}_{01} + k \underline{\mathbf{G}}_{02} + l \underline{\mathbf{G}}_{03}) (t_{21} \underline{\mathbf{R}}_{01} + t_{22} \underline{\mathbf{R}}_{02} + t_{23} \underline{\mathbf{R}}_{03}) \\ &= 2\pi (t_{21} h + t_{22} k + t_{23} l) = 0 \\ \underline{\mathbf{G}}_{(h k l)} \underline{\mathbf{R}}_3 &= (h \underline{\mathbf{G}}_{01} + k \underline{\mathbf{G}}_{02} + l \underline{\mathbf{G}}_{03}) (t_{31} \underline{\mathbf{R}}_{01} + t_{32} \underline{\mathbf{R}}_{02} + t_{33} \underline{\mathbf{R}}_{03}) \\ &= 2\pi (t_{31} h + t_{32} k + t_{33} l) = 2\pi\end{aligned}\tag{3.9}$$

resulting in a set of three **linear Diophantine equations** which can be written in matrix form as

$$\begin{pmatrix} t_{11} & t_{12} & t_{13} \\ t_{21} & t_{22} & t_{23} \\ t_{31} & t_{32} & t_{33} \end{pmatrix} \cdot \begin{pmatrix} h \\ k \\ l \end{pmatrix} = \underline{\underline{\mathbb{T}}}^{(hkl)} \cdot \begin{pmatrix} h \\ k \\ l \end{pmatrix} = \begin{pmatrix} 0 \\ 0 \\ 1 \end{pmatrix}\tag{3.10}$$

This shows that for any transformation matrix  $\underline{\underline{\mathbb{T}}}^{(h k l)}$  corresponding Miller indices  $(h k l)$  can be obtained by solving the linear equations (3.10). In fact, the solutions are already given explicitly in (3.5).

On the other hand, for given  $(h k l)$  values example transformations  $\underline{\underline{\mathbb{T}}}^{(h k l)}$  can be evaluated from (3.10) using **number theoretical** methods as has been shown elsewhere [84]. Here we mention three **example solutions** which cover all possible  $h, k, l$  values.

- (a) Let integers
- $a, b$
- solve the linear Diophantine equation

$$a h + b k = 1 \quad (3.11a)$$

then

$$\underline{\underline{\mathbf{T}}}^{(hkl)} = \begin{pmatrix} k & -h & 0 \\ l \cdot a & l \cdot b & -1 \\ a & b & 0 \end{pmatrix}, \quad \left(\underline{\underline{\mathbf{T}}}^{(hkl)}\right)^{-1} = \begin{pmatrix} b & 0 & h \\ -a & 0 & k \\ 0 & -1 & l \end{pmatrix} \quad (3.11b)$$

- (b) Let integers
- $a, c$
- solve the linear Diophantine equation

$$a h + c l = 1 \quad (3.12a)$$

then

$$\underline{\underline{\mathbf{T}}}^{(hkl)} = \begin{pmatrix} -l & 0 & h \\ k \cdot a & -1 & k \cdot c \\ a & 0 & c \end{pmatrix}, \quad \left(\underline{\underline{\mathbf{T}}}^{(hkl)}\right)^{-1} = \begin{pmatrix} -c & 0 & h \\ 0 & -1 & k \\ a & 0 & l \end{pmatrix} \quad (3.12b)$$

- (c) Let integers
- $b, c$
- solve the linear Diophantine equation

$$b k + c l = 1 \quad (3.13a)$$

then

$$\underline{\underline{\mathbf{T}}}^{(hkl)} = \begin{pmatrix} 0 & l & -k \\ -1 & h \cdot b & h \cdot c \\ 0 & b & c \end{pmatrix}, \quad \left(\underline{\underline{\mathbf{T}}}^{(hkl)}\right)^{-1} = \begin{pmatrix} 0 & -1 & h \\ c & 0 & k \\ -b & 0 & l \end{pmatrix} \quad (3.13b)$$

Thus, each of these solutions requires the computation of **one** linear Diophantine equation in two variables, equations (3.11a), (3.12a), and (3.13a), where solutions may be guessed or determined numerically, using the algorithm discussed in Appendix E.3. Table 3.2 shows which of the three solutions can be used for any triplet  $(h k l)$ . This table assumes that all non-zero Miller index values are normalized such that they do not have a common divisor greater than 1. Otherwise, all non-zero Miller indices have to be divided by  $\text{gcd}(x, y)$  or  $\text{gcd}(x, y, z)$  before transformations (3.11), (3.12), or (3.13) can be applied. (Functions  $\text{gcd}(x, y)$  and  $\text{gcd}(x, y, z)$  denote the greatest common divisor, see Appendix E.1.)

Table 3.2. Example transformations  $\underline{T}^{(hkl)}$  for different Miller index values  $(hkl)$  referring to solutions (3.11), (3.12), or (3.13), see text.

Miller indices	Transformation
$(h\ 0\ 0) \equiv (1\ 0\ 0)$	(3.11) with $a = 1, b = 0$ ; (3.12) with $a = 1, c = 0$
$(0\ k\ 0) \equiv (0\ 1\ 0)$	(3.11) with $a = 0, b = 1$ ; (3.13) with $b = 1, c = 0$
$(0\ 0\ l) \equiv (0\ 0\ 1)$	(3.12) with $a = 0, c = 1$ ; (3.13) with $b = 0, c = 1$
$(h\ k\ 0), \gcd( h ,  k ) = 1$	(3.11) compute $a, b$
$(h\ 0\ l), \gcd( h ,  l ) = 1$	(3.12) compute $a, c$
$(0\ k\ l), \gcd( k ,  l ) = 1$	(3.13) compute $b, c$
$(h\ k\ l), \gcd( h ,  k ,  l ) = 1$	(3.11) compute $a, b$ or (3.12) compute $a, c$ or (3.13) compute $b, c$

The calculation of transformation matrices  $\underline{T}^{(hkl)}$  and, hence, of corresponding netplane-adapted lattice vectors, described in this section, does not make use of any specific lattice properties like lattice type or symmetry. Further, matrices  $\underline{T}^{(hkl)}$  given by (3.11b), (3.12b), and (3.13b) represent, in each case, an **infinite number of solutions**, since the accompanying Diophantine equations (3.11a), (3.12a), and (3.13a) have infinitely many solutions, as shown in Appendix E.3. This reflects the fact that lattice descriptions are **not unique** and there is always an infinite number of alternatives. The next section shows, how to select from this infinite manifold specific lattice descriptions, which can also reflect point symmetry properties of the  $(hkl)$  netplane under consideration.

### 3.3 Symmetrically Appropriate Lattice Vectors: Minkowski Reduction

The netplane-adapted lattice vectors given by (3.11), (3.12), and (3.13) yield **mathematically exact** lattice descriptions which may, however, **not** always be **intuitive**. As an example we mention the simple cubic lattice, where  $(hkl) = (0\ 0\ 1)$  netplanes are of square shape, see Fig. 2.15, can be constructed by lattice vectors

$$\underline{R}_{o1} = a(1, 0, 0), \quad \underline{R}_{o2} = a(0, 1, 0) \quad (3.14)$$

denoting a symmetrically appropriate vector set, since the two vectors are of equal length and perpendicular to each other, suggesting a square pattern. However, there are alternative lattice vectors, e.g.

$$\underline{\mathbf{R}}_1 = a(-1, -1, 0), \quad \underline{\mathbf{R}}_2 = a(2, 1, 0) \quad (3.15)$$

which do not give any idea of the square shape of the netplane. This problem can arise, in particular, when lattice vectors are generated numerically by a computer (i.e. without visual intuition). The rather hazy notion of ‘**symmetrically appropriate**’ can be quantified by requiring that the lattice vectors  $\underline{\mathbf{R}}_1$  and  $\underline{\mathbf{R}}_2$  connect lattice points of **smallest** distance in the lattice with  $R_1^2 \leq R_2^2$ . This requirement allows additional point symmetry elements to become visible already in the lattice vector representation of the corresponding netplane. Symmetrically appropriate vectors can be constructed iteratively following an algorithm due to Minkowski (**Minkowski reduction**) [85], see Appendix D for mathematical details. The iteration starts from any two lattice vectors  $\underline{\mathbf{R}}_1$  and  $\underline{\mathbf{R}}_2$  which are **reduced** successively in length by **linear mixing** until vectors of smallest length are obtained. This is illustrated in Fig. 3.2 for the (1 1 0) netplane of an fcc monolayer. Here the initial lattice vectors  $\underline{\mathbf{R}}_1$  and  $\underline{\mathbf{R}}_2$  (labeled ‘(0)’ in the figure) are reduced in two iteration steps to yield Minkowski-reduced lattice vectors (labeled ‘(2)’) where the vectors in red illustrate the reduction in each step.

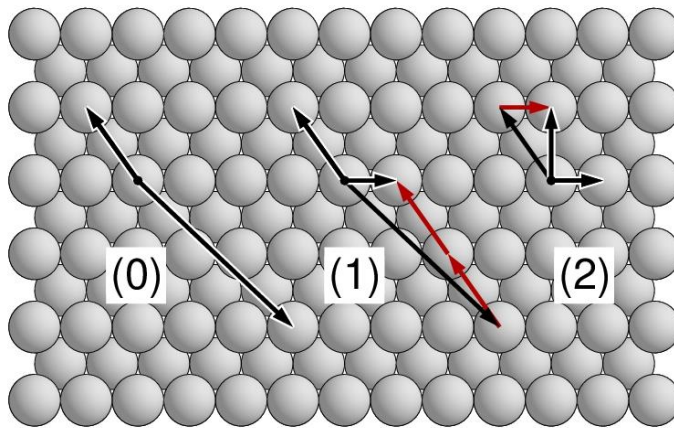


Fig. 3.2. Minkowski reduction of a lattice vector set for the (1 1 0) netplane of an fcc monolayer, see text. The underlying monolayer is added for orientation.

The reduction yields always after a **finite** number of iterations two Minkowski-reduced lattice vectors  $\underline{\mathbf{R}}_1$  and  $\underline{\mathbf{R}}_2$  of lengths  $R_1$  and  $R_2$  which can be shown to satisfy condition

$$-\min(R_1^2, R_2^2) \leq 2(\underline{\mathbf{R}}_1 \underline{\mathbf{R}}_2) < \min(R_1^2, R_2^2) \quad (3.16)$$

This means geometrically that each of the two vectors  $\underline{\mathbf{R}}_i$  projected on to the other,  $\underline{\mathbf{R}}_j$ , yields a vector along  $\underline{\mathbf{R}}_j$  of less than or equal to half the length of  $\underline{\mathbf{R}}_j$ . As shown in Appendix D, relation (3.16) guarantees that at least one of the two lattice vectors,  $\underline{\mathbf{R}}_1$  or  $\underline{\mathbf{R}}_2$ , connects lattice points of smallest distance in the lattice. If, as a result of the reduction, the vectors  $\underline{\mathbf{R}}_1$  and  $\underline{\mathbf{R}}_2$  are of the same length they must both be of smallest length. Further, relation (3.16) can be written as

$$-1 \leq -A \leq 2 \cos(\gamma) = 2 (\underline{\mathbf{R}}_1 \underline{\mathbf{R}}_2) / (\mathbf{R}_1 \mathbf{R}_2) < A \leq 1$$

$$A = \min (\mathbf{R}_1/\mathbf{R}_2, \mathbf{R}_2/\mathbf{R}_1) \quad (3.17)$$

where  $\gamma$  is the angle between vectors  $\underline{\mathbf{R}}_1$  and  $\underline{\mathbf{R}}_2$ . This proves that the angle between two Minkowski-reduced lattice vectors  $\underline{\mathbf{R}}_1$  and  $\underline{\mathbf{R}}_2$  must always lie between  $60^\circ$  and  $120^\circ$  where we distinguish between **acute**,  $60^\circ < \gamma \leq 90^\circ$ , and **obtuse** lattice vector sets,  $90^\circ < \gamma \leq 120^\circ$ .

Altogether, the Minkowski formalism leads to uniquely defined lattice vectors  $\underline{\mathbf{R}}_1$  and  $\underline{\mathbf{R}}_2$  for any two-dimensional lattice and allows an easy classification of the different types of two-dimensional Bravais lattices discussed in Sec. 3.8. Centered rectangular and hexagonal lattices yield equivalent lattice vector sets for  $\cos(\gamma) = A/2$  and  $\cos(\gamma) = -A/2$  (with  $A$  according to (3.17)) corresponding to acute and obtuse vector sets which can both be considered to be Minkowski-reduced. Here crystallographers prefer the obtuse representation referring to the strict definition given in (3.16). It should be mentioned that for three-dimensional bulk crystals analogous reduction schemes have been proposed [42], [43] to obtain unique lattice vector sets  $\underline{\mathbf{R}}_1, \underline{\mathbf{R}}_2, \underline{\mathbf{R}}_3$ , see also Sec. 2.2.2. There, the simplification to two dimensions is equivalent to the Minkowski reduction.

### 3.4 Miller Indices for Cubic and Trigonal Lattices

Generic Miller indices  $(h k l)$  are, by definition, based on reciprocal lattice vectors  $\underline{\mathbf{G}}_{01}, \underline{\mathbf{G}}_{02}, \underline{\mathbf{G}}_{03}$ , as given by (2.95), where lattice vectors  $\underline{\mathbf{R}}_{01}, \underline{\mathbf{R}}_{02}, \underline{\mathbf{R}}_{03}$ , referring to a primitive lattice representation, are the natural choice. However, in the case of **cubic** lattices scientists very often use real space and reciprocal lattice vectors of the **simple cubic** lattice even in studies of crystals with fcc and bcc lattices. This is due to the **geometric simplicity** of the sc lattice with its three orthogonal lattice vectors of equal length where the reciprocal lattice is also of sc type and direction vectors in real space are parallel to those in reciprocal space. The choice of the sc lattice for fcc and bcc lattices affects corresponding Miller index values, as will be discussed in the following.

According to (2.102), the **face-centered cubic** lattice is characterized by reciprocal lattice vectors  $\underline{\mathbf{G}}_{01}^{\text{fcc}}, \underline{\mathbf{G}}_{02}^{\text{fcc}}, \underline{\mathbf{G}}_{03}^{\text{fcc}}$ , which can be represented by those of the simple cubic (sc, cubic-P) lattice, using (2.101), where

$$\begin{aligned} \underline{\mathbf{G}}_{01}^{\text{fcc}} &= -\underline{\mathbf{G}}_{01}^{\text{sc}} + \underline{\mathbf{G}}_{02}^{\text{sc}} + \underline{\mathbf{G}}_{03}^{\text{sc}} \\ \underline{\mathbf{G}}_{02}^{\text{fcc}} &= \underline{\mathbf{G}}_{01}^{\text{sc}} - \underline{\mathbf{G}}_{02}^{\text{sc}} + \underline{\mathbf{G}}_{03}^{\text{sc}} \end{aligned}$$

$$\underline{\mathbf{G}}_{03}^{\text{fcc}} = \underline{\mathbf{G}}_{01}^{\text{sc}} + \underline{\mathbf{G}}_{02}^{\text{sc}} - \underline{\mathbf{G}}_{03}^{\text{sc}} \quad (3.18)$$

As a consequence, netplane normal directions point along vectors

$$\begin{aligned} \underline{\mathbf{G}}_{(hkl)} &= h^{\text{fcc}} \underline{\mathbf{G}}_{01}^{\text{fcc}} + k^{\text{fcc}} \underline{\mathbf{G}}_{02}^{\text{fcc}} + l^{\text{fcc}} \underline{\mathbf{G}}_{03}^{\text{fcc}} = \\ &= (-h^{\text{fcc}} + k^{\text{fcc}} + l^{\text{fcc}}) \underline{\mathbf{G}}_{01}^{\text{sc}} + (h^{\text{fcc}} - k^{\text{fcc}} + l^{\text{fcc}}) \underline{\mathbf{G}}_{02}^{\text{sc}} + (h^{\text{fcc}} + k^{\text{fcc}} - l^{\text{fcc}}) \underline{\mathbf{G}}_{03}^{\text{sc}} \\ &= h^{\text{sc}} \underline{\mathbf{G}}_{01}^{\text{sc}} + k^{\text{sc}} \underline{\mathbf{G}}_{02}^{\text{sc}} + l^{\text{sc}} \underline{\mathbf{G}}_{03}^{\text{sc}} \end{aligned} \quad (3.19)$$

suggesting, in addition to the generic notation  $(h^{\text{fcc}} k^{\text{fcc}} l^{\text{fcc}})$ , a **simple cubic** or **(sc) notation**  $(h^{\text{sc}} k^{\text{sc}} l^{\text{sc}})$  for Miller indices of the fcc lattice. According to (3.19), there is a linear transformation between the indices given by

$$\begin{pmatrix} h^{\text{sc}} \\ k^{\text{sc}} \\ l^{\text{sc}} \end{pmatrix} = \begin{pmatrix} -1 & 1 & 1 \\ 1 & -1 & 1 \\ 1 & 1 & -1 \end{pmatrix} \cdot \begin{pmatrix} h^{\text{fcc}} \\ k^{\text{fcc}} \\ l^{\text{fcc}} \end{pmatrix}, \quad \begin{pmatrix} h^{\text{fcc}} \\ k^{\text{fcc}} \\ l^{\text{fcc}} \end{pmatrix} = \frac{1}{2} \begin{pmatrix} 0 & 1 & 1 \\ 1 & 0 & 1 \\ 1 & 1 & 0 \end{pmatrix} \cdot \begin{pmatrix} h^{\text{sc}} \\ k^{\text{sc}} \\ l^{\text{sc}} \end{pmatrix} \quad (3.20a, b)$$

Here the factor 1/2 in transformation (3.20b) restricts possible values of Miller indices in simple cubic notation. Transformation (3.20b) yields integer-valued Miller indices,  $h^{\text{fcc}}, k^{\text{fcc}}, l^{\text{fcc}}$ , only if the indices in simple cubic notation,  $h^{\text{sc}}, k^{\text{sc}}, l^{\text{sc}}$ , are **all even** or **all odd** integers.

Transformation (3.20a) can also be understood as the three basic Miller index triplets  $(-1 \ 1 \ 1)$ ,  $(1 \ -1 \ 1)$ ,  $(1 \ 1 \ -1)$  defining lattice vectors in the integer vector space which describes all sc Miller indices  $(h^{\text{sc}} k^{\text{sc}} l^{\text{sc}})$  of a fcc lattice in simple cubic notation. Thus, any valid Miller index triplet  $(h^{\text{sc}} k^{\text{sc}} l^{\text{sc}})$  can be decomposed into contributions of basic Miller index triplets, where the above choice is not unique. Alternative basic lattice vectors  $(h_1 \ k_1 \ l_1)$ ,  $(h_2 \ k_2 \ l_2)$ ,  $(h_3 \ k_3 \ l_3)$  can be obtained by transformations

$$\begin{pmatrix} h_1 & k_1 & l_1 \\ h_2 & k_2 & l_2 \\ h_3 & k_3 & l_3 \end{pmatrix} = \underline{\mathbf{T}} \cdot \begin{pmatrix} -1 & 1 & 1 \\ 1 & -1 & 1 \\ 1 & 1 & -1 \end{pmatrix} \quad (3.21)$$

where  $\underline{\mathbf{T}}$  is an integer-valued  $3 \times 3$  matrix with  $\det(\underline{\mathbf{T}}) = 1$ . As an example we mention

$$\underline{\mathbf{T}} = \begin{pmatrix} 1 & 1 & 1 \\ 0 & 1 & 1 \\ 0 & 0 & 1 \end{pmatrix}, \quad \begin{pmatrix} h_1 & k_1 & l_1 \\ h_2 & k_2 & l_2 \\ h_3 & k_3 & l_3 \end{pmatrix} = \begin{pmatrix} 1 & 1 & 1 \\ 2 & 0 & 0 \\ 1 & 1 & -1 \end{pmatrix} \quad (3.22)$$

The choice of appropriate basic lattice vectors in the vector space of integers describing all possible



Miller indices will become important in connection with the decomposition of Miller indices characterizing stepped and kinked surfaces, see Sec. 4.3. Table 3.3 lists typical examples of lowest Miller index triplets  $(h k l)$  of the fcc lattice given in both generic fcc and in simple cubic notation.

Table 3.3. Typical Miller index triplets of the fcc lattice given both in simple cubic notation,  $(h^{sc} k^{sc} l^{sc})$ , and in generic fcc notation  $(h^{fcc} k^{fcc} l^{fcc})$ .

$(h^{sc} k^{sc} l^{sc})$	$(h^{fcc} k^{fcc} l^{fcc})$
(1 1 1)	(1 1 1)
(2 0 0)	(0 1 1)
(2 2 0)	(1 1 2)
(3 1 1)	(1 2 2)
(3 3 1)	(2 2 3)
(4 2 0)	(1 2 3)
(4 2 2)	(2 3 3)

The **body-centered cubic** lattice is, according to (2.103), characterized by reciprocal lattice vectors  $\underline{G}_1^{bcc}$ ,  $\underline{G}_2^{bcc}$ ,  $\underline{G}_3^{bcc}$ , which can be represented by those of the simple cubic lattice, using (2.101), where

$$\begin{aligned}
 \underline{G}_1^{bcc} &= \underline{G}_2^{sc} + \underline{G}_3^{sc} \\
 \underline{G}_2^{bcc} &= \underline{G}_1^{sc} + \underline{G}_3^{sc} \\
 \underline{G}_3^{bcc} &= \underline{G}_1^{sc} + \underline{G}_2^{sc}
 \end{aligned} \tag{3.23}$$

Therefore, netplane normal directions point along vectors

$$\begin{aligned}
 \underline{G}_{(hkl)} &= h^{bcc} \underline{G}_{01}^{bcc} + k^{bcc} \underline{G}_{02}^{bcc} + l^{bcc} \underline{G}_{03}^{bcc} = \\
 &= (k^{fcc} + l^{fcc}) \underline{G}_{01}^{sc} + (h^{fcc} + l^{fcc}) \underline{G}_{02}^{sc} + (h^{fcc} + k^{fcc}) \underline{G}_{03}^{sc} \\
 &= h^{sc} \underline{G}_{01}^{sc} + k^{sc} \underline{G}_{02}^{sc} + l^{sc} \underline{G}_{03}^{sc}
 \end{aligned} \tag{3.24}$$

which suggests, in addition to the generic notation  $(h^{bcc} k^{bcc} l^{bcc})$ , a **simple cubic** or **(sc) notation**  $(h^{sc} k^{sc} l^{sc})$  for Miller indices of the bcc lattice. According to (3.24), there is a linear transformation between the indices

$$\begin{pmatrix} h^{\text{sc}} \\ k^{\text{sc}} \\ l^{\text{sc}} \end{pmatrix} = \begin{pmatrix} 0 & 1 & 1 \\ 1 & 0 & 1 \\ 1 & 1 & 0 \end{pmatrix} \cdot \begin{pmatrix} h^{\text{bcc}} \\ k^{\text{bcc}} \\ l^{\text{bcc}} \end{pmatrix}, \quad \begin{pmatrix} h^{\text{bcc}} \\ k^{\text{bcc}} \\ l^{\text{bcc}} \end{pmatrix} = \frac{1}{2} \begin{pmatrix} -1 & 1 & 1 \\ 1 & -1 & 1 \\ 1 & 1 & -1 \end{pmatrix} \cdot \begin{pmatrix} h^{\text{sc}} \\ k^{\text{sc}} \\ l^{\text{sc}} \end{pmatrix} \quad (3.25\text{a, b})$$

Analogous to the fcc lattice, the factor 1/2 in transformation (3.25b) restricts possible values of Miller indices in simple cubic notation. Here transformation (3.25b) yields integer-valued Miller indices,  $h^{\text{bcc}}, k^{\text{bcc}}, l^{\text{bcc}}$ , only for indices in simple cubic notation,  $h^{\text{sc}}, k^{\text{sc}}, l^{\text{sc}}$ , where the **sum** of all three values, i.e.  $g = h^{\text{sc}} + k^{\text{sc}} + l^{\text{sc}}$  is an **even** integer. This is achieved by either all indices being even or by one being even and two odd.

Transformation (3.25a) can, as before, be understood as the three basic Miller index triplets (0 1 1), (1 0 1), (1 1 0) defining lattice vectors in the integer vector space which describes all sc Miller indices ( $h^{\text{sc}} k^{\text{sc}} l^{\text{sc}}$ ) of a bcc lattice in simple cubic notation. Thus, any valid Miller index triplet ( $h^{\text{sc}} k^{\text{sc}} l^{\text{sc}}$ ) can be decomposed into contributions of basic Miller index triplets, where the above choice is not unique. Alternative basic lattice vectors ( $h_1 k_1 l_1$ ), ( $h_2 k_2 l_2$ ), ( $h_3 k_3 l_3$ ) can be obtained by transformations

$$\begin{pmatrix} h_1 & k_1 & l_1 \\ h_2 & k_2 & l_2 \\ h_3 & k_3 & l_3 \end{pmatrix} = \underline{\mathbf{T}} \cdot \begin{pmatrix} 0 & 1 & 1 \\ 1 & 0 & 1 \\ 1 & 1 & 0 \end{pmatrix} \quad (3.26)$$

where  $\underline{\mathbf{T}}$  is an integer-valued  $3 \times 3$  matrix with  $\det(\underline{\mathbf{T}}) = 1$ . As an example we mention

$$\underline{\mathbf{T}} = \begin{pmatrix} 0 & 0 & 1 \\ 1 & -1 & 1 \\ 1 & 0 & 0 \end{pmatrix}, \quad \begin{pmatrix} h_1 & k_1 & l_1 \\ h_2 & k_2 & l_2 \\ h_3 & k_3 & l_3 \end{pmatrix} = \begin{pmatrix} 1 & 1 & 0 \\ 0 & 2 & 0 \\ 0 & 1 & 1 \end{pmatrix} \quad (3.27)$$

As for the fcc case, the choice of appropriate basic lattice vectors in the vector space of integers describing all possible Miller indices will become important in connection with the decomposition of Miller indices characterizing stepped and kinked surfaces, see Sec. 4.3. Table 3.4 lists typical examples of lowest Miller index triplets ( $h k l$ ) of the bcc lattice given in both generic bcc and in simple cubic notation.

Table 3.4. Typical Miller index triplets of the bcc lattice given both in simple cubic notation, ( $h^{\text{sc}} k^{\text{sc}} l^{\text{sc}}$ ), and in generic bcc notation ( $h^{\text{bcc}} k^{\text{bcc}} l^{\text{bcc}}$ ).

$(h^{\text{sc}} k^{\text{sc}} l^{\text{sc}})$	$(h^{\text{bcc}} k^{\text{bcc}} l^{\text{bcc}})$
---	--

(1 1 0)	(0 0 1)
(2 0 0)	(-1 1 1)
(2 1 1)	(0 1 1)
(3 1 0)	(-1 1 2)
(2 2 2)	(1 1 1)
(3 2 1)	(0 1 2)
(3 3 2)	(1 1 2)

The numerical constraints on Miller indices,  $h^{sc}$ ,  $k^{sc}$ ,  $l^{sc}$ , in simple cubic notation for fcc or bcc lattices become important when Miller indices (and corresponding reciprocal lattice vectors  $\underline{G}_{(hkl)}$ ) are used in **numerical calculus**. Examples are the evaluation of netplane distances  $d_{(hkl)}$  or the decomposition of Miller indices discussed in see Sec. 4.3. As an illustration, distances  $d_{(hkl)}$  between adjacent netplanes of an fcc lattice are, according to (2.101), (2.102), (3.7), given by

$$\begin{aligned}
 d_{(hkl)} &= 2\pi / |\underline{G}_{(hkl)}| = a / [3 \{ (h^{fcc})^2 + (k^{fcc})^2 + (l^{fcc})^2 \} - \\
 &\quad - 2 \{ h^{fcc} k^{fcc} + h^{fcc} l^{fcc} + k^{fcc} l^{fcc} \}]^{1/2} \\
 &= a / [(h^{sc})^2 + (k^{sc})^2 + (l^{sc})^2]^{1/2}
 \end{aligned} \tag{3.28}$$

with the three sc Miller indices,  $h^{sc}$ ,  $k^{sc}$ ,  $l^{sc}$ , required to be either all even or all odd. Thus, netplanes with (1 1 2) orientation in simple cubic notation must use  $h^{sc} = 2$ ,  $k^{sc} = 2$ ,  $l^{sc} = 4$  in the evaluation of (3.28). In general, Miller index triplets  $(hkl)$ , given in simple cubic notation for fcc lattices and representing mixtures of even and odd numbers, have to be scaled by a factor of two for any quantitative calculus. For example, the triplet (1 2 3) needs to be replaced by (2 4 6). In analogy, Miller indices, given in simple cubic notation for bcc lattices with the sum  $(h + k + l)$  being an odd number, must be scaled by a factor of two. For example, the triplet (1 1 1) needs to be replaced by (2 2 2). However, when Miller indices  $(hkl)$  are to be used only to denote **netplane directions** in the crystal, common integer factors in the indices can be omitted.

The correlations between generic fcc or bcc Miller indices and those referring to the simple cubic lattice are special cases of a more general behavior of Miller indices when lattice vectors are modified by transformations. If we assume that  $\underline{R}_1'$ ,  $\underline{R}_2'$ ,  $\underline{R}_3'$  are lattice vectors arising from a linear transformation of initial lattice vectors  $\underline{R}_1$ ,  $\underline{R}_2$ ,  $\underline{R}_3$  according to

$$\begin{pmatrix} \underline{\mathbf{R}}_1' \\ \underline{\mathbf{R}}_2' \\ \underline{\mathbf{R}}_3' \end{pmatrix} = \underline{\mathbf{T}} \cdot \begin{pmatrix} \underline{\mathbf{R}}_1 \\ \underline{\mathbf{R}}_2 \\ \underline{\mathbf{R}}_3 \end{pmatrix} \quad (3.29)$$

then the corresponding reciprocal lattice vectors  $\underline{\mathbf{G}}_1', \underline{\mathbf{G}}_2', \underline{\mathbf{G}}_3'$  and  $\underline{\mathbf{G}}_1, \underline{\mathbf{G}}_2, \underline{\mathbf{G}}_3$  are connected by

$$\begin{pmatrix} \underline{\mathbf{G}}_1' \\ \underline{\mathbf{G}}_2' \\ \underline{\mathbf{G}}_3' \end{pmatrix} = (\underline{\mathbf{T}}^{-1})^+ \cdot \begin{pmatrix} \underline{\mathbf{G}}_1 \\ \underline{\mathbf{G}}_2 \\ \underline{\mathbf{G}}_3 \end{pmatrix} \quad (3.30)$$

where the superscript '+' in  $(\underline{\mathbf{T}}^{-1})^+$  denotes the transposed matrix of  $\underline{\mathbf{T}}^{-1}$ . Thus, a general reciprocal lattice vector  $\underline{\mathbf{G}}$  which can be written in both representations as

$$\underline{\mathbf{G}} = h \underline{\mathbf{G}}_1 + k \underline{\mathbf{G}}_2 + l \underline{\mathbf{G}}_3 = h' \underline{\mathbf{G}}_1' + k' \underline{\mathbf{G}}_2' + l' \underline{\mathbf{G}}_3' \quad (3.31)$$

is given in matrix form together with (3.30) by

$$\underline{\mathbf{G}} = (h' \ k' \ l') \begin{pmatrix} \underline{\mathbf{G}}_1' \\ \underline{\mathbf{G}}_2' \\ \underline{\mathbf{G}}_3' \end{pmatrix} = (h' \ k' \ l') (\underline{\mathbf{T}}^{-1})^+ \cdot \begin{pmatrix} \underline{\mathbf{G}}_1 \\ \underline{\mathbf{G}}_2 \\ \underline{\mathbf{G}}_3 \end{pmatrix} = (h \ k \ l) \cdot \begin{pmatrix} \underline{\mathbf{G}}_1 \\ \underline{\mathbf{G}}_2 \\ \underline{\mathbf{G}}_3 \end{pmatrix} \quad (3.32)$$

This leads to a relation between the corresponding Miller indices where

$$(h' \ k' \ l') (\underline{\mathbf{T}}^{-1})^+ = (h \ k \ l) \quad , \quad (h' \ k' \ l') = (h \ k \ l) (\underline{\mathbf{T}})^+ \quad (3.33)$$

or

$$\begin{pmatrix} h' \\ k' \\ l' \end{pmatrix} = \underline{\mathbf{T}} \cdot \begin{pmatrix} h \\ k \\ l \end{pmatrix} \quad (3.34)$$

A comparison of (3.34) with (3.29) shows that the transformation between lattice vectors and that between corresponding Miller indices uses the same transformation matrix  $\underline{\mathbf{T}}$ .

As an example, lattice vectors of trigonal crystals are often expressed by those of a related hexagonal lattice where the hexagonal vectors  $\underline{\mathbf{R}}_1^{\text{hex}}, \underline{\mathbf{R}}_2^{\text{hex}}, \underline{\mathbf{R}}_3^{\text{hex}}$  are connected with those of the trigonal lattice,  $\underline{\mathbf{R}}_1^{\text{trg}}, \underline{\mathbf{R}}_2^{\text{trg}}, \underline{\mathbf{R}}_3^{\text{trg}}$ , for example, according to

$$\begin{pmatrix} \underline{\mathbf{R}}_1^{\text{hex}} \\ \underline{\mathbf{R}}_2^{\text{hex}} \\ \underline{\mathbf{R}}_3^{\text{hex}} \end{pmatrix} = \underline{\mathbf{T}} \cdot \begin{pmatrix} \underline{\mathbf{R}}_1^{\text{trg}} \\ \underline{\mathbf{R}}_2^{\text{trg}} \\ \underline{\mathbf{R}}_3^{\text{trg}} \end{pmatrix} = \begin{pmatrix} 1 & -1 & 0 \\ 0 & 1 & -1 \\ 1 & 1 & 1 \end{pmatrix} \cdot \begin{pmatrix} \underline{\mathbf{R}}_1^{\text{trg}} \\ \underline{\mathbf{R}}_2^{\text{trg}} \\ \underline{\mathbf{R}}_3^{\text{trg}} \end{pmatrix} \quad (3.35)$$

see (2.48). (There are, altogether, 6 choices of obtuse and 6 of acute representations of the corresponding hexagonal lattice of which (3.35) is an obtuse representation.) Therefore, hexagonal Miller indices  $h^{\text{hex}}, k^{\text{hex}}, l^{\text{hex}}$  are connected with those of the corresponding trigonal lattice,  $h^{\text{trg}}, k^{\text{trg}}, l^{\text{trg}}$ , by

$$\begin{pmatrix} h^{\text{hex}} \\ k^{\text{hex}} \\ l^{\text{hex}} \end{pmatrix} = \underline{\underline{\mathbf{T}}} \cdot \begin{pmatrix} h^{\text{trg}} \\ k^{\text{trg}} \\ l^{\text{trg}} \end{pmatrix} = \begin{pmatrix} 1 & -1 & 0 \\ 0 & 1 & -1 \\ 1 & 1 & 1 \end{pmatrix} \cdot \begin{pmatrix} h^{\text{trg}} \\ k^{\text{trg}} \\ l^{\text{trg}} \end{pmatrix} \quad (3.36)$$

and hence

$$\begin{pmatrix} h^{\text{trg}} \\ k^{\text{trg}} \\ l^{\text{trg}} \end{pmatrix} = \frac{1}{3} \begin{pmatrix} 2 & 1 & 1 \\ -1 & 1 & 1 \\ -1 & -2 & 1 \end{pmatrix} \cdot \begin{pmatrix} h^{\text{hex}} \\ k^{\text{hex}} \\ l^{\text{hex}} \end{pmatrix} \quad (3.37)$$

All Miller indices in (3.37) must be integer-valued which puts constraints on possible values of hexagonal Miller indices. These can be expressed as

$$\begin{aligned} -h^{\text{hex}} + k^{\text{hex}} + l^{\text{hex}} &= 3g, & 2h^{\text{hex}} + k^{\text{hex}} + l^{\text{hex}} &= 3g', \\ -h^{\text{hex}} - 2k^{\text{hex}} + l^{\text{hex}} &= 3g'' \end{aligned} \quad (3.38)$$

where  $g, g', g''$  are integers. Since

$$\begin{aligned} -h^{\text{hex}} + k^{\text{hex}} + l^{\text{hex}} &= (2h^{\text{hex}} + k^{\text{hex}} + l^{\text{hex}}) - 3h^{\text{hex}} \\ &= (-h^{\text{hex}} - 2k^{\text{hex}} + l^{\text{hex}}) + 3k^{\text{hex}} \end{aligned} \quad (3.39)$$

fulfilling one of the three conditions (3.38) will automatically satisfy the other two. Thus, constraints (3.38) can be replaced by one constraint,

$$-h^{\text{hex}} + k^{\text{hex}} + l^{\text{hex}} = 3g \quad (3.40)$$

If all 6 possible obtuse representations of the hexagonal lattice are considered three of them are subject to constraint (3.40) while the other three are subject to

$$h^{\text{hex}} - k^{\text{hex}} + l^{\text{hex}} = 3g \quad (3.41)$$

Further, it can be shown that of the 6 different acute representation of the hexagonal lattice three are subject to the constraint

$$h^{\text{hex}} + k^{\text{hex}} - l^{\text{hex}} = 3g \quad (3.42)$$

and three to

$$h^{\text{hex}} + k^{\text{hex}} + l^{\text{hex}} = 3g \quad (3.43)$$

Table 3.5 lists typical examples of lowest Miller index triplets ( $h k l$ ) of the trigonal lattice given in both generic trigonal and in hexagonal notation according to (3.36). This table also includes the corresponding Miller-Bravais indices ( $l^{\text{hex}} m^{\text{hex}} n^{\text{hex}} q^{\text{hex}}$ ) according to (3.53) as discussed in Sec. 3.5.

Table 3.5. Typical Miller index triplets of the trigonal lattice given both in generic trigonal ( $h^{\text{trg}} k^{\text{trg}} l^{\text{trg}}$ ), in obtuse hexagonal notation, ( $h^{\text{hex}} k^{\text{hex}} l^{\text{hex}}$ ) and in 4-index notation ( $l^{\text{hex}} m^{\text{hex}} n^{\text{hex}} q^{\text{hex}}$ ), see text.

$(h^{\text{trg}} k^{\text{trg}} l^{\text{trg}})$	$(h^{\text{hex}} k^{\text{hex}} l^{\text{hex}})$	$(l^{\text{hex}} m^{\text{hex}} n^{\text{hex}} q^{\text{hex}})$
(1 0 0)	(1 0 1)	(1 0 -1 1)
(0 1 0)	(-1 1 1)	(-1 1 0 1)
(0 0 1)	(0 -1 1)	(0 -1 1 1)
(1 1 0)	(0 1 2)	(0 1 -1 2)
(1 0 1)	(1 -1 2)	(1 -1 0 2)
(0 1 1)	(-1 0 2)	(-1 0 1 2)
(1 1 1)	(0 0 3)	(0 0 0 3)

### 3.5 Alternative Definition of Miller Indices, Miller-Bravais Indices

There is an alternative way to define netplanes inside a lattice, which is usually preferred by crystallographers due to its seeming simplicity. Here one considers two adjacent parallel ( $h k l$ ) netplanes in a lattice defined by lattice vectors  $\underline{R}_{01}$ ,  $\underline{R}_{02}$ ,  $\underline{R}_{03}$ , where the lattice can always be positioned such that its origin coincides with that of one of the netplanes. Then the adjacent netplane will, in general, cross the lines along the three lattice vectors  $\underline{R}_{01}$ ,  $\underline{R}_{02}$ ,  $\underline{R}_{03}$  at crossing points  $\underline{A}$ ,  $\underline{B}$ ,  $\underline{C}$  with

$$\underline{A} = \alpha_1 \underline{R}_{01}, \quad \underline{B} = \alpha_2 \underline{R}_{02}, \quad \text{and} \quad \underline{C} = \alpha_3 \underline{R}_{03} \quad (3.44)$$

as shown in the Fig. 3.3. Thus, the **intercept factors**  $\alpha_1$ ,  $\alpha_2$ ,  $\alpha_3$  can be used to characterize the

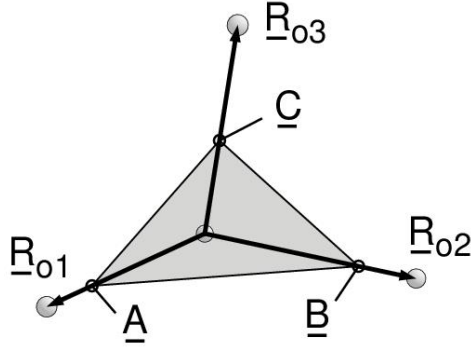


Fig. 3.3. Netplane definition by its intercepts with the three lattice vectors  $\underline{R}_{01}$ ,  $\underline{R}_{02}$ ,  $\underline{R}_{03}$  at  $\underline{A}$ ,  $\underline{B}$ ,  $\underline{C}$ . The lattice vectors and intercepts are sketched accordingly. The netplane is indicated by light gray.

netplane uniquely. If vector  $\underline{n}$  denotes the normal vector of the netplane, then the distance  $d_{(hkl)}$  between the two adjacent netplanes is given by

$$\begin{aligned} d_{(hkl)} &= \underline{A} \cdot \underline{n} = \alpha_1 \underline{R}_{01} \cdot \underline{n} = \alpha_1 \underline{R}_{01} \cdot \underline{G}_{(hkl)} / |\underline{G}_{(hkl)}| = \\ &= \alpha_1 \underline{R}_{01} \cdot (h \underline{G}_{01} + k \underline{G}_{02} + l \underline{G}_{03}) / G_{(hkl)} = \alpha_1 h 2\pi / G_{(hkl)} = 2\pi / G_{(hkl)} \end{aligned} \quad (3.45)$$

where equations (3.6), (3.7) together with the orthogonality relations (2.96) are used. This yields for the intercept factor  $\alpha_1$

$$\alpha_1 h = 1 \quad \text{or} \quad \alpha_1 = 1/h \quad (3.46)$$

In analogy, relations

$$d_{(hkl)} = \underline{B} \cdot \underline{n} \quad \text{and} \quad d_{(hkl)} = \underline{C} \cdot \underline{n} \quad (3.47)$$

result in

$$\alpha_2 = 1/k \quad \text{and} \quad \alpha_3 = 1/l \quad (3.48)$$

connecting, altogether, between inverse Miller indices  $h, k, l$  and the intercept factors  $\alpha_i$  of the three lattice vectors cut by the netplane. Since Miller indices are all integer-valued, relations (3.46), (3.48) show that for non-zero values of  $h, k, l$  the corresponding intercept factors  $\alpha_i$  are bound to  $0 \leq |\alpha_i| \leq 1$ . In addition, according to (3.46)  $h = 0$  can be considered a result of the limiting case  $\alpha_1 \rightarrow \infty$  such that the corresponding netplanes lie parallel to the lattice vector  $\underline{R}_{01}$ . Analogously,  $k = 0$  and  $l = 0$  refer to netplanes parallel to vectors  $\underline{R}_{02}$  and  $\underline{R}_{03}$ , respectively. If two Miller index values equal zero then the corresponding netplane must be parallel to two lattice vectors. For example, the  $(100)$  netplane cuts the  $\underline{R}_{01}$  axis at a lattice point ( $\alpha_1 = 1$ ) and extends parallel to the plane

spanned by  $\underline{R}_{02}$  and  $\underline{R}_{03}$ . Relations (3.46), (3.48) can be inverted to read

$$h = 1 / \alpha_1 , \quad k = 1 / \alpha_2 , \quad l = 1 / \alpha_3 \quad \text{or} \\ (h \ k \ l) = (1/\alpha_1 \ 1/\alpha_2 \ 1/\alpha_3) \quad (3.49)$$

which shows that the **inverse intercept factors** are equivalent to **Miller indices** and can, thus, be alternatively used to characterize the orientation of a netplane inside a lattice.

There is a special variant of the alternative definition (3.49) which applies only to **hexagonal lattices**. These lattices are described by two lattice vectors,  $\underline{R}_{01}$  and  $\underline{R}_{02}$ , forming a two-dimensional hexagonal lattice with angles  $\angle(\underline{R}_{01}, \underline{R}_{02}) = 120^\circ$  or  $= 60^\circ$  (obtuse or acute representation) while  $\underline{R}_{03}$  is perpendicular to both  $\underline{R}_{01}$  and  $\underline{R}_{02}$ . Assuming an **obtuse representation**, the 3-fold symmetry of the planar sublattice given by  $\underline{R}_{01}$  and  $\underline{R}_{02}$  induces a third vector  $\underline{R}_{02}' = -\underline{R}_{01} - \underline{R}_{02}$ , which forms an angle  $\angle(\underline{R}_{01}, \underline{R}_{02}') = \angle(\underline{R}_{02}, \underline{R}_{02}') = 120^\circ$  with respect to the initial lattice vectors and is of equal length, see Fig. 3.4. Thus, the vector triplet  $\underline{R}_{01}, \underline{R}_{02}, \underline{R}_{02}'$  may be considered an equivalent set and

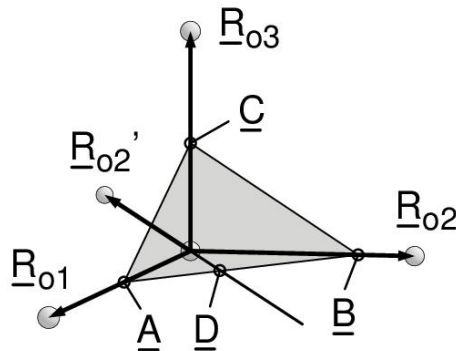


Fig. 3.4. Netplane definition (hexagonal lattices) by its intercepts with the four lattice vectors  $\underline{R}_{01}, \underline{R}_{02}, \underline{R}_{02}'$ , and  $\underline{R}_{03}$  at  $\underline{A}, \underline{B}, \underline{C}, \underline{D}$ . The lattice vectors and intercepts are sketched accordingly. The netplane is indicated by light gray.

each pair of vectors from this triplet can be used to describe the periodicity of the hexagonal netplane. Crystallographers treat the three lattice vectors  $\underline{R}_{01}, \underline{R}_{02}, \underline{R}_{02}'$  on equal footing and characterize netplanes by intercepts of the three lattice vectors  $\underline{R}_{01}, \underline{R}_{02}, \underline{R}_{03}$  and of vector  $\underline{R}_{02}'$ , i.e. by

$$\underline{A} = \alpha_1 \underline{R}_{01} , \quad \underline{B} = \alpha_2 \underline{R}_{02} , \quad \underline{C} = \alpha_3 \underline{R}_{03} , \quad \text{and} \quad \underline{D} = \alpha_2' \underline{R}_{02}' \quad (3.50)$$

as shown in the Fig. 3.4, where simple algebra yields

$$1/\alpha_2' = -1/\alpha_1 - 1/\alpha_2 \quad (3.51)$$

This is the basis of the so-called **4-index notation** of the Miller indices, also referred to as **Miller-**



**Bravais indices**, where the initial definition

$$(h \ k \ l) = (1/\alpha_1 \ 1/\alpha_2 \ 1/\alpha_3) \quad (3.52)$$

is, with the help of (3.51), replaced by

$$(l \ m \ n \ q) = (1/\alpha_1 \ 1/\alpha_2 \ 1/\alpha_2' \ 1/\alpha_3) = (h \ k \ (-h-k) \ l) \quad (3.53)$$

The quadruple  $(l \ m \ n \ q)$  is sometimes also termed  $(h \ k \ i \ l)$ . Examples of corresponding Miller and Miller-Bravais indices are listed in Table 3.6.

Table 3.6. Examples of Miller indices  $(h \ k \ l)$  and corresponding Miller-Bravais indices  $(l \ m \ n \ q)$  based on an obtuse representation of the hexagonal lattice.

$(h \ k \ l)$	$(l \ m \ n \ q)$
(1 0 0)	(1 0 -1 0)
(0 1 0)	(0 1 -1 0)
(0 0 1)	(0 0 0 1)
(1 1 0)	(1 1 -2 0)
(1 0 1)	(1 0 -1 1)
(0 1 1)	(0 1 -1 1)
(1 1 1)	(1 1 -2 1)

The **geometric equivalence** of the three lattice vectors  $\underline{R}_{01}$ ,  $\underline{R}_{02}$ ,  $\underline{R}_{02}'$  in the obtuse representation is also visible in a symmetry property of the corresponding Miller-Bravais indices. A rotation of the hexagonal lattice by  $120^\circ$  (anti-clockwise) about its symmetry axis along  $\underline{R}_{03}$ , reproduces the lattice and leads to a transformation of its lattice vectors

$$\underline{R}_{01} \rightarrow \underline{R}_{02}, \quad \underline{R}_{02} \rightarrow \underline{R}_{02}', \quad \underline{R}_{02}' \rightarrow \underline{R}_{01}, \quad \underline{R}_{03} \rightarrow \underline{R}_{03} \quad (3.54)$$

This also affects the intercepts, used for the definition of Miller-Bravais indices, see Fig. 3.4, where the transformation yields

$$\begin{aligned} (l \ m \ n \ q) &= (1/\alpha_1 \ 1/\alpha_2 \ 1/\alpha_2' \ 1/\alpha_3) \\ &\rightarrow (1/\alpha_2 \ 1/\alpha_2' \ 1/\alpha_1 \ 1/\alpha_3) = (m \ n \ l \ q) \end{aligned} \quad (3.55)$$

resulting in symmetry equivalent Miller index quadruplets. Thus, Miller-Bravais indices  $(l \ m \ n \ q)$ ,  $(m \ n \ l \ q)$ , and  $(n \ l \ m \ q)$  are symmetry equivalent and lead to netplanes of identical structure.

Assuming an **acute representation** of the hexagonal lattice the four points of Fig. 3.4 are given by

$$\underline{\mathbf{A}} = \alpha_1 \underline{\mathbf{R}}_1, \quad \underline{\mathbf{B}} = \alpha_2' (\underline{\mathbf{R}}_2 - \underline{\mathbf{R}}_1), \quad \underline{\mathbf{C}} = \alpha_3 \underline{\mathbf{R}}_3, \quad \text{and} \quad \underline{\mathbf{D}} = \alpha_2 (-\underline{\mathbf{R}}_2) \quad (3.56)$$

where

$$1/\alpha_2' = 1/\alpha_2 - 1/\alpha_1 \quad (3.57)$$

In this representation the initial definition

$$(h, k, l) = (1/\alpha_1, 1/\alpha_2, 1/\alpha_3) \quad (3.58)$$

is, with the help of (3.57), replaced by

$$(l \ m \ n \ q) = (1/\alpha_1, 1/\alpha_2', -1/\alpha_2, 1/\alpha_3) = (h \ (k-h) \ -k \ l) \quad (3.59)$$

Examples of corresponding Miller and Miller-Bravais indices are listed in Table 3.7.

Table 3.7. Examples of Miller indices  $(h \ k \ l)$  and corresponding Miller-Bravais indices  $(l \ m \ n \ q)$  based on an acute representation of the hexagonal lattice.

$(h \ k \ l)$	$(l \ m \ n \ q)$
(1 0 0)	(1 -1 0 0)
(0 1 0)	(0 1 -1 0)
(0 0 1)	(0 0 0 1)
(1 1 0)	(1 0 -1 0)
(1 0 1)	(1 -1 0 1)
(0 1 1)	(0 1 -1 1)
(1 1 1)	(1 0 -1 1)

### 3.6 Symmetry Properties of Netplanes

Netplanes can also be analyzed in terms of their symmetry behavior, i.e. by their translational symmetry and corresponding point symmetry elements. This is analogous to symmetry analyses of three-dimensional lattices discussed in Sec. 2.4. A comparison with the three-dimensional symmetry operations, available for lattices and listed in Sec. 2.4, shows immediately that there are only three different types of true point symmetry operations which qualify for two-dimensional netplanes. These are

- $i(\underline{r}_o)$       **inversion** with respect to symmetry origin  $\underline{r}_o$ , equivalent with a **180° rotation** about  $\underline{r}_o$ , as discussed below,
- $C_\varphi(\underline{r}_o)$       **rotation** by an angle  $\varphi$  about the symmetry origin  $\underline{r}_o$ ,
- $\sigma(\underline{r}_o, \underline{e})$       **mirroring (reflection)** with respect to a line through symmetry origin  $\underline{r}_o$  with the line direction defined by its normal vector  $\underline{e}$ .

In addition, netplanes may be symmetric with respect to a mixed mirror and translational symmetry operation which is known as

- $g(\underline{r}_o, \underline{g})$       **glide reflection**, combining a reflection  $\sigma(\underline{r}_o, \underline{e})$  with a translation by vector  $\underline{g}$ , where vectors  $\underline{g}$  and  $\underline{e}$  are perpendicular to each other.

As for three-dimensional lattices, translational and point symmetry elements of a netplane are subject to **compatibility constraints** which limits the number of possible point symmetry operations as well as their relation with translations. This subject is treated in full mathematical detail in this section, going beyond the analogous discussion of symmetry for three-dimensional lattices in this book. First, the different symmetry operations, mentioned above, are defined and their interplay with translational symmetry is discussed in Secs. 3.6.2 to 3.6.5. Then, Sec. 3.6.6 combines all symmetry elements to **symmetry groups** which can be used to classify the different types of netplanes according to their symmetry. These sections are rather formal and filled with mathematical details. Thus, readers, who are less interested in mathematics, may inspect the conclusions of Secs. 3.6.2 to 3.6.5 at the end of each section only or may skip these sections altogether and move to Sec. 3.7.

### 3.6.1 Centered Netplanes

Centering of three-dimensional lattices was shown in Sec. 2.2.3 to allow primitive lattice descriptions in cases where the morphological unit cells of the initial lattice are not primitive. The same considerations can also be applied to two-dimensional netplanes where the reasoning is identical to that for cell faces of three-dimensional unit cells. Consider a netplane defined by lattice vectors  $\underline{R}_1$  and  $\underline{R}_2$ , where both vectors are assumed to be of smallest length along their direction. Then the morphological unit cell spanned by  $\underline{R}_1$  and  $\underline{R}_2$  may be **primitive**, i.e. of smallest area compared with all possible unit cells in the netplane. If the cell is **non-primitive** then its area is not the smallest and, in analogy to the discussion for cell faces in Sec. 2.2.3, there is at least one **additional lattice point** inside the morphological unit cell, described by vector  $\underline{R}'$  with

$$\underline{R}' = \kappa_1 \underline{R}_1 + \kappa_2 \underline{R}_2, \quad 0 < \kappa_1, \kappa_2 < 1 \quad (3.60)$$

and for general values  $\kappa_1, \kappa_2$  there is always a second lattice point inside the cell with vector  $\underline{R}''$  given by

$$\underline{R}'' = \underline{R}_1 + \underline{R}_2 - \underline{R}' = (1 - \kappa_1) \underline{R}_1 + (1 - \kappa_2) \underline{R}_2 \quad (3.61)$$

If, however, the cell is assumed to contain **only one** additional lattice point then the vectors  $\underline{R}'$  and  $\underline{R}''$  must coincide, i.e.

$$\underline{R}'' - \underline{R}' = (1 - 2\kappa_1) \underline{R}_1 + (1 - 2\kappa_2) \underline{R}_2 = 0 \quad (3.62)$$

Here the expressions in brackets must all be zero since the vectors  $\underline{R}_1$  and  $\underline{R}_2$  are linearly independent. This leads to

$$\kappa_1 = \kappa_2 = 1/2, \quad \underline{R}' = 1/2 (\underline{R}_1 + \underline{R}_2) \quad (3.63)$$

yielding a lattice vector  $\underline{R}'$  in the **center** of the **cell** spanned by  $\underline{R}_1$  and  $\underline{R}_2$  describing a **centered** netplane. In the symmetry classification of netplanes, discussed in Sec. 3.8, it will be shown, that centering of a netplane of given symmetry type results in a new type of netplane only if the initial (non-primitive) netplane is rectangular, leading to a centered rectangular or c-rectangular netplane. As an illustration, Fig. 3.5 shows morphological unit cells of different primitive and non-primitive lattice descriptions of a centered rectangular netplane. This figure also illustrates the general result that centered netplanes imply glide reflection symmetry as discussed in detail in Sec. 3.6.5.

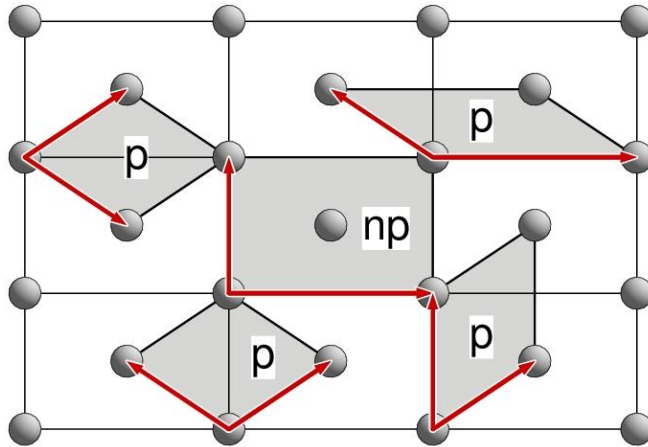


Fig. 3.5. Morphological unit cells of different primitive and non-primitive lattice descriptions of a centered rectangular netplane. The cells are shaded in gray with primitive and non-primitive cells labeled 'p' and 'np', respectively. Corresponding lattice vectors are shown as red arrows.

### 3.6.2 Inversion

**Inversion operations**  $i(\underline{r}_o)$  convert any point  $\underline{r}$  on the netplane into its image  $\underline{r}'$  such that the inversion center  $\underline{r}_o$  cuts the connecting line between  $\underline{r}$  and  $\underline{r}'$  into half, see Fig. 3.6. This can be expressed **mathematically** by a coordinate transformation of points on the netplane

$$\underline{r} = \underline{r}_o + (\underline{r} - \underline{r}_o) \rightarrow \underline{r}' = \underline{r}_o - (\underline{r} - \underline{r}_o) = 2\underline{r}_o - \underline{r} = \underline{r}_o + \underline{i}(\underline{r} - \underline{r}_o) \quad (3.64)$$

where  $\underline{i}$  is formally defined as the inversion operator. This is connected with a two-dimensional Cartesian **coordinate transformation** with respect to  $\underline{r}_o$ , applying a  $2 \times 2$  matrix  $\underline{i}$ , where

$$\begin{pmatrix} x' \\ y' \end{pmatrix} = \underline{i} \cdot \begin{pmatrix} x \\ y \end{pmatrix}, \quad \underline{i} = \begin{pmatrix} -1 & 0 \\ 0 & -1 \end{pmatrix} = -\underline{1} \quad (3.65)$$

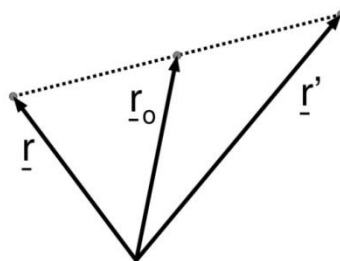


Fig. 3.6. Sketch of an inversion operation applied to vector  $\underline{r}$  to yield  $\underline{r}'$  with the inversion center at  $\underline{r}_o$ , see text.

The definition of general lattice points  $\underline{R}$  on a netplane with primitive lattice vectors  $\underline{R}_1$  and  $\underline{R}_2$  by

$$\underline{\mathbf{R}} = n_1 \underline{\mathbf{R}}_1 + n_2 \underline{\mathbf{R}}_2, \quad n_1, n_2 \text{ integer} \quad (3.66)$$

implies that the **origin** of a netplane is also an **inversion center**, since for any combination of integers  $(n_1, n_2)$  there is the negative counterpart  $(-n_1, -n_2)$  converting  $\underline{\mathbf{R}}$  into  $-\underline{\mathbf{R}}$ . In addition, the translational symmetry of the netplane yields inversion centers at all lattice points (3.66) of the netplane. There are also **other** inversion centers  $\underline{\mathbf{r}}_0$  inside the morphological unit cell of the netplane. The inversion operation (3.64) at a lattice point  $\underline{\mathbf{R}}$  given by (3.66) can be rewritten as

$$\begin{aligned} \underline{\mathbf{r}}' &= \underline{\mathbf{R}} - (\underline{\mathbf{r}} - \underline{\mathbf{R}}) = 2 \underline{\mathbf{R}} - \underline{\mathbf{r}} = [2 (\underline{\mathbf{R}} - \underline{\mathbf{r}}_0) - \underline{\mathbf{r}}] + 2 \underline{\mathbf{r}}_0 = \\ &= (\underline{\mathbf{R}} - \underline{\mathbf{r}}_0) - (\underline{\mathbf{r}} - (\underline{\mathbf{R}} - \underline{\mathbf{r}}_0)) + 2 \underline{\mathbf{r}}_0 \end{aligned} \quad (3.67)$$

where  $\underline{\mathbf{r}}_0$  may be a point inside the morphological unit cell, given by

$$\underline{\mathbf{r}}_0 = \gamma_1 \underline{\mathbf{R}}_1 + \gamma_2 \underline{\mathbf{R}}_2, \quad 0 \leq \gamma_i < 1, \quad i = 1, 2 \quad (3.68)$$

Thus, equation (3.67) can be interpreted as an inversion at lattice point  $(\underline{\mathbf{R}} - \underline{\mathbf{r}}_0)$  followed by a shift by vector  $(2 \underline{\mathbf{r}}_0)$ . As a consequence, if a netplane reproduces itself for inversions at  $\underline{\mathbf{R}}$  according to (3.66), its translational symmetry also yields inversion symmetry with respect to  $(\underline{\mathbf{R}} - \underline{\mathbf{r}}_0)$  as long as  $(2 \underline{\mathbf{r}}_0)$  is a general lattice vector. The latter allows, together with the constraints in (3.68), only parameter values  $\gamma_i = 0$  or  $\gamma_i = 1/2$ . This results, altogether, in **four** different possible inversion centers  $\underline{\mathbf{r}}_0'$  inside the unit cell at

$$\underline{\mathbf{r}}_0^{(1)} = \underline{\mathbf{0}}, \quad \underline{\mathbf{r}}_0^{(2)} = 1/2 \underline{\mathbf{R}}_1, \quad \underline{\mathbf{r}}_0^{(3)} = 1/2 \underline{\mathbf{R}}_2, \quad \underline{\mathbf{r}}_0^{(4)} = 1/2 (\underline{\mathbf{R}}_1 + \underline{\mathbf{R}}_2) \quad (3.69)$$

Thus, the primitive morphological unit cell of a netplane with inversion symmetry can contain inversion centers only at its **origin**, one at the cell **center**, and two at the **midpoints** of the cell edges, see Fig. 3.7.

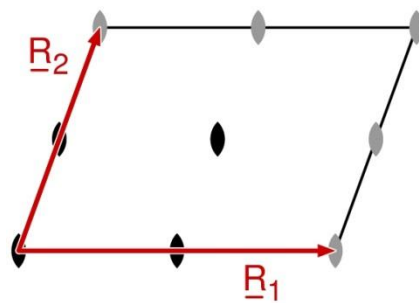


Fig. 3.7. Morphological unit cell of a netplane with lattice vectors  $\underline{\mathbf{R}}_1, \underline{\mathbf{R}}_2$ . Non-equivalent inversion centers inside the cell are shown as black ellipses while translationally equivalent inversion centers are given by gray ellipses.

This means, in particular, that, if a netplane, given by  $\underline{R}_1$  and  $\underline{R}_2$ , possesses inversion symmetry, then it can always be arranged such that there are inversion centers at positions

$$\underline{R} = n_1 \underline{R}_1 + n_2 \underline{R}_2 + \underline{r}_0^{(i)}, \quad i = 1, 4, \dots, \quad n_1, n_2 \text{ integer} \quad (3.70)$$

which, together with (3.69), can also be written as

$$\underline{R} = n_1 (\underline{R}_1/2) + n_2 (\underline{R}_2/2), \quad n_1, n_2 \text{ integer} \quad (3.71)$$

Equation (3.71) describes general lattice points on a netplane with lattice vectors  $(\underline{R}_1/2)$ ,  $(\underline{R}_2/2)$ .

**In conclusion**, inversion centers existing as symmetry elements of a netplane, defined by primitive lattice vectors  $\underline{R}_1$  and  $\underline{R}_2$ , have the following property :

- All inversion centers form a netplane with lattice vectors  $(\underline{R}_1/2)$ ,  $(\underline{R}_2/2)$ . (3.72)

### 3.6.3 Rotation

**Rotation operations**  $C_\varphi(\underline{r}_0)$  rotate any point  $\underline{r}$  on the netplane by an angle  $\varphi$  (**rotation angle**) about a center  $\underline{r}_0$  (**rotation center**) to yield an image point  $\underline{r}'$ , see Fig. 3.8. This can be expressed **mathematically** by a transformation of points on the netplane

$$\underline{r} = \underline{r}_0 + (\underline{r} - \underline{r}_0) \rightarrow \underline{r}' = \underline{r}_0 + \underline{C}_\varphi (\underline{r} - \underline{r}_0) \quad (3.73)$$

where  $\underline{C}_\varphi$  is formally defined as the rotation operator. This is connected with a two-dimensional Cartesian **coordinate transformation** with respect to the rotation center  $\underline{r}_0$ , applying a  $2 \times 2$  matrix  $\underline{C}_\varphi$ , where

$$\begin{pmatrix} x' \\ y' \end{pmatrix} = \underline{C}_\varphi \cdot \begin{pmatrix} x \\ y \end{pmatrix}, \quad \underline{C}_\varphi = \begin{pmatrix} \cos \varphi & -\sin \varphi \\ \sin \varphi & \cos \varphi \end{pmatrix} \quad (3.74)$$

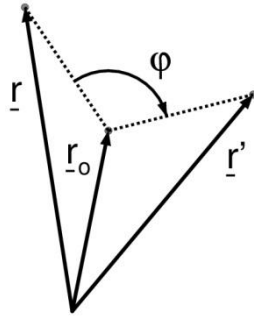


Fig. 3.8. Sketch of a rotation operation applied to vector  $\underline{r}$  to yield  $\underline{r}'$  with the rotation center at  $\underline{r}_o$ , see text.

Possible rotation **angles**  $\phi$ , which transform netplanes into themselves, are subject to **constraints**. In particular, if a rotation by angle  $\phi$  reproduces a netplane, then a rotation by  $2\phi$  must also reproduce the netplane. A repeated rotation by  $\phi$  will eventually lead to a full circular movement of the netplane after a finite number of steps. Thus, possible rotation angles  $\phi$  can only be fractions of  $360^\circ$ , i.e.

$$\phi = p (360^\circ / n) , p = 1, \dots, n , \quad n \text{ integer} \quad (3.75)$$

If a netplane reproduces itself, when rotated about a center  $\underline{r}_o$  by all angles  $\phi$  with  $p = 1, \dots, n$  in (3.75), it is said to possess an **n-fold rotation axis n** ( $C_n$ ) at  $\underline{r}_o$ . Here the symmetry symbols  $\mathbf{n}$ ,  $C_n$  refer to the Hermann-Mauguin and Schönflies notation for rotation axes, discussed in Sec. 2.4. (Both notations will be used in the following with the Schönflies notation put in parentheses.)

The angle  $\phi = 180^\circ$ , corresponding to a **2-fold rotation axis**, is special. According to (3.74), the transformation matrix  $\underline{C}_\phi$  for  $\phi = 180^\circ$  is identical to the **inversion** matrix  $\underline{i} = -\underline{1}$  in (3.65). Thus, in two dimensions a 2-fold rotation is equivalent with an inversion operation. As a consequence, the four possible inversion centers  $\underline{r}_o$ , given by (3.69) are the only centers inside the unit cell, where 2-fold rotation axes can exist.

The **compatibility** of rotational with translational symmetry of a netplane imposes **constraints** on possible **rotation angles**  $\phi$ . Let us assume a netplane to possess a rotation center at  $\underline{r}_o$ , where the netplane can always be shifted such that  $\underline{r}_o$  coincides with the netplane origin. Then, as a result of translational symmetry, there are infinitely many rotation centers at all lattice points (3.66) of the netplane. Thus, each rotation center A has an equivalent center B separated by lattice vector  $\underline{R}$  which can be assumed to be the smallest lattice vector of the netplane, see Fig. 3.9. Rotating the



netplane anti-clockwise about center A by angle  $\varphi$  transforms center B to B' while the clockwise rotation about center B transforms A to A'.

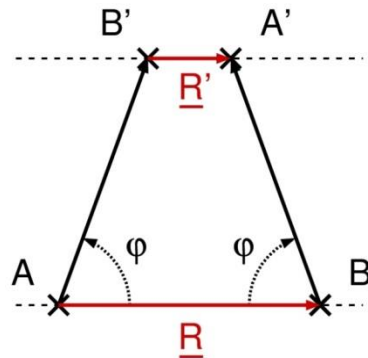


Fig. 3.9. Rotations by angles  $\pm\varphi$  applied to translationally equivalent rotation centers A and B (indicated by crosses). Lattice vector  $\underline{R}$  connects center A with B while  $\underline{R}'$  connects the image centers B' and A', see text.

Vector  $\underline{R}'$ , connecting B' with A' must be parallel to vector  $\underline{R}$  and simple algebra yields

$$\underline{R}' = \underline{R} - 2 \underline{R} \cos \varphi = \underline{R} (1 - 2 \cos \varphi) \quad (3.76)$$

Since the two rotations are assumed to transform the netplane into itself, vector  $\underline{R}'$  must be an integer multiple of  $\underline{R}$ , which means that

$$(1 - 2 \cos \varphi) = p \quad \text{or} \quad \cos \varphi = (1 - p) / 2, \quad p \text{ integer} \quad (3.77)$$

where the range of the cosine function,  $|\cos \varphi| \leq 1$ , limits the integer values p to  $-1 \leq p \leq 3$ .

Here  $p = -1$ , corresponding to  $\varphi = 0^\circ$ , can be ignored, which leaves four possible angles  $\varphi$  and corresponding n-fold rotation axes listed in Table 3.8.

Table 3.8. List of possible rotation angles  $\varphi$  and corresponding n-fold rotation axes allowed for netplanes.

$p =  \underline{R}'  /  \underline{R} $	$\varphi$	Rotation axis
0	$60^\circ$	6-fold
1	$90^\circ$	4-fold
2	$120^\circ$	3-fold
3	$180^\circ$	2-fold

Altogether, the translational symmetry of netplanes allows only **2-, 3-, 4-, and 6-fold** rotation axes. Relation (3.75) shows, in addition, that a 4-fold rotation axis implies always a 2-fold axis at the same rotation center  $\underline{r}_o$ . Further, a 6-fold rotation axis includes 2- and 3-fold axes. Since 2-fold rotations are equivalent with inversion operations, possible rotation centers  $\underline{r}_o$  for 2-, 4-, or 6-fold rotation axes must coincide with inversion centers given by (3.69). In contrast, centers of true 3-fold rotation axes (i.e. excluding 6-fold rotation) can never coincide with inversion centers.

Consider a netplane with **4-fold rotation symmetry** at  $\underline{r}_o$ , assumed to coincide with the netplane origin. Then its periodicity can be described by lattice vectors  $\underline{R}_1$  and  $\underline{R}_2$ , where  $|\underline{R}_1|$  denotes the smallest distance between lattice points of the netplane. Further,  $\underline{R}_2$  can be constructed to be the image of  $\underline{R}_1$ , rotated by  $90^\circ$ , yielding the same length as vector  $\underline{R}_1$ . Thus, the corresponding morphological unit cell is of square shape, see Fig. 3.10. A rotation of the lattice vectors  $\underline{R}_1$  and  $\underline{R}_2$  by  $90^\circ$  with respect to the netplane origin yields vectors  $\underline{R}_1'$ ,  $\underline{R}_2'$  with

$$\underline{R}_1' = C_{90}(\underline{R}_1) = \underline{R}_2, \quad \underline{R}_2' = C_{90}(\underline{R}_2) = -\underline{R}_1 \quad (3.78)$$

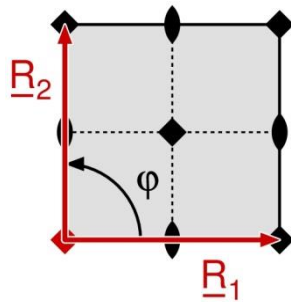


Fig. 3.10. Rotation by  $\varphi = 90^\circ$  applied to lattice vector  $\underline{R}_1$  to yield  $\underline{R}_2$ . The initial rotation center is indicated by a red square. The unit cell is emphasized in gray with its other 2- and 4-fold rotation centers shown by black ellipses and squares, respectively.

Therefore, a  $90^\circ$  rotation about a center  $\underline{r}_o$  inside the unit cell, given by

$$\underline{r}_o = \gamma_1 \underline{R}_1 + \gamma_2 \underline{R}_2, \quad 0 \leq \gamma_i < 1, \quad i = 1, 2 \quad (3.79)$$

transforms general lattice vectors  $\underline{R}$  of (3.66) to  $\underline{R}'$  according to

$$\begin{aligned} \underline{R}' &= n_1' \underline{R}_1 + n_2' \underline{R}_2 = \\ &= \underline{r}_o + C_{90}(\underline{R} - \underline{r}_o) = \underline{r}_o + C_{90}(\underline{R}) - C_{90}(\underline{r}_o) = \\ &= \gamma_1 \underline{R}_1 + \gamma_2 \underline{R}_2 + n_1 \underline{R}_2 - n_2 \underline{R}_1 - \gamma_1 \underline{R}_2 + \gamma_2 \underline{R}_1 = \\ &= (\gamma_1 + \gamma_2 - n_2) \underline{R}_1 + (\gamma_2 - \gamma_1 + n_1) \underline{R}_2 = \beta_1 \underline{R}_1 + \beta_2 \underline{R}_2 \end{aligned} \quad (3.80)$$

where

$$\begin{aligned}\beta_1 &= \gamma_1 + \gamma_2 - n_2 & \beta_2 &= \gamma_2 - \gamma_1 + n_1 \\ \gamma_1 &= 1/2 (\beta_1 - \beta_2 + n_1 + n_2) & \gamma_2 &= 1/2 (\beta_1 + \beta_2 - n_1 + n_2)\end{aligned}\quad (3.81)$$

If  $\underline{r}_0$  is the center of a 4-fold rotation axis of the netplane, then all transformed centers  $\underline{R}'$  in (3.80) must coincide with the initial centers  $\underline{R}$  given by (3.66). This requires that both  $\beta_1$  and  $\beta_2$  are integer-valued and, hence, the corresponding parameters  $\gamma_i$  in (3.81) must be integer multiples of 1/2. Together with relation (3.79), only two parameter choices ( $\gamma_1 = \gamma_2 = 0$ ) and ( $\gamma_1 = \gamma_2 = 1/2$ ) are possible. This results in **two** different possible centers of **4-fold rotation** axes inside the unit cell at

$$\underline{r}_0^{(1)} = \underline{0} \ , \quad \underline{r}_0^{(2)} = 1/2 (\underline{R}_1 + \underline{R}_2) \quad (3.82)$$

which covers only half of the 2-fold rotation centers given by (3.69), as shown in Fig. 3.10.

Next, consider a netplane with **true 3-fold rotation symmetry** at  $\underline{r}_0$  (i.e. 3- but not 6-fold rotation), assumed to coincide with the netplane origin. Then its periodicity can be described by lattice vectors  $\underline{R}_1$  and  $\underline{R}_2$ , where  $|\underline{R}_1|$ , as before, denotes the smallest distance between lattice points of the netplane. Further,  $\underline{R}_2$  can be constructed to be the image of  $\underline{R}_1$ , rotated by  $120^\circ$ , yielding the same length as vector  $\underline{R}_1$ . Thus, the corresponding morphological unit cell takes the shape of a highly symmetric **rhombus**, see Fig. 3.11. A rotation of the lattice vectors  $\underline{R}_1$  and  $\underline{R}_2$  by  $120^\circ$  with respect to the netplane origin yields vectors  $\underline{R}_1'$ ,  $\underline{R}_2'$  with

$$\underline{R}_1' = C_{120}(\underline{R}_1) = \underline{R}_2 \ , \quad \underline{R}_2' = C_{120}(\underline{R}_2) = -(\underline{R}_1 + \underline{R}_2) \quad (3.83)$$

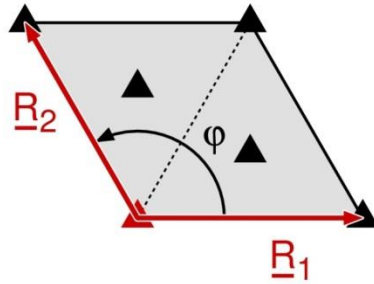


Fig. 3.11. Rotation by  $\varphi = 120^\circ$  applied to lattice vector  $\underline{R}_1$  to yield  $\underline{R}_2$ . The initial rotation center is indicated by a red triangle. The unit cell is emphasized in gray with its other 3-fold rotation centers shown by black triangles.

Therefore, a  $120^\circ$  rotation about a center  $\underline{r}_0$  inside the unit cell, given by

$$\underline{r}_0 = \gamma_1 \underline{R}_1 + \gamma_2 \underline{R}_2 \ , \quad 0 \leq \gamma_i < 1 \ , \quad i = 1, 2 \quad (3.84)$$

transforms general lattice vectors  $\underline{R}$  of (3.66) to  $\underline{R}'$  according to

$$\begin{aligned}
\underline{\mathbf{R}}' &= \underline{\mathbf{r}}_o + \mathbf{C}_{120} (\underline{\mathbf{R}} - \underline{\mathbf{r}}_o) = \underline{\mathbf{r}}_o + \mathbf{C}_{120} (\underline{\mathbf{R}}) - \mathbf{C}_{120} (\underline{\mathbf{r}}_o) = \\
&= \gamma_1 \underline{\mathbf{R}}_1 + \gamma_2 \underline{\mathbf{R}}_2 + n_1 \underline{\mathbf{R}}_2 - n_2 (\underline{\mathbf{R}}_1 + \underline{\mathbf{R}}_2) - \gamma_1 \underline{\mathbf{R}}_2 + \gamma_2 (\underline{\mathbf{R}}_1 + \underline{\mathbf{R}}_2) = \\
&= (\gamma_1 + \gamma_2 - n_2) \underline{\mathbf{R}}_1 + (2\gamma_2 - \gamma_1 + n_1 - n_2) \underline{\mathbf{R}}_2 = \beta_1 \underline{\mathbf{R}}_1 + \beta_2 \underline{\mathbf{R}}_2
\end{aligned} \tag{3.85}$$

where

$$\begin{aligned}
\beta_1 &= \gamma_1 + \gamma_2 - n_2 & \beta_2 &= 2\gamma_2 - \gamma_1 + n_1 - n_2 \\
\gamma_1 &= 1/3 (2\beta_1 - \beta_2 + n_1 + n_2) & \gamma_2 &= 1/3 (\beta_1 + \beta_2 - n_1 + 2n_2)
\end{aligned} \tag{3.86}$$

If  $\underline{\mathbf{r}}_o$  is the center of a 3-fold rotation axis of the netplane, then all transformed centers  $\underline{\mathbf{R}}'$  in (3.85) must reflect the initial centers  $\underline{\mathbf{R}}$  given by (3.66). This requires that both  $\beta_1$  and  $\beta_2$  are integer-valued and, therefore, the corresponding parameters  $\gamma_i$  must be integer multiples of 1/3. Together with relation (3.84), only three parameter choices ( $\gamma_1 = \gamma_2 = 0$ ), ( $\gamma_1 = 2/3, \gamma_2 = 1/3$ ), and ( $\gamma_1 = 1/3, \gamma_2 = 2/3$ ) are possible. This results in **three** different possible centers of true **3-fold rotation** axes at

$$\underline{\mathbf{r}}_o^{(1)} = \underline{\mathbf{0}} , \quad \underline{\mathbf{r}}_o^{(2)} = 1/3 (2 \underline{\mathbf{R}}_1 + \underline{\mathbf{R}}_2) , \quad \underline{\mathbf{r}}_o^{(3)} = 1/3 (\underline{\mathbf{R}}_1 + 2 \underline{\mathbf{R}}_2) \tag{3.87}$$

If a netplane possesses **6-fold rotation symmetry** at  $\underline{\mathbf{r}}_o$  this center must also serve for a 2- and 3-fold rotation axis. Here the former offers four distinct centers  $\underline{\mathbf{r}}_o$  inside the unit cell according to (3.69), while the latter allows three different centers, given by (3.87). The two sets of centers overlap only at  $\underline{\mathbf{r}}_o = \underline{\mathbf{0}}$ , the origin of the unit cell. Therefore, a netplane allows **6-fold rotation** symmetry only at centers coinciding with lattice points.

**In conclusion**, rotation axes existing as symmetry elements of a netplane, defined by primitive lattice vectors  $\underline{\mathbf{R}}_1$  and  $\underline{\mathbf{R}}_2$ , have the following properties :

- Netplanes allow only 2-, 3-, 4-, and 6-fold rotation axes. (3.88a)

- Centers of 2-fold rotation axes form netplanes with lattice vectors  $1/2 \underline{\mathbf{R}}_1, 1/2 \underline{\mathbf{R}}_2$ . (3.88b)

- Centers of 2-fold rotations are identical with inversion centers. (3.88c)

- Centers of true 3-fold rotations are restricted to hexagonal netplanes. They form netplanes with lattice vectors

$$1/3 (2 \underline{\mathbf{R}}_1 + \underline{\mathbf{R}}_2), \quad 1/3 (\underline{\mathbf{R}}_1 + 2 \underline{\mathbf{R}}_2) \quad (\text{obtuse representation of } \underline{\mathbf{R}}_1, \underline{\mathbf{R}}_2)$$

$$1/3 (\underline{\mathbf{R}}_1 + \underline{\mathbf{R}}_2), \quad 1/3 (-\underline{\mathbf{R}}_1 + 2 \underline{\mathbf{R}}_2) \quad (\text{acute representation of } \underline{\mathbf{R}}_1, \underline{\mathbf{R}}_2). \tag{3.88d}$$

- Centers of 4-fold rotation axes are restricted to square netplanes. They

form netplanes with lattice vectors  $1/2 (\underline{R}_1 + \underline{R}_2)$ ,  $1/2 (\underline{R}_1 - \underline{R}_2)$ . Thus, 4-fold rotation centers coincide with half of the 2-fold rotation centers, given in (3.88b). (3.88e)

- Centers of 6-fold rotation axes combine 2- with 3-fold rotation axes. They form netplanes with lattice vectors  $\underline{R}_1$  and  $\underline{R}_2$ , reflecting the initial netplane. (3.88f)

### 3.6.4 Mirror Operation

**Mirror operations**  $\sigma(\underline{r}_o, \underline{e})$  with respect to a mirror line along vector  $\underline{e}$  on the netplane create, for any point  $\underline{r}$  on one side of the line, an image point  $\underline{r}'$  on the other side, such that the connecting line between the two points is perpendicular to the mirror line and their distances from the mirror line are the same, see Fig. 3.12. This can be expressed **mathematically** by a transformation of points on the netplane

$$\underline{r} \rightarrow \underline{r}' = \underline{r} - 2 [(\underline{r} - \underline{r}_o) \underline{m}] \underline{m} = \underline{r}_o + \sigma_m (\underline{r} - \underline{r}_o) \quad (3.89)$$

where the **mirror line** is defined by its origin  $\underline{r}_o$  (**mirror center**), a direction vector  $\underline{e}$  along the line (**mirror line vector**), and a normal vector  $\underline{m}$  (**mirror line normal vector**) of unit length perpendicular to vector  $\underline{e}$ , sketched in Fig. 3.12. The mirror operation can also be connected with a

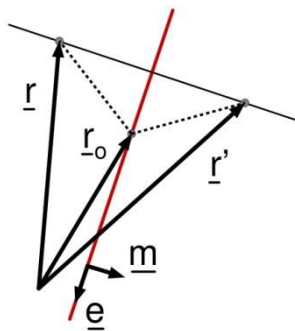


Fig. 3.12. Sketch of a mirror operation applied to vector  $\underline{r}$  to yield  $\underline{r}'$ . The mirror center  $\underline{r}_o$ , mirror line vector  $\underline{e}$ , and mirror line normal vector  $\underline{m}$  are labeled accordingly, see text.

two-dimensional Cartesian **coordinate transformation** with respect to the mirror center  $\underline{r}_o$  applying a  $2 \times 2$  matrix  $\underline{\sigma}_m$  where

$$\begin{pmatrix} x' \\ y' \end{pmatrix} = \underline{\sigma}_m \cdot \begin{pmatrix} x \\ y \end{pmatrix}, \quad \underline{\sigma}_m = \begin{pmatrix} 1 - 2m_x^2 & -2m_x m_y \\ -2m_x m_y & 1 - 2m_y^2 \end{pmatrix} \quad (3.90)$$

with

$$\underline{m} = (m_x, m_y) = (-e_y, e_x) \quad \text{and} \quad \underline{e} = (e_x, e_y) \quad \text{with} \quad e_x^2 + e_y^2 = 1 \quad (3.91)$$

The mirror line vector  $\underline{e}$  may also be written in Cartesian coordinates as

$$\underline{e} = (\cos \Phi, \sin \Phi) \quad (3.92)$$

where  $\Phi$  denotes the angle of the mirror line with respect to an x axis. Hence mirror line normal vector  $\underline{m}$  is given by

$$\underline{m} = (-\sin \Phi, \cos \Phi) \quad (3.93)$$

which, according to (3.90), leads to

$$\underline{\sigma}_m = \underline{\sigma}_\Phi = \begin{pmatrix} 1 - 2(\sin \Phi)^2 & 2 \sin \Phi \cos \Phi \\ 2 \sin \Phi \cos \Phi & 1 - 2(\cos \Phi)^2 \end{pmatrix} = \begin{pmatrix} \cos 2\Phi & \sin 2\Phi \\ \sin 2\Phi & -\cos 2\Phi \end{pmatrix} \quad (3.94)$$

Here the **mirror center**  $\underline{r}_o$  can be chosen **arbitrarily** along the mirror line, since due to the orthogonality of  $\underline{e}$  and  $\underline{m}$  a shift

$$\underline{r}_o \rightarrow \underline{r}'_o = \underline{r}_o + \chi \underline{e} \quad (3.95)$$

results, according to (3.89) with  $(\underline{e} \underline{m}) = 0$ , in a transformation

$$\underline{r}'' = \underline{r} - 2 [ (\underline{r} - \underline{r}'_o) \underline{m} ] \underline{m} = \underline{r} - 2 [ (\underline{r} - \underline{r}_o) \underline{m} ] \underline{m} + 2\chi (\underline{e} \underline{m}) \underline{m} = \underline{r}' \quad (3.96)$$

**Parallel mirror lines** given by mirror centers  $\underline{r}_{1o}, \underline{r}_{2o}$  with identical normal vectors  $\underline{m}$  are separated by a distance

$$d_m = |(\underline{r}_{2o} - \underline{r}_{1o}) \underline{m}| \quad (3.97)$$

Here a combined mirror operation with respect to the two lines can be written as

$$\underline{r} \rightarrow \underline{r}': \quad \underline{r}' = \underline{r} - 2 [ (\underline{r} - \underline{r}_{1o}) \underline{m} ] \underline{m} \quad (\text{mirror line 1}) \quad (3.98a)$$

$$\underline{r}' \rightarrow \underline{r}'': \quad \underline{r}'' = \underline{r}' - 2 [ (\underline{r}' - \underline{r}_{2o}) \underline{m} ] \underline{m} \quad (\text{mirror line 2}) \quad (3.98b)$$

yielding, after some calculus

$$\underline{r}'' = \underline{r} + 2 [ (\underline{r}_{2o} - \underline{r}_{1o}) \underline{m} ] \underline{m} \quad (3.99)$$

This corresponds to a simple **shift operation** by a shift vector perpendicular to the mirror lines with, according to (3.97), a length equal to twice the distance between the two mirror lines.

Centers  $\underline{r}_o$  of two **mirror lines** which **cross** each other can always be chosen such as to coincide with the crossing point. Thus, the mirror lines differ only by their transformation matrices  $\underline{\sigma}_m$ , where, assuming a crossing angle  $\Theta$  between the the mirror lines leads, according to (3.94), to matrices  $\underline{\sigma}_m(\Phi)$  and  $\underline{\sigma}_m(\Phi+\Theta)$  with

$$\underline{\sigma}_m(\Phi) = \begin{pmatrix} \cos 2\Phi & \sin 2\Phi \\ \sin 2\Phi & -\cos 2\Phi \end{pmatrix} \quad (3.100)$$

and

$$\underline{\sigma}_m(\Phi + \Theta) = \begin{pmatrix} \cos 2(\Phi + \Theta) & \sin 2(\Phi + \Theta) \\ \sin 2(\Phi + \Theta) & -\cos 2(\Phi + \Theta) \end{pmatrix} \quad (3.101)$$

Therefore, a combination of the two mirror operations (in the two different sequences) results in symmetry operations with their centers at  $\underline{r}_o$  and transformation matrices  $\underline{T}$ ,  $\underline{T}'$  given by the different products of  $\underline{\sigma}_m(\Phi)$  and  $\underline{\sigma}_m(\Phi+\Theta)$ , i.e. by

$$\begin{aligned} \underline{T} &= \underline{\sigma}_m(\Phi + \Theta) \cdot \underline{\sigma}_m(\Phi) = \begin{pmatrix} \cos 2(\Phi + \Theta) & \sin 2(\Phi + \Theta) \\ \sin 2(\Phi + \Theta) & -\cos 2(\Phi + \Theta) \end{pmatrix} \begin{pmatrix} \cos 2\Phi & \sin 2\Phi \\ \sin 2\Phi & -\cos 2\Phi \end{pmatrix} = \\ &= \begin{pmatrix} \cos 2\Theta & -\sin 2\Theta \\ \sin 2\Theta & \cos 2\Theta \end{pmatrix} = \underline{C}_{2\Theta} \end{aligned} \quad (3.102)$$

and

$$\begin{aligned} \underline{T}' &= \underline{\sigma}_m(\Phi) \cdot \underline{\sigma}_m(\Phi + \Theta) = \begin{pmatrix} \cos 2\Phi & \sin 2\Phi \\ \sin 2\Phi & -\cos 2\Phi \end{pmatrix} \begin{pmatrix} \cos 2(\Phi + \Theta) & \sin 2(\Phi + \Theta) \\ \sin 2(\Phi + \Theta) & -\cos 2(\Phi + \Theta) \end{pmatrix} = \\ &= \begin{pmatrix} \cos 2\Theta & \sin 2\Theta \\ -\sin 2\Theta & \cos 2\Theta \end{pmatrix} = \underline{C}_{-2\Theta} \end{aligned} \quad (3.103)$$

Comparing with (3.74), matrices  $\underline{C}_{2\Theta}$  and  $\underline{C}_{-2\Theta}$  represent clockwise and anti-clockwise rotations by an angle  $2\Theta$ , as sketched in Fig. 3.13 for the anti-clockwise case. Therefore, two mirror symmetry lines of a netplane which cross at  $\underline{r}_o$  with a finite angle  $\Theta$  are always connected with (clockwise and

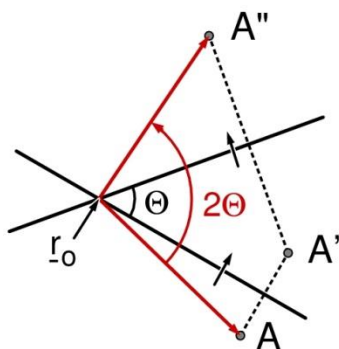


Fig. 3.13. Two subsequent mirror line operations with mirror lines crossing at  $\underline{r}_0$  and forming an angle  $\Theta$ . Point  $A$  is transformed to  $A'$ , then to  $A''$ . The mirror lines are indicated by thick black lines with small mirror normal arrows. Angles  $\Theta$ ,  $2\Theta$  are labeled accordingly.

anti-clockwise) **rotations** by  $2\Theta$ . If the two mirror lines are symmetry elements of a netplane the resulting rotation by  $\pm 2\Theta$  must also be a symmetry element. Thus, it must belong to an  $n$ -fold rotation axis of the netplane. Since these axes can only be 2-, 3-, 4-, or 6-fold, possible angles  $\Theta$  with  $0 < |\Theta| \leq 90$  amount to

$$|\Theta| = 30^\circ, 45^\circ, 60^\circ, 90^\circ \quad (3.104)$$

In particular, matrix  $\underline{T}$  of (3.102) for  $\Theta = \pm 90^\circ$  reflects a  $180^\circ$  rotation, corresponding to a 2-fold rotation axis, which was shown to be also equivalent to an inversion operation. Thus, the **crossing** point of two **orthogonal mirror** lines is always the center of a **2-fold rotation** or **inversion**.

Relation (3.102) can be modified to read

$$\underline{C}_\Theta \cdot \underline{\sigma}_m(\Phi) = \underline{\sigma}_m(\Phi + \Theta/2) \cdot \underline{\sigma}_m(\Phi) \cdot \underline{\sigma}_m(\Phi) = \underline{\sigma}_m(\Phi + \Theta/2) \quad (3.105)$$

This shows that a **mirror** operation followed by a **rotation** by an angle  $\Theta$  with respect to a center  $\underline{r}_0$  on the mirror line is equivalent to another **mirror** operation. The latter mirror line crosses the initial line at  $\underline{r}_0$  and forms an angle  $\Theta/2$  with it. This result becomes important for the symmetry analysis of netplanes discussed in the following.

The **compatibility** between translational and mirror symmetry imposes **constraints** on possible positions and directions of mirror lines in a netplane. Let us assume a netplane with lattice vectors  $\underline{R}_1$  and  $\underline{R}_2$  possesses mirror symmetry with a mirror line through  $\underline{r}_0$ . Then the netplane can always be shifted such that its origin coincides with  $\underline{r}_0$  (setting  $\underline{r}_0 = 0$ ). According to (3.89), a general lattice vector  $\underline{R}$ , given by (3.66) and not located at a mirror line, will have a mirror image  $\underline{R}'$ . Then the difference vector  $\underline{R}_{r2}$ , given by



$$\underline{\mathbf{R}}_{r2} = \underline{\mathbf{R}} - \underline{\mathbf{R}}' = 2 (\underline{\mathbf{R}} \underline{\mathbf{m}}) \underline{\mathbf{m}} = k_1 \underline{\mathbf{R}}_1 + k_2 \underline{\mathbf{R}}_2, \quad k_1, k_2 \text{ integer} \quad (3.106)$$

must also be a general lattice vector. This shows, in particular, that normal vectors  $\underline{\mathbf{m}}$  of mirror lines must always point along general lattice vectors of the netplane. Further, the vector sum  $\underline{\mathbf{R}}_{r1}$  is given by

$$\underline{\mathbf{R}}_{r1} = \underline{\mathbf{R}} + \underline{\mathbf{R}}' = 2 [\underline{\mathbf{R}} - (\underline{\mathbf{R}} \underline{\mathbf{m}}) \underline{\mathbf{m}}] = (2n_1 - k_1) \underline{\mathbf{R}}_1 + (2n_2 - k_2) \underline{\mathbf{R}}_2 \quad (3.107)$$

with

$$\underline{\mathbf{R}}_{r1} \cdot \underline{\mathbf{R}}_{r2} = 4 [\underline{\mathbf{R}} - (\underline{\mathbf{R}} \underline{\mathbf{m}}) \underline{\mathbf{m}}] \cdot [(\underline{\mathbf{R}} \underline{\mathbf{m}}) \underline{\mathbf{m}}] = 0 \quad (3.108)$$

Thus, the general lattice vector  $\underline{\mathbf{R}}_{r1}$  is perpendicular to  $\underline{\mathbf{R}}_{r2}$  and, hence, points along the mirror line.

Altogether, the existence of a **mirror plane** implies two **orthogonal** general lattice vectors  $\underline{\mathbf{R}}_{r1}$  and  $\underline{\mathbf{R}}_{r2}$  in the netplane. These may be integer multiples of smaller lattice vectors along their directions, where we consider, in each case, the smallest possible vector, calling it  $\underline{\mathbf{R}}_1$  and  $\underline{\mathbf{R}}_2$ . Vectors  $\underline{\mathbf{R}}_1$  and  $\underline{\mathbf{R}}_2$  can then be used as lattice vectors to describe the netplane periodicity and, since the vectors are perpendicular to each other the **netplane** must be **rectangular**. Therefore, in the following discussion, we will use mutually orthogonal lattice vectors  $\underline{\mathbf{R}}_1$  and  $\underline{\mathbf{R}}_2$  to describe netplanes with mirror symmetry, where primitive and centered rectangular netplanes, see Sec. 3.6.1, can be treated on the same footing.

Consider a **primitive rectangular** netplane defined by orthogonal lattice vectors  $\underline{\mathbf{R}}_1$  and  $\underline{\mathbf{R}}_2$  and a mirror operation with its **mirror line** through the netplane origin and **parallel to  $\underline{\mathbf{R}}_1$** , i.e.

$$\underline{\mathbf{m}} = \underline{\mathbf{R}}_2 / |\underline{\mathbf{R}}_2|, \quad \underline{\mathbf{r}}_0 = \underline{\mathbf{0}} \quad (3.109)$$

Then, as a result of translational symmetry, there are **infinitely** many parallel **mirror lines** through mirror centers at  $\underline{\mathbf{r}}_{0n}$  with

$$\underline{\mathbf{r}}_{0n} = n \underline{\mathbf{R}}_2, \quad n \text{ integer} \quad (3.110)$$

indicated by black horizontal lines in Fig. 3.14, where adjacent lines are separated by a distance  $d_m$  with

$$d_m = |\underline{\mathbf{R}}_2 \underline{\mathbf{m}}| = R_2 \quad (3.111)$$

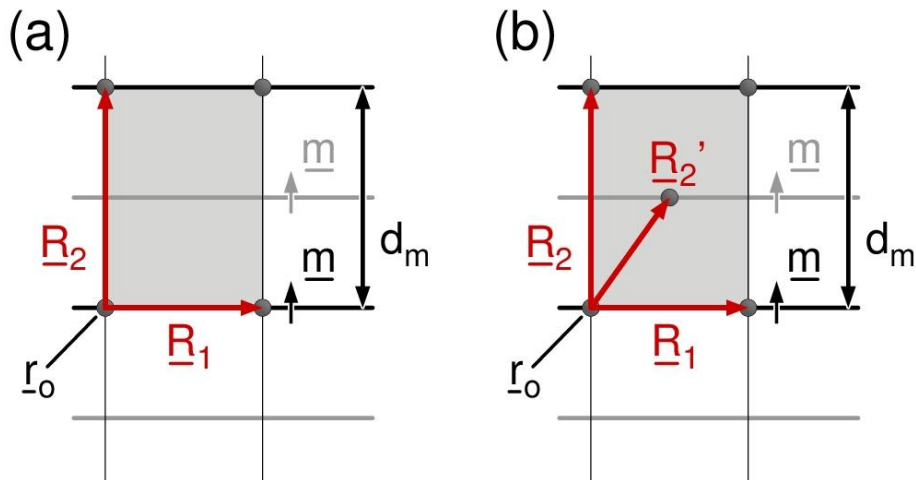


Fig. 3.14. Periodic sets of horizontal mirror lines for (a) primitive and (b) centered rectangular netplanes. The mirror lines are shown by black and gray horizontal lines (some with small mirror normal arrows) parallel to lattice vector  $\underline{R}_1$ . The unit cell is emphasized in gray.

The translational symmetry of the netplane yields **additional** parallel mirror lines beyond those given by (3.110). The mirror operation (3.89), together with (3.109), (3.110), can be written as

$$\underline{r}' = \underline{r} - 2 [ (\underline{r} - \underline{r}_{on}) \underline{m} ] \underline{m} = \underline{r} - 2 [ (\underline{r} - (\underline{r}_{on} + \underline{R}_2/2)) \underline{m} ] \underline{m} - \underline{R}_2 \quad (3.112)$$

which can be interpreted as a parallel mirror operation with respect to a mirror line at origin

$$\underline{r}_{on}' = (n + 1/2) \underline{R}_2, \quad n \text{ integer} \quad (3.113)$$

followed by a (backwards) shift by lattice vector  $\underline{R}_2$ . Thus, if a netplane reproduces itself for mirror operations with mirror lines at origins  $\underline{r}_{on}$ , according to (3.109), its translational symmetry also yields mirror symmetry with respect to additional parallel lines. The latter originate at  $\underline{r}_{on}'$ , given by (3.112), and, thus, are located in the **middle** between the adjacent mirror lines of the initial set (3.110), as indicated by gray horizontal lines in Fig. 3.14. The two sets, defined by origins (3.110) and (3.113), can be combined to one set of parallel mirror lines with  $\underline{m} = \underline{R}_2/|\underline{R}_2|$  and originating at mirror centers

$$\underline{r}_{on} = n \underline{R}_2/2, \quad n \text{ integer} \quad (3.114)$$

where even  $n$  values refer to (3.110) and odd ones to (3.113). Mirror symmetry of the netplane for additional lines parallel to those given by (3.114) cannot occur since this would violate the translational symmetry of the netplane.

The results for sets of mirror lines **parallel to  $\underline{R}_2$**  are completely analogous to those when mir-

ror lines parallel to  $\underline{R}_1$  are considered. Interchanging  $\underline{R}_1$  with  $\underline{R}_2$  in the above discussion shows that, as a result of translational symmetry, there are **infinitely** many parallel **mirror lines** through mirror centers at  $\underline{r}_{on}$  with

$$\underline{m} = \underline{R}_1/|\underline{R}_1|, \quad \underline{r}_{on} = n \underline{R}_1/2, \quad n \text{ integer} \quad (3.115)$$

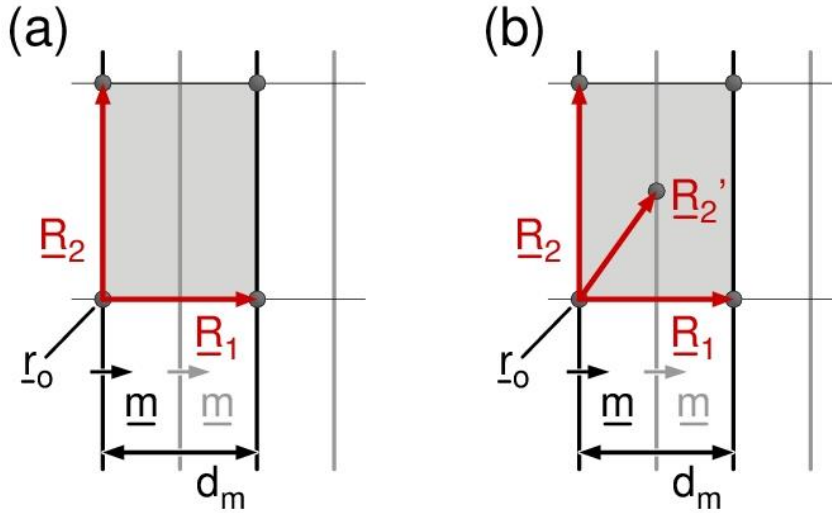


Fig. 3.15. Periodic sets of vertical mirror lines for (a) primitive and (b) centered rectangular netplanes, see text. The mirror lines are shown by black and gray vertical lines (some with small mirror normal arrows) parallel to lattice vector  $\underline{R}_2$ . The unit cell is emphasized in gray.

The sets of mirror lines parallel to lattice vectors  $\underline{R}_1$  and  $\underline{R}_2$  of a primitive rectangular netplane, given by origins (3.114) and (3.115), must also exist when the orthogonal lattice vectors  $\underline{R}_1$  and  $\underline{R}_2$  refer to a non-primitive representation of a **centered rectangular netplane**, as illustrated in Figs. 3.14b and 3.15b. The additional netplane point in the center of the morphological unit cell of the centered rectangular netplane is always positioned on a mirror line, shown in gray in the two figures. Thus, it cannot give rise to additional mirror lines and the set of parallel mirror lines at origins (3.114) and (3.115) is also **complete** for centered rectangular lattices.

Netplanes with **mirror symmetry** may also include **inversion** centers as symmetry elements. Let us assume a **primitive rectangular** netplane with orthogonal lattice vectors  $\underline{R}_1$  and  $\underline{R}_2$  to possess mirror lines **parallel to  $\underline{R}_1$**  through centers  $\underline{r}_{on}$ , given by (3.114), as symmetry elements. If the netplane also possesses inversion symmetry, then there is, according to Sec. 3.6.2, an infinite number of inversion centers which form a netplane on their own (inversion netplane), with lattice vectors  $1/2 \underline{R}_1$  and  $1/2 \underline{R}_2$ , see (3.72). The **origin** of the inversion netplane may be shifted with respect

to that of the initial netplane defining the mirror lines, but the two have to be **compatible**. Thus, mirror operations with respect to any mirror line through centers  $\underline{r}_{on}$ , given by (3.114), must reproduce all inversion centers and inversions with respect to any inversion center must reproduce all mirror lines. This is possible only if, either, the origins of the initial and its inversion netplane coincide, or the origins are shifted with respect to each other by  $\underline{R}_2/4$ . In the former case all inversion centers lie on mirror lines, while, in the latter, inversion centers lie only in the middle between mirror lines, as illustrated in Fig. 3.16.

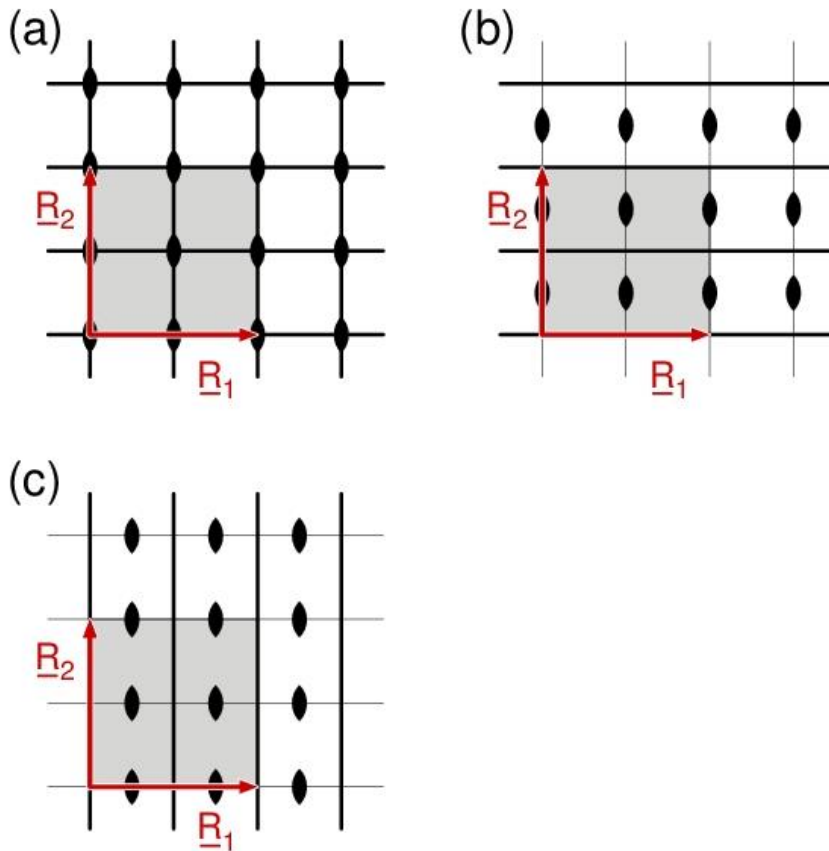


Fig. 3.16. Primitive rectangular netplanes with coexisting inversion centers (2-fold rotation axes) and mirror lines. (a) Mirror lines parallel to  $\underline{R}_1$  and  $\underline{R}_2$  with inversion centers on mirror lines. (b,c) Mirror lines with inversion centers between mirror lines parallel to  $\underline{R}_1$  and parallel to  $\underline{R}_2$ , respectively. Corresponding unit cells are emphasized in gray with lattice vectors  $\underline{R}_1$ ,  $\underline{R}_2$  indicated accordingly. Mirror lines are shown by thick lines and 2-fold rotation centers by black ellipses.

According to (3.105) an inversion center  $\underline{r}_o$  on a mirror line parallel to  $\underline{R}_1$  and through  $\underline{r}_o$  implies another mirror line through  $\underline{r}_o$  but parallel to  $\underline{R}_2$ , i.e. perpendicular to  $\underline{R}_1$ . This shows that, when all inversion centers lie on mirror lines parallel to  $\underline{R}_1$ , the netplane also includes the set (3.115) of mirror lines parallel to  $\underline{R}_2$ . This is illustrated in Fig. 3.16a, where mirror lines of both sets are sketched.

The above results apply analogously to **primitive rectangular** netplanes with orthogonal lattice vectors  $\underline{\mathbf{R}}_1$  and  $\underline{\mathbf{R}}_2$  including mirror lines **parallel to  $\underline{\mathbf{R}}_2$**  (through centers  $\underline{\mathbf{r}}_{\text{on}}$  given by (3.115)) as symmetry elements. Interchanging  $\underline{\mathbf{R}}_1$  with  $\underline{\mathbf{R}}_2$  in the previous discussion shows that inversion symmetry of the netplane is only possible if the origins of the initial and its inversion netplane coincide or, if the origins are shifted with respect to each other by  $\underline{\mathbf{R}}_1/4$ . This means that, either, all inversion centers lie on mirror lines, which implies two orthogonal sets of mirror lines, as discussed above, see Fig. 3.16a. Alternatively, inversion centers will lie only in the middle between mirror lines, as illustrated in Fig. 3.16c.

The same arguments concerning compatibility of **mirror** and **inversion** symmetry for primitive rectangular netplanes can also be used for **centered rectangular** netplanes. Starting from a non-primitive description of a centered rectangular netplane by orthogonal lattice vectors  $\underline{\mathbf{R}}_1$  and  $\underline{\mathbf{R}}_2$ , a primitive description can be obtained by lattice vectors  $\underline{\mathbf{R}}_1$  and  $\underline{\mathbf{R}}_2'$  with

$$\underline{\mathbf{R}}_2' = 1/2 (\underline{\mathbf{R}}_1 + \underline{\mathbf{R}}_2) \quad (3.116)$$

Thus, a centered rectangular netplane with inversion symmetry possesses, according to Sec. 3.6.2, an infinite number of inversion centers forming an inversion netplane with lattice vectors  $(\underline{\mathbf{R}}_1/2)$ ,  $(\underline{\mathbf{R}}_2'/2) = 1/4 (\underline{\mathbf{R}}_1 + \underline{\mathbf{R}}_2)$ . On the other hand, it was shown above that the set of mirror lines parallel to  $\underline{\mathbf{R}}_1$  is identical for primitive and centered rectangular netplanes. Therefore, **compatibility** of mirror and inversion symmetry requires that the origins of the initial and its inversion netplane coincide. This is the only choice and results in **half** of the inversion centers lying **at mirror lines** and the other half in the **middle** between mirror lines, as illustrated in Fig. 3.17. Further, the inversion centers on the mirror lines lead to two orthogonal sets of mirror lines, as discussed for primitive rectangular netplanes and sketched in Fig. 3.17.

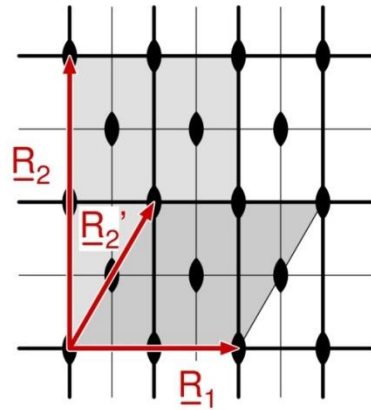


Fig. 3.17. Centered rectangular netplane with coexisting inversion centers (2-fold rotation axes) and mirror lines parallel to  $\underline{R}_1, \underline{R}_2$ . Corresponding non-primitive and primitive unit cells are emphasized in light and dark gray, respectively, with lattice vectors  $\underline{R}_1, \underline{R}_2, \underline{R}_2'$  indicated accordingly. Mirror lines are shown by thick lines and 2-fold rotation centers by black ellipses.

Since in two dimensions inversion centers and 2-fold rotation axes are equivalent the above discussion also applies to coexisting **mirror** and **2-fold rotation symmetry** in netplanes.

Netplanes with **mirror symmetry** may also possess **4-fold rotation** axes as symmetry elements. According to the discussion in Sec. 3.6.3, 4-fold rotation symmetry in a netplane results in symmetry-adapted lattice vectors  $\underline{R}_1$  and  $\underline{R}_2$  which are mutually orthogonal and both of smallest finite length. This yields a primitive morphological unit cell of square shape.

Let us assume a **square** netplane with orthogonal lattice vectors  $\underline{R}_1$  and  $\underline{R}_2$  of equal length to possess **mirror lines** parallel to  $\underline{R}_1$  through centers  $\underline{r}_{on}$ , given by (3.114), as symmetry elements. If the netplane is also symmetric with respect to **4-fold rotation**, corresponding rotation centers must coincide with positions of 2-fold rotation centers on the netplane, since 4-fold rotation implies 2-fold rotation. As shown above, the complete set of 2-fold rotation centers (= inversion centers) forms an inversion netplane with lattice vectors  $1/2 \underline{R}_1$  and  $1/2 \underline{R}_2$ . Adding 4-fold rotation centers according to (3.88e) covers half of the inversion centers in a checkerboard type arrangement, see Fig. 3.18a. The origin of this modified inversion netplane can only coincide with that of the initial square netplane or its origin is shifted, by  $\underline{R}_1/4$ ,  $\underline{R}_2/4$ , or  $(\underline{R}_1 + \underline{R}_2)/4$ , see above. Here, the presence of 4-fold rotation centers is found to yield the same structures for all cases.

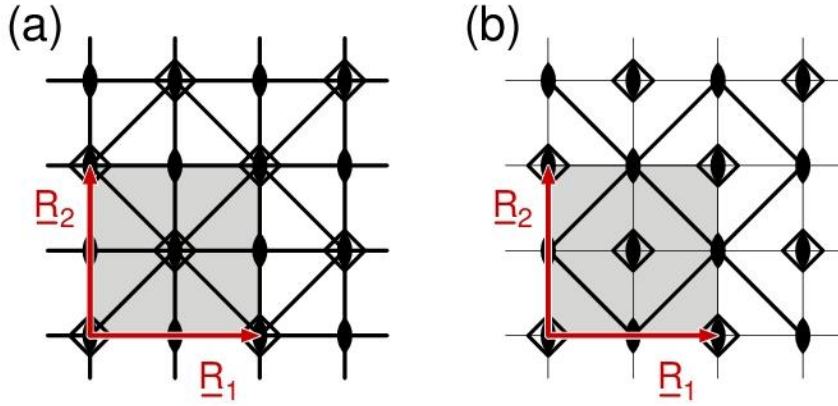


Fig. 3.18. Square netplane with coexisting 2-, 4-fold rotation axes and mirror lines. (a) Mirror lines parallel to  $\underline{R}_1$ ,  $\underline{R}_2$ , and to diagonals. (b) Mirror lines parallel to diagonals between true 2-fold rotation axes only. Corresponding unit cells are emphasized in gray. Mirror lines are shown by thick lines and 2-, 4-fold rotation centers by black ellipses and open squares, respectively.

Thus, only the coincidence geometry needs to be considered, where it can be assumed that the netplane origin  $\underline{r}_0$  also coincides with a 4-fold rotation center, as indicated in Fig. 3.18a. As a consequence, this 4-fold rotation center  $\underline{r}_0$  implies other mirror lines crossing  $\underline{r}_0$ , where, according to (3.105), mirror lines parallel to  $\underline{R}_1$  and  $\underline{R}_2$ , as well as parallel to the two diagonals ( $\underline{R}_1 \pm \underline{R}_2$ ) cover all cases, illustrated by Fig. 3.18a. This combination of mirror and 4-fold rotation symmetry does not include mirror lines parallel to the two diagonals ( $\underline{R}_1 \pm \underline{R}_2$ ) connecting true 2-fold rotation centers. The existence of such mirror lines can be shown to exclude all previous mirror lines of Fig. 3.18a, yielding an alternative geometry for coexisting mirror and 4-fold rotation symmetry, shown in Fig. 3.19b.

The coexistence of **mirror lines** and **true 3-fold** (i.e. 3- but not 6-fold) **rotation** axes as symmetry elements of a netplane is slightly more involved. First, we note that, as discussed in Sec. 3.6.3, 3-fold rotations are restricted to **hexagonal** netplanes, described by two primitive lattice vectors  $\underline{R}_1^{\text{hex}}$ ,  $\underline{R}_2^{\text{hex}}$  of equal length, forming an angle of  $120^\circ$  or  $60^\circ$ . Here we use the acute representation (i.e.  $60^\circ$ ) which yields

$$|\underline{R}_1^{\text{hex}}| = |\underline{R}_2^{\text{hex}}| = a, \quad \underline{R}_1^{\text{hex}} \cdot \underline{R}_2^{\text{hex}} = a^2 / 2 \quad (3.117)$$

where  $a$  is the lattice constant of the netplane. This allows the definition of a vector  $\underline{R}_2$

$$\underline{R}_2 = 2 \underline{R}_2^{\text{hex}} - \underline{R}_1^{\text{hex}} \quad (3.118)$$

which is orthogonal to  $\underline{R}_1^{\text{hex}}$ . Therefore, vectors  $\underline{R}_1^{\text{hex}}$ ,  $\underline{R}_2$ , together with  $\underline{R}_2^{\text{hex}}$  yield a non-primitive lattice description of the hexagonal netplane by a **centered rectangular** netplane which will be

used in the following.

Consider a **hexagonal** netplane, described as centered rectangular by orthogonal non-primitive lattice vectors  $\underline{R}_1^{\text{hex}}$ ,  $\underline{R}_2$  ( $|\underline{R}_2| = \sqrt{3} |\underline{R}_1^{\text{hex}}|$ ) and a centering lattice vector  $\underline{R}_2^{\text{hex}}$ . This netplane is further assumed to possess **mirror lines** parallel to  $\underline{R}_1^{\text{hex}}$  through centers  $\underline{r}_{\text{on}}$ , given by (3.114), as symmetry elements. If the netplane also includes symmetry with respect to **true 3-fold rotation**, then corresponding rotation centers form, according to (3.88d) and after some calculus, a separate rotation netplane with lattice vectors  $1/3 (\underline{R}_1^{\text{hex}} + \underline{R}_2^{\text{hex}})$  and  $1/3 \underline{R}_2$ . The origin  $\underline{r}_0$  of this rotation netplane, which can be assumed to be a 3-fold rotation center, must coincide with the origin of the initial hexagonal netplane, as indicated in Fig. 3.19a. The 3-fold rotation center at  $\underline{r}_0$ , positioned on a mirror line parallel to  $\underline{R}_1^{\text{hex}}$ , implies, according to (3.105), two additional mirror lines crossing  $\underline{r}_0$ , which are rotated by  $60^\circ$  and  $120^\circ$ . This yields the netplane geometry illustrated by Fig. 3.19a. The discussion for a **hexagonal** netplane assumed to possess **mirror symmetry** parallel to  $\underline{R}_2$  together with **3-fold rotation** symmetry is completely analogous and leads to the netplane geometry illustrated by Fig. 3.19b.

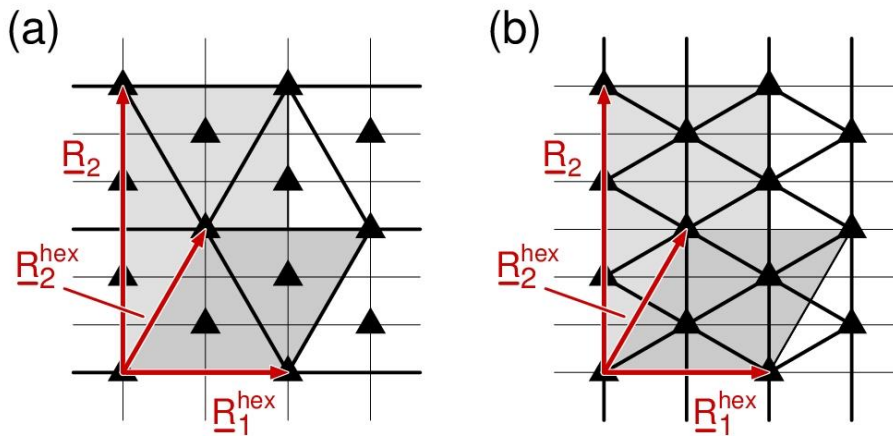


Fig. 3.19. Hexagonal netplane with coexisting true 3-fold rotation axes and mirror lines. (a) Mirror lines parallel to  $\underline{R}_1$  and corresponding rotated mirror lines. (b) Mirror lines parallel to  $\underline{R}_2$  and corresponding rotated mirror lines. Non-primitive and primitive unit cells are emphasized in light and dark gray, respectively, with lattice vectors  $\underline{R}_1$ ,  $\underline{R}_2$ ,  $\underline{R}_2'$  indicated accordingly. Mirror lines are shown by thick lines and 3-fold rotation centers by black triangles.

The coexistence of **mirror lines** and **6-fold rotation** axes as symmetry elements of a netplane is, analogous to the case of 3-fold rotation symmetry, also restricted to **hexagonal** netplanes. As before, we describe the hexagonal netplane as centered rectangular by orthogonal non-primitive lattice vectors  $\underline{R}_1^{\text{hex}}$ ,  $\underline{R}_2$  ( $|\underline{R}_2| = \sqrt{3} |\underline{R}_1^{\text{hex}}|$ ) and a centering lattice vector  $\underline{R}_2^{\text{hex}}$ . The netplane is further



assumed to possess **mirror lines** parallel to  $\underline{R}_1^{\text{hex}}$  through centers  $\underline{r}_{\text{on}}$ , given by (3.114), as symmetry elements. Allowing, in addition, for **6-fold rotational** symmetry leads to corresponding rotation centers, which form, according to (3.88f) a rotation netplane with lattice vectors  $\underline{R}_1^{\text{hex}}$ ,  $\underline{R}_2^{\text{hex}}$ , i.e. the rotation netplane is of the same periodicity than the initial hexagonal netplane. The origin  $\underline{r}_o$  of this rotation netplane, which can be assumed to be a 6-fold rotation center, must coincide with the origin of the initial hexagonal netplane, as indicated in Fig. 3.20. The 6-fold rotation center at  $\underline{r}_o$ , positioned on a mirror line parallel to  $\underline{R}_1^{\text{hex}}$ , implies, according to (3.105), five additional mirror lines crossing  $\underline{r}_o$ , which are rotated by  $30^\circ$ ,  $60^\circ$ ,  $90^\circ$ ,  $120^\circ$ , and  $150^\circ$ . This yields the netplane geometry illustrated by Fig. 3.20.

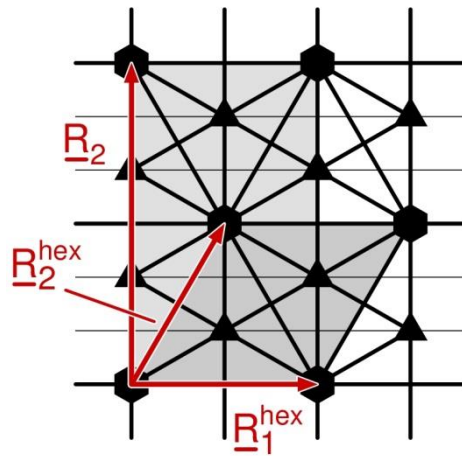


Fig. 3.20. Hexagonal netplane with coexisting 3-, 6-fold rotation axes and mirror lines parallel to  $\underline{R}_1^{\text{hex}}$ ,  $\underline{R}_2^{\text{hex}}$  and corresponding rotated mirror lines. Non-primitive and primitive unit cells are emphasized in light and dark gray, respectively, with lattice vectors  $\underline{R}_1$ ,  $\underline{R}_2$ ,  $\underline{R}_2'$  indicated accordingly. Mirror lines are shown by thick lines and 3-, 6-fold rotation centers by black triangles and hexagons, respectively.

**In conclusion**, mirror lines existing as symmetry elements of a netplane, defined by lattice vectors  $\underline{R}_1$  and  $\underline{R}_2$ , have the following properties :

- Netplanes with mirror symmetry must be either primitive or centered rectangular (including square and hexagonal netplanes as special cases). (3.119a)
- Netplanes with mirror symmetry include infinite sets of parallel mirror lines. If  $\underline{R}_1$  and  $\underline{R}_2$ , are orthogonal lattice vectors describing the primitive or non-primitive morphological unit cell, then mirror line sets can be given by normal vectors  $\underline{m} = \underline{R}_1/|\underline{R}_1|$  and centers  $\underline{r}_{\text{on}} = n \underline{R}_1/2$ , or by normal vectors  $\underline{m} = \underline{R}_2/|\underline{R}_2|$  and centers  $\underline{r}_{\text{on}} = n \underline{R}_2/2$ . (3.119b)

- In primitive rectangular netplanes with mirror symmetry inversion (2-fold rotation) centers lie either all on mirror lines or all in the middle between adjacent parallel mirror lines. (3.119c)
- In centered rectangular netplanes with mirror symmetry inversion (2-fold rotation) centers induce two orthogonal sets of parallel mirror lines. The inversion centers lie both on mirror lines and in the middle between adjacent parallel mirror lines. (3.119d)
- In square netplanes with mirror symmetry 4-fold rotation centers induce two or four orthogonal sets of parallel mirror lines. The mirror lines will either cross 2- and 4-fold rotation centers (four sets) or will only connect 2-fold centers between 4-fold rotation centers (two sets). (3.119e)
- In hexagonal netplanes with mirror symmetry true 3-fold rotation centers induce sets of parallel mirror lines which cut each other at angles of  $60^\circ$ . (3.119f)
- In hexagonal netplanes with mirror symmetry 6-fold rotation centers induce sets of parallel mirror lines which cut each other at angles of  $30^\circ$ ,  $60^\circ$ , and  $90^\circ$ , respectively. (3.119g)

### 3.6.5 Glide Reflection

**Glide reflections**  $g(\underline{r}_o, \underline{g})$  combine mirroring with translation and are, therefore, not point symmetry operations in the strict sense. They create, for any point  $\underline{r}$  on one side of a glide line along  $\underline{g}$ , a mirror point on the other side (the glide line acting as a mirror line), which is then shifted by a vector  $\underline{g}$  parallel to the glide line to yield the image point  $\underline{r}'$ , see Fig. 3.21. This can be expressed **mathematically** by a transformation of points on the netplane

$$\underline{r} \rightarrow \underline{r}' = \underline{r} - 2 [ (\underline{r} - \underline{r}_o) \underline{m} ] \underline{m} + \underline{g} = \underline{r}_o + \sigma_m (\underline{r} - \underline{r}_o) + \underline{g} \quad (3.120)$$

where the **glide line** is defined by its origin  $\underline{r}_o$  (**glide line center**), a shift vector  $\underline{g}$  along the line (**glide line vector**), and a normal vector  $\underline{m}$  (**glide line normal vector**) of unit length perpendicular to vector  $\underline{g}$ , sketched in Fig. 3.21. The glide reflection can also be connected with a two-dimensional

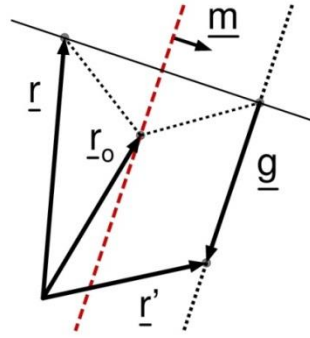


Fig. 3.21. Sketch of a glide reflection operation applied to vector  $\underline{r}$  and yielding  $\underline{r}'$ . The glide line center  $\underline{r}_0$ , glide line vector  $\underline{g}$ , and glide line normal vector  $\underline{m}$  are labeled accordingly, see text.

Cartesian **coordinate transformation** with respect to the mirror center  $\underline{r}_0$  applying a  $2 \times 2$  matrix  $\underline{\sigma}_m$  where

$$\begin{pmatrix} x' \\ y' \end{pmatrix} = \underline{\sigma}_m \cdot \begin{pmatrix} x \\ y \end{pmatrix} + \begin{pmatrix} g_x \\ g_y \end{pmatrix}, \quad \underline{\sigma}_m = \begin{pmatrix} 1 - 2m_x^2 & -2m_x m_y \\ -2m_x m_y & 1 - 2m_y^2 \end{pmatrix} \quad (3.121)$$

where matrix  $\underline{\sigma}_m$  is identical to that for mirroring, see (3.90), and

$$\underline{m} = (m_x, m_y), \quad \underline{g} = (g_x, g_y), \quad (\underline{m} \cdot \underline{g}) = 0 \quad (3.122)$$

As for mirroring the **glide line center**  $\underline{r}_0$  can be chosen **arbitrarily** along the glide line. Further, repeating a glide reflection (3.120) with the same glide line vector  $\underline{g}$  results in an operation given by

$$\begin{aligned} \underline{r} \rightarrow \underline{r}' \rightarrow \underline{r}'' &= \underline{r}' - 2 [ (\underline{r}' - \underline{r}_0) \underline{m} ] \underline{m} + \underline{g} = \\ &= \underline{r} - 2 [ (\underline{r} - \underline{r}_0) \underline{m} ] \underline{m} + 2 \underline{g} + 2 [ (\underline{r} - \underline{r}_0) \underline{m} ] \underline{m} = \\ &= \underline{r} + 2 \underline{g} \end{aligned} \quad (3.123)$$

Thus, two subsequent glide reflections with identical  $\underline{g}$  are equivalent to a **translation** by vector  $2 \underline{g}$ . In a netplane possessing glide reflection symmetry this vector must be a general lattice vector, i.e.

$$2 \underline{g} = \underline{R} = n_1 \underline{R}_1 + n_2 \underline{R}_2, \quad n_1, n_2 \text{ integer}$$

or

$$\underline{g} = 1/2 \underline{R} = 1/2 (n_1 \underline{R}_1 + n_2 \underline{R}_2) \quad (3.124)$$

This restricts possible translation vectors  $\underline{g}$  of glide lines and is the main condition for compatibility between translational and glide line symmetry in netplanes.

A **glide line**  $g(\underline{r}_o, \underline{g})$  as a symmetry element of a netplane was shown to point always along one of its **general lattice vectors**  $\underline{R}$ . Of these, the smallest vector along  $\underline{R}$ , denoted  $\underline{R}_o$ , is given, according to (3.124) by mixing factors  $n_1, n_2$ , whose common divisor is not greater than 1. This yields glide reflections  $g(\underline{r}_o, \underline{g} = \underline{R}_o/2)$  with  $\underline{R}_o$  determining the translational periodicity of the netplane along the glide line. Relation (3.124) also allows **multiples** of  $\underline{R}_o/2$  as possible glide line vectors  $\underline{g}$ , i.e. in general

$$\underline{g} = p \underline{R}_o/2, \quad p \text{ integer} \quad (3.125)$$

Here **even**  $p$  values yield vectors  $\underline{g}$  that are general lattice vectors themselves. Thus, the definition (3.120) of a glide reflection together with translational symmetry of the netplane leads to a **mirror operation**. On the other hand, **odd**  $p$  values correspond to the **glide reflection**  $g(\underline{r}_o, \underline{g} = \underline{R}_o/2)$  up to a shift by a general lattice vector which can be ignored due to translational symmetry of the netplane. Thus, in the following true glide reflection symmetry will always be connected with symmetry operations  $g(\underline{r}_o, \underline{R}_o/2)$ , where  $\underline{R}_o$  denotes the smallest vector along its direction..

The **compatibility** between translational and glide reflection symmetry imposes constraints on possible positions and directions of glide lines in a netplane. Let us assume a netplane with lattice vectors  $\underline{R}_1$  and  $\underline{R}_2$  to possess glide reflection symmetry with respect to a glide line along  $\underline{R}_o$  and through  $\underline{r}_o$ . Then the netplane can always be shifted such that its origin coincides with  $\underline{r}_o$  (setting  $\underline{r}_o = 0$ ). Further, since  $\underline{R}_o$  was shown to be a general lattice vector of smallest length along its direction, it can be used to define one of the lattice vectors of the netplane, e.g. setting  $\underline{R}_1 = \underline{R}_o$ . According to (3.120), a general lattice vector  $\underline{R}$ , given by (3.66) and not positioned on a glide line, will have a glide reflection image  $\underline{R}'$ , where

$$\underline{R}' = \underline{R} - 2(\underline{R} \cdot \underline{m}) \underline{m} + \underline{R}_o/2 \quad (3.126)$$

and applying a glide reflection to  $\underline{R}'$  creates a second image  $\underline{R}''$  with

$$\underline{R}'' = \underline{R}' - 2(\underline{R}' \cdot \underline{m}) \underline{m} + \underline{R}_o/2 \quad (3.127)$$

where both  $\underline{R}'$  and  $\underline{R}''$  are general lattice vectors. Therefore, vector  $\underline{R}_{g2}$ , given by

$$\underline{R}_{g2} = \underline{R} + \underline{R}'' - 2 \underline{R}' = 2 [(\underline{R} - \underline{R}') \cdot \underline{m}] \underline{m} \quad (3.128)$$

must also be a general lattice vector, which is orthogonal to  $\underline{R}_1 = \underline{R}_o$  since  $(\underline{m} \cdot \underline{R}_o) = 0$  according to (3.122). Thus, the lattice vector of smallest length along  $\underline{R}_{g2}$ , together with  $\underline{R}_1$  provides an **orthogonal** set of (primitive or non-primitive) lattice vectors describing the netplane periodicity. This

proves that the existence of **glide reflection** symmetry is always connected with primitive or non-primitive **rectangular** netplanes. Therefore, in the following discussion, we will use mutually orthogonal lattice vectors  $\underline{R}_1$  and  $\underline{R}_2$  to describe netplanes with glide reflection symmetry.

First, consider a **rectangular** netplane defined by orthogonal lattice vectors  $\underline{R}_1$  and  $\underline{R}_2$  and a glide reflection with its **glide line** through the netplane origin and **parallel to  $\underline{R}_1$** , i.e.

$$\underline{m} = \underline{R}_2/|\underline{R}_2|, \quad \underline{r}_o = \underline{0} \quad (3.129)$$

Then, in complete analogy with the discussion of mirror operations in Sec. 3.7.4, resulting in (3.113), there are **infinitely** many parallel **glide lines** through glide line centers at  $\underline{r}_{on}$  with

$$\underline{r}_{on} = n \underline{R}_2/2, \quad n \text{ integer} \quad (3.130)$$

which applies to both primitive and centered rectangular netplanes, as illustrated in Fig. 3.22a for the primitive rectangular case.

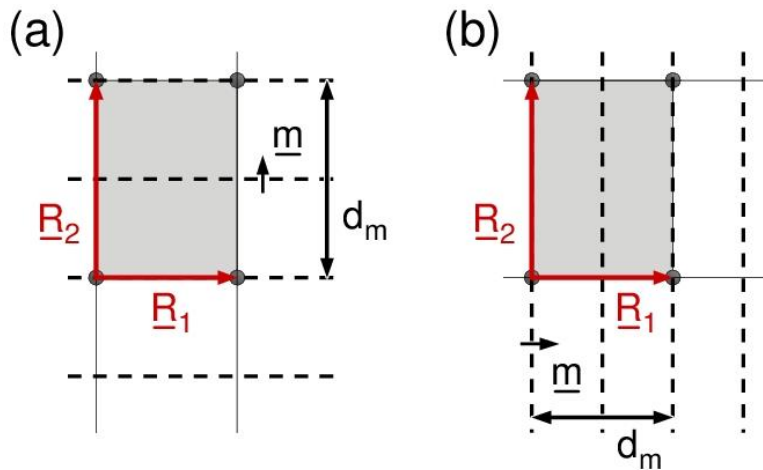


Fig. 3.22. Periodic sets of glide lines (a) parallel to lattice vector  $\underline{R}_1$ , (b) parallel to lattice vector  $\underline{R}_2$  for primitive rectangular netplanes, see text. The glide lines are shown by black horizontal and vertical dashed lines. The unit cell is emphasized in gray.

Analogously, glide reflections with their glide lines **parallel to  $\underline{R}_2$**  form an infinite set with glide line centers at

$$\underline{r}_{on} = n \underline{R}_1/2, \quad n \text{ integer} \quad (3.131)$$

for primitive and centered rectangular netplanes, shown in Fig. 3.22b.

A **glide line**  $g(\underline{r}_o, \underline{g} = \underline{R}_o/2)$  can **never** coincide with a **mirror line**  $\sigma(\underline{r}_o, \underline{e} = \underline{R}_o/|\underline{R}_o|)$  along the same direction in a netplane, since this would result in lattice vectors  $\underline{R}_o' = \underline{R}_o/2$  contradicting  $\underline{R}_o$  to

be of smallest length along its direction. However, **glide lines** may exist **between** adjacent parallel **mirror lines**. Let us assume a netplane with orthogonal lattice vectors  $\underline{R}_1$  and  $\underline{R}_2$  to possess mirror symmetry with respect to a mirror line parallel to  $\underline{R}_1$  through  $\underline{r}_o$ , chosen as the origin of the netplane. Then, according to the discussion in Sec. 3.6.4, the netplane includes an infinite set of parallel mirror lines along  $\underline{R}_1$  through centers  $\underline{r}_{on} = n \underline{R}_2/2$ ,  $n$  integer, as symmetry elements. Thus, mirror lines with  $n = 0, 1, 2$  confine or cut the morphological unit cell, see Fig. 3.23a. Let us assume that the netplane has also glide reflection symmetry with respect to a glide line parallel to  $\underline{R}_1$  and cutting the morphological unit cell, which can be achieved by setting the glide line center  $\underline{r}_{go}$  at

$$\underline{r}_{go} = \gamma \underline{R}_2, \quad 0 < \gamma < 1 \quad (3.132)$$

Then a general lattice vector  $\underline{R}$  according to (3.66) will be transformed by a glide reflection (3.120) to yield another general lattice vector  $\underline{R}'$ , where

$$\underline{R}' = \underline{R} - 2 [ (\underline{R} - \underline{r}_{go}) \underline{m} ] \underline{m} + \underline{R}_1/2, \quad \underline{m} = \underline{R}_2/|\underline{R}_2| \quad (3.133)$$

or, using representation (3.66) together with the orthogonality of  $\underline{R}_1$  and  $\underline{R}_2$ ,

$$\begin{aligned} \underline{R} &= n_1 \underline{R}_1 + n_2 \underline{R}_2, \quad n_1, n_2 \text{ integer} \\ \underline{R}' &= (n_1 + 1/2) \underline{R}_1 + (2\gamma - n_2) \underline{R}_2, \quad n_1, n_2 \text{ integer} \end{aligned} \quad (3.134)$$

which can be written as

$$\underline{R}' = 1/2 (\underline{R}_1 + \underline{R}_2) + n_1 \underline{R}_1 + [ 2(\gamma - 1/4) - n_2 ] \underline{R}_2 \quad (3.135)$$

This shows that the transformed general lattice vector  $\underline{R}'$  must belong to a **centered rectangular** lattice. Further, the prefactor  $[ 2(\gamma - 1/4) - n_2 ]$  in front of  $\underline{R}_2$  must be integer, which constrains values of  $\gamma$  to

$$2(\gamma - 1/4) = p, \quad \gamma = (2p + 1)/4, \quad p \text{ integer} \quad (3.136)$$

Thus,  $\gamma$  must be an odd valued multiple of  $1/4$  which together with constraints (3.132) allows only values  $\gamma = 1/4$  or  $\gamma = 3/4$ , yielding glide lines in the middle between mirror lines through  $\underline{r}_o = 0$  and  $\underline{r}_o = \underline{R}_2/2$ , as well as through  $\underline{r}_o = \underline{R}_2/2$  and  $\underline{r}_o = \underline{R}_2$ . Thus, a combination of glide reflection and mirror symmetry parallel to  $\underline{R}_1$  is possible only if the glide lines exist **in the middle** between adjacent mirror lines. In addition, the netplane must allow a **centered rectangular** representation by non-primitive orthogonal lattice vectors  $\underline{R}_1$  and  $\underline{R}_2$ , as illustrated in Fig. 3.23a. The corresponding result for netplane symmetry with glide and mirror lines parallel to  $\underline{R}_2$  is analogous and illustrated in Fig. 3.23b.

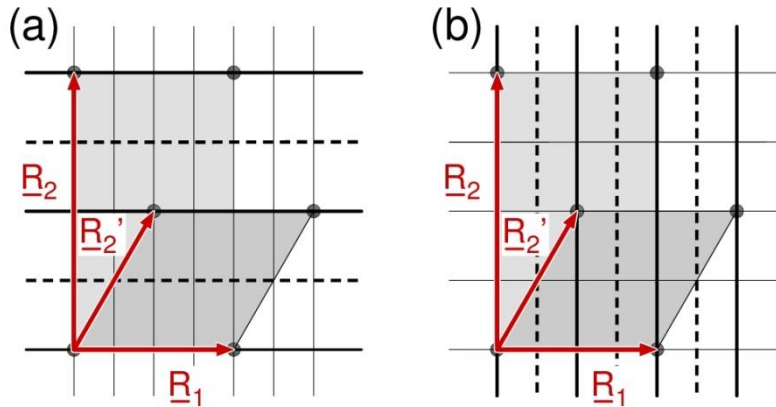


Fig. 3.23. Morphological unit cells of centered rectangular netplanes with coexisting mirror and glide line symmetry, glide and mirror lines (a) parallel to  $\underline{R}_1$ , (b) parallel to  $\underline{R}_2$ . The non-primitive lattice vectors  $\underline{R}_1$ ,  $\underline{R}_2$ , as well the centering vector  $\underline{R}_2'$  are labeled accordingly. The unit cells are emphasized in light and dark gray (non-primitive and primitive cells, respectively) with mirror lines indicated by thick and glide lines by dashed lines.

The result of the above discussion also has consequences for **primitive rectangular** netplanes described by orthogonal lattice vectors  $\underline{R}_1$  and  $\underline{R}_2$ . There, symmetry with respect to a glide line parallel to  $\underline{R}_1$  (or  $\underline{R}_2$ ) excludes mirror symmetry with lines parallel to the glide line. Primitive rectangular netplanes do **not** allow glide lines **parallel** to mirror lines.

Netplanes with **glide reflection** symmetry may also possess **inversion** symmetry. First, consider **primitive rectangular** netplanes with primitive lattice vectors  $\underline{R}_1$  and  $\underline{R}_2$ . According to (3.130) the complete set of glide lines parallel to  $\underline{R}_1$  can be positioned at centers  $\underline{r}_{on} = n \underline{R}_2/2$ . Then inversion centers, forming a netplane with lattice vectors  $1/2 \underline{R}_1$  and  $1/2 \underline{R}_2$ , see Sec. 3.6.2, can only either all lie on glide lines or all in the middle between adjacent glide lines, as illustrated in Fig. 3.24. (The prove is completely analogous to that for mirror lines given in Sec. 3.6.4.) In the former case inversion centers  $\underline{r}_{io}$  are given by

$$\underline{r}_{io} = p \underline{R}_1/2 + q \underline{R}_2/2, \quad p, q \text{ integer} \quad (3.137)$$

while in the latter  $\underline{r}_{io}$  can be defined by

$$\underline{r}_{io} = p \underline{R}_1/2 + q \underline{R}_2/2 + \underline{R}_2/4, \quad p, q \text{ integer} \quad (3.138)$$

with glide line centers  $\underline{r}_{go}$  given by

$$\underline{r}_{go} = n_2 \underline{R}_2/2, \quad n_2 \text{ integer} \quad (3.139)$$

Then a glide reflection  $g(\underline{r}_{go}, \underline{R}_1/2)$  followed by an inversion  $i(\underline{r}_{io})$  according to (3.64), (3.120) is

given by a transformation  $\underline{r} \rightarrow \underline{r}' \rightarrow \underline{r}''$ , where

$$\begin{aligned}\underline{r}' &= \underline{r} - 2 [ (\underline{r} - \underline{r}_{go}) \underline{m} ] \underline{m} + \underline{R}_1/2, \quad \underline{m} = \underline{R}_2 / |\underline{R}_2| \\ \underline{r}'' &= 2 \underline{r}_{io} - \underline{r}' = -\underline{r} + 2 [ (\underline{r} - \underline{r}_{go}) \underline{m} ] \underline{m} + 2 \underline{r}_{io} - \underline{R}_1/2 = \\ &= -\underline{r} + 2 (\underline{r} \underline{m}) \underline{m} + 2 (\underline{r}_{io} - \underline{r}_{go}) - \underline{R}_1/2\end{aligned}\quad (3.140)$$

and with

$$\underline{m}' = \underline{R}_1/|\underline{R}_1|, \quad (\underline{m} \underline{m}') = 0, \quad \underline{r} = (\underline{r} \underline{m}) \underline{m} + (\underline{r} \underline{m}') \underline{m}' \quad (3.141)$$

we obtain

$$\underline{r}'' = \underline{r} - 2 (\underline{r} \underline{m}') \underline{m}' + 2 (\underline{r}_{io} - \underline{r}_{go}) - \underline{R}_1/2 \quad (3.142)$$

If all inversion centers are positioned at glide lines, i.e for (3.137), relation (3.142) reads

$$\begin{aligned}\underline{r}'' &= \underline{r} - 2 (\underline{r} \underline{m}') \underline{m}' + p \underline{R}_1 + (q - n_2) \underline{R}_2 - \underline{R}_1/2 = \\ &= \underline{r} - 2 [ (\underline{r} - (2p-1) \underline{R}_1/4) \underline{m}' ] \underline{m}' + (q - n_2) \underline{R}_2\end{aligned}\quad (3.143)$$

This corresponds to mirror operations  $\sigma((2p-1) \underline{R}_1/4, \underline{R}_1/|\underline{R}_1|)$  with mirror lines perpendicular to the initial glide lines, followed by translations by general lattice vectors. Thus, a netplane, which is symmetric with respect to the initial glide lines parallel to  $\underline{R}_1$  and contains inversion centers on the glide lines, will also include a set of **perpendicular mirror lines** as symmetry elements, as illustrated in Fig. 3.24a.

If, on the other hand, all inversion centers are positioned in the middle between adjacent glide lines, i.e. for (3.138), relation (3.142) reads

$$\begin{aligned}\underline{r}'' &= \underline{r} - 2 (\underline{r} \underline{m}') \underline{m}' + p \underline{R}_1 + (q - n_2) \underline{R}_2 - \underline{R}_1/2 + \underline{R}_2/2 = \\ &= \underline{r} - 2 [ (\underline{r} - (2p-1) \underline{R}_1/4) \underline{m}' ] \underline{m}' + \underline{R}_2/2 + (q - n_2) \underline{R}_2\end{aligned}\quad (3.144)$$

This corresponds to glide reflections  $g((2p-1) \underline{R}_1/4, \underline{R}_2/2)$  with glide lines perpendicular to the initial glide lines, followed by translations by general lattice vectors. Thus, a netplane, which is symmetric with respect to the initial glide lines parallel to  $\underline{R}_1$  and contains inversion centers between the glide lines, will also include a set of **perpendicular glide lines** as symmetry elements, as illustrated in Fig. 3.24b.



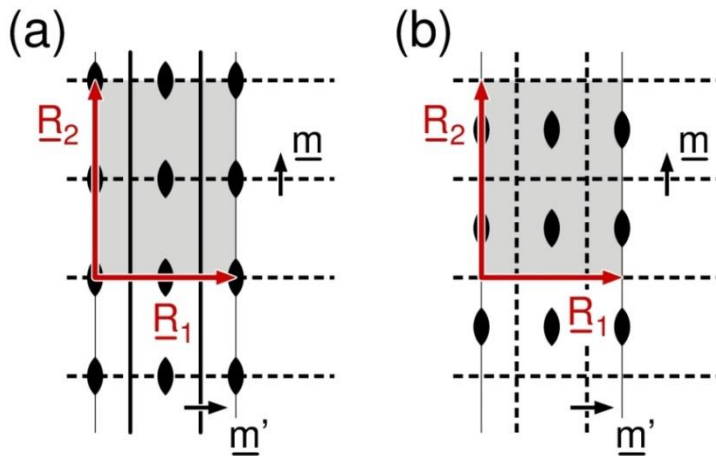


Fig. 3.24. Periodic sets of glide lines (dashed lines), parallel to  $\underline{R}_1$ , combined with corresponding inversion centers (ellipses) for a primitive rectangular netplane. (a) Inversion centers positioned on glide lines and perpendicular mirror lines, shown by thick lines. (b) Inversion centers positioned in the middle between glide lines and perpendicular glide lines. The unit cells are emphasized in gray.

**Primitive rectangular** netplanes with **inversion** and **glide reflection** symmetry, where glide lines are parallel to  $\underline{R}_2$ , yield structures, which are analogous to those obtained for glide lines parallel to  $\underline{R}_1$ . Here the two cases, inversion centers on glide lines and between glide lines, lead to additional orthogonal mirror lines and glide lines, respectively, as shown in Fig. 3.25, which is quite similar to Fig. 3.24. In fact, the structures of Figs. 3.24b and 3.25b differ only by a shift of the netplane origins.

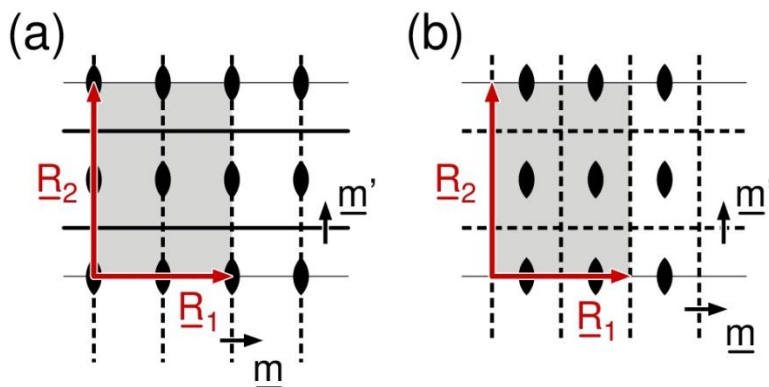


Fig. 3.25. Periodic sets of glide lines (dashed lines), parallel to  $\underline{R}_2$ , combined with corresponding inversion centers (ellipses) for a primitive rectangular netplane. (a) Inversion centers positioned on glide lines and perpendicular mirror lines, shown by thick lines. (b) Inversion centers positioned in the middle between glide lines and perpendicular glide lines. The unit cells are emphasized in gray.

**Centered rectangular** netplanes with **inversion** and **glide reflection** symmetry, where glide

lines are parallel to  $\underline{\mathbf{R}}_1$  or  $\underline{\mathbf{R}}_2$ , always yield inversion centers positioned on glide lines as well as between. According to the above discussion, this results in additional perpendicular glide and mirror lines as symmetry elements and leads to the geometry shown in Fig. 3.26.

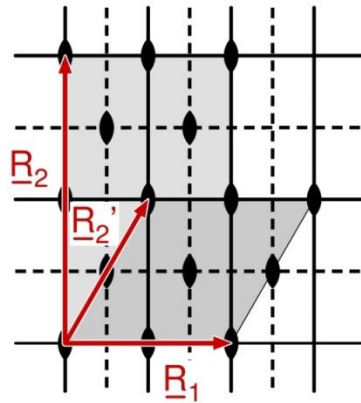


Fig. 3.26. Periodic sets of glide lines (dashed lines), parallel to  $\underline{\mathbf{R}}_1$ ,  $\underline{\mathbf{R}}_2$ , combined with corresponding inversion centers (ellipses) for a centered rectangular netplane. The non-primitive lattice vectors  $\underline{\mathbf{R}}_1$ ,  $\underline{\mathbf{R}}_2$ , as well the centering vector  $\underline{\mathbf{R}}_2'$  are shown by red arrows and labeled accordingly. The unit cells are emphasized in light and dark gray (non-primitive and primitive cells, respectively). The resulting mirror lines are indicated by thick lines.

**In conclusion**, glide lines existing as symmetry elements of a netplane, defined by lattice vectors  $\underline{\mathbf{R}}_1$  and  $\underline{\mathbf{R}}_2$ , have the following properties :

- Netplanes with glide reflection symmetry must be either primitive or centered rectangular (including square and hexagonal netplanes as special cases). (3.145a)
- Netplanes with glide reflection symmetry include infinite sets of parallel glide lines. If  $\underline{\mathbf{R}}_1$  and  $\underline{\mathbf{R}}_2$ , are orthogonal lattice vectors describing the morphological unit cell, then glide line sets can be given by normal vectors  $\underline{\mathbf{m}} = \underline{\mathbf{R}}_1/|\underline{\mathbf{R}}_1|$  and centers  $\underline{\mathbf{r}}_{\text{on}} = n \underline{\mathbf{R}}_1/2$ , or by  $\underline{\mathbf{m}} = \underline{\mathbf{R}}_2/|\underline{\mathbf{R}}_2|$  and centers  $\underline{\mathbf{r}}_{\text{on}} = n \underline{\mathbf{R}}_2/2$ . (3.145b)
- Glide lines of netplanes with glide reflection and mirror symmetry can never coincide with mirror lines. Glide lines parallel to mirror lines exist only in centered rectangular netplanes and appear in alternating equidistant sequences. Primitive netplanes do not allow parallel glide and mirror lines as symmetry elements. (3.145c)

- In primitive rectangular netplanes with glide reflection and inversion symmetry inversion (2-fold rotation) centers lie either all on glide lines or all in the middle between adjacent parallel glide lines. (3.145d)
- Primitive rectangular netplanes with glide reflection and inversion symmetry include an additional set of mirror lines perpendicular to the glide lines, if the inversion centers lie on the glide lines, and an additional set of glide lines perpendicular to the initial glide lines, if the inversion centers lie between glide lines. (3.145e)
- Centered rectangular netplanes with glide reflection and inversion symmetry include orthogonal sets of parallel glide lines as well as of mirror lines as symmetry elements. (3.145f)

### 3.6.6 Symmetry Groups

The **point symmetry** operations, i.e. inversion, n-fold rotation, and mirroring, discussed in the previous sections together with corresponding translation operations, form a **complete** set which can be used to **classify** the different types of netplanes according to their point symmetry behavior. In the following discussion, point symmetry operations are denoted by **Schönflies** symbols and their origins  $\underline{r}_o$  are assumed to coincide with the origin of a two-dimensional Cartesian coordinate system  $(x, y)$ . Further, rotation and mirror line angles are defined with respect to the x axis.

Overall, there are **16 true point symmetry operations** which can be applied and may reproduce a netplane. These are

- **eight rotation** operations  $C_\varphi(\underline{r}_o)$ , see Sec. 3.6.3, where, due to compatibility with translational symmetry, rotation angles  $\varphi$  are restricted to finite values  $\varphi = \pm 60^\circ, = \pm 90^\circ, = \pm 120^\circ, = 180^\circ$ , with the latter also shown to reflect an **inversion** operation. Further, a rotation with  $\varphi = 0^\circ$  describes the **identity** operation, which leaves a netplane unchanged and is introduced for mathematical completeness only. The corresponding  $2 \times 2$  coordinate transformation matrices  $\underline{\underline{C}}_\varphi$  are given by (3.74), i.e. by

$$\underline{\underline{C}}_\varphi = \begin{pmatrix} \cos \varphi & -\sin \varphi \\ \sin \varphi & \cos \varphi \end{pmatrix} \quad (3.146)$$

- **eight mirror** operations  $\sigma_{\Phi}(\underline{r}_o)$ , see Sec. 3.6.4, where, due to compatibility with translational symmetry, mirror line angles  $\Phi$  are restricted to values  $\Phi = 0^\circ$  (mirror line along x axis),  $= \pm 30^\circ$ ,  $= \pm 45^\circ$  (mirror line along  $\pm x/y$  diagonal),  $= \pm 60^\circ$ ,  $= 90^\circ$  (mirror line along y axis). The corresponding  $2 \times 2$  coordinate transformation matrices  $\underline{\sigma}_{\Phi}$  are given by (3.94), i.e. by

$$\underline{\sigma}_{\Phi} = \begin{pmatrix} \cos(2\Phi) & \sin(2\Phi) \\ \sin(2\Phi) & -\cos(2\Phi) \end{pmatrix} \quad (3.147)$$

Usually a netplane includes several of these 16 operations as elements describing its full point symmetry. If a netplane transforms into itself upon applying two point symmetry operations  $\mathbf{A}$ ,  $\mathbf{B}$  separately then it must also be symmetric with respect to a subsequent application of the two, formally described as a **product** operation ( $\mathbf{A} \mathbf{B}$ ) whose  $2 \times 2$  transformation matrix is given by the product of the two matrices  $\underline{\mathbf{A}}$ ,  $\underline{\mathbf{B}}$  characterizing the operations. Thus,

- the **product** of two **rotation** operations  $\mathbf{C}_{\varphi}$ ,  $\mathbf{C}_{\chi}$  (the explicit mention of the common rotation center  $\underline{r}_o$  is omitted in the following) is characterized according to (3.74) by a  $2 \times 2$  matrix  $\underline{\mathbf{T}}$  with

$$\begin{aligned} \underline{\mathbf{T}} &= \underline{\mathbf{C}}_{\varphi} \cdot \underline{\mathbf{C}}_{\chi} = \begin{pmatrix} \cos \varphi & -\sin \varphi \\ \sin \varphi & \cos \varphi \end{pmatrix} \cdot \begin{pmatrix} \cos \chi & -\sin \chi \\ \sin \chi & \cos \chi \end{pmatrix} = \\ &= \begin{pmatrix} \cos(\varphi + \chi) & -\sin(\varphi + \chi) \\ \sin(\varphi + \chi) & \cos(\varphi + \chi) \end{pmatrix} = \underline{\mathbf{C}}_{\chi} \cdot \underline{\mathbf{C}}_{\varphi} = \underline{\mathbf{C}}_{\varphi + \chi} \end{aligned} \quad (3.148)$$

which describes  $\mathbf{C}_{\varphi + \chi}$ , a rotation by an angle equal to the sum of the two initial angles.

- the **product** of two **mirror** operations  $\sigma_{\Phi}$ ,  $\sigma_{\Theta}$  is characterized according to (3.94) by a  $2 \times 2$  matrix  $\underline{\mathbf{T}}$  with

$$\begin{aligned} \underline{\mathbf{T}} &= \underline{\sigma}_{\Phi} \cdot \underline{\sigma}_{\Theta} = \begin{pmatrix} \cos(2\Phi) & \sin(2\Phi) \\ \sin(2\Phi) & -\cos(2\Phi) \end{pmatrix} \cdot \begin{pmatrix} \cos(2\Theta) & \sin(2\Theta) \\ \sin(2\Theta) & -\cos(2\Theta) \end{pmatrix} = \\ &= \begin{pmatrix} \cos 2(\Phi - \Theta) & -\sin 2(\Phi - \Theta) \\ \sin 2(\Phi - \Theta) & \cos 2(\Phi - \Theta) \end{pmatrix} = \underline{\mathbf{C}}_{2(\Phi - \Theta)} \end{aligned} \quad (3.149)$$

which describes a rotation  $\mathbf{C}_{2(\Phi - \Theta)}$  by an angle equal to twice that between the two mirror lines.

- the **mixed products** of a **rotation** and a **mirror** operation  $C_\varphi$ ,  $\sigma_\Phi$  are characterized according to (3.74) and (3.94) by  $2 \times 2$  matrices  $\underline{T}$  with

$$\begin{aligned} \underline{T} &= \underline{C}_\varphi \cdot \underline{\sigma}_\Phi = \begin{pmatrix} \cos \varphi & -\sin \varphi \\ \sin \varphi & \cos \varphi \end{pmatrix} \cdot \begin{pmatrix} \cos(2\Phi) & \sin(2\Phi) \\ \sin(2\Phi) & -\cos(2\Phi) \end{pmatrix} = \\ &= \begin{pmatrix} \cos(2\Phi + \varphi) & \sin(2\Phi + \varphi) \\ \sin(2\Phi + \varphi) & -\cos(2\Phi + \varphi) \end{pmatrix} = \underline{\sigma}_{(\Phi + \varphi/2)} \end{aligned} \quad (3.150)$$

$$\begin{aligned} \underline{T} &= \underline{\sigma}_\Phi \cdot \underline{C}_\varphi = \begin{pmatrix} \cos(2\Phi) & \sin(2\Phi) \\ \sin(2\Phi) & -\cos(2\Phi) \end{pmatrix} \cdot \begin{pmatrix} \cos \varphi & -\sin \varphi \\ \sin \varphi & \cos \varphi \end{pmatrix} = \\ &= \begin{pmatrix} \cos(2\Phi - \varphi) & \sin(2\Phi - \varphi) \\ \sin(2\Phi - \varphi) & -\cos(2\Phi - \varphi) \end{pmatrix} = \underline{\sigma}_{(\Phi - \varphi/2)} \end{aligned} \quad (3.151)$$

which describe mirror operations  $\sigma_{(\Phi \pm \varphi/2)}$  with mirror lines rotated by  $\pm\varphi/2$  with respect to the initial mirror line referring to  $\sigma_\Phi$ , where the two results depend on the sequence of the product formation.

The rotation by  $0^\circ$  (**identity** operation), described as  $C_0$  and represented, according to (3.74), by the  $2 \times 2$  unit matrix  $\underline{C}_0$  with

$$\underline{C}_0 = \begin{pmatrix} \cos \varphi & -\sin \varphi \\ \sin \varphi & \cos \varphi \end{pmatrix} \Big|_{\varphi=0^\circ} = \begin{pmatrix} 1 & 0 \\ 0 & 1 \end{pmatrix} \quad (3.152)$$

can be considered a **unit operation** whose products with rotations and mirror operations yield

$$\underline{C}_\varphi \underline{C}_0 = \underline{C}_0 \underline{C}_\varphi = \underline{C}_\varphi, \quad \underline{\sigma}_\Phi \underline{C}_0 = \underline{C}_0 \underline{\sigma}_\Phi = \underline{\sigma}_\Phi \quad (3.153)$$

On the other hand, relation (3.148) shows together with (3.152) that any rotation by angle  $\varphi$  can be undone by an inverted rotation with angle  $\varphi' = -\varphi$ . Further, applying  $\Theta = \Phi$  in (3.149) shows that any mirror operation can be undone by its own mirror operation. These two results, which are intuitively clear, can be formally expressed by the statement that each symmetry operation  $A$  of the above set possesses an **inverted operation**  $A^{-1}$ , where

$$A \cdot A^{-1} = A^{-1} \cdot A = C_0 \quad (3.154)$$

As a last result we mention the **associativity** of subsequent applications of symmetry operations  $A$ ,  $B$ ,  $C$ , i.e.

$$A \cdot (B \cdot C) = (A \cdot B) \cdot C \quad (3.155)$$

which is clear from the associativity of the matrix multiplication.

Any subset of the 16 point symmetry operations listed above forms a **point symmetry group** if all its product operations belong to the same subset. This is an example of a mathematical group  $\mathbf{G} = \{g_1, \dots, g_p\}$  with a finite number  $p$  of elements  $g_i$ , which is defined formally [40] by the four properties

- 1) a **product** of two group elements  $(g_i \cdot g_j)$  is defined and always yields an element  $g_k$  of the group (closure condition) (3.156a)

- 2) the group contains a **unit element**  $e$  with  $g_i \cdot e = e \cdot g_i = g_i$  for all elements  $g_i$  of the group, analogous to (3.153) (3.156b)

- 3) the group contains an **inverse element**  $g_i^{-1}$  with  $g_i \cdot g_i^{-1} = g_i^{-1} \cdot g_i = e$  for each element  $g_i$  of the group, analogous to (3.154) (3.156c)

- 4) group products are **associative**, i.e.  $g_i \cdot (g_j \cdot g_k) = (g_i \cdot g_j) \cdot g_k$  for all elements  $g_i$  of the group, analogous to (3.155) (3.156d)

As an example, the three rotation operations defining a 3-fold rotation axis form a set  $\{C_0, C_{120}, C_{-120}\}$  which defines a point symmetry group (denoted  $C_3$  or  $\mathbf{3}$ ).

The complete collection of two-dimensional point symmetry groups, allowed for netplanes, can be determined by considering the above 16 point symmetry operations together with their products given by (3.148) to (3.151). Then collecting sets of operations such that they satisfy the four group properties yields, altogether, **10** different **point symmetry groups**. These are listed by their operations as well as their symmetries in Table 3.9. where symmetry operation  $C_0$  defines the identity operation while  $C_{180}$  (2-fold rotation) is equivalent with inversion.

Table 3.9. List of all point symmetry groups allowed for netplanes. The list includes group members, rotations  $C_\varphi$  with  $\varphi$  denoting the rotation angle, and mirror operations  $\sigma_\Phi$ , where  $\Phi$  denotes the angle of the mirror line with respect to the x axis. The groups are labeled according to both the Hermann-Mauguin and the Schönflies notation, where the latter is put in parentheses.

Group	Symmetries	Members	Group	Symmetries	Members
<b>1 (C<sub>1</sub>)</b>	identity	$C_0$	<b>m (C<sub>s</sub>)</b>	1 mirror	$C_0, \sigma_0$
<b>2 (C<sub>2</sub>)</b>	2-fold rot.	$C_0, C_{180}$	<b>2mm (C<sub>2v</sub>)</b>	2-fold rot., 2 mirrors	$C_0, C_{180}, \sigma_0, \sigma_{90}$
<b>3 (C<sub>3</sub>)</b>	3-fold rot.	$C_0, C_{120}, C_{-120}$	<b>3m1, 31m (C<sub>3v</sub>)</b>	3-fold rot., 3 mirrors	$C_0, C_{120}, C_{-120}, \sigma_{60}, \sigma_{-60}, \sigma_0$
<b>4 (C<sub>4</sub>)</b>	2-fold rot., 4-fold rot.	$C_0, C_{90}, C_{180}, C_{-90}$	<b>4mm (C<sub>4v</sub>)</b>	2-fold rot., 4-fold rot., 4 mirrors	$C_0, C_{90}, C_{180}, C_{-90}, \sigma_0, \sigma_{45}, \sigma_{90}, \sigma_{-45}$
<b>6 (C<sub>6</sub>)</b>	2-fold rot., 3-fold rot., 6-fold rot.	$C_0, C_{60}, C_{120}, C_{180}, C_{-120}, C_{-60}$	<b>6mm (C<sub>6v</sub>)</b>	2-fold rot., 3-fold rot., 6-fold rot., 6 mirrors	$C_0, C_{60}, C_{120}, C_{180}, C_{-120}, C_{-60}, \sigma_0, \sigma_{30}, \sigma_{60}, \sigma_{90}, \sigma_{-60}, \sigma_{-30}$

Each point symmetry group in Table 3.9, except for the identity group  $C_1$ , includes subsets of symmetry elements, which themselves form groups, also called **subgroups** of the initial point symmetry group. This is shown in Table 3.10 listing all subgroups of the point symmetry groups of Table 3.9.

Table 3.10. List of all point symmetry groups allowed for netplanes together with corresponding subgroups, see text. The groups are labeled according to both the Hermann-Mauguin and the Schönflies notation, where the latter is put in parentheses. Subgroups are given only in Hermann-Mauguin notation only.

Group	Subgroups	Group	Subgroups
<b>1 (C<sub>1</sub>)</b>	--	<b>m (C<sub>s</sub>)</b>	<b>1</b>
<b>2 (C<sub>2</sub>)</b>	<b>1</b>	<b>2mm (C<sub>2v</sub>)</b>	<b>1, 2, m</b>
<b>3 (C<sub>3</sub>)</b>	<b>1</b>	<b>3m1, 31m (C<sub>3v</sub>)</b>	<b>1, 3, m</b>
<b>4 (C<sub>4</sub>)</b>	<b>1, 2</b>	<b>4mm (C<sub>4v</sub>)</b>	<b>1, 2, 4, m, 2mm</b>
<b>6 (C<sub>6</sub>)</b>	<b>1, 2, 3</b>	<b>6mm (C<sub>6v</sub>)</b>	<b>1, 2, 3, 6, m, 2mm, 3m1, 31m</b>

The formal group definition (3.156) can also be applied to describe translational symmetry of a netplane by its **translation group**. The characterization of a periodic netplane by its lattice vectors  $\underline{R}_1$  and  $\underline{R}_2$  means in particular that the netplane is symmetric with respect to translations by general lattice vectors  $\underline{R}$  with  $\underline{R} = n_1 \underline{R}_1 + n_2 \underline{R}_2$ . This can be phrased by a **translation symmetry** operation

$$\underline{r} \rightarrow \underline{r}' = \mathbf{T}_{(n_1, n_2)} \underline{r} = \underline{r} + (n_1 \underline{R}_1 + n_2 \underline{R}_2), \quad n_1, n_2 \text{ integer} \quad (3.157)$$

where the infinite set of operations  $\mathbf{T}_{(n_1, n_2)}$ ,  $n_1, n_2$  integer, together with a **product** definition,

$$\mathbf{T}_{(n_1, n_2)} \cdot \mathbf{T}_{(n_1', n_2')} = \mathbf{T}_{(n_1+n_1', n_2+n_2')} \quad (3.158)$$

a **unit** element  $\mathbf{T}_{(0,0)}$ , and **inverse** elements,

$$\mathbf{T}_{(n_1, n_2)}^{-1} = \mathbf{T}_{(-n_1, -n_2)} \quad (3.159)$$

defines the (infinite) translation group of a netplane. This group can be combined with a corresponding point symmetry group of a netplane to yield a **two-dimensional space group**, sometimes also called **plane group**. If this space group describes all symmetry properties of a netplane the netplane will be said to be characterized by a **simple** or **symmorphic** space group. This includes groups, where, due to translational symmetry, initial point symmetry operations also allow glide reflections, which combine mirroring with translation, see Sec. 3.6.5. (As discussed in Sec. 3.6.5, glide lines will appear if a netplane with mirror lines includes a primitive lattice vector which is inclined with respect to a mirror line.) In addition, there are cases where the full symmetry of a netplane requires, in addition to true point symmetry operations, glide reflections as initial generating symmetry elements. In this case the netplane will be said to be characterized by a **non-symmorphic** space group. The distinction between the different types of space groups becomes clear in Sec. 3.8, where space groups are used to classify all netplanes with respect to their possible symmetry properties.

### 3.7 Crystal Systems and Bravais Lattices in Two Dimensions

Properties of the different point symmetry operations, discussed in Sec. 3.6, together with translational symmetry allow a symmetry **classification** of all netplanes by their corresponding **space groups**. This is analogous to the classification of three-dimensional lattices discussed in Sec. 2.4. As in the three-dimensional case, we can also use the four different rotation axes, 2-, 3-, 4-, and 6-fold, to distinguish between the different types of netplanes. Here the netplane origin is



assumed to coincide with a rotation center. Further, the two lattice vectors  $\underline{R}_1$  and  $\underline{R}_2$ , describing the netplane periodicity will be described by their lengths  $a$ ,  $b$  and the angle  $\gamma$  between them, i.e.

$$|\underline{R}_1| = a, \quad |\underline{R}_2| = b, \quad \angle(\underline{R}_1, \underline{R}_2) = \gamma, \quad (\underline{R}_1 \cdot \underline{R}_2) = ab \cos(\gamma) \quad (3.160)$$

First, we note that, as a result of their periodicity, netplanes without further symmetry constraints always include an inversion center as a symmetry element at their origin, which is equivalent to **2-fold rotation symmetry**. Then the most general type of netplanes is described by primitive lattice vectors  $\underline{R}_1$  and  $\underline{R}_2$  of different length,  $a \neq b$ , and forming an angle  $\gamma$  different from  $60^\circ$ ,  $90^\circ$ , and  $120^\circ$ . This corresponds to a morphological unit cell of parallelogram shape, shown in Fig. 3.27a, and the respective netplanes are called **oblique**, forming the oblique **Bravais lattice**.

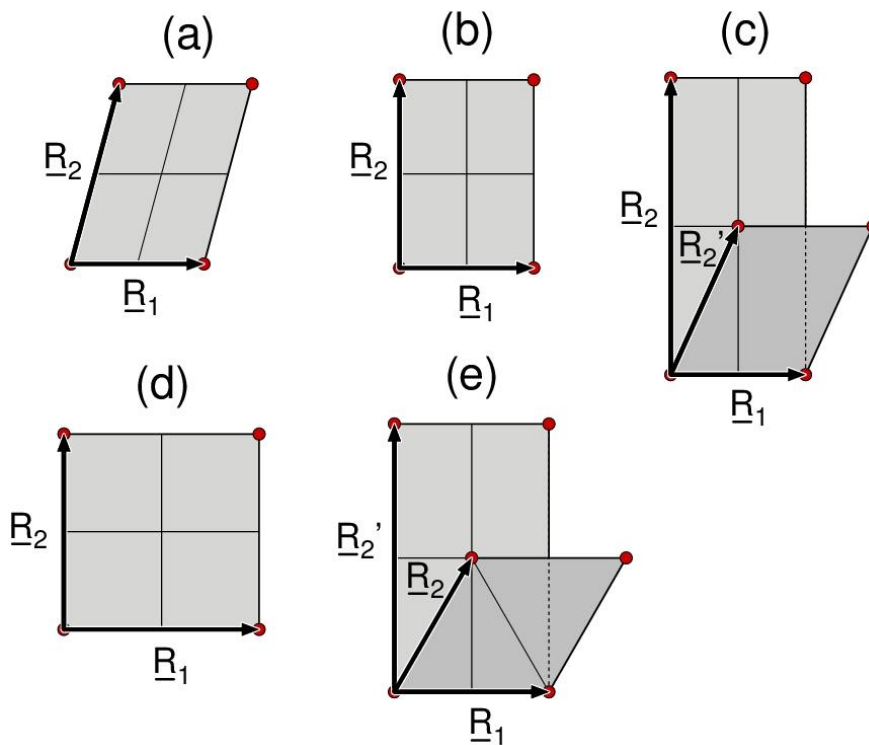


Fig. 3.27. Morphological unit cells of netplanes referring to the five Bravais lattices (a) oblique, (b) primitive rectangular, (c) centered rectangular, (d) square, and (e) hexagonal. The cells are emphasized in gray with lattice vectors  $\underline{R}_1$ ,  $\underline{R}_2$ , ( $\underline{R}_2'$ ) sketched accordingly.

A second type of netplanes is described by primitive lattice vectors  $\underline{R}_1$ ,  $\underline{R}_2$  of different length which are orthogonal to each other, i.e.  $a \neq b$ , and  $\gamma = 90^\circ$ . Here the morphological unit cell is of rectangular shape, shown in Fig. 3.27b. These netplanes are called **primitive rectangular** or **p-rectangular**, referring to the p-rectangular **Bravais lattice**.

A third type of netplane, which includes **4-fold rotation symmetry**, is described by primitive lattice vectors  $\underline{\mathbf{R}}_1$  and  $\underline{\mathbf{R}}_2$  of the same length which are orthogonal to each other, i.e.  $a = b$ , and  $\gamma = 90^\circ$ . Here the morphological unit cell is of square shape, shown in Fig. 3.27d. These netplanes are called **square**, referring to the square **Bravais lattice**.

A fourth type of netplanes, which includes **3- and 6-fold rotation symmetry**, is described by primitive lattice vectors  $\underline{\mathbf{R}}_1$  and  $\underline{\mathbf{R}}_2$  of identical length,  $a = b$ , and  $\gamma = 60^\circ$  (acute representation) or  $120^\circ$  (obtuse representation). Here the morphological unit cell has the shape of two equilateral triangles joining on one side, shown in Fig. 3.27e. These netplanes are called **hexagonal**, referring to the hexagonal **Bravais lattice**.

So far, the discussion was restricted to Bravais netplanes whose periodicity was described by primitive lattice vectors  $\underline{\mathbf{R}}_1$  and  $\underline{\mathbf{R}}_2$ . Assuming non-primitive lattice vectors  $\underline{\mathbf{R}}_1$  and  $\underline{\mathbf{R}}_2$ , the corresponding morphological unit cell will contain additional lattice points. In Sec. 3.6.1 it was shown that, if vectors  $\underline{\mathbf{R}}_1$  and  $\underline{\mathbf{R}}_2$  are of smallest length along their direction, there can only be one point located in the center of the unit cell, given by a vector  $\underline{\mathbf{R}}' = 1/2 (\underline{\mathbf{R}}_1 + \underline{\mathbf{R}}_2)$ , see (3.63). This results in a **centered netplane** which may be described by primitive lattice vectors  $\underline{\mathbf{R}}_1'$ ,  $\underline{\mathbf{R}}_2'$  with

$$\underline{\mathbf{R}}_1' = 1/2 (\underline{\mathbf{R}}_1 - \underline{\mathbf{R}}_2) , \quad \underline{\mathbf{R}}_2' = 1/2 (\underline{\mathbf{R}}_1 + \underline{\mathbf{R}}_2) \quad (3.161)$$

Centering an **oblique** netplane, sketched in Fig. 3.28a, cannot lead to different symmetry which would change the type of Bravais lattice. Therefore, a centered oblique Bravais lattice is, in its type, identical to its primitive oblique counterpart. In contrast, centering a **primitive rectangular** netplane, sketched in Fig. 3.28b, creates a new type of netplane, defining the **centered rectangular** or **c-rectangular** Bravais lattice. This lattice is not generally available by any of the other Bravais lattices. Due to the orthogonality of the initial non-primitive lattice vectors  $\underline{\mathbf{R}}_1$  and  $\underline{\mathbf{R}}_2$ , the corresponding primitive vectors  $\underline{\mathbf{R}}_1'$ ,  $\underline{\mathbf{R}}_2'$ , according to (3.161), are of equal length and can form any angle  $\gamma$  between them. This can also be used as a **definition** of the **c-rectangular** Bravais lattice being described by primitive lattice vectors  $\underline{\mathbf{R}}_1'$ ,  $\underline{\mathbf{R}}_2'$  of identical length,  $a = b$ , and any angle  $\gamma$  ( $\neq 60^\circ, 90^\circ, 120^\circ$ , see below). With this vector definition, centering the c-rectangular Bravais lattice according to (3.161) yields a primitive rectangular netplane as sketched in Fig. 3.28d. Alternatively one could use vectors  $\underline{\mathbf{R}}_1$  and  $\underline{\mathbf{R}}_2'$  as a primitive description, which is shown in Fig. 3.27c where centering results in an oblique netplane unless  $|\underline{\mathbf{R}}_1| = |\underline{\mathbf{R}}_2'|$ , corresponding to a hexagonal netplane, where centering leads to a rectangular netplane.

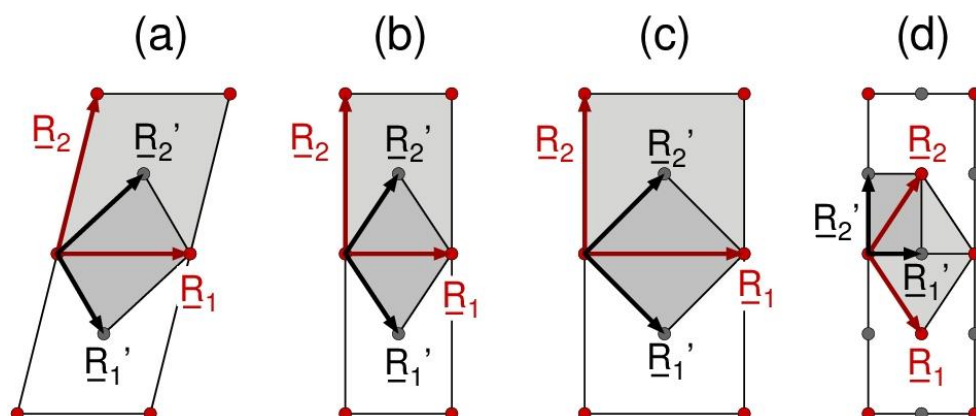


Fig. 3.28. Morphological unit cells of centered Bravais lattices, (a) oblique, (b) primitive rectangular, (c) square, and (d) c-rectangular. Lattice vectors  $\underline{R}_1$ ,  $\underline{R}_2$  refer to non-primitive and  $\underline{R}_1'$ ,  $\underline{R}_2'$  to primitive lattice descriptions, respectively. The cells are emphasized in light (non-primitive) and dark (primitive) gray. Lattice points of the initial lattice are painted red while those added by centering are painted gray.

A centered **square** netplane is described by non-primitive lattice vectors  $\underline{R}_1$  and  $\underline{R}_2$  of equal length and  $\gamma = 90^\circ$ . This results in primitive vectors  $\underline{R}_1'$ ,  $\underline{R}_2'$  according to (3.161), which are also of the same length and orthogonal, as sketched in Fig. 3.28c. Thus, the centered square netplane is identical in its type with its primitive counterpart. **Hexagonal** netplanes are described by primitive lattice vectors  $\underline{R}_1$  and  $\underline{R}_2$  of identical length,  $a = b$ , and  $\gamma = 60^\circ, 120^\circ$ . Thus, they can be considered special cases of centered rectangular netplanes according to the definition given above. This is also shown in Fig. 3.27e, where the non-primitive rectangular unit cell of a hexagonal netplane with its orthogonal lattice vectors  $\underline{R}_1$  and  $\underline{R}_2'$  is included together with the primitive unit cell, given by  $\underline{R}_1$  and  $\underline{R}_2$ . As a consequence of this close relationship between hexagonal and centered rectangular netplanes, centering hexagonal netplanes yields a primitive rectangular netplane analogous to that shown in Fig. 3.28d.

This concludes the **symmetry classification** of netplanes and yields, altogether, **five** different types, oblique, primitive and centered rectangular, square, and hexagonal. The classification describes the **two-dimensional crystal system** given by five different **Bravais lattices** in two dimensions with definitions collected in Table 3.11. In this table all lattice vectors are assumed to be primitive and defined according to (3.160).

Table 3.11. Bravais lattice members described by lattice constants  $a$ ,  $b$ , and angle  $\gamma$ , see text.

Crystal system, Bravais lattice	Definitions
Oblique	$a \neq b$ , any $\gamma \neq 60^\circ, 90^\circ, 120^\circ$
Primitive rectangular	$a \neq b$ , $\gamma = 90^\circ$
Centered rectangular	$a \neq b$ , $(\underline{R}_1 \underline{R}_2) = \pm 1/2 a^2$ or $a \neq b$ , $(\underline{R}_1 \underline{R}_2) = \pm 1/2 b^2$ or $a = b$ , any $\gamma \neq 60^\circ, 90^\circ, 120^\circ$
Square	$a = b$ , $\gamma = 90^\circ$
Hexagonal	$a = b$ , $\gamma = 60^\circ, 120^\circ$

The listing in Table 3.11 shows a **hierarchy** of the different Bravais lattices, where the oblique lattice exhibits the lowest symmetry. Thus, primitive and centered rectangular Bravais lattices can always be considered as special cases of oblique lattices. Further, the square Bravais lattice can be thought of as a special case of both primitive and centered rectangular lattices, while the hexagonal Bravais lattice represents a special case of a centered rectangular lattice. The distinction between the different lattice types becomes important when all symmetry elements of the netplanes are considered.

The **relationship** between the different **Bravais lattices** is further illustrated in Fig. 3.29 which shows all possible types of two-dimensional Bravais lattices described by Minkowski-reduced lattice vectors  $\underline{R}_1$  and  $\underline{R}_2$ , see Sec. 3.3. Here lattice vector  $\underline{R}_1$  is kept fixed and defines the x axis of the graph while all possible vectors  $\underline{R}_2$  (constrained to be Minkowski-reduced) are obtained from points inside the gray shaded area, dark gray for obtuse and light gray for acute lattice representations. The figure shows very clearly the network of lines referring to Bravais lattices of different type, where transitions between the types occur at line intersections. Further, the distinction between acute,  $60^\circ \leq \gamma \leq 90^\circ$ , and obtuse lattice vector sets,  $90^\circ < \gamma \leq 120^\circ$ , becomes clear. Centered rectangular and hexagonal lattices yield equivalent lattice vector sets for  $\cos(\gamma) = A/2$  and  $\cos(\gamma) = -A/2$  (with  $A = \min(R_1/R_2, R_2/R_1)$  according to (3.17)) corresponding to acute and obtuse vector sets which can both be considered to be Minkowski-reduced. Here crystallographers prefer the obtuse representation referring to the strict definition given in in (3.16).

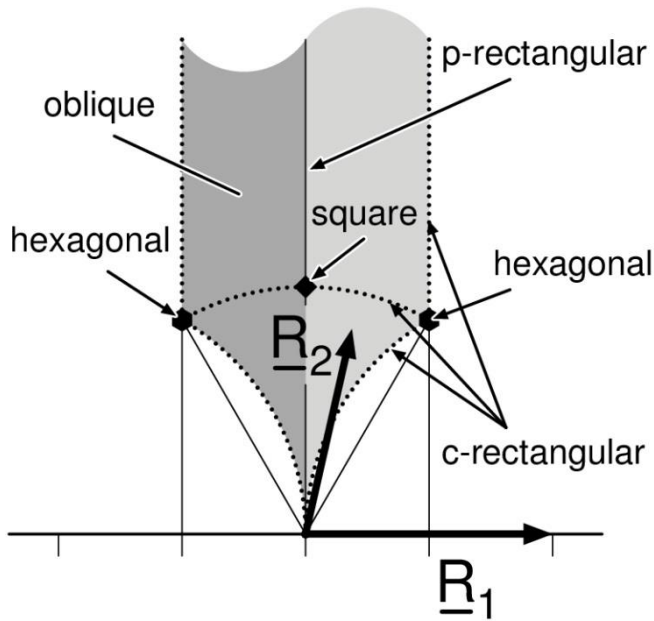


Fig. 3.29. Minkowski-reduced lattice vectors of general netplanes, see text. Lines of Bravais lattices of different type are labeled accordingly. The filled square and the two filled hexagons indicate square and hexagonal Bravais lattices, respectively.

The **symmetry classification** of netplanes discussed above also has consequences for the possible shape of compact two-dimensional unit cells, the **Wigner-Seitz cells**, discussed in Sec. 2.3. These are of interest, in particular, for theoretical studies on electronic or vibronic properties of two-dimensionally periodic systems, such as single crystal surfaces, discussed below. The basic definition of a Wigner-Seitz cell in two dimensions starts from lattice vectors  $\underline{R}_1$  and  $\underline{R}_2$  of a netplane and subdivides the netplane area into identical cells enclosing general lattice points  $\underline{R} = n_1 \underline{R}_1 + n_2 \underline{R}_2$ . Each cell is defined by including all points  $\underline{r}$  which are the nearest to  $\underline{R}$  compared with all other lattice points. Then adjacent cells about  $\underline{R}$  and  $\underline{R}'$  must be separated by sections of straight lines defined by  $\underline{r}$  assuming equal distance with respect to  $\underline{R}$  and  $\underline{R}'$ . Hence, two-dimensional Wigner-Seitz cells must be **polygonal** in shape. The edge points of these cells can be constructed for the five Bravais lattices by simple geometry considerations where we mention only the final result derived in [84].

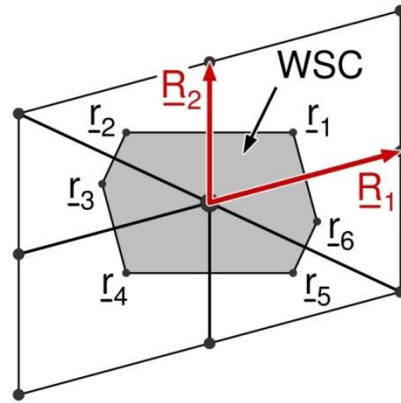


Fig. 3.30. Wigner-Seitz cell (WSC) for a general netplane with lattice vectors  $\underline{R}_1$ ,  $\underline{R}_2$ . The edges  $\underline{r}_i$ ,  $i = 1, \dots, 6$  of the polygonal cell are labeled accordingly, see text.

Let us consider a netplane with its periodicity described by Minkowski-reduced lattice vectors  $\underline{R}_1$  and  $\underline{R}_2$ . Then its (two-dimensional) Wigner-Seitz cell about the netplane origin forms, in general, an irregular hexagon, see Fig. 3.30, given by edge vectors

$$\underline{r}_i = \kappa_{i1} \underline{R}_1 + \kappa_{i2} \underline{R}_2, \quad i = 1, \dots, 6 \quad (3.162)$$

where the mixing coefficients  $\kappa_{ij}$  are listed in Table 3.12.

Table 3.12. Edge vectors of a general two-dimensional Wigner-Seitz cell based on Minkowski-reduced lattice vectors  $\underline{R}_1$ ,  $\underline{R}_2$ , see text.

Edge vector $\underline{r}_i$	$\kappa_{i1}$	$\kappa_{i2}$	
$\underline{r}_1$	$\eta_{21}$	$\eta_{12}$	$\eta_{12} = \lambda [  \underline{R}_1 ^2 ( \underline{R}_2 ^2 - \underline{R}_1 \underline{R}_2) ]$
$\underline{r}_2$	$-\eta_{21}$	$1 - \eta_{12}$	$\eta_{21} = \lambda [  \underline{R}_2 ^2 ( \underline{R}_1 ^2 - \underline{R}_1 \underline{R}_2) ]$
$\underline{r}_3$	$\eta_{21} - 1$	$\eta_{12}$	$\lambda = 1/2 [  \underline{R}_1 ^2  \underline{R}_2 ^2 - (\underline{R}_1 \underline{R}_2)^2 ]^{-1}$
$\underline{r}_4 (\equiv -\underline{r}_1)$	$-\eta_{21}$	$-\eta_{12}$	
$\underline{r}_5 (\equiv -\underline{r}_2)$	$\eta_{21}$	$\eta_{12} - 1$	
$\underline{r}_6 (\equiv -\underline{r}_3)$	$1 - \eta_{21}$	$-\eta_{12}$	

(3.163)

As a result, the edge points of Table 3.12 yield Wigner-Seitz cells shaped as

- irregular hexagons** for **oblique** netplanes, see Fig. 3.31a.
- rectangles** (coinciding edges  $\underline{r}_2$ ,  $\underline{r}_3$  and  $\underline{r}_5$ ,  $\underline{r}_6$ ) for **primitive rectangular** netplanes, see Fig. 3.31b.
- symmetrically **stretched hexagons** (two perpendicular mirror lines, one through two opposing edges) for **centered rectangular** netplanes, see Fig. 3.31c.

(d) **squares** (coinciding edges  $\underline{r}_2$ ,  $\underline{r}_3$  and  $\underline{r}_5$ ,  $\underline{r}_6$ ) for **square** netplanes, see Fig. 3.31d.

(e) **regular hexagons** for **hexagonal** netplanes, see Fig. 3.31e.

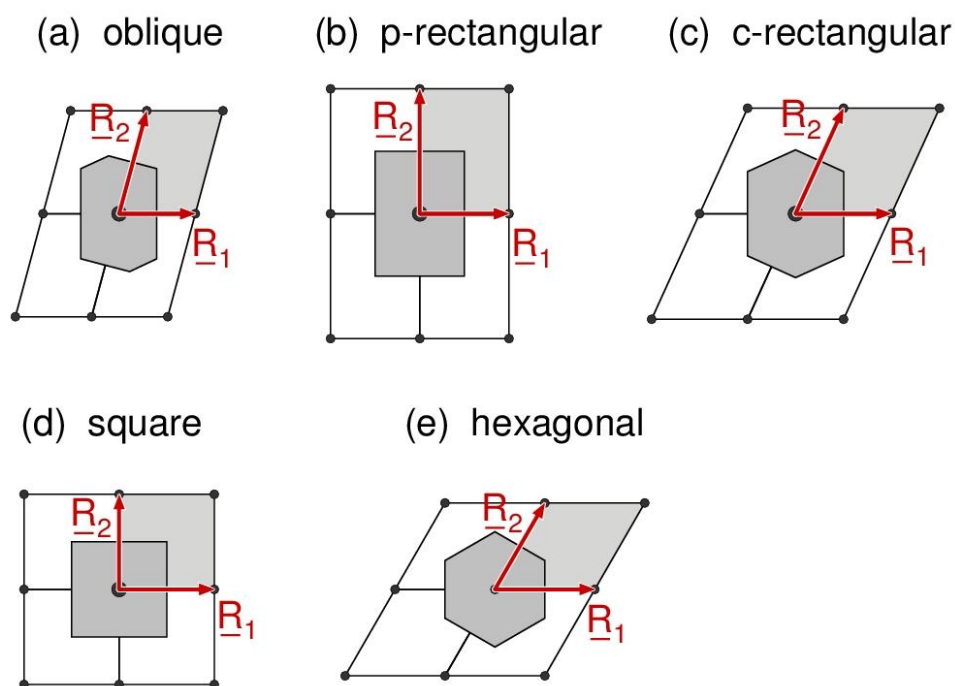


Fig. 3.31. Wigner-Seitz cells (WSC) of the five Bravais lattices in two dimensions, (a) oblique, (b) p-rectangular, (c) c-rectangular, (d) square, and (e) hexagonal. The WSCs, emphasized in dark gray, are compared with morphological unit cells spanned by lattice vectors  $\underline{R}_1$ ,  $\underline{R}_2$ , shown in lighter gray.

### 3.8 Crystallographic Classification of Netplanes and Monolayers

The symmetry classification discussed in Sec. 3.7 gave a first overview of possible types of netplanes, yielding the two-dimensional crystal systems with their five Bravais lattices. Here the discrimination between the lattice types was based only on the interplay of translational and rotational symmetry of netplanes. Monolayers are described in their translational symmetry by corresponding netplanes and can, therefore, also be classified according to the five Bravais lattices.

However, a **complete crystallographic classification** of all possible monolayer types must take into account the full set of point symmetry elements, including glide reflections, together with translational symmetry. This can be achieved formally by considering, for each of the five Bravais lattices, appropriate symmetry operations of all ten point symmetry groups, listed in Tables 3.9 and 3.10, as well as glide reflections. Here the symmetry of a monolayer may turn out to be lower than that of

its corresponding netplane due to the appearance of additional monolayer atoms at off-symmetry sites of the elementary unit cell given by the netplane. Altogether, the analysis leads to **17** different symmetry types describing netplanes and monolayers, the so-called **two-dimensional space groups**, which will be discussed in Secs. 3.8.1 to 3.8.5. These sections are rather formal and filled with geometric and group theoretical details. Thus, readers, who are less interested in the mathematics behind two-dimensional space groups, may skip these sections and move to the conclusion of the analysis, given in Sec. 3.8.6.

The classification distinguishes between symmorphic and non-symmorphic space groups. **Symmorphic space groups** result from considering any of the ten point symmetry groups of Table 3.9 (i.e. excluding glide reflections as initial symmetry elements) and adding the translation symmetry group of the Bravais lattice defined by lattice vectors  $\underline{R}_1$  and  $\underline{R}_2$ . As a consequence of combining point symmetry elements, centered at different points of the Bravais lattice, glide reflections may also appear as symmetry elements in symmorphic space groups. However, they do not act as symmetry generating elements. In contrast, **non-symmorphic space groups** arise from applying glide reflections as initial symmetry elements of a netplane or monolayer and combining them with selected point symmetry operations as well as with translational symmetry. Here only **rectangular** and **square** Bravais lattices need to be considered since glide reflection symmetry is connected with rectangular symmetry, as discussed in Sec. 3.6.5.

In the following sections, we consider the center  $\underline{r}_o$  of the **highest** point symmetry group  $\mathbf{G}$  of a netplane to coincide with the netplane origin. (The highest point symmetry group is defined as the group with the largest number of point symmetry operations that transform the netplane into itself.) Further, the symmetry elements of each space group will be sketched in **symbolic** form, according to the conventional crystallographic notation used in the International Tables for Crystallography [33] (denoted as **(ITC)** in the following). With this notation, mirror lines are indicated by thick and glide lines by dashed lines while 2-fold rotation (and inversion) centers are shown by ellipses, and 3-, 4-, and 6-fold rotation centers by filled triangles, squares, and hexagons, respectively. In addition, point symmetry and space groups will be denoted by both the international notation according to **Hermann-Mauguin** and by the **Schönflies** notation, see Sec. 2.4, where the latter will be put in parentheses. As examples, we mention the point symmetry group **4** ( $\mathbf{C}_4$ ) and the space group **p31m** ( $\mathbf{C}_{3v}^2$ ).



### 3.8.1 Oblique Netplanes

The oblique Bravais lattice with the **largest** number of symmetry elements is described by point symmetry group **2** ( $C_2$ ). The corresponding **symmorphic** space group is denoted as **p2** ( $C_2$ ) and included as no. 2 in the ITC. Fig. 3.32a shows a morphological unit cell, where the circular patterns in Fig. 3.32a represent example atoms or groups of atoms (**motifs**). The motifs are placed at **general positions** of the morphological unit cell, i.e. not located at symmetry points of the cell. As a consequence, each operation of the point symmetry group **2** ( $C_2$ ) generates a new motif at a different location, where the transformation is illustrated by the orientation of the black wedges inside the circles of the patterns. Motifs illustrating symmetry elements of the unit cell will be used throughout the following discussion. Fig. 3.32b sketches all symmetry elements of the unit cell in a symbolic form, where centers of 2-fold rotation axes (inversion centers) are indicated by ellipses, according to the conventional crystallographic notation [33].

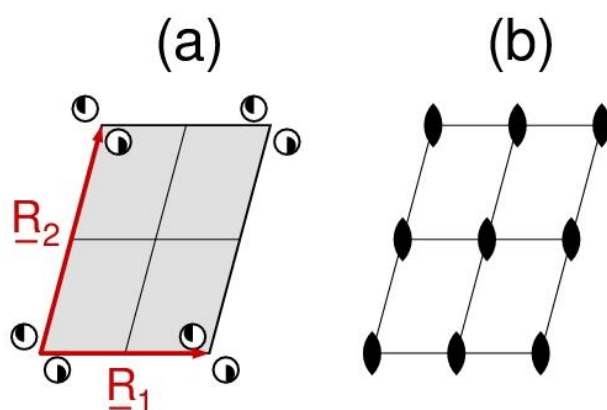


Fig. 3.32. Symmorphic oblique space group p2, no. 2 in the ITC. (a) Morphological unit cell (in gray) spanned by lattice vectors  $\underline{R}_1$ ,  $\underline{R}_2$  with example motifs shown by circular patterns. (b) Sketch of all symmetry elements of the unit cell according to ITC.

According to Table 3.10 in Sec. 3.6.6, point symmetry group **2** ( $C_2$ ) contains only one subgroup, the identity group **1** ( $C_1$ ), which can be combined with translational symmetry to yield another space group, where corresponding monolayers of the oblique Bravais lattice exhibit only translation symmetry. This **symmorphic** space group is denoted as **p1** ( $C_1$ ) and included as no. 1 in the ITC. Fig. 3.33a shows a morphological unit cell of the space group with the circular patterns illustrating its (missing) symmetry while Fig. 3.33b sketches all (i.e. none) symmetry elements of the unit cell and is added only for completeness.

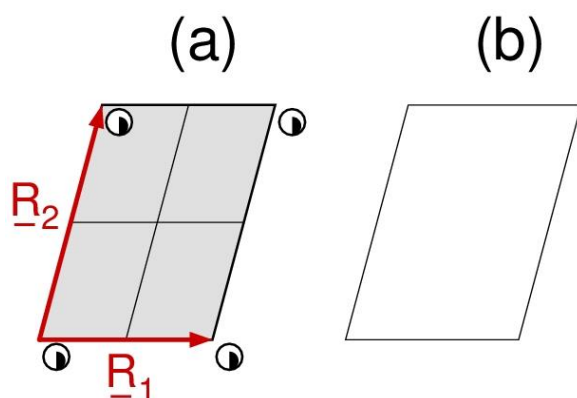


Fig. 3.33. Symmorphic oblique space group  $p1$ , no. 1 in the ITC. (a) Morphological unit cell (in gray) spanned by lattice vectors  $\underline{R}_1$ ,  $\underline{R}_2$  with example motifs shown by circular patterns. (b) Sketch of all (= no) symmetry elements of the unit cell.

### 3.8.2 Primitive Rectangular Netplanes

The primitive rectangular Bravais lattice with the **largest** number of symmetries is described by point symmetry group  $2mm$  ( $C_{2v}$ ). The corresponding **symmorphic** space group is denoted as  $p2mm$  ( $C_{2v}^1$ ), or in short as  $pmm$ , and included as no. 6 in the ITC. Fig. 3.34a shows a morphological unit cell of the space group with the circular patterns illustrating its symmetry. Fig. 3.34b sketches all symmetry elements of the unit cell following the ITC notation given in Sec. 3.8.

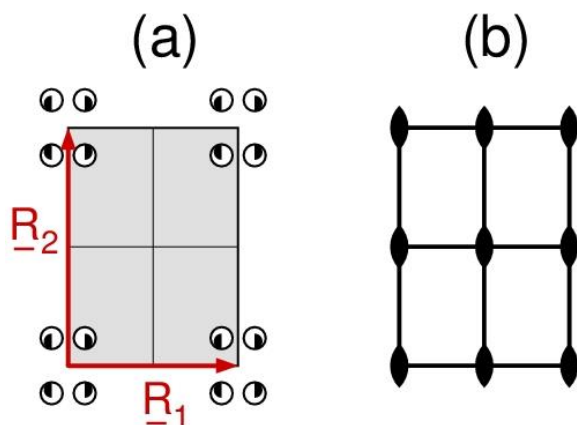


Fig. 3.34. Symmorphic primitive rectangular space group  $p2mm$ , no. 6 in the ITC. (a) Morphological unit cell (in gray) spanned by lattice vectors  $\underline{R}_1$ ,  $\underline{R}_2$  with example motifs shown by circular patterns. (b) Sketch of all symmetry elements of the unit cell according to ITC.

According to Table 3.10, point symmetry group  $2mm$  ( $C_{2v}$ ) contains three subgroups,  $1$  ( $C_1$ ),  $2$  ( $C_2$ ), and  $m$  ( $C_s$ ), which can be combined with translational symmetry of the primitive rectangular

Bravais lattice to yield three other space groups with less symmetry elements than the initial space group  $\mathbf{p2mm}$  ( $C_{2v}^1$ ). Here the cases of point symmetry groups  $\mathbf{1}$  ( $C_1$ ) and  $\mathbf{2}$  ( $C_2$ ), resulting in space groups  $\mathbf{p1}$  ( $C_1$ ) and  $\mathbf{p2}$  ( $C_2$ ), respectively, have already been discussed in Sec. 3.8.1.

Point symmetry group  $\mathbf{m}$  ( $C_s$ ) combined with a primitive rectangular Bravais lattice results in the **symmorphic** space group denoted as  $\mathbf{p1m1}$  ( $C_s^1$ ), or in short as ' $\mathbf{pm}$ ', and is included as no. 3 in the ITC. Fig. 3.35a shows a morphological unit cell of the space group with the circular patterns illustrating its symmetry. Fig. 3.35b sketches all symmetry elements of the unit cell following the ITC notation given in Sec. 3.8.

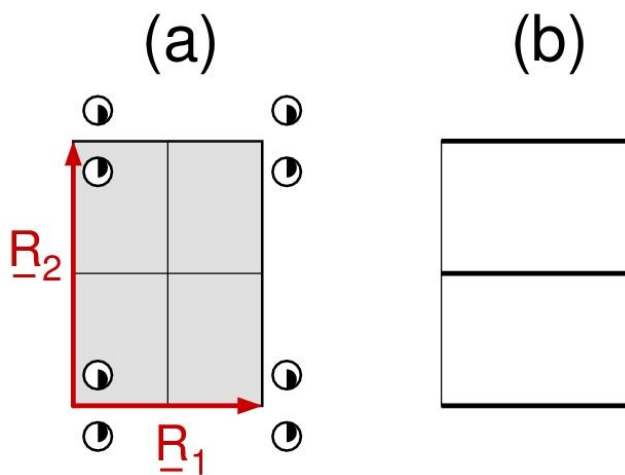


Fig. 3.35. Symmorphic primitive rectangular space group  $\mathbf{p1m1}$ , no. 3 in the ITC. (a) Morphological unit cell (in gray) spanned by lattice vectors  $\underline{R}_1$ ,  $\underline{R}_2$  with example motifs shown by circular patterns. (b) Sketch of all symmetry elements of the unit cell according to ITC.

In Sec. 3.6.5 it was shown that the existence of glide line symmetry is always connected with rectangular Bravais lattices. In particular, glide reflections as generating symmetry elements can be combined with primitive rectangular Bravais lattices to yield corresponding **non-symmorphic** space groups.

Combining the infinite set of parallel glide lines, shown to exist in primitive rectangular Bravais lattices, see Sec. 3.6.5 and Fig. 3.22, with translational symmetry leads to the **non-symmorphic** space group denoted as  $\mathbf{p1g1}$  ( $C_s^2$ ), or in short as  $\mathbf{pg}$ , and included as no. 4 in the ITC. Fig. 3.36a shows a morphological unit cell of the space group with the circular patterns illustrating its symmetry. Fig. 3.36b sketches all symmetry elements of the unit cell following the ITC notation given in Sec. 3.8.

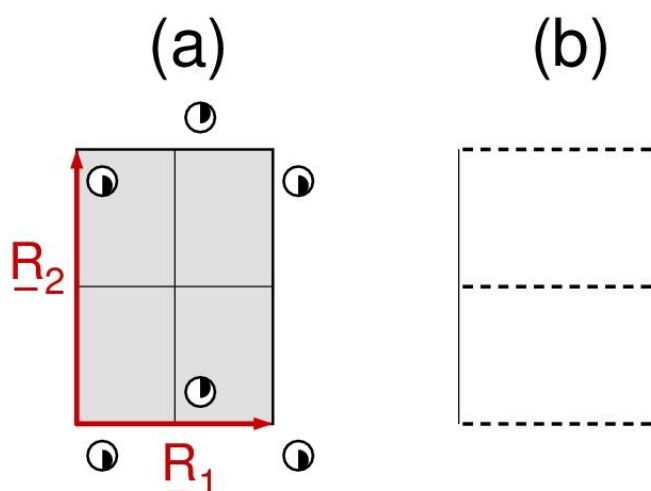


Fig. 3.36. Non-symmorphic primitive rectangular space group  $p1g1$ , no. 4 in the ITC. (a) Morphological unit cell (in gray) spanned by lattice vectors  $\underline{R}_1$ ,  $\underline{R}_2$  with example motifs shown by circular patterns. (b) Sketch of all symmetry elements of the unit cell according to ITC.

Infinite sets of parallel glide lines in primitive rectangular Bravais lattices can also be combined with symmetry described by point symmetry group  $2$  ( $C_2$ ), which includes 2-fold rotation (inversion) symmetry. As discussed in Sec. 3.6.5, there are two possible arrangements of inversion centers with respect to parallel glide lines,

- (a) All inversion centers lie on glide lines, see Fig. 3.24a. This was shown to yield additional mirror lines perpendicular to the glide lines, resulting in a **non-symmorphic** space group, denoted as  **$p2mg$**  ( $C_{2v}^2$ ), or in short as  **$pmg$** , and included as no. 7 in the ITC. Fig. 3.37a shows a morphological unit cell of the space group with the circular patterns illustrating its symmetry. Fig. 3.37b sketches all symmetry elements of the unit cell following the ITC notation given in Sec. 3.8. Note that the unit cells of Fig. 3.37 are rotated by  $90^\circ$  with respect to that of Fig. 3.24a in order to comply with the conventional notation used in the ITC.

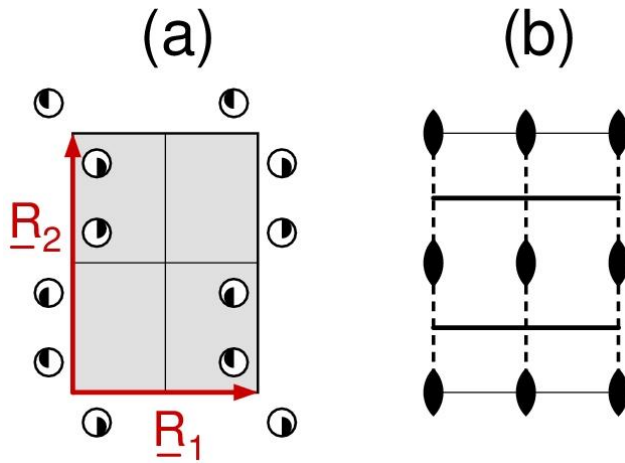


Fig. 3.37. Non-symmorphic primitive rectangular space group  $p2mg$ , no. 7 in the ITC. (a) Morphological unit cell (in gray) spanned by lattice vectors  $\underline{R}_1$ ,  $\underline{R}_2$  with example motifs shown by circular patterns. (b) Sketch of all symmetry elements of the unit cell according to ITC.

- (b) All inversion centers lie in the middle between glide lines, see Fig. 3.24b. This was shown to yield additional glide lines perpendicular to the initial glide lines resulting in an orthogonal set of glide lines. This glide line network combined with a primitive rectangular Bravais lattice leads to another **non-symmorphic** space group, denoted as  **$p2gg$**  ( $C_{2v}^3$ ), or in short as  **$pgg$** , and included as no. 8 in the ITC. Fig. 3.38a shows a morphological unit cell of the space group with the circular patterns illustrating its symmetry. Fig. 3.38b sketches all symmetry elements of the unit cell following the ITC notation given in Sec. 3.8. Note that the unit cells of Fig. 3.38 are shifted by  $1/4 \underline{R}_2$  with respect to that of Fig. 3.24b in order to comply with the conventional notation used in the ITC.

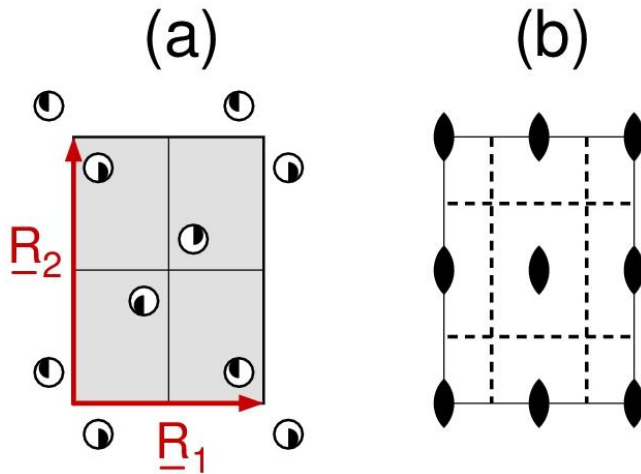


Fig. 3.38. Non-symmorphic primitive rectangular space group  $p2gg$ , no. 8 in the ITC. (a) Morphological unit cell (in gray) spanned by lattice vectors  $\underline{R}_1$ ,  $\underline{R}_2$  with example motifs shown by circular patterns. (b) Sketch of all symmetry elements of the unit cell according to ITC.

### 3.8.3 Centered Rectangular Netplanes

The centered rectangular Bravais lattice with the **largest** number of symmetries is, as the primitive rectangular lattice, described by point symmetry group  $2mm$  ( $C_{2v}$ ). The corresponding **symmorphic** space group is denoted as  $c2mm$  ( $C_{2v}^4$ ), or in short as  $cmm$ , and is included as no. 9 in the ITC. Fig. 3.39a shows two morphological unit cells of the space group, with the circular patterns illustrating its symmetry. The primitive skewed cell, defined by lattice vectors  $\underline{R}_1$  and  $\underline{R}_2$ , is emphasized by dark gray painting, while the non-primitive rectangular cell, given by vectors  $\underline{R}_1$  and  $\underline{R}_2'$  and preferred by crystallographers, is painted light gray. These two cells will be shown for all centered lattices discussed in the following. Fig. 3.39b sketches all symmetry elements of the unit cell following the ITC notation given in Sec. 3.8.

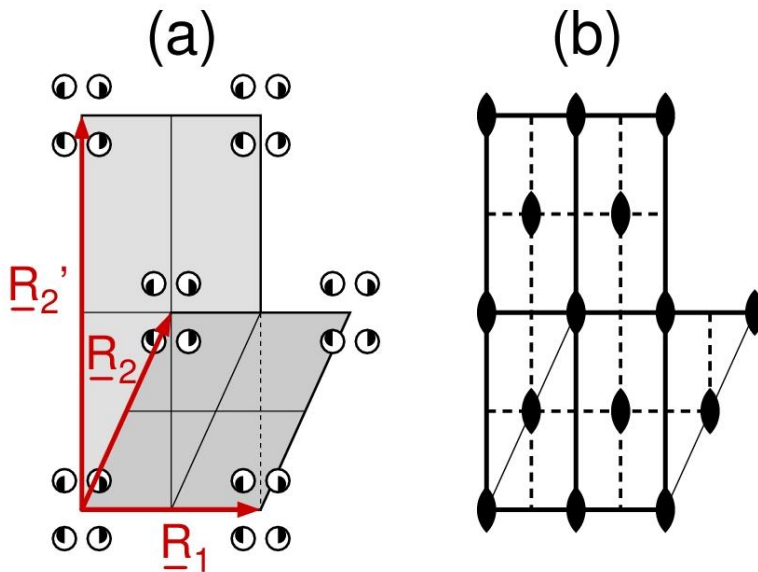


Fig. 3.39. Symmorphic centered rectangular  $c2mm$  space group, no. 9 in the ITC. (a) Morphological unit cells (in gray) spanned by lattice vectors  $\underline{R}_1$ ,  $\underline{R}_2$  (skewed cell) and  $\underline{R}_1$ ,  $\underline{R}_2'$  (rectangular cell) with example motifs shown by circular patterns. (b) Sketch of all symmetry elements of the unit cell according to ITC.

According to Table 3.10, point symmetry group  $2mm$  ( $C_{2v}$ ) contains three subgroups,  $1$  ( $C_1$ ),  $2$  ( $C_2$ ), and  $m$  ( $C_s$ ), which can be combined with translational symmetry of the centered rectangular Bravais lattice to yield three other space groups. Analogous to the discussion for the primitive rectangular case, see Sec. 3.8.2, point symmetry groups  $1$  ( $C_1$ ) and  $2$  ( $C_2$ ) can be ignored since they have been treated in Sec. 3.8.1.

Point symmetry group  $m$  ( $C_s$ ) combined with a centered rectangular Bravais lattice results in the **symmorphic** space group denoted as  $c1m1$  ( $C_s^2$ ), or in short as ' $cm$ ', and is included as no. 5 in the ITC. Fig. 3.40a shows two morphological unit cells (primitive skewed and non-primitive rectangular) of the space group with the circular patterns illustrating its symmetry. Fig. 3.40b sketches all symmetry elements of the unit cell following the ITC notation given in Sec. 3.8.

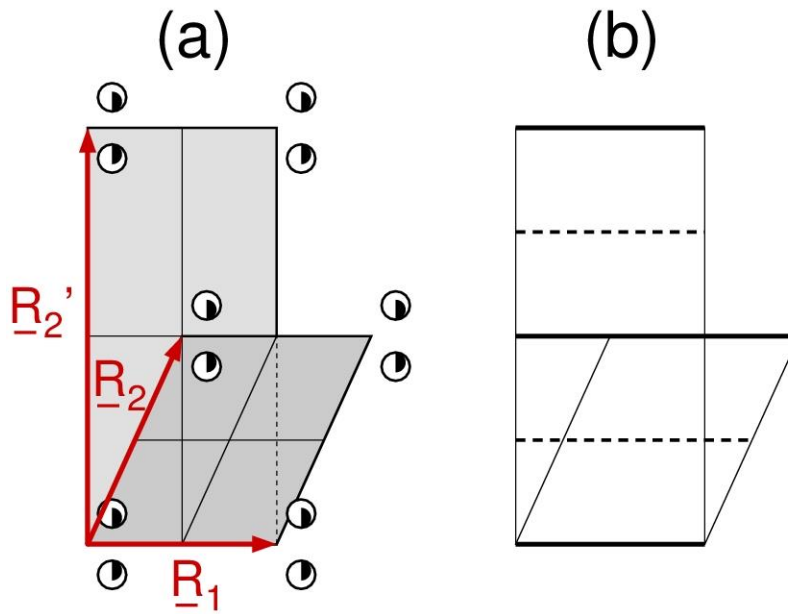


Fig. 3.40. Symmorphic centered rectangular  $c1m1$  space group, no. 5 in the ITC. (a) Morphological unit cells (in gray) spanned by lattice vectors  $\underline{R}_1, \underline{R}_2$  (skewed cell) and  $\underline{R}_1, \underline{R}_2'$  (rectangular cell) with example motifs shown by circular patterns. (b) Sketch of all symmetry elements of the unit cell according to ITC.

### 3.8.4 Square Netplanes

The square Bravais lattice with the **largest** number of symmetries is described by point symmetry group  $4mm$  ( $C_{4v}$ ). The corresponding **symmorphic** space group is denoted as  $p4mm$  ( $C_{4v}^1$ ), or in short as  $p4m$ , and included as no. 11 in the ITC. Fig. 3.41a shows a morphological unit cell of the space group with the circular patterns illustrating its symmetry. Fig. 3.41b sketches all symmetry elements of the unit cell following the ITC notation given in Sec. 3.8.



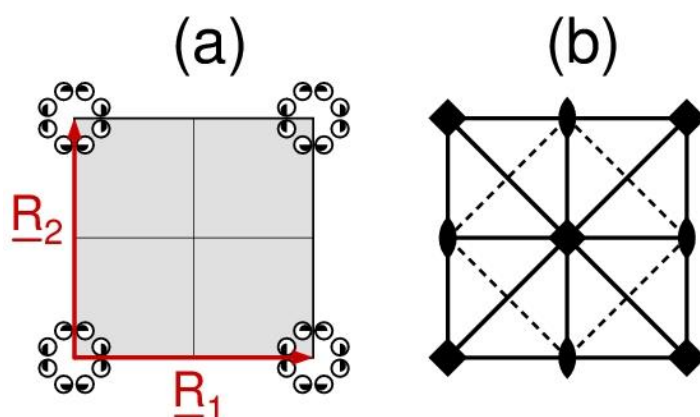


Fig. 3.41. Symmorphic square  $p4mm$  space group, no. 11 in the ITC. (a) Morphological unit cell (in gray) spanned by lattice vectors  $\underline{R}_1$ ,  $\underline{R}_2$  with example motifs shown by circular patterns. (b) Sketch of all symmetry elements of the unit cell according to ITC.

According to Table 3.10, point symmetry group  $4mm$  ( $C_{4v}$ ) contains five subgroups,  $1$  ( $C_1$ ),  $2$  ( $C_2$ ),  $4$  ( $C_4$ ),  $m$  ( $C_s$ ), and  $2mm$  ( $C_{2v}$ ), which can be combined with translational symmetry of the square Bravais lattice to yield five other space groups. Here only point symmetry groups  $4$  ( $C_4$ ) needs to be considered since the other groups have been dealt with earlier, see Secs. 3.8.1 to 3.8.3.

Point symmetry group  $4$  ( $C_4$ ) combined with a square Bravais lattice results in the **symmorphic** space group denoted as  $p4$  ( $C_4$ ) and is included as no. 10 in the ITC. Fig. 3.42a shows a morphological unit cell of the space group with the circular patterns illustrating its symmetry. Fig. 3.42b sketches all symmetry elements of the unit cell following the ITC notation given in Sec. 3.8.

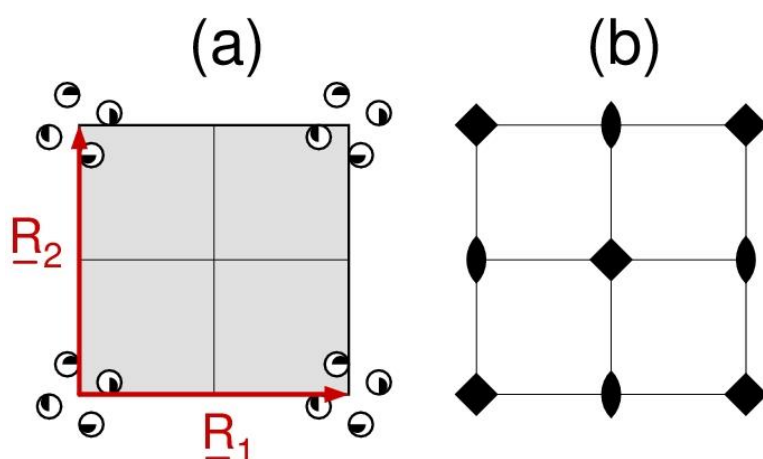


Fig. 3.42. Symmorphic square  $p4$  space group, no. 10 in the ITC. (a) Morphological unit cell (in gray) spanned by lattice vectors  $\underline{R}_1$ ,  $\underline{R}_2$  with example motifs shown by circular patterns. (b) Sketch of all symmetry elements of the unit cell according to ITC.

Infinite sets of parallel glide lines in square Bravais lattices can also be combined with symmetry described by point symmetry group **4** ( $C_4$ ), which includes 2- and 4-fold rotation symmetry. We mention without further proof that there is only one choice, where the corresponding **non-symmorphic** space group is denoted as **p4gm** ( $C_{4v}^2$ ), or in short as **p4g**, and included as no. 12 in the ITC. Fig. 3.43a shows a morphological unit cell of the space group with the circular patterns illustrating its symmetry. Fig. 3.43b sketches all symmetry elements of the unit cell following the ITC notation given in Sec. 3.8.

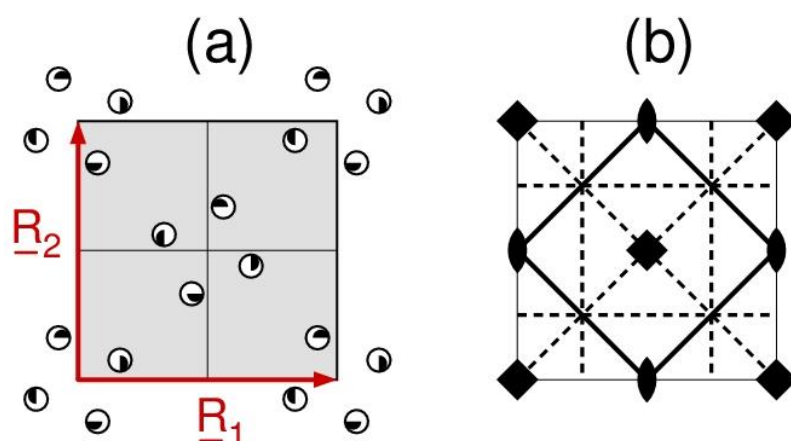


Fig. 3.43. Non-symmorphic square p4gm space group, no. 12 in the ITC. (a) Morphological unit cell (in gray) spanned by lattice vectors  $\underline{R}_1$ ,  $\underline{R}_2$  with example motifs shown by circular patterns. (b) Sketch of all symmetry elements of the unit cell according to ITC.

### 3.8.5 Hexagonal Netplanes

In Sec. 3.7 it was shown that a **hexagonal** lattice, defined by primitive lattice vectors  $\underline{R}_1$  and  $\underline{R}_2$  in acute representation ( $\gamma = 60^\circ$ ), can be described alternatively as a **centered rectangular** lattice with non-primitive lattice vectors  $\underline{R}_1$  and  $\underline{R}_2' = 2 \underline{R}_2 - \underline{R}_1$ , which are orthogonal. Therefore, all symmetry diagrams for hexagonal space groups, discussed in the following, will be shown with **two** morphological unit cells of the space group, analogous to the centered rectangular case in Sec. 3.8.3. The primitive rhombic cell, defined by lattice vectors  $\underline{R}_1$  and  $\underline{R}_2$ , is emphasized by dark gray painting, and the non-primitive rectangular cell, given by vectors  $\underline{R}_1$  and  $\underline{R}_2'$  and preferred by crystallographers, is painted light gray.

The hexagonal Bravais lattice with the **largest** number of symmetries is described by point symmetry group **6mm** ( $C_{6v}$ ). The corresponding **symmorphic** space group is denoted as **p6mm**

( $C_{6v}$ ), or in short as  $p6m$ , and included as no. 17 in the ITC. Fig. 3.44a shows two morphological unit cells (primitive rhombic and non-primitive rectangular) of the space group with the circular patterns illustrating its symmetry. Fig. 3.44b sketches all symmetry elements of the unit cell following the ITC notation given in Sec. 3.8.

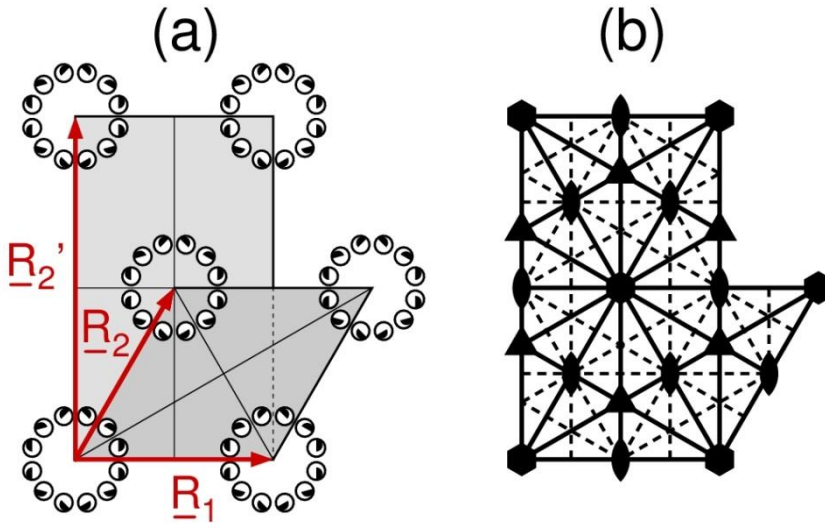


Fig. 3.44. Symmorphic hexagonal  $p6m$  space group, no. 17 in the ITC. (a) Morphological unit cells (in gray) spanned by lattice vectors  $\underline{R}_1$ ,  $\underline{R}_2$  (rhombic cell) and  $\underline{R}_1$ ,  $\underline{R}_2'$  (rectangular cell) with example motifs shown by circular patterns. (b) Sketch of all symmetry elements of the unit cell according to ITC.

According to Table 3.10, point symmetry group  $6mm$  ( $C_{6v}$ ) contains seven subgroups,  $1$  ( $C_1$ ),  $2$  ( $C_2$ ),  $3$  ( $C_3$ ),  $6$  ( $C_6$ ),  $m$  ( $C_s$ ),  $2mm$  ( $C_{2v}$ ), and  $3m1 / 31m$  ( $C_{3v}$ ) which can be combined with translational symmetry of the hexagonal Bravais lattice to yield other space groups. Here only point symmetry groups  $3$  ( $C_3$ ),  $6$  ( $C_6$ ), and  $3m1$ ,  $31m$  ( $C_{3v}$ ) need to be considered since the other groups have been dealt with earlier, see Secs. 3.8.1 to 3.8.3.

Point symmetry group  $3$  ( $C_3$ ) combined with a hexagonal Bravais lattice results in the **symmorphic** space group denoted as  $p3$  ( $C_3$ ) and is included as no. 13 in the ITC. Fig. 3.45a shows two morphological unit cells (primitive and non-primitive) of the space group with the circular patterns illustrating its symmetry. Fig. 3.45b sketches all symmetry elements of the unit cell following the ITC notation given in Sec. 3.8.

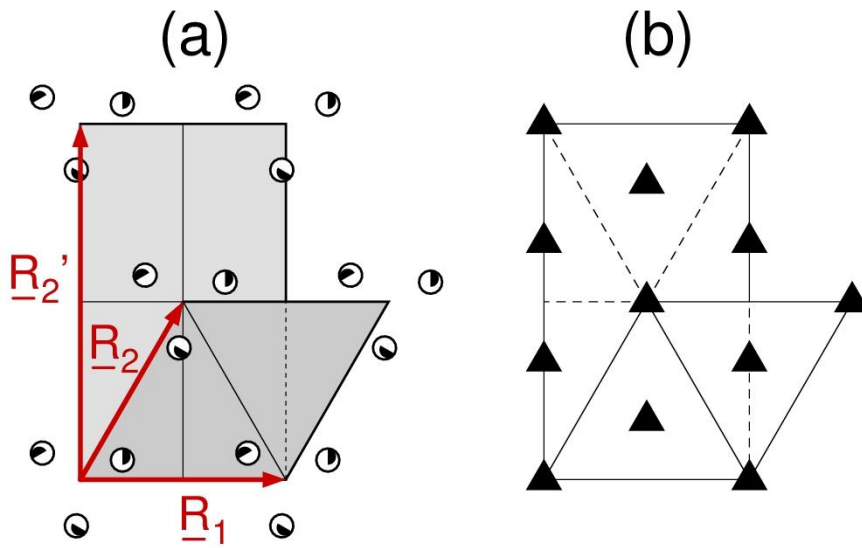


Fig. 3.45. Symmorphic hexagonal  $p3$  space group, no. 13 in the ITC. (a) Morphological unit cells (in gray) spanned by lattice vectors  $\underline{R}_1$ ,  $\underline{R}_2$  (rhombohedral cell) and  $\underline{R}_1$ ,  $\underline{R}_2'$  (rectangular cell) with example motifs shown by circular patterns. (b) Sketch of all symmetry elements of the unit cell according to ITC.

Point symmetry group  $6$  ( $C_6$ ) combined with a hexagonal Bravais lattice results in the **symmorphic** space group denoted as  $p6$  ( $C_6$ ) and is included as no. 16 in the ITC. Fig. 3.46a shows two morphological unit cells of the space group with the circular patterns illustrating its symmetry. Fig. 3.46b sketches all symmetry elements of the unit cell following the ITC notation given in Sec. 3.8.

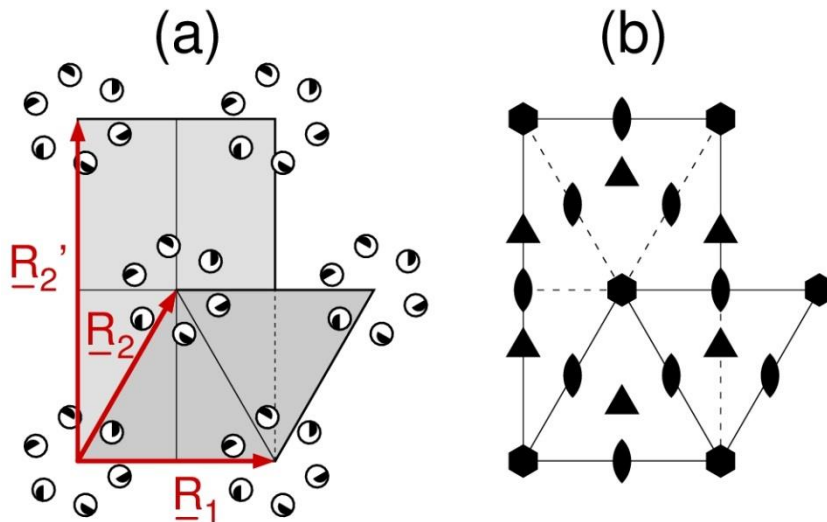


Fig. 3.46. Symmorphic hexagonal  $p6$  space group, no. 16 in the ITC. (a) Morphological unit cells (in gray) spanned by lattice vectors  $\underline{R}_1$ ,  $\underline{R}_2$  (rhombohedral cell) and  $\underline{R}_1$ ,  $\underline{R}_2'$  (rectangular cell) with example motifs shown by circular patterns. (b) Sketch of all symmetry elements of the unit cell according to ITC.

Point symmetry group  $\mathbf{3m1}$ ,  $\mathbf{31m}$  ( $C_{3v}$ ) can also be combined with a hexagonal Bravais lattice. Here the two variants depend on the orientation of the mirror lines with respect to the primitive lattice vectors  $\underline{R}_1$  and  $\underline{R}_2$  (assuming an acute representation,  $\gamma = 60^\circ$ ),

- (a) Mirror lines point between lattice vectors  $\underline{R}_1$  and  $\underline{R}_2$ , resulting in angles of  $30^\circ$  between lattice vectors and mirror lines, described by point symmetry group variant  $\mathbf{3m1}$  ( $C_{3v}$ ). This results in the **symmorphic** space group denoted as  $\mathbf{p3m1}$  ( $C_{3v}^1$ ), which is included as no. 14 in the ITC. Fig. 3.47a shows two morphological unit cells of the space group with the circular patterns illustrating its symmetry. Fig. 3.47b sketches all symmetry elements of the unit cell following the ITC notation given in Sec. 3.8.

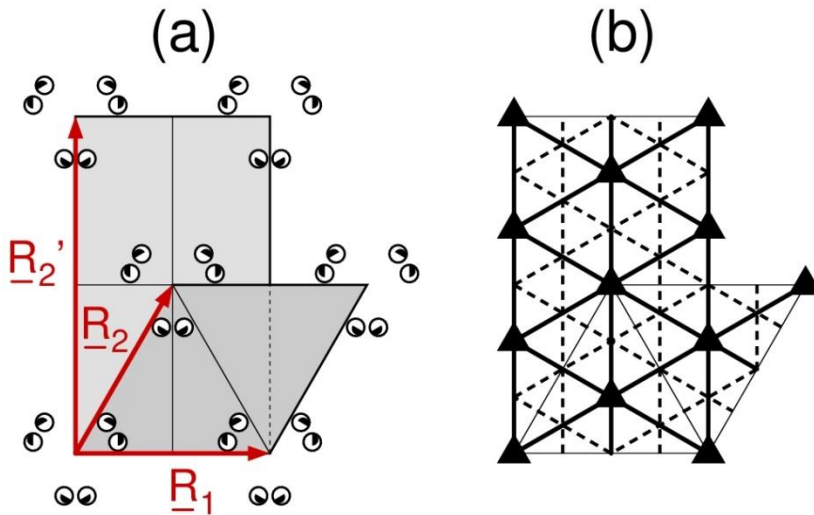


Fig. 3.47. Symmorphic hexagonal  $\mathbf{p3m1}$  space group, no. 14 in the ITC. (a) Morphological unit cells (in gray) spanned by lattice vectors  $\underline{R}_1$ ,  $\underline{R}_2$  (rhomboidal cell) and  $\underline{R}_1$ ,  $\underline{R}_2'$  (rectangular cell) with example motifs shown by circular patterns. (b) Sketch of all symmetry elements of the unit cell according to ITC.

- (b) Mirror lines coincide with lattice vectors  $\underline{R}_1$  and  $\underline{R}_2$ , described by point symmetry group variant  $\mathbf{31m}$  ( $C_{3v}$ ). This results in the **symmorphic** space group denoted as  $\mathbf{p31m}$  ( $C_{3v}^2$ ), which is included as no. 15 in the ITC. Fig. 3.48a shows two morphological unit cells of the space group with the circular patterns illustrating its symmetry. Fig. 3.48b sketches all symmetry elements of the unit cell following the ITC notation given in Sec. 3.8.

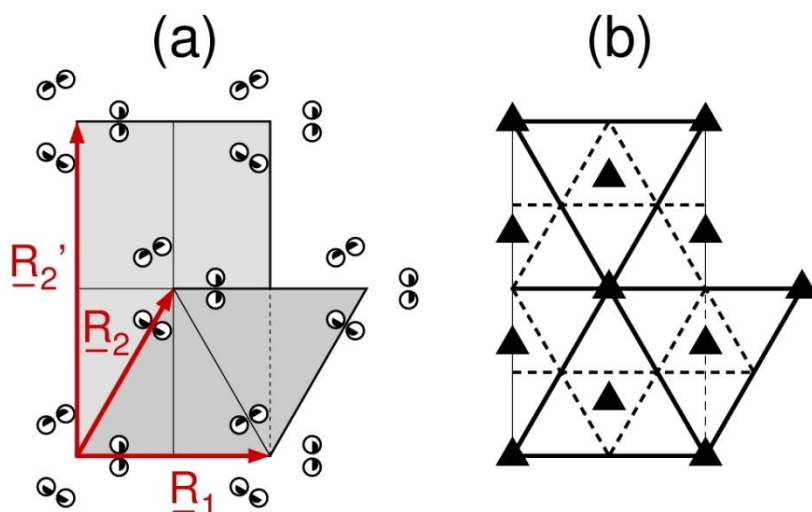


Fig. 3.48. Symmorphic hexagonal  $p31m$  space group, no. 15 in the ITC (a) Morphological unit cells (in gray) spanned by lattice vectors  $\underline{R}_1$ ,  $\underline{R}_2$  (rhomboidal cell) and  $\underline{R}_1$ ,  $\underline{R}_2'$  (rectangular cell) with example motifs shown by circular patterns. (b) Sketch of all symmetry elements of the unit cell according to ITC.

### 3.8.6 Classification Overview

Secs. 3.8.1 to 3.8.5 have covered all possible symmorphic and non-symmorphic space groups, available for a classification of netplanes and monolayers by their symmetry behavior. Altogether, there are **17 different space groups** (13 symmorphic, 4 non-symmorphic) in **two dimensions**, where two space groups refer to the oblique, five to the primitive rectangular, two to the centered rectangular, three to the square, and five to the hexagonal Bravais lattice. Table 3.13 collects all two-dimensional space groups with their properties with the numbering scheme following the sequence of the in the International Tables for Crystallography [33].

Table 3.13. Properties of the 17 space groups in two dimensions. The ITC number refers to the International Tables for Crystallography [33], where non-symmorphic space groups are labeled by asterisks (\*) and space groups with highest point symmetry of a given Bravais lattice by (+). Space and point group names are listed in Hermann-Mauguin and Schönflies notation, the latter in parentheses. The Hermann-Mauguin notation of the space groups includes also short names separated by slashes.

ITC no.	Space group	Point group	Bravais lattice
1	<b>p1</b> ( $C_1$ )	<b>1</b> ( $C_1$ )	oblique
2 <sup>+</sup>	<b>p2</b> ( $C_2$ )	<b>2</b> ( $C_2$ )	oblique
3	<b>p1m1</b> / <b>pm</b> ( $C_s^1$ )	<b>m</b> ( $C_s$ )	p-rectangular
4 <sup>*</sup>	<b>p1g1</b> / <b>pg</b> ( $C_s^2$ )	<b>1</b> ( $C_1$ )	p-rectangular
5	<b>c1m1</b> / <b>cm</b> ( $C_s^2$ )	<b>m</b> ( $C_s$ )	c-rectangular
6 <sup>+</sup>	<b>p2mm</b> / <b>pmm</b> ( $C_{2v}^1$ )	<b>2mm</b> ( $C_{2v}$ )	p-rectangular
7 <sup>*</sup>	<b>p2mg</b> / <b>pmg</b> ( $C_{2v}^2$ )	<b>2</b> ( $C_2$ )	p-rectangular
8 <sup>*</sup>	<b>p2gg</b> / <b>pgg</b> ( $C_{2v}^3$ )	<b>2</b> ( $C_2$ )	p-rectangular
9 <sup>+</sup>	<b>c2mm</b> / <b>cmm</b> ( $C_{2v}^4$ )	<b>2mm</b> ( $C_{2v}$ )	c-rectangular
10	<b>p4</b> ( $C_4$ )	<b>4</b> ( $C_4$ )	square
11 <sup>+</sup>	<b>p4mm</b> / <b>p4m</b> ( $C_{4v}^1$ )	<b>4mm</b> ( $C_{4v}$ )	square
12 <sup>*</sup>	<b>p4gm</b> / <b>p4g</b> ( $C_{4v}^2$ )	<b>4</b> ( $C_4$ )	square
13	<b>p3</b> ( $C_3$ )	<b>3</b> ( $C_3$ )	hexagonal
14	<b>p3m1</b> ( $C_{3v}^1$ )	<b>3m1</b> ( $C_{3v}$ )	hexagonal
15	<b>p31m</b> ( $C_{3v}^2$ )	<b>31m</b> ( $C_{3v}$ )	hexagonal
16	<b>p6</b> ( $C_6$ )	<b>6</b> ( $C_6$ )	hexagonal
17 <sup>+</sup>	<b>p6mm</b> / <b>p6m</b> ( $C_{6v}$ )	<b>6mm</b> ( $C_{6v}$ )	hexagonal

Fig. 3.49 gives an overview over all **symmetry elements** inside morphological unit cells of netplanes and monolayers described by the 17 two-dimensional **space groups** where the sequence follows the numbering scheme and the symbolic notation used in the ITC [33]. This collects the sketches shown already in the extended discussion of space groups in Secs. 3.8.1 to 3.8.5. Further details concerning symmetry properties of two-dimensional space groups can be found in Refs. [23], [33], [34], [40], [86], [87].

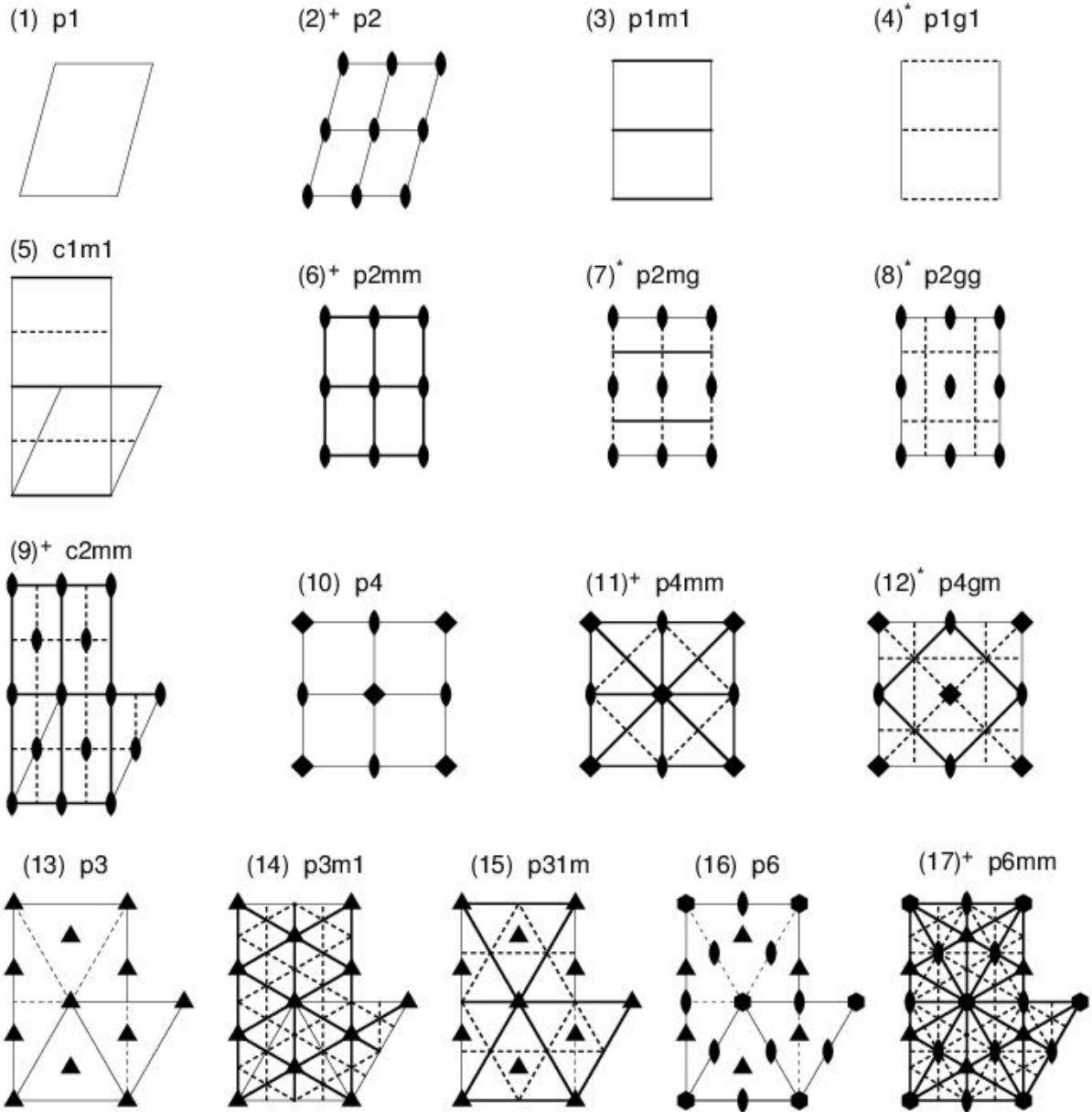


Fig. 3.49. Symmetry elements inside morphological unit cells of monolayers described by all 17 two-dimensional space groups. Non-symmorphic space groups are labeled by asterisks (\*) and space groups of highest point symmetry for a given Bravais lattice by (<sup>+</sup>). Mirror lines are indicated by thick and glide lines by dashed lines. 2-, 3-, 4-, and 6-fold rotation centers are shown by ellipses, triangles, squares, and hexagons, respectively, following the ITC notation.



### 3.9 Exercises

- 3.1. Show that the (a) sc, (b) fcc, (c) bcc, and (d) hex (hcp) lattices can be built by stacking hexagonal netplanes. Determine for each lattice relationships between the intrinsic bulk lattice constant  $a$ , the netplane lattice constant  $a_{(hkl)}$ , and the distance between adjacent netplanes  $d_{(hkl)}$ .
- 3.2. Calculate netplane-adapted lattice vectors for  $(hkl)$  monolayers described as
- (a) fcc Ni(1 1 1)
  - (b) bcc Fe(1 1 0)
  - (c) fcc Pd(1 1 3)
  - (d) hex (hcp) Co(1 1 2)
  - (e) diamond(1 2 3)
  - (f) fcc( $m$  1 1), fcc( $m$  0 1),  $m > 1$

For cubic crystals  $(hkl)$  refers to the sc notation. Determine atom densities of the monolayers and compare with those of densest monolayers.

- 3.3. Find the densest and second densest monolayers of the (a) sc, (b) fcc, (c) bcc, and (d) hex (hcp), (e) NaCl crystals. Determine for each lattice how many and which directions yield densest monolayers.
- 3.4. Determine netplane-adapted lattice vectors and atom densities of monolayers of the graphite crystal with (a) (0 0 0 1), (b) (1 1 2 1), (c) (1 -2 1 1), (d) (1 -1 0 1) orientation (Miller-Bravais indices, obtuse bulk lattice vectors). Characterize their geometric structures. What are the corresponding 3-index Miller indices?
- 3.5. Consider a hexagonal lattice with (a) obtuse and (b) acute lattice vector representation and netplanes with orientations given in 3-index notation  $(hkl)$ . Determine Miller-Bravais indices  $(lmnq)$  of the (0 0 1), (1 0 1), (1 1 1), (1 0 -1), (1 2 1), and (1 -3 5) oriented netplanes.
- 3.6. The hex(hcp) crystal can be defined by lattice vectors  $\underline{\mathbf{R}}_1, \underline{\mathbf{R}}_2, \underline{\mathbf{R}}_3$  and a basis of two atoms where

$$\begin{aligned} \underline{\mathbf{R}}_1 &= a(1, 0, 0), & \underline{\mathbf{R}}_2 &= a(-1/2, (\sqrt{3})/2, 0), & \underline{\mathbf{R}}_3 &= c(0, 0, 1) \\ \underline{\mathbf{r}}_1 &= (0, 0, 0), & \underline{\mathbf{r}}_2 &= a(1/2, 1/(\sqrt{12}), \sqrt{(2/3)}) & c/a &= \sqrt{(8/3)} \end{aligned}$$

with  $\underline{R}_i$ ,  $i = 1, 2, 3$  and  $\underline{r}_1, \underline{r}_2$  in Cartesian coordinates. Show that Miller indices  $(h k l)$  of monolayers which contain both types of atoms fulfill the Diophantine equation  $2h + 4k + 3l = 6N$ .

- 3.7. Consider the  $(1\ 2\ 3)$  oriented netplane of the (a) fcc, (b) bcc, (c) diamond, (c) cubic zincblende, and (d) graphite crystal. How many and which netplanes of the crystal are symmetrically equivalent?
- 3.8. Determine two-dimensional morphological unit cells and Wigner-Seitz cells of the monolayers described in Exercise 3.2.
- 3.9. Determine Miller indices  $(h k l)$  of all symmetry equivalent netplanes derived from a given netplane  $(h_0 k_0 l_0)$  of a (a) fcc, (b) bcc, hex (hcp) lattice.
- 3.10. Consider a crystal lattice described by initial lattice vectors  $\underline{R}_{o1}, \underline{R}_{o2}, \underline{R}_{o3}$  and by  $(h k l)$  netplane-adapted lattice vectors  $\underline{R}_1, \underline{R}_2, \underline{R}_3$  where the transformation is given by

$$\begin{pmatrix} \underline{R}_1 \\ \underline{R}_2 \\ \underline{R}_3 \end{pmatrix} = \begin{pmatrix} t_{11} & t_{12} & t_{13} \\ t_{21} & t_{22} & t_{23} \\ t_{31} & t_{32} & t_{33} \end{pmatrix} \cdot \begin{pmatrix} \underline{R}_{o1} \\ \underline{R}_{o2} \\ \underline{R}_{o3} \end{pmatrix} = \underline{T}^{(hkl)} \cdot \begin{pmatrix} \underline{R}_{o1} \\ \underline{R}_{o2} \\ \underline{R}_{o3} \end{pmatrix}$$

with integer-valued matrix elements  $t_{ij}$ . Corresponding reciprocal lattice vectors of the two lattice representations are  $\underline{G}_{o1}, \underline{G}_{o2}, \underline{G}_{o3}$  and  $\underline{G}_1, \underline{G}_2, \underline{G}_3$ , respectively, with

$$\begin{pmatrix} \underline{G}_1 \\ \underline{G}_2 \\ \underline{G}_3 \end{pmatrix} = \begin{pmatrix} q_{11} & q_{12} & q_{13} \\ q_{21} & q_{22} & q_{23} \\ q_{31} & q_{32} & q_{33} \end{pmatrix} \cdot \begin{pmatrix} \underline{G}_{o1} \\ \underline{G}_{o2} \\ \underline{G}_{o3} \end{pmatrix} = \underline{Q}^{(hkl)} \cdot \begin{pmatrix} \underline{G}_{o1} \\ \underline{G}_{o2} \\ \underline{G}_{o3} \end{pmatrix}$$

Determine the relationship between the transformation matrices  $\underline{T}^{(hkl)}$  and  $\underline{Q}^{(hkl)}$ .

- 3.11. Consider a crystal lattice described by initial lattice vectors  $\underline{R}_{o1}, \underline{R}_{o2}, \underline{R}_{o3}$  and by  $(h k l)$  netplane-adapted lattice vectors  $\underline{R}_1, \underline{R}_2, \underline{R}_3$  with a vector transformation  $\underline{T}^{(hkl)}$  as in Exercise 3.10. Determine Miller indices  $(h' k' l')$  corresponding to a vector transformation  $\underline{T}^{(h'k'l')} = (\underline{T}^{(hkl)})^{-1}$ .
- 3.12. Consider a crystal lattice described by lattice vectors  $\underline{R}_{o1}, \underline{R}_{o2}, \underline{R}_{o3}$  and Miller indices  $(h_0 k_0 l_0)$  with respect to the corresponding reciprocal lattice vectors. Further, transformed lattice vectors  $\underline{R}_1, \underline{R}_2, \underline{R}_3$  with a vector transformation  $\underline{T}^{(hkl)}$  are assumed to provide an

equivalent lattice description, analogous to Exercise 3.10, and yield Miller indices  $(h k l)$ . Determine the Miller index transformation matrix  $\underline{\underline{M}}$  where

$$\begin{pmatrix} h \\ k \\ l \end{pmatrix} = \begin{pmatrix} m_{11} & m_{12} & m_{13} \\ m_{21} & m_{22} & m_{23} \\ m_{31} & m_{32} & m_{33} \end{pmatrix} \cdot \begin{pmatrix} h_o \\ k_o \\ l_o \end{pmatrix} = \underline{\underline{M}} \cdot \begin{pmatrix} h_o \\ k_o \\ l_o \end{pmatrix}$$

- 3.13. A netplane is defined in a Cartesian coordinate system  $(x, y)$  by lattice vectors

$$\underline{\underline{R}}_1 = a (0, \sqrt{3}), \quad \underline{\underline{R}}_2 = a/2 (1, \sqrt{27})$$

Show by Minkowski reduction that the netplane is hexagonal.

- 3.14. Determine Miller indices of polar and non-polar monolayers of the NaCl and CsCl crystals. Hint: polar monolayers are monoatomic.

- 3.15. Show that the atom density  $\rho_{(hkl)}$  of  $(h k l)$  monolayers of sc, fcc, and bcc crystals (Miller indices in sc notation) is determined by

$$\rho_{(hkl)} = \frac{p}{\sqrt{(h^2 + k^2 + l^2)}} \quad \text{with } p = 1, 4, 2 \text{ for sc, fcc, and bcc, respectively.}$$

- 3.16. Find structurally different monolayers of equal atom density for crystals with (a) fcc and (b) bcc lattice.
- 3.17. Consider a netplane with two inversion centers at  $\underline{\underline{r}}_{o1}$  and  $\underline{\underline{r}}_{o2}$ . Show that the combination of two inversion operations  $\mathbf{i}(\underline{\underline{r}}_{o2}) \cdot \mathbf{i}(\underline{\underline{r}}_{o1})$  corresponds to a shift by  $\pm 2 (\underline{\underline{r}}_{o2} - \underline{\underline{r}}_{o1})$ .
- 3.18. The xy plane (in Cartesian coordinates) includes two 4-fold rotation axes along z whose centers are separated by vector  $\underline{\underline{R}}_1 = a (1, 0, 0)$ . Consider subsequent rotation operations by  $90^\circ$ ,  $180^\circ$ ,  $270^\circ$  about the two centers generating new rotation centers in the xy plane. Show that infinitely many rotation operations create a periodic structure of rotation centers, corresponding to a square netplane with perpendicular lattice vectors  $\underline{\underline{R}}_1 = a (1, 0, 0)$ ,  $\underline{\underline{R}}_2 = a (0, 1, 0)$ .
- 3.19. Consider a netplane with inversion centers at  $\underline{\underline{r}}^i = n_1 \underline{\underline{r}}_1 + n_2 \underline{\underline{r}}_2$ ,  $n_i$  integer. Determine lattice vectors of the netplane.
- 3.20. Consider a netplane with  $n_1$ - and  $n_2$ -fold rotation axes at the same center  $\underline{\underline{r}}_{o1}$ . Prove that that the netplane has a  $p$ -fold rotation axis at  $\underline{\underline{r}}_{o1}$  with  $p = \text{lcm}(n_1, n_2)$ .

- 3.21. Consider a rectangular netplane with orthogonal lattice vectors  $\underline{R}_1$  and  $\underline{R}_2$  and mirror symmetry. Show that if the netplane includes a mirror line, which does not point parallel or perpendicular to the lattice vectors, the netplane must also include glide lines.
- 3.22. Which of the point symmetry elements of the bulk lattice are conserved in the netplanes referring to the monolayers described in Exercise 3.2?
- 3.23. Which  $(h k l)$  netplanes of an fcc lattice can be described by rectangular unit cells? Determine general conditions for  $(h k l)$ .
- 3.24. The hcp crystal can be defined by lattice vectors  $\underline{R}_1, \underline{R}_2, \underline{R}_3$  given in Exercise 3.6. Show that the atom density of primitive  $(h k l)$  monolayers is given by

$$\rho_{(hkl)} = \frac{1}{\sqrt{\frac{8}{3}(h^2 + k^2 + hk) + \frac{3}{4}l^2}}$$

- 3.25. Consider a primitive monolayer and its different netplane descriptions. Which alternative Bravais lattices can be used to describe a monolayer corresponding to a (a) square, (b) primitive rectangular, (c) centered rectangular, (d) hexagonal netplane?
- 3.26. Lattice vectors of trigonal lattices,  $\underline{R}_1^{\text{trg}}, \underline{R}_2^{\text{trg}}, \underline{R}_3^{\text{trg}}$ , can be represented by those of corresponding hexagonal lattices,  $\underline{R}_1^{\text{hex}}, \underline{R}_2^{\text{hex}}, \underline{R}_3^{\text{hex}}$ , where transformation (3.35)

$$\begin{pmatrix} \underline{R}_1^{\text{hex}} \\ \underline{R}_2^{\text{hex}} \\ \underline{R}_3^{\text{hex}} \end{pmatrix} = \begin{pmatrix} 1 & -1 & 0 \\ 0 & 1 & -1 \\ 1 & 1 & 1 \end{pmatrix} \cdot \begin{pmatrix} \underline{R}_1^{\text{trg}} \\ \underline{R}_2^{\text{trg}} \\ \underline{R}_3^{\text{trg}} \end{pmatrix}$$

is one example of an obtuse representation.

- (a) Show that there are, altogether, 6 choices of obtuse and 6 of acute hexagonal representations and determine the corresponding transformations.
- (b) Evaluate the Miller index transformation  $(h^{\text{trg}} k^{\text{trg}} l^{\text{trg}}) \rightarrow (h^{\text{hex}} k^{\text{hex}} l^{\text{hex}})$  for each of the lattice transformations in (a).
- (c) The Miller index transformations in (b) results in constraints for  $h^{\text{hex}}, k^{\text{hex}}, l^{\text{hex}}$  reading
- $$-h^{\text{hex}} + k^{\text{hex}} + l^{\text{hex}} = 3g, \quad h^{\text{hex}} - k^{\text{hex}} + l^{\text{hex}} = 3g, \quad h^{\text{hex}} + k^{\text{hex}} - l^{\text{hex}} = 3g$$
- $$h^{\text{hex}} + k^{\text{hex}} + l^{\text{hex}} = 3g$$

Which transformation belongs to which constraint?

## 4 IDEAL SINGLE CRYSTAL SURFACES

Ideal single crystal surfaces, which result from **truncating** perfect three-dimensional bulk crystals, provide only an approximate description of structural properties of many crystal surfaces that appear in nature. However, these model surfaces can be treated in an **exact** way mathematically and show **general concepts** which can easily be transferred to real crystal surfaces. Examples are the general classification of stepped and kinked surfaces or the treatment of chiral surfaces which will be discussed in detail in this section.

In the present section (also in Secs. 5, 6) a number of examples deal with crystals of **cubic** symmetry, specifically fcc and bcc. In these examples we will always use Miller indices referring to **simple cubic** notation, see Sec. 3.4, without further specification since this notation is commonly used by surface scientists. Further, in all cases where Miller indices are used to denote only directions of netplane normal vectors their values will be **normalized** such that the indices do not have a common divisor. As an example, Miller indices of (3 9 18) and (1 3 6) netplanes are equivalent, where the latter notation will be used. Further, **negative** Miller indices will be written with a **minus sign** in front, i.e.  $h = -2$ , rather than given in crystallographic notation, i.e.  $h = \bar{2}$ .

### 4.1 Basic Definition, Termination

The exact definition of an ideal single crystal surface starts from the **truncation** of a perfect three-dimensional **bulk** crystal parallel to one of its  $(h k l)$  monolayers which acts as a top layer with the crystal substrate below and vacuum above. (By convention the corresponding reciprocal lattice vector  $\underline{G}_{(h k l)}$  is defined such that it points from the substrate into vacuum.) As a result, the surface is **periodic** in two dimensions and its periodicity is determined by lattice vectors  $\underline{R}_1$  and  $\underline{R}_2$ , which define the periodicity of the corresponding  $(h k l)$  netplane. Therefore, one can use **Miller indices**  $(h k l)$  to characterize the **surface orientation** and apply mathematical descriptions of monolayers and netplanes also to ideal single crystal surfaces. This is illustrated in Fig. 4.1 which shows an irregular grain of an ideal fcc nickel single crystal exposing different bulk truncated surface sections which are labeled by their Miller indices  $(h k l)$ .

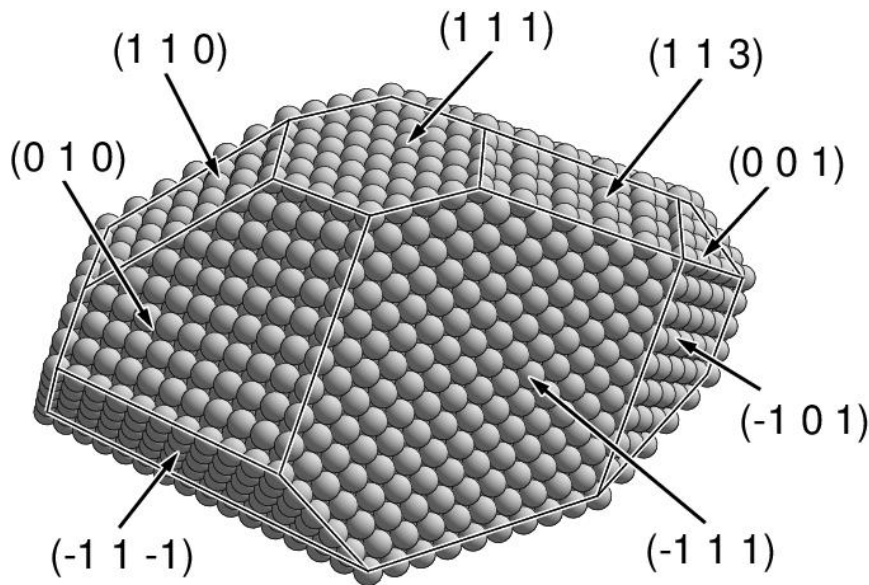


Fig. 4.1. Different bulk truncated surface sections of an ideal fcc nickel single crystal with atoms shown as balls. The surfaces are indicated by their Miller indices.

Single crystals with more than one atom type in the primitive unit cell can exhibit **differently terminated** surfaces for the same  $(h k l)$  orientation. If the crystal contains  $p > 1$  non-equivalent atoms in the primitive unit cell then there are  $p$  parallel primitive monolayers originating at each atom of the cell which may describe the topmost layer of an ideal single crystal surface. Of these monolayers, some may fall on the **same spatial plane** depending on the actual  $(h k l)$  direction. This yields monolayers with identical netplanes but a (planar) basis with more than one atom type. As a result, for polyatomic crystals there are  $q \leq p$  different terminations of corresponding ideal single crystal surfaces described by  $(h k l)$ .

As an example, the **sodium chloride**, NaCl, crystal is described by an **fcc** lattice (as defined in (2.38)) of lattice constant  $a$  and **two** different elements, one sodium and one chlorine each, in its primitive unit cell, yielding  $p = 2$ . (The  $\text{Na}^+$  and  $\text{Cl}^-$  ions are positioned at  $\underline{r}_1^{\text{Na}} = a(0, 0, 0)$  and  $\underline{r}_2^{\text{Cl}} = a/2(1, 1, 1)$  inside the fcc unit cell.) For  $(1 0 0)$  monolayers one obtains  $q = 1$  since  $\text{Na}^+$  and  $\text{Cl}^-$  ions fall on the same plane. This results in only one  $(1 0 0)$  surface termination, where  $\text{Na}^+$  and  $\text{Cl}^-$  ions exist in equal amounts giving rise to a non-polar surface, see Fig. 4.2a. On the other hand,  $(1 1 1)$  monolayers of  $\text{Na}^+$  and  $\text{Cl}^-$  ions are separated from each other, hence  $q = 2$ , which leads to two possible  $(1 1 1)$  surface terminations, one with  $\text{Na}^+$  and one with  $\text{Cl}^-$  ions at the top, see Fig. 4.2b for the  $\text{Na}^+$  termination. These surfaces are highly polar and quite difficult to prepare experimentally. The NaCl crystal structure also applies to **MgO**, resulting in the same surface termina-

tions which were shown in Fig. 1.1.

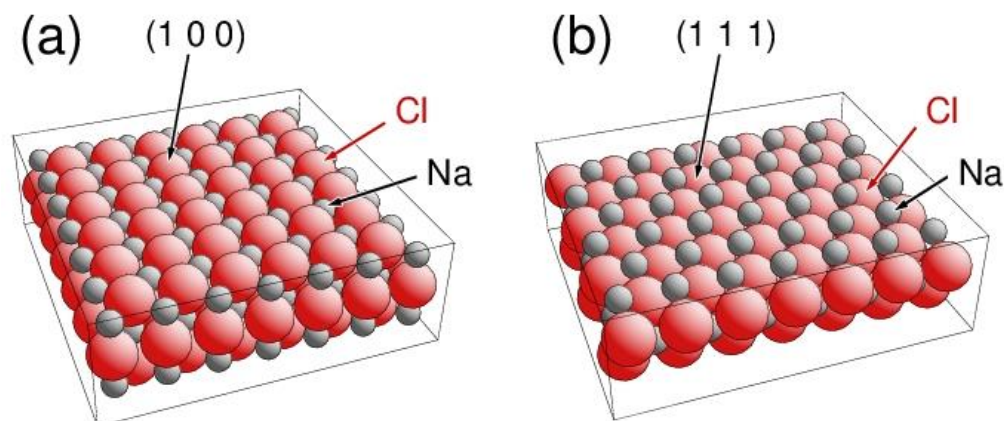


Fig. 4.2. Different NaCl single crystal surfaces. (a) Non-polar NaCl(1 0 0) surface, (b) polar NaCl(1 1 1) surface with Na termination.

A more complex example is given by the **vanadium sesquioxide**,  $V_2O_3$ , crystal whose structure is of corundum type with a **trigonal-R** (or equivalent hexagonal) lattice [31], see Sec. 2.4. The primitive unit cell of  $V_2O_3$  contains **ten** atoms,  $4 \times V$  and  $6 \times O$ , yielding  $p = 10$ . Along the (1 1 1) direction (corresponding to (0 0 0 1) in the hexagonal 4-index notation) there are two sets of three different hexagonal monolayers each, hence  $q = 6$ , where the two sets are connected by inversion symmetry. Each set contains two monolayers with  $V^{3+}$  ions (originating from two different  $V^{3+}$  ions in the unit cell) and one with  $O^{2-}$  ions of higher density (originating from three different  $O^{2-}$  ions in the unit cell). This allows three different (0 0 0 1) surface terminations shown in Fig. 4.3, the **full metal** termination  $VV'O\dots$ , the **half metal** termination  $V'OV\dots$ , and the **oxygen** termination  $OVV'\dots$ . Experimental and theoretical studies on real  $V_2O_3(0\ 0\ 0\ 1)$  surfaces indicate that the half-metal  $V'OV\dots$  termination which is the least polar of the three terminations is energetically preferred [88].

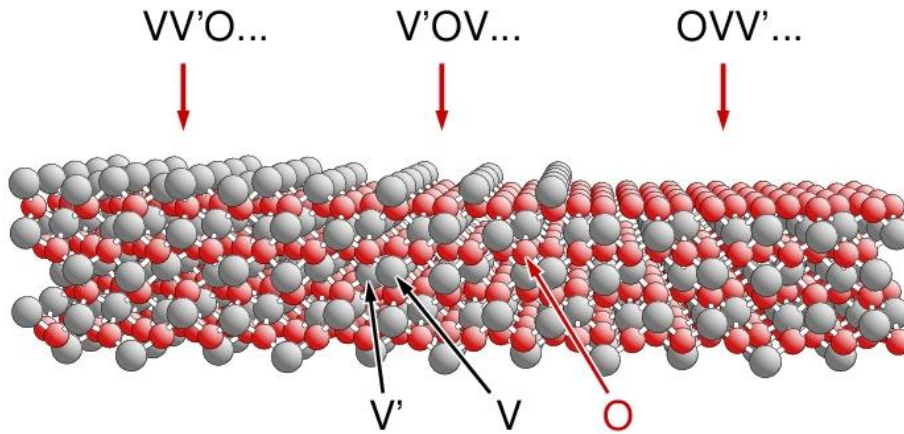


Fig. 4.3. Structure of the  $V_2O_3$  crystal (corundum lattice, trigonal-R) with three differently terminated  $(0\ 0\ 0\ 1)$  surfaces, denoted  $VV'O\dots$ ,  $V'OV\dots$ ,  $OVV'\dots$  and indicated by red arrows.

An even more complex example is the **vanadium pentoxide**,  $V_2O_5$ , crystal with an **orthorhombic-P** lattice [31], see Sec. 2.4. The primitive unit cell of  $V_2O_5$  contains **14** atoms,  $4 \times V$ ,  $10 \times O$ , yielding  $p = 14$ . This crystal has a **layer structure** and can be described by a periodic arrangement of weakly binding physical layers along the  $(0\ 1\ 0)$  direction. (Note that, depending on the choice of the orthorhombic crystal axes, this termination may also be called  $(0\ 0\ 1)$ .) Each physical layer contains **eight** different monolayers (two with  $V^{5+}$  ions, six with  $O^{2-}$  ions) indicated in Fig. 4.4, hence  $q = 8$ . This results formally in **eight** different  $(0\ 1\ 0)$  surface terminations. However, for chemical reasons, i.e. as a result of strong local binding between the atoms, the termination of the real surface is assumed to be described always as shown in Fig. 4.4. Here singly coordinated vanadyl oxygen (dark red balls), labeled '8' in the figure, forms the terminating monolayer [7].



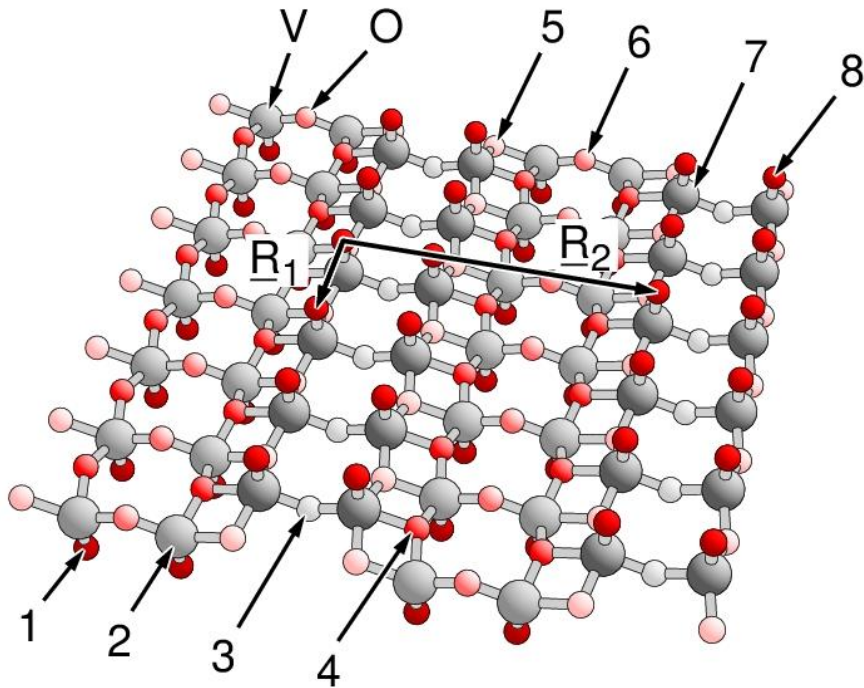


Fig. 4.4. Structure of a physical layer of the (0 1 0) surface of a  $V_2O_5$  crystal (orthorhombic lattice). Atoms (gray for V, red for O) are numbered with respect to their monolayer sequence inside the physical layer. The lattice vectors  $\underline{R}_1$ ,  $\underline{R}_2$  of the layer illustrate the surface periodicity.

All previous examples refer to single crystals which contain **inversion symmetry**. Therefore,  $(h k l)$  and  $(-h -k -l)$  oriented surfaces are equivalent and show the same termination schemes. This does not apply to single crystals without inversion centers, where  $(h k l)$  and  $(-h -k -l)$  oriented surfaces can be structurally different, which is also manifested in different physical and chemical properties. For example, **gallium arsenide**, GaAs, forms a crystal with a cubic **zincblende** lattice [31]. The primitive unit cell (fcc type) contains **two** atoms, Ga and As, yielding  $p = 2$ . This crystal has **no inversion symmetry** and, therefore, its monolayer stacking along the  $(1 1 1)$  direction differs from that along  $(-1 -1 -1)$ . Fig. 4.5 illustrates the structure of the two surfaces. The  $(1 1 1)$  surface allows two terminations, see Fig. 4.5a. Termination 1 yields arsenic atoms sitting on top of gallium at a large perpendicular distance to form the topmost hexagonal surface layer. Termination 2 yields a hexagonal surface layer of gallium atoms at the top, where these atoms are 3-fold coordinated with respect to the underlying As at a small perpendicular distance. The  $(-1 -1 -1)$  surface, see Fig. 4.5b offers the same two types of terminations as  $(1 1 1)$  except that the gallium and arsenic atoms are interchanged. Experiments indicate that termination 2 is energetically preferred for both surfaces resulting in a gallium terminated  $(1 1 1)$  and an arsenic terminated  $(-1 -1 -1)$  surface.

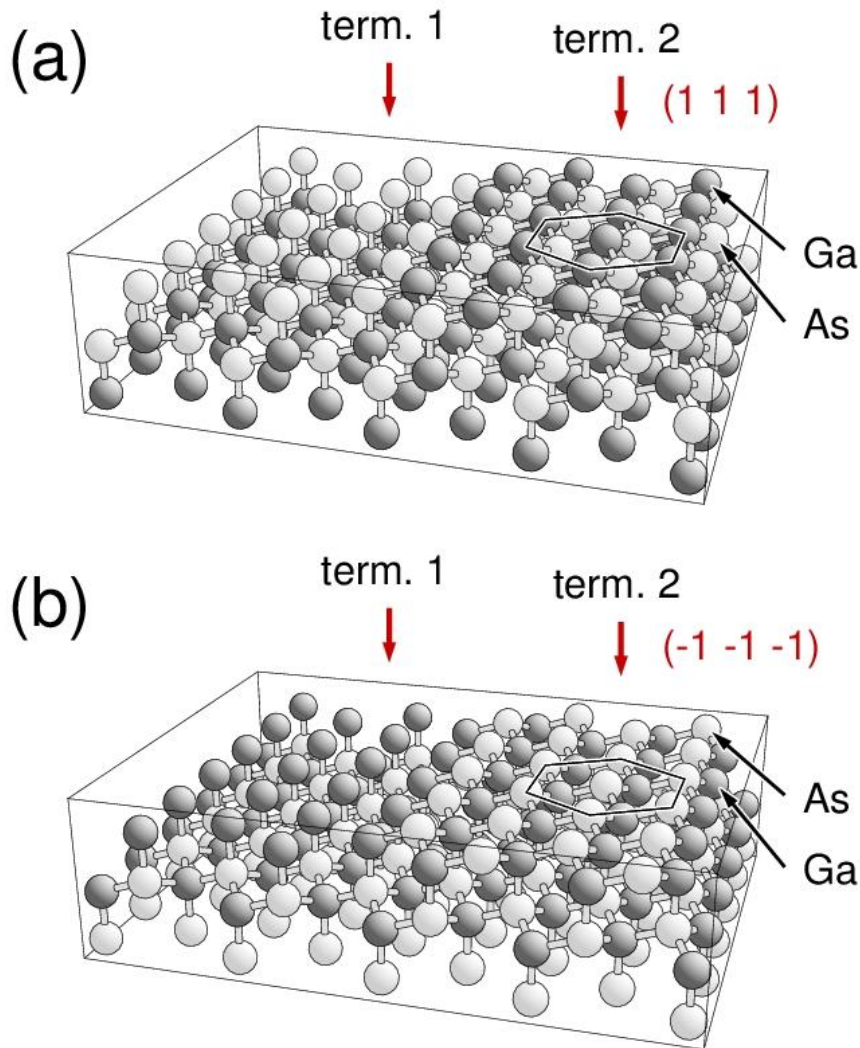


Fig. 4.5. Structure of different terminations of the ideal (a) (1 1 1) and (b) (-1 -1 -1) oriented surface of GaAs. In both cases, the two terminations are labeled 'term. 1' and 'term. 2' and atom balls are labeled accordingly. The hexagon to the right connects neighboring atoms of the topmost surface layer.

The truncation of a perfect three-dimensional crystal by a periodic surface yields the crystal substrate with atoms below and vacuum above. This poses the question as to which of the substrate atoms are assigned to the surface and which need to be considered as bulk atoms. The definition of **surface atoms** is not unique and depends to some extent on the physical or chemical parameters which are to be described. Considering structural properties, a reasonable choice is to define surface atoms by their neighbor environment. As discussed in Sec. 2.6, each atom inside a bulk crystal is surrounded by atom neighbors which can be grouped into shells depending on their distance from the atom under consideration. The distances and numbers of atoms of the shells are determined only by the bulk crystal structure. When atoms from the substrate are close to the surface their neighbor

shells become incomplete compared with the perfect bulk environment since atoms above the surface are missing. This shell behavior can be used to discriminate between bulk and surface atoms in a simple way: for a given number of shells, starting with the smallest, an atom will be considered a surface atom if any of its shells contains fewer atom members than obtained for the perfect bulk. Otherwise, the atom will be denoted as a bulk atom. In practice, for many low-Miller-index surfaces, first and second nearest neighbor shells are considered sufficient for a reasonable definition of surface atoms. The definition yields different results depending on the topmost layers of the  $(h k l)$  oriented surfaces. In particular, the number of surface layers required to reach the bulk part of the substrate will vary with  $(h k l)$ . As an example, Table 4.1 lists for selected  $(h k l)$  surfaces of the fcc crystal the number of atoms in neighbor shells (1<sup>st</sup> to 3<sup>rd</sup>) surrounding atoms of the topmost four monolayers of the surface. The different  $(h k l)$  entries are grouped according to decreasing monolayer density which shows that the number of topmost layers to reach the bulk from the surface increases as the monolayer density decreases. This is clear from the present definition of bulk atoms requiring a distance from the surface which is determined by bulk crystal parameters irrespective of the surface orientation. In contrast, the  $(h k l)$  oriented monolayers are separated by distances which decrease with decreasing monolayer density. This is clear for the vicinal stepped  $(9 9 7)$  surface with wide  $(1 1 1)$  terraces, shown in Fig. 4.6, where the first and second atom neighbor shells are completed only after 10 monolayers, and the third atom neighbor shell only after 18 monolayers. Thus, at stepped and (kinked) surfaces, all atoms on the terraces should be viewed as surface atoms.

Table 4.1. Atom neighbor shell behavior of selected  $(hkl)$  surfaces of the fcc crystal. Columns 2 to 5 give for each atom in monolayer 1 to 4 from the surface the number of atoms  $n_1, n_2, n_3$  in its 1<sup>st</sup> to 3<sup>rd</sup> neighbor shells. Numbers  $n_i$  are **boldfaced** if they reflect the bulk value. Column 6 lists smallest indices of layers with bulk atoms only, corresponding to  $n_1, n_2, n_3 = 12, 6, 24$ .

$(hkl)$	layer 1	2	3	4	Bulk layer
(1 1 1)	9, 3, 15	<b>12, 6, 21</b>	<b>12, 6, 24</b>	<b>12, 6, 24</b>	3
(1 0 0)	8, 5, 12	<b>12, 5, 20</b>	<b>12, 6, 24</b>	<b>12, 6, 24</b>	3
(1 1 0)	7, 4, 14	11, 4, 18	<b>12, 6, 20</b>	<b>12, 6, 24</b>	4
(3 1 1)	7, 3, 14	10, 5, 16	<b>12, 5, 19</b>	<b>12, 6, 23</b>	5
(3 3 1)	7, 3, 12	9, 4, 16	11, 4, 19	<b>12, 6, 19</b>	6
(2 1 0)	6, 4, 14	9, 4, 16	11, 5, 16	<b>12, 5, 20</b>	7
(2 1 1)	7, 3, 12	9, 3, 16	10, 5, 17	<b>12, 5, 19</b>	7
(9 9 7)	7, 3, 12	9, 3, 14	9, 3, 15	9, 3, 15	18

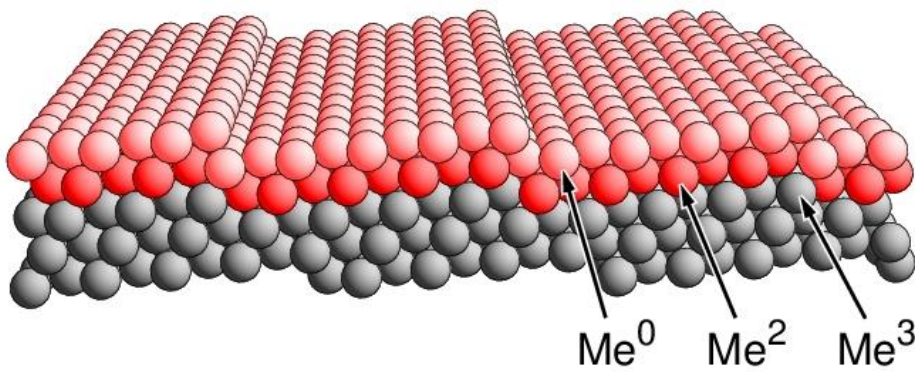


Fig. 4.6. Structure of the  $(9\ 9\ 7)$  surface of an fcc crystal with atoms near the surface emphasized. Atom balls with all neighbor shells incomplete ('true' surface atoms,  $Me^0$ ) are painted light red, those with first and second neighbor shells completed ( $Me^2$ ) dark red, and those with the first to third neighbor shells completed ('true' bulk atoms,  $Me^3$ ) gray.

## 4.2 Morphology of Surfaces, Stepped and Kinked Surfaces

The overall shapes (**morphology**) of  $(h k l)$  oriented single crystal surfaces are only partly determined by the geometry of corresponding  $(h k l)$  monolayers. Local binding between atoms, which may involve several monolayers, will also become important. This is particularly evident for oxide surfaces, where local binding dominates the detailed surface structure, as illustrated in Fig. 4.4 for the  $V_2O_5(0 1 0)$  surface. Here atoms from eight different  $(h k l)$  monolayers contribute to the shape of the surface. In more compact crystals the morphology of  $(h k l)$  oriented surfaces is characterized often by sections referring to **densest monolayers** of the crystal (microfacets) forming **terraces** and being separated by steps which may be straight **steps** or broken steps ('stepped steps', commonly called kinked steps or **kinks**). Since the  $(h k l)$  orientation of these surfaces is often quite close to those of the densest monolayers, they are usually called **vicinal** surfaces. As an example, the  $(7 7 9)$  surface of an fcc crystal, see Fig. 4.7, is described by  $(1 1 1)$  terraces (the  $(1 1 1)$  monolayers of the crystal are the densest) separated by steps originating from  $(0 0 1)$  monolayers. Thus, the  $(7 7 9)$  monolayer, which consists of a rather open set of parallel atom rows, shown in Fig. 4.7 by light balls, does not show the surface morphology.

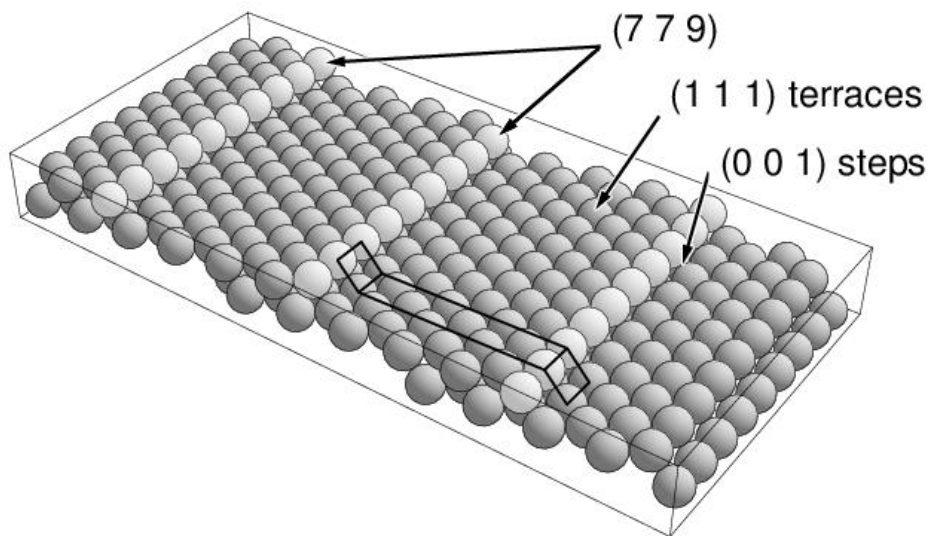


Fig. 4.7. Structure of the stepped  $(7 7 9)$  surface of an fcc crystal. Atom balls along the step lines (defining the  $(7 7 9)$  monolayer) are emphasized in light gray. Steps and terraces are labeled accordingly and illustrated by line frames.

Further, the  $(5 6 8)$  surface of an fcc crystal, see Fig. 4.8, is characterized by  $(1 1 1)$  terraces separated by periodically broken steps (kinked steps) originating from  $(0 0 1)$  and  $(-1 1 1)$  monolayers. As in the example before, the  $(5 6 8)$  monolayer which forms a very open set of atoms describ-

ing the kink corners, shown in Fig. 4.7 by red balls, does not show the surface morphology.

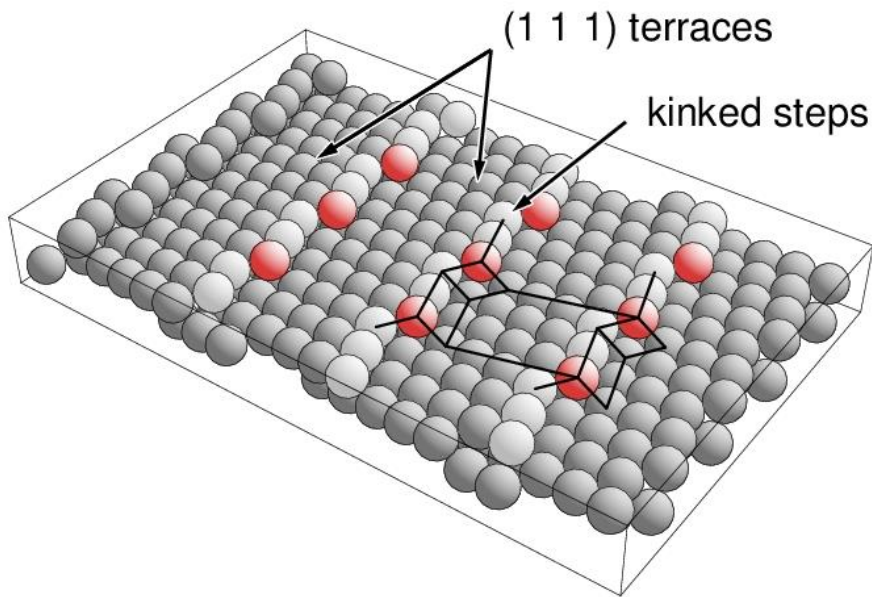


Fig. 4.8. Structure of the kinked (5 6 8) surface of an fcc crystal. Atom balls along the kink lines are emphasized in light gray and red (the latter defining the (5 6 8) monolayer). Kinks and terraces are illustrated by line frames.

Another complication can arise for crystal surfaces referring to **large Miller indices**. For example, fcc single crystal surfaces corresponding to  $(h k l) = (2m 1 1)$  and  $m > 1$  in sc notation can form alternating (1 0 0) terraces of widths given by  $m$  and  $m+1$  atom rows, respectively. The terraces are separated by (1 1 1) single height steps, see right part of Fig. 4.9 for  $m = 3$  corresponding to an fcc(6 1 1) surface. Removing all atoms from the smaller of the two terraces results in a stepped surface of identical (1 0 0) terraces of widths given by  $2m$  atom rows which are separated by (1 1 1) oriented double height steps as shown in the left part of Fig. 4.9. The appearance of steps (and kinks) of **multiple atom height** will be discussed in more detail in the next section. Other surface structures have also been discussed in Refs. [89], [90], [91], [92].

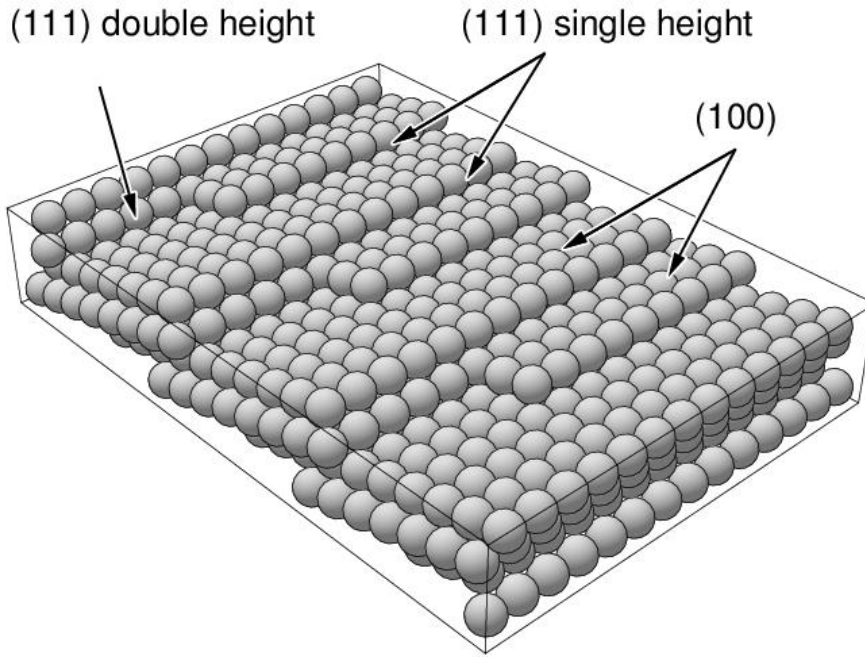


Fig. 4.9. Structure of the stepped  $(6\ 1\ 1)$  surface of a crystal with an fcc lattice, left part with double height steps and identical terraces, right part with single height steps and alternating narrow and wide terraces.

From the examples of Fig. 4.7 it is clear that **step edges** at single crystal surfaces are formed by periodic atom rows along general lattice vectors  $\underline{\mathbf{R}}_N$  (**step edge vectors**) which connect neighboring atoms referring to rather small interatomic distances. Thus, the periodicity of surfaces containing steps along  $\underline{\mathbf{R}}_N$  is described by netplanes parallel to  $\underline{\mathbf{R}}_N$ . As a consequence, corresponding monolayer normal vectors, pointing along reciprocal lattice vectors  $\underline{\mathbf{G}}_{(h\ k\ l)}$  according to (3.6), must be perpendicular to  $\underline{\mathbf{R}}_N$ . Thus, representations

$$\underline{\mathbf{R}}_N = p_1 \underline{\mathbf{R}}_1 + p_2 \underline{\mathbf{R}}_2 + p_3 \underline{\mathbf{R}}_3 \quad , \quad \underline{\mathbf{G}}_{(h\ k\ l)} = h \underline{\mathbf{G}}_1 + k \underline{\mathbf{G}}_2 + l \underline{\mathbf{G}}_3 \quad (4.1)$$

with integer  $p_i$  and  $h, k, l$  yield

$$\begin{aligned} \underline{\mathbf{R}}_N \underline{\mathbf{G}}_{(h\ k\ l)} &= (p_1 \underline{\mathbf{R}}_1 + p_2 \underline{\mathbf{R}}_2 + p_3 \underline{\mathbf{R}}_3) (h \underline{\mathbf{G}}_1 + k \underline{\mathbf{G}}_2 + l \underline{\mathbf{G}}_3) = \\ &= 2\pi (p_1 h + p_2 k + p_3 l) = 0 \end{aligned} \quad (4.2)$$

where the orthogonality relation of real and reciprocal lattice vectors (2.96) has been applied. Relation (4.2) can be used to find  $(h\ k\ l)$ -indexed surfaces for a given edge vector  $\underline{\mathbf{R}}_N$  but also to verify edge vectors  $\underline{\mathbf{R}}_N$  at a stepped  $(h\ k\ l)$  surface.

As an example, we consider the **fcc lattice**, defined by (2.102) and represented by simple cubic lattice vectors  $\underline{\mathbf{R}}_1, \underline{\mathbf{R}}_2, \underline{\mathbf{R}}_3$  in Cartesian coordinates. Then vectors  $\underline{\mathbf{R}}_N$  connecting nearest neighbors

are given by

$$\underline{\mathbf{R}}_N = \pm a/2 (0, 1, \pm 1), \pm a/2 (1, 0, \pm 1), \pm a/2 (1, \pm 1, 0) \quad (4.3)$$

Relation (4.2) together with (4.3) and using  $(h k l)$  in sc notation results in six linear Diophantine equations

$$h \pm k = 0, \quad h \pm l = 0, \quad k \pm l = 0 \quad (4.4)$$

with solutions

$$(h k l) = (m \pm m n), \quad = (m n \pm m), \quad = (m n \pm n), \quad m, n \text{ integer} \quad (4.5)$$

These Miller index triplets characterize orientations of all fcc surfaces with steps formed by rows of nearest neighbor atoms (which also include the atomically flat surfaces given by  $(\pm 1 \pm 1 \pm 1)$ ,  $(0 0 \pm 1)$ ).

If vectors  $\underline{\mathbf{R}}_N$  connecting second nearest neighbors, given by

$$\underline{\mathbf{R}}_N = \pm a (1, 0, 0), \pm a (0, 1, 0), \pm a (0, 0, 1) \quad (4.6)$$

are considered, an analogous procedure yields Miller index triplets

$$(h k l) = (0 m n), \quad = (m 0 n), \quad = (m n 0), \quad m, n \text{ integer} \quad (4.7)$$

defining orientations of all fcc surfaces with steps formed by rows of second nearest neighbor atoms (which also include the atomically flat surfaces given by  $(\pm 1 0 0)$ ,  $(0 \pm 1 0)$ ,  $(0 0 \pm 1)$ ).

### 4.3 Miller Index Decomposition

Surfaces with large Miller index values  $(h k l)$  correspond, according to (3.8), to rather open monolayers of low atom density. They can be characterized in many cases morphologically by combinations of **terraces** with  $(h_t k_t l_t)$  orientation separated by **steps** with  $(h_s k_s l_s)$  orientation, as discussed in the previous section. Here the Miller index triplets  $(h k l)$ ,  $(h_t k_t l_t)$ , and  $(h_s k_s l_s)$  are connected by an **additivity theorem** which is discussed in the following.

Starting from a **monoatomic** single crystal with its primitive lattice described by lattice vectors  $\underline{\mathbf{R}}_{o1}$ ,  $\underline{\mathbf{R}}_{o2}$ ,  $\underline{\mathbf{R}}_{o3}$  a **stepped surface** looks like that shown in Fig. 4.10, which sketches the stepped  $(3 3 5)$  surface of an fcc crystal. Here, step-adapted lattice vectors  $\underline{\mathbf{R}}_1$ ,  $\underline{\mathbf{R}}_2$ ,  $\underline{\mathbf{R}}_3$  can be constructed where  $\underline{\mathbf{R}}_1$  and  $\underline{\mathbf{R}}_2$  describe the periodicity of the terrace monolayers



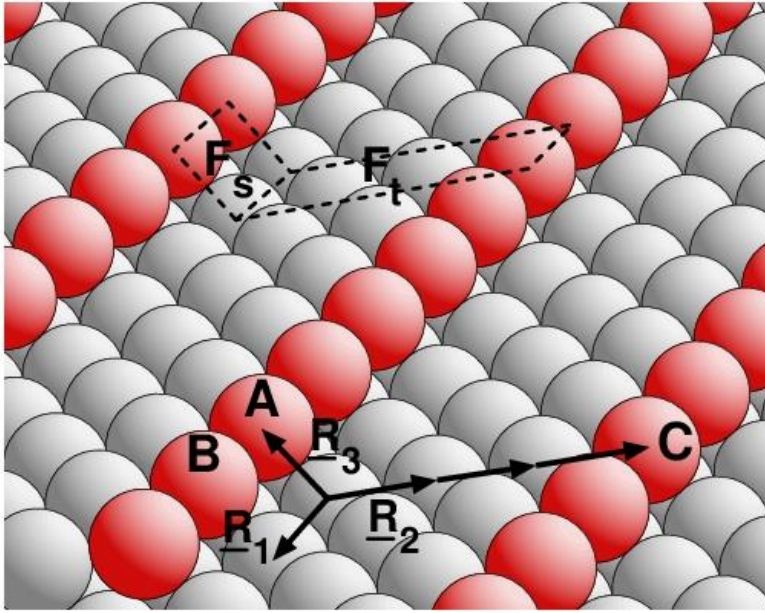


Fig. 4.10. Scheme of a Miller index decomposition for the stepped (3 3 5) surface of an fcc crystal. The atom balls along the step lines, forming a (3 3 5) monolayer are emphasized in red. The step-adapted lattice vectors  $\underline{R}_1$ ,  $\underline{R}_2$ ,  $\underline{R}_3$  are sketched accordingly. The elementary terrace and step sections of area  $F_t$  and  $F_s$ , respectively, are framed by dashed lines.

with  $\underline{R}_1$  pointing along the step edges and  $\underline{R}_3$  along the connection between the lower and upper edge of each step. Let us assume further that terraces are  $n_t$  vector lengths  $\underline{R}_2$  ‘wide’ and the steps are  $n_s$  vector lengths  $\underline{R}_3$  ‘high’ ( $n_t = 3$  and  $n_s = 1$  in Fig. 4.10). Then the atoms at two adjacent step edges, A, B, and at C in Fig. 4.10, determine a plane with a normal vector defining the  $(h k l)$  direction of the stepped surface while  $\underline{R}_1$  and  $\underline{R}_2$  refer to  $(h_t k_t l_t)$  of the terrace and  $\underline{R}_3$  and  $\underline{R}_1$  to  $(h_s k_s l_s)$  of the step side ( $(h k l) = (3 3 5)$ ,  $(h_t k_t l_t) = (1 1 1)$ , and  $(h_s k_s l_s) = (0 0 2)$  in Fig. 4.10). As a result, the **reciprocal lattice vector**  $\underline{G}_{(h k l)}$  of the **stepped surface**, which is perpendicular to the plane through atoms A, B, and C, is determined by

$$\begin{aligned} \underline{G}_{(h k l)} &= 2\pi/\beta (\underline{AB} \times \underline{AC}) = 2\pi/\beta \{ \underline{R}_1 \times (n_t \underline{R}_2 - n_s \underline{R}_3) \} = \\ &= 2\pi/\beta \{ n_t (\underline{R}_1 \times \underline{R}_2) + n_s (\underline{R}_3 \times \underline{R}_1) \} = n_t \underline{G}_{(h k l)_t} + n_s \underline{G}_{(h k l)_s} \\ \beta &= (\underline{R}_1 \times \underline{R}_2) \underline{R}_3 \end{aligned} \quad (4.8)$$

Thus, after the three reciprocal lattice vectors have been decomposed into their Miller index combinations, one obtains the **additivity theorem for stepped surfaces**

$$(h k l) = n_t (h_t k_t l_t) + n_s (h_s k_s l_s) \quad (4.9)$$

The **scalar factors**  $n_t$ ,  $n_s$  in this equation have a simple geometric meaning. The elementary

terrace section defined as the periodic repeat cell along the terrace, sketched by dashed lines in Fig. 4.10, has an area  $F_t$ , where

$$F_t = n_t | \underline{\mathbf{R}}_1 \times \underline{\mathbf{R}}_2 | = n_t (V_{el}/2\pi) |G_{(h k l)_t}| \quad (4.10)$$

while the area  $F_s$  of the repeat cell of step side, also sketched by dashed lines in Fig. 4.10, is given by

$$F_s = n_s | \underline{\mathbf{R}}_3 \times \underline{\mathbf{R}}_1 | = n_s (V_{el}/2\pi) |G_{(h k l)_s}| \quad (4.11)$$

where  $| \underline{\mathbf{R}}_i \times \underline{\mathbf{R}}_j |$  are the unit cell areas of the corresponding terrace and step planes. Thus, the factors  $n_t$  and  $n_s$  in (4.8) and (4.9), respectively, define the relative sizes of the periodic repeat cells along the terraces and the steps with respect to their corresponding unit cell areas. The definition of terraces and steps requires that the terrace area  $F_t$  be larger than that of the separating step  $F_s$ . Thus, if the elementary cells  $| \underline{\mathbf{R}}_1 \times \underline{\mathbf{R}}_2 |$  and  $| \underline{\mathbf{R}}_3 \times \underline{\mathbf{R}}_1 |$  are of comparable size the scalar factor  $n_t$  in (4.9) will be larger than  $n_s$  and  $(h_t k_t l_t)$  will be the dominant component of the  $(h k l)$  triplet. In this spirit, the  $(h k l)$  oriented surface will be called **vicinal surface** with the  $(h_t k_t l_t)$  (terrace) surface representing the **vicinal partner**. Thus, the stepped fcc(3 3 5) surface shown in Fig. 4.10 which decomposes to

$$(3 \ 3 \ 5) = 3 (1 \ 1 \ 1) + 1 (0 \ 0 \ 2)$$

is vicinal, with  $(1 \ 1 \ 1)$  being the vicinal partner.

The additivity theorem (4.9) is the basis of the so-called **step notation** [93], [94] of stepped vicinal surfaces according to which an  $(h k l)$  surface is, in its general form, denoted as

$$(h k l) \equiv [ p_1 (h_t k_t l_t) \times p_2 (h_s k_s l_s) ] , \quad p_1 = n_t + 1 , \quad p_2 = n_s \quad (4.12)$$

Here the terrace width of  $n_t \underline{\mathbf{R}}_2$  used above corresponds to  $(n_t + 1)$  rows of terrace atoms used in the definition of the step notation. This definition was initially proposed for surfaces of **cubic crystals** (face- and body-centered) with Miller indices of simple cubic notation and single steps ( $n_s = 1$ ) [93] whereas the additivity theorem is more general and independent of the lattice type. Further, each of the Miller index triplets  $(h k l)$ ,  $(h_t k_t l_t)$ , and  $(h_s k_s l_s)$  in notation (4.12) is assumed to be scaled such that its indices do not have a common divisor. For example  $(2 \ 2 \ 0)$  is written as  $(1 \ 1 \ 0)$ . Examples of the additivity theorem (4.9) for crystals with simple (sc), face-centered (fcc), and body-centered (bcc) cubic lattices together with the corresponding step notations are given in the Table 4.2.

Table 4.2. Decomposition of Miller indices of vicinal stepped surfaces of crystals with sc, fcc, and bcc lattices. The table includes corresponding step notations, see

text. Labels (sc) and (gen) refer to simple cubic and generic index notation. Constant  $p$  can assume any positive integer value.

$(h\ k\ l) = n_t (h_t\ k_t\ l_t) + n_s (h_s\ k_s\ l_s)$	Step notation
<b>fcc (sc):</b> $(7\ 7\ 5) = 6(1\ 1\ 1) + (1\ 1\ -1)$ $(3\ 3\ 5) = 3(1\ 1\ 1) + (0\ 0\ 2)$ $(9\ 1\ 1) = 4(2\ 0\ 0) + (1\ 1\ 1)$ $(p+2\ p+2\ p) = (p+1)(1\ 1\ 1) + (1\ 1\ -1)$ $(p+2\ p\ p) = p(1\ 1\ 1) + (2\ 0\ 0)$ $(2p+1\ 1\ 1) = p(2\ 0\ 0) + (1\ 1\ 1)$	$[7(1\ 1\ 1) \times (1\ 1\ -1)]$ $[4(1\ 1\ 1) \times (0\ 0\ 1)]$ $[5(1\ 0\ 0) \times (1\ 1\ 1)]$ $[(p+2)(1\ 1\ 1) \times (1\ 1\ -1)]$ $[(p+1)(1\ 1\ 1) \times (1\ 0\ 0)]$ $[(p+1)(1\ 0\ 0) \times (1\ 1\ 1)]$
<b>fcc (gen):</b> $(5\ 5\ 1) = 4(1\ 1\ 0) + (1\ 1\ 1)$ $(4\ 3\ 2) = 3(1\ 1\ 1) + (1\ 0\ -1)$	$[5(1\ 1\ 0) \times (1\ 1\ 1)]$ $[4(1\ 1\ 1) \times (1\ 0\ -1)]$
<b>bcc (sc):</b> $(5\ 5\ 2) = 5(1\ 1\ 0) + (0\ 0\ 2)$ $(6\ 6\ 10) = 5(1\ 1\ 2) + (1\ 1\ 0)$ $(8\ 1\ 1) = 4(2\ 0\ 0) + (0\ 1\ 1)$ $(p\ p\ 2) = p(1\ 1\ 0) + (0\ 0\ 2)$ $(p+1\ p+1\ 2p) = p(1\ 1\ 2) + (1\ 1\ 0)$ $(2p\ 1\ 1) = p(2\ 0\ 0) + (0\ 1\ 1)$	$[6(1\ 1\ 0) \times (0\ 0\ 1)]$ $[6(1\ 1\ 2) \times (1\ 1\ 0)]$ $[5(2\ 0\ 0) \times (0\ 1\ 1)]$ $[(p+1)(1\ 1\ 0) \times (0\ 0\ 1)]$ $[(p+1)(1\ 1\ 2) \times (1\ 1\ 0)]$ $[(p+1)(1\ 0\ 0) \times (0\ 1\ 1)]$
<b>bcc (gen):</b> $(4\ 1\ 1) = 4(1\ 0\ 0) + (0\ 1\ 1)$ $(1\ 1\ 2) = 2(0\ 0\ 1) + (1\ 1\ 0)$	$[5(1\ 0\ 0) \times (0\ 1\ 1)]$ $[3(0\ 0\ 1) \times (1\ 1\ 0)]$
<b>sc (gen):</b> $(9\ 1\ 1) = 9(1\ 0\ 0) + (0\ 1\ 1)$	$[10(1\ 0\ 0) \times (0\ 1\ 1)]$

Surfaces, for which the decomposition (4.9) suggests **multiple-atom-height steps**,  $n_s > 1$ , can give rise to more complex structural behavior depending on local binding. For strong nearest neighbor binding, like in metals with fcc and bcc lattices, these surfaces still form single-height steps with minimal variation of their terrace widths even if  $n_s > 1$ . Here the multiple-atom-height step region, which has terraces of ‘width’  $n_t \underline{R}_2$  and steps of ‘height’  $n_s \underline{R}_3$ , is partitioned in  $n_s$  additional **subterraces**,

$$\begin{aligned}
 &((p+1)n_s - n_t) \quad \text{terraces A of width } p \underline{R}_2 \quad \text{and} \\
 &(n_t - p n_s) \quad \text{terraces B of width } (p+1) \underline{R}_2, \quad p = [n_t / n_s] \quad (4.13)
 \end{aligned}$$

where  $[x]$  denotes the integer truncation function. (The mathematics behind this partitioning is

spelled out in Appendix E.1.) As an example, the (15 15 23) surface of a crystal with an fcc lattice, see Fig. 4.11, is decomposed in (1 1 1) terraces and (0 0 1) steps according to

$$(15\ 15\ 23) = 15(1\ 1\ 1) + 4(0\ 0\ 2)$$

with four subterraces, one type A of width  $3\ \underline{R}_2$  and three type B of widths  $4\ \underline{R}_2$  filling the initial multiple-step region with  $4\ \underline{R}_3$  'high' steps and  $15\ \underline{R}_2$  'wide' terraces.

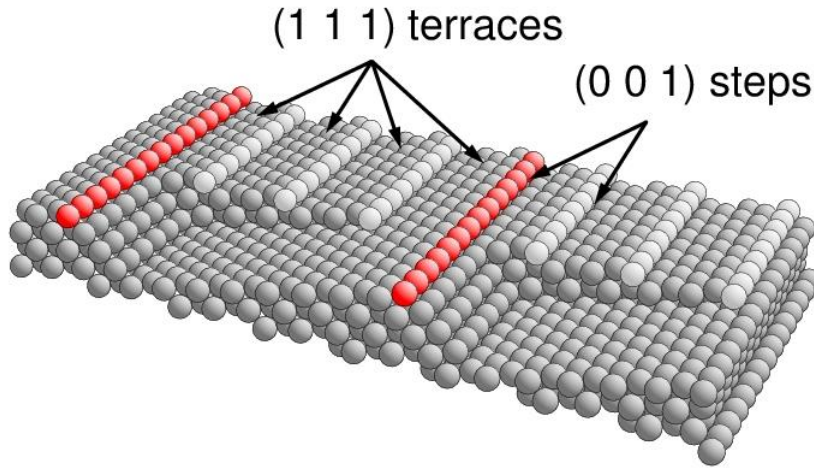


Fig. 4.11. Structure of the stepped (15 15 23) surface of an fcc crystal, with multiple-atom-height steps (front) as well as with single-height steps and subterraces of variable width (back).

The partitioning of multiple-atom-height step regions into subterraces A, B separated by single-height steps according to (4.13) yields subterrace sequences which in general are not regular and can be evaluated by number theoretical methods as described in Appendix E.1. However, these exact mathematical sequences may not be observed at real crystal surfaces where diffusion processes also determine the different widths of subterraces with single-height steps for a given surface orientation  $(h\ k\ l)$ .

Surfaces with large Miller index values  $(h\ k\ l)$  can also be characterized morphologically in some cases by combinations of terraces with  $(h_t\ k_t\ l_t)$  orientation separated by **kinked steps** with  $(h_{s1}\ k_{s1}\ l_{s1})$  and  $(h_{s2}\ k_{s2}\ l_{s2})$  orientation. Analogous to stepped surfaces the Miller index triplets  $(h\ k\ l)$ ,  $(h_t\ k_t\ l_t)$ ,  $(h_{s1}\ k_{s1}\ l_{s1})$ , and  $(h_{s2}\ k_{s2}\ l_{s2})$  are connected by an **additivity theorem** which is proven in the following.

Starting from a **monoatomic** single crystal with its primitive lattice described by  $\underline{R}_{o1}$ ,  $\underline{R}_{o2}$ ,  $\underline{R}_{o3}$  a **kinked surface** looks like that shown in Fig. 4.12 which sketches the kinked fcc(11 13 19) surface. Here, kink-adapted lattice vectors  $\underline{R}_1$ ,  $\underline{R}_2$ ,  $\underline{R}_3$  can be constructed where  $\underline{R}_1$  and  $\underline{R}_2$  describe the

periodicity of the terrace monolayers, with the two vectors pointing along the two kink directions and  $\underline{R}_3$  along the connection between the lower and upper corner of a kink.

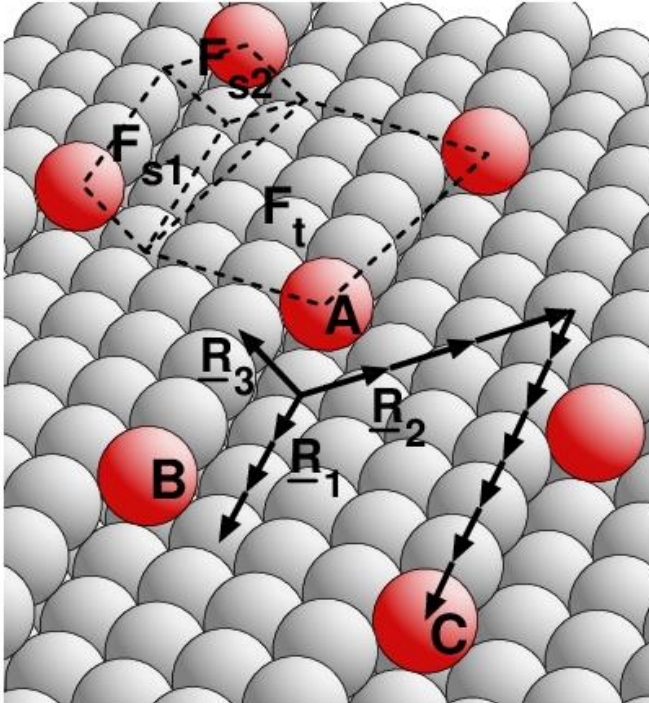


Fig. 4.12. Scheme of a Miller index decomposition for the kinked  $(11\ 13\ 19)$  surface of an fcc crystal. The atom balls at the kink centers, forming a  $(11\ 13\ 19)$  monolayer are emphasized in red. The kink-adapted lattice vectors  $\underline{R}_1$ ,  $\underline{R}_2$ ,  $\underline{R}_3$  are sketched accordingly. The elementary terrace and two kink sections of area  $F_t$ ,  $F_{s1}$  and  $F_{s2}$  are framed by dashed lines.

Let us assume further that the two kink edges are  $m_1$ ,  $m_2$  vector lengths  $\underline{R}_1$ ,  $\underline{R}_2$  ‘long’ ( $m_1 = 3$  and  $m_2 = 1$  in Fig. 4.12) and the terrace width between kinked steps is described by a vector  $\underline{R}_t = n_1 \underline{R}_1 + n_2 \underline{R}_2$  connecting the lower corner of one kink with the upper corner of an adjacent kink ( $n_1 = 6$  and  $n_2 = 3$  in Fig. 4.12). In addition, the kinks are assumed to be  $n_s$  vector lengths  $\underline{R}_3$  ‘high’ ( $n_s = 1$  in Fig. 4.12). Then the atoms at corners of adjacent kink lines, A, B, and C in Fig. 4.12, determine a plane with a normal vector defining the  $(h\ k\ l)$  direction of the kinked surface. Further,  $\underline{R}_1$  and  $\underline{R}_2$  refer to  $(h_t\ k_t\ l_t)$  of the terrace,  $\underline{R}_3$  and  $\underline{R}_1$  to  $(h_{s1}\ k_{s1}\ l_{s1})$  of one kink side, and  $\underline{R}_2$  and  $\underline{R}_3$  to  $(h_{s2}\ k_{s2}\ l_{s2})$  of the other kink side ( $(h\ k\ l) = (11\ 13\ 19)$ ,  $(h_t\ k_t\ l_t) = (1\ 1\ 1)$ ,  $(h_{s1}\ k_{s1}\ l_{s1}) = (0\ 0\ 2)$ ,  $(h_{s2}\ k_{s2}\ l_{s2}) = (-1\ 1\ 1)$  in Fig. 4.12). As a result, the **reciprocal lattice vector**  $\underline{G}_{(h\ k\ l)}$  of the **kinked surface**, which is perpendicular to the plane through atoms A, B, and C, is determined by

$$\begin{aligned}
\underline{G}_{(hkl)} &= 2\pi/\beta (\underline{AB} \times \underline{AC}) \\
&= 2\pi/\beta (m_1 \underline{R}_1 - m_2 \underline{R}_2) \times (n_1 \underline{R}_1 + n_2 \underline{R}_2 - m_2 \underline{R}_2 - n_s \underline{R}_3) \\
&= 2\pi/\beta \{ (m_1 n_2 + m_2 n_1 - m_1 m_2) (\underline{R}_1 \times \underline{R}_2) + m_1 n_s (\underline{R}_3 \times \underline{R}_1) + m_2 n_s (\underline{R}_2 \times \underline{R}_3) \} \\
&= (m_1 n_2 + m_2 n_1 - m_1 m_2) \underline{G}_{(hkl)_t} + m_1 n_s \underline{G}_{(hkl)_{s1}} + m_2 n_s \underline{G}_{(hkl)_{s2}} \\
\beta &= (\underline{R}_1 \times \underline{R}_2) \cdot \underline{R}_3 \tag{4.14}
\end{aligned}$$

Thus, after the four reciprocal lattice vectors have been decomposed into their Miller index combinations, one obtains the **additivity theorem for kinked surfaces**

$$(hkl) = (m_1 n_2 + m_2 n_1 - m_1 m_2) (h_t k_t l_t) + m_1 n_s (h_{s1} k_{s1} l_{s1}) + m_2 n_s (h_{s2} k_{s2} l_{s2}) \tag{4.15}$$

The **scalar factors** in this equation have a simple geometric meaning. The elementary terrace section defined as the periodic repeat cell along the terrace, sketched by dashed lines in Fig. 4.12, has an area  $F_t$ , where

$$F_t = p_t |\underline{R}_1 \times \underline{R}_2| = p_t (V_{el}/2\pi) |\underline{G}_{(hkl)_t}|, \quad p_t = (m_1 n_2 + m_2 n_1 - m_1 m_2) \tag{4.16}$$

while the areas  $F_{s1}$ ,  $F_{s2}$  of the two kink step sides, also sketched by dashed lines, are given by

$$F_{s1} = p_{s1} |\underline{R}_3 \times \underline{R}_1| = p_{s1} (V_{el}/2\pi) |\underline{G}_{(hkl)_{s1}}|, \quad p_{s1} = m_1 n_s \tag{4.17}$$

$$F_{s2} = p_{s2} |\underline{R}_2 \times \underline{R}_3| = p_{s2} (V_{el}/2\pi) |\underline{G}_{(hkl)_{s2}}|, \quad p_{s2} = m_2 n_s \tag{4.18}$$

where  $|\underline{R}_i \times \underline{R}_j|$  are the unit cell areas of the corresponding terrace and step planes. Thus, the factors  $p_t$ ,  $p_{s1}$ ,  $p_{s2}$  in (4.14), (4.15) define the relative sizes of the periodic repeat cells along the terraces and the two types of steps along the kink line with respect to their corresponding unit cell areas. The definition of terraces and steps requires that the terrace area  $F_t$  is larger than that of the separating steps  $F_{s1}$  and  $F_{s2}$ . Thus, if the elementary cells  $|\underline{R}_1 \times \underline{R}_2|$ ,  $|\underline{R}_3 \times \underline{R}_1|$ , and  $|\underline{R}_2 \times \underline{R}_3|$  are of comparable size the scalar factor  $p_t$  in (4.16) will be larger than  $p_{s1}$  and  $p_{s2}$  and  $(h_t k_t l_t)$  will be the dominant component of the  $(hkl)$  triplet. In this spirit, the  $(hkl)$  oriented surface will be called **vicinal surface** with the  $(h_t k_t l_t)$  (terrace) surface representing the **vicinal partner**. Thus, the kinked fcc(11 13 19) surface shown in Fig. 4.12 which decomposes to

$$(11\ 13\ 19) = 12(1\ 1\ 1) + 3(0\ 0\ 2) + 1(-1\ 1\ 1) \tag{4.19}$$

is vicinal with  $(1\ 1\ 1)$  being the vicinal partner.

The additivity theorem (4.15) for kinked surfaces can be written alternatively as

$$(hkl) = p_t (h_t k_t l_t) + n_s (h'_s k'_s l'_s) \tag{4.20}$$

with  $p_t$  according to (4.16) and

$$(h_s' k_s' l_s') = m_1 (h_{s1} k_{s1} l_{s1}) + m_2 (h_{s2} k_{s2} l_{s2}) \quad (4.21)$$

where relations (4.20) and (4.21) are identical to the additivity theorem (4.9) for stepped surfaces. Therefore, the kinked surface can also be understood as a stepped surface whose terraces are separated by 'steps' which themselves are characterized in their orientation by stepped surfaces. As an example, the kinked fcc(11 13 19) surface shown in Fig. 4.12 with a decomposition according to (4.19) can also be interpreted as a combination of the 'stepped' surface

$$(11\ 13\ 19) = 12(1\ 1\ 1) + 1(-1\ 1\ 7)$$

with the stepped surface

$$(-1\ 1\ 7) = 3(0\ 0\ 2) + 1(-1\ 1\ 1)$$

The distinction between kinked and stepped surfaces becomes questionable in cases where the kink line sections are very short. As an illustration, Fig. 4.13 shows the fcc(10 2 0) surface which allows an interpretation as a kinked surface with (2 0 0) terraces and (1 1 1) / (1 1 -1) kink steps (sections a, b, c) according to

$$(10\ 2\ 0) = 4(2\ 0\ 0) + 1(1\ 1\ 1) + 1(1\ 1\ -1)$$

but also as a stepped surface with (2 0 0) terraces separated by (2 2 0) steps (sections a, d) according to

$$(10\ 2\ 0) = 4(2\ 0\ 0) + 1(2\ 2\ 0)$$

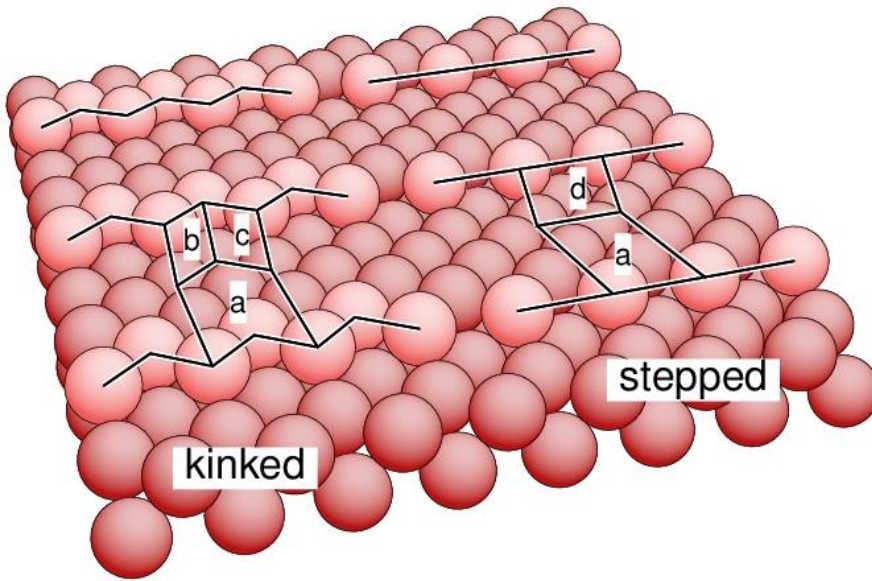


Fig. 4.13. Structure of the  $(10\ 2\ 0)$  surface of an fcc crystal. Step and kink atoms are emphasized by lighter color. The kink decomposition is shown to the left (repeat cells labeled a, b, c and outlined by black lines). The step decomposition is shown to the right (repeat cells labeled a, d).

The additivity theorem (4.15) is the basis of the so-called **microfacet notation** [94], [95] of vicinal surfaces according to which an  $(h\ k\ l)$  surface is, in its general form, denoted as

$$(h\ k\ l) = a_{\lambda} (h_t\ k_t\ l_t) + b_{\mu} (h_{s1}\ k_{s1}\ l_{s1}) + c_{\nu} (h_{s2}\ k_{s2}\ l_{s2}) \quad (4.22)$$

This notation was initially proposed for crystals with **cubic lattices** (face- and body-centered) and Miller indices of simple cubic notation and single steps only, whereas the additivity theorem is more general and independent of the lattice type. Further, each of the Miller index triplets  $(h\ k\ l)$ ,  $(h_t\ k_t\ l_t)$ ,  $(h_{s1}, k_{s1}, l_{s1})$ , and  $(h_{s2}, k_{s2}, l_{s2})$  in (4.22) is assumed to be scaled such that its indices do not have a common divisor. For example  $(12\ 8\ 4)$  is written as  $(3\ 2\ 1)$ . In addition, parameters a, b, c and  $\lambda$ ,  $\mu$ ,  $\nu$  are chosen as independent numbers (resulting in indexed number quantities like ‘ $3_4$ ’), where  $\lambda$ ,  $\mu$ ,  $\nu$  denote the true decomposition given by (4.15) with

$$\lambda = p_1 \quad , \quad \mu = p_2 \quad , \quad \nu = p_3 \quad (4.23)$$

according to (4.16), (4.17), (4.18) while parameters a, b, c are scaled further to guarantee the additivity of the Miller indices in (4.22) which can be expressed formally by

$$\begin{aligned} a &= (p_1 / \chi) \gcd(h_t, k_t, l_t) \quad , \quad b = (p_2 / \chi) \gcd(h_{s2}, k_{s2}, l_{s2}) \\ c &= (p_3 / \chi) \gcd(h_{s2}, k_{s2}, l_{s2}) \quad , \quad \chi = \gcd(h, k, l) \end{aligned} \quad (4.24)$$

with  $\gcd(n_1, n_2, n_3)$  denoting the greatest common divisor of the three integers  $n_1, n_2, n_3$ , see Appen-



dix E.1.

As an example, for a crystal with an fcc lattice the additivity theorem for the (20 16 14) indexed surface (simple cubic notation) reads

$$(20\ 16\ 14) = 15(1\ 1\ 1) + 2(2\ 0\ 0) + (1\ 1\ -1)$$

while the corresponding microfacet notation reads

$$(10\ 8\ 7) = (15/2)_{15}(1\ 1\ 1) + 2_2(1\ 0\ 0) + (1/2)_1(1\ 1\ -1)$$

Using generic Miller indices or simple cubic Miller indices with the correct numerical constraints, see (3.20b), (3.25b), yields

$$\mathbf{a} = \lambda = p_1 \quad , \quad \mathbf{b} = \mu = p_2 \quad , \quad \mathbf{c} = \nu = p_3 \quad (4.25)$$

making the indexed numbers unnecessary and resulting in a notation according to the additivity theorem (4.15). Examples of the additivity theorem for crystals with fcc and bcc lattices together with corresponding microfacet notations are given in Table 4.3.

Table 4.3. Decomposition of Miller indices of vicinal kinked surfaces of crystals with fcc and bcc lattices. The table includes corresponding microfacet notations, see text. Labels (sc) and (gen) refer to the Miller index notations, simple cubic and generic Bravais, see above, and constant p can assume any positive integer value.

$(h, k, l) = \mathbf{a}(h_t k_t l_t) + \mathbf{b}(h_{s1} k_{s1} l_{s1}) + \mathbf{c}(h_{s2} k_{s2} l_{s2})$	Microfacet notation
<b>fcc (sc):</b> $(17\ 11\ 9) = 10(1\ 1\ 1) + 3(2\ 0\ 0) + (1\ 1\ -1)$ $(11\ 3\ 1) = 4(2\ 0\ 0) + 2(1\ 1\ 1) + (1\ 1\ -1)$ $(17\ 15\ 1) = 7(2\ 2\ 0) + (1\ 1\ 1) + (2\ 0\ 0)$ $(2p+7\ 2p+1\ 2p-1) = 2p(1\ 1\ 1) + 3(2\ 0\ 0) + (1\ 1\ -1)$ $(2p+1\ 3\ 1) = (p-1)(2\ 0\ 0) + 2(1\ 1\ 1) + (1\ 1\ -1)$ $(2p+1\ 2p-1\ 1) = (p-1)(2\ 2\ 0) + (1\ 1\ 1) + (2\ 0\ 0)$	$10_{10}(1\ 1\ 1) + 6_3(1\ 0\ 0) + 1_1(1\ 1\ -1)$ $8_4(1\ 0\ 0) + 2_2(1\ 1\ 1) + 1_1(1\ 1\ -1)$ $14_7(1\ 1\ 0) + 1_1(1\ 1\ 1) + 2_1(1\ 0\ 0)$ $(2p)_{2p}(1\ 1\ 1) + 6_3(1\ 0\ 0) + 1_1(1\ 1\ -1)$ $(2p-2)_{(p-1)}(1\ 0\ 0) + 2_2(1\ 1\ 1) +$ $\quad\quad\quad + 1_1(1\ 1\ -1)$ $(2p-2)_{(p-1)}(1\ 1\ 0) + 2_1(1\ 0\ 0) +$ $\quad\quad\quad + 1_1(1\ 1\ 1)$
<b>fcc (gen):</b> $(10\ 13\ 14) = 10(1\ 1\ 1) + 3(0\ 1\ 1) + (0\ 0\ 1)$ $(2\ 6\ 7) = 4(0\ 1\ 1) + 2(1\ 1\ 1) + (0\ 0\ 1)$	$10_{10}(1\ 1\ 1) + 3_3(0\ 1\ 1) + 1_1(0\ 0\ 1)$ $4_4(0\ 1\ 1) + 2_2(1\ 1\ 1) + 1_1(0\ 0\ 1)$
<b>bcc (sc):</b> $(8\ 7\ 3) = 6(1\ 1\ 0) + 2(1\ 0\ 1) + (0\ 1\ 1)$ $(15\ 10\ 3) = 10(1\ 1\ 0) + 3(1\ 0\ 1) + (2\ 0\ 0)$ $(18\ 16\ 4) = 15(1\ 1\ 0) + 3(1\ 0\ 1) + (0\ 1\ 1)$ $(2p+2\ 2p+1\ 3) = 2p(1\ 1\ 0) + 2(1\ 0\ 1) + (0\ 1\ 1)$ $(2p+5\ 2p\ 3) = 2p(1\ 1\ 0) + 3(1\ 0\ 1) + (2\ 0\ 0)$	$6_6(1\ 1\ 0) + 2_2(1\ 0\ 1) + 1_1(0\ 1\ 1)$ $10_{10}(1\ 1\ 0) + 3_3(1\ 0\ 1) + 2_1(1\ 0\ 0)$ $(15/2)_{15}(1\ 1\ 0) + (3/2)_3(1\ 0\ 1) +$ $\quad\quad\quad + (1/2)_1(0\ 1\ 1)$ $(2p)_{2p}(1\ 1\ 0) + 2_2(1\ 0\ 1) + 1_1(0\ 1\ 1)$ $(2p)_{2p}(1\ 1\ 0) + 3_3(1\ 0\ 1) + 2_1(1\ 0\ 0)$
<b>bcc (gen):</b> $(1\ 2\ 6) = 6(0\ 0\ 1) + 2(0\ 1\ 0) + (1\ 0\ 0)$ $(1\ 3\ 15) = 15(0\ 0\ 1) + 3(0\ 1\ 0) + (1\ 0\ 0)$	$6_6(0\ 0\ 1) + 2_2(0\ 1\ 0) + 1_1(1\ 0\ 0)$ $15_{15}(0\ 0\ 1) + 3_3(0\ 1\ 0) + 1_1(1\ 0\ 0)$

Surfaces, for which the decomposition (4.15) suggests **multiple-atom-height kinks**,  $n_s > 1$ , can result in much more complex structural behavior depending on local binding. This is analogous to stepped surfaces described above. For strong nearest neighbor binding, like in metals with fcc and bcc lattices, these surfaces still form kinks with single atom steps even if  $n_s > 1$ . As an example the  $(37\ 25\ 17)$  surface of a crystal with an fcc lattice, see Fig. 4.14, decomposes into  $(1\ 1\ 1)$  terraces and  $(1\ 1\ -1) / (2\ 0\ 0)$  kinks of double step height which is clear from the decomposition

$$(37\ 25\ 17) = 21(1\ 1\ 1) + 2 \cdot 2(1\ 1\ -1) + 2 \cdot 3(2\ 0\ 0)$$

with  $m_1 = 2$ ,  $m_2 = 3$ ,  $n_s = 2$ ,  $n_1 = 7$ ,  $n_2 = 3$  according to (4.15). Here single step height kink lines contain two sections differing in length and separate terraces of different width. Further, the corre-

sponding kink lines are structurally more complex as indicated by the black lines in Fig. 4.14.

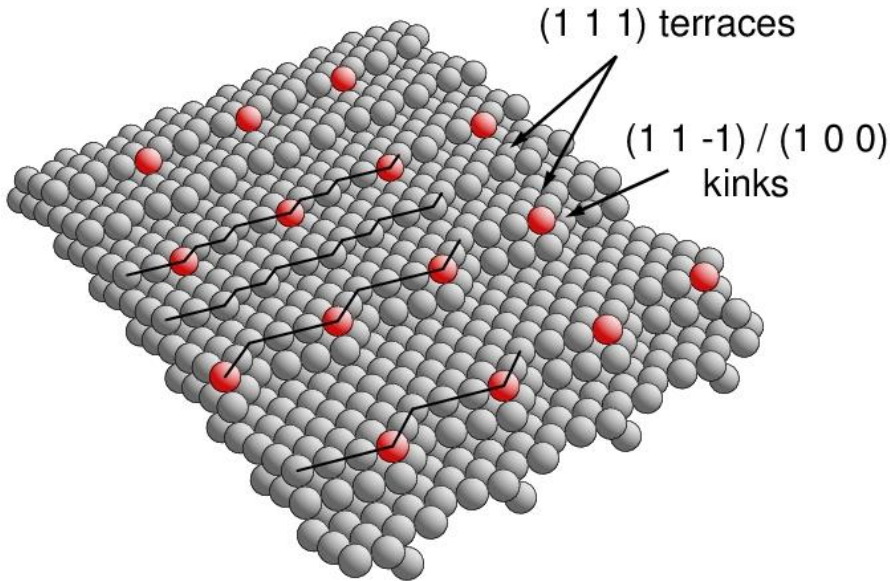


Fig. 4.14. Structure of the kinked fcc(37 25 17) surface with alternating single-height kinks (back) and two lines of double-height kinks (front). The red atom balls define the (37 25 17) monolayer. Kink edges are emphasized by black lines.

So far, the discussion of the shape of vicinal surfaces was restricted to monoatomic single crystals with only one atom in the primitive unit cell (primitive crystals). A generalization to **polyatomic crystals** with more than one atom in the primitive unit cell and/or different elements is straight forward since, according to Sec. 2.2.1, any general crystal can be decomposed formally into a set of primitive crystals with lattices which are identical to that of the general crystal. Thus, vicinal surfaces of polyatomic crystals can be considered as superpositions of those of their primitive component crystals. However, the detailed local structure at the surfaces may be rather complicated depending on the crystal type. As an illustration Fig. 4.15 shows an example of moderate complexity, the kinked (15 11 9) surface of cubic MgO. This surface can be decomposed in (1 1 1) terraces and (1 1 -1) / (2 0 0) kinks, where the terrace sections alternate between the two atom types leading to a highly polar ‘zebra-striped’ surface.

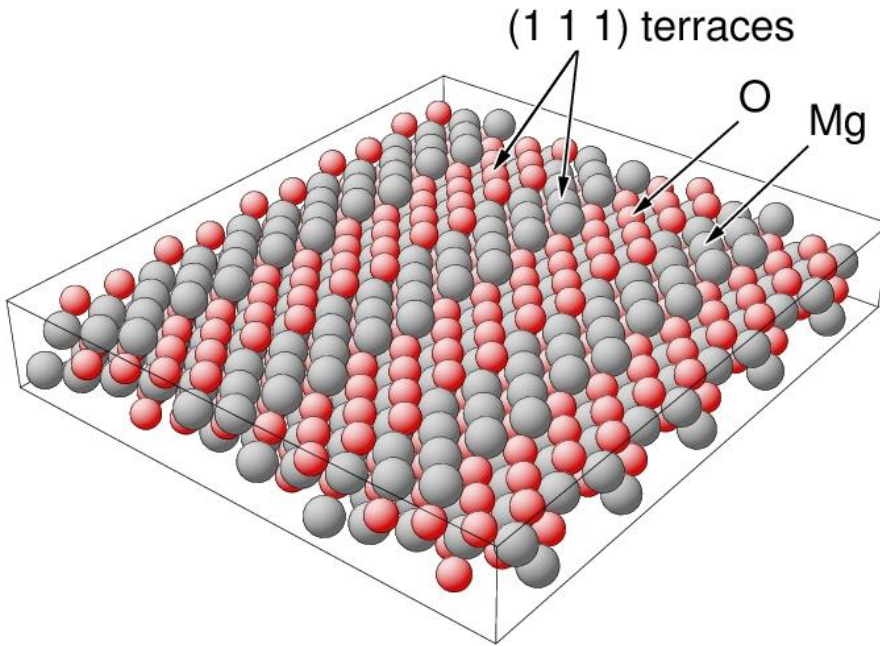


Fig. 4.15. Structure of the kinked  $(15\ 11\ 9)$  surface of cubic MgO with alternating  $(1\ 1\ 1)$  terraces of Mg and O atoms. The atoms are shown in different color and labeled accordingly.

A more complex example is given in Fig. 4.16 showing the structure of the stepped  $(0\ 1\ 8)$  surface of cubic **strontium titanate**,  $\text{SrTiO}_3$ , (perovskite lattice). This surface exhibits alternating  $(0\ 0\ 1)$  oriented terraces of binary  $\text{TiO}_2$  and  $\text{SrO}$  units. However, it must be emphasized that the structures of the  $\text{MgO}(15\ 11\ 9)$  and  $\text{SrTiO}_3(0\ 1\ 8)$  surfaces shown in Figs. 4.15 and 4.16, respectively, are to some extent academic. The corresponding real crystal surfaces that can be measured are very likely to be modified by interatomic binding effects leading to local relaxation of atom positions and reconstruction at the surface. This will be discussed in greater detail in Sec. 5.

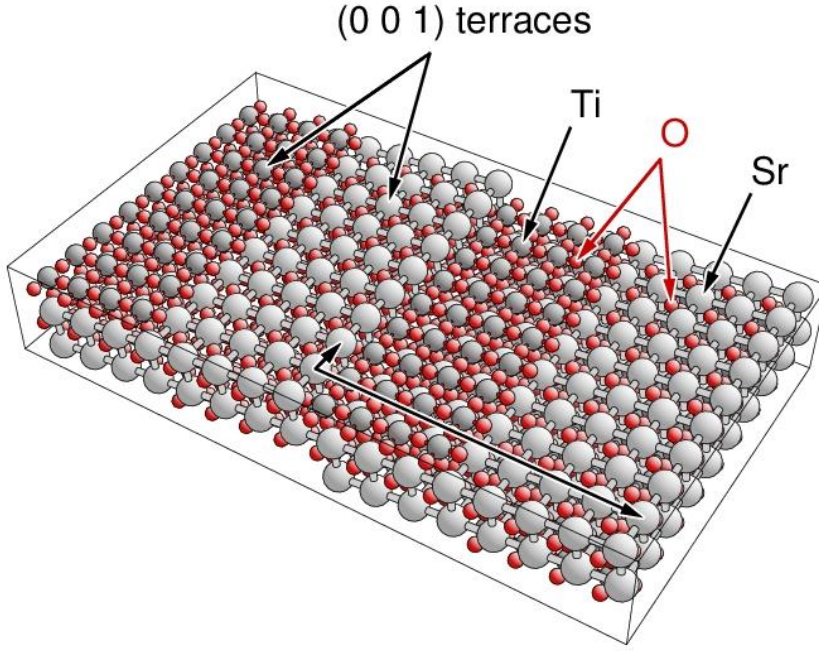


Fig. 4.16. Structure of the stepped (0 1 8) surface of a  $\text{SrTiO}_3$  crystal (perovskite lattice, cubic-P). The atoms are shown in different color and labeled accordingly. The surface-adapted lattice vectors illustrate the surface periodicity.

Altogether, the two **decomposition theorems** (4.9) and (4.15) can be used to characterize general  $(h k l)$ -indexed surfaces of single crystals by surfaces of high atom density, usually corresponding to low Miller index values, which describe the surface morphology by combinations of dense terraces separated by steps and/or kinks. This can be achieved in the most general case by replacing the initial reciprocal lattice vectors  $\underline{\mathbf{G}}_{o1}$ ,  $\underline{\mathbf{G}}_{o1}$ ,  $\underline{\mathbf{G}}_{o1}$  which describe vector  $\underline{\mathbf{G}}_{(h k l)}$  of the  $(h k l)$ -indexed surface according to

$$\underline{\mathbf{G}}_{(h k l)} = h \underline{\mathbf{G}}_{o1} + k \underline{\mathbf{G}}_{o2} + l \underline{\mathbf{G}}_{o3} \quad (4.26)$$

by a set of transformed reciprocal lattice vectors  $\underline{\mathbf{G}}_1$ ,  $\underline{\mathbf{G}}_2$ ,  $\underline{\mathbf{G}}_3$ . The latter also form a basis of the reciprocal lattice but at the same time refer to normal directions of high density monolayers. If the transformed vectors are represented by

$$\underline{\mathbf{G}}_i = h_i \underline{\mathbf{G}}_{o1} + k_i \underline{\mathbf{G}}_{o2} + l_i \underline{\mathbf{G}}_{o3}, \quad i = 1, 2, 3 \quad (4.27)$$

with corresponding Miller indices  $(h_i k_i l_i)$  then the transformation reads

$$\begin{pmatrix} \underline{\mathbf{G}}_1 \\ \underline{\mathbf{G}}_2 \\ \underline{\mathbf{G}}_3 \end{pmatrix} = \begin{pmatrix} h_1 & k_1 & l_1 \\ h_2 & k_2 & l_2 \\ h_3 & k_3 & l_3 \end{pmatrix} \cdot \begin{pmatrix} \underline{\mathbf{G}}_{o1} \\ \underline{\mathbf{G}}_{o2} \\ \underline{\mathbf{G}}_{o3} \end{pmatrix}, \quad \begin{pmatrix} \underline{\mathbf{G}}_{o1} \\ \underline{\mathbf{G}}_{o2} \\ \underline{\mathbf{G}}_{o3} \end{pmatrix} = \begin{pmatrix} h_1 & k_1 & l_1 \\ h_2 & k_2 & l_2 \\ h_3 & k_3 & l_3 \end{pmatrix}^{-1} \cdot \begin{pmatrix} \underline{\mathbf{G}}_1 \\ \underline{\mathbf{G}}_2 \\ \underline{\mathbf{G}}_3 \end{pmatrix} \quad (4.28)$$

Together with (4.26) this leads to

$$\underline{\mathbf{G}}_{(hkl)} = (h \ k \ l) \cdot \begin{pmatrix} \underline{\mathbf{G}}_{o1} \\ \underline{\mathbf{G}}_{o2} \\ \underline{\mathbf{G}}_{o3} \end{pmatrix} = (h \ k \ l) \cdot \begin{pmatrix} h_1 & k_1 & l_1 \\ h_2 & k_2 & l_2 \\ h_3 & k_3 & l_3 \end{pmatrix}^{-1} \cdot \begin{pmatrix} \underline{\mathbf{G}}_1 \\ \underline{\mathbf{G}}_2 \\ \underline{\mathbf{G}}_3 \end{pmatrix} \stackrel{\text{def.}}{=} (\mathbf{a}_1 \ \mathbf{a}_2 \ \mathbf{a}_3) \cdot \begin{pmatrix} \underline{\mathbf{G}}_1 \\ \underline{\mathbf{G}}_2 \\ \underline{\mathbf{G}}_3 \end{pmatrix} \quad (4.29)$$

where  $\mathbf{a}_i$ ,  $i = 1, 2, 3$ , are integer-valued coefficients which can be calculated by solving the system of linear Diophantine equations

$$\begin{pmatrix} \mathbf{a}_1 \\ \mathbf{a}_2 \\ \mathbf{a}_3 \end{pmatrix} = \begin{pmatrix} h_1 & h_2 & h_3 \\ k_1 & k_2 & k_3 \\ l_1 & l_2 & l_3 \end{pmatrix}^{-1} \cdot \begin{pmatrix} h \\ k \\ l \end{pmatrix} \quad (4.30)$$

with solutions

$$\mathbf{a}_1 = \frac{1}{\Delta} [h(k_2 l_3 - k_3 l_2) + k(l_2 h_3 - l_3 h_2) + l(h_2 k_3 - h_3 k_2)] \quad (4.31a)$$

$$\mathbf{a}_2 = \frac{1}{\Delta} [h(k_3 l_1 - k_1 l_3) + k(l_3 h_1 - l_1 h_3) + l(h_3 k_1 - h_1 k_3)] \quad (4.31b)$$

$$\mathbf{a}_3 = \frac{1}{\Delta} [h(k_1 l_2 - k_2 l_1) + k(l_1 h_2 - l_2 h_1) + l(h_1 k_2 - h_2 k_1)] \quad (4.31c)$$

$$\Delta = h_3(k_1 l_2 - k_2 l_1) + k_3(l_1 h_2 - l_2 h_1) + l_3(h_1 k_2 - h_2 k_1) \quad (4.31d)$$

where for generic Miller indices  $\Delta = 1$  while for simple cubic Miller indices of fcc and bcc lattices  $\Delta = 4$  and  $\Delta = 2$ , respectively, must be used, see Exercise 4.17. Thus, if the Miller indices  $(h \ k \ l)$  of the surface to be analyzed and those,  $(h_i \ k_i \ l_i)$ , of the corresponding high atom density surfaces are known, relations (4.31) provide the decomposition coefficients  $\mathbf{a}_i$ . This suggests a simple **trial-and-error** method to characterize the structure of a general  $(h \ k \ l)$  surface by terraces, steps, and kinks of surfaces with high atom density.

In a first step, a set of reciprocal lattice vectors  $\underline{\mathbf{G}}$  with Miller indices  $(h \ k \ l)$ , representing surfaces of high atom density, is evaluated. Of these, three reciprocal lattice vectors  $\underline{\mathbf{G}}_1$ ,  $\underline{\mathbf{G}}_2$ ,  $\underline{\mathbf{G}}_3$ , and Miller indices  $(h_1 \ k_1 \ l_1)$ ,  $(h_2 \ k_2 \ l_2)$ , and  $(h_3 \ k_3 \ l_3)$  according to (4.27), are chosen such that they form a reciprocal lattice basis, i.e.

$$\det \begin{pmatrix} h_1 & k_1 & l_1 \\ h_2 & k_2 & l_2 \\ h_3 & k_3 & l_3 \end{pmatrix} = \Delta \quad (4.32)$$

where  $\Delta = 1$  for generic Miller indices,  $\Delta = 4$  and  $\Delta = 2$  for sc Miller indices in fcc and bcc lattices, respectively. Then for each vector triplet  $\underline{G}_1, \underline{G}_2, \underline{G}_3$  the decomposition coefficients  $a_1, a_2, a_3$  are evaluated using (4.31) where only vector triplets with coefficients  $a_i \geq 0$  need to be considered. For these solutions the Miller indices  $(h_1 k_1 l_1), (h_2 k_2 l_2), (h_3 k_3 l_3)$  and coefficients  $a_i$  are rearranged such that  $a_1 \geq a_2 \geq a_3 \geq 0$  after which three different scenarios of surface structures can be distinguished

- (a) For  $\mathbf{a}_2 = \mathbf{a}_3 = \mathbf{0}$  the  $(h k l) = (h_1 k_1 l_1)$  oriented surface is characterized as a surface of **high atom density**.
- (b) For  $\mathbf{a}_1 \geq \mathbf{a}_2 > \mathbf{0}$  and  $\mathbf{a}_3 = \mathbf{0}$  the  $(h k l)$  oriented surface is **stepped** with  $(h_1 k_1 l_1)$  representing the terrace surface (vicinal partner), with terraces of ‘width’  $a_1$  and step ‘heights’  $a_2$ . Here the value  $a_2 = 1$  yields single atom steps while  $a_2 > 1$  refers to multiple atom steps where the latter may lead to subterraces with single atom steps as discussed above.
- (c) For  $\mathbf{a}_1 \geq \mathbf{a}_2 \geq \mathbf{a}_3 > \mathbf{0}$  the  $(h k l)$  oriented surface is **kinked** with  $(h_1 k_1 l_1)$  representing the terrace surface (vicinal partner). If  $\mathbf{g} = \mathbf{gcd}(\mathbf{a}_2, \mathbf{a}_3)$ , then two cases can be distinguished,
  - (ca)  $\mathbf{g} = \mathbf{1}$  there are continuous kink lines of  $a_2$  and  $a_3$  atom vectors long sections and adjacent terraces are separated by single atom steps. Here  $a_3 = 1$  yields single atom kinks while  $a_3 > 1$  refers to multiple atom kinks where the latter may result in more complex single atom kinks.
  - (cb)  $\mathbf{g} > \mathbf{1}$  there are continuous kink lines of  $a_2/g$  and  $a_3/g$  atom vectors long sections and adjacent terraces are separated by multiple atom steps that are  $g$  atoms high which may result in more complex single atom steps with single atom kinks.

The decomposition is most evident for  $(h k l)$  oriented surfaces where the decomposition coefficients  $a_i$  are rather different with large terraces, corresponding to  $a_1$  distinctly larger than  $a_2, a_3$ , and, in the case of kinked surfaces, large kink lines with small kink edges, corresponding to  $a_2 > 1$  and  $a_3 = 1$ . This must be considered when choosing meaningful vector triplets  $\underline{G}_1, \underline{G}_2, \underline{G}_3$  and Miller indices  $(h_1 k_1 l_1), (h_2 k_2 l_2), (h_3 k_3 l_3)$  for the decomposition. An example is the fcc(16 10 8) surface which decomposes to

$$(16\ 10\ 8) = 9(1\ 1\ 1) + 3(2\ 0\ 0) + (1\ 1\ -1)$$

On the other hand, decompositions with very similar values  $a_i$  may not yield a clear structural description. Here an example is the fcc(21 13 3) surface shown in Fig. 4.17 which decomposes to

$$(21\ 13\ 3) = 5(2\ 2\ 0) + 4(2\ 0\ 0) + 3(1\ 1\ 1)$$

showing (1 1 1) terraces with a fairly complex kink structure. Surfaces of this type may not be called vicinal.

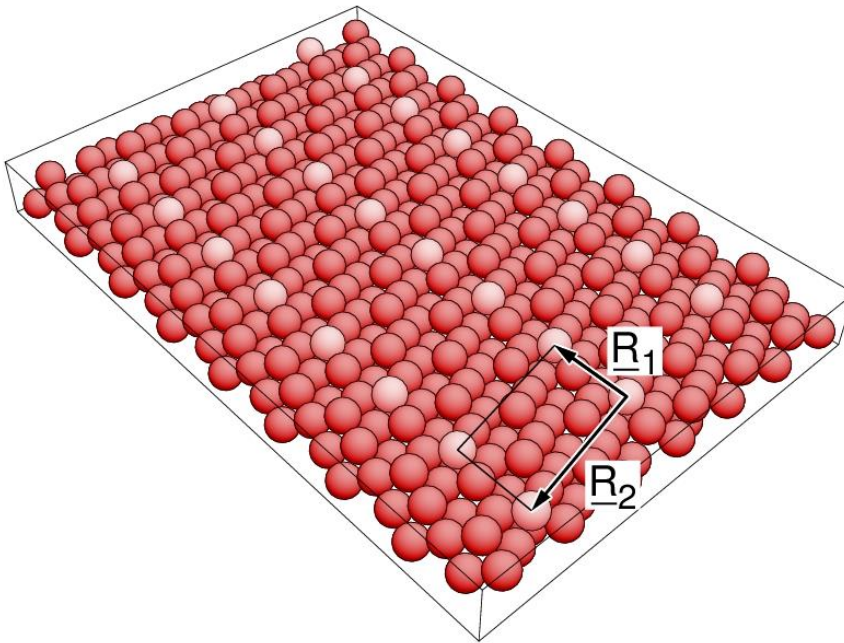


Fig. 4.17. Structure of the (21 13 3) surface of an fcc crystal. The atoms of the top-most monolayer are emphasized by lighter color. The surface unit cell is outlined by black lines with surface lattice vectors  $\underline{R}_1$ ,  $\underline{R}_2$  labeled accordingly.

As examples of general decompositions, we consider crystals with an **fcc lattice**, where high-density surfaces are given by the Miller index families  $\{1\ 1\ 1\}$ ,  $\{2\ 0\ 0\}$ ,  $\{2\ 2\ 0\}$  with altogether 26  $(h\ k\ l)$  members. Here useful example decompositions are

$$\begin{aligned}
 (h\ k\ l) &= (k+l)/2 \cdot (1\ 1\ 1) + (h-l)/2 \cdot (1\ 1\ -1) + (h-k)/2 \cdot (1\ -1\ 1) \\
 &= (k+l)/2 \cdot (1\ 1\ 1) + (k-l)/2 \cdot (1\ 1\ -1) + (h-k)/2 \cdot (2\ 0\ 0) \\
 &= l \cdot (1\ 1\ 1) + (h-l)/2 \cdot (2\ 0\ 0) + (k-l)/2 \cdot (0\ 2\ 0) \\
 &= h/2 \cdot (2\ 0\ 0) + k/2 \cdot (0\ 2\ 0) + l/2 \cdot (0\ 0\ 2) \quad \{\text{even } (h\ k\ l) \text{ only}\} \\
 &= l \cdot (1\ 1\ 1) + (k-l)/2 \cdot (2\ 2\ 0) + (h-k)/2 \cdot (2\ 0\ 0)
 \end{aligned} \tag{4.33}$$



Crystals of **bcc lattices** offer high-density surfaces described by the Miller index families  $\{1\ 1\ 0\}$ ,  $\{2\ 0\ 0\}$ ,  $\{2\ 1\ 1\}$  with altogether 42  $(h\ k\ l)$  members. Here useful example decompositions are

$$\begin{aligned}
 (h\ k\ l) &= (-h + k + l)/2 \cdot (0\ 1\ 1) + (h - k + l)/2 \cdot (1\ 0\ 1) + (h + k - l)/2 \cdot (1\ 1\ 0) \\
 &= k \cdot (1\ 1\ 0) + l \cdot (1\ 0\ 1) + (h - k - l)/2 \cdot (2\ 0\ 0) \\
 &= -k \cdot (1\ -1\ 0) + (h + k - l)/2 \cdot (2\ 0\ 0) + l \cdot (1\ 0\ 1) \\
 &= (h - k) \cdot (2\ 1\ 1) + (-h + 2k) \cdot (1\ 1\ 0) + (-h + k + l)/2 \cdot (0\ 0\ 2)
 \end{aligned} \tag{4.34}$$

The characterization of general  $(h\ k\ l)$ -indexed surfaces according to the above recipe allows one to distinguish between surfaces of high atom density, stepped, and kinked vicinal surfaces. While the underlying Miller index decomposition is not unique it is most general and applies to surfaces of crystals with **any Bravais lattice type**. An alternative distinction between stepped and kinked surfaces has been proposed for crystals with highly symmetric cubic and hexagonal (hcp) lattices [96]. Here a stepped surface is defined by the atoms of its terrace edges forming linear arrays with nearest neighbor distances separating the atoms. This definition is rather intuitive but may not be applicable to crystals with general Bravais lattices.

#### 4.4 Chiral and Achiral Surfaces

There is an additional structural property, **handedness** or **chirality** (kheir ( $\chi\epsilon\iota\rho$ ) is Greek for 'hand'), which can be used to discriminate between surfaces of single crystals [96] but is of much more general relevance [97]. For example, chiral molecules have been found to be optically active in the presence of circularly polarized light [97], and large organic biomolecules can react quite differently with their environment depending on their chiral components [98]. Further, chiral crystal surfaces have attracted much interest since their interaction with large (chiral) adsorbates has been found, in some cases, to differ dramatically depending on their chiral orientation (enantioselective adsorption) [99], [100]. This will be discussed in Sec. 6.7.

The formal **definition** of a general three-dimensional **chiral** object is that it cannot be superimposed onto its mirror image. This definition has also been used to describe symmetry properties of molecules: applying a mirror operation creates an image molecule, which may or may not be brought in coincidence with the initial species by a simple rotation and translation. If there is no coincidence possible the molecule will be called **chiral** and in the coincidence case it will be called

**achiral.** The two mirror partners of a chiral molecule are also known as **enantiomers**. As an example, Fig. 4.18 shows the two enantiomers of bromochlorofluoromethane, BrClFCH, where mirroring creates two different species, a right-handed R-BrClFCH ('R-' for 'rectus', latin for right) and a left-handed S-BrClFCH molecule ('S-' for 'sinister', latin for left) using a nomenclature according to the stereochemical rules [101]. Here the peripheral atoms see different arrangements of atom neighbors. For example, rotating R-BrClFCH clockwise about its C-H axis moves the bromine towards the chlorine atom whereas rotating S-BrClFCH about its C-H axis to move the bromine

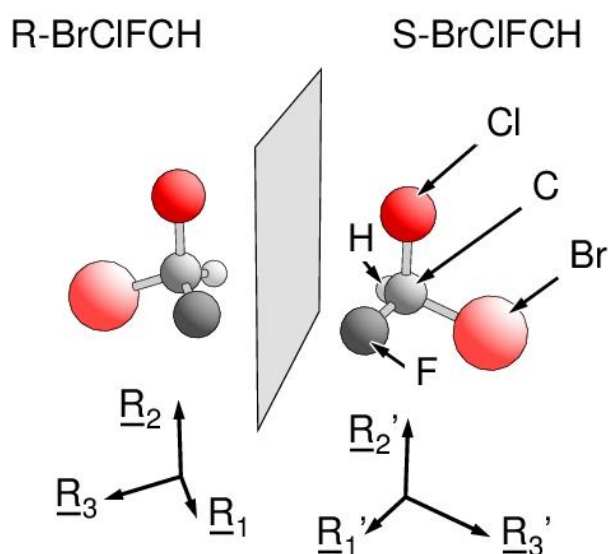


Fig. 4.18. Balls-and-sticks models of the two enantiomers of bromochlorofluoromethane, BrClFCH, with a mirror plane in between. The right- and left-handed vector triplets  $\underline{R}_1, \underline{R}_2, \underline{R}_3$ , and  $\underline{R}'_1, \underline{R}'_2, \underline{R}'_3$ , referring to the R-BrClFCH and S-BrClFCH species, respectively, are shown at the bottom.

towards chlorine requires an anticlockwise rotation. The different orientation is also clear from the interatomic vectors  $\underline{R}_1, \underline{R}_2, \underline{R}_3$ , pointing from the central carbon to fluorine, chlorine, and bromine, and shown at the bottom of Fig. 4.18. These vectors form a right-handed triplet while their mirror images  $\underline{R}'_1, \underline{R}'_2, \underline{R}'_3$  form a left-handed triplet.

The example shows that the concept of chirality is connected mathematically with the handedness of vector triplets in three-dimensional space. A non-coplanar vector triplet  $\underline{R}_1, \underline{R}_2, \underline{R}_3$  is called **right-handed** if the corresponding volume product,  $V = (\underline{R}_1 \times \underline{R}_2) \cdot \underline{R}_3$ , see Appendix F, assumes a **positive** value, whereas the triplet is considered to be **left-handed** if  $V$  is **negative**. The three point symmetry operations, mirroring, inversion, and rotation, affect the handedness of a vector triplet differently depending on the operation.

- (a) A **mirror operation**  $\sigma(\underline{r}_0, \underline{m})$  with respect to a plane of normal vector  $\underline{m}$  through the origin  $\underline{r}_0 = \underline{0}$  is, according to (3.89), defined by a transformation

$$\underline{r}' = \sigma(\underline{0}, \underline{m}) \underline{r} = \underline{r} - 2(\underline{r} \cdot \underline{m}) \underline{m} \quad (4.35)$$

As a result, the vector triplet  $\underline{R}_1, \underline{R}_2, \underline{R}_3$  is transformed to  $\underline{R}_1', \underline{R}_2', \underline{R}_3'$ , where, as proven in Appendix F,

$$V' = (\underline{R}_1' \times \underline{R}_2') \cdot \underline{R}_3' = -(\underline{R}_1 \times \underline{R}_2) \cdot \underline{R}_3 = -V \quad (4.36)$$

This shows that mirroring **changes** the **handedness** of vector triplets.

- (b) An **inversion**  $i(\underline{r}_0)$  with respect to the origin  $\underline{r}_0 = \underline{0}$  is, according to (3.64), defined by a transformation

$$\underline{r}' = i(\underline{0}) \underline{r} = -\underline{r} \quad (4.37)$$

Therefore, the vector triplet  $\underline{R}_1, \underline{R}_2, \underline{R}_3$  is transformed to  $\underline{R}_1', \underline{R}_2', \underline{R}_3'$ , where the volume product with respect to the inversion center yields

$$V' = (\underline{R}_1' \times \underline{R}_2') \cdot \underline{R}_3' = [(-\underline{R}_1) \times (-\underline{R}_2)] \cdot (-\underline{R}_3) = -V \quad (4.38)$$

This shows that inversion **changes** also the **handedness** of vector triplets.

- (c) A (clockwise) **rotation**  $C_\varphi(\underline{r}_0, \underline{e})$  by an angle  $\varphi$  about an axis along  $\underline{e}$  through the rotation center at the origin  $\underline{r}_0 = \underline{0}$  is, according to (3.73), (3.74) and using a representation

$$\underline{r} = x_1 \underline{e}_1 + x_2 \underline{e}_2 + x_3 \underline{e}_3 \quad x_i = \underline{r} \cdot \underline{e}_i, \quad i = 1, 2, 3 \quad (4.39)$$

where  $\underline{e}_1, \underline{e}_2, \underline{e}_3 = \underline{e}$  are Cartesian unit vectors with respect to the rotation axis along  $\underline{e}_3$ , defined by a transformation

$$\underline{r}' = C_\varphi(\underline{r}) = x_1' \underline{e}_1 + x_2' \underline{e}_2 + x_3' \underline{e}_3 \quad (4.40)$$

with

$$\begin{pmatrix} x_1' \\ x_2' \\ x_3' \end{pmatrix} = \begin{pmatrix} \cos \varphi & \sin \varphi & 0 \\ -\sin \varphi & \cos \varphi & 0 \\ 0 & 0 & 1 \end{pmatrix} \cdot \begin{pmatrix} x_1 \\ x_2 \\ x_3 \end{pmatrix} \quad (4.41)$$

Thus, the vector triplet  $\underline{R}_1, \underline{R}_2, \underline{R}_3$  is transformed to  $\underline{R}_1', \underline{R}_2', \underline{R}_3'$ , where the volume product with respect to the rotation center at the origin  $\underline{r}_0 = \underline{0}$  is yields

$$V' = (\underline{R}_1' \times \underline{R}_2') \cdot \underline{R}_3' = (\underline{R}_1 \times \underline{R}_2) \cdot \underline{R}_3 = V \quad (4.42)$$

as can be proven by simple calculus using (4.39) and (4.40). This shows that rotation **does not change** the **handedness** of vector triplets.

Altogether, inversion and mirroring change the handedness of corresponding vector triplets while rotation does not. Thus, applying a combination of different rotations with a mirror operation or with an inversion will always change the handedness of vector triplets describing the atom positions of a molecule and may lead to a molecule of different conformation. In this case the molecule is called **chiral**. On the other hand, a molecule with mirror or inversion symmetry will not change its shape when combinations of mirroring, inversion, or rotation are applied and the molecule is called **achiral**. Therefore, **chirality** can be based on the behavior of a system with respect to mirroring or inversion and, hence, the existence of corresponding **mirror planes** or **inversion centers**. This equivalence is also clear from the fact that the inversion operation  $i(\underline{r}_o)$  can always be represented by a combination of mirroring  $\sigma(\underline{r}_o, \underline{m})$  and a  $180^\circ$  rotation  $C_{180}(\underline{r}_o, \underline{m})$

$$i(\underline{r}_o) = \sigma(\underline{r}_o, \underline{m}) C_{180}(\underline{r}_o, \underline{m}) = C_{180}(\underline{r}_o, \underline{m}) \sigma(\underline{r}_o, \underline{m}) \quad (4.43)$$

which can be proven using the above transformations. In the following, we will focus on the definition of chirality based on mirror symmetry which is common practice in the literature.

It should be mentioned in passing that in general chirality is associated with atom centers in a molecule, so-called **chiral centers**, where mirror operations change the handedness of the atom arrangement near the center. In the BrClFCH molecule shown in Fig. 4.18 the carbon center acts as the chiral center distinguishing between R-BrClFCH and S-BrClFCH. However, larger molecules may contain several chiral centers. As an example, Fig. 4.19 shows the tartaric acid (TA) molecule [102],  $C_4O_6H_6$ , which includes two chiral carbon centers, denoted as  $C^*$  in the figure, which can be both left- and right-handed. Hence, there are four possible isomeric species. In (R,R)-TA and (S,S)-TA, see Fig. 4.19, both carbon centers are left-handed or both right-handed according to the Cahn-Ingold-Prelog rules [101] and the two species are enantiomers connected by mirror imaging. In the other two, (L,R)-TA and (R,L)-TA, one of the carbon centers is left- and the other right-handed such that they are structurally identical and achiral (usually referred to as meso tartaric acid and diastereoisomeric with respect to the chiral species).

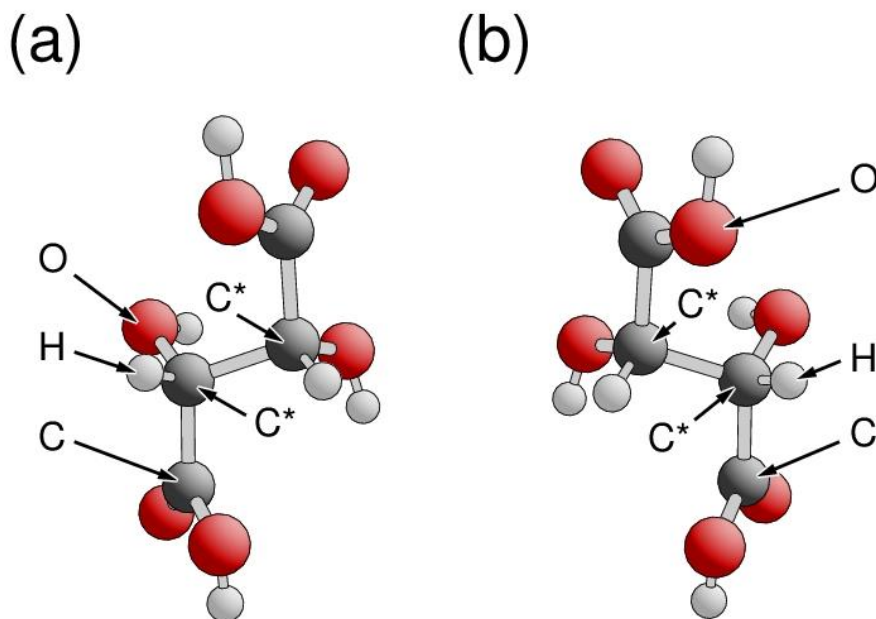


Fig. 4.19. Balls-and-sticks models of the two enantiomers of tartaric acid (TA) from crystal data [102], (a) (R,R)-TA and (b) (S,S)-TA. The atom balls labeled C\* refer to the two chiral carbon centers.

The concept of **chirality** can also be applied to extended systems such as **bulk** single crystals. For example, according to the basic definition, a primitive crystal which contains inversion centers by definition will always be achiral. Surfaces of ideal single crystals are terminated by  $(h k l)$  oriented monolayers which are described by netplane-adapted lattice vectors  $\underline{R}_1$  and  $\underline{R}_2$ , where a stacking vector  $\underline{R}_3$  connects adjacent parallel monolayers, see Sec. 4.1. Here a **surface** can be considered to be **chiral** if it does not exhibit mirror symmetry along any plane perpendicular to the surface. These surfaces always have chiral partners which can be obtained by applying a mirror operation to the initial surface with the mirror plane perpendicular to the surface. The mirroring transforms the netplane-adapted lattice vectors  $\underline{R}_1$  and  $\underline{R}_2$  such that the vector product  $\underline{R}_1 \times \underline{R}_2$  changes its sign but not its absolute value. This vector  $\underline{R}_1 \times \underline{R}_2$  defines (up to a constant factor) the reciprocal lattice vector  $\underline{G}_{(h k l)}$  and, hence, the Miller indices of the surface, see (3.6). Therefore, the **chiral partner** of the  $(h k l)$  surface is defined by Miller indices  $(-h -k -l)$ .

The two chiral partners of an  $(h k l)$  oriented surface may also be assigned a **handedness** which is most evident for kinked surfaces of primitive crystals. It was shown previously, see (4.14), that the reciprocal lattice vector  $\underline{G}_{(h k l)}$  of a kinked surface can be written as a sum of three contributions,  $\{(m_1 n_2 + m_2 n_1 - m_1 m_2) \underline{G}_{(h k l)t}\}$ ,  $\{m_1 n_s \underline{G}_{(h k l)s1}\}$ , and  $\{m_2 n_s \underline{G}_{(h k l)s2}\}$ , characterizing its terrace orientation and those of the two steps defining the kink. Sorting the three contributions accord-

ing to their lengths yields the three vectors  $\underline{G}_i$ ,  $i = 1, 2, 3$ , pointing out of the surface where  $\underline{G}_1$  is assumed to be of smallest and  $\underline{G}_3$  of largest length. Then the  $(h k l)$  surface is called **right-handed**, also denoted as  $(h k l)^R$ , if the vectors  $\underline{G}_1, \underline{G}_2, \underline{G}_3$  form a right-handed system, quantified by the volume product

$$V_{\text{ch}} = (\underline{G}_1 \times \underline{G}_2) \cdot \underline{G}_3 \quad (4.44)$$

being **positive**, whereas the surface is called **left-handed**, denoted as  $(h k l)^S$ , if  $\underline{G}_1, \underline{G}_2, \underline{G}_3$  form a left-handed system and  $V_{\text{ch}}$  is **negative**. This assignment is **unique** if the lengths of the three vectors  $\underline{G}_i$  are all different and is compatible with the nomenclature proposed in the literature [103], [104].

As an example, Fig. 4.20a shows the chiral  $(11\ 9\ 5)$  surface of an fcc crystal, described by  $(1\ 1\ 1)$  terraces with kinks of  $(1\ 1\ -1)$  and  $(1\ 0\ 0)$  steps (confirming the additivity relation  $(11\ 9\ 5) = 7(1\ 1\ 1) + 2(1\ 1\ -1) + (2\ 0\ 0)$ ). The corresponding volume product  $V_{\text{ch}}$  equals to

$$V_{\text{ch}} = \alpha ((2\ 0\ 0) \times (2\ 2\ -2)) \cdot (7\ 7\ 7) = 28\ \alpha > 0$$

where  $\alpha$  is a global positive constant. Hence, the surface is right-handed and may be written as  $(11\ 9\ 5)^R$ . The chiral partner surface  $(-11\ -9\ -5)$  shown in Fig. 4.20b (a mirrored copy of the surface section in Fig. 4.20a) is left-handed and may be termed  $(-11\ -9\ -5)^S$ . The kink lines, emphasized by light balls in Fig. 4.20, show the difference between the two surfaces quite clearly. In contrast, fcc bulk crystals are intrinsically achiral in three dimensions since they contain multiple mirror symmetry. However, none of the mirror planes is perpendicular to the  $(11\ 9\ 5)$  surface which is why the corresponding surface is chiral.

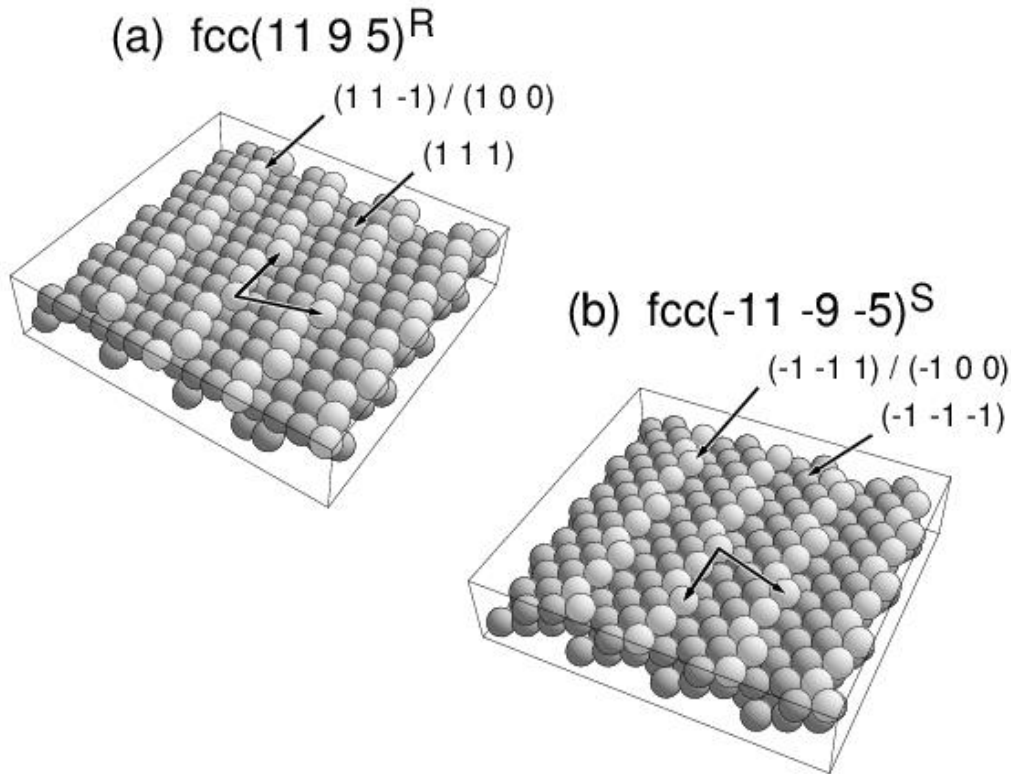


Fig. 4.20. Structure of the (a) kinked  $\text{fcc}(11\ 9\ 5)^R$  surface with  $(1\ 1\ 1)$  terraces and  $(1\ 1\ -1) / (1\ 0\ 0)$  kinks, (b) chiral partner surface  $\text{fcc}(-11\ -9\ -5)^S$ . The atoms along the kink lines are emphasized by light balls. The surface-adapted lattice vectors illustrate the surface periodicity.

There are cases where, after sorting, two of the vectors  $\underline{G}_i$  are equal in length. Then the above sorting process does not lead to a unique solution and the volume product  $V_{\text{ch}}$  can become positive or negative depending on the sequence chosen for the vectors  $\underline{G}_i$ . This can appear for general Bravais lattices where the concept of dense monolayers, forming terraces separated by steps and kinks, is less evident and the concept of chirality may not be applicable. Here sorting the reciprocal lattice vectors  $\underline{G}_{(h\ k\ l)_t}$ ,  $\underline{G}_{(h\ k\ l)_{s1}}$ ,  $\underline{G}_{(h\ k\ l)_{s2}}$  themselves according to their length can provide a unique assignment. In cases where two vectors  $\underline{G}_i$  are equal in length and also their scalar prefactors agree with each other the assignment of a handedness of the surface becomes unclear and the surface has to be considered **achiral**. This happens for example for stepped surfaces with open step edges such that the edges may also be interpreted as kink lines. A simple example is the achiral  $\text{fcc}(4\ 1\ 0)$  surface shown in Fig. 4.21 whose Miller indices can be decomposed as

$$(4\ 1\ 0) \equiv (8\ 2\ 0) = 3(2\ 0\ 0) + (2\ 2\ 0)$$

suggesting a stepped surface with  $(1\ 0\ 0)$  oriented terraces separated by  $(1\ 1\ 0)$  steps or as

$$(4\ 1\ 0) \equiv (8\ 2\ 0) = 3(2\ 0\ 0) + (1\ 1\ 1) + (1\ 1\ -1)$$

suggesting a kinked surface with  $(1\ 0\ 0)$  oriented terraces separated by kink lines of symmetric  $(1\ 1\ 1)$  and  $(1\ 1\ -1)$  step sections.

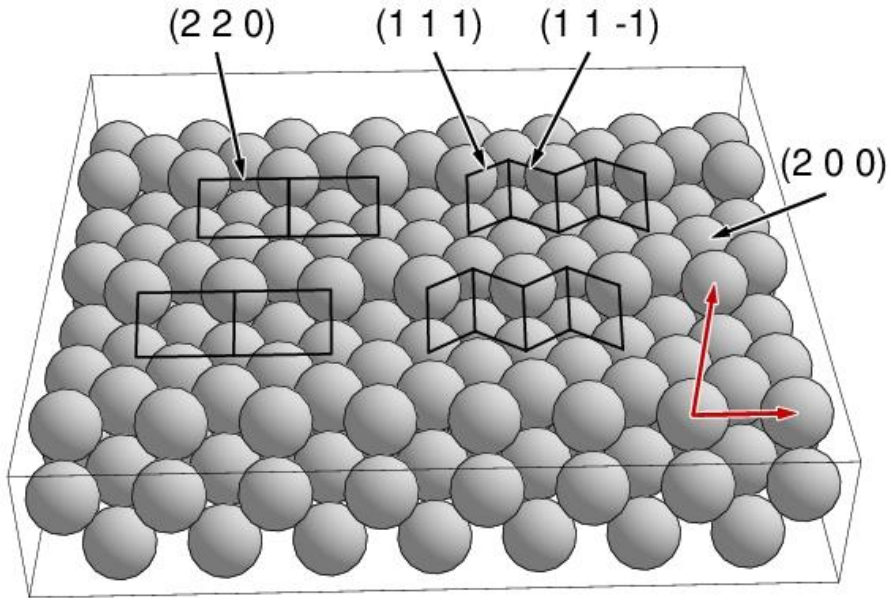


Fig. 4.21. Structure of the fcc(4 1 0) surface described by  $(1\ 0\ 0)$  terraces with  $(1\ 1\ 0)$  steps (left part) or with  $(1\ 1\ -1) / (1\ 1\ -1)$  kinks (right part). The step and kink areas are outlined by black lines. The surface-adapted lattice vectors in red illustrate the overall surface periodicity.

As stated earlier, an  $(h\ k\ l)$  surface is considered to be **achiral** only if there is at least one mirror plane of the crystal which is perpendicular to the surface. Thus, all parallel  $(h\ k\ l)$  **monolayers** which are stacked from the surface towards the bulk must **share** one or several **mirror planes** perpendicular to the surface. As an example, Fig. 4.22 shows the achiral  $(3\ 3\ 1)$  surface of an fcc crystal, described by  $(1\ 1\ 1)$  terraces with  $(1\ 1\ -1)$  steps (confirming the additivity relation  $(3\ 3\ 1) = 2(1\ 1\ 1) + (1\ 1\ -1)$ ). The mirror plane perpendicular to the steps and, thus, perpendicular to the surface is indicated in Fig. 4.22 by the red line labeled  $\sigma$ . In addition, the isolated topmost monolayer (formed by the atoms at the step edges) as well as all underlying isolated monolayers contain a mirror line on the mirror plane labeled  $\sigma$ .



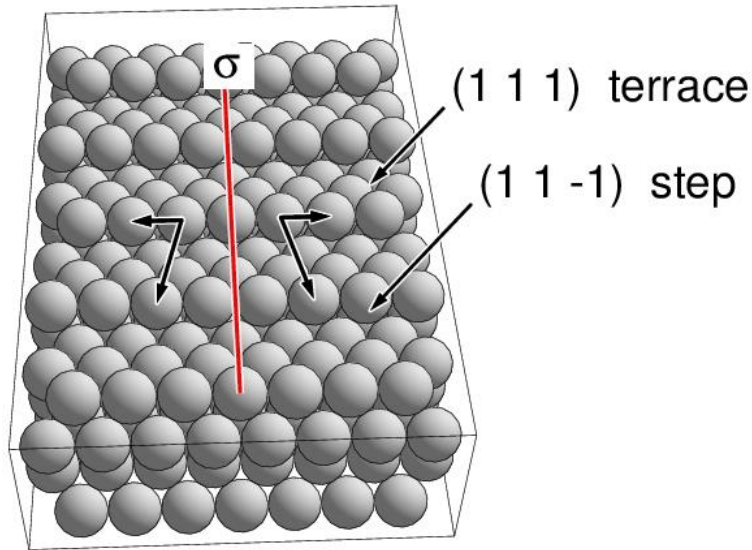


Fig. 4.22. Structure of the achiral stepped fcc(3 3 1) surface with (1 1 1) terraces and (1 1 -1) steps. The mirror plane perpendicular to the surface is indicated by a red line labeled  $\sigma$ . The netplane-adapted lattice vectors (left- and right-handed) illustrate the surface periodicity.

In Sec. 3.6.4 it was shown that netplanes containing mirror lines correspond to either primitive rectangular (including square) or centered rectangular (including hexagonal) lattices in two dimensions. This **two-dimensional** symmetry applies to each separate monolayer near the  $(h k l)$  surface. However, the overall **three-dimensional** symmetry and morphology near the surface, determining the surface chirality, is also influenced by the netplane-adapted vector  $\underline{R}_3$  connecting adjacent monolayers. For example, the fictitious monoatomic triclinic crystal with lattice vectors

$$\underline{R}_1 = a(1, 0, 0), \quad \underline{R}_2 = a(0, 1, 0), \quad \underline{R}_3 = a(1/\sqrt{2}, 1/\sqrt{3}, 1/2) \quad (4.45)$$

yields a (0 0 1) oriented surface shown in Fig. 4.23 in a parallel projection perpendicular to the surface. Here each of the (0 0 1) monolayers with lattice vectors  $\underline{R}_1, \underline{R}_2$  given by (4.45) is of square symmetry including mirror lines. However, the (0 0 1) surface combining all monolayers has no mirror symmetry and is chiral.

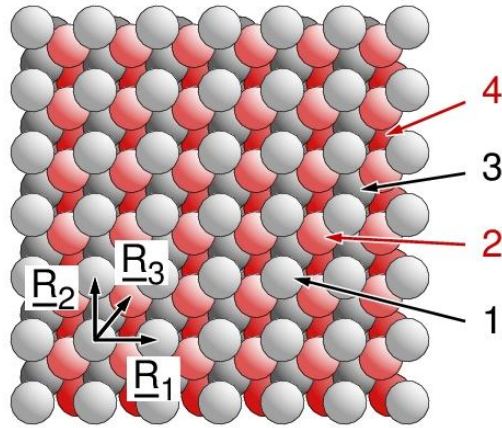


Fig. 4.23. Structure of the chiral (0 0 1) surface of a fictitious primitive triclinic crystal, see text. The netplane-adapted lattice vectors  $\underline{R}_1$ ,  $\underline{R}_2$ ,  $\underline{R}_3$  illustrate the mono-layer and bulk periodicity. The atoms of the topmost four monolayers are painted differently and labeled accordingly.

In addition to chiral surfaces, there is often an infinite but discrete set of **achiral** ( $h k l$ ) surfaces of a crystal depending on its symmetry. This set can be determined by simple geometric considerations. Achiral ( $h k l$ ) surfaces have been defined by the existence of at least one mirror plane of the corresponding bulk crystal pointing perpendicular to the surface. This means, in particular, that the **mirror plane normal** vector  $\underline{m}$  must point **parallel** to the surface. Hence, vector  $\underline{m}$  must be perpendicular to the surface normal vector pointing along the reciprocal lattice vector  $\underline{G}_{(h k l)}$ . This can be used to find the Miller indices of all possible achiral ( $h k l$ ) surfaces of a single crystal.

Consider an ( $h k l$ ) surface of an ideal single crystal with lattice vectors  $\underline{R}_{01}$ ,  $\underline{R}_{02}$ ,  $\underline{R}_{03}$ . Then the normal vector  $\underline{m}$  of any mirror plane defined by  $\sigma(\underline{r}_0, \underline{m})$  in the crystal can be represented by

$$\underline{m} = x_1 \underline{R}_{01} + x_2 \underline{R}_{02} + x_3 \underline{R}_{03} \quad (4.46)$$

The corresponding reciprocal lattice of the crystal is given by vectors  $\underline{G}_{01}$ ,  $\underline{G}_{02}$ ,  $\underline{G}_{03}$  according to (2.95) and an ( $h k l$ ) surface is defined by its normal vector along

$$\underline{G}_{(h k l)} = h \underline{G}_{01} + k \underline{G}_{02} + l \underline{G}_{03} \quad (4.47)$$

Thus, the **condition** of an **achiral** surface with vector  $\underline{m}$  perpendicular to  $\underline{G}_{(h k l)}$  results in a linear equation

$$\underline{G}_{(h k l)} \underline{m} = x_1 h + x_2 k + x_3 l = 0 \quad (4.48)$$

where the orthogonality relation of real and reciprocal lattice vectors (2.96) has been used. Therefore, all achiral ( $h k l$ ) surfaces of a single crystal can be obtained by considering normal vectors  $\underline{m}$  of all mirror planes of the crystal and then selecting ( $h k l$ ) according to (4.48) for each vector  $\underline{m}$ .

This procedure is most general and applies to single crystals with any lattice.

As examples of finding all achiral surfaces we consider **cubic crystals** which may be simple, face-, or body-centered. The simple cubic lattice with lattice vectors

$$\underline{R}_1^{\text{sc}} = a(1, 0, 0), \quad \underline{R}_2^{\text{sc}} = a(0, 1, 0), \quad \underline{R}_3^{\text{sc}} = a(0, 0, 1) \quad (4.49)$$

in Cartesian coordinates offers **nine** mirror planes, shown in Fig. 4.24, which are described by normal vectors  $\underline{m}$  with

$$\begin{aligned} \underline{m} &= (1, 0, 0), (0, 1, 0), (0, 0, 1), \text{ and} \\ \underline{m} &= \alpha(1, \pm 1, 0), \alpha(1, 0, \pm 1), \alpha(0, 1, \pm 1), \quad \alpha = 1/\sqrt{2} \end{aligned} \quad (4.50)$$

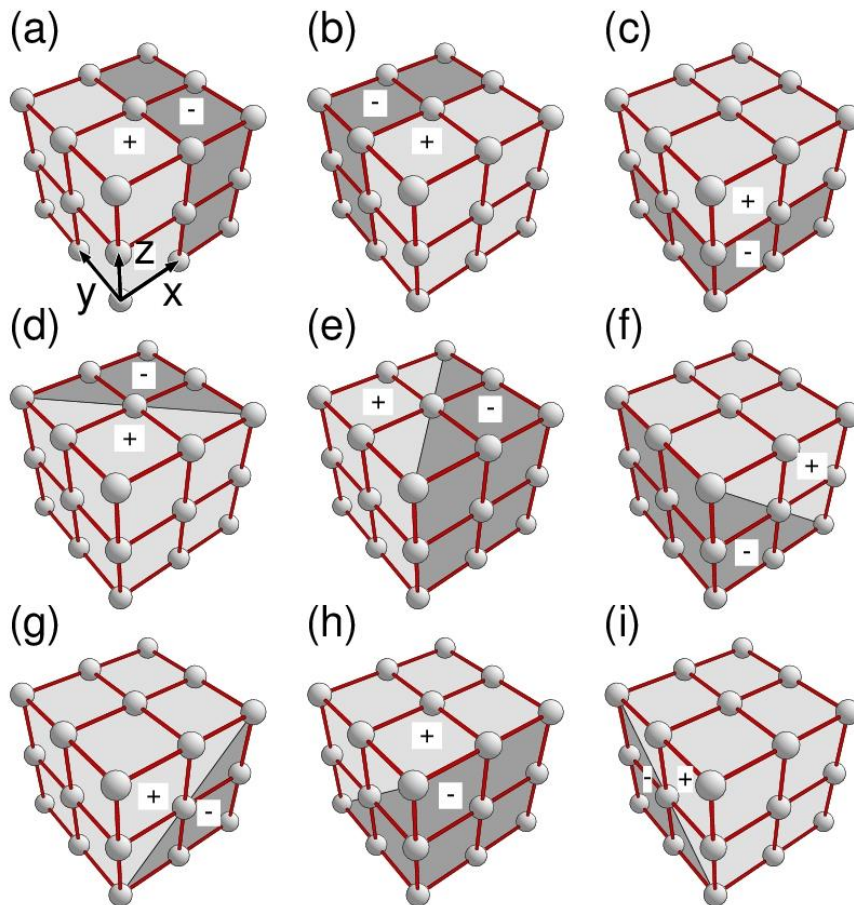


Fig. 4.24. The nine mirror planes of a primitive simple cubic crystal, (a) - (i). Crystal atoms of nearest neighbors are connected by sticks. Mirror planes are indicated by boundaries between light and dark regions labeled + and -. All mirror planes go through the center of the cube. Cartesian coordinates are included in (a).

This results, according to (4.48), in **nine** different sets of Miller indices  $(h k l)$  describing normal directions of achiral surfaces of simple cubic crystals, which are listed in Table 4.4.

Table 4.4. Possible sets of Miller indices ( $h k l$ ) describing orientations of achiral surfaces of cubic crystals. Parameters  $m, n$  are integer-valued with at least one being non-zero.

Set	Constraint (4.48)	( $h k l$ )
1	$h = 0$	(0 $m$ $n$ )
2	$k = 0$	( $m$ 0 $n$ )
3	$l = 0$	( $m$ $n$ 0)
4, 5	$h \pm k = 0$	( $m$ $\pm m$ $n$ )
6, 7	$h \pm l = 0$	( $m$ $n$ $\pm m$ )
8, 9	$k \pm l = 0$	( $m$ $n$ $\pm n$ )

Fcc and bcc lattices, describing many metal single crystals, share all mirror planes with those of the sc lattice. Therefore, achiral surfaces of the corresponding crystals are characterized by all sets of Miller indices (in simple cubic notation) given in Table 4.4. This also applies to the polyatomic crystals MgO and NaCl, described by fcc lattices, or to CsCl, described by a simple cubic lattice. Note that the Miller indices in simple cubic notation given in Table 4.4 can be applied to fcc and bcc crystals without the constraints discussed in Sec. 3.4 since they describe directions only.

The **achiral** surfaces of **fcc** crystals listed in Table 4.4 can all be connected with flat high density surfaces, determined by low Miller index directions (1 1 1), (0 0 1), and (0 1 1) including their symmetry equivalents. They also appear for stepped surfaces composed of high density terraces and steps as discussed in Secs. 4.2 and 4.3. This is clear from the additivity theorem of Miller indices (4.9) for stepped surfaces which allows decomposing the indices of all sets in Table 4.4. As examples, consider sets 1 and 4 with positive indices  $m, n$ . Here the additivity theorem (note the fcc constraints for Miller indices in simple cubic notation required for quantitative evaluations) yields

$$\begin{aligned}
 \text{set 1 : } (0 \ 2m \ 2n) &= m (0 \ 2 \ 0) + n (0 \ 0 \ 2) \\
 &= (m-n) (0 \ 2 \ 0) + n (0 \ 2 \ 2) && m \geq n \\
 &= (n-m) (0 \ 0 \ 2) + m (0 \ 2 \ 2) && m \leq n \quad (4.51a)
 \end{aligned}$$

$$\begin{aligned} \text{set 4: } (2m \pm 2m \ 2n) &= (m+n) (1 \pm 1 \ 1) + (m-n) (1 \pm 1 \ -1) & m \geq n \\ &= 2m (1 \pm 1 \ 1) + (n-m) (0 \ 0 \ 2) & m \leq n \end{aligned}$$

$$\begin{aligned} (2m+1 \pm(2m+1) \ 2n+1) &= \\ &= (m+n+1) (1 \pm 1 \ 1) + (m-n) (1 \pm 1 \ -1) , \quad m \geq n \\ &= (2m+1) (1 \pm 1 \ 1) + (n-m) (0 \ 0 \ 2) , \quad m \leq n \quad (4.51b) \end{aligned}$$

with the other sets leading to analogous results. As an illustration, Fig. 4.22 shows a model of the achiral stepped fcc(3 3 1). This may suggest that all stepped ( $h k l$ ) surfaces of fcc crystals are achiral which can be proven mathematically for surfaces with steps formed by atom rows with smallest or second smallest interatomic distance, see Sec. 4.2. Larger interatomic distances result in kinked surfaces which are chiral.

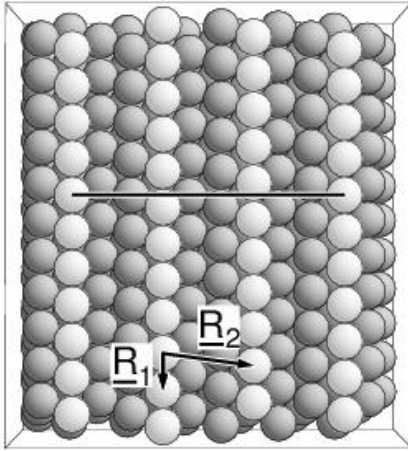
The **achiral** surfaces of **bcc** crystals listed in Table 4.4 can also be connected with flat high density surfaces, determined here by low Miller index directions (1 1 0), (1 0 0), (2 1 1) including their symmetry equivalents. However, in contrast to fcc crystals stepped ( $h k l$ ) surfaces of bcc crystals may be either achiral or chiral. Examples of achiral stepped surfaces from Table 4.4 (with bcc constraints for Miller indices in simple cubic notation and  $m, n > 0$ ) are

$$\text{set 1: } (0 \ m \ m+2n) = m (0 \ 1 \ 1) + n (0 \ 0 \ 2) \quad (4.52a)$$

$$\text{set 4: } (m \pm m \ 2n) = m (1 \pm 1 \ 0) + n (0 \ 0 \ 2) \quad (4.52b)$$

In contrast, Fig. 4.25 shows a model of the stepped chiral (1 2 3) surface of a bcc iron crystal (according to the additivity theorem  $(1 \ 2 \ 3) = 2 (0 \ 1 \ 1) + (1 \ 0 \ 1)$ ) together with its chiral (-1 -2 -3) partner surface. In this figure the black lines perpendicular to the steps at both surfaces illustrate the missing mirror symmetry which results in chirality.

(a) bcc (1 2 3)



(b) bcc (-1 -2 -3)

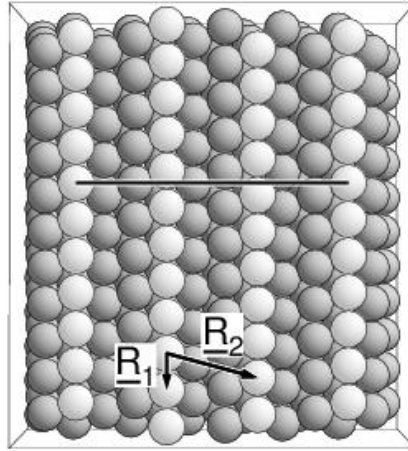


Fig. 4.25. Structure of the (a) perfect stepped (1 2 3) surface of bcc iron with (0 1 1) terraces and (1 0 1) steps, and (b) its chiral partner surface given by (-1 -2 -3). The atom balls along the step lines are emphasized by light color. Black lines perpendicular to the steps indicate the chirality of the surfaces, see text. The netplane-adapted lattice vectors  $\underline{R}_1$  and  $\underline{R}_2$  illustrate the surface periodicity.

The three-dimensional lattice of a **hexagonal** crystal can be described in Cartesian coordinates by lattice vectors (obtuse representation, see Sec. 2.2.2.1.)

$$\underline{R}_1 = a (1, 0, 0), \quad \underline{R}_2 = a (-1/2, \sqrt{3}/2, 0), \quad \underline{R}_3 = c (0, 0, 1) \quad (4.53)$$

and includes **seven** mirror planes, shown in Fig. 4.26. The corresponding normal vectors  $\underline{m}$  can be described by

$$\begin{aligned} \underline{m} &= (\cos \varphi, \sin \varphi, 0), \quad \varphi = 0^\circ, 30^\circ, 60^\circ, 90^\circ, 120^\circ, 150^\circ, \text{ and} \\ \underline{m} &= (0, 0, 1) \end{aligned} \quad (4.54)$$

or by seven lattice directions along

$$\begin{aligned} \underline{R} &= \underline{R}_1, & \underline{R} &= 2 \underline{R}_1 + \underline{R}_2, & \underline{R} &= \underline{R}_1 + \underline{R}_2, & \underline{R} &= \underline{R}_1 + 2 \underline{R}_2 \\ \underline{R} &= \underline{R}_2, & \underline{R} &= -\underline{R}_1 + \underline{R}_2, & \underline{R} &= \underline{R}_3 \end{aligned} \quad (4.55)$$

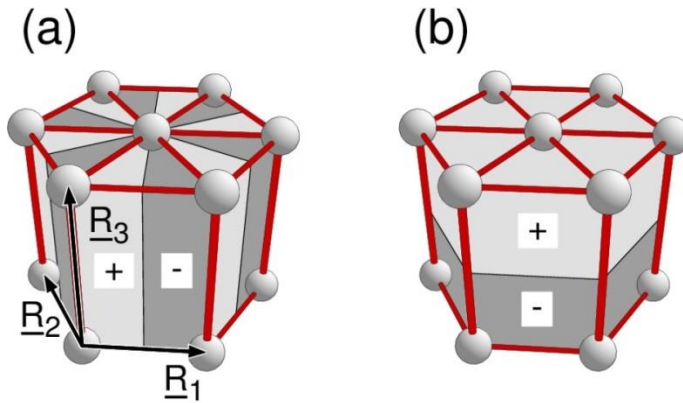


Fig. 4.26. The seven mirror planes of a hexagonal crystal, (a) six vertical planes, (b) one horizontal plane. Crystal atoms of nearest neighbors are connected by sticks. Mirror planes are indicated by boundaries between light and dark regions labeled + and -. All mirror planes go through the center of the hexagonal prism. The lattice vectors are included in (a).

This results, according to (4.48), in **seven** different sets of Miller indices  $(h k l)$ ,  $(l m n q)$  describing normal directions of achiral single crystal surfaces which are listed in Table 4.5.

Table 4.5. Possible sets of Miller indices  $(h k l)$ ,  $(l m n q)$  describing orientations of achiral surfaces of hexagonal crystals. The Miller indices are given in generic and in Miller-Bravais (4-index) notation. Parameters  $m, n$  are integer-valued with at least one being non-zero.

Set	Constraint (4.48)	$(h k l)$ generic	$(l m n q)$ Miller-Bravais
1	$h = 0$	$(0 m n)$	$(0 m -m n)$
2	$2 h + k = 0$	$(m -2m n)$	$(m -2m m n)$
3	$h + k = 0$	$(m -m n)$	$(m -m 0 n)$
4	$h + 2 k = 0$	$(2m -m n)$	$(2m -m -m n)$
5	$k = 0$	$(m 0 n)$	$(m 0 -m n)$
6	$h - k = 0$	$(m m n)$	$(m m -2m n)$
7	$l = 0$	$(m, n, 0)$	$(m, n, -m-n 0)$

As an illustration, Fig. 4.27 shows a model of the perfect stepped  $(1 0 -1 5)$  surface of a **hexagonal cobalt** crystal which is achiral. According to the additivity theorem, the corresponding Miller-Bravais indices can be decomposed according to

$$(1 0 -1 5) = 5 (0 0 0 1) + (1 0 -1 0)$$

which refers to set 5 of Table 4.5. Here the crystal lattice is given by hexagonal lattice vectors  $\underline{R}_1, \underline{R}_2, \underline{R}_3$  according to (4.53) with  $c/a = 1.623$  for cobalt, quite close to the value  $\sqrt{(8/3)} = 1.633$  for

the ideal hexagonal close-packed crystal. Further, the primitive unit cell contains two atoms located at

$$\mathbf{r}_1 = \underline{0}, \quad \mathbf{r}_2 = \frac{2}{3} \underline{\mathbf{R}}_1 + \frac{1}{3} \underline{\mathbf{R}}_2 + \frac{1}{2} \underline{\mathbf{R}}_3 \quad (4.56)$$

These atoms, denoted  $\text{Co}^1$  and  $\text{Co}^2$  in Fig. 4.27, form alternating hexagonal  $(0001)$  terraces of different widths on the  $(10\bar{1}5)$  surface and are separated by  $(10\bar{1}0)$  steps. The hexagonal shape of the terraces and their relative positioning leads to mirror planes perpendicular to the steps and, thus, to an achiral  $(10\bar{1}5)$  surface.

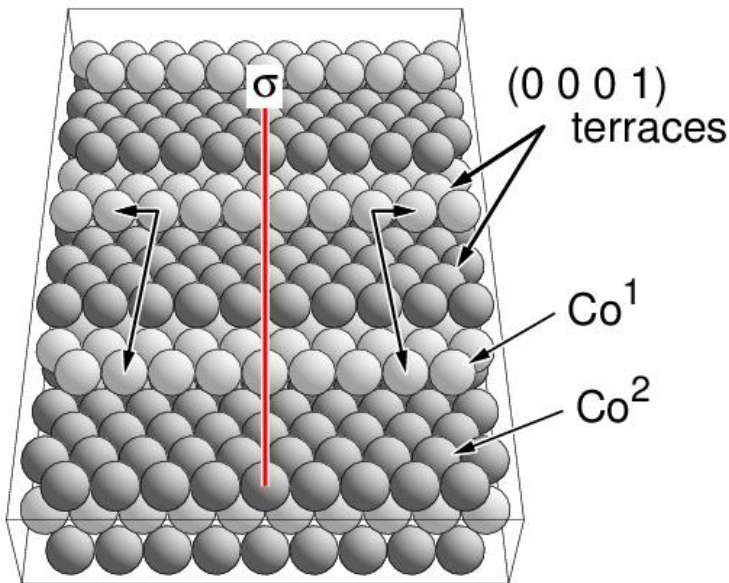


Fig. 4.27. Structure of the stepped  $(10\bar{1}5)$  surface of hexagonal (hcp) cobalt with  $(0001)$  terraces. The atoms  $\text{Co}^1$  and  $\text{Co}^2$ , referring to the two atoms in the primitive hcp unit cell, are distinguished by light and dark gray. The mirror plane perpendicular to the surface is indicated by a red line labeled  $\sigma$ . The netplane-adapted lattice vectors (left- and right-handed) illustrate the surface periodicity.



#### 4.5 Exercises

- 4.1. Determine the densest (close-packed) surfaces of (a) sc, (b) fcc, (c) bcc, (d) hex (hcp), (e) diamond, and (f) CsCl crystals.
- 4.2. How many differently terminated surfaces for given  $(h k l)$  are there for perfect crystals of Ni, GaAs, NaCl, CsCl, graphite? Give the maximum number of terminations and determine Miller indices of corresponding surface orientations. Find orientations with less than the maximum number of terminations.
- 4.3. Determine Miller indices of polar and non-polar surfaces of NaCl and CsCl crystals. Hint: polar surfaces of these crystals are monoatomic.
- 4.4. Analyze surfaces of an fcc crystal with sc Miller indices

- (a)  $(0\ 1\ m)$              $m > 1$   
 (b)  $(1\ 1\ m)$              $m > 1$   
 (c)  $(m-1\ m\ m+1)$      $m > 1$   
 (d)  $(m\ m\ m+2)$          $m > 1$   
 (e)  $(m\ m\ m+4)$          $m > 1$   
 (d)  $(7\ 8\ 11)$   
 (d)  $(1\ 31\ 108)$

by their structure. Characterize terraces, steps, and kinks by their orientations and widths/heights.

- 4.5. Consider the rutile  $\text{TiO}_2$  crystal defined in Exercise 2.23. Analyze ideal surfaces of the bulk truncated crystal with orientations

- (a)  $(0\ 0\ 1)$ ,    (b)  $(1\ 0\ 0)$ ,    (c)  $(0\ 1\ 1)$ ,    (d)  $(1\ 1\ 1)$

Determine for each orientation the number and structure of different terminations. Find point symmetry elements of the  $\text{TiO}_2$  bulk crystal which also appear at the surface.

- 4.6. Which Miller index values  $(h k l)$  of the simple cubic lattice are not strictly valid for numerical evaluations of fcc and bcc lattices when sc indexing is used? Characterize netplanes and surface structures described by Miller indices (in sc notation)

- (a)  $(h k l) = (2m\ 2m\ 2p+1)$             for crystals with an fcc lattice.  
 (b)  $(h k l) = (2m\ 2m\ 2p+1)$             for crystals with a bcc lattice.

Discuss example surfaces.

- 4.7. Determine conditions for surfaces of bcc crystals to possess steps consisting of
- atom rows with smallest interatomic distance. Show that corresponding Miller indices can be represented by  $(m \ n \ \pm(m+n))$ ,  $(m \ n \ \pm(m-n))$  in sc notation.
  - atom rows with second smallest interatomic distance. Show that corresponding Miller indices can be represented by  $(0 \ m \ n)$ ,  $(m \ 0 \ n)$ ,  $(m \ n \ 0)$  in sc notation.
- 4.8. Determine Miller indices of a crystal with a bcc lattice and a surface of consisting of 6 (nearest neighbor) atom distances wide terraces with single atom steps.
- 4.9. Give an example of a kinked surface of a silicon crystal with  $(1 \ 1 \ 1)$  terraces.
- 4.10. Visualize the facet edge of a stepped surface of an fcc crystal where  $(1 \ 1 \ 1)$  and  $(1 \ 0 \ 0)$  indexed surfaces join (Miller indices in sc notation).
- 4.11. Determine neighbor shells ( $1^{\text{st}}$  to  $5^{\text{th}}$  neighbors) for atoms of the  $1^{\text{st}}$ ,  $2^{\text{nd}}$ , ... surface layer of the
- $(1 \ 0 \ 0)$ ,  $(1 \ 1 \ 0)$ , and  $(1 \ 1 \ 1)$  surfaces of an fcc crystal.
  - $(1 \ 0 \ 0)$ ,  $(1 \ 1 \ 0)$ , and  $(1 \ 1 \ 1)$  surfaces of an bcc crystal.

From which surface layer on are the  $3^{\text{rd}}$  neighbor shells complete (reflecting those of the bulk)?

- 4.12. Decompose the Miller index triplets  $(h \ k \ l)$  of netplanes into those of densely packed netplanes and give the formal decomposition relations for
- fcc $(7 \ 9 \ 9)$
  - bcc $(1 \ 1 \ 10)$
  - hex (hcp) $(0 \ 0 \ 0 \ 1)$
  - hex (hcp) $(5 \ 1 \ -6 \ 0)$
  - sc $(7 \ 8 \ 11)$

Characterize surfaces with Miller index orientations  $(h \ k \ l)$  given in (a) - (e).

- 4.13. Give alternative netplane decompositions for the  $(4 \ 3 \ 1)$  surface of a crystal with an fcc lattice (sc notation). Visualize the decompositions.

- 4.14. Build a surface of a crystal with an fcc lattice which consists of alternating 6 and 7 atom distances long kinks and determine corresponding sc Miller indices. Which general irregularities of the kink sequences can arise for crystals with an fcc lattice?
- 4.15. Show that the stepped (1 2 3) surface of a crystal with a bcc lattice is chiral. Discuss the geometric structure of the two chiral partner surfaces.
- 4.16. Show that the hexagonal graphite crystal, defined in Exercise 2.7, allows all achiral surfaces given in Table 4.5.
- 4.17. Prove that in the Miller index decomposition for Miller indices of fcc and bcc lattices using the sc notation a scaling factor  $\Delta = 4$  and  $\Delta = 2$ , respectively, is required in relations (4.31).
- 4.18. Molecules with  $n > 1$  chiral centers allow  $2^n$  different arrangements of their left- and right-handed centers distinguishing between isomeric species. Of these, pairs of molecules are enantiomers if their chiral centers are complementary in handedness. (The members of other pairs are called diastereomers.)
- Show that there are up to  $2^{(n-1)}$  different enantiomer pairs.
  - For which chiral arrangements can the molecules with  $n > 1$  chiral centers become achiral?
- 4.19. Determine the chirality (left- or right-handedness, denoted  $X = L, S$  in  $(h k l)^X$ ) of the following kinked surfaces of cubic bulk substrate (Miller indices in sc notation)
- sc :  $(6 2 1)^X, (7 5 1)^X, (10 3 1)^X, (10 7 1)^X, (13 3 1)^X$ .
  - fcc :  $(5 3 1)^X, (6 4 3)^X, (8 5 4)^X, (8 7 4)^X, (10 8 5)^X, (17 1 3)^X$ .
  - bcc :  $(11 10 3)^X, (12 7 1)^X, (16 3 1)^X, (16 -3 -1)^X, (16 1 3)^X$ .

## 5 REAL CRYSTAL SURFACES

Atoms at **real crystal surfaces** appearing in nature experience a different local binding environment (connected with different atom coordination) as compared to atom sites inside the bulk crystal. This leads to **structures** of real surfaces which **differ** from those of simple **bulk truncation** discussed for ideal single crystal surfaces. The differences may be rather small, examples are many elemental metal surfaces, but can also be quite substantial for semiconductor or oxide surfaces. Real surfaces can be restructured locally by bond changes including making and breaking of bonds which may result in an overall **disordered** structure. In many other cases, surfaces will still exhibit a two-dimensionally periodic atom arrangement. However, the periodicity, specific atom positions, and the placement of atom layers may be different from those of bulk layers. These effects are usually described by surface **relaxation** and **reconstruction**, where details as well as nomenclature have been treated differently in the literature [94]. However, the basic concepts discussed in this section are universal. Real crystal surfaces are often covered by adsorbates which introduces additional structural features as will be treated in Sec. 6.

### 5.1 Surface Relaxation

The effect of surface **relaxation** is the simplest modification observed for real surfaces. It assumes that the  $(h k l)$  surface of a substrate, whose bulk lattice is given by a netplane-adapted lattice vectors  $\underline{R}_1, \underline{R}_2, \underline{R}_3$ , is terminated by overlayers forming  $(h k l)$  monolayers, identical to those of the substrate. However, **relative positions** of the **overlayer atoms** near the surface, expressed by inter-layer distances and lateral shifts, **deviate** from corresponding positions in the **bulk**. This is described in the simplest case by complete overlayers shifting slightly with respect to their bulk positions. In most cases that are observed in experiments [22], [23] these shifts happen **perpendicular** to the surface, either towards (**inwards** relaxation) or away from the substrate (**outwards** relaxation).

**Formally**, atom positions of **relaxed overlayers** near the surface are described by

$$\underline{R}^{(m)} = \underline{r}_i + n_1 \underline{R}_1 + n_2 \underline{R}_2 + \underline{s}^{(m)}, \quad n_1, n_2 \text{ integer}, \quad i = 1, \dots, p \quad (5.1)$$

for layer  $m$  near the surface where  $\underline{r}_i$  refers to positions of atoms inside the unit cell of the bulk lattice,  $n_1, n_2$  are integer-valued coefficients accounting for the overlayer (netplane) periodicity, and

$\underline{s}^{(m)}$  is a shift vector corresponding to the absolute positioning of layer  $m$ . As an illustration, Fig. 5.1 shows the (0 0 1) surface of a fictitious crystal with a simple cubic lattice (lattice constant  $a$ ), where the topmost layer no. 1 is relaxed inwards by 10% and shifted sideways by vector  $\underline{v}$  and layer no. 2 is relaxed inwards by 30%.

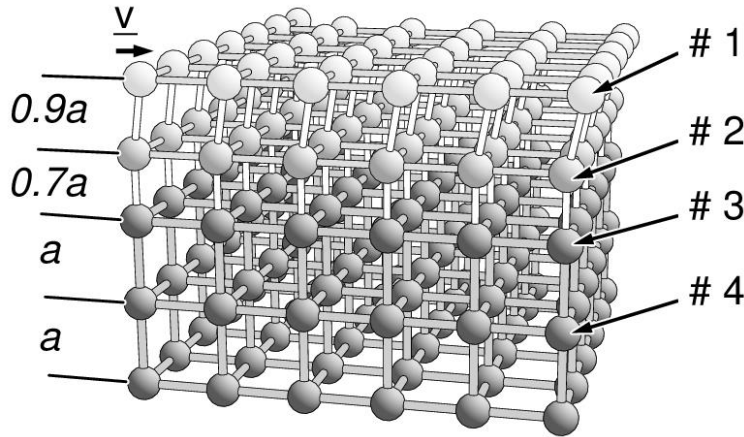


Fig. 5.1. Hypothetical (0 0 1) surface section of a crystal with a simple cubic lattice (lattice constant  $a$ ) with the two topmost overlayers relaxed, see text. Layer indices (by '# i') and inter-layer distances are indicated.

Shift vectors  $\underline{s}^{(m)}$  are equal to  $(n_3 \underline{R}_3)$  for **bulk truncated** surfaces of ideal single crystals. Further,  $\underline{s}^{(m)}$  is expected to approach the bulk value  $(n_3 \underline{R}_3)$  for layers positioned well **below** the surface. Relaxation occurs for most metal surfaces, where, so far, mainly monolayer shifts perpendicular to the surface have been considered [105] (typical shifts amount to 1 - 5% of the inter-layer spacing), with only few examples of lateral shifts in cases of stepped surfaces [22], [23].

## 5.2 Surface Reconstruction

Real surfaces which differ structurally from simple bulk truncation other than by relaxation are described as **reconstructed** surfaces. Reconstruction of a single crystal surface may result in surface **disorder** or may yield a **periodic** surface structure including minor or sizeable displacements of the atoms and different periodicity compared with the bulk. Further, **additional** or **fewer atoms** may exist in the layer unit cells compared with those of an ideal bulk truncation. In the periodic case the  $(h k l)$  surface of the substrate is terminated by monolayers that exhibit a two-dimensional periodicity given by vectors  $\underline{R}_1'$  and  $\underline{R}_2'$ . These vectors can differ from those of the corresponding  $(h k l)$  bulk netplanes,  $\underline{R}_1$  and  $\underline{R}_2$ , to form **superlattices**. In addition, the building units (two-

dimensional unit cells) of the surface monolayers may contain a number of atoms different from that of the bulk layers. These monolayers will be called **overlayers** in the following.

Surface reconstruction is usually **combined** with relaxation such that atom positions of monolayers near the surface are described mathematically by

$$\underline{\mathbf{R}}^{(m)} = \underline{\mathbf{r}}_i' + n_1 \underline{\mathbf{R}}_1' + n_2 \underline{\mathbf{R}}_2' + \underline{\mathbf{s}}^{(m)} \quad (5.2)$$

for layer  $m$  near the surface where  $\underline{\mathbf{r}}_i'$  refer to atom positions inside the reconstructed overlayers (which may or may not include positions of the initial bulk crystal),  $n_1, n_2$  are integer-valued coefficients accounting for the overlayer periodicity, and  $\underline{\mathbf{s}}^{(m)}$  is a shift vector which describes possible layer relaxation. The periodicity vectors  $\underline{\mathbf{R}}_1'$  and  $\underline{\mathbf{R}}_2'$  can be connected with those of the  $(h k l)$  bulk netplanes,  $\underline{\mathbf{R}}_1$  and  $\underline{\mathbf{R}}_2$ , by linear  $2 \times 2$  **transformations**, written in matrix form as

$$\begin{pmatrix} \underline{\mathbf{R}}_1' \\ \underline{\mathbf{R}}_2' \end{pmatrix} = \begin{pmatrix} m_{11} & m_{12} \\ m_{21} & m_{22} \end{pmatrix} \cdot \begin{pmatrix} \underline{\mathbf{R}}_1 \\ \underline{\mathbf{R}}_2 \end{pmatrix} = \underline{\mathbf{M}} \cdot \begin{pmatrix} \underline{\mathbf{R}}_1 \\ \underline{\mathbf{R}}_2 \end{pmatrix} \quad (5.3)$$

assuming surface-adapted lattice vectors  $\underline{\mathbf{R}}_1, \underline{\mathbf{R}}_2, \underline{\mathbf{R}}_2$  describing the bulk periodicity. As a consequence, the **unit cell area**  $F'$  of a reconstructed overlayer is given by

$$\begin{aligned} F' &= |\underline{\mathbf{R}}_1' \times \underline{\mathbf{R}}_2'| = |(m_{11} \underline{\mathbf{R}}_1 + m_{12} \underline{\mathbf{R}}_2) \times (m_{21} \underline{\mathbf{R}}_1 + m_{22} \underline{\mathbf{R}}_2)| = \\ &= |(m_{11} m_{22} - m_{12} m_{21}) (\underline{\mathbf{R}}_1 \times \underline{\mathbf{R}}_2)| = |\det(\underline{\mathbf{M}})| F \end{aligned} \quad (5.4)$$

where  $F$  is the unit cell area of the  $(h k l)$  bulk netplane. Thus,  $|\det(\underline{\mathbf{M}})|$  gives the ratio of the unit cell area  $F'$  of the overlayer and that,  $F$ , of the corresponding bulk layers. The transformation matrix  $\underline{\mathbf{M}}$  in (5.3), called **reconstruction matrix** and sometimes written as  $(\mathbf{m}_{11} \mathbf{m}_{12} | \mathbf{m}_{21} \mathbf{m}_{22})$  for convenience, allows a classification of reconstructed periodic surfaces into three categories,

- (a) Reconstruction with **commensurate** superlattices is described by a reconstruction matrix  $\underline{\mathbf{M}}$  according to (5.3) containing only **integer-valued** elements  $m_{ij}$ . In this case the periodicity vectors  $\underline{\mathbf{R}}_1', \underline{\mathbf{R}}_2'$  of the overlayer are also general vectors of the  $(h k l)$  bulk netplane and the unit cell area of the overlayer is an integer multiple of that of the bulk netplane. This includes systems, for which matrix  $\underline{\mathbf{M}}$  equals the **unit matrix** and the reconstructed overlayer is of the same periodicity as the  $(h k l)$  bulk netplane. As a simple example Fig. 5.2 compares the ideal  $(1 1 0)$  surface of fcc platinum with the so-called  $(1 \times 2)$ -missing-row reconstructed surface [106] taken from the **Surface Structure Database**, SSD 78.77, where every second row of atoms of the topmost  $(1 1 0)$  layer is missing. This results in a reconstruction matrix

$$\underline{\underline{\mathbf{M}}} = \begin{pmatrix} 1 & 0 \\ 0 & 2 \end{pmatrix}, \quad F' = 2 F \quad (5.5)$$

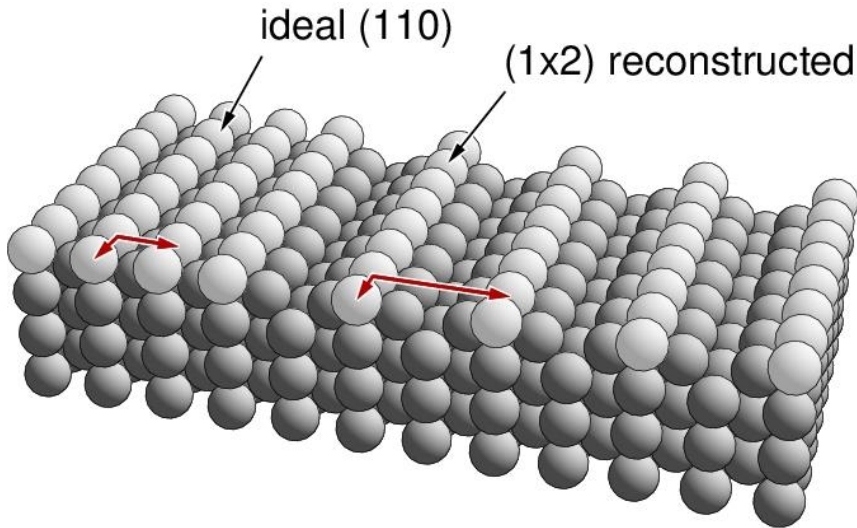


Fig. 5.2. Ideal (left) and the  $(1 \times 2)$  reconstructed Pt(1 1 0) surface (right). The layer periodicity vectors are indicated in red for both surface structures.

Note that in this example and the following ones we make use of the so-called **Wood notation** to denote the overlayer periodicity such as ‘ $(1 \times 2)$ ’ or (centered) ‘ $c(2 \times 2)$ ’. This notation will be discussed in detail in Sec. 6.3.

Another example is the centered  $(2 \times 2)$  reconstruction of the  $(1 0 0)$  surface of bcc tungsten [22] taken from the Surface Structure Database, SSD 74.14, and illustrated by Fig. 5.3. Here the reconstruction matrix  $\underline{\underline{\mathbf{M}}}$  is given by

$$\underline{\underline{\mathbf{M}}} = \begin{pmatrix} 1 & -1 \\ 1 & 1 \end{pmatrix}, \quad F' = 2 F \quad (5.6)$$

In addition to the transformed periodicity, atom positions of the topmost overlayer are displaced by alternating lateral shifts as indicated by red arrows in Fig. 5.3 which yields diagonal zig-zag rows of tungsten atoms. Thus, this type of reconstruction may also be called **displacive**.

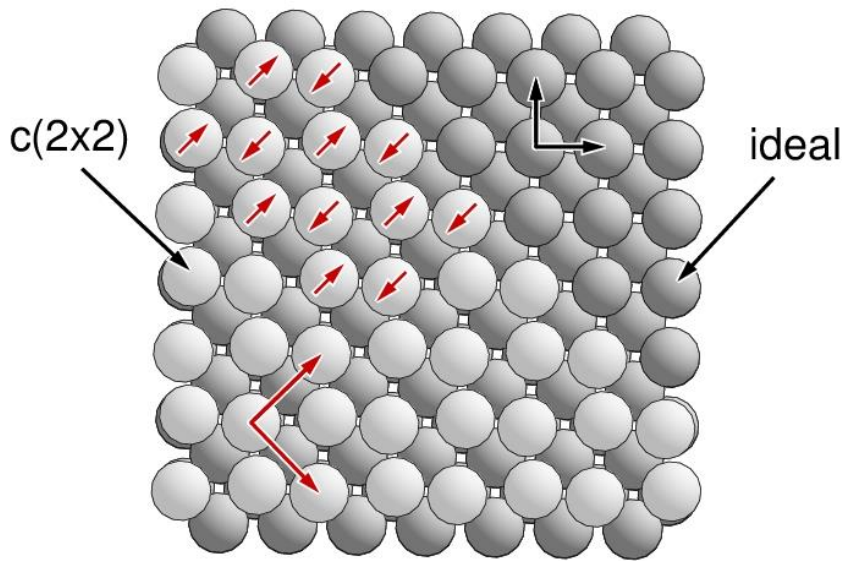


Fig. 5.3. Ideal (upper right) and  $c(2 \times 2)$ -reconstructed  $W(100)$  surface (lower left). The layer periodicity vectors are shown separately for the ideal substrate (black) and the reconstructed overlayer (red). Corresponding atom displacements are indicated by red arrows.

As more complicated examples, we mention surface structures, in which commensurate **reconstruction** is **combined** with major **repositioning** of individual atoms near the surface. An example is given by the symmetric dimer  $(2 \times 1)$  [107] and the buckled dimer  $c(4 \times 2)$  reconstructed  $(100)$  surfaces of silicon [108], see Fig. 5.4, where alternating rows of surface atoms are shifted laterally as well as up and down forming surface **dimers** in order to optimize their Si-Si bonds.



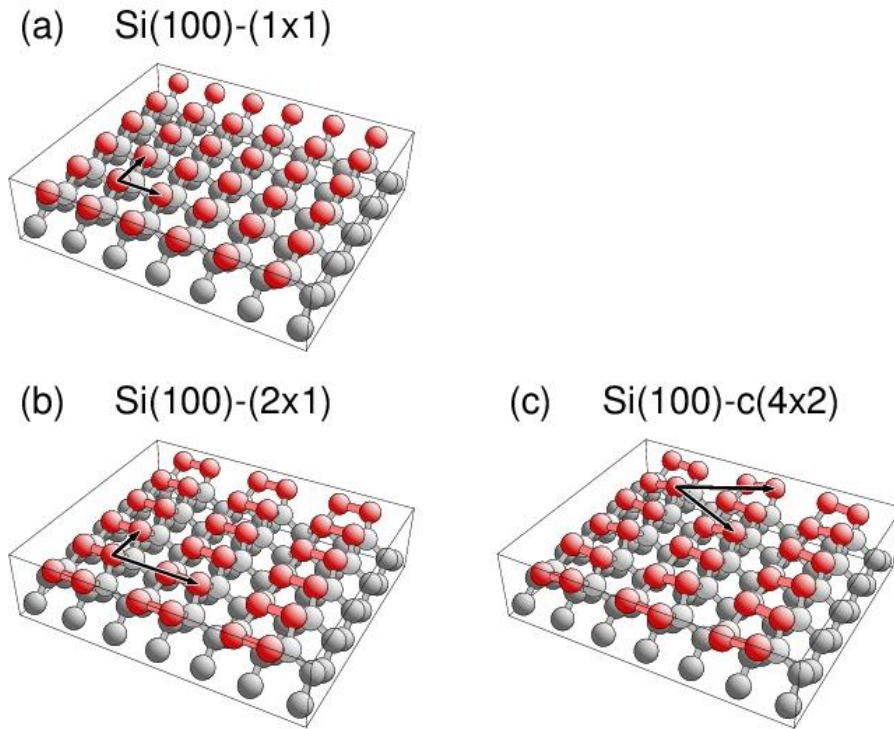


Fig. 5.4. The Si(1 0 0) surface, (a) ideal unreconstructed ( $1 \times 1$ ), (b) reconstructed ( $2 \times 1$ ) with symmetric dimers in top layer, (c) reconstructed  $c(4 \times 2)$  with buckled dimers in top layer. The corresponding overlayers are shown in red with their lattice vectors sketched in black.

The buckled dimer  $c(4 \times 2)$  reconstruction [108] shown in Fig. 5.4c is an example of a more general behavior of reconstructed overlayers which, as a result of their coupling with the substrate, are not strictly planar with atoms shifted up and down resulting in **buckled surfaces**. In general, these perpendicular shifts can be described by **modulation functions**  $\Delta z(\underline{r})$ , where  $\underline{r}$  denotes lateral positions along the surface. Due to the lateral periodicity of the overlayers  $\Delta z(\underline{r})$  is also a periodic function. Thus, it may be represented by a **Fourier expansion** with respect to the overlayer periodicity. The modulation of atom positions is not restricted to reconstructed overlayers only but may also reach deeper into the substrate making the definition of corresponding modulation functions for substrate layers necessary. Further, the concept of modulated atom positions, described by appropriate modulation functions, can also be applied to all other types of reconstruction discussed below.

A very complex example is given by the **dimer-adatom-stacking-fault (DAS) model** of the  $(7 \times 7)$  reconstructed  $(1\ 1\ 1)$  surface of silicon [109], [110], see Fig. 5.5, where the topmost three monolayers of the surface reconstruct. Here Si adatoms stick out of the surface,  $\text{Si}_2$  dimers stabilize in long trenches which cross to form open holes, and the rest atoms

together with the adatoms yield a mirror symmetry inside the surface unit cell (not existing in the bulk) described as a stacking fault

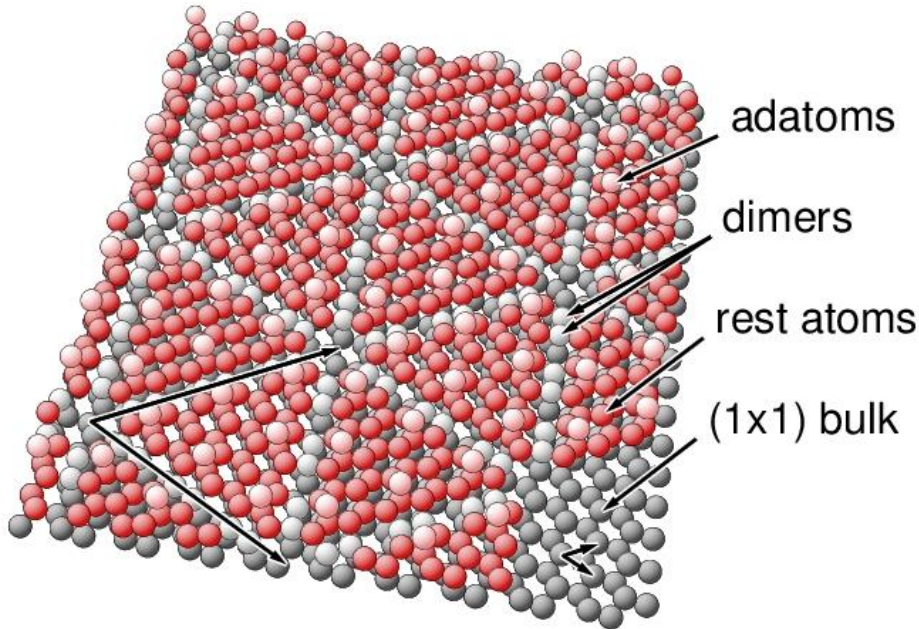


Fig. 5.5. Structure of the reconstructed  $\text{Si}(1\ 1\ 1) - (7 \times 7)$  surface according to the dimer-atom-stacking-fault (DAS) model. The overlayer is removed at the bottom right to reveal the ideal bulk termination of  $\text{Si}(1\ 1\ 1)$ . The different Si atom types are labeled accordingly. The periodicity vectors of the overlayer and of the ideal bulk termination are sketched in black.

- (b) Reconstruction with **coincidence superlattices**, sometimes also called **high-order commensurate (HOC)** or **scaled commensurate** lattices, is described by a reconstruction matrix  $\underline{\underline{\mathbf{M}}}$  according to (5.3) which contains **rational**- and **integer**-valued elements  $m_{ij}$  with at least one being rational. Thus, matrix  $\underline{\underline{\mathbf{M}}}$  can be written as

$$\underline{\underline{\mathbf{M}}} = \begin{pmatrix} r_{11} & r_{12} \\ r_{21} & r_{22} \end{pmatrix}, \quad r_{ij} = \frac{p_{ij}}{q_{ij}}, \quad p_{ij}, q_{ij} \text{ integer} \quad (5.7)$$

where  $q_{ij} = 1$  corresponds to an integer  $r_{ij}$ . Together with  $c_i = \text{lcm}(q_{i1}, q_{i2})$  denoting the least common multiple (see Appendix E.1) of the two denominators  $q_{i1}, q_{i2}$ ,  $i = 1, 2$ , this matrix can be written as a **reconstruction matrix**

$$\underline{\underline{\mathbf{M}}} = \begin{pmatrix} \frac{r_{11}'}{c_1} & \frac{r_{12}'}{c_1} \\ \frac{r_{21}'}{c_2} & \frac{r_{22}'}{c_2} \end{pmatrix} = \begin{pmatrix} c_1 & 0 \\ 0 & c_2 \end{pmatrix}^{-1} \begin{pmatrix} r_{11}' & r_{12}' \\ r_{21}' & r_{22}' \end{pmatrix}, \quad r_{ij}' = c_i \cdot r_{ij} = \frac{c_i}{q_{ij}} \cdot p_{ij} \quad (5.8)$$

to yield

$$\begin{pmatrix} \underline{\mathbf{R}}_1'' \\ \underline{\mathbf{R}}_2'' \end{pmatrix} = \begin{pmatrix} c_1 & 0 \\ 0 & c_2 \end{pmatrix} \begin{pmatrix} \underline{\mathbf{R}}_1' \\ \underline{\mathbf{R}}_2' \end{pmatrix} = \begin{pmatrix} r_{11}' & r_{12}' \\ r_{21}' & r_{22}' \end{pmatrix} \cdot \begin{pmatrix} \underline{\mathbf{R}}_1 \\ \underline{\mathbf{R}}_2 \end{pmatrix} \quad (5.9)$$

where elements  $r_{ij}'$  and  $c_i$  are **integer**-valued. Thus, if the initial overlayer lattice  $\underline{\mathbf{R}}_1', \underline{\mathbf{R}}_2'$  in (5.3) is represented by a lattice with a larger unit cell given by scaled lattice vectors

$$\underline{\mathbf{R}}_1'' = c_1 \underline{\mathbf{R}}_1', \quad \underline{\mathbf{R}}_2'' = c_2 \underline{\mathbf{R}}_2' \quad (5.10)$$

then the resulting matrix  $\underline{\mathbf{M}}$  in (5.8) is replaced by an integer-valued matrix and the superlattice will be commensurate. This property of matrix  $\underline{\mathbf{M}}$  explains the nomenclature ‘scaled commensurate’ for this type of reconstruction. The **distinction** between simple commensurate and coincidence superlattices may be considered somewhat artificial. However, we will keep this distinction to indicate that **coincidence** superlattices connect **non-primitive** unit cells of the overlayer, larger than corresponding primitive cells, with those of the substrate. In contrast, (**simple**) **commensurate** superlattices connect **primitive** unit cells of the overlayer with those of the substrate.

As an example of a coincidence superlattice, Fig. 5.6 shows a postulated structure of the (1 1 1) oriented gold surface [111], referred to as Au(1 1 1) - ( $\sqrt{3} \times 22$ )rect, where the top-most gold layer forms a hexagonal lattice which is compressed unilaterally along  $\underline{\mathbf{R}}_2$  by 4.35% (= 1/23) such that 23 atom distances of the overlayer along  $\underline{\mathbf{R}}_2$  coincide with 22 atoms distances of the substrate. As a consequence, the primitive unit cell of the surface is rectangular and given by scaled lattice vectors

$$\underline{\mathbf{R}}_1'' = 2 \underline{\mathbf{R}}_1 - \underline{\mathbf{R}}_2, \quad \underline{\mathbf{R}}_2'' = 22 \underline{\mathbf{R}}_2 \quad (5.11)$$

which are orthogonal and where  $|\underline{\mathbf{R}}_1''| = \sqrt{3} |\underline{\mathbf{R}}_1|$  (explaining the nomenclature ‘( $\sqrt{3} \times 22$ )rect’). The overlayer atoms of the rows along  $\underline{\mathbf{R}}_2$  compensate their lateral **compressive stress** by gradually shifting their positions normal to the surface, as illustrated in Fig. 5.6b. This results in a periodically **buckled surface**, where the buckling can be described by a modulation function  $\Delta z(\mathbf{r})$  as discussed before.

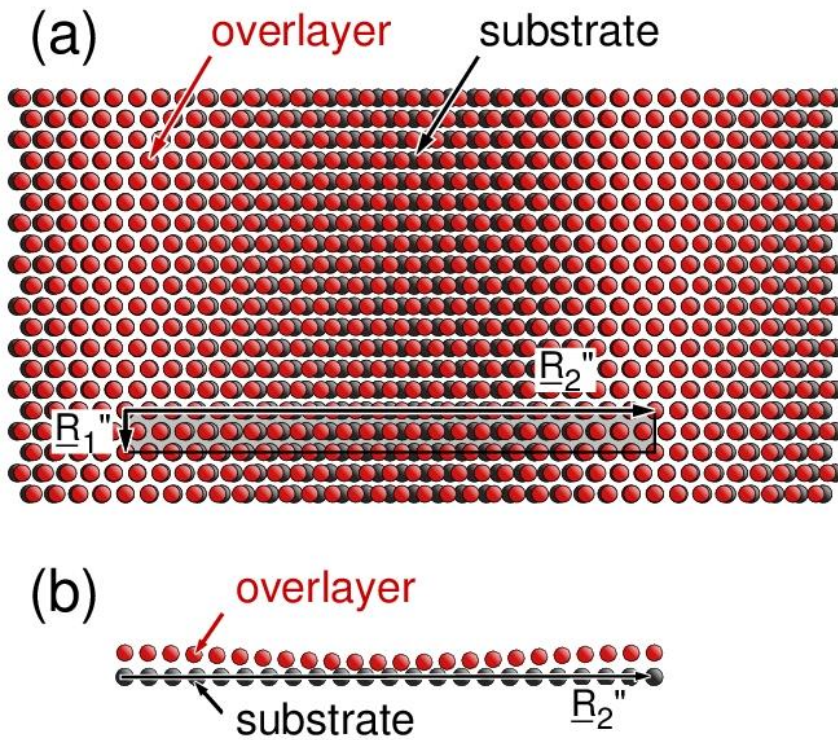


Fig. 5.6. (a) Coincidence superlattice of the Au(1 1 1) -  $(\sqrt{3} \times 22)$ rect surface shown by its overlayer (red) and the topmost substrate layer (black) for a normal view. The common unit cell is emphasized in gray with scaled lattice vectors  $\underline{R}_1''$ ,  $\underline{R}_2''$  indicated. (b) Parallel view of the unit cell along  $\underline{R}_1''$  illustrating the perpendicular displacement (buckling) of the overlayer atoms.

As another example, Fig. 5.7 shows a fictitious surface with two graphene layers, i.e. graphite monolayers with honeycomb structure, corresponding to a reconstruction matrix

$$\underline{\underline{M}} = \frac{1}{12} \begin{pmatrix} 11 & 2 \\ -2 & 13 \end{pmatrix} = \begin{pmatrix} 0.9167 & 0.1667 \\ -0.1667 & 1.0833 \end{pmatrix} \quad (5.12)$$

discussed below, see also (5.27). This surface forms a **coincidence lattice** with scaled lattice vectors  $\underline{R}_i'' = 12 \underline{R}_i'$  according to (5.10) and shows a **hexagonal moiré pattern** whose periodicity vectors  $\underline{R}_1^p$ ,  $\underline{R}_2^p$  (not included in Fig. 5.7) can be described by

$$\begin{pmatrix} \underline{R}_1^p \\ \underline{R}_2^p \end{pmatrix} = \begin{pmatrix} 3 & 5 \\ -5 & 8 \end{pmatrix} \cdot \begin{pmatrix} \underline{R}_1 \\ \underline{R}_2 \end{pmatrix} \quad (5.13)$$

as discussed in detail in Sec. 6.5. This leads to

$$\begin{pmatrix} \underline{R}_1'' \\ \underline{R}_2'' \end{pmatrix} = 12 \underline{\underline{M}} \begin{pmatrix} 3 & 5 \\ -5 & 8 \end{pmatrix}^{-1} \cdot \begin{pmatrix} \underline{R}_1^p \\ \underline{R}_2^p \end{pmatrix} = \begin{pmatrix} 2 & -1 \\ 1 & 1 \end{pmatrix} \cdot \begin{pmatrix} \underline{R}_1^p \\ \underline{R}_2^p \end{pmatrix} \quad (5.14)$$

which shows that the coincidence lattice is also **commensurate** with the **moiré lattice** and the unit cell area given by the scaled lattice vectors  $\underline{R}_1''$ ,  $\underline{R}_2''$  is three times, i.e. an integer multiple of, the periodicity cell area suggested by the moiré pattern. This is a more general result of coincidence lattices forming moiré patterns as shown in Sec. 6.5.

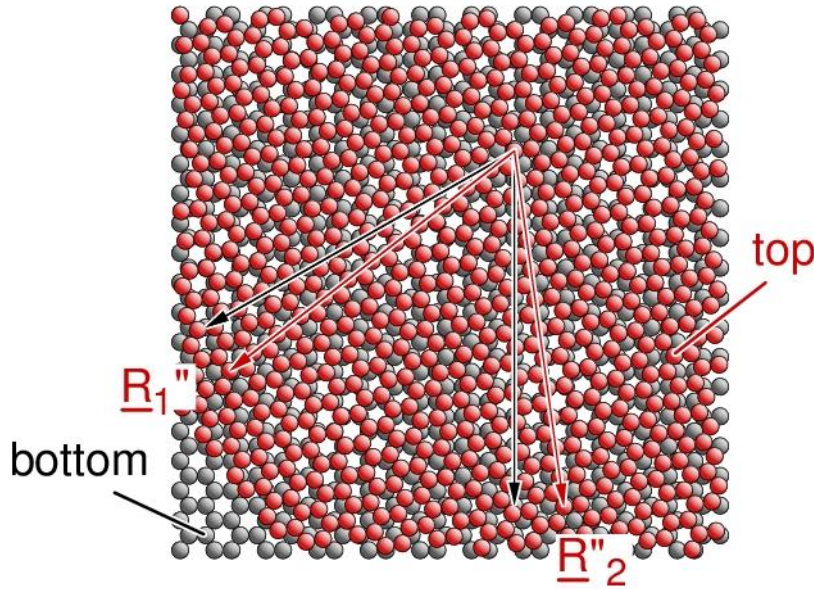


Fig. 5.7. Coincidence superlattice of two graphene sheets, see text. The scaled lattice vectors  $\underline{R}_1''$ ,  $\underline{R}_2''$  of the top layer are shown in red, those of the bottom layer in black.

- (c) Reconstruction with **incommensurate** superlattices is described by a reconstruction matrix  $\underline{\underline{M}}$  containing elements  $m_{ij}$  of which at least one is **irrational**, i.e. cannot be represented by an integer or a rational number. In this case at least one of the periodicity vectors  $\underline{R}_1'$ ,  $\underline{R}_2'$  in (5.3) cannot be described by lattice vectors of the corresponding  $(h k l)$  substrate netplane using integer- or rational-valued linear combinations. Further, the **combined** surface system (overlayer with substrate layers) is **not strictly periodic** in two dimensions. As an example, Fig. 5.8 shows a  $(1 0 0)$  surface of fcc gold [112] taken from the Surface Structure Database, SSD 79.80. Here the topmost overlayer is reconstructed with a slightly distorted hexagonal structure, while the  $(1 0 0)$  monolayers of the substrate are of square geometry and also slightly distorted near the surface. Assuming a perfectly hexagonal overlayer on a substrate with exact square lattice this results in a reconstruction matrix

$$\underline{\underline{M}} = \eta \begin{pmatrix} 1 & 0 \\ -1/2 & \sqrt{3}/2 \end{pmatrix} \quad (5.15)$$

where  $\eta$  ( $\approx 0.95$ ) is the ratio of the lattice constants of the reconstructed layer and the initial (1 0 0) monolayer.

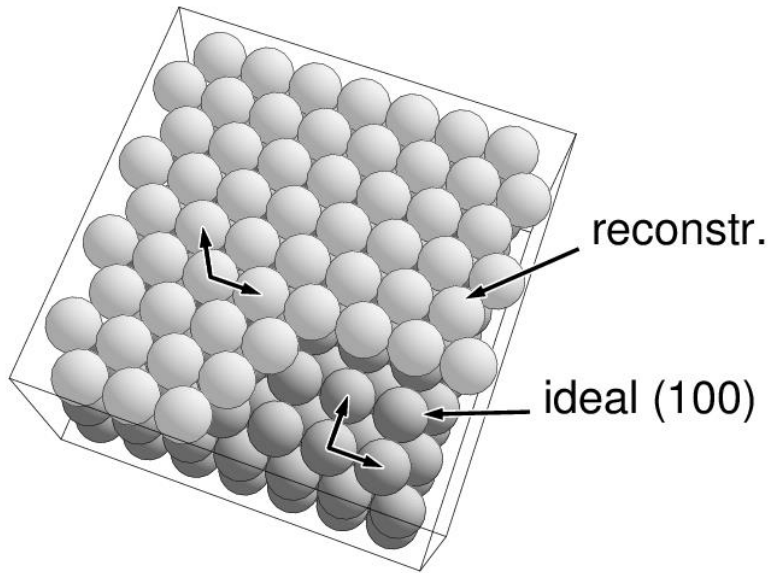


Fig. 5.8. Hexagonal reconstructed Au(1 0 0) surface. Atoms of the top reconstructed and the underlying substrate layers are painted differently with periodicity vectors sketched accordingly.

An esthetically pleasing class of incommensurate superlattices is given by surfaces with **rotational superlattices**. Here the topmost overlayer retains its internal lattice (except for minor lateral distortions and buckling) but is rotated by an angle  $\alpha$  with respect to the underlying substrate layer. Simple algebraic calculus shows that the reconstruction matrix  $\underline{\underline{M}}$  of a rotational superlattice is given by

$$\underline{\underline{M}} = \frac{1}{\sin(\omega)} \begin{pmatrix} \sin(\omega - \alpha) & q^{-1} \sin(\alpha) \\ -q \sin(\alpha) & \sin(\omega + \alpha) \end{pmatrix}, \quad q = \frac{R_2}{R_1} \quad (5.16)$$

assuming an anti-clockwise rotation of the overlayer by an angle  $\alpha$ , where the angle between the lattice vectors  $\underline{R}_1$  and  $\underline{R}_2$  of the  $(h k l)$  bulk netplane is  $\omega$ . These surface systems exhibit **spatial interference** patterns, so-called **moiré** patterns as shown above, which have been observed for many surfaces as will be discussed in great detail in Sec. 6.5.

While rotational superlattices are **incommensurate** in general a detailed mathematical analysis shows that, depending on the angles  $\omega$ ,  $\alpha$ , and the ratio  $q$  of the vector lengths  $R_2$  and  $R_1$ , they can also yield **coincidence superlattices** which bridges between incommensurate and high-order commensurate surface systems. As a conceptual example, we consider a

simple cubic substrate with a (0 0 1) oriented surface, where the monolayers of the substrate are described by square lattices with lattice vectors given by

$$\underline{\mathbf{R}}_1 = a (1, 0), \quad \underline{\mathbf{R}}_2 = a (0, 1) \quad (5.17)$$

(ignoring the third dimension normal to the surface). Further, we assume that the topmost monolayer (overlayer) is rotated with respect to the substrate layers by an angle  $\alpha$  with  $\tan(\alpha) = n_2/n_1$  where  $n_1, n_2$  are positive integers. Then the reconstruction matrix (5.16) with  $q = 1, \omega = 90^\circ$  reads

$$\underline{\underline{\mathbf{M}}} = \begin{pmatrix} \cos(\alpha) & \sin(\alpha) \\ -\sin(\alpha) & \cos(\alpha) \end{pmatrix} = \frac{1}{\sqrt{n_1^2 + n_2^2}} \begin{pmatrix} n_1 & n_2 \\ -n_2 & n_1 \end{pmatrix} \quad (5.18)$$

and the lateral lattice vectors of the overlayer,  $\underline{\mathbf{R}}_1', \underline{\mathbf{R}}_2'$  are given by

$$\begin{pmatrix} \underline{\mathbf{R}}_1' \\ \underline{\mathbf{R}}_2' \end{pmatrix} = \frac{1}{\sqrt{n_1^2 + n_2^2}} \begin{pmatrix} n_1 & n_2 \\ -n_2 & n_1 \end{pmatrix} \begin{pmatrix} \underline{\mathbf{R}}_1 \\ \underline{\mathbf{R}}_2 \end{pmatrix} \quad (5.19)$$

Thus, the lattice vectors (5.19) describe, in general, an **incommensurate** overlayer. However, for selected integer values  $n_1, n_2$  with

$$n_1^2 + n_2^2 = N^2, \quad N \text{ integer} \quad (5.20)$$

which correspond to a discrete set of angles  $\alpha$  where

$$\cos(\alpha) = n_1/N, \quad \sin(\alpha) = n_2/N \quad (5.21)$$

the reconstruction matrix (5.18) becomes

$$\underline{\underline{\mathbf{M}}} = \begin{pmatrix} \cos(\alpha) & \sin(\alpha) \\ -\sin(\alpha) & \cos(\alpha) \end{pmatrix} = \frac{1}{N} \begin{pmatrix} n_1 & n_2 \\ -n_2 & n_1 \end{pmatrix} \quad (5.22)$$

and describes a **coincidence lattice** reconstruction, as discussed above. Thus, if the rotated overlayer lattice  $\underline{\mathbf{R}}_1', \underline{\mathbf{R}}_2'$  of (5.3) is represented by non-primitive lattice vectors  $\underline{\mathbf{R}}_1'', \underline{\mathbf{R}}_2''$  with

$$\underline{\mathbf{R}}_1'' = N \underline{\mathbf{R}}_1', \quad \underline{\mathbf{R}}_2'' = N \underline{\mathbf{R}}_2' \quad (5.23)$$

the resulting matrix transformation between  $(\underline{\mathbf{R}}_1, \underline{\mathbf{R}}_2)$  and  $(\underline{\mathbf{R}}_1'', \underline{\mathbf{R}}_2'')$  based on (5.19), (5.22), and (5.23) is integer-valued and the overlayer will be high-order commensurate. This is illustrated in Fig. 5.9 for  $n_1 = 4, n_2 = 3$  (hence  $N = 5$  corresponding to  $\alpha = 36.87^\circ$ ). The supercell, given by  $\underline{\mathbf{R}}_1'', \underline{\mathbf{R}}_2''$ , is common to both the substrate and overlayer lattice, and contains 25 atoms per unit cell in each layer. However, it does not represent the primitive cell of the

compound system, which is given by vectors  $\underline{R}_{o1}''$ ,  $\underline{R}_{o2}''$  with

$$\begin{pmatrix} \underline{R}_{o1}'' \\ \underline{R}_{o2}'' \end{pmatrix} = \begin{pmatrix} 2 & -1 \\ 1 & 2 \end{pmatrix} \cdot \begin{pmatrix} \underline{R}_1 \\ \underline{R}_2 \end{pmatrix} \quad (5.24)$$

as sketched in Fig. 5.9 where only 5 atoms are included in the unit cell of each layer.

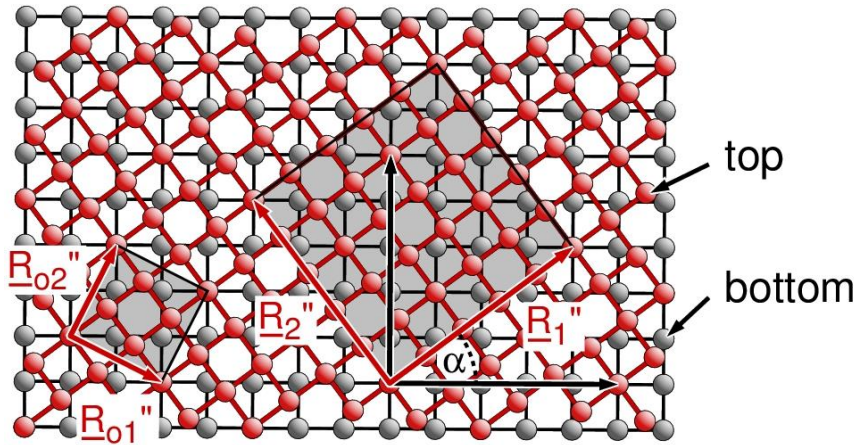


Fig. 5.9. Commensurate rotational overlayer on a substrate with square lattice corresponding to  $\alpha = 36.87^\circ$ , see text. The common unit cells, primitive cell with overlayer lattice vectors  $\underline{R}_{o1}''$ ,  $\underline{R}_{o2}''$  to the left, scaled cell with vectors  $\underline{R}_1''$ ,  $\underline{R}_2''$  to the right, are emphasized in gray.

The above relations (5.17) to (5.23) are valid for any rotational overlayer on a substrate with a **square lattice** and corresponding values  $n_1$ ,  $n_2$ ,  $N$  result in **coincidence lattices**. This includes cases where  $n_1$  and  $N$  become quite large while  $n_2$  remains much smaller, leading to rotational superlattices with quite small rotation angles  $\alpha$ . (Actually, solutions of the Pythagorean equation (5.20) can be generated explicitly by an algorithm discussed in Appendix E.4.) As an example, Fig. 5.10 shows the superlattice corresponding to  $n_1 = 84$ ,  $n_2 = 13$ ,  $N = 85$  (reflecting an angle  $\alpha = 8.797^\circ$ ) exhibiting a clear moiré pattern. Here a supercell, defined by  $\underline{R}_1''$ ,  $\underline{R}_2''$  according to (5.23), with  $85^2 = 7225$  overlayer atoms would be common to the substrate and the overlayer lattice. As before, a more detailed analysis evidences periodicity with much smaller lattice vectors  $\underline{R}_{o1}''$ ,  $\underline{R}_{o2}''$  where

$$\begin{pmatrix} \underline{R}_{o1}'' \\ \underline{R}_{o2}'' \end{pmatrix} = \begin{pmatrix} 6 & 7 \\ -7 & 6 \end{pmatrix} \cdot \begin{pmatrix} \underline{R}_1 \\ \underline{R}_2 \end{pmatrix} \quad (5.25)$$

as sketched in Fig. 5.10. Here only 85 overlayer atoms are included in the primitive cell.



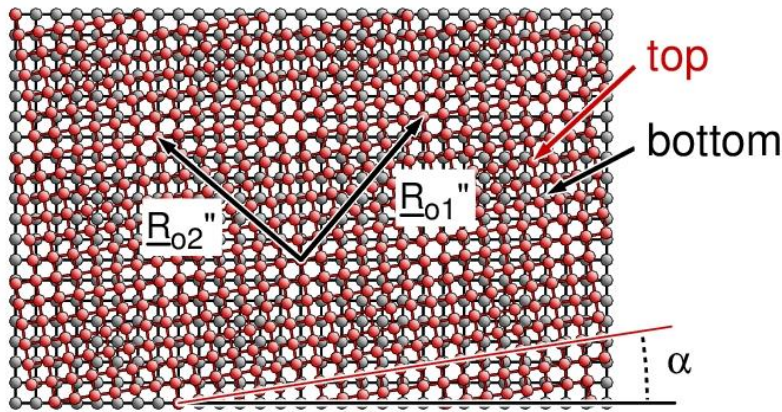


Fig. 5.10. Commensurate rotational overlayer on substrate with square lattice corresponding to  $\alpha = 8.797^\circ$  sketched at the bottom, see text. The lattice vectors  $\underline{R}_{o1}$ ,  $\underline{R}_{o2}$  of the primitive common unit cell are indicated accordingly.

In cases of **truly incommensurate** rotational superlattices the reconstruction matrix  $\underline{\underline{M}}$  according to (5.16) must contain irrational elements. However, these elements can always be approximated by rational numbers which, altogether, results in an approximate reconstruction matrix  $\underline{\underline{M}}$  which describes a coincidence lattice as discussed above for substrates with square lattice. As an example for hexagonal lattices, a reconstructed surface with two graphene layers, rotated by  $\alpha = 8^\circ$  with respect to each other, corresponds to a reconstruction matrix  $\underline{\underline{M}}$  according to (5.16) (setting  $\omega = 60^\circ$ )

$$\underline{\underline{M}} = \frac{2}{\sqrt{3}} \begin{pmatrix} \sin(52^\circ) & \sin(8^\circ) \\ -\sin(8^\circ) & \sin(68^\circ) \end{pmatrix} = \begin{pmatrix} 0.909916 & 0.160703 \\ -0.160703 & 1.070620 \end{pmatrix} \quad (5.26)$$

This matrix can be approximated by

$$\underline{\underline{M}} = \frac{1}{12} \begin{pmatrix} 11 & 2 \\ -2 & 13 \end{pmatrix} = \begin{pmatrix} 0.916667 & 0.166667 \\ -0.166667 & 1.083333 \end{pmatrix} \quad (5.27)$$

describing reconstruction with a coincidence superlattice, shown in Fig. 5.7, which is visually indistinguishable from that of the incommensurate overlayer structure describing  $8^\circ$  rotation.

The transformation matrix  $\underline{\underline{M}}$  describing transformations between lattice vectors of the ideal bulk-truncated and the reconstructed surface forms the basis of the  **$2 \times 2$  matrix notation** to characterize **reconstructed surfaces**. For a general single crystal surface of a substrate Sub with Miller indices  $(h \ k \ l)$  and its topmost layer reconstructed according to reconstruction matrix  $\underline{\underline{M}}$  the

$2 \times 2$  matrix notation can be written as

$$\text{Sub } (h k l) - \underline{\underline{\mathbf{M}}} = \text{Sub } (h k l) - \begin{pmatrix} m_{11} & m_{12} \\ m_{21} & m_{22} \end{pmatrix} \quad (5.28)$$

with an alternative notation

$$\text{Sub } (h k l) - (m_{11} \ m_{12} \mid m_{21} \ m_{22}) \quad (5.29)$$

where the latter in its one-line format is easier to write than (5.28). Examples are

- $\text{Pt}(1\ 1\ 0) - \begin{pmatrix} 1 & 0 \\ 0 & 2 \end{pmatrix}$  or  $\text{Pt}(1\ 1\ 0) - (1\ 0 \mid 0\ 2)$

describing the  $(1 \times 2)$  reconstructed  $\text{Pt}(1\ 1\ 0)$  surface, see Fig. 5.2,

- $\text{W}(1\ 0\ 0) - \begin{pmatrix} 1 & 1 \\ -1 & 1 \end{pmatrix}$  or  $\text{W}(1\ 0\ 0) - (1\ 1 \mid -1\ 1)$

describing the  $c(2 \times 2)$  reconstructed  $\text{W}(1\ 0\ 0)$  surface, see Fig. 5.3,

- $\text{Si}(1\ 0\ 0) - \begin{pmatrix} 2 & -1 \\ 2 & 1 \end{pmatrix}$  or  $\text{Si}(1\ 0\ 0) - (2\ -1 \mid 2\ 1)$

describing the  $c(4 \times 2)$  reconstructed  $\text{Si}(1\ 0\ 0)$  surface, see Fig. 5.4c,

- $\text{C}(0\ 0\ 0\ 1) - \begin{pmatrix} 3 & 5 \\ -5 & 8 \end{pmatrix}$  or  $\text{C}(0\ 0\ 0\ 1) - (3\ 5 \mid -5\ 8)$

yielding an approximate description of a graphite  $\text{C}(0\ 0\ 0\ 1)$  surface with its topmost layer rotated by  $8^\circ$  at its top, see Fig. 5.7.

These notations have been introduced some time ago [94] and have also been recommended by the International Union of Pure and Applied Chemistry (IUPAC) [86]. However, they are used by surface scientists much less frequently compared with the Wood notation, see Sec. 6.3.

### 5.3 Growth Processes

The geometric structure of crystal surfaces is determined, apart from static inter-atomic coupling, also by dynamic details of diffusion and nucleation which eventually result in thin film formation and crystal growth. These processes are completely analogous for thin film and adsorbate layer formation, and the corresponding structural details can be discussed on the same footing, see also Sec. 6.1. Overlayers (**adsorbate layers**) are composed of foreign atoms or molecules at a substrate surface which, depending on layer thickness, may also be called **heteroepitaxial (thin) films**. These are distinguished from overlayers whose atoms are of the same chemical type as those of the substrate surface, usually termed **homoepitaxial (thin) films** and which become important for crystal growth.

The growth of an overlayer has to be initiated by **nucleation centers** at the substrate surface where adsorbing atoms or molecules, from gas phase or diffusing at the substrate surface, can stabilize to form larger surface aggregates which may eventually lead to closed overlayers. These nucleation centers can be adsorbate particles, which approach the surface and bind at preferred surface sites (e.g. near steps or kinks), or surface perturbations, such as lattice imperfections (e.g. dislocations, defects, or vacancies) and impurities. Their position and arrangement is governed by complex individual binding properties, surface diffusion, and thermodynamic behavior. Thus, there are only few general qualitative criteria as to structural details of nucleation centers. This aspect goes beyond the scope of the present book and further details of the underlying physics can be found in Ref. [35].

The growth of adsorbate overlayers and thin films has been discussed for a long time where three basic **growth modes** have been considered [113] and verified by experiment [35]. These modes can be distinguished roughly by energetic quantities which consider binding between atoms within the overlayer as well as between overlayer and substrate atoms. In the following, we restrict our discussion of crystal growth to elemental overlayers and substrates, e.g. elemental metal systems with growth modes shown schematically in Fig. 5.11. However, it must be emphasized that growth mechanisms of molecular adsorbate overlayers can be described in a completely analogous way.

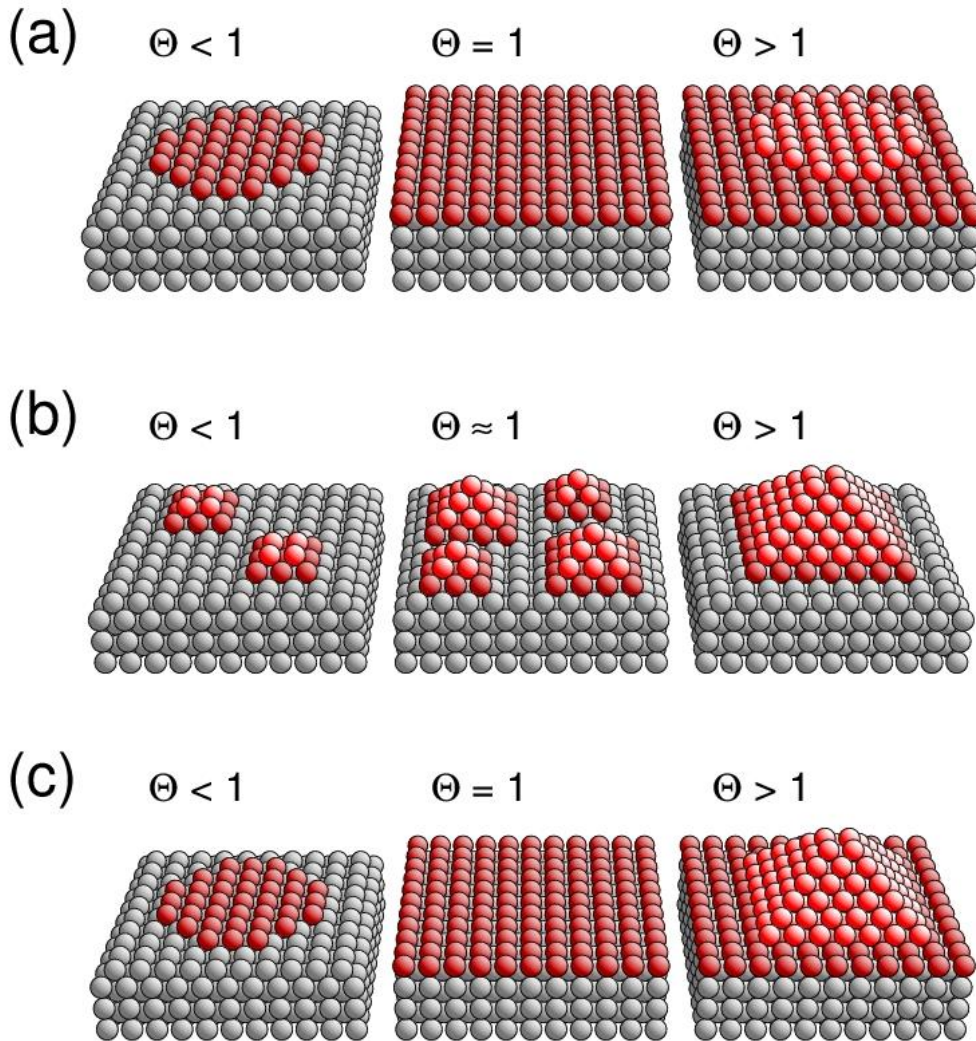


Fig. 5.11. Schematic sketch of the three different growth modes, (a) Frank-Van-der-Merwe (layer-by-layer), (b) Volmer-Weber (three-dimensional clusters), (c) Stranski-Krastanov (clusters above monolayer). Overlayer (substrate) atoms are shown in red (gray) where those above the first adsorbate layer are painted in lighter red. The amount of deposited species is denoted by a coverage  $\Theta$  (monolayer coverage where  $\Theta = 1$  refers to one overlayer atom per substrate atom).

- (a) **Frank-Van-der-Merwe (FM)** growth mode (**layer-by-layer** growth, see Fig. 5.11a). This mode assumes that binding between overlayer and substrate atoms dominates or is comparable in strength with binding between overlayer atoms. Here, adsorbing atoms stabilize at neighboring surface sites, forming monolayer islands at small coverage. With increasing coverage these islands grow until a complete monolayer film is obtained. At larger coverage (and assuming inter-layer binding to dominate), a second monolayer film starts to build above the first continuing the layer-by-layer growth process where each single layer is completed before the next starts to build. For heteroepitaxial growth, where the atoms of the

overlayers differ from those of the substrate, the building process is often accompanied by local stress or strain acting on each overlayer which, after equilibration, gives rise to layer dependent structural variations.

As an example, ultra-thin films of iron, 1 - 20 monolayers (ML) thick, are found to grow in layer-by-layer mode on the (1 0 0) surface of the fcc copper single crystal substrate [114], [115] with different structural phases. For very thin Fe layers, 1-4 ML, the lateral lattice constants of the overlayers and of the Cu substrate agree while the distances between adjacent monolayers in the film are larger by 4% compared with those of the substrate, resulting in a centered tetragonal film lattice. Above 10ML thickness the Fe films assume a bcc lattice structure, the generic bulk structure of iron, with a (1 1 0) surface termination [114].

- (b) **Volmer-Weber (VW)** growth mode (**three-dimensional cluster** growth, see Fig. 5.11b). This mode assumes that binding between overlayer atoms dominates or is comparable in strength with binding between overlayer and substrate atoms. Here, adsorbing atoms stabilize at the substrate surface forming three-dimensional clusters, often in the shape of several layers thick islands, where the size of the clusters and/or their density at the surface increases with increasing adsorbate coverage. Only at very large coverage do the clusters combine to form a closed and often quite rough overlayer surface.

Many noble metals grow on insulator or semiconductor substrate in the Volmer-Weber mode; for an overview see e.g. [116]. Examples are silver clusters growing on a mica substrate or gold growing on  $\text{MgF}_2$  [116].

- (c) **Stranski-Krastanov (SK)** growth mode (**mixed layer-by-layer and cluster** growth, see Fig. 5.11c). This mode combines the two previous modes where it is assumed that binding between overlayer atoms and between overlayer and substrate atoms are of comparable strength. Here adsorbing atoms stabilize initially at the substrate surface forming monolayer islands which grow until one or a few complete monolayers (often called **wetting layers**) are reached. After this, additional adatoms bind on top of the wetting layers in three-dimensional clusters of increasing size and/or density.

Metals are found to often grow on metal and insulator substrates in the Stranski-Krastanov mode; for an overview see e.g. [117]. Examples are gold and silver growing on a tungsten substrate [118] or silver growing on a silicon substrate [119].

At vicinal metal surfaces with flat terraces separated by steps or kinks, sites near step or kink atoms can be assumed to act as nucleation centers for homoepitaxial growth. As a consequence, atoms from the gas phase, or adsorbed at terrace sites and diffusing along the terrace, will stabilize at regular surface sites next to step or kink atoms. This leads to a continuation of the terraces, possibly changing terrace widths and causing additional step irregularities. Here one can distinguish between two different growth scenarios. First, with increasing coverage atoms may stabilize by forming single atom rows along step or kink lines where each row is completed before atoms adsorb at sites of the next row. This is the 1-dimensional equivalent of Frank-Van-der-Merwe growth and does not introduce new structural features except for kinks due to incomplete atom rows. Alternatively, atoms may adsorb near step or kink lines also allowing for incomplete rows which results in irregular step and kink structures and can be considered equivalent to Volmer-Weber growth. As an illustration, Fig. 5.12 shows a stepped (5 5 3) surface of a fictitious fcc metal substrate where atoms of the same element type adsorb according to a Frank-Van-der-Merwe type, Fig. 5.12a, and a Volmer-Weber type growth scenario, see Fig. 5.12b.

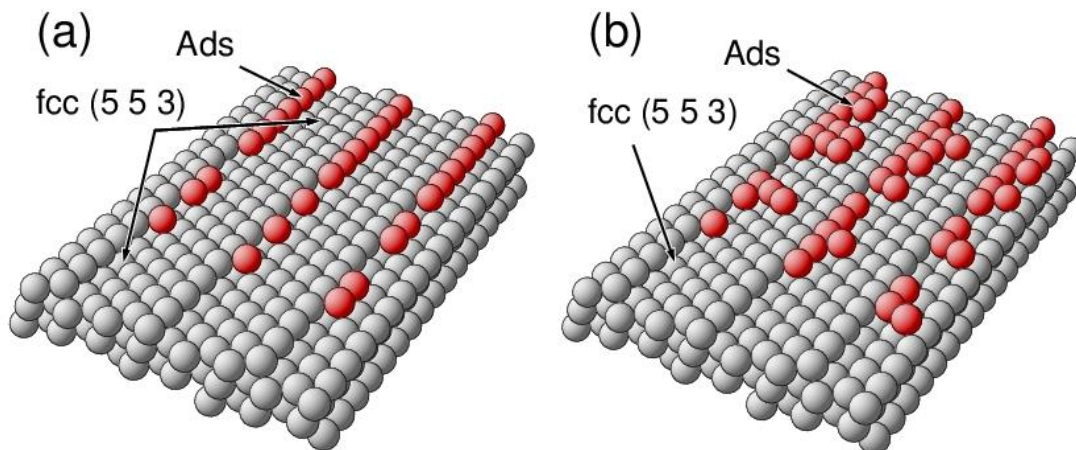


Fig. 5.12. Schematic sketch of (a) Frank-Van-der-Merwe type and (b) Volmer-Weber type growth at a stepped (5 5 3) surface of a fcc metal substrate. Adsorbate (substrate) atoms (of the same element type) are shown in red (gray).

So far, heteroepitaxial growth processes at the substrate surface have been considered only for systems where the adsorbing species does not intermix with substrate atoms. Intermixing can happen if the adsorbates react chemically with substrate atoms which results in a surface composition with an interface region where there is no clear phase separation between adsorbate and substrate. Examples are surface oxides or sulfides originating from oxygen and sulfur adsorption at metal substrates. Further, adsorbing metal atoms can mix with surface atoms of a metal substrate to form sur-

face alloy layers which, in their composition, may not exist as bulk alloys, see Ref. [120]. Structural details of these systems can be very complex and have to be treated on an individual basis, going beyond the scope of this book. As an illustration, Fig. 5.13 shows experimental structures of indium adsorbed on the Cu(1 1 1) surface [121] where alloying of the topmost surface layer occurs according to a  $(2 \times 2)$  overlayer, representing a  $\text{Cu}_3\text{In}$  surface alloy, Fig. 5.13a, as well as according to a  $(\sqrt{3} \times \sqrt{3})\text{R}30^\circ$  overlayer with  $\text{Cu}_2\text{In}$  composition, see Fig. 5.13b. So far,  $\text{Cu}_2\text{In}$  and  $\text{Cu}_3\text{In}$  have not been observed as bulk alloys.

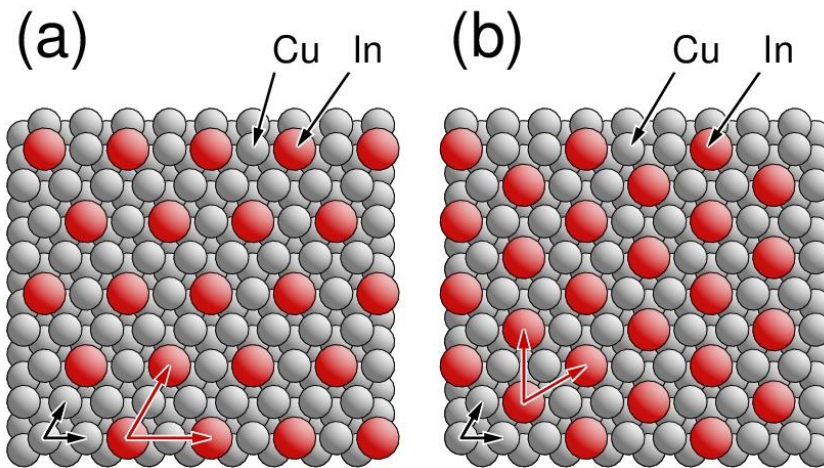


Fig. 5.13. Cu(1 1 1) + In surface section with alloy formation at the topmost layer, (a)  $(2 \times 2)$  overlayer with  $\text{Cu}_3\text{In}$  composition, (b)  $(\sqrt{3} \times \sqrt{3})\text{R}30^\circ$  overlayer with  $\text{Cu}_2\text{In}$  composition. Indium (copper) atoms are shown in red (gray). The lattice vectors of the overlayer and of the Cu substrate are sketched in red and black, respectively.

#### 5.4 Facetting

Real surfaces of single crystals may be **rough** beyond simple buckling of their topmost layers and can combine **small** flat surface sections of different  $(h k l)$ -indexed orientation. This structural feature is called **facetting**. Facets are also found in crystallites and nanoparticles where they confine the particle surface and determine the global shape as discussed in Sec. 2.7. At extended single crystal surfaces, facet formation is often observed as a consequence of thermal equilibration after sputtering by atom or ion beams or as a result of etching and polishing. It originates from physical and chemical processes, where an  $(h k l)$  surface of a flat single crystal can be stabilized energetically by introducing finite sections of differently oriented  $(h' k' l')$  surface sections.

Other examples are **oxide crystals**, where surfaces with highly polar termination can lower their electrostatic energy by forming local facets with non-polar termination. This has been proposed for the highly polar  $(1\ 1\ 1)$  surface of MgO (NaCl lattice, see Sec. 1), where thermal treatment (annealing at high temperatures) produces facets, whose sides resemble non-polar  $(0\ 0\ 1)$ ,  $(0\ 1\ 0)$ , and  $(1\ 0\ 0)$  terminated surfaces [122]. This is illustrated in Fig. 5.14 showing a section of a MgO $(1\ 1\ 1)$  surface with two pyramids terminated by non-polar facets.

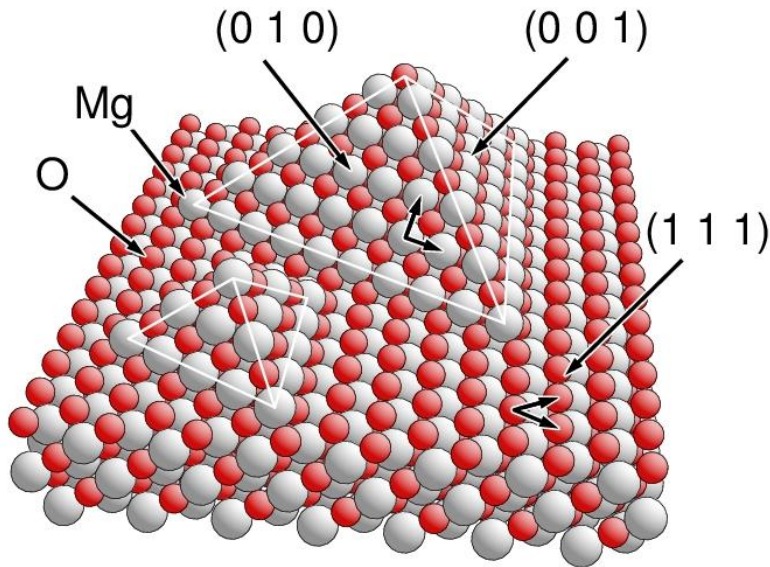


Fig. 5.14. Ionic MgO $(1\ 1\ 1)$  surface section with two pyramids terminated by facets of non-polar  $(0\ 0\ 1)$ ,  $(0\ 1\ 0)$ , and  $(1\ 0\ 0)$  monolayers. The facet edges are emphasized by white lines. Corresponding netplane orientations are labeled with adapted lattice vectors indicated accordingly.

Another example is given in Fig. 5.15, where two stepped surfaces of an fcc $(7\ 1\ 1)$  crystal, describing  $(1\ 0\ 0)$  terraces with  $(1\ 1\ 1)$  steps, and fcc $(10\ 0\ 2)$ , describing  $(1\ 0\ 0)$  terraces with  $(0\ 0\ 1)$  steps, join to form a facet edge.



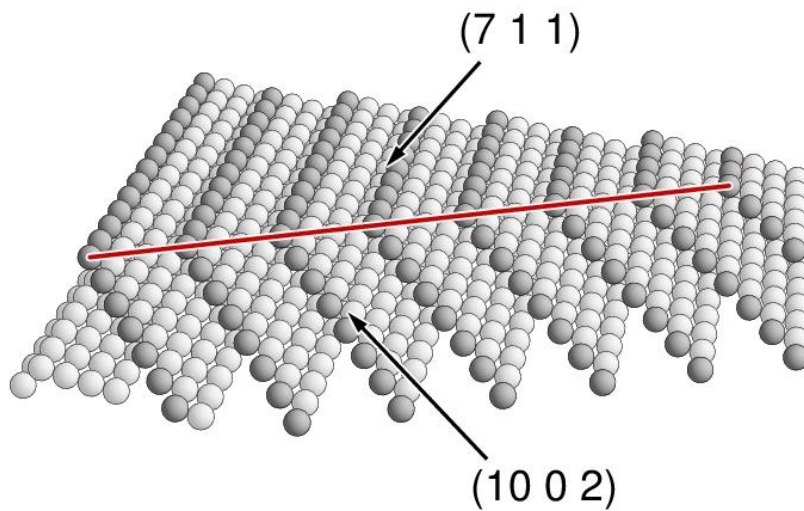


Fig. 5.15. Facet edge separating stepped  $(7\ 1\ 1)$  and  $(10\ 0\ 2)$  surfaces of an fcc crystal. Step edges are indicated by darker balls and facet edge atoms are connected by a red line.

**Facet edges** will be **denoted** in the following by  $(h\ k\ l) / (h'\ k'\ l')$ , where  $(h\ k\ l)$  and  $(h'\ k'\ l')$  are the Miller indices of the two surface sections which join to form the edge. Further, facet edges are called **positive** if the two joining surface sections form a **roof-shaped** arrangement with respect to the underlying crystal bulk. In contrast, **negative** facet edges result from surface sections forming a **trough-shaped** arrangement with respect to the bulk. This is illustrated in Fig. 5.16, where positive and negative edges of  $(0\ 0\ 1) / (1\ 1\ 1)$  facets of a fcc crystal surface are shown. Evidently, a faceted surface which still gives the appearance to be flat on a larger scale must contain both positive and negative facet edges.

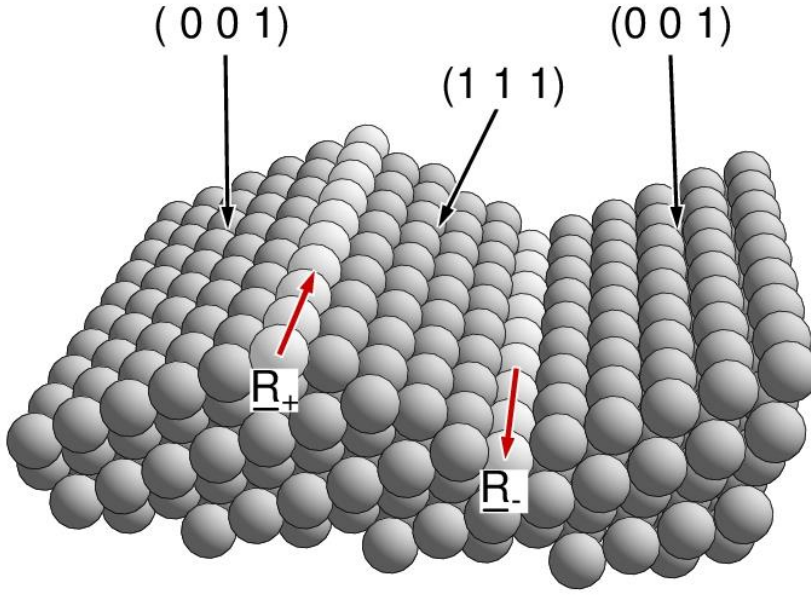


Fig. 5.16. Structure of surface sections near positive and negative edges of (0 0 1) / (1 1 1) facets of a crystal with an fcc lattice. The positive (negative) edge is indicated by its facet edge vector  $\underline{R}_+$  ( $\underline{R}_-$ ) in red.

The direction of a facet edge is defined by the **facet edge vector**,  $\underline{R}_{\text{facet}}$ , which points parallel to the cutting line of the corresponding two surface sections. If their orientations are defined by Miller indices  $(h k l)$  and  $(h' k' l')$ , respectively, then vector  $\underline{R}_{\text{facet}}$ , common to both netplanes, is perpendicular to both reciprocal lattice vectors  $\underline{G}_{(h k l)}$  and  $\underline{G}_{(h' k' l')}$  as given by (3.6). Therefore,  $\underline{R}_{\text{facet}}$  can be represented by the (scaled) vector product

$$\begin{aligned}
 \underline{R}_{\text{facet}} &= \chi (\underline{G}_{(h k l)} \times \underline{G}_{(h' k' l')}) = \\
 &= \chi (h \underline{G}_{01} + k \underline{G}_{02} + l \underline{G}_{03}) \times (h' \underline{G}_{01} + k' \underline{G}_{02} + l' \underline{G}_{03}) = \\
 &= \chi \{ (k l' - l k') (\underline{G}_{02} \times \underline{G}_{03}) + (l h' - h l') (\underline{G}_{03} \times \underline{G}_{01}) \\
 &\quad + (h k' - k h') (\underline{G}_{01} \times \underline{G}_{02}) \} = \\
 &= \chi (2\pi)^2 / \beta \{ (k l' - l k') \underline{R}_{01} + (l h' - h l') \underline{R}_{02} + (h k' - k h') \underline{R}_{03} \} \\
 \beta &= (\underline{R}_{01} \times \underline{R}_{02}) \cdot \underline{R}_{03}
 \end{aligned} \tag{5.30}$$

where the reciprocity between real space and reciprocal lattice vectors, discussed in Sec. 2.5, has been applied. Thus, fixing the scaling factor  $\chi$  in (5.30) at

$$\chi = \frac{\beta}{(2\pi)^2} \tag{5.31}$$

yields a facet edge vector  $\underline{R}_{\text{facet}}$  which equals a **general lattice vector**. Vector  $\underline{R}_{\text{facet}}$  is of smallest length along its direction if the Miller indices  $(h k l)$  and  $(h' k' l')$  have no common divisor larger

than 1, i.e. if  $\gcd(h\ k\ l) = \gcd(h'\ k'\ l') = 1$ . Relation (5.30) with (5.31) can also be expressed mathematically in a simpler **determinantal form** as

$$\underline{\mathbf{R}}_{\text{facet}} = \det \begin{pmatrix} h & k & l \\ h' & k' & l' \\ \underline{\mathbf{R}}_{o1} & \underline{\mathbf{R}}_{o2} & \underline{\mathbf{R}}_{o3} \end{pmatrix} \quad (5.32)$$

Swapping the two top rows in matrix (5.32) changes only the sign of its determinant and, hence, the direction of  $\underline{\mathbf{R}}_{\text{facet}}$ . Thus, edge vectors  $\underline{\mathbf{R}}_{\text{facet}}$  of an  $(h\ k\ l) / (h'\ k'\ l')$  facet and of its corresponding  $(h'\ k'\ l') / (h\ k\ l)$  facet (one belongs to a positive and the other to a negative facet edge, see Fig. 5.16) are always equal in length but opposite in direction.

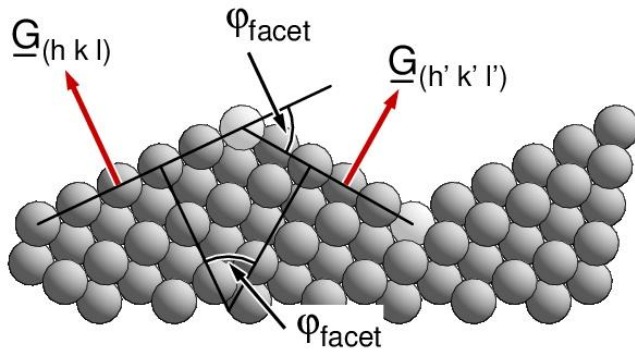


Fig. 5.17. Structure of a facet edge separating  $(h\ k\ l)$  and  $(h'\ k'\ l')$  oriented surface sections. The facet angle  $\varphi_{\text{facet}}$  and the corresponding reciprocal lattice vectors  $\underline{\mathbf{G}}_{(h\ k\ l)}$  and  $\underline{\mathbf{G}}_{(h'\ k'\ l')}$  are labeled accordingly. Edge atoms are emphasized by light balls.

The two surface sections joining at the facet edge form a **facet angle**  $\varphi_{\text{facet}}$ , as illustrated in Fig. 5.17. This angle can be evaluated by considering the scalar product of the corresponding normal vectors along  $\underline{\mathbf{G}}_{(h\ k\ l)}$  and  $\underline{\mathbf{G}}_{(h'\ k'\ l')}$  as

$$\cos \varphi_{\text{facet}} = (\underline{\mathbf{G}}_{(h\ k\ l)} \underline{\mathbf{G}}_{(h'\ k'\ l')}) / (|\underline{\mathbf{G}}_{(h\ k\ l)}| |\underline{\mathbf{G}}_{(h'\ k'\ l')}|) \quad (5.33)$$

As examples, Table 5.1 lists angles  $\varphi_{\text{facet}}$  and edge vectors  $\underline{\mathbf{R}}_{\text{facet}}$  of facets formed by high-density  $(h\ k\ l)$  surfaces of crystals with fcc and bcc lattices calculated using (5.32) and (5.33).

Table 5.1. Angles  $\phi_{\text{facet}}$  and edge vectors  $\underline{\mathbf{R}}_{\text{facet}}$  of facets formed by selected  $(h k l)$  surfaces of crystals with (a) fcc and (b) bcc lattices. The facets  $(h k l) / (h' k' l')$  are listed according to monolayer density with  $\rho(h k l) \geq \rho(h' k' l')$ . All Miller indices are given in sc notation. The edge vectors are defined by Cartesian coordinates  $(x, y, z)$ , normalized to lattice constant  $a$ , and refer to the vectors of smallest length.

## (a) Face-centered cubic lattice

	Facet $(h k l) / (h' k' l')$	$\cos \phi_{\text{facet}}$ , $\phi_{\text{facet}} [^\circ]$	$\underline{\mathbf{R}}_{\text{facet}} / a$
1	(1 1 1) / (-1 1 1)	1/3 , 70.53	(0, -1/2, 1/2)
2	(1 1 1) / (0 0 2)	1/√3 , 54.74	(1/2, -1/2, 0)
3	(1 1 1) / (0 2 2)	√(2/3) , 35.26	(0, -1/2, 1/2)
4	(0 0 2) / (0 2 0)	0 , 90.00	(-1, 0, 0)
5	(0 0 2) / (0 2 2)	1/√2 , 45.00	(-1, 0, 0)
6	(1 1 1) / (1 1 3)	5/√33 , 29.50	(1/2, -1/2, 0)
7	(0 0 2) / (1 1 3)	3/√11 , 25.24	(-1/2, 1/2, 0)
8	(7 1 1) / (10 0 2)	34/√1326 , 20.98	(1/2, -1, 5/2)

## (b) Body-centered cubic lattice

	Facet $(h k l) / (h' k' l')$	$\cos \phi_{\text{facet}}$ , $\phi_{\text{facet}} [^\circ]$	$\underline{\mathbf{R}}_{\text{facet}} / a$
1	(0 1 1) / (1 0 1)	1/2 , 60.00	(1/2, 1/2, -1/2)
2	(0 1 1) / (1 1 0)	1/2 , 60.00	(-1/2, 1/2, -1/2)
3	(1 0 1) / (1 1 0)	1/2 , 60.00	(-1/2, 1/2, 1/2)
4	(0 1 1) / (0 0 2)	1/√2 , 45.00	(1, 0, 0)
5	(0 1 1) / (1 1 2)	√(3/4) , 30.00	(1/2, 1/2, -1/2)
6	(0 0 2) / (1 2 1)	1/√6 , 65.91	(-2, 1, 0)
7	(0 0 2) / (1 1 2)	2/√6 , 35.26	(-1, 1, 0)
8	(1 1 2) / (1 2 1)	5/6 , 33.56	(-3/2, 1/2, 1/2)

Many **open surfaces** of single crystals expose small local planar sections of high atom density corresponding to low Miller index netplanes. Therefore, they are often considered to be **(micro) faceted**. As an illustration, the (2 1 1) oriented surface of bcc tungsten can conceptually be thought of as being stepped with (1 0 1) oriented terraces and (1 1 0) oriented steps. (The additivity theorem for Miller indices (4.9) of stepped surfaces yields  $(2 1 1) = (1 0 1) + (1 1 0)$ ). But this surface may also be described as consisting of faceted stripes with (1 0 1) and (1 1 0) orientation reflecting the densest monolayers of the bcc lattice, see Fig. 5.18. This is one simple example where **stepped** (or

**kinked**) surfaces of single crystals may also be called **(micro) faceted**.

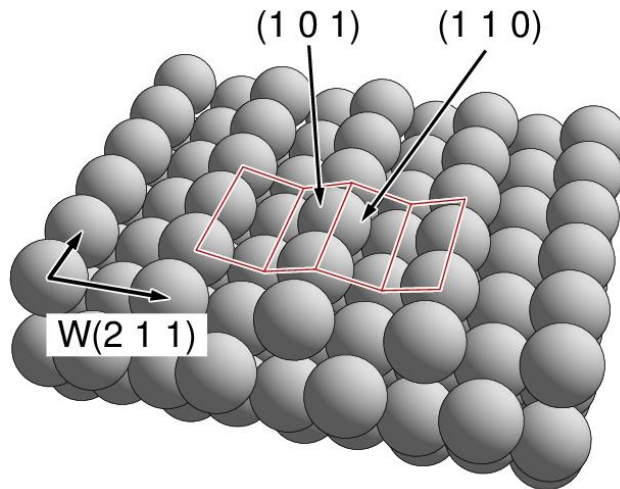


Fig. 5.18. Perspective view of a  $W(2\ 1\ 1)$  surface with  $(1\ 0\ 1)$  and  $(1\ 1\ 0)$  facet stripes. The  $(2\ 1\ 1)$ -adapted lattice vectors are shown at the lower left. Joining facet areas are sketched by red lines and labeled accordingly.

More complex examples of facetting, where many facet edges of different type can occur, are given, for example, by curved surfaces. These appear at crystalline spheres, cylinders, and tips, and are of great physical interest in connection with metal tips used in field emission or for scanning tunneling microscopy [34]. As an illustration, Fig. 5.19 shows a spherical section of an fcc crystal which may model the tip of a scanning tunneling microscope. This hemisphere exposes facets of different  $(h\ k\ l)$  oriented surfaces of high density (labeled in the figure) with stepped and kinked transitions between them.

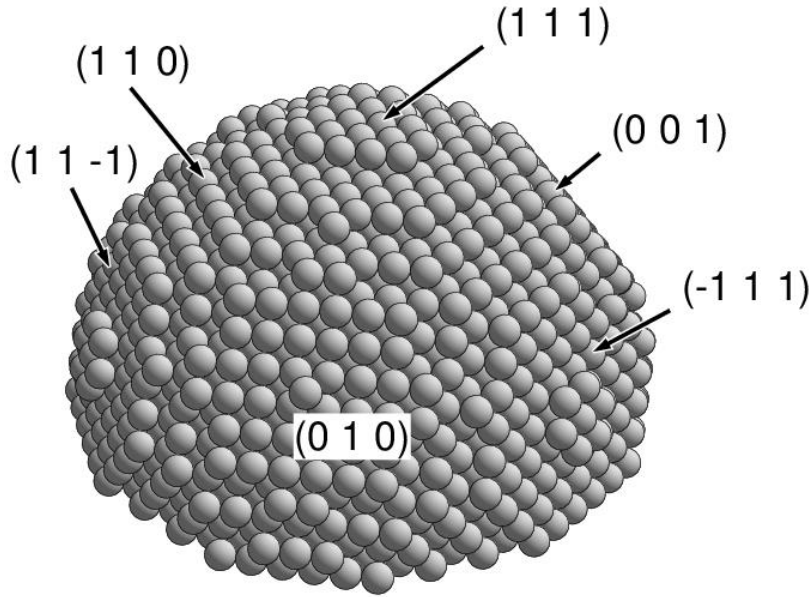


Fig. 5.19. Spherical section of an fcc crystal exposing different  $(h k l)$  oriented facets of high atom density. The facets are labeled by their Miller indices.

## 5.5 Exercises

- 5.1. Consider a  $(0 0 1)$  oriented surface of a fictitious monoatomic crystal with an sc lattice described by Minkowski-reduced lattice vectors  $\underline{R}_{01}$ ,  $\underline{R}_{02}$ ,  $\underline{R}_{03}$ . As a result of surface relaxation the inter-layer separation  $d_{i,i+1}$  along  $\underline{R}_{03}$  is affected according to

$$d_{i,i+1} = R_{03} (1 + q_i) , \quad i = 1, 2 \dots$$

where index  $i$  counts monolayers from the surface top. Discuss variations in the neighbor shells (up to 5<sup>th</sup> shell) of atoms of the three topmost surface layers assuming  $q_i$  values  $q_1 = -0.2$ ,  $q_2 = -0.1$ ,  $q_3 = 0.05$ ,  $q_i = 0.0$  for  $i > 4$ .

- 5.2. Consider the  $(0 0 1)$  oriented surface of a Pd crystal (fcc lattice, lattice constant  $a = 3.89 \text{ \AA}$ ). The topmost four monolayers are relaxed perpendicular to the surface with interlayer distances  $d_{i,i+1}$  varying according to  $d_{12} = 1.0487 d_0$ ,  $d_{23} = 1.0025 d_0$ ,  $d_{34} = 0.9922 d_0$ ,  $d_{45} = 1.0025 d_0$  ( $d_0$  denotes the bulk interlayer spacing). Determine the geometric structure of neighbor shells (up to 3<sup>rd</sup> nearest neighbors) of atoms of the three topmost surface layers.
- 5.3. Consider a Ni $(0 0 1)$  surface (fcc lattice) with  $c(2 \times 2)$  reconstruction of the topmost surface layer. Give alternative representations of the reconstructed layer (matrix definition).

- 5.4. Consider a Cu(1 1 1) and (0 0 1) surface (fcc lattice) with the surface layer rotated by  $10^\circ$ . Determine the approximate lateral lattice constant of the resulting superlattice.
- 5.5. Consider the superposition of two adjacent fcc monolayers which are rotated by small angles  $\alpha$  with respect to each other. Determine the resulting geometry as a function of the rotation angle  $\alpha$  and discuss corresponding superlattices for monolayers oriented (1 1 1) and (0 0 1).
- 5.6. Discuss the Cu(1 1 0) surface (fcc lattice) with missing row reconstructions,  $(2 \times 1)$  and  $(1 \times 2)$ , of the first layer.
- Determine corresponding reconstruction matrices.
  - Evaluate monolayer orientations of the corresponding microfacets.
- 5.7. Discuss the structure of a Si(0 0 1) surface (diamond lattice) with a missing row reconstruction of the first layer. Determine the reconstruction matrix. Calculate distances of neighbor shells (up to 3<sup>rd</sup> neighbors) of atoms of the three topmost surface layers
- 5.8. Discuss the structure of a Si(1 1 0) surface (diamond lattice). Show that this surface allows only one unique termination.
- 5.9. Consider a Si(0 0 1) surface (diamond lattice)
- without relaxation or reconstruction. Show that the two possible terminations differ only by a  $90^\circ$  rotation about the surface normal.
  - with a buckling  $c(4 \times 2)$  dimer reconstruction of the first layer. Determine neighbor shell radii of the atoms of the reconstruction layer.
- 5.10. Discuss the model of the  $(7 \times 7)$  reconstructed Si(1 1 1) surface according to a LEED analysis by S.Y. Tong et al. [110], see Fig. 5.5. How many atoms does each of the elementary cells of the first three surface layers contain?
- 5.11. Consider rotational reconstruction with isotropic scaling of the top layer (overlayer) of a primitive simple cubic lattice at the (0 0 1), (0 1 1), and (1 1 1) surface. Determine rotation angles which yield coincidence lattice overlayers. Which values do the scaling constants of the lattice vectors assume for a given rotation? Hint: use results of Appendix E.4.
- 5.12. Consider rotational reconstruction with isotropic scaling of the top layer (overlayer) of a primitive hexagonal lattice. Determine rotation angles which yield coincidence lattice over-

- layers. Which values do the scaling constants of the lattice vectors assume for a given rotation? Hint: use results of Appendix E.4.
- 5.13. Consider rotational reconstruction of the topmost overlayer of a primitive tetragonal crystal. Determine constraints for the lattice constants  $a$ ,  $c$  and for Miller indices  $(h k l)$  to yield coincidence lattice overlayers.
  - 5.14. Consider rotational reconstruction of the topmost overlayer of the  $(0 0 1)$ ,  $(1 0 0)$ , and  $(1 0 1)$  oriented surface of a primitive tetragonal crystal. Determine lattice constants  $a$ ,  $c$  to yield coincidence lattice overlayers.
  - 5.15. Consider a Pd $(0 0 1)$  surface (fcc lattice) with a crystallite of palladium forming a pyramid of square base of on top of it. (The internal structure of the crystallite is assumed to be identical to that of the bulk crystal.)
    - (a) Determine Miller indices of the four facet planes of the pyramid.
    - (b) Calculate the angle between two crossing facet planes of the pyramid.
  - 5.16. Consider a Ni $(1 1 1)$  surface (fcc lattice) with a crystallite of palladium forming a pyramid of triangular base of on top of it. (The internal structure of the crystallite is assumed to be identical to that of the bulk crystal.)
    - (a) Determine Miller indices of the three facet planes of the pyramid.
    - (b) Calculate the angle between two crossing facet planes of the pyramid.
  - 5.17. Consider fcc metal single crystals terminated by surfaces of orientations given by Miller indices  $(1 1 0)$ ,  $(1 1 3)$ ,  $(2 1 1)$ . These surfaces may be interpreted as microfaceted. Determine Miller indices of corresponding facets.
  - 5.18. Consider bcc metal single crystals terminated by surfaces of orientations given by Miller indices  $(0 0 1)$ ,  $(1 1 2)$ ,  $(0 1 3)$ ,  $(1 1 1)$ . These surfaces may be interpreted as microfaceted. Determine Miller indices of corresponding facets.
  - 5.19. Consider an fcc crystal sphere with an atom in its center and including all atoms up to a distance  $r = 5a$  from the center ( $a =$  lattice constant).
    - (a) Characterize surface sections of the ball corresponding to densest monolayers.
    - (b) Discuss transitions between sections of low  $(h k l)$  index monolayers as a result of the ball curvature.
    - (c) How many atoms does the ball contain?



- 5.20. Consider a lattice being described by two equivalent lattice vector sets  $\underline{R}_1, \underline{R}_2, \underline{R}_3$  and  $\underline{R}_1', \underline{R}_2', \underline{R}_3'$  with

$$\begin{pmatrix} \underline{R}_1' \\ \underline{R}_2' \\ \underline{R}_3' \end{pmatrix} = \underline{\underline{T}} \cdot \begin{pmatrix} \underline{R}_1 \\ \underline{R}_2 \\ \underline{R}_3 \end{pmatrix}$$

Then facet edge vectors  $\underline{R}_{\text{facet}}$  can be represented by either of the lattice vector sets. Show that

$$\underline{R}_{\text{facet}} = \det \begin{pmatrix} H & K & L \\ H' & K' & L' \\ \underline{R}_1' & \underline{R}_2' & \underline{R}_3' \end{pmatrix} = \det(\underline{\underline{T}}) \cdot \det \begin{pmatrix} h & k & l \\ h' & k' & l' \\ \underline{R}_1 & \underline{R}_2 & \underline{R}_3 \end{pmatrix}$$

where  $(h \ k \ l)$ ,  $(h' \ k' \ l')$  and  $(H \ K \ L)$ ,  $(H' \ K' \ L')$  are Miller indices referring to the two lattice vector sets. Hint: use results of Secs. 5.4 and 3.4.

## 6 ADSORBATE LAYERS

### 6.1 Definition and Classification

Adsorption at single crystal surfaces of  $(h k l)$  orientation can be described by foreign atoms and/or molecules - they will be called **adsorbates** or adparticles in this section - binding to a substrate and forming overlayers. Hence, adsorption processes are closely related with growth mechanisms at single crystal surfaces where different growth modes have been discussed in Sec. 5.3, and structural aspects are completely analogous in both types of systems. If the adparticles are identical in type with atoms of the substrate, adsorption increases only the substrate at its corresponding surface, possibly introducing additional surface reconstruction treated in Sec. 5.2. This will not lead to new structure details and can be ignored in the present section.

Structural properties of adsorbate overlayers depend strongly on the interaction between the adsorbates and the substrate surface, as well as between different adsorbates within the overlayer depending on the overlayer density. The latter is usually defined by an adsorbate **coverage**  $\Theta$  which is given by the ratio of the number density of adsorbates in the overlayer and the atom density of the topmost substrate layer, where  $\Theta = 1$  is defined as **monolayer coverage**. In cases of very weak adsorbate-substrate and adsorbate-adsorbate interactions at low coverage, adsorbate particles can diffuse easily on the substrate surface and corresponding overlayers cannot be expected to show any structural order. They will form completely **disordered two-dimensional gas or liquid films**. Examples are light rare gas atoms, like helium or neon, physisorbed at low coverage  $\Theta \ll 1$  at metal surfaces, where interatomic coupling is governed by Van-der-Waals type interactions [123]. These cases are not relevant for general crystallographic considerations.

If the adsorbate-substrate interaction becomes stronger while the adsorbate-adsorbate interaction is still weak, the adsorbates may bind only at specific geometric sites of the substrate surface. At low adsorbate coverage,  $\Theta < 1$ , not all equivalent surface sites will be populated by adsorbates and there is a disordered distribution of populated sites. Thus, corresponding adsorbate overlayers can be described structurally by fixed overlayer lattices, which are commensurate with the lattice of the substrate surface. However, not all overlayer lattice sites are occupied by adsorbates. These disordered systems are usually called two-dimensional **lattice gas systems**. An example is given by the adsorption of ammonia on the Cu(1 1 1) surface at low coverage [124]. Fig. 6.1 illustrates a possible structure of a the Cu(1 1 1) + (disordered) - NH<sub>3</sub> system for an NH<sub>3</sub> coverage  $\Theta = 1/3$ . Here

$\text{NH}_3$  molecules stabilize always on top of copper atoms of the substrate surface (which forms a hexagonal lattice) where only  $1/3$  of the top sites are occupied.

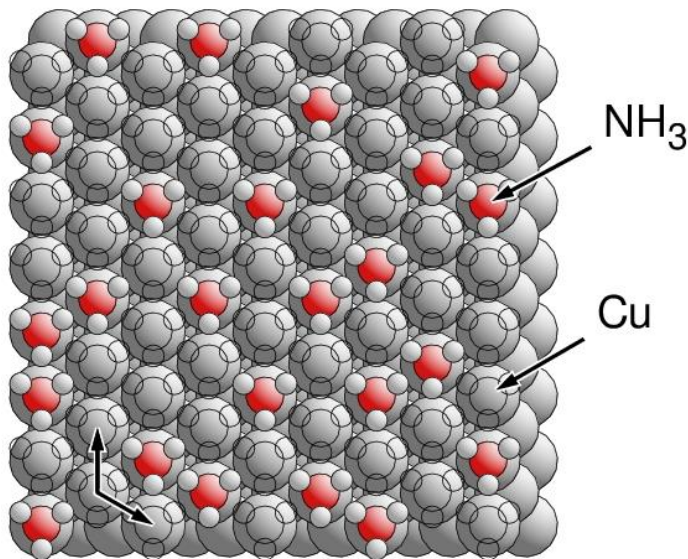


Fig. 6.1. Structure of the  $\text{Cu}(1\ 1\ 1) + (\text{disordered}) - \text{NH}_3$  adsorbate system. The lattice vectors of the  $\text{NH}_3$  adsorbate lattice for a complete  $(1 \times 1)$  overlayer are shown in black. The random population of the lattice sites by  $\text{NH}_3$  molecules corresponds to a coverage  $\Theta = 1/3$ . Unoccupied lattice sites are indicated by open circles.

If, on the other hand, the adsorbate-substrate interaction is weak while the adsorbate-adsorbate interaction becomes strong, then adsorbates may, at lower coverage, combine to two-dimensional **islands** or form three-dimensional **clusters** at the surface which are randomly distributed. Their structural properties are influenced very little by those of the substrate surface and have to be treated individually. At higher adsorbate coverage islands and clusters can increase in size and form defect-free periodic overlayers which are oriented randomly on the surface and whose lattices are, in general, not expected to be commensurate with that of the substrate. There are also cases of **partially disordered** adsorbate systems. Here we mention only overlayers which are periodic in one dimension and disordered in the other forming periodic adsorbate rows on the surface that are positioned in a disordered fashion.

In addition, there are many adsorbate systems [22] where the adsorbates interact strongly with the substrate and also couple with each other at large enough coverage forming two-dimensionally **periodic overlayers**. Thus, the discussion of structural properties of these adsorbate systems is, from a crystallographic point of view, completely **analogous** to that of single crystal surfaces with topmost layers that are relaxed or reconstructed, see Secs. 5.1 and 5.2. It is also strongly connected

with structural aspects of homoepitaxial crystal growth discussed in Sec. 5.3. Differences arise only in that the atom types (elements) in adsorbate overlayers will differ from those of the substrate. On the other hand, heteroepitaxial thin films are in their structural description analogous to adsorbate overlayers and can be treated at the same footing. Altogether, we can distinguish between three cases.

- (a) Adsorbate overlayers can form **commensurate** overlayer lattices. Here the lattice vectors of the overlayers,  $\underline{R}_1'$  and  $\underline{R}_2'$ , are connected with those of the substrate,  $\underline{R}_1$  and  $\underline{R}_2$ , by an **integer-valued** transformation matrix  $\underline{M}$  according to (5.3). Further, the adsorbates stabilize in one or several specific sites at the substrate surface as will be discussed below. An example from the Surface Structure Database, SSD 28.6.8.45, is the adsorption of CO on the Ni(1 1 0) surface, formally described as Ni(1 1 0) + p2mg(2 × 1) - 2CO [125], shown in Fig. 6.2, where

$$\underline{\underline{M}} = \begin{pmatrix} 2 & 0 \\ 0 & 1 \end{pmatrix}$$

Here the CO molecules stabilize in bridge sites between Ni atoms of the topmost substrate layer, where their molecular axes are tilted alternatingly to the left and right of the Ni ridges, with two CO molecules in each overlayer unit cell.

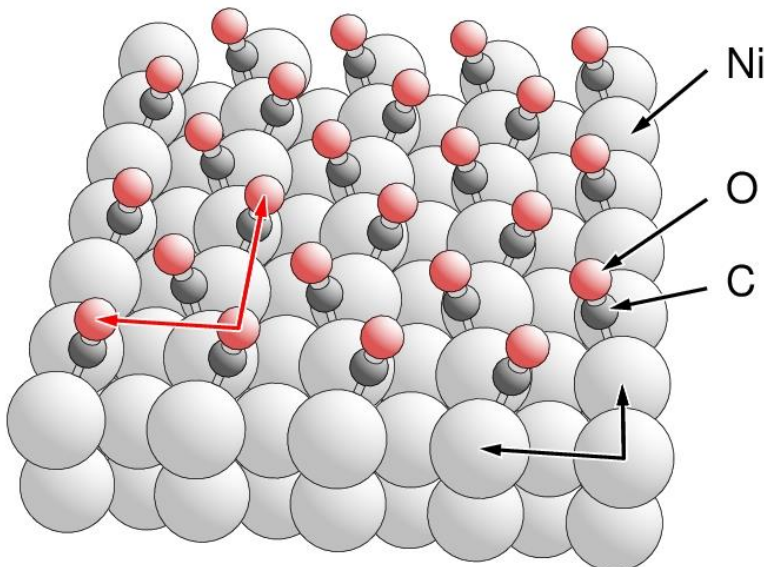


Fig. 6.2. Structure of the Ni(1 1 0) + p2mg(2 × 1) - 2CO adsorbate system. The lattice vectors of the CO adsorbate layer and of the Ni substrate are sketched in red and black, respectively.

More complex cases of commensurate superlattices include large molecular adsorbates at reconstructed single crystal surfaces of metals where the adsorbates bind at preferred surface sites. As an example,  $C_{60}$  adsorbate molecules, so-called ‘buckyballs’, form a  $4 \times 4$  superlattice on the  $Cu(1\ 1\ 1)$  surface [126] which is described as

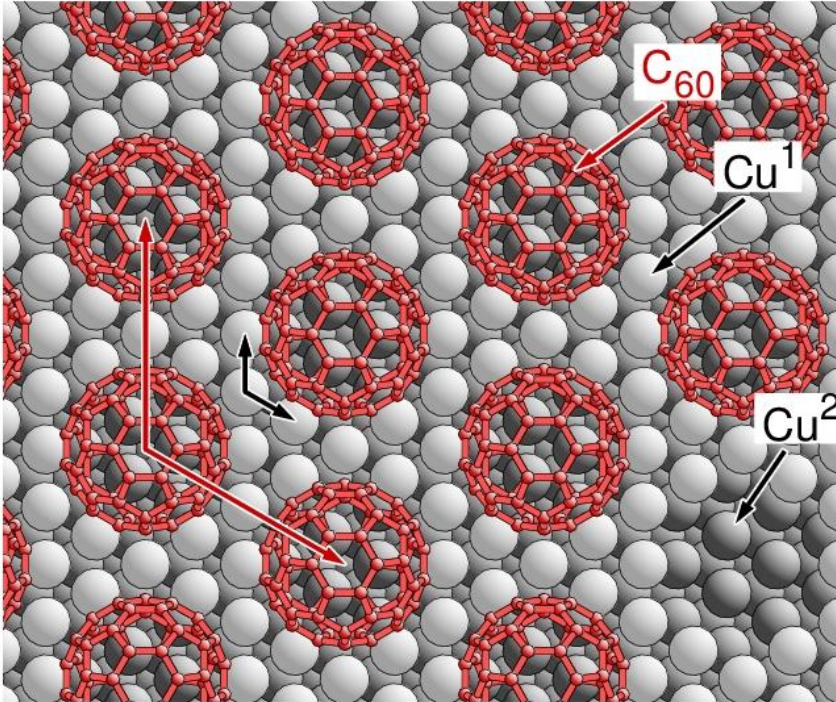


Fig. 6.3. Structure of the  $Cu(1\ 1\ 1) + (4 \times 4) - C_{60}$  adsorbate system. The lattice vectors of the  $C_{60}$  adsorbate layer and of the  $Cu$  substrate are sketched in red and black, respectively.  $Cu$  atoms of the 1<sup>st</sup> and 2<sup>nd</sup> substrate surface layer, labeled  $Cu^1$  and  $Cu^2$ , are shown in light and dark gray, the  $C_{60}$  adsorbates in red with bond sticks. One adsorbate is removed to illustrate the missing 1<sup>st</sup> layer  $Cu$  atoms.

$Cu(1\ 1\ 1) + (4 \times 4) - C_{60}$ , see Fig. 6.3. Here the topmost layer of the  $Cu$  substrate (1<sup>st</sup> layer) is reconstructed forming a  $4 \times 4$  overlayer with hexagonal holes described by seven missing  $Cu$  atoms. These holes act as binding sites for the  $C_{60}$  adsorbates which sit above 3-fold hollow sites of the 2<sup>nd</sup> surface layer where they bind with three copper atoms of the layer.

- (b) Adsorbate overlayers can form **coincidence** lattices, sometimes also called **high-order commensurate (HOC)** or **scaled commensurate** lattices. Here the transformation matrix  $\underline{M}$ , connecting lattice vectors of the overlayer with those of the substrate surface according to (5.3), contains integer and **rational** matrix elements  $m_{ij}$  with at least one rational. Coincidence lattices can appear for metal overlayers on a substrate of a different metal where the two metal lattice constants do not match each other. As an illustration, Fig. 6.4 shows a fic-

titious adsorbate system with a hexagonal overlayer of fcc metal B adsorbed at a (1 1 1) surface of an fcc metal A (only the topmost hexagonal substrate layer is shown). Here the lattice constant of metal B is larger than that of metal A by 6.25% ( $= 1/16$ ). This results in a coincidence lattice overlayer structure described by a transformation matrix

$$\underline{\underline{M}} = \frac{1}{16} \begin{pmatrix} 17 & 0 \\ 0 & 17 \end{pmatrix} \quad (6.1)$$

In this system the overlayer of metal B forms a hexagonal coincidence lattice with the substrate. The common hexagonal supercell is given by multiples of the substrate lattice vectors,  $\underline{R}_1'' = 17 \underline{R}_1$  and  $\underline{R}_2'' = 17 \underline{R}_2$ , also evidenced by the hexagonal interference pattern in Fig. 6.4.

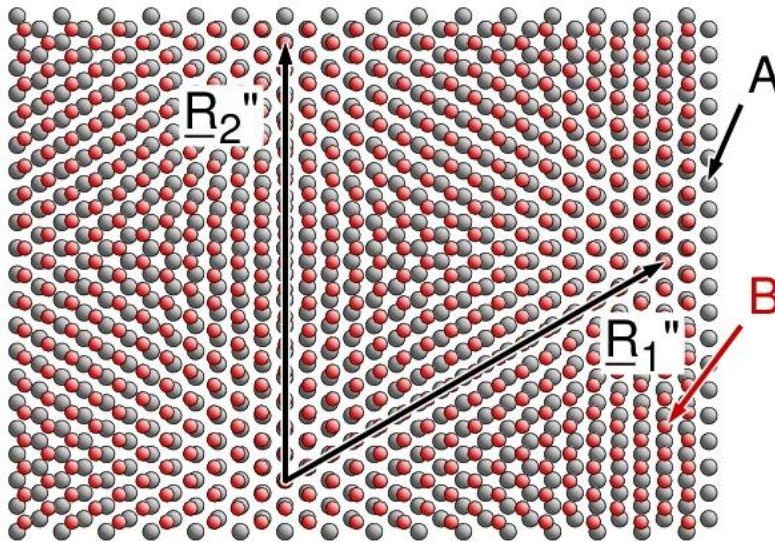


Fig. 6.4. Structure of a fictitious adsorbate system with a hexagonal overlayer of fcc metal B (red balls) on a (1 1 1) surface of an fcc metal A (gray balls). The substrate is represented by its topmost layer. The lattice constant of metal B is larger than that of metal A by  $6.25\% = 1/16$ . The lattice vectors of the common superlattice,  $\underline{R}_1''$ ,  $\underline{R}_2''$ , are sketched accordingly.

In real adsorbate overlayer systems, **coincidence lattices** are usually combined with a **modulation** of overlayer (and substrate) **atom positions** perpendicular and parallel to the surface as a result of local binding effects. Therefore, overlayer atom positions inside the unit cell of the coincidence lattice are described only **approximately** by lattice vectors defined by rational-valued transformation matrices  $\underline{\underline{M}}$  such as (6.1). An example is the adsorption of graphene, a graphite monolayer with honeycomb structure, on the (0 0 0 1) surface of ruthenium which has been observed by LEED and STM [127]. Here the graphene overlayer forms,

together with the topmost Ru layers, a coincidence superlattice where very small lateral distortions are combined with perpendicular warping, see Fig. 6.5b. High-order commensurate (HOC) overlayers will be discussed in more detail in Secs. 6.4 and 6.5.

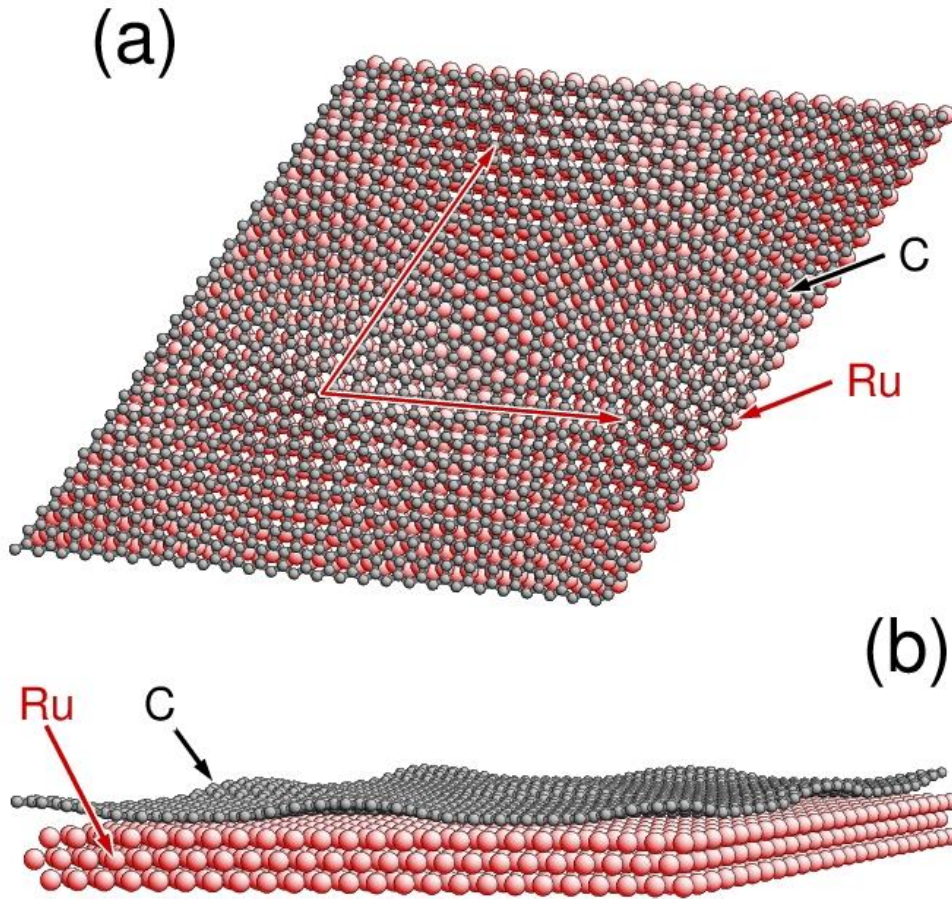


Fig. 6.5. Graphene overlayer adsorbed on the Ru(0 0 0 1) surface. The Ru surface is shown by its topmost three layers. (a) View perpendicular to the surface. The superlattice periodicity,  $12 \times 12$  for the Ru substrate and  $13 \times 13$  for graphene from DFT simulations, is indicated by lattice vectors. (b) View almost parallel to the surface demonstrating the overlayer warping.

- (c) Adsorbate overlayers can form **incommensurate** overlayer lattices. Here the transformation matrix  $\underline{M}$ , connecting lattice vectors of the overlayer with those of the substrate surface according to (5.3), contains matrix elements  $m_{ij}$ , of which at least one is **irrational**. In this case the combined adsorbate-substrate system is not strictly periodic in two dimensions. An example from the Surface Structure Database, SSD 47.54.1, is the adsorption of Xe atoms adsorbed on the Ag (1 1 1) surface [128] shown in Fig. 6.6. Here both the Xe adsorbate overlayer and the topmost substrate layer form hexagonal lattices. However, their lattice constants are different and, in addition, the relative orientation of the two layers with respect

to each other may vary. The orientation shown in Fig. 6.6 is only one of many possibilities where the overlayer can be rotated and shifted laterally. Analogous to the earlier examples, the Xe overlayer may not be completely flat with modulations due to local binding effects which are, however, expected to be small in the present case. Also, the slightest lateral adsorbate-substrate interaction may contract or expand the overlayer into a commensurate relationship, perhaps with a large coincidence supercell reflecting a high-order commensurate lattice. The latter corresponds formally to approximating all elements of the real-valued transformation matrix  $\underline{M}$  by rational numbers for which many mathematical algorithms have been proposed [129].

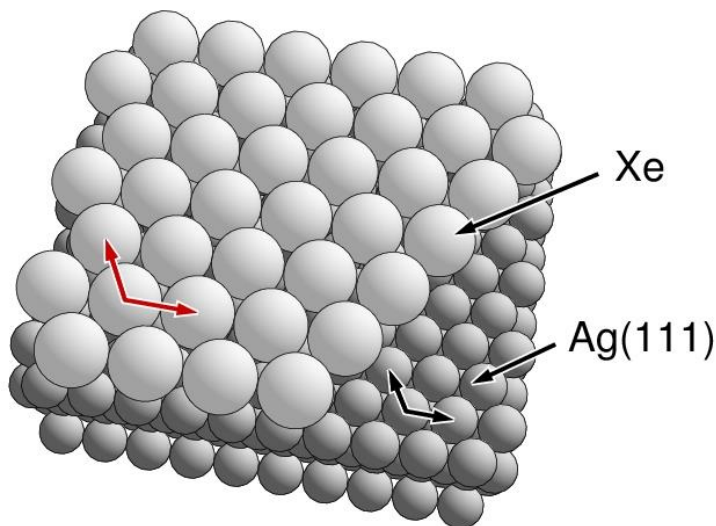


Fig. 6.6. Structure of the incommensurate Ag(1 1 1) + Xe system. The periodicity vectors of the Xe adsorbate layer and of the Ag substrate are shown for one possible orientation only with overlayer vectors chosen to be parallel to those of the substrate.

## 6.2 Adsorbate Sites

The structural characterization of an adsorbate covered surface also includes quantitative details about all surface positions where the adsorbates stabilize as well as about orientation and changed internal structure in cases of molecular adsorbates. These details are basically determined by the local binding of each adsorbate with its nearby atoms of the substrate surface, i.e. those of the topmost substrate layers. The planar substrate surface of a single crystal with ideal bulk termination, i.e. of two-dimensional lateral periodicity and defined by Miller indices  $(h k l)$ , is also characterized by its **lateral point symmetry** reflecting a two-dimensional point symmetry group, see Sec.



3.8. As a result, there are preferred lateral sites inside the elementary cell of the substrate surface which are compatible with its symmetry, so-called **high-symmetry sites**. In many surface systems adsorbates are found to stabilize laterally at or near these high-symmetry sites with a perpendicular distance  $z_{\text{ads}}$ . The latter is usually measured from the plane through the topmost ( $h k l$ ) monolayer of the substrate where  $z_{\text{ads}} > 0$  will be called **above** and  $z_{\text{ads}} < 0$  **below** the surface. In the following, examples of high-symmetry sites at surfaces of different symmetry are discussed and illustrated by results from measured adsorbate systems. Additional sites can be inspected in Appendix A which collects the most important high-symmetry sites of common surfaces. In the following, all example structures are denoted by ‘SSD n.m’ where n.m refers the corresponding structure to the entry number of the Surface Structure Database (NIST Version 5 or oSSD), see Sec. 7.2 and Appendix H.

At ideal substrate surfaces with **square** netplanes and appropriate point symmetry, see Section 3.8.4, the primitive periodicity cell offers three distinct lateral high-symmetry sites, shown in Fig. 6.7, (a) the top site, (b) the 4-fold hollow site, and (c) the 2-fold bridge site.

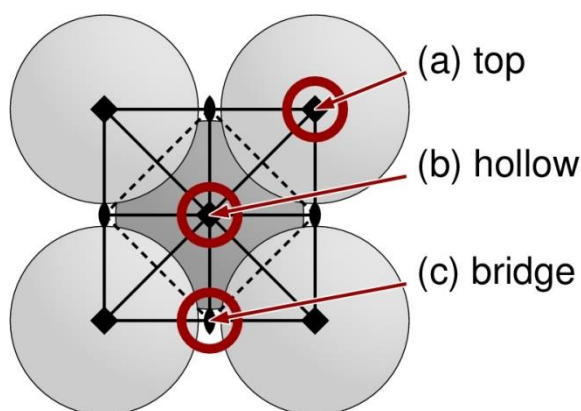


Fig. 6.7. Primitive periodicity cell of a substrate with square lattice. The lateral high-symmetry sites, (a) top, (b) hollow, and (c) bridge, are shown by red circles. The gray balls indicate substrate atoms of different layers and all possible point symmetry elements of the cell are included by corresponding symbols, see Sec. 3.8.4.

At the **top** site the adsorbate atom or molecule stabilizes directly above a substrate atom at the surface, see Fig. 6.7, site (a). This allows strong directional binding of the adsorbate with the substrate which can be a result of strong covalent bond formation at the surface. An example of periodically ordered **molecular** adsorbates is Ni(1 0 0) + c(2 × 2) - CO [130], SSD 28.6.8.8, shown in Fig. 6.8, where the CO molecules adsorb in top sites with carbon pointing to the surface and  $z_{\text{ads}}(\text{C}) = 1.70 \text{ \AA}$ .

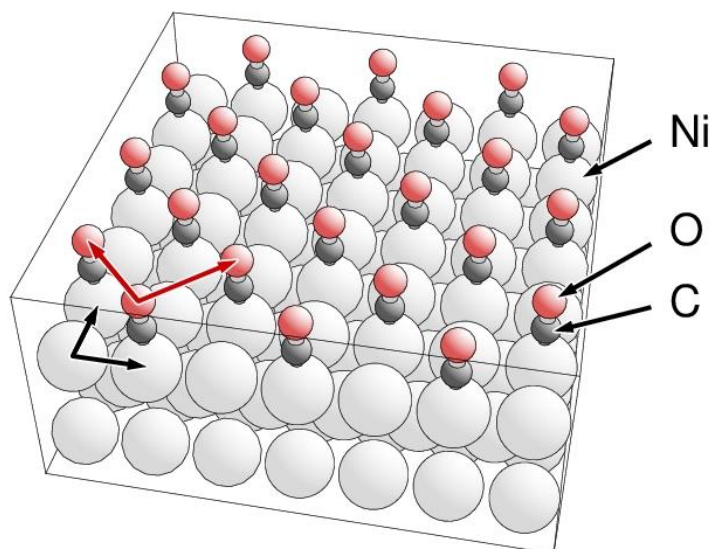


Fig. 6.8. Structure of the Ni(1 0 0) + c(2 × 2) - CO adsorbate system. The lattice vectors of the CO adsorbate layer and of the Ni substrate are shown in red and black, respectively.

At the **4-fold hollow** site the adsorbate atom or molecule stabilizes laterally in the center between four substrate atoms at the surface which form the periodicity cell, see Fig. 6.7, site (b). This allows for largest coordination at the surface which can be due to major electrostatic interactions appearing for ionic adsorbates. An example of periodically ordered **atomic** adsorbates is Cu(1 0 0) + c(2 × 2) - Cl [131], SSD 29.17.7, shown in Fig. 6.19 below, where the chlorine atoms adsorb in hollow sites with  $z_{\text{ads}} = 1.59 \text{ \AA}$ .

At the **2-fold bridge** site the adsorbate atom or molecule stabilizes laterally between two adjacent substrate atoms at the surface, see Fig. 6.7, site (c). An example of periodically ordered **atomic** adsorbates is Ir(1 0 0) + (1 × 2) - O [132], SSD 77.8.4, where the oxygen atoms adsorb in bridge sites with  $z_{\text{ads}} = 1.30 \text{ \AA}$ .

At ideal substrate surfaces with **hexagonal** netplanes and appropriate point symmetry, see Section 3.8.5, the primitive periodicity cell offers four distinct lateral high-symmetry sites, shown in Fig. 6.9, (a) the top site, (b) the 3-fold hcp hollow site, (c) the 3-fold fcc hollow site, and (d) the 2-fold bridge site.

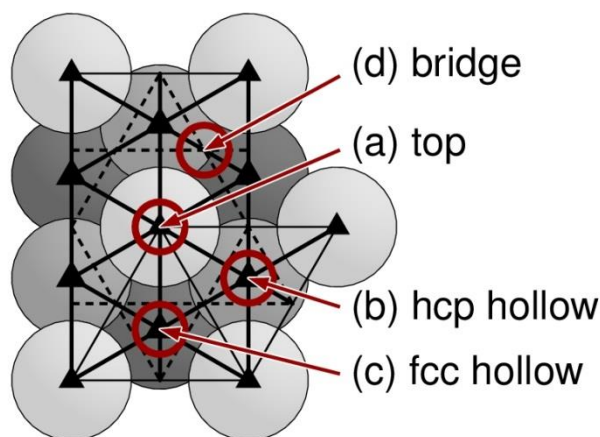


Fig. 6.9. Primitive and rectangular periodicity cells of a substrate with hexagonal lattice based on cubic and hexagonal close-packed bulk structures. The lateral high-symmetry sites, (a) top, (b) hcp hollow, (c) fcc hollow, and (d) bridge, are shown by red circles. The gray balls indicate substrate atoms of different layers and the point symmetry elements of the cell are included by corresponding symbols, see Sec. 3.8.5.

At the **top** site the adsorbate atom or molecule stabilizes directly above a substrate atom at the surface, see Fig. 6.9, site (a), which allows strong directional binding of the adsorbate with the substrate. An example of periodically ordered **atomic** adsorbates is  $\text{Cu}(1\ 1\ 1) + (2 \times 2) - \text{Cs}$  [133], SSD 29.55.1, where the Cs atoms adsorb in top sites with  $z_{\text{ads}} = 3.01\ \text{\AA}$ . Further,  $\text{Rh}(1\ 1\ 1) + (\sqrt{3} \times \sqrt{3})R30^\circ - \text{CO}$  [134], SSD 45.6.8.7a, is an example of periodically ordered **molecular** adsorbates where the CO molecules adsorb in top sites with carbon pointing to the surface and  $z_{\text{ads}}(\text{C}) = 1.81\ \text{\AA}$ .

Surfaces with hexagonal netplanes can offer two different **3-fold hollow** sites depending on the structure of the substrate layers below the topmost layer. For cubic and hexagonal close-packed crystals these are the **hcp hollow** site, see Fig. 6.9, site (b), where there is a substrate atom of the 2<sup>nd</sup> surface layer directly underneath the adsorbate site and the **fcc hollow** site, see Fig. 6.9, site (c), where an atom of the 3<sup>rd</sup> surface layer is underneath. An example of periodically ordered **atomic** adsorbates is  $\text{Ni}(1\ 1\ 1) + (2 \times 2) - \text{O}$  [135], SSD 28.8.75a, where oxygen atoms adsorb in fcc hollow sites with  $z_{\text{ads}} = 1.09\ \text{\AA}$ . Also the CO molecules of the **molecular** adsorbate system  $\text{Pd}(1\ 1\ 1) + (\sqrt{3} \times \sqrt{3})R30^\circ - \text{CO}$  [136], SSD 46.6.8.13, shown in Fig. 6.20 below, adsorb in fcc hollow sites with carbon pointing to the surface and  $z_{\text{ads}}(\text{C}) = 1.25\ \text{\AA}$ . Further, the NO molecules of  $\text{Ni}(1\ 1\ 1) + c(4 \times 2) - 2\text{NO}$  [137], SSD 28.7.8.8, shown in Fig. 6.10, adsorb in both fcc and hcp hollow sites with nitrogen pointing to the surface and  $z_{\text{ads}}(\text{N})$  varying between 1.18 and 1.32  $\text{\AA}$ . (Actually, the topmost nickel layer is not exactly planar while the nitrogen centers are co-planar, resulting

in different  $z_{\text{ads}}(\text{N})$  values.)

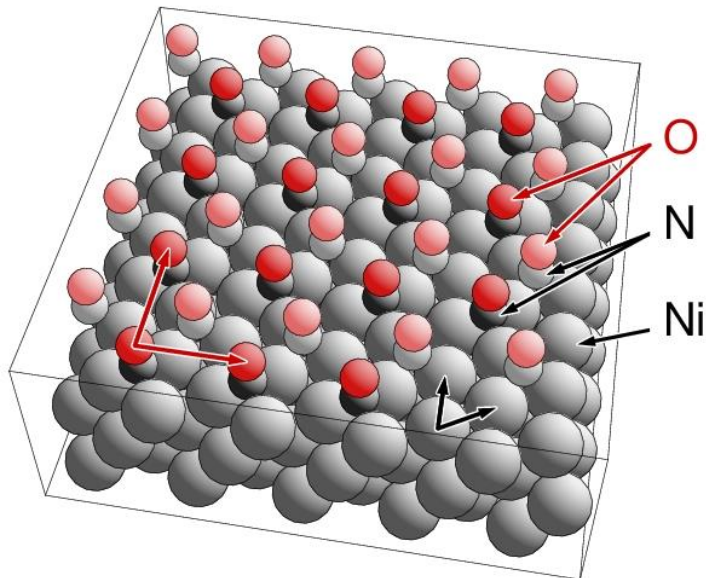


Fig. 6.10. Structure of the  $\text{Ni}(1\ 1\ 1) + c(4 \times 2) - 2\text{NO}$  adsorbate system. NO molecules in fcc hollow sites are painted lighter than those in hcp hollow sites. The lattice vectors of the NO adsorbate layer and of the Ni substrate are shown in red and black, respectively.

At the **2-fold bridge** site the adsorbate atom or molecule stabilizes laterally between two adjacent substrate atoms at the surface, see Fig. 6.9, site (d). An example of **molecular** adsorption is  $\text{Cu}(1\ 1\ 1) + (\text{disordered}) - \text{C}_2\text{H}_2$  [138], SSD 29.6.1.6, shown in Fig. 6.11, where the two carbon atoms of the acetylene adsorbate bend slightly asymmetrically over bridge sites such that they approach adjacent fcc and hcp hollow sites where  $z_{\text{ads}}(\text{C})$  amounts to  $1.38\ \text{\AA}$  (fcc) and  $1.44\ \text{\AA}$  (hcp), respectively. Due to the 3-fold symmetry of the clean  $\text{Cu}(1\ 1\ 1)$  surface there are three equivalent bridge site structures with the orientation of the  $\text{C}_2\text{H}_2$  adsorbate rotated by  $\pm 120^\circ$ . Of these only one orientation is shown in Fig. 6.11.

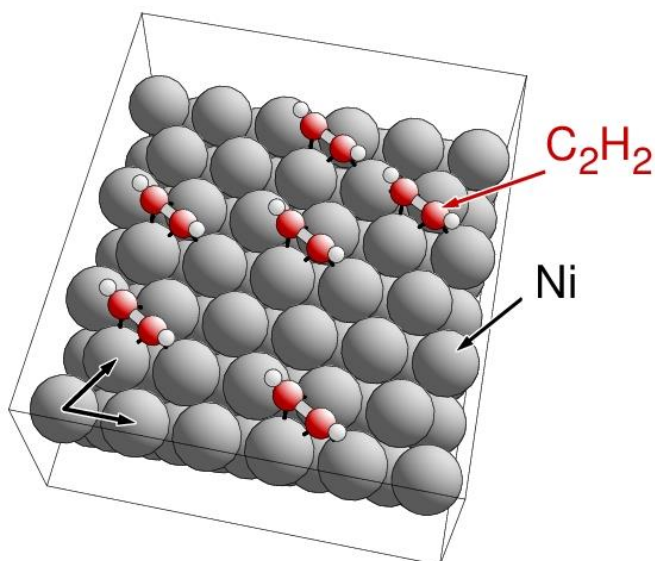


Fig. 6.11. Structure of the Cu(1 1 1) + (disordered) -  $C_2H_2$  adsorbate system. The lattice vectors of the Cu substrate are shown in black.

At ideal substrate surfaces with **primitive rectangular** netplanes and appropriate point symmetry, see Section 3.8.2, the primitive periodicity cell offers four distinct lateral high-symmetry sites, shown in Fig. 6.12, (a) the top site, (b) the 2-fold long bridge site, (c) the 2-fold short bridge site, and (d) the 4-fold hollow site, sometimes also called center site.

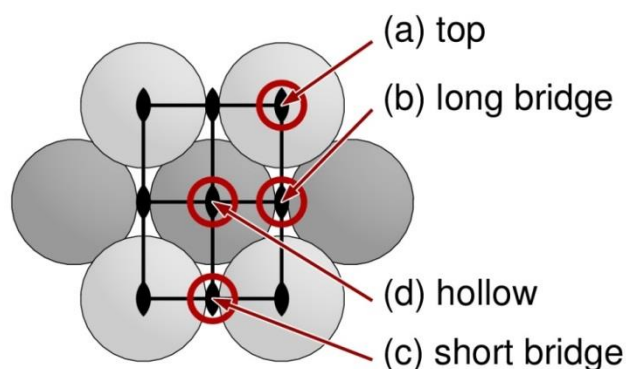


Fig. 6.12. Primitive cell of a substrate with primitive rectangular lattice based on cubic bulk structures. The lateral high-symmetry sites, (a) top, (b) long bridge, (c) short bridge, and (d) hollow, are shown by red circles. The gray balls indicate substrate atoms of different layers and the point symmetry elements of the cell are included by corresponding symbols, see Sec. 3.8.2.

At the **top** site the adsorbate atom or molecule stabilizes directly above a substrate atom at the surface, see Fig. 6.12, site (a). An example of periodically ordered **molecular** adsorbates is Cu(1 1 0) +  $(2 \times 1)$  - CO [139], SSD 29.6.8.7, where the CO molecules adsorb in top sites with carbon pointing to the surface and  $z_{\text{ads}}(\text{C}) = 1.87 \text{ \AA}$ .

At the **2-fold long bridge** site the adsorbate atom or molecule stabilizes laterally between two adjacent substrate atoms at the surface, see Fig. 6.12, site (b). An example of **atomic** adsorption was suggested for  $\text{Ag}(1\ 1\ 0) + (2 \times 1) - \text{O}$  [140], SSD 47.8.4, shown in Fig. 6.13, where the oxygen atoms stabilize between silver atoms of the topmost substrate row with  $z_{\text{ads}} = 0.2\ \text{\AA}$ , i.e. only slightly above the surface plane through the rows.

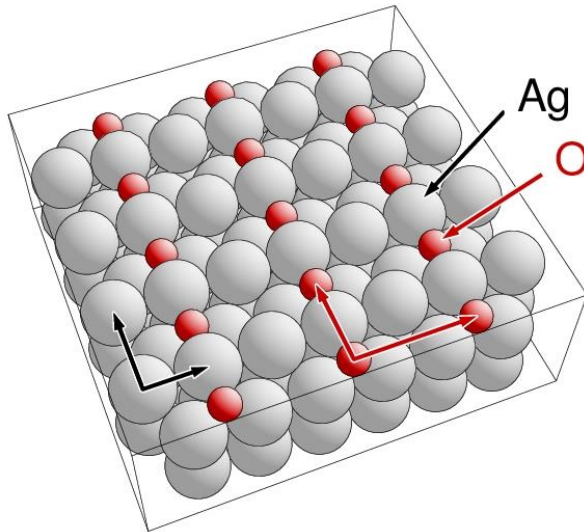


Fig. 6.13. Structure of the  $\text{Ag}(1\ 1\ 0) + (2 \times 1) - \text{O}$  adsorbate system. The lattice vectors of the O adsorbate layer and of the Ag substrate are shown in red and black, respectively.

At the **2-fold short bridge** site the adsorbate atom or molecule also stabilizes laterally between two adjacent substrate atoms at the surface but the substrate atoms are closer together than at the long bridge site, see Fig. 6.12, site (c). An example of periodically ordered **atomic** adsorbates is  $\text{Pt}(1\ 1\ 0) + c(2 \times 2) - \text{Br}$  [106], SSD 78.35.1, shown in Fig. 6.14, where the bromine atoms adsorb in short bridge sites above the topmost substrate rows with  $z_{\text{ads}} = 2.04\ \text{\AA}$ . Further, the CO molecules of the **molecular** adsorbate system  $\text{Ni}(1\ 1\ 0) + p2mg(2 \times 1) - 2\text{CO}$  [125], SSD 28.6.8.45, shown in Fig. 6.2, adsorb quite near short bridge sites. Here their molecular axes are alternately tilted with respect to the surface normal as discussed below.

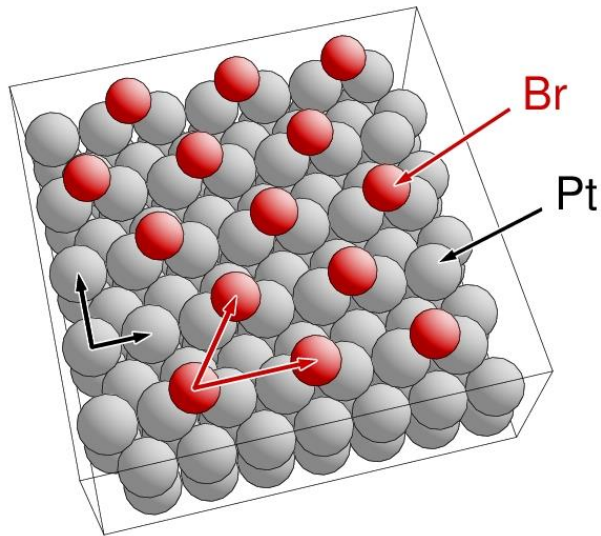


Fig. 6.14. Structure of the Pt(1 1 0) + c(2 × 2) - Br adsorbate system. The lattice vectors of the Br adsorbate layer and of the Pt substrate are shown in red and black, respectively.

At the **4-fold hollow** site the adsorbate atom or molecule stabilizes laterally in the center between four substrate atoms at the surface which form the periodicity cell, see Fig. 6.12, site (d). An example of periodically ordered **atomic** adsorbates is Ni(1 1 0) + c(2 × 2) - S [141], SSD 28.16.57b, where the sulfur atoms adsorb in hollow sites with  $z_{\text{ads}} = 0.77 \text{ \AA}$ .

At ideal substrate surfaces with **centered rectangular** netplanes and appropriate point symmetry, see Section 3.8.3, the primitive periodicity cell offers two distinct lateral high-symmetry sites, shown in Fig. 6.15, (a) the top site and (b) the 4-fold hollow site. Further, there is an additional site, (c) the so-called 3-fold hollow site, which is not exactly of high symmetry but is treated on the same footing since it has been observed in a number of surface systems.

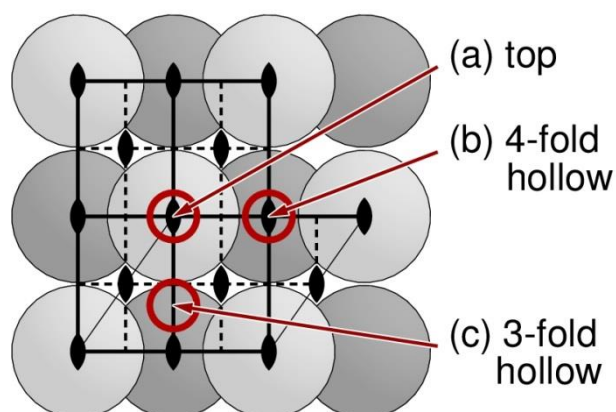


Fig. 6.15. Primitive cell of a substrate with centered rectangular lattice based on cubic bulk structures. The lateral high-symmetry sites, (a) top, (b) 4-fold hollow, and (c) 3-fold hollow, are shown by red circles. The gray balls indicate substrate atoms of different layers and the point symmetry elements of the cell are included by corresponding symbols, see Sec. 3.8.3.

At the **top** site the adsorbate atom or molecule stabilizes directly above a substrate atom at the surface, see Fig. 6.15, site (a). Examples for this type of site do not seem to exist in the literature.

At the **4-fold hollow** site the adsorbate atom or molecule stabilizes laterally between four substrate atoms at the surface, two adjacent and two at larger distance, see Fig. 6.15, site (b). An example of periodically ordered **atomic** adsorbates is Fe(1 1 0) + (2 × 2) - S [142], SSD 26.16.4, where the sulfur atoms adsorb with  $z_{\text{ads}} = 0.77 \text{ \AA}$ .

At the **3-fold hollow** site the adsorbate atom or molecule stabilizes laterally between three substrate atoms at the surface forming a triangle with two equal sides and one larger by only 15%, see Fig. 6.15, site (c). An example of periodically ordered **atomic** adsorbates is W(1 1 0) + (2 × 1) - O [143], SSD 74.8.1, shown in Fig. 6.16, where the oxygen atoms adsorb with  $z_{\text{ads}} = 1.25 \text{ \AA}$ .



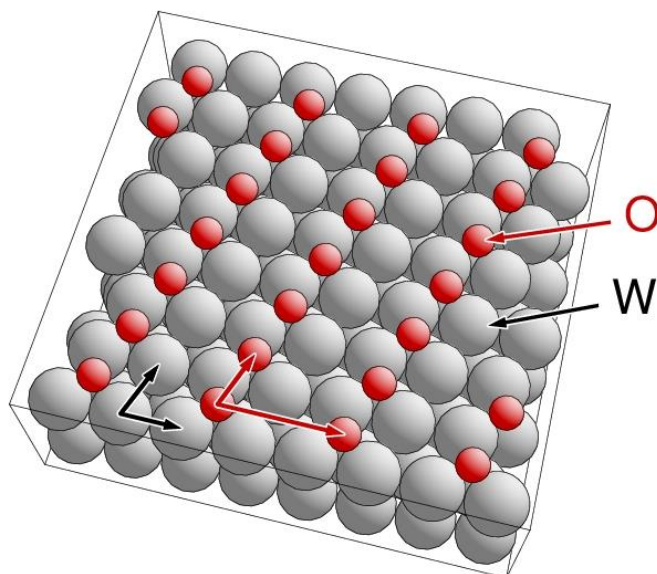


Fig. 6.16. Structure of the  $W(1\ 1\ 0) + (2 \times 1) - O$  adsorbate system. The lattice vectors of the O adsorbate layer and of the W substrate are shown in red and black, respectively.

In the example system  $Ni(1\ 1\ 1) + c(4 \times 2) - 2NO$  [137] discussed above, see Fig. 6.10, adsorption at both fcc and hcp hollow sites of the hexagonal substrate surface appears in the same structure. This illustrates that ordered adsorbate overlayers are not always connected with only one single adsorption site and **mixed site adsorption** can occur. Another example is  $Pt(1\ 1\ 1) + c(4 \times 2) - 2CO$  [144], SSD 78.6.8.4, shown in Fig. 6.40 below, where CO molecules adsorb in both top and bridge sites of the hexagonal substrate surface with carbon pointing to the surface and  $z_{ads}(C) = 1.85\ \text{\AA}$  for the top site and  $1.55\ \text{\AA}$  for the bridge site.

Apart from adsorption at sites near substrate atoms of the otherwise unreconstructed surface, adsorbates can also replace substrate atoms at the surface (**substitutional adsorption**). A simple example is  $Cu(1\ 0\ 0) + c(2 \times 2) - Pd$  [145], SSD 29.46.2, where palladium and copper atoms of the topmost layer form a checkerboard structure resulting in surface alloying. Another example is  $Cu(1\ 1\ 0) + c(2 \times 2) - Mn$  [146], SSD 29.25.8, shown in Fig. 6.17, where manganese and copper atoms in alternating sequence form the topmost surface rows.

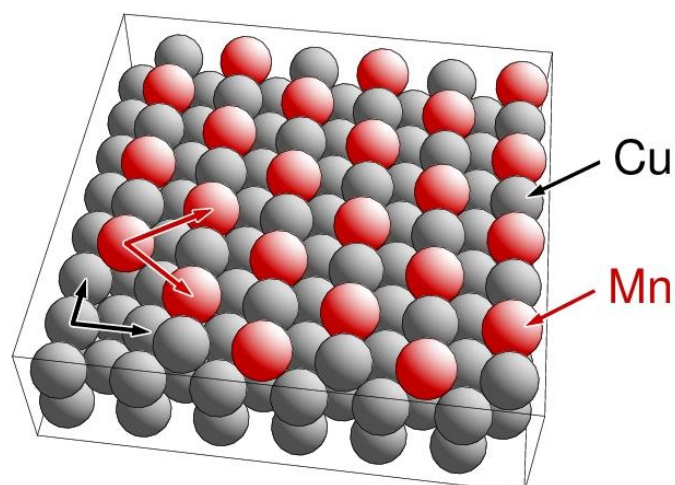


Fig. 6.17. Structure of the  $\text{Cu}(1\ 1\ 0) + c(2 \times 2) - \text{Mn}$  adsorbate system. The lattice vectors of the Mn / Cu atoms of the topmost layer and of the Cu substrate are shown in red and black, respectively.

So far, adsorbate structure has been characterized by lateral surface sites and perpendicular distances  $z_{\text{ads}}$  of the adsorbate from the topmost substrate plane. For **molecular adsorbates** this needs to be supplemented by parameters which describe the **orientation** of the adsorbate relative to the surface and the **internal** molecular structure where the latter may be distorted if compared with structure of the free molecule. For example, the information stating which part of an adsorbate molecule points to the substrate and the inclination of a molecular axis with respect to the surface normal of the substrate are essential for a complete structural characterization. Assuming no internal distortion of the adsorbed molecule, three angles are needed to specify the orientation of a non-symmetrical molecule relative to a surface. As a simple example, the CO molecule is found to adsorb in many cases with its molecular axis along the surface normal and with its carbon end pointing towards the substrate, see  $\text{Ni}(1\ 0\ 0) + c(2 \times 2) - \text{CO}$  in Fig. 6.8. However, the molecular axis of CO can also be tilted away from the surface normal as shown for  $\text{Ni}(1\ 1\ 0) + p2mg(2 \times 1) - 2\text{CO}$  in Fig. 6.2. The latter illustrates the more general result that adsorbates may adsorb differently depending on their coverage on the substrate surface due to adsorbate-adsorbate interaction. In the  $\text{Ni}(1\ 1\ 0) + p2mg(2 \times 1) - 2\text{CO}$  system adjacent CO adsorbate molecules, getting quite near to each other, try to minimize their mutual repulsion by tilting in different direction whereas in the  $\text{Ni}(1\ 0\ 0) + c(2 \times 2) - \text{CO}$  system the adsorbates are further away and stabilize in equal orientation.

Further, adsorbate atoms or molecules are expected to influence the structure of the underlying **substrate** by inducing relaxation and reconstruction. This may create new adsorption sites which do not exist at the clean surface. As an example, the clean  $\text{Cu}(1\ 1\ 0) - (1 \times 1)$  surface [147], SSD 29.65, exists as an unreconstructed bulk terminated structure with primitive rectangular lattice. In contrast, in the  $\text{Cu}(1\ 1\ 0) + (2 \times 3) - 4\text{N}$  system [148], SSD 29.7.10, see Fig. 6.18, the nitrogen adsorbate reconstructs the top copper layer to form a buckled nearly square lattice. Another example of large structural effects of the adsorbate on the substrate is the  $\text{Si}(1\ 1\ 1)$  surface. Without adsorbates this surface shows a complex  $(7 \times 7)$  reconstruction [109], [110] described by the DAS model, see Fig. 5.5. After hydrogen adsorption the reconstruction disappears completely, yielding a simple  $\text{Si}(1\ 1\ 1) + (1 \times 1) - \text{H}$  adsorbate system [149], SSD 14.1.30, with an unreconstructed substrate and top-site-bonded hydrogen atoms.

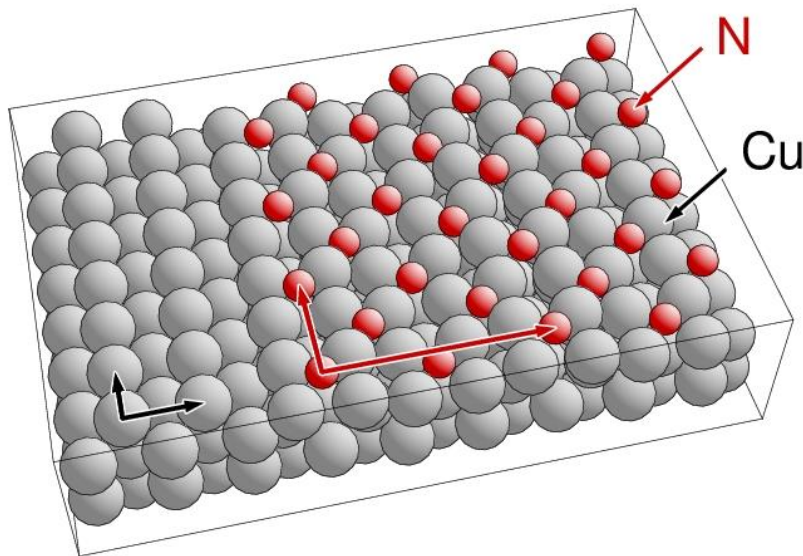


Fig. 6.18. Structure of the  $\text{Cu}(1\ 1\ 0) + (2 \times 3) - 4\text{N}$  adsorbate system. The lattice vectors of the unreconstructed substrate to the left are shown in black while those of the reconstructed surface to the right are shown in red.

### 6.3 Wood Notation of Surface Structure

As a simpler alternative to the matrix notation, the structure of ordered **reconstructed** single crystal surfaces as well as of ordered **adsorbate layers** is often characterized by the **Wood notation** [150]. Here we adopt mainly the nomenclature used in Ref. [94]. It should be mentioned in passing that a number of attempts have been made to suggest alternative notation schemes which could give

a unique description of surface structure of any complexity [44], analogous to notations used in bulk crystallography [33]. These include generalizations of the  $2 \times 2$  matrix notation [100] or a scheme proposed by the authors of the NIST Surface Structure Database (SSD) [23], see Sec. 7. However, these schemes have never been widely accepted within the surface science community, in contrast to the Wood notation.

As a first example of the Wood notation the so-called  $(1 \times 2)$ -missing-row reconstructed platinum surface was discussed in Sec. 5.2. This surface is denoted as  $\text{Pt}(1\ 1\ 0) - (1 \times 2)$  where the periodicity of the topmost  $(1\ 1\ 0)$  surface layer is described as ‘ $(1 \times 2)$ ’ and every second row of atoms of this layer is missing. The notation refers to a rectangular lattice of the topmost layer whose second lattice vector is enlarged by a factor 2 compared with that of the underlying substrate lattice while the first remains unchanged, see Fig. 5.2. As a result, the corresponding reconstruction matrix  $\underline{M}$  is given by (5.5).

A slightly more complex example is given by the  $\text{Cu}(1\ 0\ 0)$  surface with a periodic chlorine overlayer of half the density of the topmost Cu layer [131] shown in Fig. 6.19.

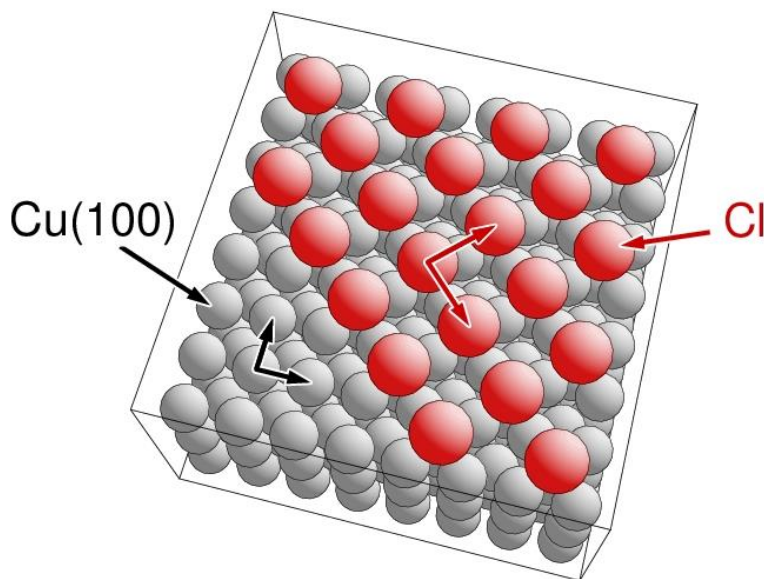


Fig. 6.19. Structure of the  $\text{Cu}(1\ 0\ 0) + c(2 \times 2) - \text{Cl}$  adsorbate system. The periodicity vectors of the Cl adsorbate layer and of the Cu substrate are shown in red and black, respectively.

The example, taken from the Surface Structure Database, SSD 29.17.7, is commonly denoted as  $\text{Cu}(1\ 0\ 0) + c(2 \times 2) - \text{Cl}$  following the Wood notation, where the periodicity of the Cl adsorbate layer is characterized by ‘ $c(2 \times 2)$ ’. This corresponds to a centered rectangular overlayer with rec-

tangular lattice vectors twice those of the underlying substrate layer. The overlayer periodicity can also be described by a primitive square lattice with lattice vectors increased by a factor  $\sqrt{2}$  and rotated by  $45^\circ$  with respect to those of the substrate. Thus, the corresponding reconstruction matrix  $\underline{\underline{M}}$  is given by

$$\underline{\underline{M}} = \begin{pmatrix} 1 & -1 \\ 1 & 1 \end{pmatrix}$$

and, within the Wood notation scheme, the overlayer structure can be written as  $\text{Cu}(1\ 0\ 0) + (\sqrt{2} \times \sqrt{2})\text{R}45^\circ - \text{C1}$ . The appearance of irrational numbers,  $\sqrt{2}$ , in the notation still leads to an integer-valued reconstruction matrix characterizing the commensurate overlayer. This applies also to the  $\text{Pd}(1\ 1\ 1) + (\sqrt{3} \times \sqrt{3})\text{R}30^\circ - \text{CO}$  adsorbate structure [136], SSD 46.6.8.13, shown in Fig. 6.20. Here the lattices of both the substrate and the CO overlayer are hexagonal with the lattice vectors of the overlayer increased by a factor  $\sqrt{3}$  and rotated by  $30^\circ$  with respect to those of the

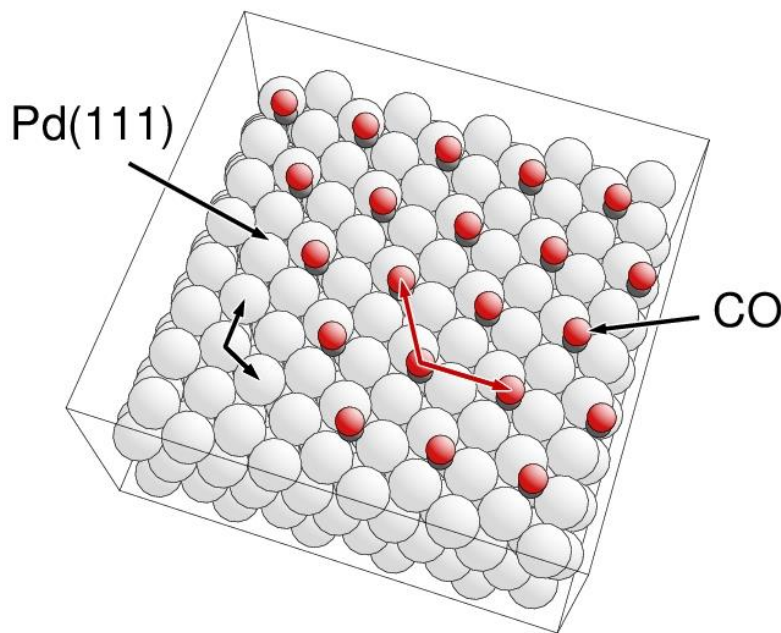


Fig. 6.20. Structure of the  $\text{Pd}(1\ 1\ 1) + (\sqrt{3} \times \sqrt{3})\text{R}30^\circ - \text{CO}$  adsorbate system. The periodicity vectors of the CO adsorbate layer and of the Pd substrate are shown in red and black, respectively.

substrate. For this structure, using obtuse hexagonal vector pairs, the transformation matrix  $\underline{\underline{M}}$  is given by

$$\underline{\underline{\mathbf{M}}} = \begin{pmatrix} 2 & 1 \\ -1 & 1 \end{pmatrix}$$

The **general** case of the **Wood notation** of a **reconstructed** surface is formally given by

$$\text{Sub}(h k l) - \kappa(\gamma_1 \times \gamma_2) \mathbf{R}\alpha - \eta \text{Sub} \quad (6.2a)$$

and a general surface with an **adsorbate overlayer** is written as

$$\text{Sub}(h k l) + \kappa(\gamma_1 \times \gamma_2) \mathbf{R}\alpha - \eta \text{Ovl} \quad (6.2b)$$

where it is assumed that the substrate '**Sub**' is described by stacking two-dimensionally periodic layers with periodicity vectors  $\underline{\mathbf{R}}_1$  and  $\underline{\mathbf{R}}_2$  representing  $(h k l)$  Miller index planes. In addition, either the topmost substrate layer at the surface is reconstructed yielding a periodic **reconstruction layer** (which may actually include more than one substrate layers), formula (6.2a), or the surface is covered by a **periodic overlayer** '**Ovl**', formula (6.2b). In both cases, the periodicity vectors  $\underline{\mathbf{R}}_1'$  and  $\underline{\mathbf{R}}_2'$  of the topmost (over)layer are given by **linear combinations** of the substrate surface vectors  $\underline{\mathbf{R}}_1$  and  $\underline{\mathbf{R}}_2$  where for

(a)  $\kappa = \text{'p'}$  (**primitive**) vector  $\underline{\mathbf{R}}_1'$  equals the substrate surface vector  $\underline{\mathbf{R}}_1$  rotated anti-clockwise by an angle  $\alpha$  along the surface plane and scaled by factor  $\gamma_1$  to yield  $|\underline{\mathbf{R}}_1'| = \gamma_1 |\underline{\mathbf{R}}_1|$ . The same procedure is applied to  $\underline{\mathbf{R}}_2$  using angle  $\alpha$  and scaling factor  $\gamma_2$  to yield  $\underline{\mathbf{R}}_2'$ . (6.3a)

(b)  $\kappa = \text{'c'}$  (**centered**) vectors  $\underline{\mathbf{R}}_1'$ ,  $\underline{\mathbf{R}}_2'$  describe a centered two-dimensional lattice starting from a primitive set  $\underline{\mathbf{R}}_{1p}'$ ,  $\underline{\mathbf{R}}_{2p}'$  constructed according to (a) followed by a linear transformation

$$\underline{\mathbf{R}}_1' = 1/2 (\underline{\mathbf{R}}_{1p}' + \underline{\mathbf{R}}_{2p}'), \quad \underline{\mathbf{R}}_2' = 1/2 (-\underline{\mathbf{R}}_{1p}' + \underline{\mathbf{R}}_{2p}') \quad . \quad (6.3b)$$

Further, the unit cell of the reconstructed substrate surface is assumed to contain  $\eta \geq 1$  non-equivalent species '**Sub**' and in the adsorbate system the unit cell of the overlayer may contain  $\eta \geq 1$  non-equivalent species '**Ovl**' of the same type. The general Wood notation (6.2) is often **simplified** by omitting  $\kappa$  if  $\kappa = \text{'p'}$ , omitting  $\eta$  if  $\eta = 1$ , and omitting '**R**  $\alpha$ ' if  $\alpha = 0^\circ$ . The qualifier  $\kappa$  has been used in a few cases to also give **additional information** about the overlayer lattice and its symmetry. An example is given by the  $\text{Ni}(1\ 1\ 0) + \text{p}2\text{mg}(2 \times 1) - 2\text{CO}$  adsorbate system [125], see Fig. 6.2, where the unit cell of the CO overlayer is described in its two-dimensional symmetry by symmetry group  $\text{p}2\text{mg}$ .

The most complex case, adsorption of a reconstructed overlayer at a reconstructed substrate surface, would be denoted as

$$\text{Sub}(h k l) - \kappa_o(\gamma_{o1} \times \gamma_{o2})\mathbf{R}\alpha_o - \eta_o \text{Sub} + \kappa(\gamma_1 \times \gamma_2)\mathbf{R}\alpha - \eta \text{Ovl} \quad (6.4)$$

where in addition to (6.2b) the substrate reconstruction would be described in analogy with that of the overlayer as ‘ $-\kappa_o(\gamma_{o1} \times \gamma_{o2})\mathbf{R}\alpha_o - \eta_o \text{Sub}$ ’. This added complication which has been observed only rarely will be ignored in the following.

The Wood notation can describe both **commensurate** and **incommensurate** overlayers. However, it is **not general** due to its restrictions in the overlayer periodicity introduced by (6.3) which equates the angle between the lattice vectors  $\underline{\mathbf{R}}_1'$  and  $\underline{\mathbf{R}}_2'$  with that between  $\underline{\mathbf{R}}_1$  and  $\underline{\mathbf{R}}_2$  as discussed in Appendix C. The periodicity information of the Wood notation can be expressed alternatively by a **2 × 2 matrix transformation** according to (5.3), i.e. given by

$$\begin{pmatrix} \underline{\mathbf{R}}_1' \\ \underline{\mathbf{R}}_2' \end{pmatrix} = \begin{pmatrix} m_{11} & m_{12} \\ m_{21} & m_{22} \end{pmatrix} \cdot \begin{pmatrix} \underline{\mathbf{R}}_1 \\ \underline{\mathbf{R}}_2 \end{pmatrix} = \underline{\underline{\mathbf{M}}}_{p,c} \cdot \begin{pmatrix} \underline{\mathbf{R}}_1 \\ \underline{\mathbf{R}}_2 \end{pmatrix} \quad (6.5)$$

referring to the reconstruction matrix  $\underline{\underline{\mathbf{M}}}_{p,c}$  which may also be written as  $(m_{11} \ m_{12} \mid m_{21} \ m_{22})$ .

If the periodicity vectors  $\underline{\mathbf{R}}_1$  and  $\underline{\mathbf{R}}_2$  of the substrate form an angle  $\omega$ , i.e.  $(\underline{\mathbf{R}}_1 \ \underline{\mathbf{R}}_2) = R_1 R_2 \cos(\omega)$ , then simple algebra, see Appendix C, yields

- for ‘**primitive**’ overlayers denoted by ‘... - p( $\gamma_1 \times \gamma_2$ ) $\mathbf{R}\alpha$  - ...’

$$\underline{\underline{\mathbf{M}}}_p = \frac{1}{\sin(\omega)} \begin{pmatrix} \gamma_1 \sin(\omega - \alpha) & \gamma_1 q^{-1} \sin(\alpha) \\ -\gamma_2 q \sin(\alpha) & \gamma_2 \sin(\omega + \alpha) \end{pmatrix}, \quad q = \frac{R_2}{R_1} \quad (6.6a)$$

- for ‘**centered**’ overlayers denoted by ‘... - c( $\gamma_1 \times \gamma_2$ ) $\mathbf{R}\alpha$  - ...’

$$\underline{\underline{\mathbf{M}}}_c = \frac{1}{2\sin(\omega)} \begin{pmatrix} \gamma_1 \sin(\omega - \alpha) - \gamma_2 q \sin(\alpha) & \gamma_1 q^{-1} \sin(\alpha) + \gamma_2 \sin(\omega + \alpha) \\ -\gamma_1 \sin(\omega - \alpha) - \gamma_2 q \sin(\alpha) & -\gamma_1 q^{-1} \sin(\alpha) + \gamma_2 \sin(\omega + \alpha) \end{pmatrix} \quad (6.6b)$$

In the following, **examples** of Wood notations are listed together with corresponding transformation matrices describing the overlayer periodicity for different types of Bravais lattices characterized by the parameters  $q$  and  $\omega$ .

- Overlayers on a substrate with **square** netplane (e.g. fcc(1 0 0), bcc(1 0 0), diamond(0 0 1), zinblende(0 0 1) ), where  $R_1 = R_2$ ,  $\omega = 90^\circ$ , see Fig. 6.21. Example notations are

$$(a) \quad p(a \times b) = (a \times b) \quad : \quad \underline{\underline{M}}_p = \begin{pmatrix} a & 0 \\ 0 & b \end{pmatrix} \quad a, b \text{ integer} \quad (6.7a)$$

$$(b) \quad c(4 \times 2) \quad : \quad \underline{\underline{M}}_c = \begin{pmatrix} 2 & 1 \\ -2 & 1 \end{pmatrix} \quad (6.7b)$$

$$(c) \quad c(2 \times 2) = (\sqrt{2} \times \sqrt{2})R45^\circ \quad : \quad \underline{\underline{M}}_c = \underline{\underline{M}}_p = \begin{pmatrix} 1 & 1 \\ -1 & 1 \end{pmatrix} \quad (6.7c)$$

$$(d) \quad p(a\sqrt{2} \times b\sqrt{2}) 45^\circ \quad : \quad \underline{\underline{M}}_p = \begin{pmatrix} a & a \\ -b & b \end{pmatrix} \quad (6.7d)$$

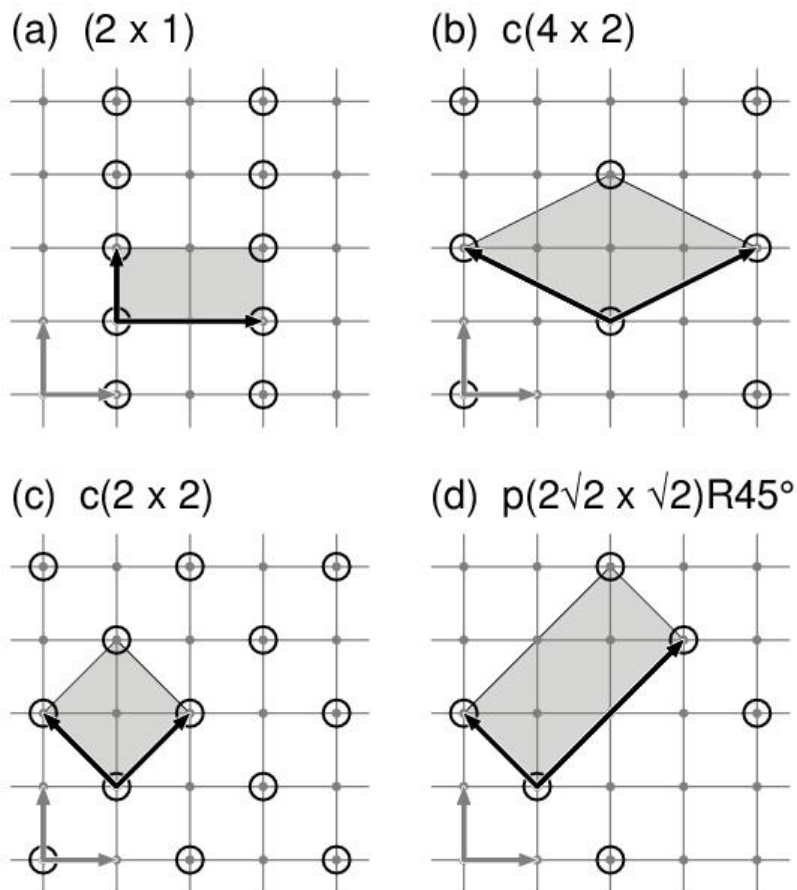


Fig. 6.21. Overlayer unit cells on a substrate with square lattice, (a) to (d), see text. Overlayer and substrate lattice vectors are shown in black and gray, respectively. The overlayer unit cell is emphasized in gray.



- Overlayers on a substrate with **rectangular** netplane (e.g. fcc(1 1 0), diamond(1 1 0), zinblende(1 1 0)), where  $R_1 \neq R_2$ ,  $\omega = 90^\circ$ , see Fig. 6.22. Example notations are

$$(a) \quad p(a \times b) = (a \times b) \quad : \quad \underline{\underline{M}}_p = \begin{pmatrix} a & 0 \\ 0 & b \end{pmatrix} \quad a, b \text{ integer} \quad (6.8a)$$

$$(b) \quad p(2 \times 2) = (2 \times 2) \quad : \quad \underline{\underline{M}}_p = \begin{pmatrix} 2 & 0 \\ 0 & 2 \end{pmatrix} \quad (6.8b)$$

$$(c) \quad \text{fcc}(1 1 0): c(2 \times 2) \quad : \quad \underline{\underline{M}}_c = \begin{pmatrix} 1 & 1 \\ -1 & 1 \end{pmatrix} \quad (6.8c)$$

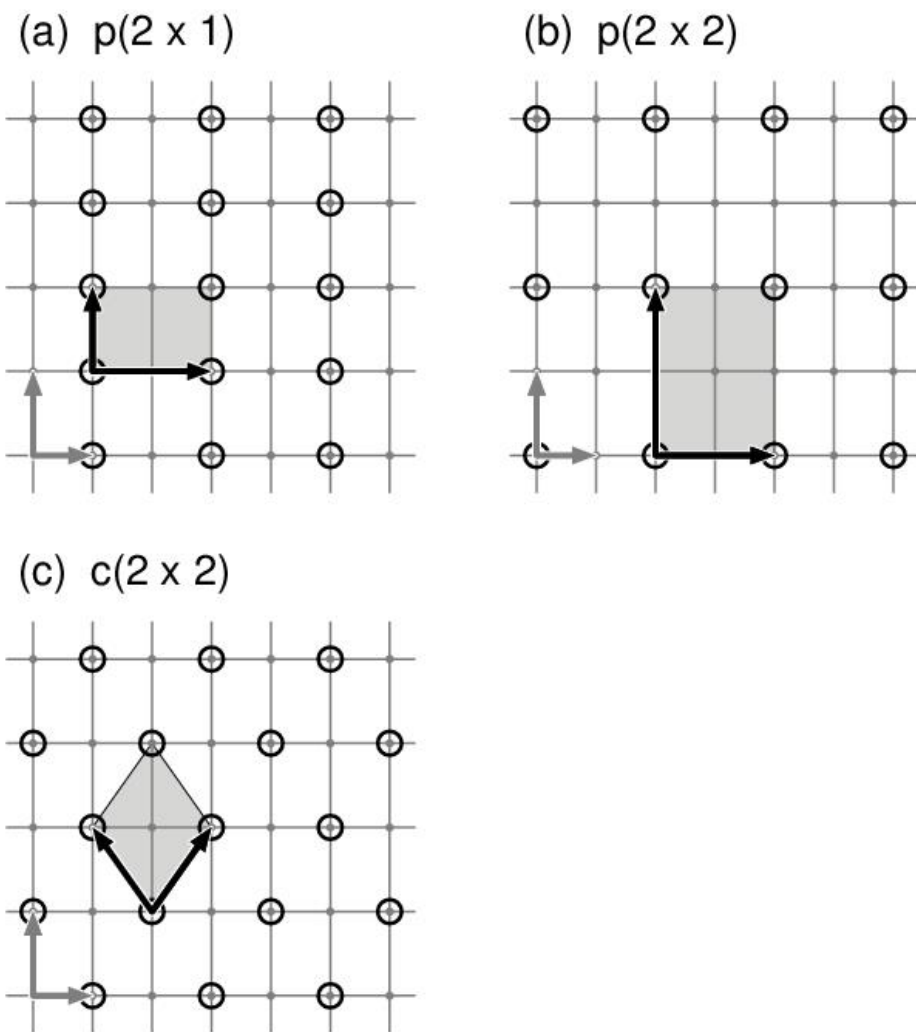


Fig. 6.22. Overlayer unit cells on a substrate with rectangular lattice, (a) to (c), see text. Overlayer and substrate lattice vectors are shown in black and gray, respectively. The overlayer unit cell is emphasized in gray.

- Overlayers on a substrate with **hexagonal** netplane (e.g. fcc(1 1 1), diamond(1 1 1), zinblende(1 1 1), graphite(0 0 0 1)), where  $R_1 = R_2$ ,  $\omega = 120^\circ$  (obtuse representation), see Fig. 6.23. Example notations are

$$(a) \quad p(a \times b) = (a \times b) \quad : \quad \underline{\underline{M}}_p = \begin{pmatrix} a & 0 \\ 0 & b \end{pmatrix} \quad a, b \text{ integer} \quad (6.9a)$$

$$(b) \quad c(2 \times 2) \text{ (also called } (2 \times 1) \text{)} : \quad \underline{\underline{M}}_p = \begin{pmatrix} 1 & -1 \\ 1 & 1 \end{pmatrix} \quad (6.9b)$$

$$(c) \quad c(4 \times 2) \quad : \quad \underline{\underline{M}}_p = \underline{\underline{M}}_c = \begin{pmatrix} 0 & -2 \\ 2 & 1 \end{pmatrix} \quad (6.9c)$$

$$(d) \quad p(\sqrt{(a^2 - ab + b^2)} \times \sqrt{(a^2 - ab + b^2)}) R\alpha \text{ with}$$

$$\cos \alpha = (a - 1/2 b) / (\sqrt{(a^2 - ab + b^2)}) \quad : \quad \underline{\underline{M}}_p = \begin{pmatrix} a & b \\ -b & a - b \end{pmatrix} \quad (6.9d)$$

Specific cases are

$$(d1) \quad (a, b) = (2, 1)$$

$$(\sqrt{3} \times \sqrt{3})R30^\circ : \quad \underline{\underline{M}}_p = \begin{pmatrix} 2 & 1 \\ -1 & 1 \end{pmatrix} \quad (6.9e)$$

$$(d2) \quad (a, b) = (3, 1)$$

$$(\sqrt{7} \times \sqrt{7})R19.1^\circ : \quad \underline{\underline{M}}_p = \begin{pmatrix} 3 & 1 \\ -1 & 2 \end{pmatrix} \quad (6.9f)$$

$$(d3) \quad (a, b) = (4, 1)$$

$$(\sqrt{13} \times \sqrt{13})R13.9^\circ : \quad \underline{\underline{M}}_p = \begin{pmatrix} 4 & 1 \\ -1 & 3 \end{pmatrix} \quad (6.9g)$$

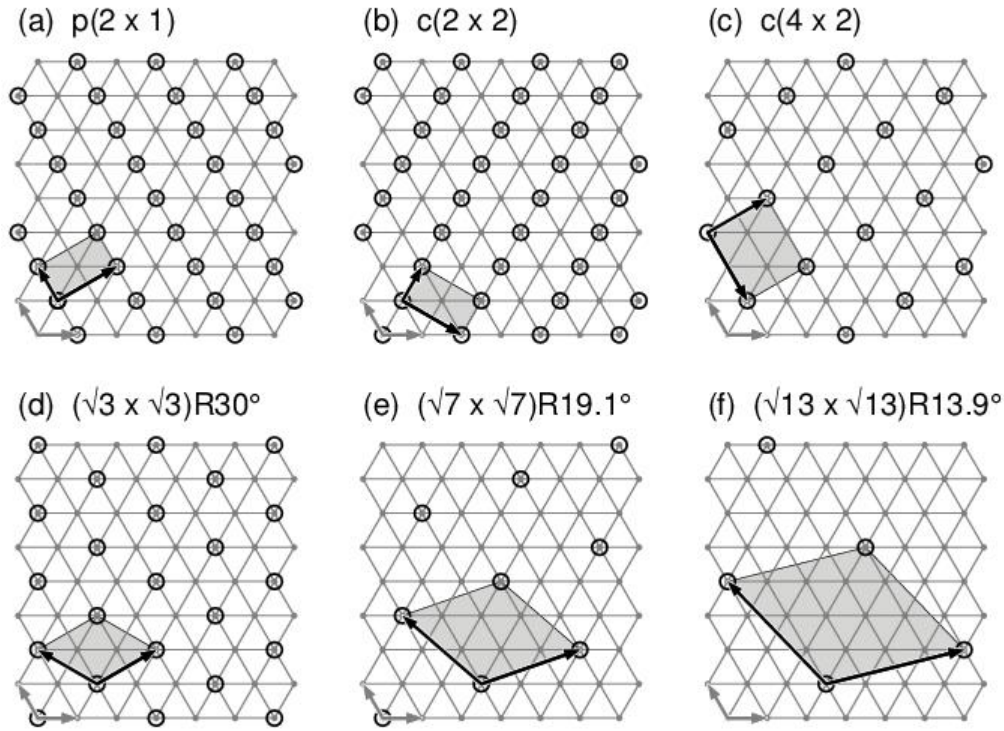


Fig. 6.23. Overlayer unit cells on a substrate with hexagonal lattice, (a) to (f), see text. Overlayer and substrate lattice vectors are shown in black and gray, respectively. The overlayer unit cell is emphasized in gray.

Further mathematical details as well as special cases of Wood notations are given in Appendix C.

#### 6.4 High-Order Commensurate (HOC) Overlayers

As mentioned in Sec. 6.1 adsorbate overlayers can form a **high-order commensurate (HOC)** lattice structure which is formally defined by a transformation matrix  $\underline{\underline{M}}$ , connecting lattice vectors of the overlayer  $\underline{\underline{R}}_{o1}'$ ,  $\underline{\underline{R}}_{o2}'$  with those of the substrate surface,  $\underline{\underline{R}}_{o1}$  and  $\underline{\underline{R}}_{o2}$ , according to

$$\begin{pmatrix} \underline{\underline{R}}_{o1}' \\ \underline{\underline{R}}_{o2}' \end{pmatrix} = \begin{pmatrix} m_{11} & m_{12} \\ m_{21} & m_{22} \end{pmatrix} \cdot \begin{pmatrix} \underline{\underline{R}}_{o1} \\ \underline{\underline{R}}_{o2} \end{pmatrix} = \underline{\underline{M}} \cdot \begin{pmatrix} \underline{\underline{R}}_{o1} \\ \underline{\underline{R}}_{o2} \end{pmatrix} \quad (6.10)$$

where all elements  $m_{ij}$  are **rational** or integer-valued with at least one being rational. Thus, the transformation matrix can be written as

$$\underline{\underline{M}} = \begin{pmatrix} p_{11} & p_{12} \\ q_{11} & q_{12} \\ p_{21} & p_{22} \\ q_{21} & q_{22} \end{pmatrix} = \begin{pmatrix} n_1 & 0 \\ 0 & n_2 \end{pmatrix}^{-1} \cdot \begin{pmatrix} a_{11} & a_{12} \\ a_{21} & a_{22} \end{pmatrix} \stackrel{\text{def.}}{=} \underline{\underline{B}}^{-1} \underline{\underline{A}}, \quad p_{ij}, q_{ij}, n_i, a_{ij} \text{ integer} \quad (6.11)$$

with

$$n_i = \frac{q_{i1} q_{i2}}{\gcd(q_{i1}, q_{i2})}, \quad a_{ij} = n_i \frac{p_{ij}}{q_{ij}}, \quad b_{ij} = n_i \delta_{ij}, \quad i, j = 1, 2 \quad (6.12)$$

(Function  $\gcd(x, y)$  denotes the greatest common divisor, see Appendix E.1.) This means that matrix  $\underline{\mathbf{M}}$  can always be represented by a product of an inverted matrix  $\underline{\mathbf{B}}$  and a matrix  $\underline{\mathbf{A}}$  where both matrices are integer-valued. As a consequence, relation (6.10) with (6.11) can be rewritten as

$$\begin{pmatrix} \underline{\mathbf{R}}_1' \\ \underline{\mathbf{R}}_2' \end{pmatrix} \stackrel{\text{def.}}{=} \begin{pmatrix} n_1 \underline{\mathbf{R}}_{o1}' \\ n_2 \underline{\mathbf{R}}_{o2}' \end{pmatrix} = \underline{\mathbf{B}} \begin{pmatrix} \underline{\mathbf{R}}_{o1}' \\ \underline{\mathbf{R}}_{o2}' \end{pmatrix} = \underline{\mathbf{A}} \begin{pmatrix} \underline{\mathbf{R}}_{o1}' \\ \underline{\mathbf{R}}_{o2}' \end{pmatrix} \quad (6.13)$$

Therefore, in a HOC lattice structure one can always find a superlattice with superlattice vectors  $\underline{\mathbf{R}}_1'$  and  $\underline{\mathbf{R}}_2'$  of the overlayer which are commensurate with those of the substrate  $\underline{\mathbf{R}}_{o1}$  and  $\underline{\mathbf{R}}_{o2}$ . The corresponding supercell describing the periodicity shared by the two vector sets,  $\underline{\mathbf{R}}_1', \underline{\mathbf{R}}_2'$  and  $\underline{\mathbf{R}}_{o1}', \underline{\mathbf{R}}_{o2}'$ , has an area

$$F_s = |\underline{\mathbf{R}}_1' \times \underline{\mathbf{R}}_2'| = |\det(\underline{\mathbf{B}})| |\underline{\mathbf{R}}_{o1}' \times \underline{\mathbf{R}}_{o2}'| = |\det(\underline{\mathbf{A}})| |\underline{\mathbf{R}}_{o1} \times \underline{\mathbf{R}}_{o2}| \quad (6.14)$$

with

$$|\det(\underline{\mathbf{B}})| = |n_1 n_2| \quad (6.15)$$

The supercell spanned by  $\underline{\mathbf{R}}_1', \underline{\mathbf{R}}_2'$  may not be the smallest possible cell, the **primitive** supercell of the HOC lattice structure. This is clear by a simple numerical example. Let us assume a transformation matrix  $\underline{\mathbf{M}}$  and its representation by (6.11), (6.12) where

$$\underline{\mathbf{M}} = \frac{1}{13} \begin{pmatrix} 14 & -5 \\ 5 & 14 \end{pmatrix} = \underline{\mathbf{B}}^{-1} \underline{\mathbf{A}} = \begin{pmatrix} 13 & 0 \\ 0 & 13 \end{pmatrix}^{-1} \cdot \begin{pmatrix} 14 & -5 \\ 5 & 14 \end{pmatrix} \quad (6.16)$$

which according to (6.14) leads to a supercell size  $F_s = 169 |\underline{\mathbf{R}}_{o1}' \times \underline{\mathbf{R}}_{o2}'|$ . However, an alternative representation of matrix  $\underline{\mathbf{M}}$  as

$$\underline{\mathbf{M}} = \frac{1}{13} \begin{pmatrix} 14 & -5 \\ 5 & 14 \end{pmatrix} = \underline{\mathbf{B}}'^{-1} \underline{\mathbf{A}}' = \begin{pmatrix} 3 & 2 \\ -2 & 3 \end{pmatrix}^{-1} \cdot \begin{pmatrix} 4 & 1 \\ -1 & 4 \end{pmatrix} \quad (6.17)$$

leads to a supercell size  $F_s = 13 |\underline{\mathbf{R}}_{o1}' \times \underline{\mathbf{R}}_{o2}'|$  which is smaller by a factor 13 and represents the primitive supercell. This is illustrated for a rectangular substrate lattice and  $\underline{\mathbf{M}}$  according to (6.16) in Fig. 6.24 where the supercell corresponding to the initial matrix  $\underline{\mathbf{A}}$  in (6.16) and the primitive supercell corresponding to matrix  $\underline{\mathbf{A}}'$  in (6.17) are sketched.

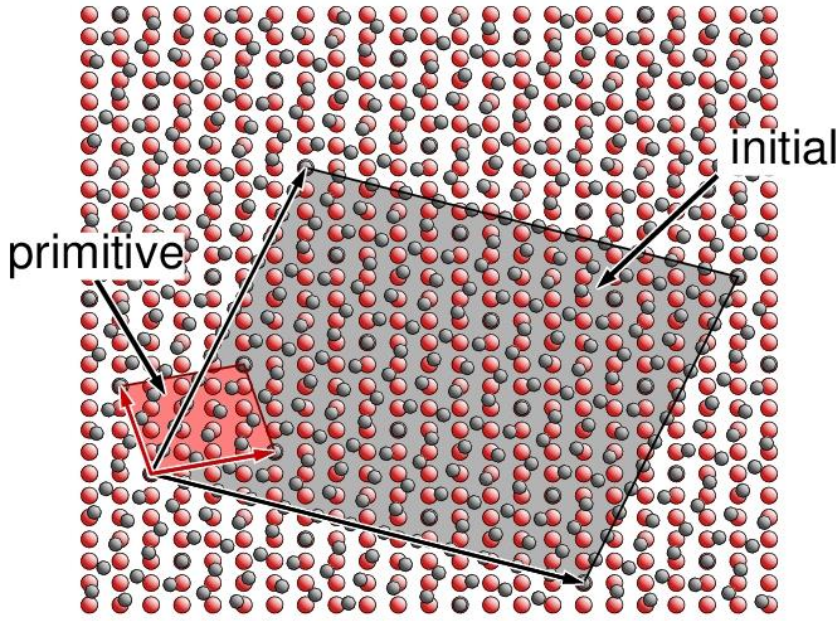


Fig. 6.24. Fictitious rectangular substrate with HOC overlayer structure according to (6.16). The initial and primitive supercells with superlattice vectors are outlined in gray and red, respectively.

The reduction of superlattice vector sets  $\mathbf{R}_1', \mathbf{R}_2'$ , determined initially by (6.11), (6.12), (6.13), to yield a primitive set  $\mathbf{R}_1'', \mathbf{R}_2''$  (providing the smallest supercell) can be achieved by number theoretical methods as described in detail in Appendix E.5. The basic idea is that if  $\mathbf{R}_1', \mathbf{R}_2'$  can be reduced then there must be an alternative set of reduced (primitive) superlattice vectors  $\mathbf{R}_1'', \mathbf{R}_2''$  which represent the initial superlattice vectors with

$$\begin{pmatrix} \mathbf{R}_1' \\ \mathbf{R}_2' \end{pmatrix} = \underline{\underline{\mathbf{T}}} \begin{pmatrix} \mathbf{R}_1'' \\ \mathbf{R}_2'' \end{pmatrix}, \quad \underline{\underline{\mathbf{T}}} \text{ integer} \quad (6.18)$$

As a result, the reduced vectors  $\mathbf{R}_1'', \mathbf{R}_2''$  yield according to (6.13)

$$\begin{pmatrix} \mathbf{R}_1'' \\ \mathbf{R}_2'' \end{pmatrix} = \underline{\underline{\mathbf{T}}}^{-1} \begin{pmatrix} \mathbf{R}_1' \\ \mathbf{R}_2' \end{pmatrix} = \underline{\underline{\mathbf{T}}}^{-1} \underline{\underline{\mathbf{B}}} \begin{pmatrix} \mathbf{R}_{o1}' \\ \mathbf{R}_{o2}' \end{pmatrix} = \underline{\underline{\mathbf{T}}}^{-1} \underline{\underline{\mathbf{A}}} \begin{pmatrix} \mathbf{R}_{o1} \\ \mathbf{R}_{o2} \end{pmatrix} \quad (6.19)$$

In addition, the vectors  $\mathbf{R}_1'', \mathbf{R}_2''$  also represent general lattice vectors of both the overlayer and the substrate surface. This means that the transformation matrices  $\underline{\underline{\mathbf{A}}}', \underline{\underline{\mathbf{B}}}'$  with

$$\underline{\underline{\mathbf{A}}}' = \underline{\underline{\mathbf{T}}}^{-1} \underline{\underline{\mathbf{A}}}, \quad \underline{\underline{\mathbf{B}}}' = \underline{\underline{\mathbf{T}}}^{-1} \underline{\underline{\mathbf{B}}} \quad (6.20)$$

must be integer-valued and leave the transformation matrix  $\underline{\underline{\mathbf{M}}}$  unchanged, i.e.

$$\underline{\underline{\mathbf{M}}} = \underline{\underline{\mathbf{B}}}^{-1} \underline{\underline{\mathbf{A}}} = \underline{\underline{\mathbf{B}}}'^{-1} \underline{\underline{\mathbf{A}}}' \quad (6.21)$$

As a result, the size of the reduced supercell of the overlayer is determined by

$$\begin{aligned} F_s^{\text{red}} &= |\underline{\mathbf{R}}_1'' \times \underline{\mathbf{R}}_2''| = |\det(\underline{\mathbf{A}}')| |\underline{\mathbf{R}}_{o1} \times \underline{\mathbf{R}}_{o2}| = \frac{|\det(\underline{\mathbf{A}})|}{|\det(\underline{\mathbf{T}})|} |\underline{\mathbf{R}}_{o1} \times \underline{\mathbf{R}}_{o2}| = \\ &= |\det(\underline{\mathbf{B}}')| |\underline{\mathbf{R}}_{o1}' \times \underline{\mathbf{R}}_{o2}'| = \frac{|\det(\underline{\mathbf{B}})|}{|\det(\underline{\mathbf{T}})|} |\underline{\mathbf{R}}_{o1}' \times \underline{\mathbf{R}}_{o2}'| = \frac{F_s}{|\det(\underline{\mathbf{T}})|} \end{aligned} \quad (6.22)$$

such that  $|\det(\underline{\mathbf{T}})|$  can be understood as a reduction factor of the cell sizes corresponding to the two representations. Since the determinants of  $\underline{\mathbf{A}}$ ,  $\underline{\mathbf{A}}'$ ,  $\underline{\mathbf{B}}$ ,  $\underline{\mathbf{B}}'$ , and  $\underline{\mathbf{T}}$  are all integer-valued, relation (6.22) shows further that the integer  $\det(\underline{\mathbf{T}})$  must be a common divisor of both integers  $\det(\underline{\mathbf{A}})$  and  $\det(\underline{\mathbf{B}})$  with an upper limit given by

$$1 \leq |\det(\underline{\mathbf{T}})| \leq g \stackrel{\text{def.}}{=} \text{gcd}(|\det(\underline{\mathbf{A}})|, |\det(\underline{\mathbf{B}})|) \quad (6.23)$$

Thus, relations (6.22), (6.23) show that for  $g = 1$ , and hence  $|\det(\underline{\mathbf{T}})| = 1$ , the initial supercell vectors  $\underline{\mathbf{R}}_1'$ ,  $\underline{\mathbf{R}}_2'$  cannot be reduced further and  $\underline{\mathbf{R}}_1'$ ,  $\underline{\mathbf{R}}_2'$  yields already the primitive cell size. On the other hand, a value of  $g > 1$  indicates that reduction is possible with a largest reduction factor given by  $|\det(\underline{\mathbf{T}})| = g$ . This can be used to quantify the cell size reduction in going from the initial HOC lattice representation (6.13) to the primitive representation (6.19). Further, the reduced transformation matrices  $\underline{\mathbf{A}}'$ ,  $\underline{\mathbf{B}}'$  for  $|\det(\underline{\mathbf{T}})| = g$  can be evaluated by a number theoretical algorithm given in Appendix E.5. In the numerical example (6.16) the corresponding values are  $g = \text{gcd}(221, 169) = 13$ , yielding a supercell size which is 13 times larger than that given by the matrices of (6.17), which confirms the above result.

Recent experimental studies on the adsorption of  $C_{60}$  fullerene molecules ('buckyballs') at the hexagonal  $\text{Pb}(1\ 1\ 1)$  surface have shown an ordered  $C_{60}$  overlayer with HOC lattice structure described as  $\text{Pb}(1\ 1\ 1) + (\sqrt{403}/7 \times \sqrt{403}/7)\text{R}22.85^\circ - C_{60}$  [151], see Fig. 6.25. This corresponds to a transformation matrix  $\underline{\mathbf{M}}$  with

$$\underline{\mathbf{M}} = \frac{1}{7} \begin{pmatrix} 14 & 9 \\ -9 & 23 \end{pmatrix} = \underline{\mathbf{B}}^{-1} \underline{\mathbf{A}} = \begin{pmatrix} 7 & 0 \\ 0 & 7 \end{pmatrix}^{-1} \cdot \begin{pmatrix} 14 & 9 \\ -9 & 23 \end{pmatrix} \quad (6.24)$$

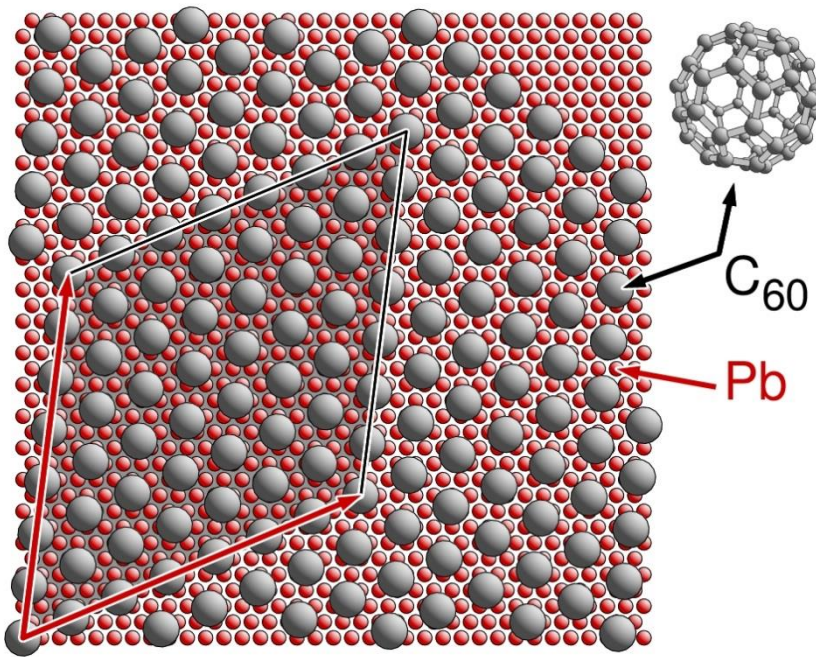


Fig. 6.25. Structure of the  $\text{Pb}(1\ 1\ 1) + (\sqrt{403}/7 \times \sqrt{403}/7)\text{R}22.85^\circ - \text{C}_{60}$  adsorbate system. The lattice vectors of the primitive superlattice are sketched in red and the supercell is outlined in black.

Here  $\text{gcd}(|\det(\underline{A})|, |\det(\underline{B})|) = \text{gcd}(403, 49) = 1$ . Thus, representation (6.24) cannot be reduced further and the superlattice vectors sketched in Fig. 6.25 reflect the primitive cell of the HOC lattice structure.

The  $\text{Pb}(1\ 1\ 1) - \text{C}_{60}$  adsorbate system is an example of a more general group of HOC lattice structures, **hexagonal** overlays on hexagonal substrate, which has also been discussed in the literature [152]. Using an acute representation for the substrate lattice vectors  $\underline{R}_{o1}$  and  $\underline{R}_{o2}$  with  $\underline{R}_{o1} = \underline{R}_{o2} = \underline{R}$ , any commensurate hexagonal overlayer with lattice vectors  $\underline{R}_{o1}'$ ,  $\underline{R}_{o2}'$  can be described by a transformation

$$\begin{pmatrix} \underline{R}_{o1}' \\ \underline{R}_{o2}' \end{pmatrix} = \begin{pmatrix} m & n \\ -n & m+n \end{pmatrix} \begin{pmatrix} \underline{R}_{o1} \\ \underline{R}_{o2} \end{pmatrix}, \quad m, n \text{ integer} \quad (6.25)$$

since the resulting vectors  $\underline{R}_{o1}'$ ,  $\underline{R}_{o2}'$  are of equal length

$$\underline{R}_{o1}' = \underline{R}_{o2}' = \left( \sqrt{m^2 + n^2 + mn} \right) \underline{R} \quad (6.26)$$

and form an angle of  $60^\circ$  as can be shown by simple vector calculus. As a consequence, HOC lattice structures involving hexagonal overlayer and substrate lattices can be defined by transformations

$$\begin{pmatrix} m' & n' \\ -n' & m'+n' \end{pmatrix} \begin{pmatrix} \underline{R}_{o1}' \\ \underline{R}_{o2}' \end{pmatrix} = \begin{pmatrix} m & n \\ -n & m+n \end{pmatrix} \begin{pmatrix} \underline{R}_{o1} \\ \underline{R}_{o2} \end{pmatrix}, \quad m, n, m', n' \text{ integer} \quad (6.27)$$

or

$$\begin{pmatrix} \underline{R}_{o1}' \\ \underline{R}_{o2}' \end{pmatrix} = \begin{pmatrix} m' & n' \\ -n' & m'+n' \end{pmatrix}^{-1} \begin{pmatrix} m & n \\ -n & m+n \end{pmatrix} \begin{pmatrix} \underline{R}_{o1} \\ \underline{R}_{o2} \end{pmatrix} = \begin{pmatrix} a & b \\ -b & a+b \end{pmatrix} \begin{pmatrix} \underline{R}_{o1} \\ \underline{R}_{o2} \end{pmatrix} \quad (6.28)$$

with

$$a = (m(m'+n') + n n') / \Delta, \quad b = (n m' - m n') / \Delta, \quad \Delta = m^2 + n^2 + m' n' \quad (6.29)$$

Here the corresponding vector lengths are

$$\underline{R}_{o1}' = \underline{R}_{o2}' = \left( \sqrt{a^2 + b^2 + a b} \right) \underline{R} = \sqrt{\frac{m^2 + n^2 + m n}{m'^2 + n'^2 + m' n'}} \underline{R} \quad (6.30)$$

Relations (6.28), (6.29) allow determining a joint superlattice with vectors  $\underline{R}_1'$ ,  $\underline{R}_2'$  where

$$\begin{pmatrix} \underline{R}_1' \\ \underline{R}_2' \end{pmatrix} = \begin{pmatrix} m' & n' \\ -n' & m'+n' \end{pmatrix} \begin{pmatrix} \underline{R}_{o1}' \\ \underline{R}_{o2}' \end{pmatrix} = \begin{pmatrix} m & n \\ -n & m+n \end{pmatrix} \begin{pmatrix} \underline{R}_{o1} \\ \underline{R}_{o2} \end{pmatrix} \quad (6.31)$$

and

$$\underline{R}_1' = \underline{R}_2' = \left( \sqrt{m^2 + n^2 + m n} \right) \underline{R} \quad (6.32)$$

According to the discussion above, the superlattice cell spanned by vectors  $\underline{R}_1'$ ,  $\underline{R}_2'$  cannot be reduced further in size if the integer-valued determinants in (6.31) are coprime, i.e. if

$$\text{gcd}(m^2 + n^2 + m n, m'^2 + n'^2 + m' n') = 1 \quad (6.33)$$

For the Pb(1 1 1) - C<sub>60</sub> adsorbate system the present general formalism yields

$$m = 14, \quad n = 9, \quad m' = 7, \quad n' = 0 \quad \text{and hence} \quad \text{gcd}(403, 49) = 1 \quad (6.34)$$

which verifies the result obtained above.

HOC lattice structures formed by overlayers on substrate where both lattices are **square** can be treated analogous to the hexagonal case. Here commensurate overlayers with square lattice vectors  $\underline{R}_{o1}'$ ,  $\underline{R}_{o2}'$  of the overlayer and  $\underline{R}_{o1}$ ,  $\underline{R}_{o2}$  of the substrate ( $\underline{R}_{o1} = \underline{R}_{o2} = \underline{R}$ ) can be described by a transformation



$$\begin{pmatrix} \underline{\mathbf{R}}_{o1}' \\ \underline{\mathbf{R}}_{o2}' \end{pmatrix} = \begin{pmatrix} m & n \\ -n & m \end{pmatrix} \begin{pmatrix} \underline{\mathbf{R}}_{o1} \\ \underline{\mathbf{R}}_{o2} \end{pmatrix}, \quad m, n \text{ integer} \quad (6.35)$$

since the resulting vectors  $\underline{\mathbf{R}}_{o1}'$ ,  $\underline{\mathbf{R}}_{o2}'$  are of equal length

$$\mathbf{R}_{o1}' = \mathbf{R}_{o2}' = \left( \sqrt{m^2 + n^2} \right) \mathbf{R} \quad (6.36)$$

and form an angle of  $90^\circ$  as can be shown by simple vector calculus. Thus, HOC lattice structures involving square overlayer and substrate lattices can be defined by transformations

$$\begin{pmatrix} m' & n' \\ -n' & m' \end{pmatrix} \begin{pmatrix} \underline{\mathbf{R}}_{o1}' \\ \underline{\mathbf{R}}_{o2}' \end{pmatrix} = \begin{pmatrix} m & n \\ -n & m \end{pmatrix} \begin{pmatrix} \underline{\mathbf{R}}_{o1} \\ \underline{\mathbf{R}}_{o2} \end{pmatrix}, \quad m, n, m', n' \text{ integer} \quad (6.37)$$

or

$$\begin{pmatrix} \underline{\mathbf{R}}_{o1}' \\ \underline{\mathbf{R}}_{o2}' \end{pmatrix} = \begin{pmatrix} m' & n' \\ -n' & m' \end{pmatrix}^{-1} \begin{pmatrix} m & n \\ -n & m \end{pmatrix} \begin{pmatrix} \underline{\mathbf{R}}_{o1} \\ \underline{\mathbf{R}}_{o2} \end{pmatrix} = \begin{pmatrix} a & b \\ -b & a \end{pmatrix} \begin{pmatrix} \underline{\mathbf{R}}_{o1} \\ \underline{\mathbf{R}}_{o2} \end{pmatrix} \quad (6.38)$$

with

$$a = (mm' + nn')/\Delta, \quad b = (nm' - mn')/\Delta, \quad \Delta = m^2 + n^2 \quad (6.39)$$

where the corresponding vector lengths are

$$\mathbf{R}_{o1}' = \mathbf{R}_{o2}' = \left( \sqrt{a^2 + b^2} \right) \mathbf{R} = \sqrt{\frac{m^2 + n^2}{m'^2 + n'^2}} \mathbf{R} \quad (6.40)$$

As before, relations (6.38), (6.39) allow to determine a joint superlattice with vectors  $\underline{\mathbf{R}}_1'$ ,  $\underline{\mathbf{R}}_2'$  where

$$\begin{pmatrix} \underline{\mathbf{R}}_1' \\ \underline{\mathbf{R}}_2' \end{pmatrix} = \begin{pmatrix} m' & n' \\ -n' & m' \end{pmatrix} \begin{pmatrix} \underline{\mathbf{R}}_{o1}' \\ \underline{\mathbf{R}}_{o2}' \end{pmatrix} = \begin{pmatrix} m & n \\ -n & m \end{pmatrix} \begin{pmatrix} \underline{\mathbf{R}}_{o1} \\ \underline{\mathbf{R}}_{o2} \end{pmatrix} \quad (6.41)$$

and

$$\mathbf{R}_1' = \mathbf{R}_2' = \left( \sqrt{m^2 + n^2} \right) \mathbf{R} \quad (6.42)$$

The superlattice cell spanned by vectors  $\underline{\mathbf{R}}_1'$ ,  $\underline{\mathbf{R}}_2'$  cannot be reduced further in size if the integer-valued determinants in (6.41) are coprime, i.e. if

$$\gcd(m^2 + n^2, m'^2 + n'^2) = 1 \quad (6.43)$$

## 6.5 Interference Lattices

Interference lattices and quasi-periodic long-range order at adsorbate covered surfaces expressed by one- and two-dimensional **moiré patterns** have been known for some time but have attracted considerable attention more recently in connection with graphene, a graphite monolayer with honeycomb structure, adsorbing at metal surfaces. (In the following, graphene will be named ‘**Gra**’ in all structure formulas using the Wood notation.) As an example, experimental LEED and STM studies [127] suggest that graphene adsorbing on the hexagonal (0 0 0 1) surface of ruthenium forms a commensurate phase with a coincidence lattice described by a supercell of  $25 \times 25$  carbon honeycombs on a  $23 \times 23$  supercell of the hexagonal Ru(0 0 0 1) substrate. This was simulated by DFT calculations with different (smaller than observed) coincidence lattices [127] where Fig. 6.5 shows results for the Ru(0 0 0 1) + (12/13  $\times$  12/13) - Gra structure. Here the lateral long-range order is evident in the view perpendicular to the substrate surface, see Fig. 6.5a. In addition, the lateral structure is combined with perpendicular warping of the graphene layer shown in Fig. 6.5b, which is characterized by local distortion away from the substrate when carbon gets near the ruthenium surface.

Boron nitride (h-BN) monolayers adsorbed on the (1 1 1) surface of rhodium have also been found to form coincidence lattices. These are described by  $13 \times 13$  supercells of hexagonal  $B_3N_3$  rings on top of  $12 \times 12$  supercells of the Rh(1 1 1) substrate surface [153]. Analogous to the previous example, the coincidence lattice structure includes warping of the boron nitride overlayer. Interestingly, the warping of this overlayer leads to local indentation towards the substrate when adsorbate atoms get near the rhodium surface which is opposite to the previous example. However, in this section structural details of overlayer warping will be ignored and focus will be put on the lateral structure.

Another example is an observed rotational superlattice formed by a silver monolayer on the Ni(1 1 1) substrate surface described as Ni(1 1 1) + (1.167  $\times$  1.167)R2.4° - Ag [154] in Wood notation. This structure can be represented approximately by a HOC lattice structure with a transformation matrix

$$\underline{\underline{\mathbf{M}}} = \frac{1}{39} \begin{pmatrix} 46 & -2 \\ 2 & 44 \end{pmatrix} = \begin{pmatrix} 5 & 2 \\ -2 & 7 \end{pmatrix}^{-1} \cdot \begin{pmatrix} 6 & 2 \\ -2 & 8 \end{pmatrix} \quad (6.44)$$

reflecting Ni(1 1 1) + (1.155  $\times$  1.155)R2.2° - Ag which is shown in Fig. 6.26 (only the overlayer

and the topmost substrate layer are included). The figure illustrates nicely that the combination of

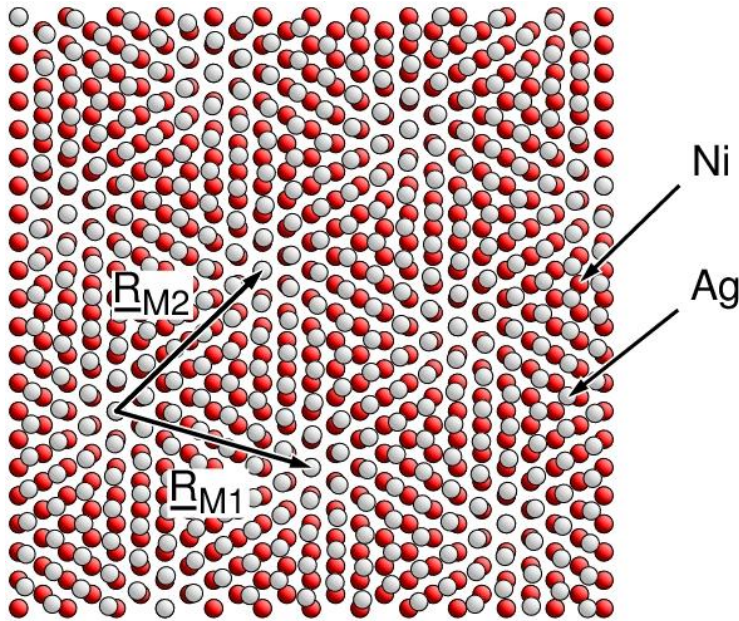


Fig. 6.26. Structure of the Ni(1 1 1) + (1.155 × 1.155)R2.2° - Ag adsorbate system. The lattice vectors  $\underline{R}_{M1}$ ,  $\underline{R}_{M2}$  of the moiré pattern are labeled accordingly.

the Ag adsorbate and the Ni substrate lattices yields a structure with a clear lateral interference pattern (moiré pattern) of local areas (**moirons**) which form a hexagonal lattice with lattice vectors  $\underline{R}_{M1}$  and  $\underline{R}_{M2}$ . The general formalism to describe these two-dimensional interference lattices quantitatively will be discussed in the following.

### 6.5.1 Basic formalism

The basis of the formalism [155], [156] is a lateral surface structure combining a two-dimensional periodic substrate layer described by lattice vectors  $\underline{R}_{o1}$  and  $\underline{R}_{o2}$ , with an overlayer whose periodicity is given by lattice vectors  $\underline{R}_{o1}'$ ,  $\underline{R}_{o2}'$  with

$$\begin{pmatrix} \underline{R}_{o1}' \\ \underline{R}_{o2}' \end{pmatrix} = \underline{M} \cdot \begin{pmatrix} \underline{R}_{o1} \\ \underline{R}_{o2} \end{pmatrix} \quad (6.45)$$

where the  $2 \times 2$  matrix  $\underline{M}$  quantifies the linear transformation as discussed in Sec. 6.1. For real-valued  $\underline{M}$  we define an integer approximant matrix  $\underline{M}_I$  whose elements  $a_{ij}$  are the integers nearest to  $m_{ij}$ , see Appendix E.5. Therefore,  $\underline{M}_I$  characterizes the commensurate structure closest to that given by matrix  $\underline{M}$ .

As discussed in Appendix G, any functions  $f^S(\underline{r})$ ,  $f^O(\underline{r})$ , describing lateral spatial properties of the **substrate** surface and of the **overlayer** by themselves can be represented by corresponding infinite Fourier series as

$$f^S(\underline{r}) = \sum_{j,k} c_{j,k}^S \exp[i(j\underline{G}_{o1} + k\underline{G}_{o2})\underline{r}] = \sum_{j,k} c_{j,k}^S \exp\left[i(j \ k) \begin{pmatrix} \underline{G}_{o1} \\ \underline{G}_{o2} \end{pmatrix} \underline{r}\right] \quad (6.46a)$$

$$f^O(\underline{r}) = \sum_{j',k'} c_{j',k'}^O \exp\left[i(j' \ k') \begin{pmatrix} \underline{G}_{o1}' \\ \underline{G}_{o2}' \end{pmatrix} \underline{r}\right], \quad j, k, j', k' \text{ integer} \quad (6.46b)$$

with, in general, complex valued coefficients  $c_{j,k}^S$  and  $c_{j',k'}^O$ , respectively, (which, at the real three-dimensional surface, may depend on a third coordinate perpendicular to the surface) and reciprocal lattice vectors  $\underline{G}_{o1}$ ,  $\underline{G}_{o2}$  and  $\underline{G}_{o1}'$ ,  $\underline{G}_{o2}'$  derived from orthogonality relations (2.96), i.e.

$$\underline{G}_{oi} \underline{R}_{oj} = \underline{G}_{oi}' \underline{R}_{oj}' = 2\pi \delta_{ij}, \quad j, k = 1, 2 \quad (6.47)$$

as discussed in Sec. 2.5. Note that in (6.46) we use a matrix notation for scalar products with vectors

$$p \underline{v}_1 + q \underline{v}_2 \stackrel{\text{def.}}{=} (p \ q) \begin{pmatrix} \underline{v}_1 \\ \underline{v}_2 \end{pmatrix} \quad (6.48)$$

which proves to be useful for the following.

The real space transformation (6.45) together with orthogonality relations (6.47) leads to a transformation of the reciprocal space lattice vectors of the substrate and the overlayer given by

$$\begin{pmatrix} \underline{G}_{o1}' \\ \underline{G}_{o2}' \end{pmatrix} = \underline{\underline{m}} \begin{pmatrix} \underline{G}_{o1} \\ \underline{G}_{o2} \end{pmatrix} \quad \text{with} \quad \underline{\underline{m}} = (\underline{\underline{M}}^{-1})^+ = (\underline{\underline{M}}^+)^{-1} = \underline{\underline{M}}^{-1+} \quad (6.49)$$

where  $\underline{\underline{M}}^+$  denotes the transposed and  $\underline{\underline{M}}^{-1}$  the inverted matrix  $\underline{\underline{M}}$  with  $\underline{\underline{M}}^{-1+}$  being the combination.

According to (6.46) the **superposition** of the property functions  $f^S(\underline{r})$  of the substrate and  $f^O(\underline{r})$  of the overlayer describing spatial properties of the combined system can be written as

$$\begin{aligned}
f(\mathbf{r}) &= f^S(\mathbf{r}) + f^O(\mathbf{r}) = \\
&= \sum_{j,k} c_{j,k}^S \exp \left[ i (\mathbf{j} \ \mathbf{k}) \begin{pmatrix} \underline{\mathbf{G}}_{o1} \\ \underline{\mathbf{G}}_{o2} \end{pmatrix} \mathbf{r} \right] + \sum_{j',k'} c_{j',k'}^O \exp \left[ i (\mathbf{j}' \ \mathbf{k}') \begin{pmatrix} \underline{\mathbf{G}}_{o1}' \\ \underline{\mathbf{G}}_{o2}' \end{pmatrix} \mathbf{r} \right] \\
&\qquad\qquad\qquad j, k, j', k' \text{ integer} \qquad\qquad\qquad (6.50)
\end{aligned}$$

This superposition is **non-periodic** for real-valued transformation matrices  $\underline{\mathbf{M}}$ . In contrast, for **commensurate** lateral surface structures the matrix  $\underline{\mathbf{M}}$  is integer-valued, thus, agreeing with its **integer approximant**  $\underline{\mathbf{M}}_I$ . Then in reciprocal space

$$\begin{pmatrix} \underline{\mathbf{G}}_{o1}' \\ \underline{\mathbf{G}}_{o2}' \end{pmatrix} = \underline{\mathbf{m}} \begin{pmatrix} \underline{\mathbf{G}}_{o1} \\ \underline{\mathbf{G}}_{o2} \end{pmatrix} = \underline{\mathbf{m}}_I \begin{pmatrix} \underline{\mathbf{G}}_{o1} \\ \underline{\mathbf{G}}_{o2} \end{pmatrix} \quad \text{with} \quad \underline{\mathbf{m}}_I = (\underline{\mathbf{M}}_I)^{-1+} \quad (6.51)$$

and we can write

$$(\mathbf{j} \ \mathbf{k}) \begin{pmatrix} \underline{\mathbf{G}}_{o1} \\ \underline{\mathbf{G}}_{o2} \end{pmatrix} = (\mathbf{j} \ \mathbf{k}) \underline{\mathbf{m}}_I^{-1} \underline{\mathbf{m}}_I \begin{pmatrix} \underline{\mathbf{G}}_{o1} \\ \underline{\mathbf{G}}_{o2} \end{pmatrix} \stackrel{\text{def.}}{=} (\mathbf{j}' \ \mathbf{k}') \begin{pmatrix} \underline{\mathbf{G}}_{o1}' \\ \underline{\mathbf{G}}_{o2}' \end{pmatrix} \quad (6.52)$$

where

$$\begin{pmatrix} \mathbf{j}' \\ \mathbf{k}' \end{pmatrix} = (\underline{\mathbf{m}}_I^{-1})^+ \begin{pmatrix} \mathbf{j} \\ \mathbf{k} \end{pmatrix} = \underline{\mathbf{M}}_I \begin{pmatrix} \mathbf{j} \\ \mathbf{k} \end{pmatrix} \quad (6.53)$$

Thus, each substrate component in (6.46a) can be written as

$$f_{j,k}^S(\mathbf{r}) = c_{j,k}^S \exp \left[ i (\mathbf{j} \ \mathbf{k}) \begin{pmatrix} \underline{\mathbf{G}}_{o1} \\ \underline{\mathbf{G}}_{o2} \end{pmatrix} \mathbf{r} \right] = \frac{c_{j,k}^S}{c_{j',k'}^O} f_{j',k'}^O(\mathbf{r}) \quad (6.54)$$

where  $f_{j',k'}^O(\mathbf{r})$  is an overlayer component in (6.46b) referring to indices  $j', k'$  which can be different from  $j, k$ . Thus, for commensurate structures each substrate component (6.54) can be combined with a corresponding overlayer component and Fourier expansion (6.50) becomes altogether periodic with the overlayer lattice vectors  $\underline{\mathbf{R}}_{o1}', \underline{\mathbf{R}}_{o2}'$  describing its periodicity.

The basic mathematical idea of an interference lattice in a combined substrate/overlayer system is that all or an infinite subset of components  $f_{j,k}^S(\mathbf{r})$  of the substrate expansion (6.50) interfere with corresponding components  $f_{j',k'}^O(\mathbf{r})$  of the overlayer which exhibit identical or very similar spatial variation.

If each component  $f_{j,k}^S(\underline{\mathbf{r}})$  interferes with a corresponding component  $f_{j',k'}^O(\underline{\mathbf{r}})$  (**basic** or **first order interference**) the superposition component can, together with (6.49), (6.53), be written as

$$\begin{aligned} f_{j,k}(\underline{\mathbf{r}}) &= f_{j,k}^S(\underline{\mathbf{r}}) + f_{j',k'}^O(\underline{\mathbf{r}}) = \\ &= c_{j,k}^S \exp \left[ i (\mathbf{j} \cdot \mathbf{k}) \begin{pmatrix} \underline{\mathbf{G}}_{o1} \\ \underline{\mathbf{G}}_{o2} \end{pmatrix} \underline{\mathbf{r}} \right] + c_{j',k'}^O \exp \left[ i (\mathbf{j} \cdot \mathbf{k}) \underline{\mathbf{m}}_I^{-1} \underline{\mathbf{m}} \begin{pmatrix} \underline{\mathbf{G}}_{o1} \\ \underline{\mathbf{G}}_{o2} \end{pmatrix} \underline{\mathbf{r}} \right] = \\ &= c_{j,k}^S \exp \left[ i (\mathbf{j} \cdot \mathbf{k}) \begin{pmatrix} \underline{\mathbf{G}}_{o1} \\ \underline{\mathbf{G}}_{o2} \end{pmatrix} \underline{\mathbf{r}} \right] \cdot \kappa_{j,k}(\underline{\mathbf{r}}) \end{aligned} \quad (6.55)$$

with a modulation factor  $\kappa_{j,k}(\underline{\mathbf{r}})$  given by

$$\kappa_{j,k}(\underline{\mathbf{r}}) = 1 + \frac{c_{j',k'}^O}{c_{j,k}^S} \exp \left[ i (\mathbf{j} \cdot \mathbf{k}) \begin{pmatrix} \underline{\mathbf{G}}_{M1} \\ \underline{\mathbf{G}}_{M2} \end{pmatrix} \underline{\mathbf{r}} \right] \quad (6.56)$$

and

$$\begin{pmatrix} \underline{\mathbf{G}}_{M1} \\ \underline{\mathbf{G}}_{M2} \end{pmatrix} = \left( \underline{\mathbf{m}}_I^{-1} \underline{\mathbf{m}} - \underline{\mathbf{1}} \right) \begin{pmatrix} \underline{\mathbf{G}}_{o1} \\ \underline{\mathbf{G}}_{o2} \end{pmatrix} \quad (6.57)$$

Thus, the superposition component  $f_{j,k}(\underline{\mathbf{r}})$  of (6.55) is a periodic function modulated by a factor  $\kappa_{j,k}(\underline{\mathbf{r}})$  which itself is a periodic function with lattice vectors  $\underline{\mathbf{G}}_{M1}$  and  $\underline{\mathbf{G}}_{M2}$  in reciprocal space. This corresponds to a lattice in real space with lattice vectors  $\underline{\mathbf{R}}_{M1}$  and  $\underline{\mathbf{R}}_{M2}$  (**moiré lattice vectors**) according to

$$\begin{pmatrix} \underline{\mathbf{R}}_{M1} \\ \underline{\mathbf{R}}_{M2} \end{pmatrix} = \left( \underline{\mathbf{m}}_I^{-1} \underline{\mathbf{m}} - \underline{\mathbf{1}} \right)^{-1+} \begin{pmatrix} \underline{\mathbf{R}}_{o1} \\ \underline{\mathbf{R}}_{o2} \end{pmatrix} = \left( \underline{\mathbf{M}}_I - \underline{\mathbf{M}} \right)^{-1} \underline{\mathbf{M}} \begin{pmatrix} \underline{\mathbf{R}}_{o1} \\ \underline{\mathbf{R}}_{o2} \end{pmatrix} = \underline{\mathbf{P}} \begin{pmatrix} \underline{\mathbf{R}}_{o1} \\ \underline{\mathbf{R}}_{o2} \end{pmatrix} \quad (6.58)$$

with a transformation matrix  $\underline{\mathbf{P}}$  (**moiré matrix**) given by

$$\underline{\mathbf{P}} = \left( \underline{\mathbf{M}}_I - \underline{\mathbf{M}} \right)^{-1} \underline{\mathbf{M}} = \left[ \underline{\mathbf{1}} - \underline{\mathbf{M}}_M \right]^{-1} \underline{\mathbf{M}}_M \quad \text{where} \quad \underline{\mathbf{M}}_M = \left( \underline{\mathbf{m}}_I^{-1} \underline{\mathbf{m}} \right) \quad (6.59)$$

If the structure of the combined substrate/overlayer system is approaching commensurability, which is expressed mathematically by the transformation matrix  $\underline{\mathbf{M}}$  in (6.45), (6.58) getting near its integer approximant  $\underline{\mathbf{M}}_I$ , then matrix  $\underline{\mathbf{P}}$  becomes rather large and the moiré lattice vectors  $\underline{\mathbf{R}}_{M1}$  and  $\underline{\mathbf{R}}_{M2}$  in (6.58) will be considerably larger than the lattice vectors  $\underline{\mathbf{R}}_{o1}$  and  $\underline{\mathbf{R}}_{o2}$  of the substrate. This geometry describes a long-range modulation whose periodicity is perceived as a periodic interference pattern

associated with moiré patterns as will be illustrated in the following.

Moiré patterns have been found for graphene overlayers on a number of hexagonal metal substrate surfaces where an isotropically scaled ( $\gamma \times \gamma$ ) overlayer structure has been discussed in the literature, for references see e.g. [155]. Here the transformation matrix  $\underline{\underline{M}}$  connecting lattice vectors  $\underline{R}_{o1}'$  and  $\underline{R}_{o2}'$  of the graphene layer with those,  $\underline{R}_{o1}$  and  $\underline{R}_{o2}$ , of the metal substrate according to (6.45) is given by

$$\underline{\underline{M}} = \begin{pmatrix} \gamma & 0 \\ 0 & \gamma \end{pmatrix} = \gamma \underline{\underline{1}}, \quad \gamma = \frac{a_{\text{Gra}}}{a_{\text{Me}}} \quad (6.60)$$

where  $\gamma$  is a scaling factor determined by the ratio of the lattice constants  $a_{\text{gra}}$  and  $a_{\text{Me}}$  of the graphene overlayer and of the metal substrate, respectively. Table 6.1 lists experimental  $\gamma$  values

Table 6.1. Scaling factors  $\gamma$  and moiré factors  $\lambda$  for scaled ( $\gamma \times \gamma$ ) overlayers of graphene on different metal substrates, see text. The references denote experimental studies where the moiré patterns have been identified.

Substrate	$\gamma$	$\lambda$
Pt(1 1 1) [157]	0.89	8.09
Ir(1 1 1) [158], [159]	0.91	10.11
Ru(0 0 0 1) [127]	0.92	11.50
Rh(1 1 1) [157], [160]	0.93	13.28
Cu(1 1 1) [161]	0.97	32.33
Ni(1 1 1) [162]	1.00	$\infty$

for different metal substrates where moiré patterns have been observed. This shows that for graphene  $\gamma$  values lie always near  $\gamma = 1$  such that the integer approximant of  $\underline{\underline{M}}$  equals the unit matrix  $\underline{\underline{M}}_I = \underline{\underline{1}}$ . This leads to a moiré matrix  $\underline{\underline{P}}$  according to (6.59)

$$\underline{\underline{P}} = \begin{pmatrix} \lambda & 0 \\ 0 & \lambda \end{pmatrix} = \lambda \underline{\underline{1}}, \quad \lambda = \frac{\gamma}{|1-\gamma|} \quad (6.61)$$

with  $\lambda$  denoting the **moiré factor**. As an example, Fig. 6.27 shows a simulation of a graphene overlayer on the Pt(1 1 1) surface where  $\gamma = 0.89$ . Here a hexagonal moiré lattice corresponding to a lat-

tice constant  $a_{\text{moiré}} = 8.09 a_{\text{Pt}}$  is obtained which confirms the moiré pattern observed by experiment [157].

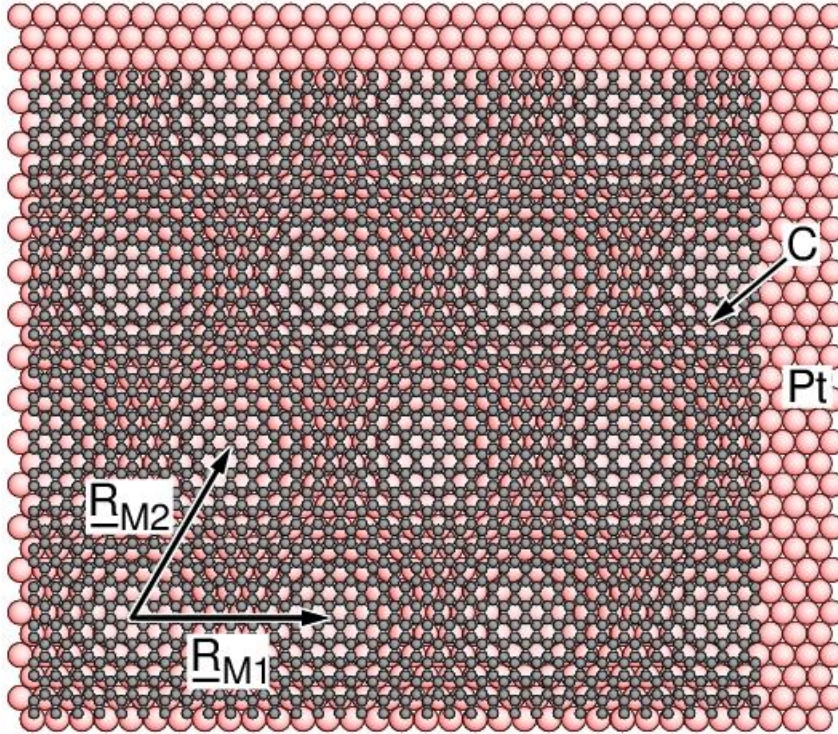


Fig. 6.27. Moiré pattern of a graphene overlayer on the Pt(1 1 1) surface for a view perpendicular to the surface with moiré lattice vectors  $\underline{R}_{M1}$ ,  $\underline{R}_{M2}$  included.

The moiré matrix  $\underline{P}$  of (6.61) shows in general that isotropic overlayer scaling always results in moiré lattice vectors  $\underline{R}_{M1}$  and  $\underline{R}_{M2}$  that point along the directions of the substrate lattice vectors  $\underline{R}_{o1}$  and  $\underline{R}_{o2}$ , respectively. Thus, the moiré lattice is of the same Bravais lattice type as that of the substrate. Further, (6.58) together with (6.61) shows that moiré lattice vectors diverge in their lengths when  $\gamma$  approaches  $\gamma = 1$  which corresponds to lattice constants of the overlayer and substrate lattices getting very close. In this limit the moiré arrangement will become very open with extremely large moirons (giant scaling) that may be too large to be observable. This is consistent with experimental findings for graphene overlayers on Ni(1 1 1) substrate [162] where the surface lattice constants differ by less than 1%.

**High-order interference** is obtained by an infinite subset of substrate components  $f_{j,k}^{S,d}(\underline{r})$ , given by



$$f_{j,k}^{S,d}(\underline{\mathbf{r}}) = c_{j'',k''}^S \exp \left[ i (j'' \ k'') \begin{pmatrix} \underline{\mathbf{G}}_{o1} \\ \underline{\mathbf{G}}_{o2} \end{pmatrix} \underline{\mathbf{r}} \right] \quad \text{with} \quad \begin{pmatrix} j'' \\ k'' \end{pmatrix} = \underline{\mathbf{d}} \begin{pmatrix} j \\ k \end{pmatrix} \quad (6.62)$$

in the Fourier expansion (6.46a), interfering with corresponding overlay components  $f_{j,k}^O(\underline{\mathbf{r}})$ . Here the integer-valued matrix  $\underline{\mathbf{d}}$  selects the infinite subset and can thus be considered an **interference order matrix** where  $\underline{\mathbf{d}} = \underline{\mathbf{1}}$  (or more generally  $\det(\underline{\mathbf{d}}) = 1$ ) refers to first order interference discussed above. Then analogous to (6.55) the superposition components can be written as

$$\begin{aligned} f_{j,k}^d(\underline{\mathbf{r}}) &= f_{j,k}^{S,d}(\underline{\mathbf{r}}) + f_{j,k}^O(\underline{\mathbf{r}}) = \\ &= c_{j'',k''}^S \exp \left[ i (j \ k) \underline{\mathbf{d}}^+ \begin{pmatrix} \underline{\mathbf{G}}_{o1} \\ \underline{\mathbf{G}}_{o2} \end{pmatrix} \underline{\mathbf{r}} \right] \cdot \kappa_{j,k}^d(\underline{\mathbf{r}}) \end{aligned} \quad (6.63)$$

with a modulation factor  $\kappa_{j,k}^d(\underline{\mathbf{r}})$  where

$$\kappa_{j,k}^d(\underline{\mathbf{r}}) = 1 + \frac{c_{j'',k''}^O}{c_{j'',k''}^S} \exp \left[ i (j \ k) \begin{pmatrix} \underline{\mathbf{G}}_{M1}^d \\ \underline{\mathbf{G}}_{M2}^d \end{pmatrix} \underline{\mathbf{r}} \right] \quad (6.64)$$

and

$$\begin{pmatrix} \underline{\mathbf{G}}_{M1}^d \\ \underline{\mathbf{G}}_{M2}^d \end{pmatrix} = \left( \underline{\mathbf{m}}_I^{-1} \underline{\mathbf{m}} - \underline{\mathbf{d}}^+ \right) \begin{pmatrix} \underline{\mathbf{G}}_{o1} \\ \underline{\mathbf{G}}_{o2} \end{pmatrix} \quad (6.65)$$

As before, the superposition component  $f_{j,k}^d(\underline{\mathbf{r}})$  of (6.62) is a periodic function modulated by a factor  $\kappa_{j,k}^d(\underline{\mathbf{r}})$  which itself is a periodic function with a lattice  $\underline{\mathbf{G}}_{M1}^d, \underline{\mathbf{G}}_{M2}^d$  in reciprocal space that corresponds to a lattice with lattice vectors  $\underline{\mathbf{R}}_{M1}^d, \underline{\mathbf{R}}_{M2}^d$  (**high-order moiré lattice vectors**) in real space according to

$$\begin{pmatrix} \underline{\mathbf{R}}_{M1}^d \\ \underline{\mathbf{R}}_{M2}^d \end{pmatrix} = \left( \underline{\mathbf{m}}_I^{-1} \underline{\mathbf{m}} - \underline{\mathbf{d}}^+ \right)^{-1+} \begin{pmatrix} \underline{\mathbf{R}}_{o1} \\ \underline{\mathbf{R}}_{o2} \end{pmatrix} = \left( \underline{\mathbf{M}}_I - \underline{\mathbf{M}}_d \right)^{-1} \underline{\mathbf{M}} \begin{pmatrix} \underline{\mathbf{R}}_{o1} \\ \underline{\mathbf{R}}_{o2} \end{pmatrix} = \underline{\mathbf{P}}^d \begin{pmatrix} \underline{\mathbf{R}}_{o1} \\ \underline{\mathbf{R}}_{o2} \end{pmatrix} \quad (6.66)$$

with a transformation matrix  $\underline{\mathbf{P}}$  (**high-order moiré matrix**) given by

$$\underline{\mathbf{P}}^d = \left( \underline{\mathbf{M}}_I - \underline{\mathbf{M}}_d \right)^{-1} \underline{\mathbf{M}} = \left[ \underline{\mathbf{1}} - \underline{\mathbf{M}}_M \underline{\mathbf{d}} \right]^{-1} \underline{\mathbf{M}}_M \quad \text{where} \quad \underline{\mathbf{M}}_M = \left( \underline{\mathbf{M}}_I^{-1} \underline{\mathbf{M}} \right) \quad (6.67)$$

If the structure of the combined substrate/overlay system is approaching high-order commensurability, expressed formally by the transformation matrix  $(\underline{\mathbf{M}} \ \underline{\mathbf{d}})$  in (6.66) getting near its integer ap-

proximant  $\underline{\underline{M}}_I$ , then matrix  $\underline{\underline{P}}^d$  is diverging and the moiré lattice vectors  $\underline{\underline{R}}_{M1}^d$  and  $\underline{\underline{R}}_{M2}^d$  in (6.66) will be considerably larger than the lattice vectors  $\underline{\underline{R}}_{o1}$  and  $\underline{\underline{R}}_{o2}$  of the substrate. The resulting long-range modulation can explain periodic high-order moiré patterns. Since these patterns refer to interference of only a subset of Fourier components representing the substrate periodicity their visual perception may not be as pronounced as that of first order moiré patterns. Further, high-order interference in two dimensions will in general depend on a  $2 \times 2$  order matrix  $\underline{\underline{d}}$  rather than on a scalar quantity unless the matrix is restricted to an integer multiple  $d$  of the unit matrix as assumed elsewhere [163].

As an example, high-order moiré patterns have been found in experiment for graphene overlayers on the Ir(1 1 1) surface [158], [159] where the overlayer is rotated by almost  $30^\circ$  with respect to the hexagonal substrate surface. This system, characterized in Wood notation as Ir(1 1 1) + (0.9  $\times$  0.9)R29.5° - Gra, can be approximated by a HOC lattice structure with a transformation matrix (using the acute representation of the hexagonal lattice)

$$\underline{\underline{M}} = \frac{1}{151} \begin{pmatrix} 80 & 78 \\ -78 & 158 \end{pmatrix} = \begin{pmatrix} 5 & 9 \\ -9 & 14 \end{pmatrix}^{-1} \cdot \begin{pmatrix} -2 & 12 \\ -12 & 10 \end{pmatrix}$$

describing Ir(1 1 1) + ( $\sqrt{(124/151)} \times \sqrt{(124/151)}$ )R29.5° - Gra which is shown in Fig. 6.28 (only the overlayer and the topmost substrate layer are included). Here the hexagonal interference pattern is clearly visible with moiré lattice vectors  $\underline{\underline{R}}_{M1}$  and  $\underline{\underline{R}}_{M2}$  included in Fig. 6.28.

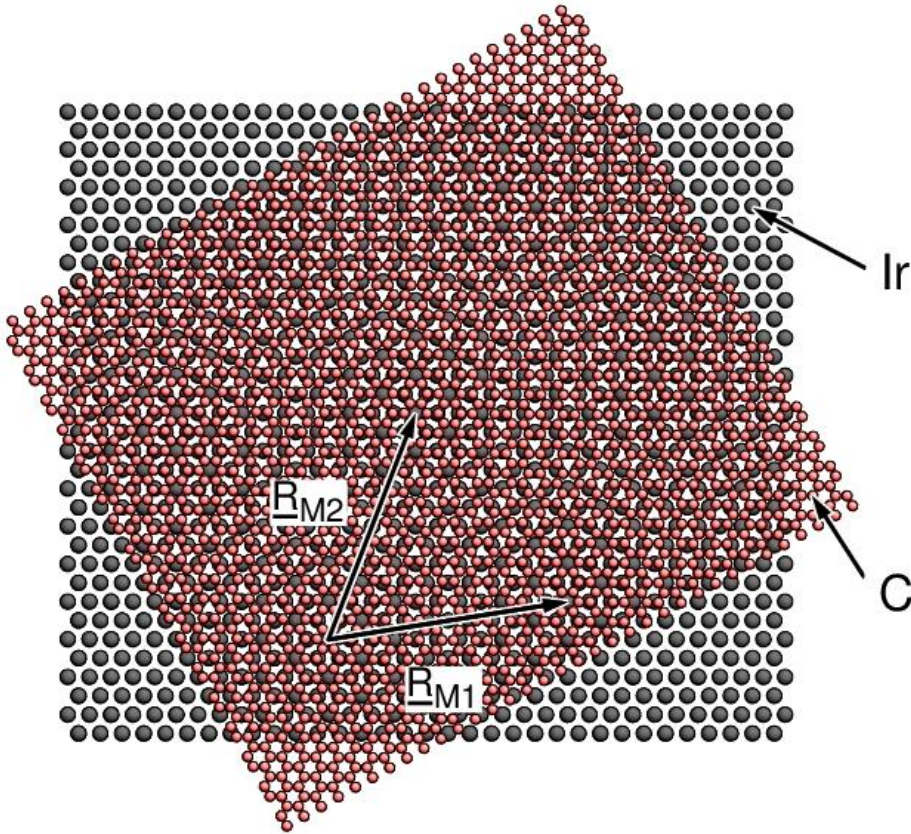


Fig. 6.28. High-order moiré pattern of a graphene overlayer on the Ir(1 1 1) surface for a perpendicular view with high-order moiré lattice vectors  $\underline{\mathbf{R}}_{M1}$ ,  $\underline{\mathbf{R}}_{M2}$  included.

This pattern can be described by high-order interference [163] assuming a simplified ‘second’ order matrix  $\underline{\mathbf{d}}$  and an appropriate integer approximant  $\underline{\mathbf{M}}_I$  with

$$\underline{\mathbf{M}} = \begin{pmatrix} 0.530 & 0.517 \\ -0.530 & 1.046 \end{pmatrix} \approx \frac{1}{2} \begin{pmatrix} 1 & 1 \\ -1 & 2 \end{pmatrix} = \frac{1}{2} \underline{\mathbf{M}}_I = \underline{\mathbf{M}}_I \underline{\mathbf{d}}^{-1}, \quad \underline{\mathbf{d}} = \begin{pmatrix} 2 & 0 \\ 0 & 2 \end{pmatrix} \quad (6.68)$$

which yields for the moiré matrix according to (6.67) after some calculus

$$\underline{\mathbf{P}}^d = \underline{\mathbf{d}}^{-1} (\underline{\mathbf{M}}_I \underline{\mathbf{d}}^{-1} - \underline{\mathbf{M}})^{-1} \underline{\mathbf{M}} = - \begin{pmatrix} 10 & 2 \\ -2 & 12 \end{pmatrix}$$

and results, in agreement with experiment [159], in a hexagonal moiré lattice with vectors  $\underline{\mathbf{R}}_{M1}$  and  $\underline{\mathbf{R}}_{M2}$  of lengths

$$|\underline{\mathbf{R}}_{M1}| = |\underline{\mathbf{R}}_{M2}| = \sqrt{124} |\underline{\mathbf{R}}_{oI}| = \sqrt{124} a_{Ir} \quad (6.69)$$

where  $a_{Ir}$  is the lattice constant of the hexagonal Ir(1 1 1) substrate. Further, the moiré lattice is ro-

tated by  $8.948^\circ$  with respect to the substrate lattice which confirms the previous analysis [163].

If matrix  $\underline{\underline{M}}$  in (6.45) describes a coincidence lattice of a HOC lattice structure, see Sec. 6.4, i.e. if  $\underline{\underline{M}}$  can be represented by two integer matrices  $\underline{\underline{A}}$ ,  $\underline{\underline{B}}$  with

$$\underline{\underline{M}} = \underline{\underline{B}}^{-1} \underline{\underline{A}} \quad (6.70)$$

then the moiré matrix (6.67) describing interference yields

$$\underline{\underline{P}}^d = \left( \underline{\underline{M}}_1 - \underline{\underline{B}}^{-1} \underline{\underline{A}} \underline{\underline{d}} \right)^{-1} \left( \underline{\underline{B}}^{-1} \underline{\underline{A}} \right) = \left( \underline{\underline{B}} \underline{\underline{M}}_1 - \underline{\underline{A}} \underline{\underline{d}} \right)^{-1} \underline{\underline{A}} \quad (6.71)$$

with  $\underline{\underline{d}} = \underline{\underline{1}}$  referring to basic interference. As a consequence, the transformation between the moiré lattice vectors,  $\underline{\underline{R}}_{M1}^d$  and  $\underline{\underline{R}}_{M2}^d$ , and those of the substrate lattice,  $\underline{\underline{R}}_{o1}$  and  $\underline{\underline{R}}_{o2}$ , given by (6.66), can be written as

$$\begin{pmatrix} \underline{\underline{R}}_1 \\ \underline{\underline{R}}_2 \end{pmatrix} = \underline{\underline{A}} \begin{pmatrix} \underline{\underline{R}}_{o1} \\ \underline{\underline{R}}_{o2} \end{pmatrix} = \left( \underline{\underline{B}} \underline{\underline{M}}_1 - \underline{\underline{A}} \underline{\underline{d}} \right) \begin{pmatrix} \underline{\underline{R}}_{M1}^d \\ \underline{\underline{R}}_{M2}^d \end{pmatrix} \quad (6.72)$$

where  $\underline{\underline{R}}_1$  and  $\underline{\underline{R}}_2$  are the superlattice vectors describing the HOC supercell according to (6.13). Since the matrices  $\underline{\underline{A}}$ ,  $\underline{\underline{B}}$ ,  $\underline{\underline{M}}_1$ , and  $\underline{\underline{d}}$  appearing on the right side of (6.72) are all integer-valued the superlattice vectors  $\underline{\underline{R}}_1$  and  $\underline{\underline{R}}_2$  are given by integer-valued linear combinations of vectors  $\underline{\underline{R}}_{M1}$  and  $\underline{\underline{R}}_{M2}$ . Therefore, the moiré lattice with vectors  $\underline{\underline{R}}_{M1}$  and  $\underline{\underline{R}}_{M2}$  can serve as a basis to define the coincidence lattice of the HOC structure.

As a simple example, graphene adsorbed on the hexagonal Ru(0 0 0 1) surface, which has been discussed earlier, was found to form a HOC coincidence lattice structure where 25 graphene cells fit on 23 Ru unit cells. This yields a lattice transformation (6.10) with a transformation matrix

$$\underline{\underline{M}} = \frac{23}{25} \begin{pmatrix} 1 & 0 \\ 0 & 1 \end{pmatrix} \quad \text{and} \quad \underline{\underline{M}}_1 = \begin{pmatrix} 1 & 0 \\ 0 & 1 \end{pmatrix} \quad (6.73)$$

Hence, according to (6.58), (6.59) the moiré lattice vectors  $\underline{\underline{R}}_{M1}$  and  $\underline{\underline{R}}_{M2}$  are given by

$$\begin{pmatrix} \underline{\underline{R}}_{M1} \\ \underline{\underline{R}}_{M2} \end{pmatrix} = \frac{23}{2} \begin{pmatrix} 1 & 0 \\ 0 & 1 \end{pmatrix} \begin{pmatrix} \underline{\underline{R}}_{o1} \\ \underline{\underline{R}}_{o2} \end{pmatrix} \quad (6.74)$$

while the superlattice vectors  $\underline{\underline{R}}_1$  and  $\underline{\underline{R}}_2$  of the overlayer defined by (6.13) are

$$\begin{pmatrix} \underline{R}_1 \\ \underline{R}_2 \end{pmatrix} = 23 \begin{pmatrix} 1 & 0 \\ 0 & 1 \end{pmatrix} \begin{pmatrix} \underline{R}_{o1} \\ \underline{R}_{o2} \end{pmatrix} = 2 \begin{pmatrix} \underline{R}_{M1} \\ \underline{R}_{M2} \end{pmatrix} \quad (6.75)$$

Thus, the superlattice vectors  $\underline{R}_1$  and  $\underline{R}_2$  are twice as large as their moiré counterparts,  $\underline{R}_{M1}$  and  $\underline{R}_{M2}$ , as shown in Fig. 6.29 which confirms relation (6.72).

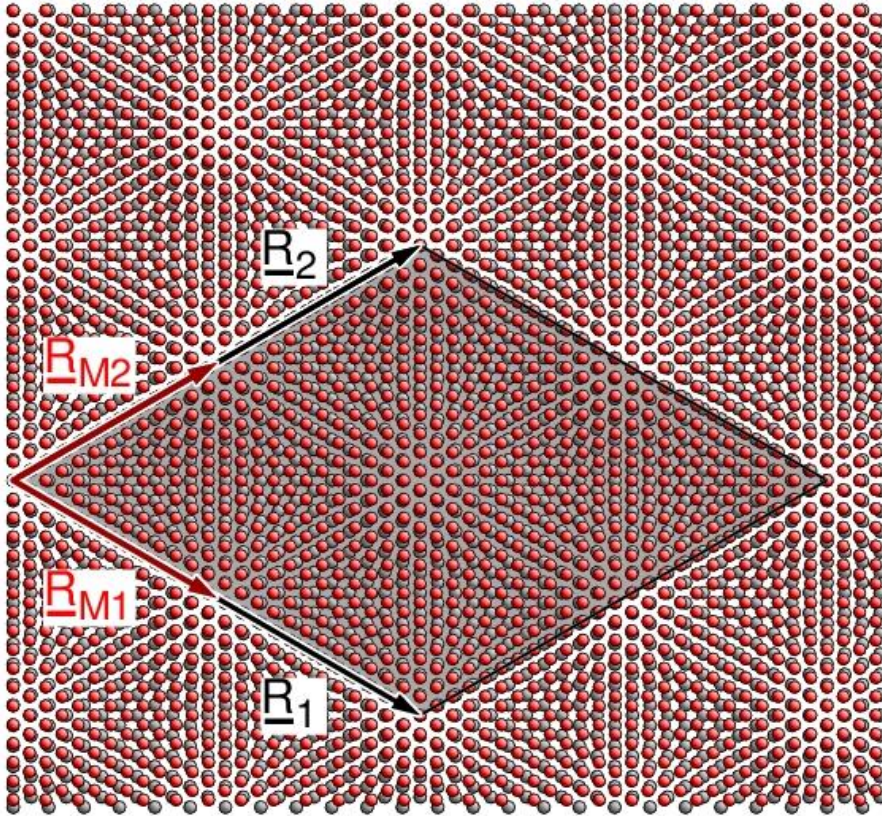


Fig. 6.29. Graphene overlayer adsorbed on the Ru(0 0 0 1) surface. The Ru substrate is shown by its topmost layer with gray atom balls while the honeycomb elements of the graphene are simplified by red balls. The supercell is emphasized in gray with superlattice vectors  $\underline{R}_1$ ,  $\underline{R}_2$  and moiré lattice vectors  $\underline{R}_{M1}$ ,  $\underline{R}_{M2}$  labeled accordingly.

### 6.5.2 Interference and Wood Notation

Further quantification of moiré lattices is obtained for surfaces where the overlayer structure can be characterized using the Wood notation (6.2), see Sec. 6.3. In the present section only the primitive notation ‘... -  $p(\gamma_1 \times \gamma_2)R\alpha$  - ...’ (or ‘... -  $(\gamma_1 \times \gamma_2)R\alpha$  - ...’ in short) will be considered. According to (6.6a), the  $2 \times 2$  transformation matrix of an overlayer structure characterized as ‘... -  $(\gamma_1 \times \gamma_2)R\alpha$  - ...’ is given by

$$\underline{\underline{\mathbf{M}}} = \frac{1}{\sin(\omega)} \begin{pmatrix} \gamma_1 \sin(\omega - \alpha) & \gamma_1 q^{-1} \sin(\alpha) \\ -\gamma_2 q \sin(\alpha) & \gamma_2 \sin(\omega + \alpha) \end{pmatrix}, \quad q = \frac{\mathbf{R}_2}{\mathbf{R}_1} \quad (6.76)$$

where  $q$ ,  $\omega$  refer to the type of Bravais lattice. If the nearby commensurate overlayer structure described by the integer approximant  $\underline{\underline{\mathbf{M}}}_I$  corresponds to a Wood notation ‘... -  $(\gamma_{I1} \times \gamma_{I2})\mathbf{R}\alpha_I$  - ...’ based on the same Bravais lattice, i.e. if

$$\underline{\underline{\mathbf{M}}}_I = \frac{1}{\sin(\omega)} \begin{pmatrix} \gamma_{I1} \sin(\omega - \alpha_I) & \gamma_{I1} q^{-1} \sin(\alpha_I) \\ -\gamma_{I2} q \sin(\alpha_I) & \gamma_{I2} \sin(\omega + \alpha_I) \end{pmatrix} \quad (6.77)$$

then the transformation matrix  $\underline{\underline{\mathbf{M}}}_M$  in (6.67) can be represented in Wood notation as

$$"... - (\gamma_{M1} \times \gamma_{M2})\mathbf{R}\alpha_M - ..." \quad , \quad \gamma_{Mi} = \frac{\gamma_i}{\gamma_{Ii}}, \quad i=1,2, \quad \alpha_M = \alpha - \alpha_I \quad (6.78)$$

with a transformation matrix  $\underline{\underline{\mathbf{M}}}_M$  given by

$$\underline{\underline{\mathbf{M}}}_M = \frac{1}{\sin(\omega)} \begin{pmatrix} \gamma_{M1} \sin(\omega - \alpha_M) & \gamma_{M1} q^{-1} \sin(\alpha_M) \\ -\gamma_{M2} q \sin(\alpha_M) & \gamma_{M2} \sin(\omega + \alpha_M) \end{pmatrix} \quad (6.79)$$

If we further assume that the order matrix for high-order interference can be restricted to a multiple of the unit matrix, i.e. to

$$\underline{\underline{\mathbf{d}}} \cong \underline{\underline{\mathbf{d}}} \cdot \underline{\underline{\mathbf{1}}} = \underline{\underline{\mathbf{d}}} \begin{pmatrix} 1 & 0 \\ 0 & 1 \end{pmatrix} \quad (6.80)$$

then the (high-order) moiré matrix  $\underline{\underline{\mathbf{P}}}^d$  according to (6.67) can be written as

$$\begin{aligned} \underline{\underline{\mathbf{P}}}^d &= [\underline{\underline{\mathbf{1}}} - \underline{\underline{\mathbf{M}}}_M \underline{\underline{\mathbf{d}}}]^{-1} \underline{\underline{\mathbf{M}}}_M = \\ &= \frac{1}{\Delta \sin(\omega)} \cdot \begin{pmatrix} \gamma_{M1} [\sin(\omega - \alpha_M) - \underline{\underline{\mathbf{d}}} \gamma_{M2} \sin(\omega)] & q^{-1} \gamma_{M1} \sin(\alpha_M) \\ -q \gamma_{M2} \sin(\alpha_M) & \gamma_{M2} [\sin(\omega + \alpha_M) - \underline{\underline{\mathbf{d}}} \gamma_{M1} \sin(\omega)] \end{pmatrix} \end{aligned} \quad (6.81)$$

where

$$\Delta = 1 + \underline{\underline{\mathbf{d}}}^2 \gamma_{M1} \gamma_{M2} - \underline{\underline{\mathbf{d}}} (\gamma_{M1} + \gamma_{M2}) \cos(\alpha_M) - \underline{\underline{\mathbf{d}}} (\gamma_{M2} - \gamma_{M1}) \cot(\omega) \sin(\alpha_M) \quad (6.82)$$

Using (6.81), (6.82) together with (6.66) one can derive parameters which are quite intuitive and can be actually measured in experiments performed for the overlayer structures. A comparison of the lengths of the moiré lattice vectors  $\underline{\underline{\mathbf{R}}}_{M1}^d, \underline{\underline{\mathbf{R}}}_{M2}^d$  with those of the substrate surface,  $\underline{\underline{\mathbf{R}}}_{01}$  and  $\underline{\underline{\mathbf{R}}}_{02}$  yields the **moiré factors**  $\lambda_i$  with

$$\lambda_i = \frac{\mathbf{R}_{\text{Mi}}}{\mathbf{R}_{\text{oi}}} = \frac{\gamma_{\text{Mi}}}{\Delta} \sqrt{1 + d^2 \gamma_{\text{Mj}}^2 - 2d \gamma_{\text{Mj}} \cos(\alpha_{\text{M}})} , \quad (\text{i,j}) = (1,2), (2,1) \quad (6.83)$$

and the **moiré angles**  $\varphi_i$  defined by the angles between the moiré lattice vectors and their substrate counterparts, are given by

$$\cos(\varphi_i) = \frac{\mathbf{R}_{\text{Mi}} \mathbf{R}_{\text{oi}}}{\mathbf{R}_{\text{Mi}} \mathbf{R}_{\text{oi}}} = \frac{\cos(\alpha_{\text{M}}) - d \gamma_{\text{Mj}}}{\sqrt{1 + d^2 \gamma_{\text{Mj}}^2 - 2d \gamma_{\text{Mj}} \cos(\alpha_{\text{M}})}} , \quad (\text{i,j}) = (1,2), (2,1) \quad (6.84)$$

Special cases are systems where the integer approximant matrix  $\underline{\mathbf{M}}_i$  equals the unit matrix which refers to  $\gamma_{\text{fi}} = 1$ ,  $\alpha_i = 0^\circ$  resulting in

$$\lambda_i = \frac{\mathbf{R}_{\text{Mi}}}{\mathbf{R}_{\text{oi}}} = \frac{\gamma_i}{\Delta} \sqrt{1 + d^2 \gamma_j^2 - 2d \gamma_j \cos(\alpha)} , \quad (\text{i,j}) = (1,2), (2,1)$$

$$\Delta = 1 + d^2 \gamma_1 \gamma_2 - d(\gamma_1 + \gamma_2) \cos(\alpha) - d(\gamma_2 - \gamma_1) \cot(\omega) \sin(\alpha)$$

$$\cos(\varphi_i) = \frac{\mathbf{R}_{\text{Mi}} \mathbf{R}_{\text{oi}}}{\mathbf{R}_{\text{Mi}} \mathbf{R}_{\text{oi}}} = \frac{\cos(\alpha) - d \gamma_j}{\sqrt{1 + d^2 \gamma_j^2 - 2d \gamma_j \cos(\alpha)}} , \quad (\text{i,j}) = (1,2), (2,1) \quad (6.85)$$

for the moiré parameters as discussed in detail in [155]. This simplifies further for isotropic scaling combined with rotation, where  $\gamma_1 = \gamma_2 = \gamma$ , to yield

$$\lambda_1 = \lambda_2 = \lambda = \frac{\mathbf{R}_{\text{Mi}}}{\mathbf{R}_{\text{oi}}} = \frac{\gamma}{\sqrt{\Delta}} , \quad \Delta = 1 + d^2 \gamma^2 - 2d \gamma \cos(\alpha)$$

$$\cos(\varphi_1) = \cos(\varphi_2) = \cos(\varphi) = \frac{\mathbf{R}_{\text{Mi}} \mathbf{R}_{\text{oi}}}{\mathbf{R}_{\text{Mi}} \mathbf{R}_{\text{oi}}} = \frac{\cos(\alpha) - d \gamma}{\sqrt{\Delta}} \quad (6.86)$$

As a first example, we consider the graphene overlayer on the Pt(1 1 1) surface discussed earlier. This system which has been observed in experiments [157] can be described in Wood notation as Pt(1 1 1) + (0.89 × 0.89) - Gra, reflecting an isotropically scaled overlayer with  $\gamma = 0.89$  and no rotation,  $\alpha = 0^\circ$ . Here the integer approximant structure is (1 × 1) corresponding to  $\alpha_i = 0^\circ$  such that equations (6.86) are applicable and yield a hexagonal first order moiré lattice with

$$\lambda = \frac{\gamma}{|1 - \gamma|} = 8.09 , \quad \varphi_i = 0^\circ \quad (6.87)$$

which is shown in Fig. 6.27 confirming the result discussed above.

Another example where equations (6.86) can be applied is a rotated graphene overlayer ad-

sorbed on top of graphene. For this system a rotation angle  $\alpha = 3.5^\circ$  has been claimed by experiment [164]. Thus, in Wood notation the overlayer structure is described as Gra +  $(1 \times 1)R3.5^\circ$  - Gra and exhibits a hexagonal first order moiré pattern where according to (6.86)

$$\lambda = \left( 2 \left| \sin\left(\frac{\alpha}{2}\right) \right| \right)^{-1} = 16.37, \quad \cos(\varphi) = \frac{\cos(\alpha) - 1}{\sqrt{2(1 - \cos(\alpha))}}, \quad \varphi = 90^\circ + \frac{\alpha}{2} = 91.75^\circ \quad (6.88)$$

which is shown in Fig. 6.30.

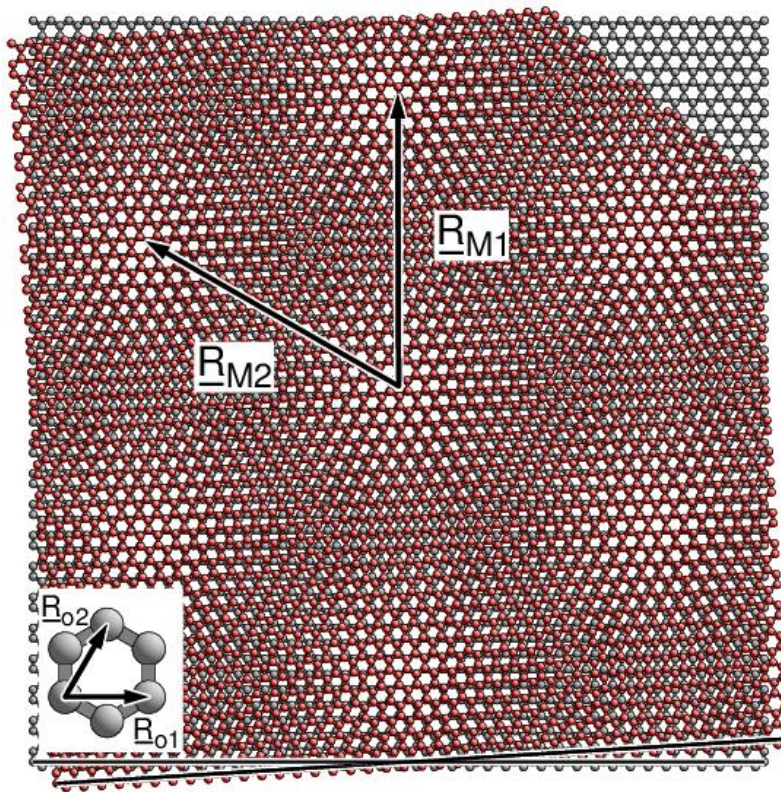


Fig. 6.30. Graphene overlayer adsorbed on a graphene layer for a rotation angle  $\alpha = 3.5^\circ$  (indicated by lines at the bottom) with moiré vectors  $\underline{R}_{M1}$ ,  $\underline{R}_{M2}$  included. The lattice vectors  $\underline{R}_{o1}$ ,  $\underline{R}_{o2}$  of the underlying graphene monolayer are sketched at the lower left where a magnification by a factor 5 is applied for better visibility.

The combination of rotated and scaled overlayers has been found in experiments for graphene adsorbed on hexagonal boron nitride (h-BN) [165]. In this system the lattice constant of the graphene overlayer is smaller by 3% compared with that of the h-BN lattice and the overlayer is rotated by a rather small angle of  $3^\circ$  yielding a h-BN +  $(0.97 \times 0.97)R3^\circ$  - Gra structure in Wood notation. This can be approximated by a HOC lattice structure with a transformation matrix



$$\underline{\underline{\mathbf{M}}} = \frac{1}{17} \begin{pmatrix} 16 & 1 \\ -1 & 17 \end{pmatrix} = \begin{pmatrix} 17 & 0 \\ 0 & 17 \end{pmatrix}^{-1} \begin{pmatrix} 16 & 1 \\ -1 & 17 \end{pmatrix}$$

representing h-BN + (0.971 × 0.971)R3° - Gra. The resulting hexagonal first order moiré pattern according to (6.86) leads to  $\lambda = 16.52$  and  $\varphi = 63.00^\circ$ . This is illustrated in Fig. 6.31a where in the simulation the graphene C<sub>6</sub> and B<sub>3</sub>N<sub>3</sub> honeycombs are replaced by gray and red balls for better visibility. For comparison, Fig. 6.31b shows a corresponding simulation of the overlayer structure h-BN + (0.971 × 0.971)R0° - Gra, i.e. without rotation, defined by a transformation matrix

$$\underline{\underline{\mathbf{M}}} = \frac{1}{35} \begin{pmatrix} 34 & 0 \\ 0 & 34 \end{pmatrix} = \begin{pmatrix} 35 & 0 \\ 0 & 35 \end{pmatrix}^{-1} \begin{pmatrix} 34 & 0 \\ 0 & 34 \end{pmatrix}$$

The resulting moiré pattern is dramatically changed, representing a much larger moiré lattice,  $\lambda = 34.00$  and  $\varphi = 0.00^\circ$ , with well separated moirons compared to those of the overlayer structure with a small rotation. Further, the rotation of the overlayer by only 3° leads to a moiron lattice rotated by a sizeable 63.00° which may be described as a giant rotation. This is a more general result found for overlayer structures with small rotation angles  $\alpha$  and where the lattice mismatch is small, reflected by scaling factors  $\gamma_i \approx 1$ . In fact, it can be shown by simple Taylor expansion that for even smaller values of  $\alpha$  the moiré angle  $\varphi$  in (6.86) can be approximated by

$$\varphi \approx \frac{\alpha}{|1-\gamma|} \quad (6.89)$$

which substantiates the general result.

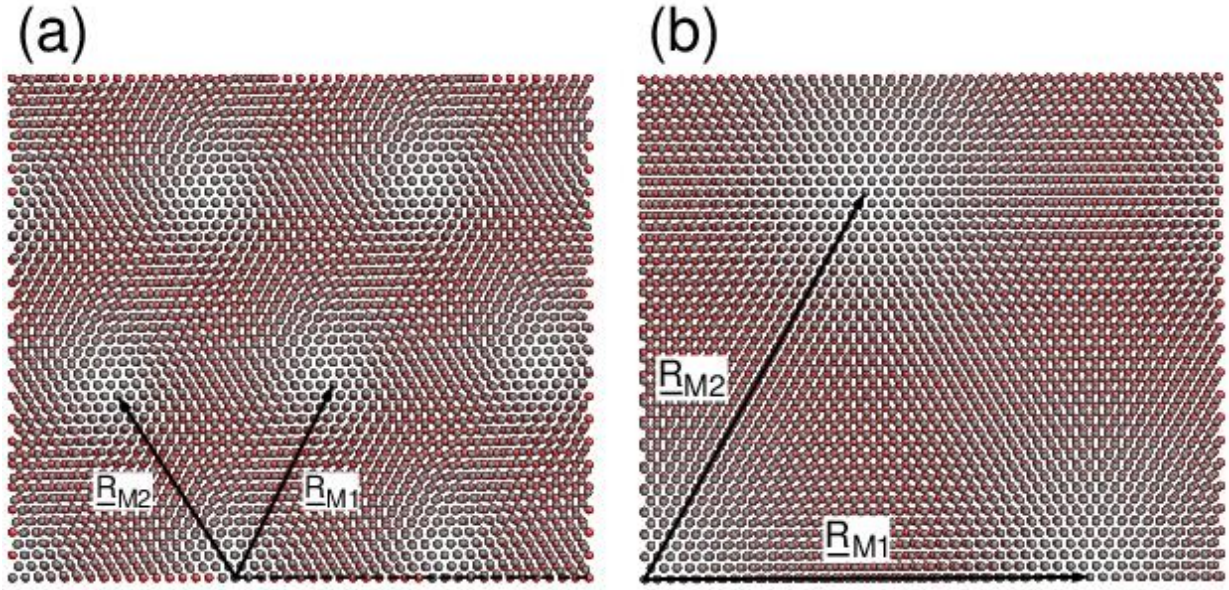


Fig. 6.31. Graphene overlayer adsorbed on a hexagonal boron nitride layer for a rotation angle of (a)  $\alpha = 3.0^\circ$ , (b)  $\alpha = 0.0^\circ$ . The graphene  $C_6$  and  $B_3N_3$  honeycombs are simulated by gray and red balls for better visibility. Moiré vectors  $\underline{R}_{M1}$ ,  $\underline{R}_{M2}$  are indicated accordingly.

Another interesting example of a rotated and scaled overlayer is the

$Ir(1\ 1\ 1) + (\sqrt{(124/151)} \times \sqrt{(124/151)})R29.5^\circ$  - Gra adsorbate system [159] discussed above, see Fig. 6.28, which exhibits a second order moiré pattern. Here the integer approximant  $\underline{M}_I$ , given by (6.68) can be written as

$$\underline{\underline{M}}_I = \begin{pmatrix} 1 & 1 \\ -1 & 2 \end{pmatrix} = \frac{1}{\sin(60^\circ)} \begin{pmatrix} \sqrt{3} \sin(30^\circ) & \sqrt{3} \sin(30^\circ) \\ -\sqrt{3} \sin(30^\circ) & \sqrt{3} \sin(90^\circ) \end{pmatrix}$$

reflecting a  $(\sqrt{3} \times \sqrt{3})R30^\circ$  structure in Wood notation according to (6.77). Using (6.78) this results in scaling factors  $\gamma_M = \sqrt{(124/453)} = 0.5232$  and rotation angles  $\alpha_M = -0.4187^\circ$ . Thus, applying (6.82), (6.83), (6.84) for second order interference,  $d = 2$ , yields moiré factors  $\lambda_i = \sqrt{124}$  and moiré angles  $\varphi_i = 8.948^\circ$  which confirms the previous analysis.

An important result of the present formalism is that for isotropically scaled overlayers with scaling factors  $\gamma_{M1} = \gamma_{M2} = \gamma_M$  the moiré factors  $\lambda_1$  and  $\lambda_2$  given by (6.83) are equal and do not depend explicitly on the type of Bravais lattice. Likewise, the moiré angles  $\varphi_1$  and  $\varphi_2$  defined by (6.84) agree with each other and are independent of the Bravais lattice type. Thus, for isotropically scaled and rotated overlayers the type of Bravais lattice of a possible moiré lattice is always that of the initial substrate. As an illustration, Fig. 6.32 shows moiré patterns for fictitious surface struc-

tures with different Bravais lattices where the patterns result from rotation by  $\alpha = 4^\circ$  and isotropic scaling by  $p = 0.95$ . This corresponds in all examples to a moiré angle  $\varphi = 55.71^\circ$  and a moiré factor  $\lambda = 11.252$ . For all four Bravais lattice types with symmetry, i.e. for primitive and centered rectangular, square, and hexagonal lattices, the moiré lattice type agrees with that of the substrate and overlayer lattice. While this theoretical result is quite clear its experimental verification seems to exist only for hexagonal surface systems so far.

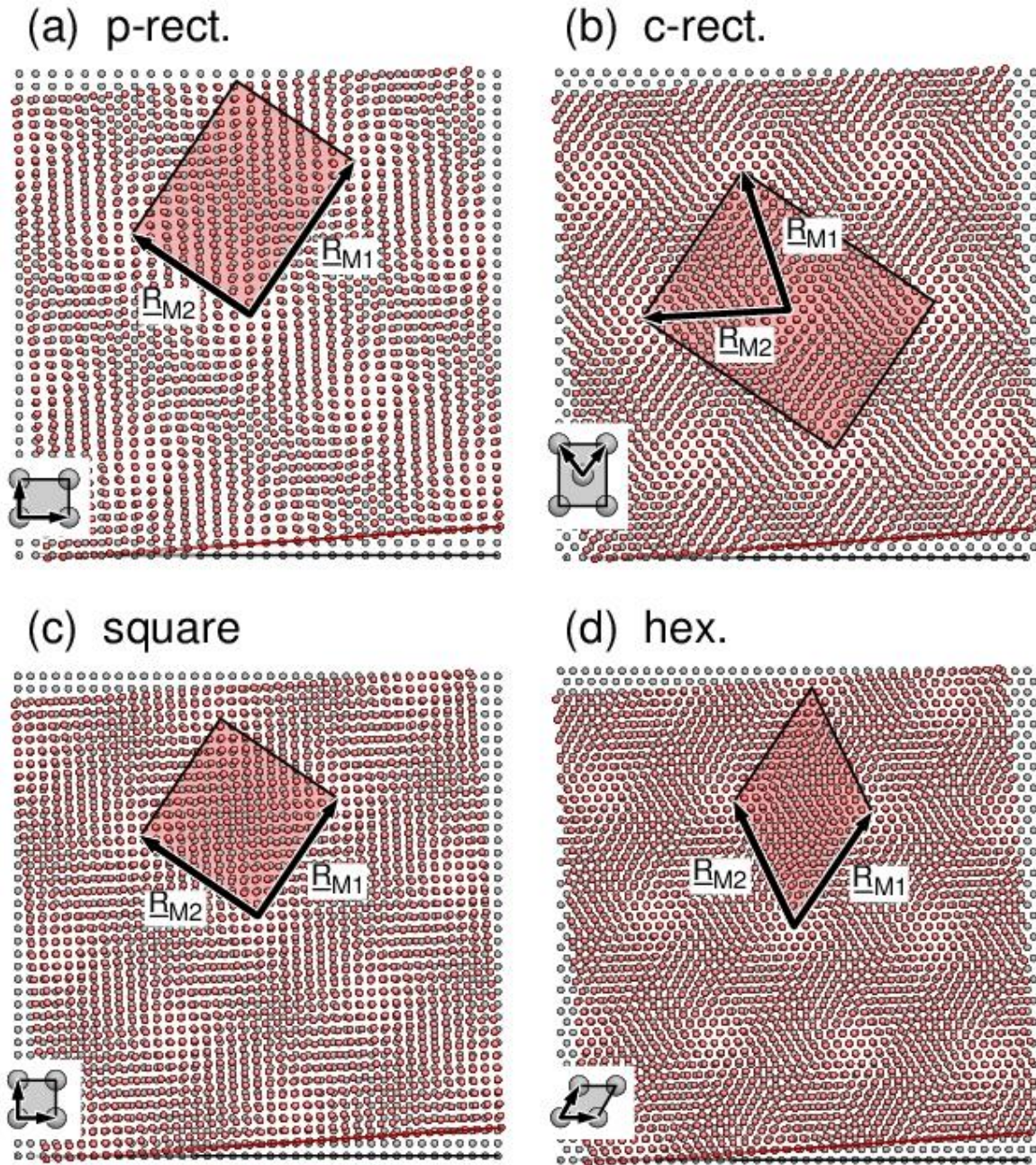


Fig. 6.32. Moiré patterns of overlayers with different Bravais lattices, (a) primitive rectangular (p-rect.,  $R_{o1}/R_{o2} = 1.3$ ), (b) centered rectangular (c-rect.,  $\angle(\mathbf{R}_{o1}, \mathbf{R}_{o2}) = 75^\circ$ ), (c) square, (d) hexagonal (hex.) reflecting a  $(0.95 \times 0.95)R_4^\circ$  overlayer structure. Moiré unit cells are emphasized in red with moiré vectors  $\mathbf{R}_{M1}$ ,  $\mathbf{R}_{M2}$  labeled accordingly. Substrate unit cells and lattice vectors  $\mathbf{R}_{o1}$ ,  $\mathbf{R}_{o2}$  are included at the lower left insets with a magnification factor 3 applied for better visibility.

### 6.5.3 Anisotropic Scaling, Stretching and Shifting

While the Bravais lattice type of moiré lattices resulting from rotated and isotropically scaled overlayers always agrees with that of the overlayer structure, anisotropic scaling with scaling factors  $\gamma_{M1} \neq \gamma_{M2}$  can lead to moiré patterns which do not reflect the initial Bravais lattice. As an illustration Fig. 6.33 shows two moiré patterns of a fictitious (distorted) hexagonal overlayer on hexagonal substrate which refer to  $(0.94 \times 0.98)R5^\circ$  (Fig. 6.33a) and to  $(0.98 \times 0.94)R(-5^\circ)$  (Fig. 6.33b) in Wood notation. In both cases the moiré pattern is characterized by distorted ellipsoidal moirons forming an almost rectangular lattice. In addition, the moirons are frizzy at their boundaries exhibiting a spiral structure where the spirals rotate clockwise in the left and anti-clockwise in the right pattern of Fig. 6.33. Thus, the two patterns may be considered chiral pairs.

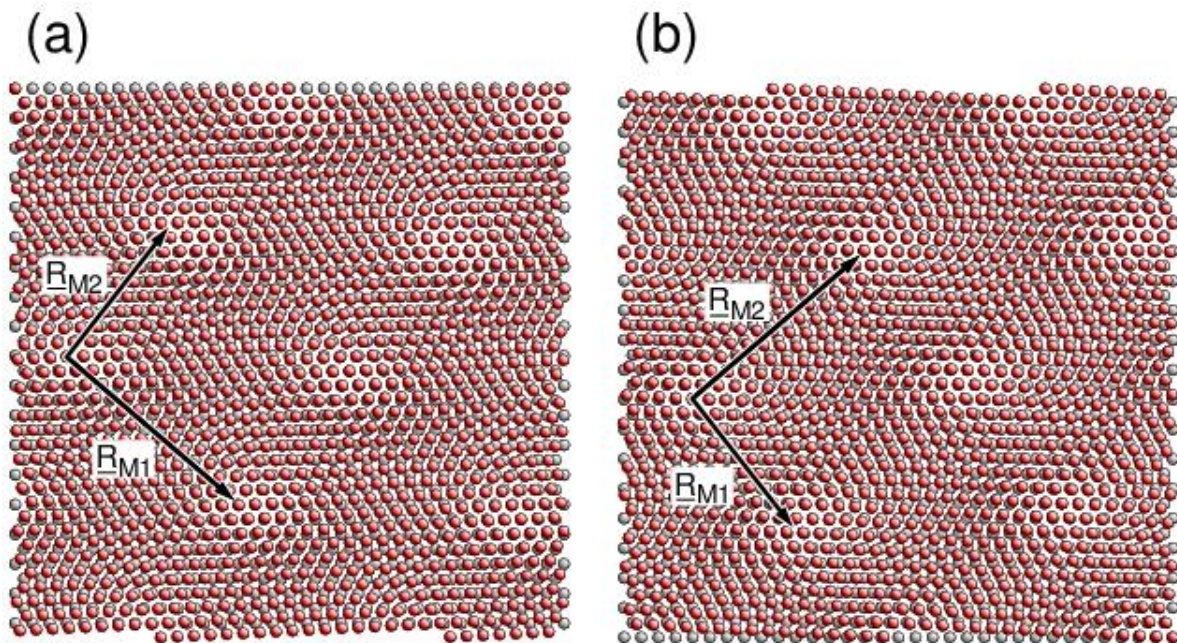


Fig. 6.33. Moiré patterns of a fictitious (distorted) hexagonal overlayer on hexagonal substrate described as (a)  $(0.94 \times 0.98)R5^\circ$ , (b)  $(0.98 \times 0.94)R(-5^\circ)$ . Moiré vectors  $\underline{R}_{M1}$ ,  $\underline{R}_{M2}$  are labeled accordingly.

Anisotropically scaled overlayers without rotation, reflecting  $(\gamma_1 \times \gamma_2)$  overlayers in Wood notation with  $(1 \times 1)$  as the integer approximant, i.e.  $\underline{M}_1 = \underline{1}$ , are characterized by transformation matrices  $\underline{M}$  according to (6.45) with

$$\underline{M} = \begin{pmatrix} \gamma_1 & 0 \\ 0 & \gamma_2 \end{pmatrix} \quad (6.90)$$

Thus, they can lead to periodic first order moiré patterns with lattice vectors  $\underline{\mathbf{R}}_{M1}$  and  $\underline{\mathbf{R}}_{M2}$  defined by (6.58) with a moiré matrix  $\underline{\mathbf{P}}$  according to (6.59) given as

$$\underline{\mathbf{P}} = \begin{pmatrix} \frac{\gamma_1}{1-\gamma_1} & 0 \\ 0 & \frac{\gamma_2}{1-\gamma_2} \end{pmatrix} \quad (6.91)$$

yielding moiré factors  $\lambda_i$  and moiré angles  $\varphi_i$  according to (6.83), (6.84)

$$\lambda_i = \frac{\mathbf{R}_{Mi}}{\mathbf{R}_{oi}} = \frac{\gamma_i}{|1-\gamma_i|}, \quad \varphi_i = 0^\circ, \quad i=1, 2 \quad (6.92)$$

Here the limit  $\gamma_1 = 1, \gamma_2 \neq 1$ , corresponding to a  $(1 \times \gamma_2)$  overlayer, leads to a diverging moiré factor  $\lambda_1$ . This means that the moiré lattice vector  $\underline{\mathbf{R}}_{M1}$  tends to infinity such that the interference along  $\underline{\mathbf{R}}_{M1}$  disappears while that along  $\underline{\mathbf{R}}_{M2}$  remains. As a result the moiré pattern is periodic only in one dimension, exhibiting moirons as parallel infinite stripes (**1-dimensional moirons**) rather than confined regions where the stripes are perpendicular to  $\underline{\mathbf{R}}_{o2}$ . This has been observed in experiments for the gold surface whose reconstruction has been characterized as Au(1 1 1) -  $(\sqrt{3} \times 22)$ rect [111]. As discussed in Sec. 5.2, the topmost surface layer experiences a lateral compression such that 23 atoms of the overlayer fit in a cell with 22 atoms of the substrate along  $\underline{\mathbf{R}}_{o2}$ . This leads to a transformation matrix  $\underline{\mathbf{M}}$  and to a moiré matrix  $\underline{\mathbf{P}}$  with

$$\underline{\mathbf{M}} = \begin{pmatrix} 1 & 0 \\ 0 & \frac{22}{23} \end{pmatrix}, \quad \underline{\mathbf{P}} = \begin{pmatrix} \infty & 0 \\ 0 & 22 \end{pmatrix}$$

which confirms the observed arrangement of striped moirons, shown in Fig. 5.6.

One-dimensional moiré patterns can also be found in overlayer structures where the overlayer lattice is **stretched** with respect to the substrate lattice. The lattice vectors  $\underline{\mathbf{R}}_{o1}'$ ,  $\underline{\mathbf{R}}_{o2}'$  of stretched overlayers are described by a transformation

$$\underline{\mathbf{R}}_{oi}' = \underline{\mathbf{R}}_{oi} + \gamma(\underline{\mathbf{R}}_{oi} \cdot \underline{\mathbf{e}})\underline{\mathbf{e}}, \quad i=1,2 \quad (6.93)$$

where  $\gamma$  is a stretch factor and  $\underline{\mathbf{e}}, \underline{\mathbf{e}}'$  are unit vectors with  $\underline{\mathbf{e}}$  defining the stretch direction and  $\underline{\mathbf{e}}'$  being perpendicular to  $\underline{\mathbf{e}}$ . Overlayer structures resulting from stretching cannot be described by Wood notation since the angle between  $\underline{\mathbf{R}}_{o1}'$  and  $\underline{\mathbf{R}}_{o2}'$  differs in general from that between  $\underline{\mathbf{R}}_{o1}$  and  $\underline{\mathbf{R}}_{o2}$ . However, transformation (6.93) can be written as

$$\begin{pmatrix} \underline{\mathbf{R}}_{o1}' \\ \underline{\mathbf{R}}_{o2}' \end{pmatrix} = \underline{\mathbf{M}} \cdot \begin{pmatrix} \underline{\mathbf{R}}_{o1} \\ \underline{\mathbf{R}}_{o2} \end{pmatrix} \quad (6.94)$$

with

$$\underline{\mathbf{M}} = \frac{1}{(x_1 x_2' - x_2 x_1')} \begin{pmatrix} (1+\gamma)x_1 x_2' - x_2 x_1' & -\gamma x_1 x_1' \\ \gamma x_2 x_2' & x_1 x_2' - (1+\gamma)x_2 x_1' \end{pmatrix} \quad (6.95)$$

where

$$x_i = (\underline{\mathbf{R}}_{oi} \cdot \underline{\mathbf{e}}), \quad x_i' = (\underline{\mathbf{R}}_{oi}' \cdot \underline{\mathbf{e}}), \quad i=1,2 \quad (6.96)$$

After some calculation this leads to

$$\underline{\mathbf{1}} - \underline{\mathbf{M}} = \frac{\gamma}{(x_1 x_2' - x_2 x_1')} \begin{pmatrix} x_1 & 0 \\ 0 & x_2 \end{pmatrix} \begin{pmatrix} -x_2' & x_1' \\ -x_2' & x_1' \end{pmatrix}, \quad \det(\underline{\mathbf{1}} - \underline{\mathbf{M}}) = 0 \quad (6.97)$$

As a result, the moiré matrix  $\underline{\mathbf{P}}$  according to (6.59) with  $\underline{\mathbf{M}}_I = \underline{\mathbf{1}}$  becomes singular, thus, excluding a two-dimensional moiré pattern. However, stretching along direction  $\underline{\mathbf{e}}$  can lead to spatial variations which are perceived as 1-dimensional moiré stripes but the detailed analysis is rather complex. As an illustration, Fig. 6.34 shows a fictitious (distorted) hexagonal overlayer on hexagonal substrate where the overlayer (red balls) is stretched by a factor  $\gamma = 8/7$  along vector  $\underline{\mathbf{e}} = (2 \underline{\mathbf{R}}_{o1} + \underline{\mathbf{R}}_{o2})/\sqrt{7}$  with respect to the substrate layer (gray balls). Thus, the moiré stripes repeat periodically along  $\underline{\mathbf{e}}$  with a periodicity length given by vector  $\underline{\mathbf{R}} = 8 (2 \underline{\mathbf{R}}_{o1} + \underline{\mathbf{R}}_{o2})$  while the stripes are not exactly perpendicular to  $\underline{\mathbf{e}}$ .

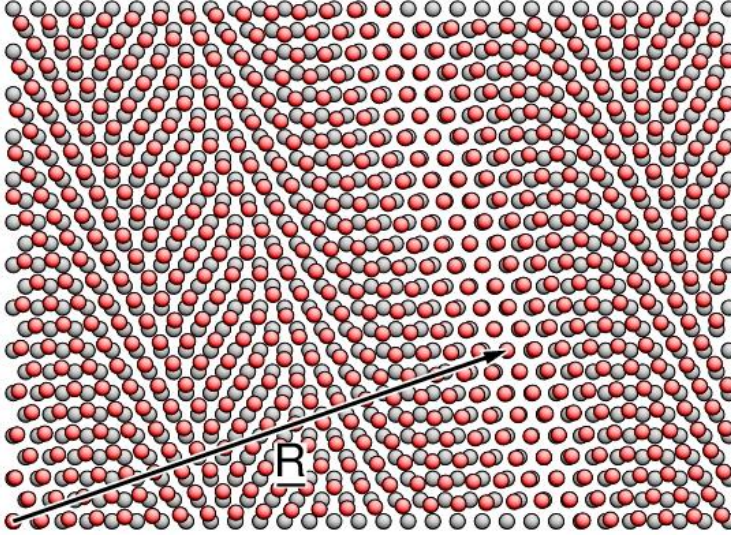


Fig. 6.34. Moiré patterns of a fictitious (distorted) hexagonal overlayer (red balls) on hexagonal substrate (gray balls) where the overlayer is stretched by a factor  $\gamma = 8/7$  along vector  $\underline{R}$  included in the figure.

Moiré lattices are also affected by lateral shifts of the overlayer. A global shift vector  $\underline{s}$  translating the otherwise rigid overlayer can always be represented by lattice vectors  $\underline{R}_{o1}$  and  $\underline{R}_{o2}$  of the substrate, i.e. by

$$\underline{s} = x_1 \underline{R}_{o1} + x_2 \underline{R}_{o2} = \begin{pmatrix} x_1 & x_2 \end{pmatrix} \begin{pmatrix} \underline{R}_{o1} \\ \underline{R}_{o2} \end{pmatrix} \quad (6.98)$$

where the shift does not influence the periodicity of the overlayer structure but changes the origin of the corresponding lattice. As a result, the origin of the moiré lattice vectors  $\underline{R}_{M1}^d, \underline{R}_{M2}^d$  given by (6.66) is shifted by

$$\underline{S}_M = x_1 \underline{R}_{M1}^d + x_2 \underline{R}_{M2}^d = \begin{pmatrix} x_1 & x_2 \end{pmatrix} \begin{pmatrix} \underline{R}_{M1}^d \\ \underline{R}_{M2}^d \end{pmatrix} = \begin{pmatrix} x_1 & x_2 \end{pmatrix} \underline{P}^d \begin{pmatrix} \underline{R}_{o1} \\ \underline{R}_{o2} \end{pmatrix} \quad (6.99)$$

Since moiré lattice vectors  $\underline{R}_{M1}$  and  $\underline{R}_{M2}$  do in general not point along directions of the substrate lattice vectors  $\underline{R}_{o1}$  and  $\underline{R}_{o2}$ , vectors  $\underline{s}$  and  $\underline{S}_M$  may also point in different directions. Further, the lengths of the corresponding shift vectors may be quite different. As an illustration, we assume an overlayer structure to represent a combination of isotropic scaling and rotation described as  $(\gamma \times \gamma)R\alpha$  in Wood notation. Thus, the lattice vectors of the moiré lattice,  $\underline{R}_{M1}^d$  and  $\underline{R}_{M2}^d$ , are connected with those of the substrate lattice,  $\underline{R}_{o1}$  and  $\underline{R}_{o2}$ , where moiré parameters  $\lambda, \varphi$  are given by (6.86). Then the ratio of the shift lengths is given by



$$\begin{aligned} \left( \frac{\underline{S}_M}{\underline{s}} \right)^2 &= \frac{x_1^2 (\underline{R}_{M1}^d)^2 + x_2^2 (\underline{R}_{M2}^d)^2 + x_1 x_2 (\underline{R}_{M1}^d \underline{R}_{M2}^d)}{x_1^2 (\underline{R}_{01})^2 + x_2^2 (\underline{R}_{02})^2 + x_1 x_2 (\underline{R}_{01} \underline{R}_{02})} = \\ &= \frac{x_1^2 (\lambda \underline{R}_{01})^2 + x_2^2 (\lambda \underline{R}_{02})^2 + x_1 x_2 (\lambda \underline{R}_{01} \lambda \underline{R}_{02})}{x_1^2 (\underline{R}_{01})^2 + x_2^2 (\underline{R}_{02})^2 + x_1 x_2 (\underline{R}_{01} \underline{R}_{02})} = \lambda^2 \end{aligned} \quad (6.100)$$

and the angle between the shift vectors  $\underline{s}$  and  $\underline{S}_M$  yields with (6.86) after some calculus

$$\cos(\angle(\underline{S}_M, \underline{s})) = \frac{\underline{S}_M \underline{s}}{S_M s} = \cos(\varphi) \quad (6.101)$$

Thus, for  $(\gamma \times \gamma)R\alpha$  overlayer structures the shift vectors of the moiré lattice and of the substrate lattice,  $\underline{S}_M$  and  $\underline{s}$ , respectively, are connected by the same relationships (6.86) as the lattice vectors themselves. This is evident from Fig. 6.35 which shows shift directions of the overlayer and of the moiré lattice for two overlayer structures. In Fig. 6.35a, referring to  $\text{Ir}(1\ 1\ 1) + (0.906 \times 0.906)R0^\circ - \text{Gra}$  [159], the graphene overlayer is scaled but not rotated such that the moiré lattice vectors are parallel to those of the iridium substrate. Thus, the moiré lattice and the overlayer both shift in parallel, i.e. horizontally in Fig. 6.35a. In Fig. 6.35b, referring to (fictitious)  $\text{Ir}(1\ 1\ 1) + (0.906 \times 0.906)R5^\circ - \text{Gra}$ , the graphene overlayer is scaled and rotated leading to moiré lattice vectors which point in directions different from those of the substrate lattice vectors. Therefore, the moiré lattice shifts in a diagonal direction while the overlayer shifts horizontally. However, in both cases the moiré shifts are much larger than the corresponding overlayer shifts, where according to (6.100) amplification factors  $S_M/s = 9.61$  (without rotation) and 7.22 (with rotation) are found.

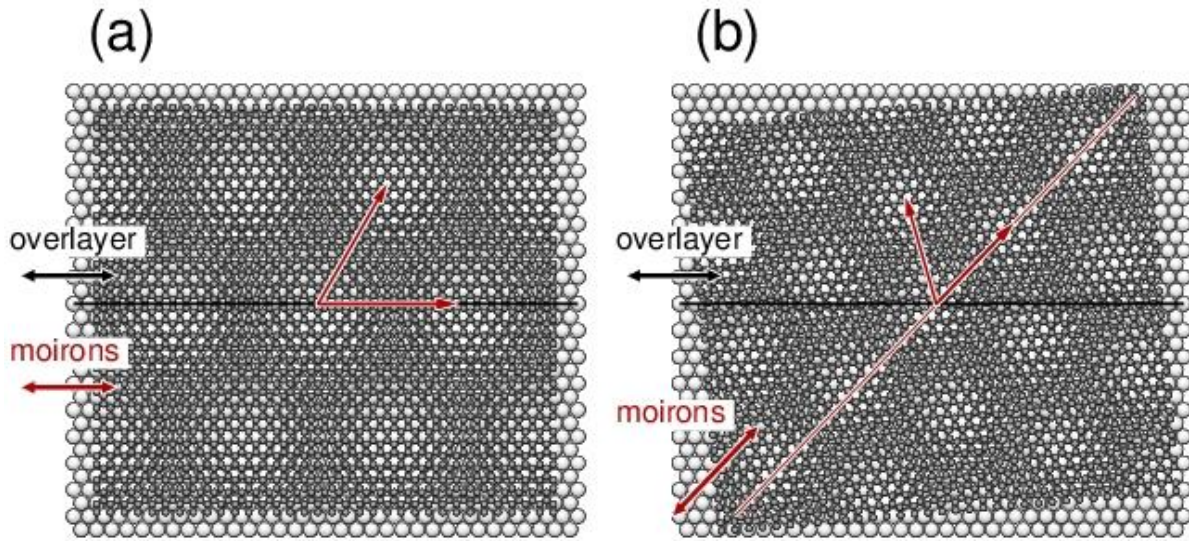


Fig. 6.35. Graphene overlayer adsorbed on the Ir(1 1 1) surface for structures (a) Ir(1 1 1) + (0.906 × 0.906) - Gra, (b) Ir(1 1 1) + (0.906 × 0.906)R5° - Gra (fictitious). The moiré vectors  $\underline{R}_{M1}$ ,  $\underline{R}_{M2}$  are shown in red. Shift directions of the overlayer and of the moiré lattice are denoted by black and red double headed arrows

Moiré lattices of shifted overlayers can be observed at stepped metal surfaces. As an illustration, Fig. 6.36 shows the simulation of a moiré pattern for graphene spreading over a monoatomic step on the Ir(1 1 1) surface [155], [166]. Here the Ir atoms at adjacent terraces experience a lateral shift of  $-\underline{s} = (\underline{R}_{o1} - 2 \underline{R}_{o2}) / 3$  (shown by a red arrow denoted ‘ $-\underline{s}$ ’ in the figure inset at the bottom right), corresponding to a relative shift  $\underline{s}$  of the graphene layer. This results, according to (6.98), (6.99), in a parallel shift  $\underline{S}_M = (\underline{R}_{M1} - 2 \underline{R}_{M2}) / 3$  (shown by a red arrow denoted ‘ $\underline{S}_M$ ’ in the figure) of the moirion arrangement between the terraces.

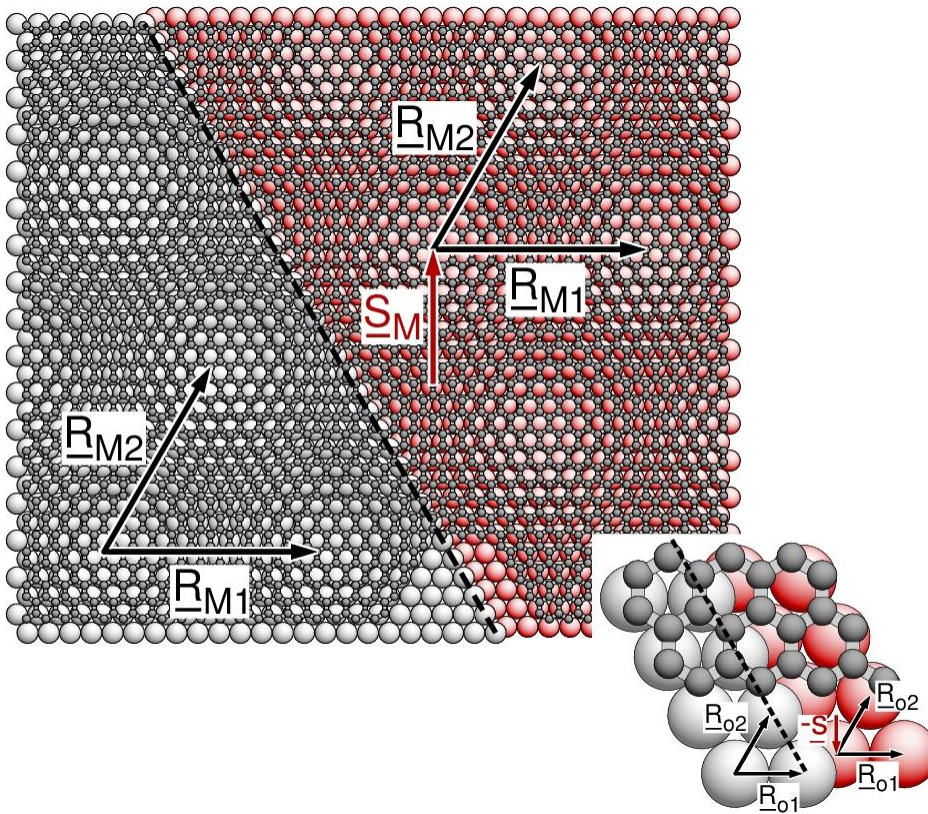


Fig. 6.36. Graphene overlayer adsorbed at a stepped Ir(1 1 1) surface. Adjacent terraces are shown in red (lower terrace) and light gray (upper terrace) with moiré vectors  $\underline{R}_{M1}$ ,  $\underline{R}_{M2}$  included. The inset at the bottom right shows an enlarged local area near the step edge with lattice vectors  $\underline{R}_{o1}$ ,  $\underline{R}_{o2}$  at the two terraces. The vector labeled ' $\underline{s}$ ' denotes the lateral atom shift between upper and lower terrace.

## 6.6 Symmetry and Domain Formation

As pointed out in Sec. 6.1, structure concepts discussed for the topmost layers of relaxed or reconstructed surfaces of real crystals can be used analogously to characterize adsorbate layers at surfaces. This applies in particular to **symmetry** properties. In the case of reconstructed or adsorbate layers at surfaces - both will be called overlayers in the following - those with **commensurate superlattices** are expected to exhibit **highest symmetry**, where **two aspects** are important. **First**, the overlayer and the substrate surface share a common periodicity (i.e. translational symmetry), that of the superlattice, with lattice vectors  $\underline{R}_1'$ ,  $\underline{R}_2'$ . These lattice vectors are given by integer-valued combinations of the two-dimensional lattice vectors of the substrate surface,  $\underline{R}_1$  and  $\underline{R}_2$ , according to (5.3). Further, the area of the superlattice unit cell is an integer multiple of that of the substrate surface. **Second**, point symmetry elements, common to the overlayer and the substrate surface, will

combine to form the two-dimensional space group of the superlattice representing the joint overlayer / substrate surface. This space group may be identical to that of the overlayer (and can never include additional symmetry elements). But it can also represent lower symmetry compared with that of each subsystem given by the two corresponding space groups.

**Formally**, the combination of two-dimensional space groups of overlayer and substrate lattices can be based on the notion that all **two-dimensional** symmetry elements appearing in an atom layer can be translated into **three-dimensional** ones at the surface. Thus, rotation axes in two-dimensional atom layers reflect rotation axes pointing perpendicular to the layers in three-dimensional space. Likewise, mirror lines in two-dimensional layers correspond to mirror planes perpendicular to the layers in three dimensions. Finally, glide lines in two-dimensional layers translate to glide planes perpendicular to the layers in three dimensions. Then the **joint** two-dimensional **space group** of the overlayer and substrate layers **collects** the two-dimensional equivalents of all those three-dimensional symmetry elements that are shared by both layers.

As an example, we consider the adsorption of oxygen on the (1 1 0) surface of fcc rhodium, for which experimental studies [167], SSD 45.8.7, have shown a  $\text{Rh}(1\ 1\ 0) + \text{p}2\text{mg}(2 \times 1) - 2\text{O}$  overlayer structure shown in Fig. 6.37. Here oxygen atoms are placed at tilted bridge sites along the

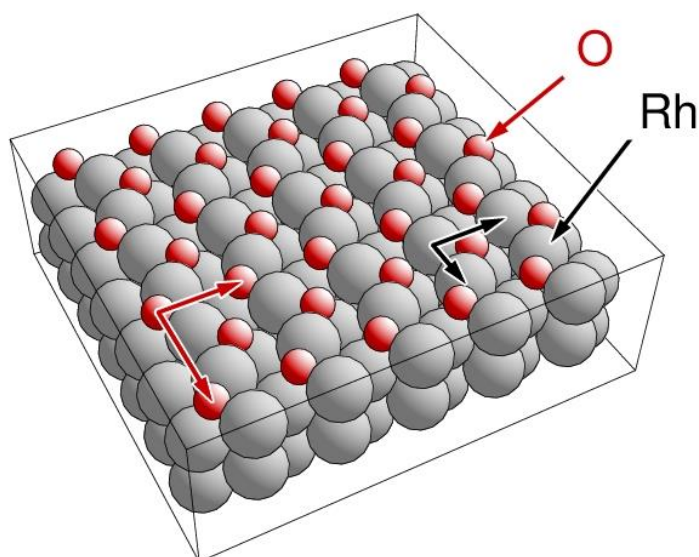


Fig. 6.37. Structure of the  $\text{Rh}(1\ 1\ 0) + \text{p}2\text{mg}(2 \times 1) - 2\text{O}$  adsorbate system. O adsorbate and Rh substrate atoms are shown in red and gray. Lattice vectors of the adsorbate layer and substrate are shown in red and black.

topmost rows of Rh atoms in an alternating fashion (left and right tilt). As a result, the unit cell of

the oxygen overlayer, containing two oxygen atoms, is rectangular with lattice vectors along and perpendicular to the substrate atom rows, where  $\underline{R}_1' = 2 \underline{R}_1$  and  $\underline{R}_2' = \underline{R}_2$  define the superlattice. Further, the point symmetry elements of the overlayer are those of space group  $p2mg$  sketched in Fig. 6.38a. In contrast, point symmetry elements of the substrate lattice, shown in Fig. 6.38b, form the space group  $p2mm$  (for group notations see Sec. 3.8.6), where the unit cell area is half that of the superlattice cell. (The sketch of Fig. 6.38a includes two unit cells of the substrate to reflect the superlattice periodicity.) All 2-fold rotation centers of the oxygen overlayer as well as the two

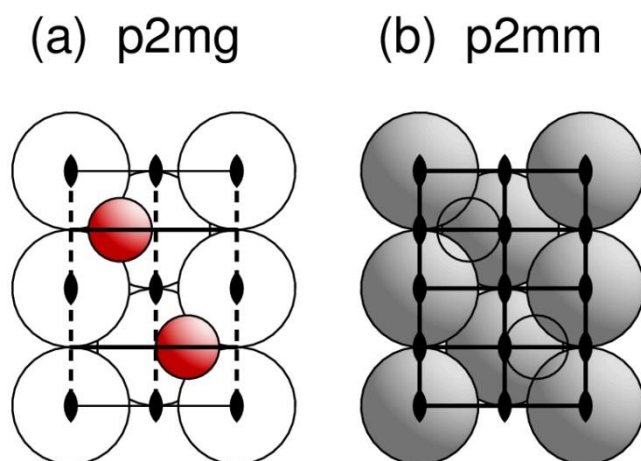


Fig. 6.38. Surface symmetry elements of the  $\text{Rh}(1\ 1\ 0) + p2mg(2 \times 1) - 2\text{O}$  adsorbate system. (a) O adsorbate symmetry elements, space group  $p2mg$ . (b)  $\text{Rh}(1\ 1\ 0)$  substrate symmetry elements, space group  $p2mm$ . The sketch includes two unit cells of the substrate to reflect the adsorbate periodicity. All symmetry elements are denoted according to ITC.

mirror lines also appear in the symmetry sketch of the substrate. Further, the glide lines of the overlayer with periodicity vectors  $\underline{R}_1' = 2 \underline{R}_1$  are consistent with the parallel mirror lines of the substrate along  $\underline{R}_1$ . Thus, all symmetry elements of space group  $p2mg$  exist in both subsystems and this space group describes all point symmetry elements of the combined overlayer / substrate surface. So in this example the space group of the **overlayer** happens to be **identical** to that of the **combined system**.

An example where the space group of the **combined** system represents **lower symmetry** compared with that of the **overlayer** superlattice is the  $\text{Al}(1\ 1\ 1) + (1 \times 1) - \text{O}$  adsorbate system [168], SSD 13.8.19, shown in Fig. 6.39. Here the unit cell of the separate oxygen overlayer includes point symmetry elements described by the hexagonal space group  $p6mm$ , see upper left pattern of Fig. 6.39 which is identical to the symmetry of the unit cells of each underlying aluminum substrate layer. However, the substrate layer cells are **shifted** laterally with respect to those of the adsorbate

overlayer. As a result, there are **fewer** point symmetry elements in the combined overlayer / substrate system than in the adsorbate and substrate layers themselves and the symmetry of the combined system is described by space group  $p3m1$ , see lower right pattern of Fig. 6.39.

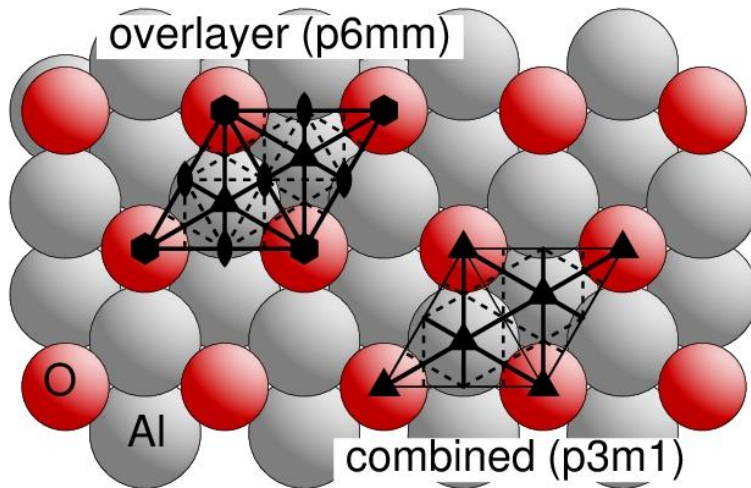


Fig. 6.39. Structure of the Al(1 1 1) + (1 × 1) - O adsorbate system. The figure includes symmetry patterns of space group  $p6mm$  of the separate overlayer and substrate (top left) as well as of space group  $p3m1$  of the combined overlayer/substrate surface (bottom right). All symmetry elements are denoted according to ITC.

Table 6.2 gives an overview of **allowed space groups** for all **combinations** of commensurate overlayer and substrate lattices sharing point symmetry elements (including glide lines). Here the **rows** denote the two-dimensional **substrate lattice** at the surface and **columns** refer to space groups of the **combined** overlayer / substrate **superlattice**. The table shows that in numerous cases the symmetry of the substrate lattice allows **different** superlattice symmetries depending on the lattice vectors  $\underline{R}_1'$ ,  $\underline{R}_2'$  of the superlattice. A full analysis of compatible overlayer symmetries can be obtained by an interactive computational tool, **LEEDpat** [169], which allows finding all possible overlayer space groups for a given commensurate superlattice and a substrate space group.



(b) Space groups no. 10 - 12 (square), 13 - 17 hexagonal) of the combined overlayer / substrate superlattice

Substrate lattice	Combined overlayer / substrate superlattice							
	(10) p4	(11) p4mm	(12) p4gm	(13) p3	(14) p3m1	(15) p31m	(16) p6	(17) p6mm
(1) p1	--	--	--	--	--	--	--	--
(2) p2	--	--	--	--	--	--	--	--
(3) p1m1, m=0	--	--	--	--	--	--	--	--
(4) p1g1, g=0	--	--	--	--	--	--	--	--
(5) c1m1, m=0	--	--	--	--	--	--	--	--
(6) p2mm, m=0,90	--	--	--	--	--	--	--	--
(7) p2mg, m=0, g=90	--	--	--	--	--	--	--	--
(8) p2gg, g=0,90	--	--	--	--	--	--	--	--
(9) c2mm, m=0,90	--	--	--	--	--	--	--	--
(10) p4	any	--	--	--	--	--	--	--
(11) p4mm, m=0,45	any	0, 45	0, 45	--	--	--	--	--
(12) p4gm, g=0	any	--	0	--	--	--	--	--
(13) p3	--	--	--	any	--	--	--	--
(14) p3m1, m=90	--	--	--	any	0	90	--	--
(15) p31m, m=0	--	--	--	any	90	0	--	--
(16) p6	--	--	--	any	--	--	any	--
(17) p6mm, m=0,90	--	--	--	any	0, 90	0, 90	any	0, 90

In the tables lattice vectors  $\underline{R}_1$ ,  $\underline{R}_2$  of the substrate are oriented such that  $\underline{R}_1$  points along the horizontal x axis, except for centered rectangular lattices where  $(\underline{R}_1 + \underline{R}_2)$  is assumed to point along x, see Fig. 3.49. The table entries 'any', 0, 45, and 90 denote allowed azimuthal angles (in degrees) of mirror (m) and glide (g) lines or planes relative to the substrate lattice while '--' refers to incompatible symmetries. Symmetry degenerate orientations, such as 120° rotations for hexagonal lattices, are not included in the list. The numbering sequence follows the scheme used in the ITC [33].

In addition to the compatibility rules given in Table 6.2, **overlayers** of the same structure can be **oriented differently** with respect to a substrate surface with symmetry, where the resulting over-



layer / substrate systems are energetically degenerate. At real crystal surfaces this degeneracy gives rise to **domain formation** where finite patches of the differently oriented overlayers coexist and can be observed by diffraction or imaging experiments [34], [94]. As an example, we consider the adsorption of carbon monoxide on the (1 1 1) surface of fcc platinum, where experimental studies [144], SSD 78.6.8.4, have yielded a  $\text{Pt}(1\ 1\ 1) + c(4 \times 2) - 2\text{CO}$  overlayer structure as shown in a perspective view in Fig. 6.40. Here CO molecules are placed at top and bridge sites above the

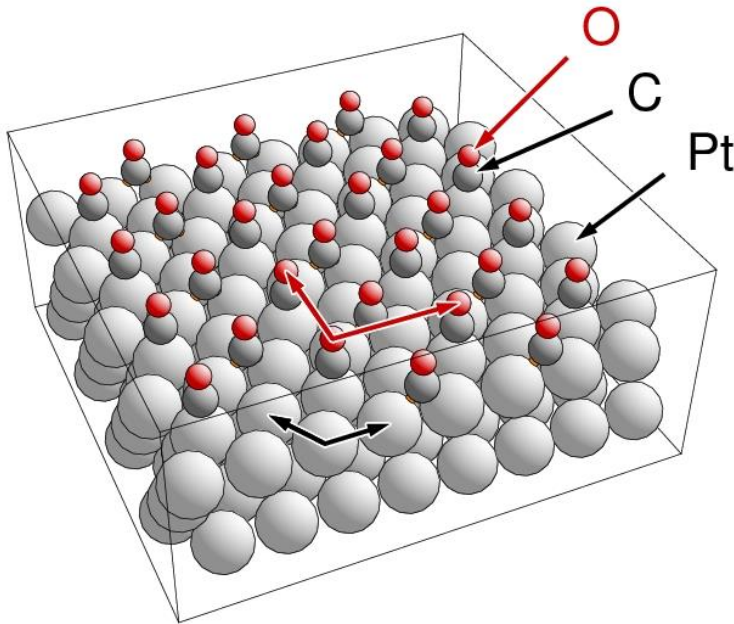


Fig. 6.40. Structure of the  $\text{Pt}(1\ 1\ 1) + c(4 \times 2) - 2\text{CO}$  adsorbate system. The periodicity vectors of the CO adsorbate layer and of the Pt substrate are shown in red and black, respectively.

hexagonal Pt surface layer, where the unit cell of the CO overlayer, containing two molecules, is rectangular with lattice vectors  $\underline{R}_1' = 2 \underline{R}_1$  and  $\underline{R}_2' = \underline{R}_1 + 2 \underline{R}_2$  defining the superlattice. The point symmetry elements of the overlayer are those of space group  $p2mm$  while the substrate symmetry is described by  $p3m1$ . This yields a combined two-dimensional symmetry pattern represented by space group  $p1m1$ . The symmetry is more evident in the view normal to the surface shown in Fig. 6.41. This figure shows the three energetically degenerate orientations of CO overlayers which are rotated by  $120^\circ$  with respect to each other as a consequence of the 3-fold rotational symmetry of the substrate lattice. Thus, the substrate symmetry gives rise to three different **rotational domains** on the real surface.

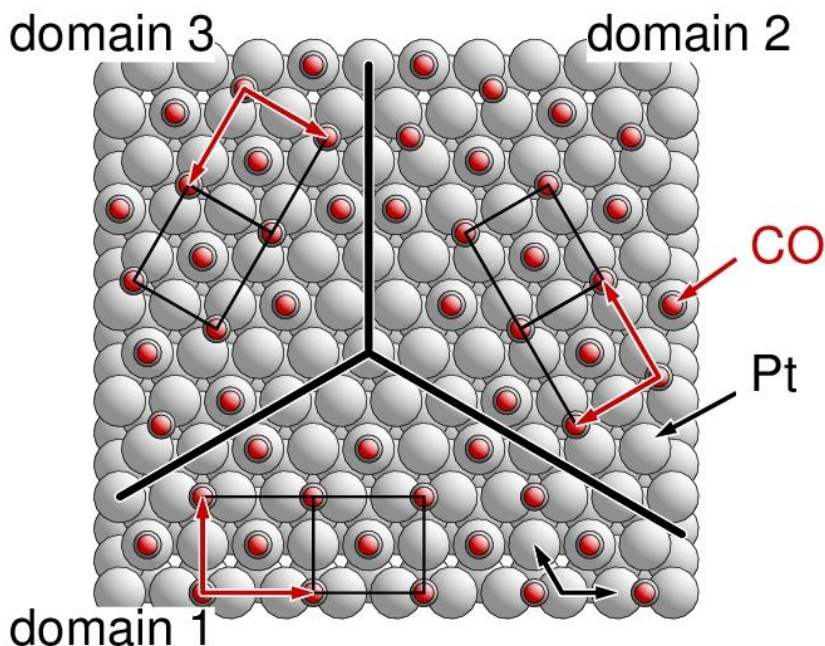


Fig. 6.41. Structure of rotational domains of the Pt(1 1 1) + c(4 × 2) - 2CO adsorbate system with the three equivalent rotational domains. The domains are separated by black lines.

Rotational domains of overlayers can appear whenever the substrate surface symmetry includes a rotation axis which is not shared by the overlayer. Domain formation can also be found for other symmetry elements of the substrate surface. A mirror plane of the substrate can induce two **mirrored domains** of overlayers as suggested by experiments for the Ni(1 1 0) + c(2 × 2) - CN adsorbate system [170], SSD 28.6.7.2, shown in Fig. 6.42. Here CN molecules are found to adsorb as tilted species at bridging sites along the topmost rows of Ni atoms with the tilt pointing always in the same direction laterally. This offers a second, energetically degenerate, geometric configuration where the tilt occurs to the other side, which can give rise to two mirrored domains. Actually, in the present system the two domains can be connected by a 2-fold rotation perpendicular to the surface and can, therefore, also be considered 2-fold rotational domains.

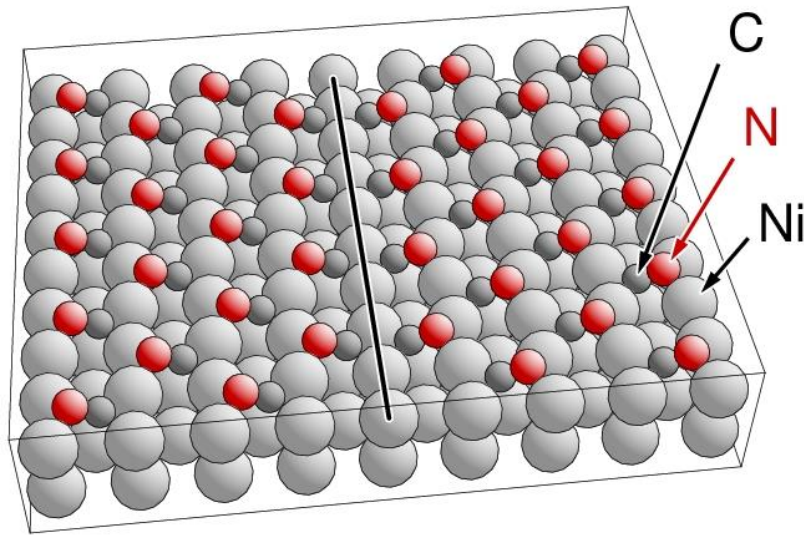


Fig. 6.42. Structure of mirror domains of the  $\text{Ni}(1\ 1\ 0) + c(2 \times 2)$  - CN adsorbate system. The two domains are separated by a black line.

Further, a glide line of the substrate surface can induce two **glide line domains** of overlayers which may also appear for the  $\text{Ni}(1\ 1\ 0) + c(2 \times 2)$  - CN adsorbate system [170] as illustrated in Fig. 6.43. Here the glide line operation creates a second, energetically degenerate, structure of the CN adsorbate with its tilt pointing to the other side with respect to the surface normal. This is combined with a shift by half an overlayer lattice vector along the glide line indicated by a red arrow in Fig. 6.43.

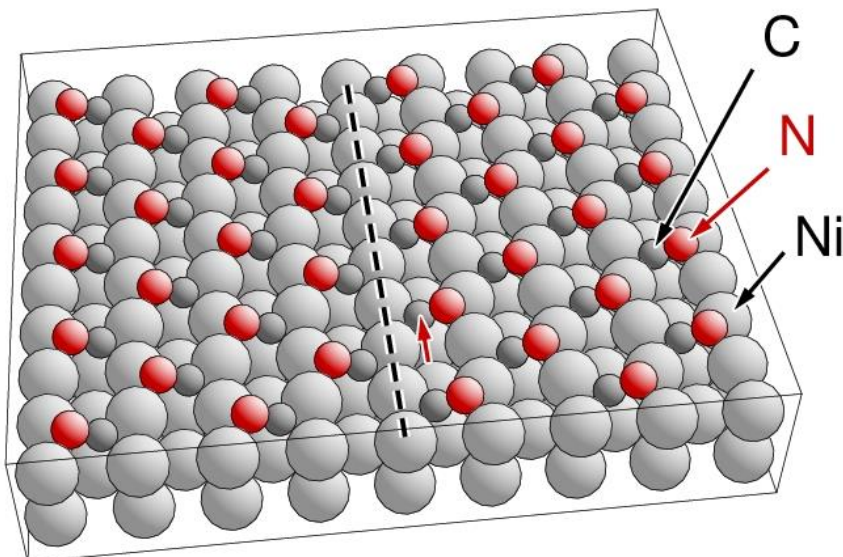


Fig. 6.43. Structure of glide line domains of the  $\text{Ni}(1\ 1\ 0) + c(2 \times 2)$  - CN adsorbate system. The domains are separated by a black dashed line. The shift vector along the glide line is indicated by a red arrow.

In addition to point symmetry elements of the substrate surface its translational symmetry can also induce different domains, so-called **translational domains**. As an example, we consider the adsorption of atomic hydrogen on the (1 1 0) surface of rhodium where experiments found a  $\text{Rh}(1\ 1\ 0) + (1 \times 3) - \text{H}$  adsorbate structure [171], SSD 45.1.5, as illustrated by Fig. 6.44. Here hydrogen atoms adsorb in 3-fold sites at the slopes of the (1 1 0) troughs of the rhodium surface. The hydrogen rows can be moved laterally in their perpendicular direction by a lattice vector of the substrate lattice, indicated by a red arrow in Fig. 6.44, to yield altogether three energetically degenerate configurations. This results in three different translational domains.

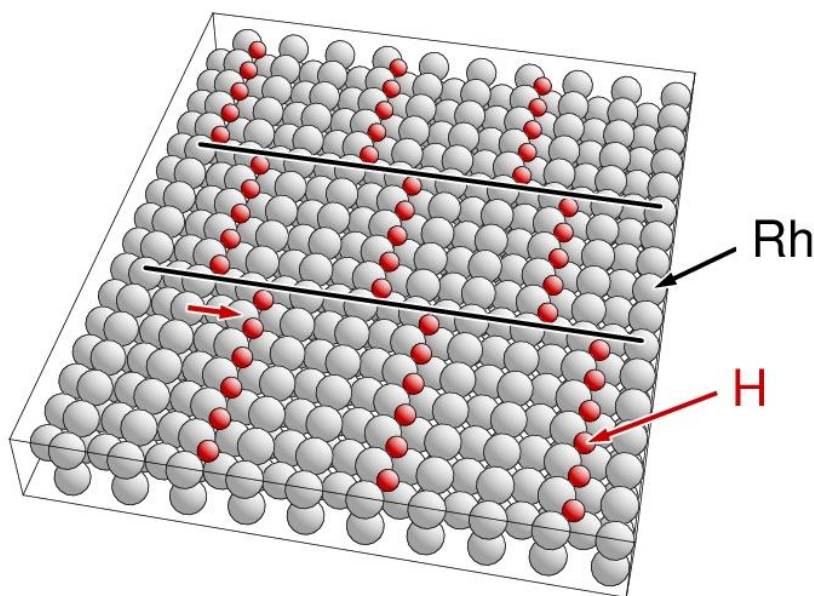


Fig. 6.44. Structure of translational domains of the  $\text{Rh}(1\ 1\ 0) + (1 \times 3) - \text{H}$  adsorbate system. The domains are separated by a black line with the shift vector indicated in red.

Another example of translational domains is given by the adsorption of atomic oxygen on the (1 1 0) surface of silver, where experiments show a  $\text{Ag}(1\ 1\ 0) + (2 \times 1) - \text{O}$  adsorbate structure [172], as illustrated by Fig. 6.45. Here oxygen atoms adsorb between silver atoms of the topmost rows of the  $(2 \times 1)$  reconstructed substrate forming rows of alternating Ag and O atoms. These rows may be shifted laterally in their perpendicular direction by a lattice vector of the substrate lattice, illustrated by a red arrow in Fig. 6.45, which yields an energetically degenerate configuration. The resulting two structures form different translational domains. While the two domains are completely equivalent the lateral shift between them, reflecting a structural phase inversion, can be observed in electron scattering experiments [34], [94] since it gives rise to scattering phase changes between adjacent domains. Therefore, these translational domains are sometimes also called **anti-phase do-**

mains.

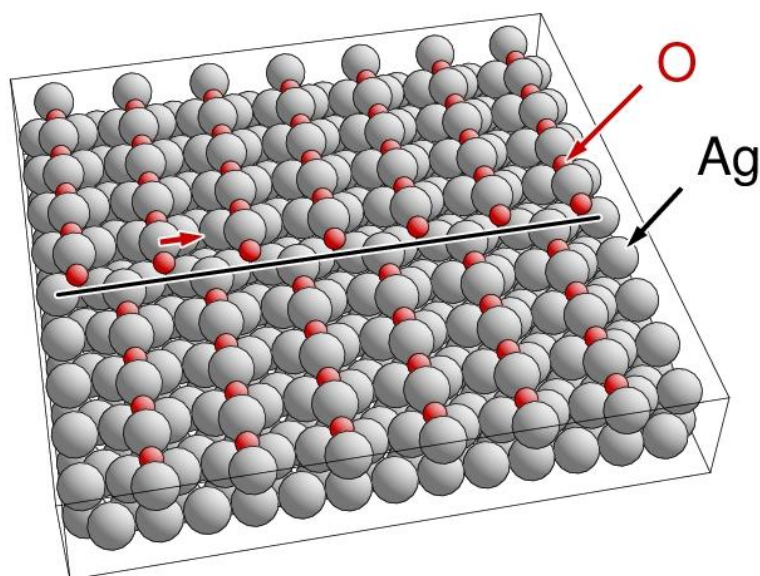


Fig. 6.45. Structure of translational (anti-phase) domains of the  $\text{Ag}(1\ 1\ 0) + (2 \times 1) - \text{O}$  adsorbate system. The domains are separated by a black line with the shift vector indicated in red.

## 6.7 Adsorption at Surfaces and Chirality

Structural aspects of adsorption involving chiral adsorbates as well as chiral substrate surfaces have attracted wide scientific interest because these systems have been found to show exciting physical and chemical properties which are also important for practical applications. Examples are enantioselective catalytic reactions which are used by the chemical industry to produce different drugs. In many cases, chiral adsorption systems refer to organic molecular adsorbates and/or kinked metal surfaces [173], [174], [175] where a large variety of structural elements have been observed. These can be rather complex and have to be studied on a case-by-case basis which goes far beyond the scope of this book. Therefore, this section focuses only on a few general guidelines and basic results that can be illustrated by simple examples.

The chirality of adsorbate systems can be classified into four different groups depending on the chirality of the overlayer and the substrate taken separately. Achiral or chiral overlayers may combine with achiral or chiral substrate surfaces. Here achiral overlayers on achiral substrate represent the simplest group while chiral overlayers on chiral substrate are the most complex.

The adsorption of **single achiral** molecules on an **achiral** surface can create either an achiral or a chiral adsorbate system depending on the adsorption site and on the orientation of the adsorbate at the surface. If the substrate and the adsorbate share a mirror plane perpendicular to the surface the combined adsorbate system is achiral. This is illustrated in Fig. 6.46 for ammonia adsorption on the Cu(1 1 1) surface where experiments for Cu(1 1 1) + (disordered) - NH<sub>3</sub> [124], SSD 29.7.1.3, yield at rather low coverage a disordered overlayer structure with NH<sub>3</sub> stabilizing with its nitrogen end at top sites of the metal substrate while positions of the hydrogen centers could not be determined. In Fig. 6.46a it is assumed that the NH<sub>3</sub> is structurally analogous to the free molecule with its 3-fold rotation axis perpendicular to the surface. The three hydrogen centers are rotated such that one of the three molecular mirror planes, indicated by a red line in Fig. 6.46a, coincides with a substrate mirror plane, parallel to the horizontal black line. As a consequence, a mirror operation with respect to the common mirror plane reproduces the adsorbate system and the system is **achiral**. It should be mentioned in passing that the adsorption of single atoms at mirror-symmetry sites of an achiral surface will always result in an achiral adsorbate system whereas other adsorption sites of the atom result in chirality.

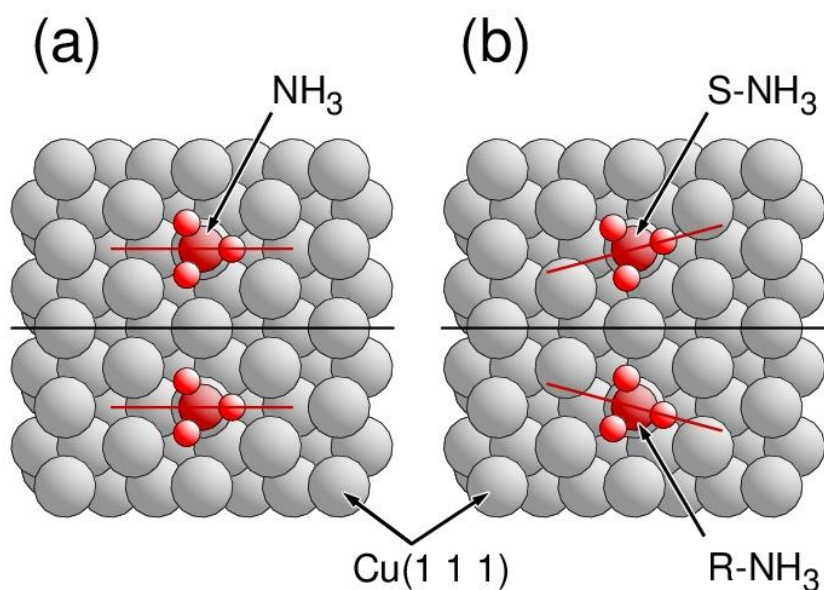


Fig. 6.46. Structure of the Cu(1 1 1) + (disordered)-NH<sub>3</sub> adsorbate system with ammonia in different orientation, (a) achiral and (b) chiral. The upper and lower parts of the figures show the adsorbate and its mirror image. The black line indicates a mirror plane perpendicular to the substrate surface while the red lines refer to mirror planes of the separate NH<sub>3</sub> adsorbate.

In Fig. 6.46b the upper half shows the NH<sub>3</sub> adsorbate at the top site where, however, the three hydrogen centers are rotated about the molecular rotation axis anti-clockwise by 15°, indicated by

the label S-NH<sub>3</sub>. As a consequence, the adsorbate does not share a mirror plane with the substrate surface. This is clear from comparing the upper red line in Fig. 6.46b, denoting a molecular mirror plane, with the horizontal black line referring to the closest mirror plane of the substrate. Thus, applying a mirror operation with respect to the mirror plane of the substrate leads to an adsorbate structure shown in the lower half of Fig. 6.46b with ammonia labeled R-NH<sub>3</sub>. The two adsorbate structures are different and cannot be brought into coincidence by rotation about the surface normal and/or translation. Thus, they are chiral partners and the adsorbate system is **chiral**. The structural difference between the two enantiomeric forms may be emphasized further by relaxation of the substrate and lifting of its mirror symmetry due to the presence of the asymmetrically positioned adsorbate. While the two enantiomers are energetically equivalent there may be an energy barrier between them which hinders easy transformation such that the two species become stable and can, at higher coverages, exist in well separated domains. For the present Cu(1 1 1)+NH<sub>3</sub> adsorbate system, this is difficult to observe and one would assume an achiral structure to be preferred since the asymmetric adsorbate structure may not reflect equilibrium. However, more complex achiral molecules are expected to yield adsorption with two enantiomeric structures which are well separated by energetic barriers and can be clearly identified.

So far, chirality was discussed as a local phenomenon occurring near the adsorbate site (**local chirality**). Chiral structures can also be formed by atoms or achiral molecules arranged as chiral clusters or islands at achiral surfaces, which can be considered as **cooperative chirality**. This is illustrated by Fig. 6.47 which shows a fictitious chiral arrangement of six NH<sub>3</sub> adsorbates on the Cu(1 1 1) surface together with its enantiomeric image where the two structures are denoted R-(NH<sub>3</sub>)<sub>6</sub> and S-(NH<sub>3</sub>)<sub>6</sub>.

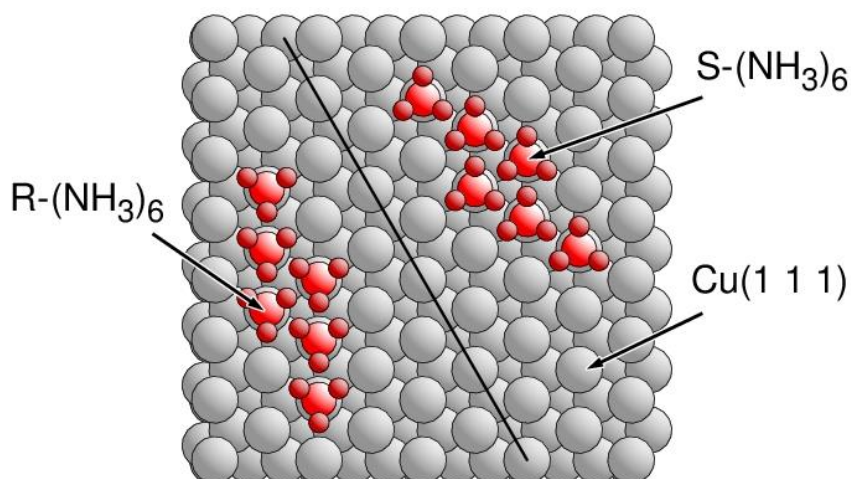


Fig. 6.47. Structure of the two enantiomers of a cooperative chiral arrangement of  $\text{NH}_3$  adsorbates on the  $\text{Cu}(1\ 1\ 1)$  surface, denoted  $\text{R}-(\text{NH}_3)_6$  and  $\text{S}-(\text{NH}_3)_6$ , in a view along the surface normal. The black line indicates a mirror plane perpendicular to the substrate surface.

Cooperative chirality at achiral surfaces can be obtained with both chiral and achiral adsorbates and is found for large molecular networks assembling at metal surface. A fairly complex example is rubrene adsorbed on the  $\text{Au}(1\ 1\ 1)$  surface [176]. This aromatic molecule,  $\text{C}_{42}\text{H}_{28}$ , combining tetracene with four phenyl rings, is chiral and can form large symmetric flower-like supramolecular structures with up to 150 molecules on the  $\text{Au}(1\ 1\ 1)$  surface where both left- and right-handed structures have been identified [176].

The adsorption of **single chiral** molecules on an **achiral** surface will always create a chiral adsorbate system with energetically equal or different enantiomeric structures. As an example, the adsorption of tartaric acid (TA),  $\text{C}_4\text{O}_6\text{H}_6$ , on the  $\text{Cu}(1\ 1\ 0)$  surface has been studied experimentally in great detail [174], [177], [178]. As discussed in Sec. 4.4, the free TA molecule contains two chiral carbon centers and forms two enantiomers, right-handed (R,R)-TA and left-handed (S,S)-TA, see Fig. 4.19. Upon adsorption the TA molecule is deprotonated, losing hydrogen from its opposite COOH ends, and the resulting tartrate,  $\text{C}_4\text{O}_6\text{H}_4$ , is distorted, bridging between the dense copper atom rows on the (1 1 0) surface with its two COO ends binding with copper along the rows. This is illustrated in Fig. 6.48 where the two tartrate adsorbates are labeled according to their free TA molecule enantiomers, (R,R)-TA and (S,S)-TA. As a consequence of the substrate symmetry the two species are expected to be energetically equivalent if they bind in symmetrically equivalent sites.



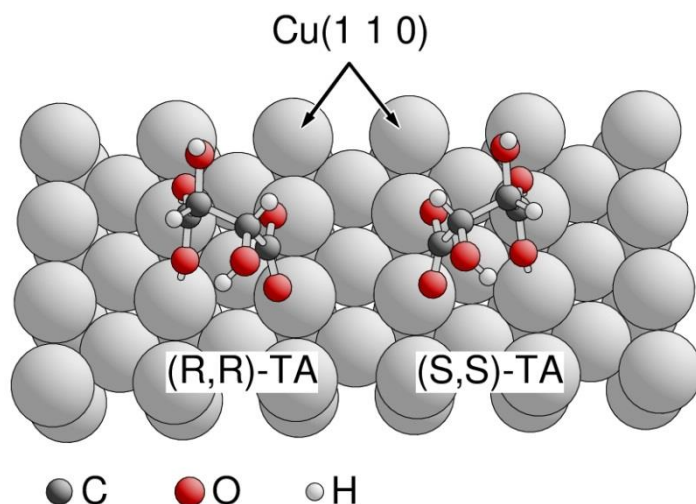


Fig. 6.48. Structure of the two enantiomers of tartrate, (R,R)-TA (left) and (S,S)-TA (right), adsorbed on the Cu(1 1 0) surface. The adsorbate atoms are color coded as explained at the bottom.

At higher adsorbate coverage chiral adsorbates can form ordered overlayer structures with different two-dimensional periodicity in larger domains. As an illustration, Fig. 6.49 shows the observed structures [177], [178] of **enantiopure** overlayers of the two chiral tartrate species (R,R)-TA and (S,S)-TA, on the Cu(1 1 0) surface. They refer to an adsorbate coverage  $\Theta = 16.7\%$  (1/6) and can be described as Cu(1 1 0) - (9 0 | 1 2) - 3(R,R)-TA and Cu(1 1 0) - (9 0 | -1 2) - 3(S,S)-TA in  $2 \times 2$  matrix notation. When mixtures of left- and right-handed tartrate are adsorbed on the Cu(1 1 0) surface the two species are found to form well separated enantiopure domains [178] with the geometric structures shown in Fig. 6.49. However, enantiomers may also mix at the surface to produce two-dimensionally periodic or randomly structured overlayers. The latter seems to occur for the adsorption of 1:1 (i.e. **racemic**) mixtures of left- and right-handed tartrate on the Cu(1 1 0) substrate where some patches suggest disorder [178].

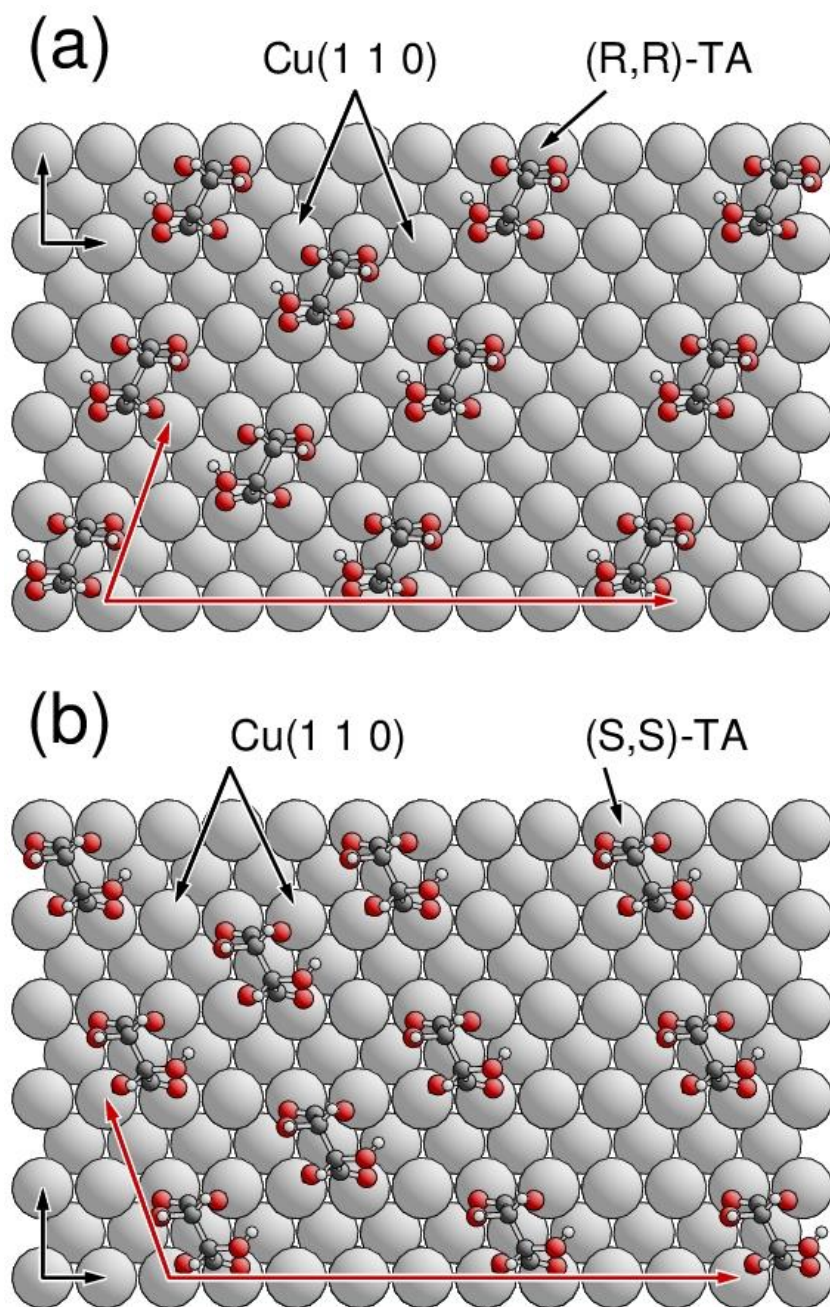


Fig. 6.49. Structure of enantiopure tartrate overlayers on the Cu(1 1 0) surface, (a) Cu(1 1 0)-(9 0 | 1 2)-(R,R)-TA and (b) Cu(1 1 0)-(9 0 | -1 2)-(S,S)-TA. The color coding of the adsorbate atoms is identical to that used in Fig. 6.48.

Fig. 6.48 illustrates further that the combined adsorption of the two (R,R)-TA and (S,S)-TA enantiomers on the Cu(1 1 0) surface leads to an achiral adsorbate pair and, thus, to an altogether achiral adsorbate system. This is a more general result which can be associated with **cooperative achi-rality** where clusters of chiral adsorbates with different chirality on an achiral substrate can result in an achiral adsorbate system.

The adsorption of single atoms or **single achiral** molecules on a **chiral** surface will always create a chiral system independent of the actual adsorption site or orientation of the adsorbate at the surface. Here the resulting chirality is determined by that of the substrate. However, at higher coverage achiral adsorbates may arrange as **chiral clusters** or islands reflecting cooperative chirality as discussed earlier. At chiral surfaces this leads to four different chiral conformations where the substrate / adsorbate combinations with equal handedness,  $\text{Sub}^{\text{R}} + \text{R-Ads}$  and  $\text{Sub}^{\text{S}} + \text{S-Ads}$ , form enantiomers as do combinations with opposite handedness,  $\text{Sub}^{\text{R}} + \text{S-Ads}$  and  $\text{Sub}^{\text{S}} + \text{R-Ads}$ . As an illustration, Fig. 6.50 shows kinked chiral iron surfaces described as left-handed  $\text{Fe}(25\ 20\ 3)^{\text{S}}$  and right-handed  $\text{Fe}(-25\ -20\ -3)^{\text{R}}$ , which form substrate enantiomers. These surfaces are both covered by two chiral islands of nine cobalt atoms each, denoted  $\text{R-Co}_9$  and  $\text{S-Co}_9$ , which are island enantiomers. Transitions between the two island types of these fictitious systems can be achieved by surface diffusion of cobalt along the substrate terraces, oriented  $(1\ 1\ 0)$  for  $\text{Fe}(25\ 20\ 3)^{\text{S}}$  and  $(-1\ -1\ 0)$  for  $\text{Fe}(-25\ -20\ -3)^{\text{R}}$ . As a result of differences in the adsorbate sites and binding the two island enantiomers at the left-handed substrate surface, Fig. 6.50a, are energetically different, which also holds for the right-handed substrate surface, Fig. 6.50b. However, for symmetry reasons the  $\text{S-Co}_9$  island at  $\text{Fe}(25\ 20\ 3)^{\text{S}}$  and the  $\text{R-Co}_9$  island at  $\text{Fe}(-25\ -20\ -3)^{\text{R}}$  are energetically equivalent, which is also true for  $\text{R-Co}_9$  at  $\text{Fe}(25\ 20\ 3)^{\text{S}}$  and  $\text{S-Co}_9$  at  $\text{Fe}(-25\ -20\ -3)^{\text{R}}$ .

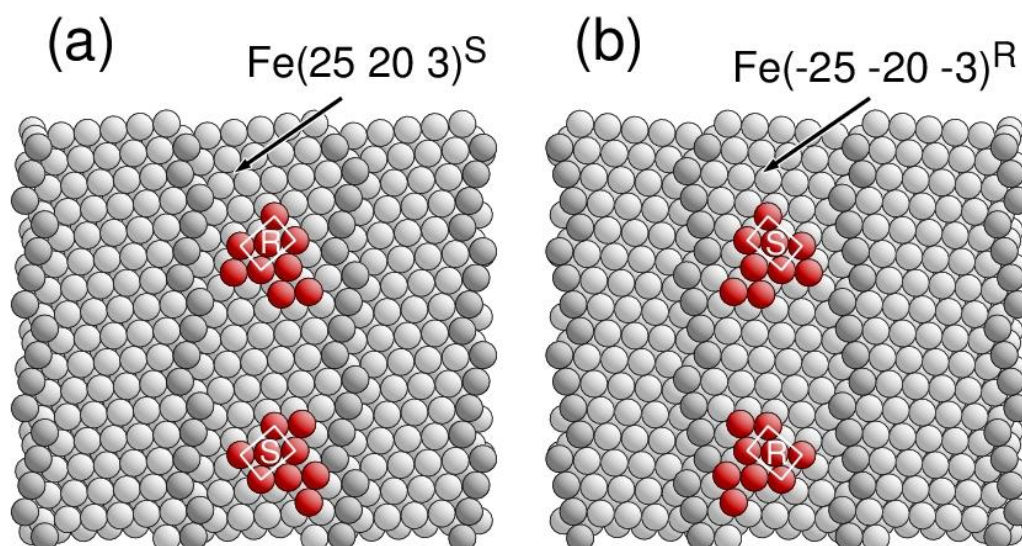


Fig. 6.50. Structure of chiral cobalt islands,  $\text{R-Co}_9$  and  $\text{S-Co}_9$ , at a kinked chiral iron surface, (a) left-handed  $\text{Fe}(25\ 20\ 3)^{\text{S}}$  and (b) right-handed  $\text{Fe}(-25\ -20\ -3)^{\text{R}}$ . Adsorbate (substrate) atoms are shown in red (gray) with those along the kink lines emphasized in dark gray. The islands are denoted R for right- and S for left-handed and their orientations are outlined by white rectangles.

The adsorption of **single chiral** molecules on a **chiral** surface will always create a chiral system. Assuming adsorbates with only one chiral center leads to an overall chiral adsorbate system with four different conformers, completely analogous to the discussion for cooperative chirality of chiral clusters at chiral surfaces. For the following, we consider chiral substrates, represented by kinked vicinal surfaces, right-handed  $\text{Sub}(h\ k\ l)^{\text{R}}$  and left-handed  $\text{Sub}(h\ k\ l)^{\text{S}}$ , and chiral adsorbates R-Ads and S-Ads. For vicinal surfaces with wide (locally achiral) terraces between the chiral kink lines we can distinguish two different scenarios. First, chiral adsorbates may stabilize at terrace sites far away from the kink sites. Then the handedness of the substrate may be irrelevant. Thus, the discussion of local chiral behavior is analogous to that of chiral molecules at achiral surfaces. Second, chiral adsorbates may stabilize near kink sites forming the chiral substrate centers. Here all four conformers need to be considered and can lead to different structural behavior.

As an example, the adsorption of chiral fluoro-amino-methoxy (FAM) on the kinked copper surface  $\text{Cu}(8\ 7\ 4)$  has been examined in theoretical (DFT) studies [179] where it was found that stabilization near the chiral centers of the kink lines is energetically preferred. The free FAM molecule,  $\text{FNH}_2\text{CHO}$ , with a chiral carbon center, is distorted by adsorption such that its nitrogen end binds on top of a kink atom of the copper substrate while its oxygen end binds at a 3-fold fcc site near the kink edge, as shown on Fig. 6.51. This basic binding scheme is independent of the chirality of the adsorbate. However, further structural details are quite different between the adsorbed R-FAM and S-FAM enantiomers. At the right-handed  $\text{Cu}(8\ 7\ 4)^{\text{R}}$  surface, Fig. 6.51a, the left-handed S-FAM bends over the kink edge with a CH group sticking out of the surface and its C-F bond pointing towards the lower terrace. In contrast, the right-handed R-FAM, while bending over the kink edge, stabilizes with its fluorene sticking out of the surface and its CH group pointing towards the lower terrace. For both adsorbates the local surface structure is also affected by relaxation of the substrate atoms near the adsorption site. At the left-handed  $\text{Cu}(-8\ -7\ -4)^{\text{S}}$  surface, Fig. 6.51b, the equilibrium structures of the adsorbates are complementary to those at the  $\text{Cu}(8\ 7\ -4)^{\text{R}}$  surface, with a C-F bond parallel and a C-H bond perpendicular to the substrate surface for R-FAM and viceversa for S-FAM. This creates, altogether, four adsorbate structures which can interact differently with approaching reactants.

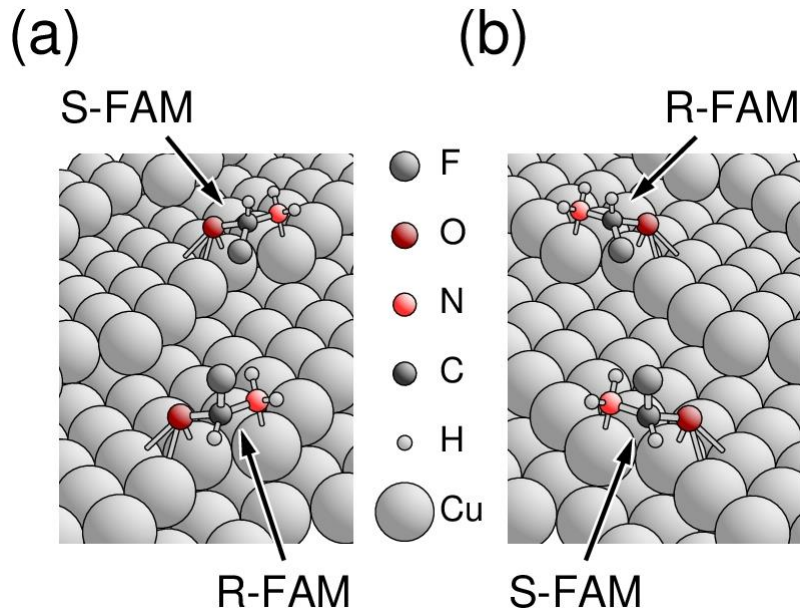


Fig. 6.51. Structure of chiral fluoro-amino-methoxy (FAM) adsorbates at chiral centers of a kinked copper surface, (a) right-handed  $\text{Cu}(8\ 7\ 4)^{\text{R}}$ , (b) left-handed  $\text{Cu}(-8\ -7\ -4)^{\text{S}}$ . Both figures include the two adsorbate enantiomers, R-FAM and S-FAM labeled accordingly. The color coding of the atoms is explained between the figures. The figures illustrate the general adsorption behavior but do not reflect exact computed atom coordinates.

## 6.8 Exercises

- 6.1. Consider the unrelaxed  $(0\ 0\ 1)$  surface of a tungsten single crystal (bcc lattice, lattice constant  $a = 3.160\ \text{\AA}$ ) with sulfur atoms adsorbed in a  $c(2 \times 2)$  overlayer. Sulfur is assumed to adsorb in hollow sites at a distance from the nearest tungsten atoms of  $d(\text{W-S}) = 2.456\ \text{\AA}$ . Discuss structural details of the adsorbate system. Evaluate neighbor shells of the adsorbate center.
- 6.2. Consider unrelaxed surfaces of a nickel single crystal (fcc lattice, lattice constant  $a = 3.520\ \text{\AA}$ ) with CO adsorbed in periodic overlayers (interatomic distance  $d(\text{C-O}) = 1.137\ \text{\AA}$ ). Discuss adsorbate structure and symmetry at the surface for adsorbate systems
  - (a)  $\text{Ni}(1\ 0\ 0) + c(2 \times 2) - \text{CO}$  ; perpendicular CO in on top positions ,
  - (b)  $\text{Ni}(1\ 1\ 0) - (2 \times 1) + (2 \times 2) - \text{CO}$  ; Ni substrate missing row reconstructed, tilted CO in bridge positions above topmost Ni rows ,

- (c)  $\text{Ni}(1\ 1\ 1) + (\sqrt{3} \times \sqrt{3})R30^\circ - \text{CO}$  ; CO in bridge positions ,
- (d)  $\text{Ni}(1\ 1\ 0) - p2mg(2 \times 1) + (2 \times 2) - 2\text{CO}$  ; tilted CO in bridge positions above topmost Ni rows , analogous to structure shown in Fig. 6.2,
- (e)  $\text{Ni}(1\ 1\ 1) + c(4 \times 2) - \text{CO}$  ; perpendicular CO in hollow positions .

Assume, for all systems, CO adsorption with carbon pointing towards the substrate with a distance  $d(\text{Ni-C}) = 1.840 \text{ \AA}$  and tilt angles of  $15^\circ$ .

- 6.3. Consider the unreconstructed  $(1\ 1\ 1)$  surface of a silicon single crystal (diamond lattice, lattice constant  $a = 5.431 \text{ \AA}$ ) with hydrogen atoms in a  $(1 \times 1)$  overlayer adsorbed at on top positions (hydrogen ‘terminators’). Evaluate neighbor shells of the hydrogen center up to 6<sup>th</sup> nearest neighbors assuming an adsorbate distance  $d(\text{H-Si}) = 1.000 \text{ \AA}$ .
- 6.4. Consider the  $(0\ 0\ 1)$  surface of a copper single crystal (fcc lattice, lattice constant  $a = 3.610 \text{ \AA}$ ) with atomic oxygen adsorbed

- (a) in an ideal  $c(2 \times 2)$  overlayer structure with oxygen in 4-fold centered hollow sites at a perpendicular distance  $z(\text{O-Cu}) = 0.800 \text{ \AA}$  from the topmost Cu layer, see Fig. 6.52.

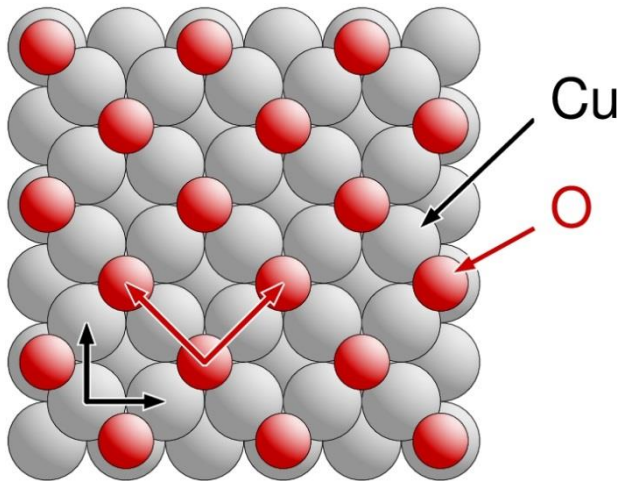


Fig. 6.52. Structure of the  $\text{Cu}(0\ 0\ 1) + c(2 \times 2) - \text{O}$  adsorbate system. Substrate and adsorbate lattice vectors are indicated in red and black.

- (b) in a  $(2\sqrt{2} \times \sqrt{2})R45^\circ$  overlayer with the topmost Cu layer  $(2\sqrt{2} \times \sqrt{2})R45^\circ$  missing row reconstructed, see Fig. 6.53. Oxygen is assumed to adsorb at 3-fold centered hol-

low sites of the reconstructed substrate layer (substrate atoms Cu' in Fig. 6.53, perpendicular distance  $z(\text{O}-\text{Cu}) = 0.700 \text{ \AA}$ ).

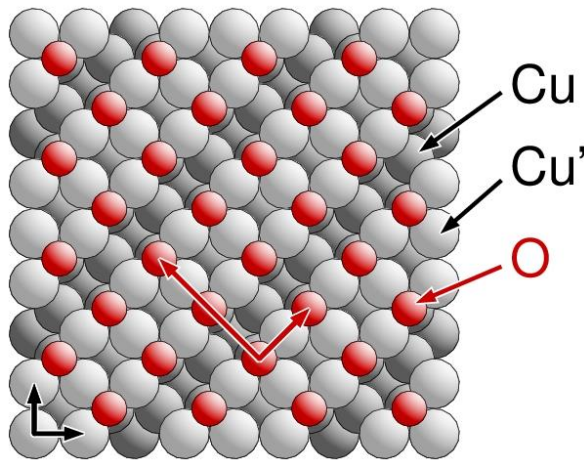


Fig. 6.53. Structure of the  $\text{Cu}(0\ 0\ 1) - (2\sqrt{2} \times \sqrt{2})R45^\circ + 2\text{O}$  adsorbate system. Substrate and adsorbate lattice vectors are indicated in red and black.

Describe both systems in  $2 \times 2$  matrix notation. Determine symmetry elements of the surfaces and evaluate corresponding space groups. Evaluate neighbor shells of the adsorbate centers.

- 6.5. Consider the (1 1 1) surface of a palladium single crystal (fcc lattice, lattice constant  $a = 3.890 \text{ \AA}$ ) with atomic xenon adsorbed in a hexagonal overlayer (interatomic distance  $d(\text{Xe}-\text{Xe}) = 4.384 \text{ \AA}$ ). One lattice vector of the Xe overlayer is assumed to be co-linear with one lattice vector of the topmost Pd substrate layer. Further, one Xe atom is assumed to adsorb in on top position. Determine minimum and maximum Xe-Pd neighbor distances for a planar Xe overlayer.
- 6.6. Consider the (1 1 1) surface of an aluminum single crystal (fcc lattice, lattice constant  $a = 4.050 \text{ \AA}$ ) with carbon dioxide,  $\text{CO}_2$ , adsorbed at very low coverage  $\Theta$ . Discuss possible structures with commensurate overlayers and determine supercells with corresponding  $2 \times 2$  matrices and Wood notations. Calculate intermolecular distances at the surface. Discuss possible adsorbate sites.
- 6.7. Consider the stepped (1 1 3) surface of a silver single crystal (fcc lattice, lattice constant  $a = 4.090 \text{ \AA}$ ) with sulfur atoms adsorbed at very low coverage  $\Theta$ . Assume adsorbate structures to be described by a model of hard spheres. Here interatomic distances  $d(\text{S}-\text{Ag})$  are determined by touching spheres of radii corresponding to the covalent radii  $r_{\text{cov}}$  of the atoms

involved, where  $r_{\text{cov}}(\text{Ag}) = 1.45 \text{ \AA}$ ,  $r_{\text{cov}}(\text{S}) = 1.02 \text{ \AA}$ . Determine perpendicular distances  $z$  of the adsorbate at different substrate positions (on top, bridge, central sites; at terraces, near steps). Here perpendicular distances  $z$  are defined with respect to the normal vector of the (1 1 3) surface. For which structure is  $z$  smallest?

- 6.8. Consider sulfur adsorption with a  $(5 \times 5)$  coincidence lattice on the unrelaxed Ag(1 1 1) surface in a model of hard spheres as in Exercise 6.7 using the same structure parameters. Determine possible symmetric structures with 9, 16, 25, 36, 49 sulfur atoms in the coincidence supercell. Calculate interatomic distances  $d(\text{S-S})$  accounting for possible buckling of the sulfur layer according to the model of hard spheres.
- 6.9. Determine the Wood notation of the adsorbate systems defined by  $2 \times 2$  matrix notation as
- |  |                                   |
|--|-----------------------------------|
| (a) Cu(1 0 0) + (1 1   -1 1) - O               | (b) Ni(1 1 1) + (1 2   -1 1) - CO |
| (c) Ni(1 1 1) + (4 1   -1 3) - NH <sub>3</sub> | (d) Pd(1 1 0) + (1 1   -1 2) - NO |
| (e) W(1 1 0) + (2 2   -2 4) - O                | (e) W(1 1 1) + (6 1   -1 5)       |

Determine adsorbate coverages  $\Theta$  of these adsorbate systems.

- 6.10. Quantify Wood notation parameters  $p$ ,  $\alpha$  of commensurate surface overlayers at different crystal faces
- |   |   |
|---|---|
| (a) fcc(1 1 1) + $(\sqrt{3} \times p)R\alpha$ - ...         | (b) fcc(1 1 1) + $(p \times \sqrt{(7/2)})R\alpha$ - ...       |
| (c) fcc(1 1 1) + $(p \times p)R13.898^\circ$ - ...          | (d) fcc(1 1 1) + $c(p \times 4p)R7.598^\circ$ - ...           |
| (e) fcc(1 1 0) + $(2\sqrt{3} \times \sqrt{3})R\alpha$ - ... | (f) fcc(1 1 0) + $(3\sqrt{2} \times 3/\sqrt{2})R\alpha$ - ... |
| (g) fcc(1 0 0) + $(\sqrt{5} \times \sqrt{5})R\alpha$ - ...  | (h) fcc(1 0 0) + $(p \times 2p)R26.565^\circ$ - ...           |
| (i) bcc(1 1 0) + $c(3 \times 5)R\alpha$ - ...               | (j) bcc(1 0 0) + $(5 \times 5) R\alpha^\circ$ - ...           |
- 6.11. Consider the adsorbate system Ni(1 1 1) +  $(\sqrt{3} \times \sqrt{3})R30^\circ$  - CO where CO adsorbs in bridge positions with its molecular axis (a) perpendicular, (b) parallel to the surface. Identify possible rotational and mirror domains. Evaluate corresponding  $2 \times 2$  matrices connecting the lattice vectors of each domain with those of the substrate.
- 6.12. Consider benzene, C<sub>6</sub>H<sub>6</sub>, adsorption on the (1 1 1) surface of a substrate with an fcc lattice. Give examples of commensurate overlayers for different coverage and orientations of the adsorbate which allow 2, 3, and 6 domains at the surface.
- 6.13. Show that the (1 0 0) surface of an ideal fcc or bcc single crystal cannot have commensurate overlayers with hexagonal lattice. Hint: use results from Appendix E.4.



- 6.14. Show that the (1 1 0) surface of an ideal fcc or bcc single crystal cannot have commensurate overlayers with hexagonal lattice. Hint: use results from Appendix E.4.
- 6.15. Assume that a substrate surface has two overlayers with different lattice where both overlayers are commensurate with respect to the substrate. Show that the overlayers are in general high-order commensurate with respect to each other. When are they (1<sup>st</sup> order) commensurate?
- 6.16. Consider an overlayer on top of a substrate layer with given Bravais lattice type (square, rectangular, hexagonal). Which lattice types are allowed for the overlayer to be commensurate?
- 6.17. Show that all commensurate hexagonal overlayers on top of hexagonal substrate can be described in Wood notation as  $(p \times p)R\alpha$  with  $p = \sqrt{(m^2 + n^2 + mn)}$  and  $\tan(\alpha) = 3n / (2m + n)$  where  $m, n$  are integers. Determine corresponding  $2 \times 2$  transformation matrices between overlayer and substrate lattice vectors. Discuss acute and obtuse representations of the hexagonal lattice.
- 6.18. Consider a commensurate overlayer (lattice vectors  $\underline{R}_{o1}'$  and  $\underline{R}_{o2}'$ ) on top of hexagonal substrate with lattice vectors  $\underline{R}_{o1}$  and  $\underline{R}_{o2}$  in acute representation. Show that the transformation according to

$$\begin{pmatrix} \underline{R}_{o1}' \\ \underline{R}_{o2}' \end{pmatrix} = \begin{pmatrix} m & n \\ -n & m+n \end{pmatrix} \begin{pmatrix} \underline{R}_{o1} \\ \underline{R}_{o2} \end{pmatrix}, \quad m, n \text{ integer}$$

results in a hexagonal overlayer lattice.

- 6.19. Consider a high-order commensurate (HOC) overlayer with square lattice vectors  $\underline{R}_{o1}'$  and  $\underline{R}_{o2}'$  on top of substrate with square lattice vectors  $\underline{R}_{o1}$  and  $\underline{R}_{o2}$ .

(a) Show that in the lattice vector transformation can be written as

$$\begin{pmatrix} \underline{R}_{o1}' \\ \underline{R}_{o2}' \end{pmatrix} = \begin{pmatrix} m' & n' \\ -n' & m' \end{pmatrix}^{-1} \begin{pmatrix} m & n \\ -n & m \end{pmatrix} \begin{pmatrix} \underline{R}_{o1} \\ \underline{R}_{o2} \end{pmatrix}, \quad m, n, m', n' \text{ integer}$$

- (b) Assume further that the vector lengths of  $\underline{R}_{o1}'$  and  $\underline{R}_{o1}$  are identical and show that the matrix elements  $m, n, m', n'$  must be solutions of the Diophantine equation

$$m^2 + n^2 = m'^2 + n'^2$$

- 6.20. Consider a high-order commensurate (HOC) overlayer with hexagonal lattice vectors  $\underline{\mathbf{R}}_{o1}'$  and  $\underline{\mathbf{R}}_{o2}'$  on top of hexagonal substrate with lattice vectors  $\underline{\mathbf{R}}_{o1}$  and  $\underline{\mathbf{R}}_{o2}$  (both lattices in acute representation). Assume further that the vector lengths of  $\underline{\mathbf{R}}_{o1}'$  and  $\underline{\mathbf{R}}_{o1}$  are identical. Show that in the corresponding transformation according to (6.27) the integer parameters  $m, n, m', n'$  must be solutions of the Diophantine equation

$$m^2 + n^2 + mn = m'^2 + n'^2 + m'n'$$

- 6.21. Show that a commensurate hexagonal overlayer with lattice vectors  $\underline{\mathbf{R}}_{o1}'$  and  $\underline{\mathbf{R}}_{o2}'$  on hexagonal substrate with lattice vectors  $\underline{\mathbf{R}}_{o1}$  and  $\underline{\mathbf{R}}_{o2}$  (both lattices in obtuse representation) can be described by a transformation

$$\begin{pmatrix} \underline{\mathbf{R}}_{o1}' \\ \underline{\mathbf{R}}_{o2}' \end{pmatrix} = \begin{pmatrix} m & n \\ -n & m-n \end{pmatrix} \begin{pmatrix} \underline{\mathbf{R}}_{o1} \\ \underline{\mathbf{R}}_{o2} \end{pmatrix}, \quad m, n \text{ integer}$$

- 6.22. Consider an overlayer structure where the substrate is Wood-representable and the overlayer is stretched with respect to the substrate along direction  $\underline{\mathbf{e}}$  by a factor  $\gamma$ . For which directions  $\underline{\mathbf{e}}$  and Bravais lattice types is the overlayer structure Wood-representable?
- 6.23. Relations (6.86) can be inverted to compute the parameters  $\gamma, \alpha$  of a  $p(\gamma \times \gamma)\mathbf{R}\alpha$  overlayer structure from (measured) moiré parameters  $\lambda, \varphi$ . Determine the inverted relationships and prove that

$$\gamma = \frac{\lambda}{\sqrt{\Delta'}}, \quad \cos(\alpha) = \frac{\cos(\varphi) + d\lambda}{\sqrt{\Delta'}}, \quad \Delta' = 1 + d^2\lambda^2 + 2d\lambda \cos(\varphi)$$

- 6.24. Well separated moiré patterns are observed for moiré factors  $\lambda > 5$ . Consider isotropically scaled and rotated overlayers with an integer approximant  $\underline{\mathbf{M}}_I = \underline{\mathbf{1}}$  and evaluate the range of scaling factors  $\gamma$  and rotation angles  $\alpha$  which fulfill the condition  $\lambda > 5$ .

## 7 EXPERIMENTAL ANALYSIS OF REAL CRYSTAL SURFACES

### 7.1 Experimental Methods

**Truly quantitative** structure determinations of single crystal surfaces and adsorbate systems by experiment are intrinsically **difficult**. While three-dimensionally periodic bulk crystal structures can be measured routinely with the help of X-ray diffraction methods, a complete surface structure analysis requires usually a **combination of different experimental methods** to yield a unique result. Methods that can contribute to a quantitative analysis of structural details of real crystal surfaces must be able to probe **mainly** atoms **near the surface**, ignoring those of the inner substrate. This excludes standard X-ray diffraction methods from surface analyses. X-ray photons can penetrate deep in to the bulk and, therefore, yield structural bulk information, with that from surface atoms representing only a minor perturbation. However special geometric arrangements of the **X-ray** beam with respect to the single crystal surface, so-called **grazing incidence** geometry [34], can also yield structural information pertaining to the surface. Other diffraction methods, such as low energy electron diffraction (**LEED**), have proven to be particularly useful in identifying surface structure. These methods rely on the interference of particles that scatter (often multiple times) from periodic arrangements of atoms at single crystal surfaces which are ordered over a relatively wide area. If the surface structure deviates strongly from periodic ordering, for example, as a result of large size imperfections or disordered adsorbate structure, local (small-area) diffraction becomes more useful. For these systems local diffraction methods, such as photoelectron diffraction (**PED**) or surface extended X-ray absorption fine structure (**SEXAFS**), can be used to obtain quantitative information about local environments of surface atoms including coordination and binding angles.

**In general**, methods that can provide information about structural details at real crystal surfaces and adsorbate systems include those based on **scattering, diffraction, imaging**, as well as **spectroscopy**, and use **photons, electrons, or atoms and ions**. A detailed discussion of each method as well as of its merits in connection with quantitative determination of surface structure is beyond the scope of this book. Corresponding methods are well documented in the **surface science** literature, see e.g. Refs. [34], [94], [180]. In Table 7.1 we list only example methods by their names where the list may not be exhaustive.

Table 7.1. Experimental methods used to determine surface structure. The methods are given by their names, where capital letters in the names are meant to explain the acronyms included in the table. Details of the different methods are given, for example, in Ref. [34].

<b>Method by name</b>	<b>Acronym</b>
<b>(a) Imaging methods</b>	
Scanning Tunneling Microscopy	STM
Atomic Force Microscopy	AFM
Transmission Electron Microscopy	TEM
<b>(b) Diffraction methods</b>	
Low Energy Electron Diffraction	LEED
Medium Energy Electron Diffraction	MEED
Reflection High Energy Electron Diffraction	RHEED
Transmission Electron Diffraction	TED
Low Energy Positron Diffraction	LEPD
PhotoElectron Diffraction	PED
X-Ray Diffraction	XRD
(Surface) Extended X-ray Absorption Fine Structure	(S)EXAFS
Grazing Incidence X-Ray Diffraction	GI-XRD
X-ray Standing Wavefield absorption	XSW
Atom diffraction	AD
<b>(c) Scattering methods</b>	
High-Resolution Helium Atom Scattering	HRHAS
Low Energy Ion Scattering	LEIS / IS
Medium Energy Ion Scattering	MEIS / IS
High Energy Ion Scattering	HEIS / IS
Thermal Energy Atom Scattering	TEAS
Inelastic Molecular Beam Scattering	IMBS
Time-Of-Flight Scattering And Recoiling Spectroscopy	TOF-SARS
<b>(d) Spectroscopy methods</b>	
Near-Edge X-ray Absorption Fine Structure or X-ray Absorption Near-Edge Spectroscopy	NEXAFS XANES
(High-Resolution) Electron Energy Loss Spectroscopy	(HR)EELS
Surface Electron Energy Loss Fine Structure	SEELFS
(Fourier Transform) Reflection Absorption Infrared Spectroscopy	(FT)RAIRS

## 7.2 Surface Structure Compilations

As a result of the experimental **complexity** the number of **quantitatively** solved surface structures is rather **small** compared to that of bulk crystal structures. As of 2012, more than 800,000 bulk crystal structures have been published and stored in crystal structure databases, such as CSD (Cambridge Structural Database) [181], ICSD (Inorganic Crystal Structure Database) [182], Crystmet [183], NAD (Nucleic Acid Database) [184], or PDB (Protein Data Bank) [185]. In contrast, as of 2004 (when there were about 400,000 published bulk crystal structures) the NIST Surface Structure Database (SSD) listed only about 1400 surface structures that are quantitatively complete in all details, with an estimated additional 150 structures published between 2004 and 2014.

A number of compilations of crystallographic information on surfaces and interfaces have been published in the literature or are available in electronic form. Early tabulations by Somorjai and Van Hove [36] give mostly **two-dimensional** structure information, i.e. lateral periodicity patterns, of ordered monolayers of atoms and molecules with only few results of three-dimensional parameters. Examples are adsorbate layer spacings and adsorption bond lengths. Here the lateral periodicity was derived mainly from LEED measurements. A more detailed listing of **three-dimensional** structure parameters with many early literature references is included in the LEED book by Van Hove et al. [94]. The structure information in the review by Ohtani et al. [186] with an extensive list of references for surfaces with and without ordered adsorbates is strictly **two-dimensional** describing the surfaces only by their lateral symmetry pattern. Most of the tables of [186] can also be found in the textbook by Somorjai [12].

More recent **three-dimensional** structure parameters have been published in the **Atlas of Surface Structures** [23] based on data of the electronic **NIST Surface Structure Database**, Version 1, discussed below which includes all quantitatively known surface structures until 1991. The second volume of this Atlas also gives graphical representations of the surfaces yielding a good qualitative overview of the structures examined at that time. (Many of these structures are still relevant at present.) Further, a review chapter of the **Landolt-Börnstein Series** [187] lists quantitative structure parameters from experiments on adsorbates at metal and semiconductor surfaces where the data are complete until 2002.

Another resource of quantitative surface structure data is the **Surface Crystallographic Information Service (SCIS)** where the printed version [25] includes references until the end of 1987. The SCIS book was complemented by database software allowing an easy search and basic visualization of published surface structure on a personal computer. The SCIS software was updated in a second version to include references until the end of 1992. The SCIS software project was succeeded by the development of the **NIST Surface Structure Database (SSD)** which was published and distributed by the National Institute of Science and Technology (NIST) between 1992 and 2010 with biennial updates until the end of 2003. The distribution of the latest version 5 of SSD by NIST has been discontinued but it remains available as an open source database (**open SSD**, oSSD) and can be downloaded from the web, see Appendix H. Complete compilations of quantitative surface structure data published after 2004 have not yet appeared in the literature.

So far, the NIST Surface Structure Database (**SSD**) [22], [23], [24] is the only **complete critical compilation** of reliable crystallographic information available on surfaces and interfaces. The database provides access to detailed text and graphical information for 1379 experimentally determined atomic-scale structures which have been published until 2004 (SSD version 5). It can be considered to cover all **classical** surface structures which have not been revised after 2004 or have only experienced very minor modifications in distances or angles since then. More recent published surface structures, which are not included in SSD, concern mainly single crystal surfaces with rather complex reconstruction and/or large molecules or molecular networks [188], [189]. An example is shown in Fig. 7.1 where scanning tunneling microscopy (STM) measurements together with theoretical DFT studies have identified large organic molecules, 1,3,5-tris(pyridyl)benzene (TPyB) forming an ordered hexagonal network on the hexagonal Cu(1 1 1) surface [190] which is described in Wood notation as  $\text{Cu}(1\ 1\ 1) - (6\sqrt{3} \times 6\sqrt{3})R30^\circ + 2\text{TPyB} - 3\text{Cu}$ .

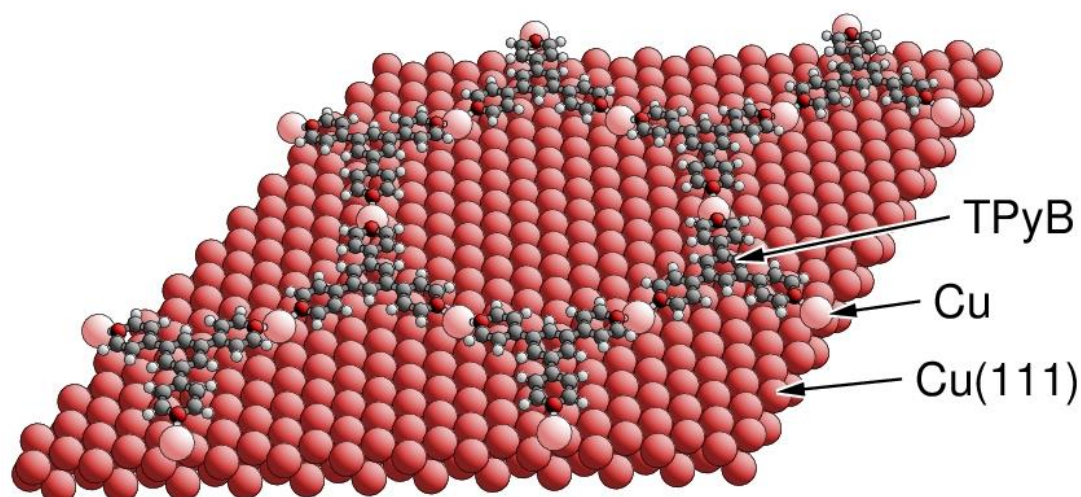


Fig. 7.1. Structure of a molecular adsorbate network on copper substrate described as  $\text{Cu}(1\ 1\ 1) - (6\sqrt{3} \times 6\sqrt{3})R30^\circ + 2\text{TPyB} - 3\text{Cu}$ . The adsorbate atoms are shown in different size and color, small / dark gray for carbon, small / dark red for nitrogen, very small / light gray for hydrogen, and large / light red for adsorbate copper. Substrate copper is shown by large / dark red balls.

SSD is a **critical** compilation of published structure data. This means, in particular, that structure information provided by experimentalists or taken from the literature was **checked** for **completeness** and **consistency** before being included in the database. Symmetry or qualitative geometry information only, which is available for many single crystal surfaces and adsorbate systems, did **not** qualify a surface system to be entered in SSD. This applies specifically to numerous recent structure studies on complex overlayers where only scanning tunneling microscopy (STM) is used to obtain a qualitative impression of the surface with very limited quantitative structural details.

In the following, we discuss a few results from **statistical analyses** of the SSD data which have been provided by M. A. Van Hove (Hong Kong Baptist University) and refer to structures solved until 2004. These results can shed some light on the types of surfaces and interfaces that are known quantitatively but also on the use of different experimental methods to obtain quantitative surface structure. First, of the 1379 entries contained in the SSD database the majority, 1363 (98.8%), concerns the clean substrate surface with or without adsorbate overlayers while 16 (1.2%) are interstitial structures with foreign atoms inside the substrate. Table 7.2 lists further details about the

Table 7.2. Number of quantitatively solved surface and interface structures until 2004 taken from the Surface Structure Database (SSD, V. 5). The data are grouped according to substrate type, element composition, electronic property, basic structure, see text.

<b>Element composition</b>	<b>Entries</b>	<b>Electronic property</b>	<b>Entries</b>	<b>Basic structure</b>	<b>Entries</b>
Elemental	1148 (83%)	Metal	1124 (81%)	Unreconstructed	1054 (76%)
Compound	121 (9%)	Semiconductor	215 (16%)	Reconstructed	325 (24%)
Alloy	106 (8%)	Insulator	40 (3%)		
Other	4 (< 1%)	Semimetal	7 (< 1%)		

kinds of substrates that were examined. The majority of substrates appearing in SSD are **elemental** substrates, where transition **metals**, such as Co, Ni, V, Mo, Ru, Rh, Pd, Pt, and W dominate due to the relatively easy growth and preparation of corresponding single crystals and their surfaces. In addition, substrates of elemental **semiconductors**, such as Si and Ge, and of compound semiconductors, such as GaAs, CdSe, CdTe, and InP, have been analyzed by their surface structure due to their great technological importance. They account for 16% of all entries in SSD. Finally, the majority of entries in SSD, 76%, refer to **unreconstructed** substrate surfaces.

Table 7.3 lists details about the kinds of adsorbates that were examined. Of all SSD entries 961 (68%) refer to adsorbate systems. Of these, the majority, 720 entries, concern **atomic** adsorbates, such as H, N, O, Cl, S, Na, K, Cs, Al, Fe, and Mn, while a smaller group includes **molecular** adsorbates, such as CO, CN, NO, N<sub>2</sub>, PF<sub>x</sub>, and small hydrocarbons. An even smaller group is given by **compound** adsorbate systems where the adsorbates can mix with atoms of the substrate surface



Table 7.3. Number of quantitatively solved surface and interface structures until 2004 taken from the Surface Structure Database (SSD, V. 5). The data are grouped according to adsorbate type and adsorbate structure, see text.

Adsorbate type	Entries	Adsorbate structure	Entries
Atomic	720 (52%)	Overlayer	716 (52%)
Molecular	173 (13%)	Pseudomorphic	101 (7%)
Compound	38 (3%)	Substitutional	74 (5%)
Mixed atomic / molecular	18 (1%)	Epitaxial	39 (3%)
Thin films	12 (1%)	Interstitial	15 (1%)
		Other	16 (1%)

forming mixed surface layers. Examples are surface alloy layers, such as those formed by Na which penetrates into the top layer of the Al(1 1 1) surface [191]. Finally, there are a small number of entries with both atoms and molecules **coadsorbed** at the surface, such as O and C<sub>6</sub>H<sub>6</sub> on the Ru(0 0 0 1) surface, as well as with metal adsorbates that form **thin overlayer films**, such as Ni films on top of a Cu(1 0 0) substrate.

As to details of the adsorbate morphology, Table 7.3 shows that the majority, 716 (52%), of all SSD entries describe adsorbates that form ordered or disordered **overlayers**, such as CO on the Ni(1 0 0) surface. A smaller group of entries, 101 (7%), concerns **pseudomorphic** layers of adsorbates in positions which continue the crystal structure of the substrate. Examples are metal adsorbates on a metal substrate, such as Fe films on top of a Cu(1 1 0) substrate. Another group, 74 entries (5%), is given by adsorbates that occupy positions of substrate atoms at the surface forming mixed adsorbate / substrate atom layers (**substitution**). Examples are again metal adsorbates on a metal substrate which yield surface alloy layers, such as Au adsorbates at a Cu(1 0 0) substrate. Mixed adsorbate / substrate atom layers can also occur when adsorbate atoms assume **interstitial** positions between atoms of substrate layers near the surface. This group includes 15 entries (1%), where an example is given by O atoms adsorbing onto and penetrating into the Al(1 1 1) surface. Further, one group of 39 systems (3%) is described by (**epitaxial**) adsorbate overlayers of crystalline structure where the overlayer lattice does not match that of the substrate. An example is the adsorption of Xe atoms forming (slightly distorted) hexagonal overlayers on top of a Ag(1 1 1) substrate, whose substrate surface is also hexagonal but whose lattice constant differs from that of the overlayer. There are numerous examples of surface systems that **do not fit uniquely** into one of the different groups

discussed above but the above schemes can give a sound basis for a general classification of surface structure.

Further, an inspection of the SSD data shows that of all **experimental methods** used in surface structure evaluations low-energy electron diffraction (**LEED**) is by far the **most often** applied method which covers about 65% of all surface structure determinations contained in SSD. In fact, in the beginning of quantitative surface structure analysis, between 1969 and 1980, LEED was the only method available. This is illustrated in Fig. 7.2 which shows the number of quantitatively solved surface and interface structures as a function of the publication year until 2004 according to the

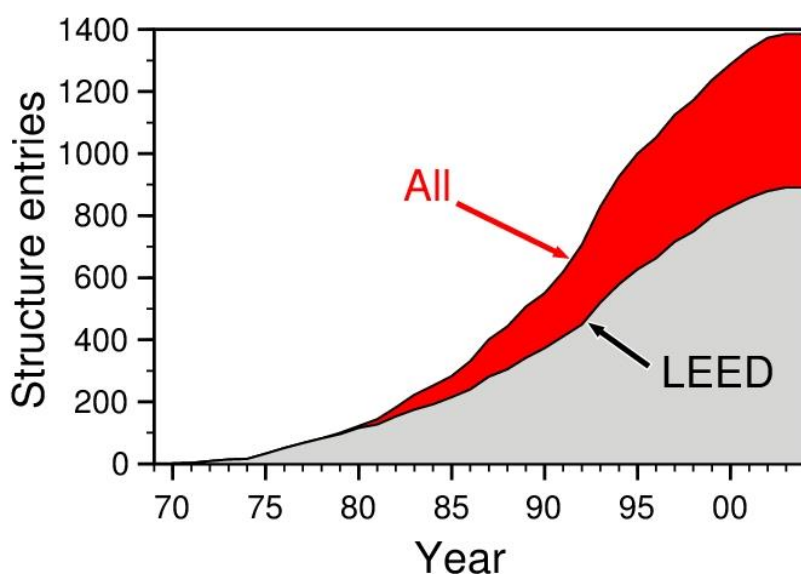


Fig. 7.2. Number of quantitatively solved surface and interface structures as a function of the publication year, see text. The data are given separately for all measured structures and for those using LEED.

SSD data. Quantitative results from experimental methods **other** than LEED have started to appear in the literature only **after 1980**, and even in 2004 surface structure studies applying LEED still outnumbered those using other methods. This is also clear from a listing of all surface and interface structures solved until 2004 as a function of the methods applied as given in Table 7.4.

Table 7.4. Number of quantitatively solved surface and interface structures until 2004 as a function of the methods used. The methods are given by their acronyms explained in Table 7.1.

Method	Entries	Method	Entries	Method	Entries
LEED	891 (65%)	TOF-SARS	13 (1%)	AED	3 (<1%)
PED	132 (10%)	NEXAFS	11 (1%)	SEELFS	2 (<1%)
IS	117 (8%)	RHEED	10 (1%)	TED	1 (<1%)
SEXAFS	67 (5%)	LEPD	5 (<1%)	AD	1 (<1%)
XSW	63 (5%)	HREELS	4 (<1%)	STM	1 (<1%)
XRD	55 (4%)	MEED	3 (<1%)		

The table shows that, besides LEED, photoelectron diffraction (**PED**), ion scattering (**IS**), surface extended X-ray absorption (**SEXAFS**), and X-ray Standing Wavefield absorption (**XSW**) were the five topmost experimental methods applied to quantitative surface analysis covering 93% of all solved surface and interface structures.

### 7.3 Database Formats for Surface and Nanostructures

The collection of quantitative surface and nanostructure data is of vital importance for a scientific understanding and documentation of many properties of these systems. This is required for archiving purposes but also when structural data of a group of systems are analyzed by their similarities or screened in their characteristic differences. Further, quantitative structure data are needed for theoretical postprocessing when ‘intelligent guesses’ from experiments are used as input for visualization and for numerical simulation.

In general, structure information includes quantitative numerical parameters, such as lattice constants, interatomic distances, or bond angles, as well as symmetry properties. Further, a complete characterization must contain textual descriptions, such as system preparation and experimental methods together with estimates of instrumental and methodological errors. This requires standard data formats which are commonly accepted and widely adopted. The issue has been discussed extensively in the surface science literature [192], [193], [194] of which we mention in the following only some of the most important points raised [194].

In the past, numerous data formats for documenting structural parameters derived from bulk

and surface crystallography have been proposed for different purposes. Examples are three-dimensional crystal data formats, such as

- **CIF** (Crystallographic Information Framework) [195] which is adopted by the International Union of Crystallography for the documentation of bulk crystal data,
- **PDB** (Protein Data Bank) [196] which is a generally accepted documentation format for crystals of biological macromolecules,
- different formats used in simulations and theoretical studies with standard computer codes, such as **VASP** (Vienna Ab initio Simulation Package) [197],

or data formats developed specifically for surface structure, such as

- **SSD** (Surface Structure Database) [23], [27] which was proposed as a combined numerical and textual data format for submitting quantitative surface structures to the NIST SSD database [22],
- **SURVIS** (SURface VISualizer) [27] which was developed for the visualizer tool Survis inside the NIST SSD project and documented in the Survis and Balsac manuals,
- **BALSAC** (Build and Analyze Lattices, Surfaces, And Clusters) [26] which is the standard format of the visualizer and analysis tool Balsac,

or general data formats for documenting atom positions, such as

- **XYZ** which is widely supported by quantum chemical and solid state physics codes (although no formal specification has been published so far) and collects Cartesian coordinates and element specifications of all atoms in the bulk, at a surface, or in a molecule.

While the data formats mentioned above (and many others) have been used and proven valuable for information exchange within different scientific communities no format has been generally adopted as a single data format for documenting structure and properties of the bulk, of surfaces or of nanoparticles. This is partly due to the fact that different scientific groups put emphasis on different aspects of structure data. Thus, formats which are complete in one community may not be flexible enough to serve the purposes of another. As a consequence, a generally acceptable structure data format has to be either developed from scratch or updated from an existing format addressing the kind of structures which are examined today and may be studied in the near future. These will be mainly nanostructures and complex surfaces including molecular networks, i.e. structures that very

often have lower dimensionality and order than two-dimensionally periodic surfaces.

In the following, we list the most important requirements which an ideal structure data format has to fulfill according to Ref. [194] to conveniently document experimental and theoretical results from surface and nanostructures. The data format should

- describe all theoretical and experimental methods in enough detail to enable reproduction of the results. This may require different accuracies depending on the experiment but also on the theoretical methods applied.
- allow the combination of results from multiple techniques in a single structure determination. This includes experimentally as well as theoretically obtained data.
- have a consistent scheme allowing coordinate listings of all three- and lower-dimensional structures as well as combinations thereof. Examples include carbon nanotubes or graphene layers adsorbed incommensurately on a single-crystal surface.
- allow documenting incomplete structural results which may arise in complex systems. Examples include hydrogen atom positions at surfaces which may not be determined in a given structure while all other atoms have been evaluated. In nanostructures many more partial structure determinations are to be expected.
- be unique and machine-readable but also include human-readable tags. It should be described in the open literature and should be free of copyright protection.
- be sufficiently simple and intuitive to allow easy conversion of past published results to complement a structure collection. This could be achieved by appropriate conversion utilities.

Further, there should be an a priori agreement on the data format within the community of experimental and theoretical crystallographers, surface scientists and nanoscientists. This can be enforced by consensus between the major journal and book publishers in publication policies.

The development of a general structure data format which obeys all or most of the above requirements is a major task which requires a lot of conceptual work but also the ability of convincing the scientific community of its value and need. Besides, such a development project may not be ‘scientifically rewarding’. Therefore, the authors of Ref. [194] have proposed a ‘hybrid universal format’ in which different already existing file formats may appear in the same structure file for dif-

ferent parts of a complex structure; for further details see [194].

#### 7.4 Exercises

- 7.1. Discuss the basic physical mechanisms which are applied in the different structure determination methods listed in Table 7.1. Explain the need of different methods to arrive at a unique structure determination.
- 7.2. Consider a (fictitious) database of experimental and theoretical surface structures where each structure needs to be documented in complete form.
- Which structure parameters are required for each entry?
  - Which additional information should be included for each surface structure?
- 7.3. Consider the entry of a surface structure in a database with the following parameters
- crystal: monoatomic nickel, fcc lattice, bulk symmetry, lattice constant, lattice vectors, bulk unit cell (shape and volume), atom density.
  - surface: orientation (1 0 0), square lattice, monolayer symmetry, monolayer spacing lateral and perpendicular (bulk value),  $2 \times 2$  reconstruction matrix, perpendicular relaxation of the topmost monolayers (in % of monolayer spacing), surface unit cell (shape and volume).

Which of these data entries can be generated from a minimal set of parameters? Determine a minimal set.

- 7.4. What are possible uses of a surface structure database? Discuss examples.
- 7.5. Why are different formats for surface structure documentation needed? Discuss examples of possible advantages and disadvantages.

## 8 NANOTUBES

Nanotubes form an important class of **nanoparticles** which may exhibit **spatial periodicity** and can, thus, be described structurally in a way analogous to crystalline material. They have become a major area of research in recent years since these systems exhibit extremely interesting new electronic and chemical properties. Examples are nanotubes that provide new substrate material for catalytically active particles but may also act as catalysts themselves [14], [16]. The most prominent and oldest members of the nanotube family are **carbon nanotubes** observed as early as 1952 [198] but attracting attention only much later [199], [200]. Meanwhile, very different materials, such as Si, BN,  $\text{VO}_x$ ,  $\text{TiO}_2$ ,  $\text{WS}_2$ ,  $\text{MoS}_2$ , and MnO have been found to form nanotubes [14], [15], [16]. While physical and chemical properties of these systems have been widely discussed in the literature, the present section focuses on **crystallographic aspects**. The structure of nanotubes depends very much on their **preparation** [14], [201], where the crystal structure of the corresponding bulk material may give some hints. In the following, we consider a **special class** of **nanotubes** derived from rolling sections of single crystal layers, which also includes carbon nanotubes. It should be emphasized that the nanotubes discussed as examples in this section, originating from NaCl crystal layers, are meant only to illustrate the basic crystallographic concepts. They have not been prepared by experiments so far and may be difficult to produce due to the highly ionic character of their constituent atoms.

### 8.1 Basic Definition

The construction of **nanotubes** considered in this section starts from infinitely **long strips** of finite width, cut out of a planar two-dimensionally periodic layer parallel to an  $(h\ k\ l)$  netplane of a perfect single crystal. These strips are then rolled up joining their parallel borders to yield long **cylindrical tubes** whose circumference equals the strip width. For the sake of simplicity, we confine ourselves first to nanotubes originating from  $(h\ k\ l)$  **monolayers**. As an example, Fig. 8.1 shows a part of the NaCl(1 2 2) (6, 1) nanotube representing a rolled up section of a (1 2 2) monolayer of the perfect cubic NaCl crystal with (6, 1) denoting the rolling direction explained in the following.

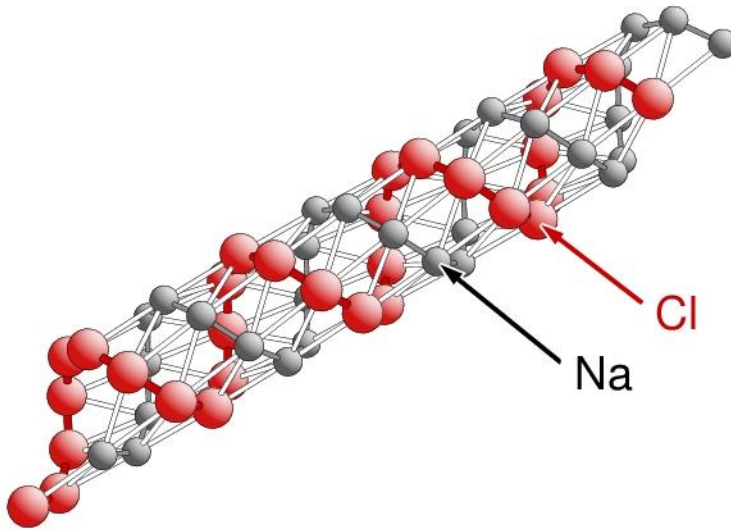


Fig. 8.1. Structure of a NaCl(1 2 2) (6, 1) nanotube section, see text.

As discussed in Sec. 3.2, the periodicity of an  $(h k l)$  monolayer is given by **netplane-adapted lattice vectors**  $\underline{R}_1$  and  $\underline{R}_2$  which result from linear transformations of the initial lattice vectors  $\underline{R}_{01}$ ,  $\underline{R}_{02}$ ,  $\underline{R}_{03}$  of the bulk crystal according to

$$\underline{R}_1 = t_{11} \underline{R}_{01} + t_{12} \underline{R}_{02} + t_{13} \underline{R}_{03} \quad (8.1a)$$

$$\underline{R}_2 = t_{21} \underline{R}_{01} + t_{22} \underline{R}_{02} + t_{23} \underline{R}_{03} \quad (8.1b)$$

where  $t_{ij}$  are (integer-valued) elements of a transformation matrix  $\underline{\mathbf{T}}^{(h k l)}$  referring to Miller indices  $(h k l)$  as given by (3.11), (3.12), or (3.13). The definition of a nanotube requires an additional lattice vector along the monolayer, called **rolling vector**  $\underline{R}_r$ , which can be written as

$$\underline{R}_r = m \underline{R}_1 + n \underline{R}_2, \quad m, n \text{ integer} \quad (8.2)$$

where  $m, n$  are commonly referred to as **rolling indices**. The rolling vector, starting at any point of the  $(h k l)$  monolayer, is used to construct an **infinitely** long strip extending perpendicular to vector  $\underline{R}_r$  with a width equal to the length of  $\underline{R}_r$ . This is illustrated in Fig. 8.2 for the (1 2 2) monolayer of a NaCl crystal where a strip section (emphasized by a gray background in Fig. 8.2) is defined in its width by a rolling vector  $\underline{R}_r$  with  $m = 6, n = 1$ . **Rolling** the strip along  $\underline{R}_r$  such that its two edges



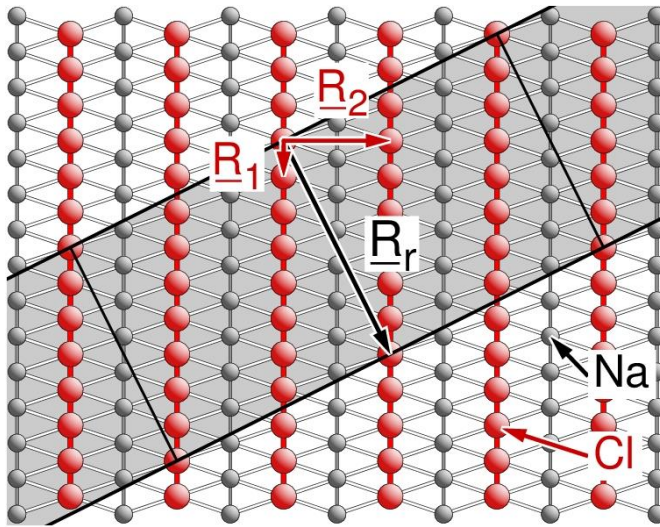


Fig. 8.2. Structure of a NaCl(1 2 2) monolayer including a section of the nanotube strip defined by a rolling vector  $m = 6$ ,  $n = 1$ . The strip is emphasized in gray with netplane-adapted lattice vectors  $\underline{R}_1$ ,  $\underline{R}_2$  and the rolling vector  $\underline{R}_r$  labeled accordingly.

**coincide** creates a circular **tube** where atoms positioned exactly at one edge of the planar strip will coincide with their counterparts connected by vector  $\underline{R}_r$  on the other edge. The resulting nanotube is commonly labeled by the decomposition (8.2) of the rolling vector  $\underline{R}_r$  as an **(m, n) nanotube**. Thus, the strip shown in Fig. 8.2 corresponds to the (6, 1) nanotube of NaCl(1 2 2) displayed in Fig. 8.1.

In **mathematical** terms, the rolling procedure can be achieved by a **non-linear** coordinate **transformation**  $(x, y, z) \rightarrow (x_t, y_t, z_t)$  in Cartesian space with

$$\begin{aligned} x_t &= \kappa \cdot \cos \varphi, & y_t &= \kappa \cdot \sin \varphi, & z_t &= z \\ \kappa &= (\underline{R}_r - x) / 2\pi, & \varphi &= (y / \underline{R}_r) 360^\circ & x &\leq \underline{R}_r \end{aligned} \quad (8.3)$$

where the Cartesian coordinate system is chosen such that the  $x$  axis is perpendicular to the monolayer with  $x = 0$  defining the monolayer plane. Further, the  $y$  axis points along the rolling vector  $\underline{R}_r$ , and the  $z$  axis points along the strip border in the monolayer. Inverting the rolling vector direction by going from  $\underline{R}_r$  to  $-\underline{R}_r$  corresponds in (8.3) to a transformation

$$(x, y, z) \rightarrow (x, -y, -z) \rightarrow (x_t, -y_t, -z_t) \quad (8.4)$$

which does not change the structure of the nanotube. Thus, rolling indices  $(m, n)$  and  $(-m, -n)$  reflect identical nanotubes.

As mentioned earlier, the oldest examples of nanotubes are **carbon nanotubes** created by rolling sections of honeycomb structured (0 0 0 1) monolayers of hexagonal graphite (so-called graphene layers), shown in Fig. 8.3. These monolayers form the basis of layer-type graphite crystals but can also exist in nature as separate graphene sheets, either in aqueous solution or adsorbed at solid surfaces. Carbon nanotubes have been **classified** according to their structure and symmetry

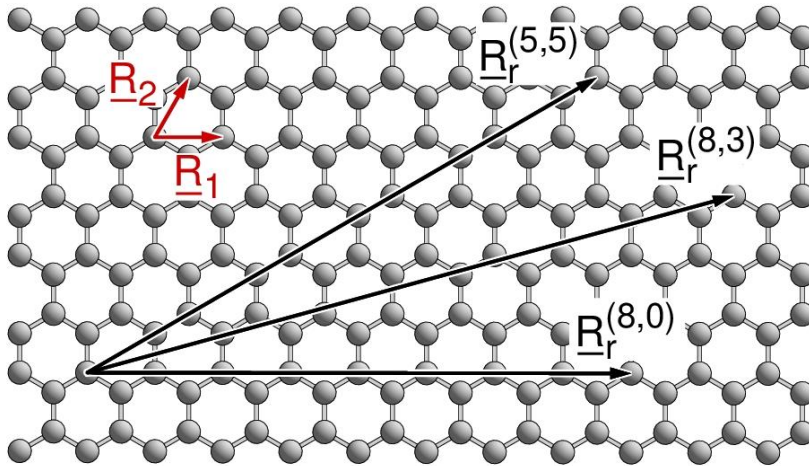


Fig. 8.3. Structure of a graphite(0 0 0 1) monolayer (graphene). The monolayer includes three different nanotube rolling vectors,  $\underline{R}_r^{(8,0)}$ ,  $\underline{R}_r^{(8,3)}$  and  $\underline{R}_r^{(5,5)}$ , see text. The lattice vectors  $\underline{R}_1$  and  $\underline{R}_2$  of the monolayer are shown in red.

given by the **rolling indices** ( $m, n$ ) in (8.2). Here the indices are commonly based on an acute representation of the graphene netplane lattice vectors  $\underline{R}_1$  and  $\underline{R}_2$  ( $\angle(\underline{R}_1, \underline{R}_2) = 60^\circ$ ), which is also used for the present discussion. The following three types of nanotubes can be distinguished:

- (a) For  $\mathbf{m} \neq \mathbf{0}, \mathbf{n} = \mathbf{0}$ , nanotubes are described as **zigzag** tubes which is evident from the direction of the corresponding rolling vectors  $\underline{R}_r$  pointing along zigzag carbon rows of the graphene sheet. As an illustration, Fig. 8.4a shows a section of the (8, 0) carbon nanotube defined by the rolling vector  $\underline{R}_r^{(8,0)}$  sketched in Fig. 8.3. Due to the 6-fold rotational symmetry of the graphene layer there are three equivalent zigzag nanotubes described by  $\pm(m, 0)$ ,  $\pm(0, m)$ , and  $\pm(m, -m)$ .
- (b) For  $\mathbf{m} = \mathbf{n} \neq \mathbf{0}$ , nanotubes are described as **armchair** tubes which is also clear from the direction of the corresponding rolling vectors  $\underline{R}_r$  pointing along meandering carbon rows of the graphene sheet. As an illustration, Fig. 8.4b shows a section of the (5, 5) carbon nanotube defined by the rolling vector  $\underline{R}_r^{(5,5)}$  sketched in Fig. 8.3. Due to the 6-fold rotational symmetry of the graphene layer there are six equivalent armchair nanotubes de-

scribed by  $\pm(m, m)$ ,  $\pm(-m, 2m)$ , and  $\pm(2m, -m)$ .

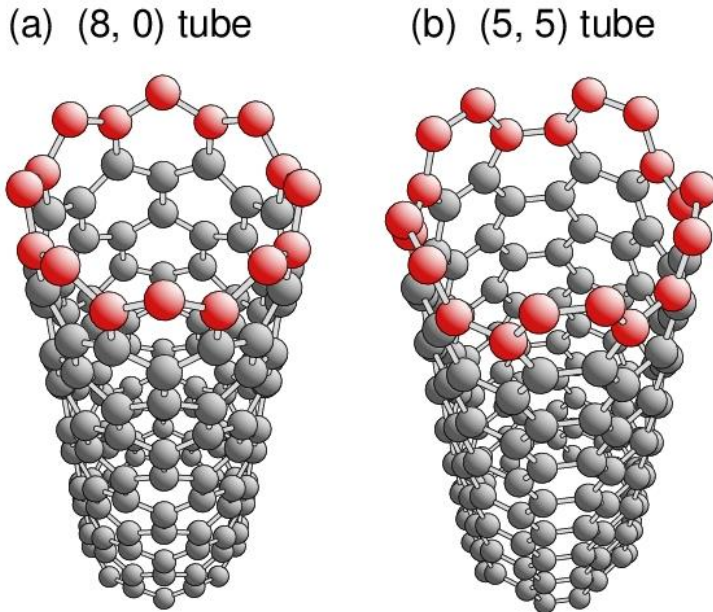
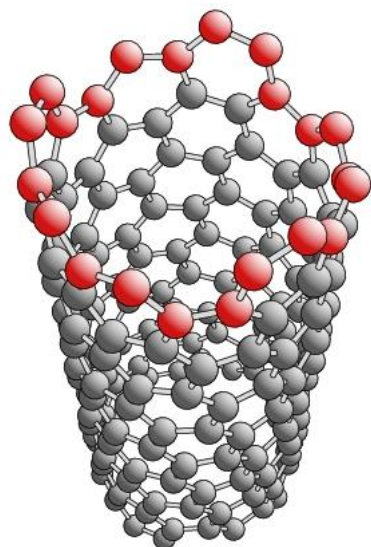


Fig. 8.4. Structure of symmetric carbon nanotubes, (a) zigzag (8, 0) and (b) arm-chair (5, 5) tube. The zigzag and armchair cuts are emphasized by red atom balls at the top.

- (c) For  $m, n \neq 0$ ,  $m \neq n$ , nanotubes are described by spiral networks of carbon honeycombs without mirror symmetry along the tube axis. This implies that there are always **chiral pairs** of nanotubes, where one arises from the other by mirroring with respect to a plane along the nanotube axis. As an illustration, Fig. 8.5 shows a sections of a chiral pair of carbon nanotubes, denoted (8, 3) and (3, 8); the rolling vector  $R_r^{(8, 3)}$  is sketched in Fig. 8.3. Here the spiral networks of the two nanotubes proceed in different directions. Due to the mirror symmetry of the graphene layer there are three equivalent chiral pairs of nanotubes for each (m, n) described by (m, n) with  $\pm(n, m)$ , with  $\pm(m+n, -n)$ , and with  $\pm(-m, m+n)$ .

(a) (8, 3) tube



(b) (3, 8) tube

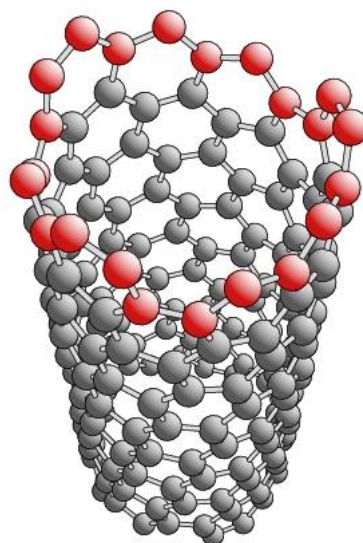


Fig. 8.5. Chiral pair of carbon nanotubes, (a) (8, 3) and (b) (3, 8) tube. The spiral structures are emphasized by red atom balls at the top.

## 8.2 Nanotubes and Symmetry

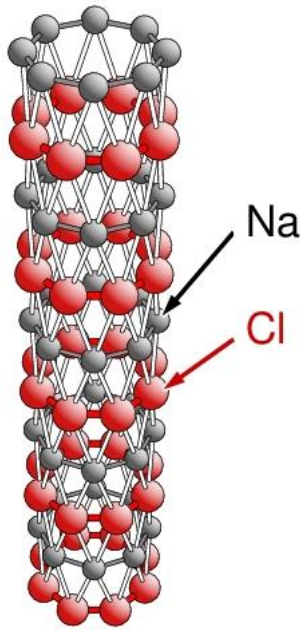
Ideal linear nanotubes can also be characterized by their **symmetry properties**, which derive from translational and point symmetry of their defining **monolayers**. As a result of translational symmetry of these layers, defined by lattice vectors  $\underline{R}_1$  and  $\underline{R}_2$ , nanotubes can exhibit combined translational and rotational symmetry. Considering a general lattice vector  $\underline{R}$  of the netplane with

$$\underline{R} = k_1 \underline{R}_1 + k_2 \underline{R}_2, \quad k_1, k_2 \text{ integer} \quad (8.5)$$

the rolling transformation (8.3) shows immediately that changes of its components **along** the rolling vector  $\underline{R}_r$ , pointing along coordinate  $y$  and affecting only angle  $\varphi$  in (8.3), are transformed to **rotational increments** on the tube. In contrast, changes of its components **perpendicular** to  $\underline{R}_r$ , pointing along coordinate  $z$  in (8.3), are transformed to linear shifts **parallel to the axis** of the tube. This means, in particular, that rows of atoms at equal distances along vector  $\underline{R}$ , with components both parallel and perpendicular to  $\underline{R}_r$ , on the monolayer, yield **spiral** arrangements on the corresponding nanotube. This is illustrated by the NaCl(1 2 2) (6, 1) nanotube in Fig. 8.1 where the Na and Cl spirals, relating to dense atom rows along  $\underline{R}_1$  on the monolayer, see Fig. 8.2, are evident. In contrast, if vector  $\underline{R}$  points **along** the rolling vector  $\underline{R}_r$ , then atom rows along  $\underline{R}$  on the monolayer lead to **rings** on the nanotube. This is shown in Fig. 8.6a for the NaCl(1 2 2) (8, 0) nanotube with its the Na and

Cl rings. On the other hand, if vector  $\underline{R}$  is **perpendicular** to  $\underline{R}_r$  then atom rows along  $\underline{R}$  on the monolayer result in rows **parallel** to the axis of the nanotube, as demonstrated in Fig. 8.6b for the NaCl(1 2 2) (0, 6) nanotube showing Na and Cl rows.

(a) (8, 0) tube



(b) (0, 6) tube

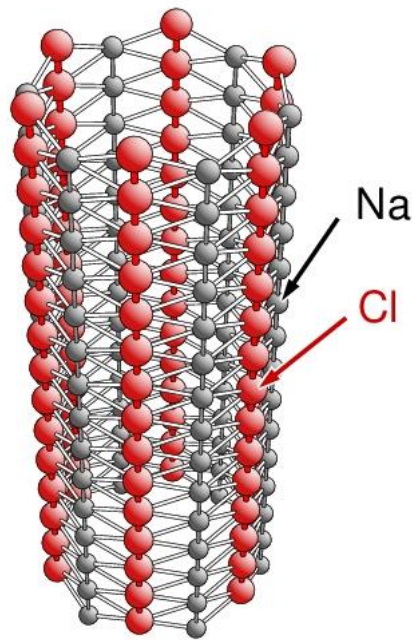


Fig. 8.6. Structures of symmetric NaCl(1 2 2) nanotubes, (a) (8, 0) and (b) (0, 6) tubes.

Nanotubes originating from **general monolayers** appear usually as **chiral pairs** of tubes, where one derives from the other by **mirroring** with respect to a plane along the nanotube axis. The two tubes can be thought of as arising from rolling monolayer strips **above** and **below** the layer which corresponds to the coordinate transformation (8.3) as well as to the complementary transformation  $(x, y, z) \rightarrow (x_t', y_t', z_t')$  in Cartesian space with

$$\begin{aligned} x_t' &= \kappa \cdot \cos \varphi, & y_t' &= \kappa \cdot \sin \varphi, & z_t' &= z \\ \kappa &= (R_r + x) / 2\pi, & \varphi &= (-y / R_r) \cdot 360^\circ & x &\geq -R_r \end{aligned} \quad (8.6)$$

For monolayers with **mirror symmetry** (mirror lines in the corresponding netplane) chiral pairs of nanotubes can also be obtained by two different rolling vectors  $\underline{R}_r$  and  $\underline{R}_r'$  (rolling at the same side of the layer) where  $\underline{R}_r'$  is a mirror image of  $\underline{R}_r$ . As an illustration, Fig. 8.7 shows the chiral pairs of NaCl(1 2 2) (6, 1) and (6, -1) nanotubes.

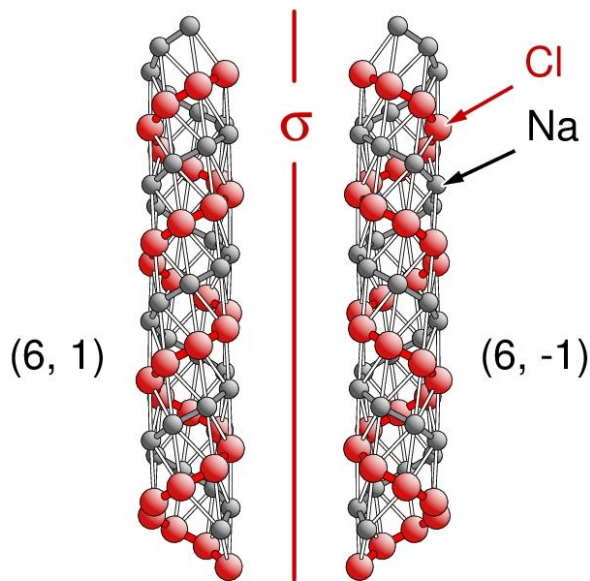


Fig. 8.7. Chiral pair of NaCl(1 2 2) nanotubes, (6, 1) to the left and (6, -1) to the right. The red line between the tubes denoted  $\sigma$  is meant to indicate the mirror symmetry between the two tubes.

If a **mirror line**  $\sigma$  exists **perpendicular** to the **rolling vector**  $\underline{R}_r$  in the monolayer then there is always a **second** mirror line  $\sigma'$  parallel to the first at a distance  $1/2 R_r$  which can be proven analogous to the discussion of mirror lines in Sec. 3.6.4. Then the rolling transformation converts the two mirror lines,  $\sigma$  and  $\sigma'$ , on the monolayer into a mirror plane which goes through the axis of the corresponding nanotube. As a result, the nanotube exhibits **mirror symmetry** along its tube axis and is **achiral**. This is illustrated in Fig. 8.8 for a (1 1 1) monolayer of an fcc crystal and a rolling vector  $\underline{R}_r^{(6,0)}$ . The mirror lines,  $\sigma$  and  $\sigma'$  of the monolayer in Fig. 8.8a lie on a mirror plane of the nanotube along its axis, see Fig. 8.8b, illustrating its mirror symmetry and achirality.

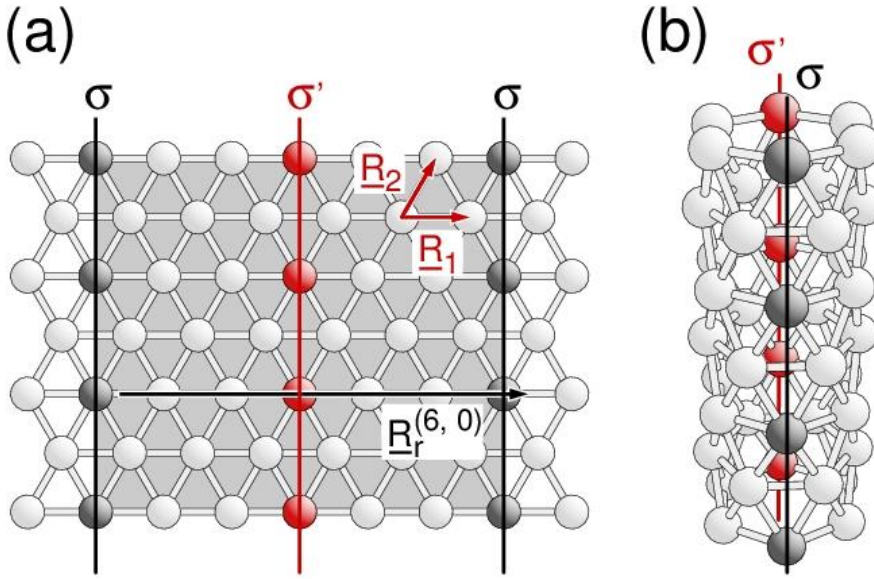


Fig. 8.8. (a) Structure of a fcc(1 1 1) monolayer including a nanotube strip (emphasized in gray) with rolling vector  $\underline{R}_r^{(6,0)}$ . The netplane-adapted lattice vectors  $\underline{R}_1$  and  $\underline{R}_2$  are shown in red and mirror lines  $\sigma$ ,  $\sigma'$  as thick lines. (b) fcc(1 1 1) (6, 0) nanotube corresponding to the nanotube strip in (a).

**Mirror lines  $\sigma$  parallel to the rolling vector  $\underline{R}_r$**  in the monolayer are converted by the rolling transformation to mirror planes pointing **perpendicular** to the nanotube **axis**. Thus, corresponding nanotubes exhibit again **mirror symmetry** and are **achiral**. Fig. 8.8 can also be used to illustrate this behavior. The fcc(1 1 1) monolayer contains, in addition to its mirror lines perpendicular to  $\underline{R}_r^{(6,0)}$  indicated in Fig. 8.8a, mirror lines parallel to  $\underline{R}_r^{(6,0)}$ . The resulting mirror symmetry of the nanotube perpendicular to its axis is quite clear from Fig. 8.8b.

According to (8.3) and (8.6), the netplane coordinate  $z$  **perpendicular** to the **rolling vector  $\underline{R}_r$**  in the monolayer is transformed by the tube rolling procedure to yield coordinate  $z_t$  or  $z_t'$  **along** the **nanotube axis**. Thus, **translational periodicity** of the nanotube along its axis is connected with periodicity of the corresponding monolayer along the direction perpendicular to the rolling vector. This means, in particular, that the monolayer must contain **lattice vectors  $\underline{R}_s$  perpendicular** to the **rolling vector  $\underline{R}_r$**  to yield a nanotube with translational symmetry. If vector  $\underline{R}_s$ , represented as

$$\underline{R}_s = p \underline{R}_1 + q \underline{R}_2, \quad p, q \text{ integer} \quad (8.7)$$

denotes the smallest of these perpendicular vectors then according to (8.2)

$$\begin{aligned} \underline{R}_s \underline{R}_r &= (p \underline{R}_1 + q \underline{R}_2) (m \underline{R}_1 + n \underline{R}_2) = \\ &= (m \underline{R}_1^2 + n \underline{R}_1 \underline{R}_2) p + (n \underline{R}_2^2 + m \underline{R}_1 \underline{R}_2) q = 0 \end{aligned} \quad (8.8)$$

Together with representation (8.1) of the lattice vectors  $\underline{R}_1$  and  $\underline{R}_2$  this yields equations

$$F_1 p + F_2 q = 0 \quad \text{or} \quad F_1 / F_2 = -q / p \quad (8.9)$$

where

$$F_1 = \sum_{i=1}^3 \sum_{j=1}^3 (m t_{1i} t_{1j} + n t_{1i} t_{2j}) \underline{R}_{oi} \underline{R}_{oj} \quad (8.10a)$$

$$F_2 = \sum_{i=1}^3 \sum_{j=1}^3 (n t_{2i} t_{2j} + m t_{1i} t_{2j}) \underline{R}_{oi} \underline{R}_{oj} \quad (8.10b)$$

Thus, **translational periodicity** of a nanotube along its axis requires that the **ratio**  $F_1 / F_2$  assumes a **rational** value. This requirement can be satisfied for **all** ( $h k l$ ) **monolayers** of crystals whose lattices are

(a) **cubic** (sc, fcc, bcc), since

$$\begin{aligned} \underline{R}_{oi}^2 &= a^2, \quad \underline{R}_{oi} \underline{R}_{oj} = 0, i \neq j, & \text{for sc lattices} \\ \underline{R}_{oi}^2 &= 1/2 a^2, \quad \underline{R}_{oi} \underline{R}_{oj} = 1/4 a^2, i \neq j, & \text{for fcc lattices} \\ \underline{R}_{oi}^2 &= 3/4 a^2, \quad \underline{R}_{oi} \underline{R}_{oj} = -1/4 a^2, i \neq j, & \text{for bcc lattices} \end{aligned}$$

(b) **hexagonal close-packed** (hcp) (i.e. hexagonal with a ratio  $c/a = \sqrt{8/3}$ ), since

$$\underline{R}_{o1}^2 = \underline{R}_{o2}^2 = a^2, \quad \underline{R}_{o3}^2 = 8/3 a^2, \quad \underline{R}_{o1} \underline{R}_{o2} = 1/2 a^2, \quad \underline{R}_{oi} \underline{R}_{o3} = 0, i \neq 3$$

(c) **primitive orthorhombic** or **tetragonal** with lattice constants  $a, b, c$ , resulting in rational values of  $(b/a)^2$  and  $(c/a)^2$ , since

$$\underline{R}_{o1}^2 = a^2, \quad \underline{R}_{o2}^2 = (b/a)^2 a^2, \quad \underline{R}_{o3}^2 = (c/a)^2 a^2, \quad \underline{R}_{oi} \underline{R}_{oj} = 0, i \neq j$$

Further, **translational periodicity** of nanotubes is also guaranteed for **selected** ( $h k l$ ) monolayers crystals with other Bravais lattices. As examples we mention

(d) (0 0 0 1) monolayers of **hexagonal** lattices,

(e) (0 0 1) monolayers of **tetragonal** lattices,

(f) (1 1 1) monolayers of **trigonal** lattices.

In general, a nanotube can be **achiral** only if it exhibits **mirror symmetry** where possible mirror planes are either perpendicular to the tube axis or contain the axis. Thus, unrolling an achiral nanotube will always create a strip inside an ( $h k l$ ) monolayer which contains a mirror line  $\sigma$  either



perpendicular or parallel to the rolling vector  $\underline{R}_r$ . This means, in particular, that symmetry properties of the corresponding  $(h k l)$  monolayer must be described by a two-dimensional space group which contains at least one mirror line. This excludes, according to Table 3.13 and Fig. 3.49, monolayers with symmetry described by space groups 1, 2 (oblique), 4, 8 (p-rectangular), 10 (square), and 13, 16 (hexagonal).

### 8.3 Complex Nanotubes

Nanotubes can assume much more complex geometric arrangements compared with those defined by rolling single crystal monolayers which were discussed so far. In particular, structural details of **thicker nanotubes** do not need to be immediately connected with rolling single crystal layers. As an example, silicon nanotubes with thicker walls have been proposed to possess polygonal rather than circular cross sections consisting of distorted crystalline material and described as **hollow nanowires** [201]. This is illustrated by Fig. 8.9 which shows a model of a silicon nanotube with thick walls made of single crystal bulk silicon and a hexagonal cross section.

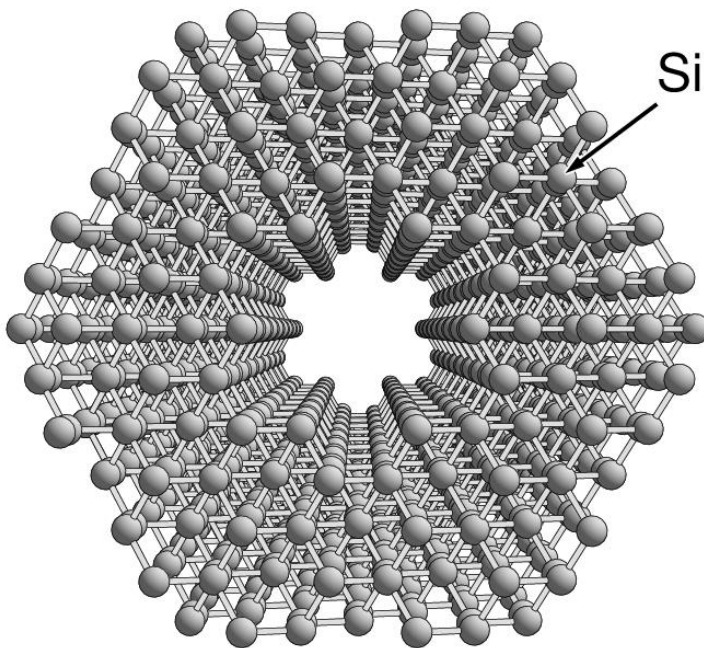


Fig. 8.9. Structure of a thick silicon nanotube of hexagonal cross section simulated by a balls-and-sticks model based on the crystal structure of bulk silicon.

On the other hand, rolled nanotubes can also exhibit rather complex structures. As an example, we mention **multi-walled** nanotubes of carbon, which have been observed [202]. Here foreign at-

oms may be inserted between the walls to yield **intercalation nanotubes**. As an illustration, Fig. 8.10 shows a fictitious double-walled carbon nanotube composed of a (12, 3) tube (outer wall) and a (7, 3) tube (inner wall).

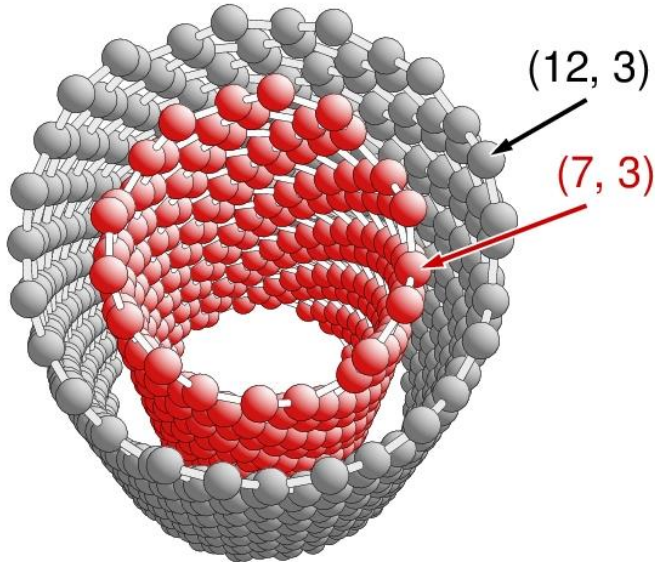


Fig. 8.10. Structure of a fictitious double-walled carbon nanotube combining a (12, 3) tube (outer wall, gray) with a (7, 3) tube (inner wall, red).

Rolled nanotubes can be composed of even **thicker crystal layers**. This is of particular interest for crystals with **layer-type lattices**, where strong chemical binding exists inside physical layers combining several monolayers. These **physical layers** can then be **rolled** to form **complex nanotubes**. As an example, vanadium pentoxide,  $V_2O_5$ , discussed in Sec. 4.1, is described by a layer-type orthorhombic lattice with 14 atoms (4 vanadium, 10 oxygen atoms) in the unit cell. Here (0 1 0) oriented physical layers (of 8 monolayers each, see Fig. 4.4,) are loosely coupled to form the layer-type crystal. These physical layers may serve as building units for  $V_2O_5$  nanotubes, which has also been confirmed experimentally [203]. As an example, Fig. 8.11 shows a model of a section of a  $V_2O_5(0\ 1\ 0)$  (0, 5) nanotube (referring to netplane-adapted lattice vectors  $\underline{R}_1$  and  $\underline{R}_2$  given in Fig. 4.4) which arises from one physical layer. The singly coordinated vanadyl oxygen atoms sticking out of this nanotube surface are assumed to be catalytically active.

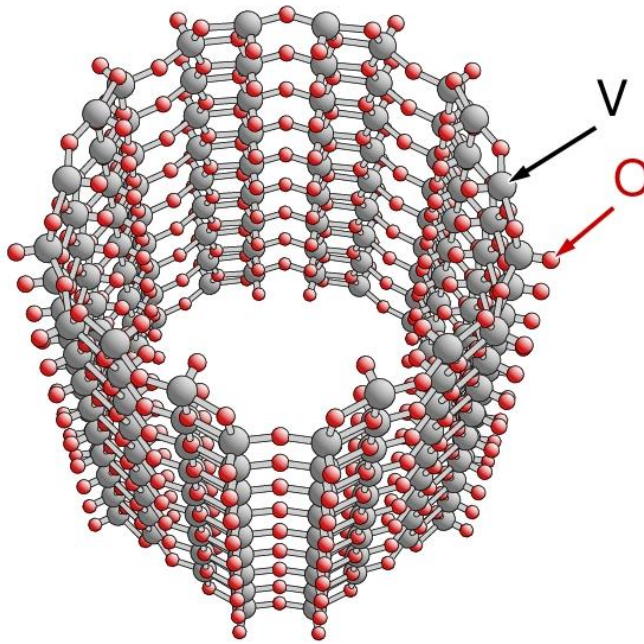


Fig. 8.11. Structure of a (0, 5) nanotube of a (0 1 0) oriented physical layer of the  $V_2O_5$  crystal.

Even more complex shapes of nanotubes have been observed by experiment [202], in particular, for carbon. Examples are flexible ('spaghetti' type) carbon nanotubes, nanotube **junctions** (reminiscent of junctions of tree branches), or **toruses**, which together with many other nanotube structures can be viewed at the nanotube web site [202]. However, from a crystallographic point of view these systems have to be considered on a system-by-system basis and are, therefore, of limited interest for the present general discussion of nanotubes.

## 8.4 Exercises

- 8.1. Consider a (1 1 0) oriented monolayer of an fcc crystal (lattice constant  $a$ ) and nanotubes originating from the monolayer with rolling vectors  $\underline{R}_r^{(m,n)}$  according to (8.2).
- Determine radii  $R_{\text{tube}}(m, n)$  of the nanotubes as a function of  $a$ ,  $m$ ,  $n$ . Hint: the required netplane-adapted lattice vectors  $\underline{R}_1$  and  $\underline{R}_2$  can be represented by
 
$$\underline{R}_1 = a/\sqrt{2} (1, 0, 0), \quad \underline{R}_2 = a (0, 1, 0)$$
  - Which of the  $(m, n)$  nanotubes are translationally periodic? Along which direction?
  - Determine indices  $(m, n)$  and  $(m', n')$  of chiral pairs of nanotubes. Which  $(m, n)$  nanotubes are achiral?

- 8.2. Show that  $(m, n)$  nanotubes of  $(0\ 0\ 0\ 1)$  monolayers of graphite are always translationally periodic along the tube axis. Calculate periodicity lengths  $L(m, n)$ . Calculate tube radii  $R_{\text{tube}}(m, n)$ .
- 8.3. Discuss symmetry elements of  $(m, n)$  nanotubes of fcc(1 1 1) and bcc(1 1 0) monolayers.
- 8.4. Consider a (monoatomic) monolayer with Minkowski-reduced lattice vectors  $\underline{R}_1$  and  $\underline{R}_2$  describing a Bravais lattice with symmetry and a rolling vector  $\underline{R}_r^{(m, n)}$  according to (8.2).
- Calculate radii  $R_{\text{tube}}(m, n)$  and periodicity lengths  $L(m, n)$  (if applicable) of translationally periodic  $(m, n)$  nanotubes referring to different Bravais lattices.
  - Find constraints for the lattice vectors  $\underline{R}_1$  and  $\underline{R}_2$  such that there are no translationally periodic  $(m, n)$  nanotubes. Discuss examples for different Bravais lattices.
- 8.5. Consider a nanotube constructed from a p-rectangular monolayer with symmetry properties according to space group no. 6, see Table 3.13, and a rolling vector  $\underline{R}_r^{(m, n)}$  according to (8.2). Show that all chiral partners of the  $(m, n)$  nanotube are given by  $(m', n') = \pm(m, -n)$ . For which  $(m, n)$  values are the nanotubes achiral?
- 8.6. Consider a nanotube constructed from a c-rectangular monolayer with symmetry properties according to space group no. 9, see Table 3.13, and a rolling vector  $\underline{R}_r^{(m, n)}$  according to (8.2). Show that with orthogonal lattice vectors all chiral partners of the  $(m, n)$  nanotube are given by  $(m', n') = \pm(m, -n)$ . For which  $(m, n)$  values are the nanotubes achiral?
- 8.7. Consider a nanotube constructed from a square monolayer with symmetry properties according to space group no., see Table 3.13, and a rolling vector  $\underline{R}_r^{(m, n)}$  according to (8.2). Show that all chiral partners of the  $(m, n)$  nanotube are given by  $(m', n') = \pm(m, -n), \pm(n, -m)$ . For which  $(m, n)$  values are the nanotubes achiral?

- 8.8. Consider a nanotube constructed from a hexagonal monolayer with symmetry properties according to space group no. 17 of ITC [33], see Table 3.13, and a rolling vector  $\underline{R}^{(m,n)}$  according to (8.2). Show that all chiral partners of the  $(m, n)$  nanotube are given by

acute lattice vectors:  $(m', n') = \pm(n, m), \pm(m+n, -n), \pm(-m, m+n)$

obtuse lattice vectors:  $(m', n') = \pm(n, m), \pm(m-n, -n), \pm(m, m-n)$

For which  $(m, n)$  values are the nanotubes achiral?

- 8.9. Discuss chiral pairs of  $(m, n)$  nanotubes of  $(1\ 0\ 0)$ ,  $(1\ 1\ 0)$ , and  $(1\ 1\ 1)$  oriented monolayers of gold crystals. For which values of  $m, n$  are corresponding nanotubes achiral?
- 8.10. Compare  $(m, n)$  nanotubes of  $(1\ 1\ 0)$  oriented monolayers of nickel crystals with those of vanadium. Which nanotubes are achiral for both nickel and vanadium?
- 8.11. Consider fictitious  $(m, n)$  nanotubes of dense  $(h\ k\ l)$  monolayers of NaCl and CsCl crystals. Which nanotubes include both elements? Discuss examples.

- 8.12. Hexagonal boron nitride, BN, is described by a layer-type crystal structure which is analogous to that of graphite. Thus,  $(0\ 0\ 0\ 1)$  monolayers of BN have a honeycomb appearance and can be defined by a two-dimensional lattice with lattice and lattice basis vectors

$$\underline{R}_1 = a(1, 0), \quad \underline{R}_2 = a(1/2, \sqrt{3}/2), \quad \underline{r}_1^B = (0, 0), \quad \underline{r}_2^N = (1/3, 1/3)$$

Determine achiral  $(m, n)$  nanotubes of  $(0\ 0\ 0\ 1)$  BN and show that there are only two different types.

- 8.13. Consider a monolayer with lattice vectors of a square netplane and two different elements A, B in the unit cell, described by

$$\underline{R}_1 = a(1, 0), \quad \underline{R}_2 = a(0, 1), \quad \underline{r}_1^A = (0, 0), \quad \underline{r}_2^B = (x, y), \quad 0 < x, y < 1$$

Determine values  $x, y$  which allow achiral  $(m, n)$  nanotubes.

## APPENDICES

### A Sketches of High-Symmetry Adsorbate Sites

This appendix gives an overview of the most common sites which are considered for adsorbates stabilizing at single crystal surfaces of high symmetry. Each site is sketched in (a) a view along the surface normal and (b) a view parallel to the surface where the sites are grouped according to bulk crystal structure, A.1 fcc, A.2 bcc, A.3 hcp, A.4 diamond, and A.5 zincblende and surface orientation ( $h k l$ ). Here the substrate is shown as a collection of gray and light red shaded atom balls near the adsorption site where the gray shading distinguishes between different atom layers becoming darker for layers deeper below the surface. Neighboring atoms of each layer are labeled  $Nx$  according to their layer index ( $N = 1$  (topmost), 2, 3, ...) and distance from the adsorption site ( $x = a$  (nearest), b, c, ...). The adsorption site is shown by a small dark red ball representing the adsorbate center and larger light red balls referring the substrate atoms nearest to the adsorbate. The dashed line in each view (a) denotes the cutting plane used for the view in (b).

#### A.1 Face-centered cubic (fcc) surface sites

Details of the sketches are explained in the beginning of Appendix A.

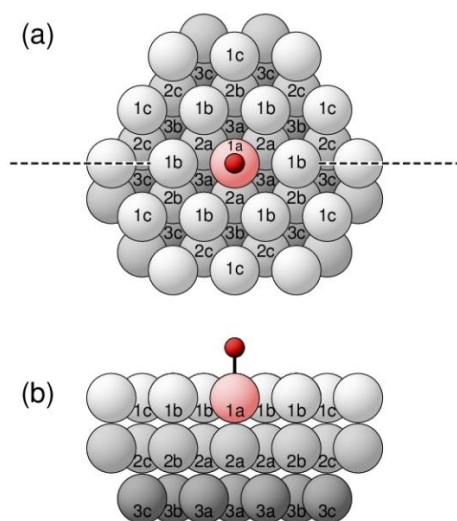


Fig. A.1. fcc(1 1 1) top

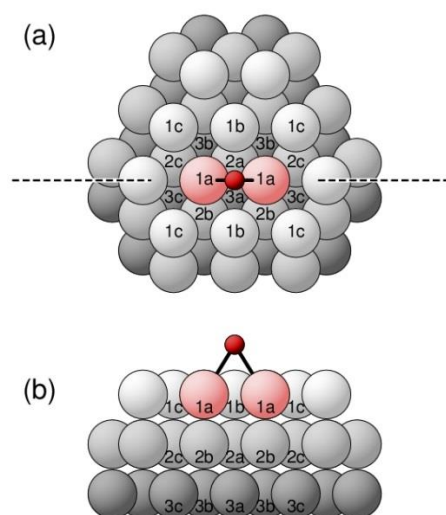


Fig. A.2. fcc(1 1 1) bridge

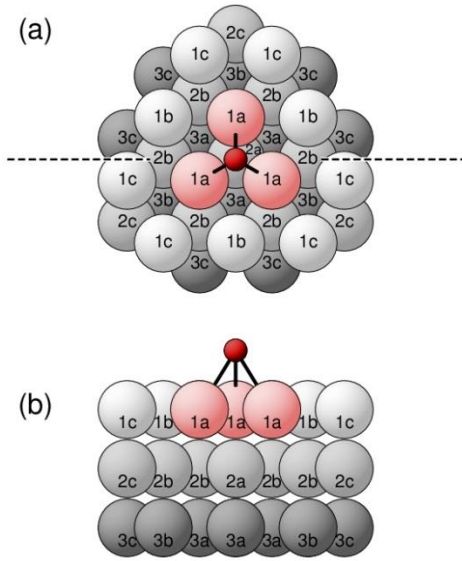


Fig. A.3. fcc(1 1 1) hcp-hollow

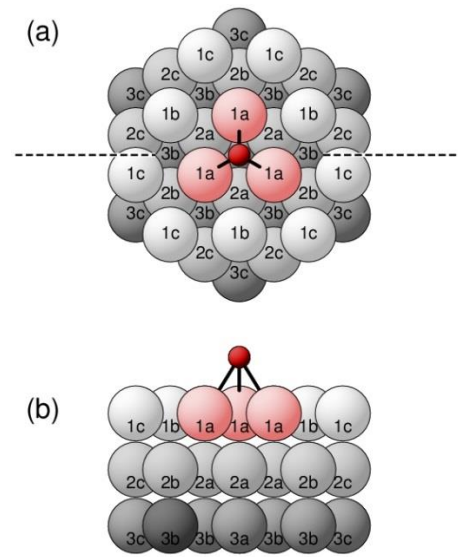


Fig. A.4. fcc(1 1 1) fcc-hollow

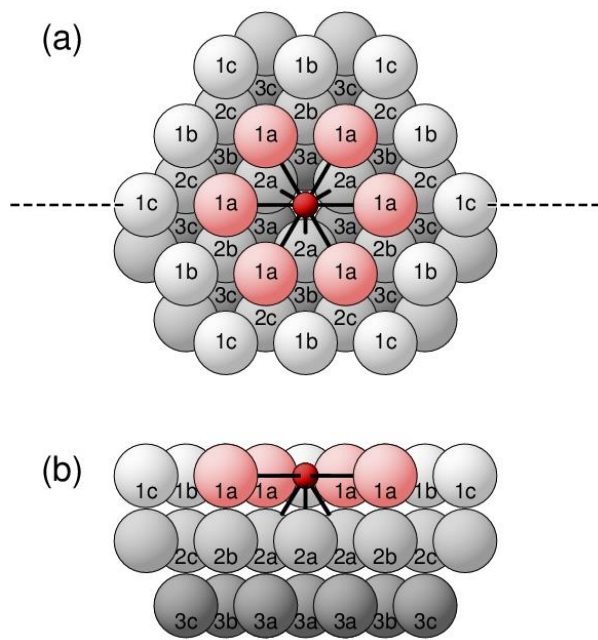


Fig. A.5. fcc(1 1 1) substitutional

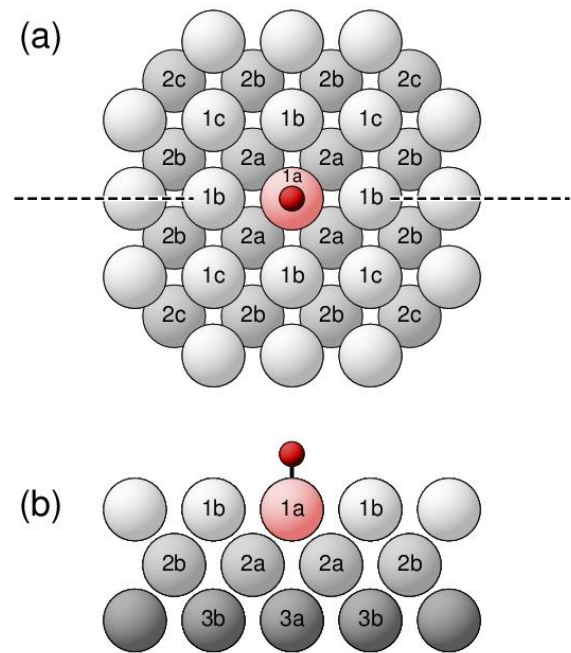


Fig. A.6. fcc(1 0 0) top

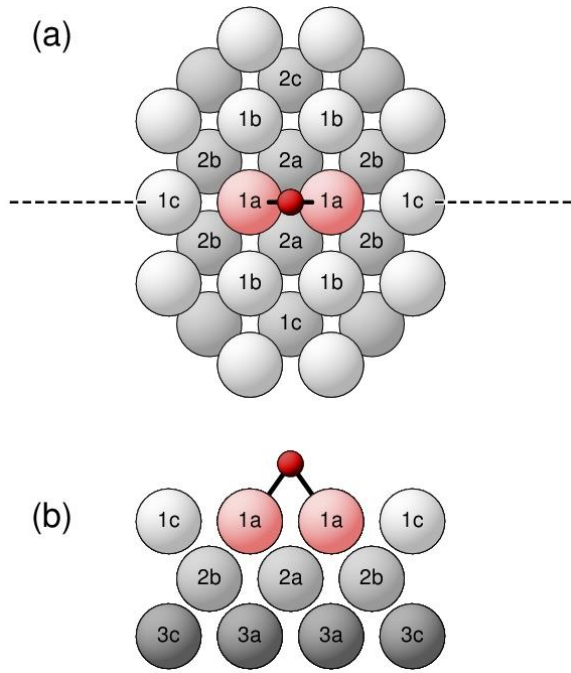


Fig. A.7. fcc(1 0 0) bridge

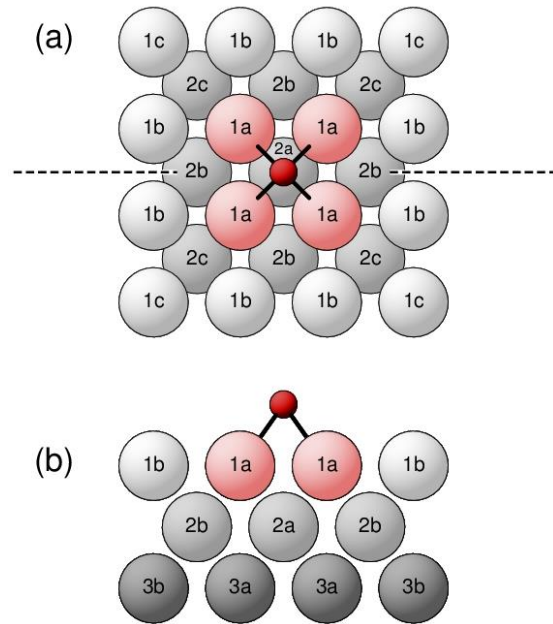


Fig. A.8. fcc(1 0 0) 4-fold hollow

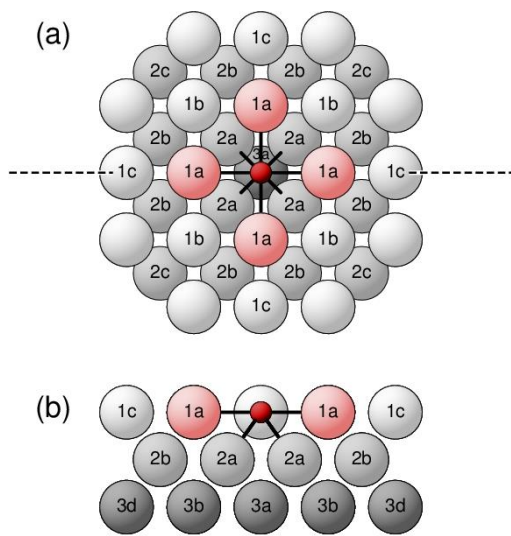


Fig. A.9. fcc(1 0 0) substitutional

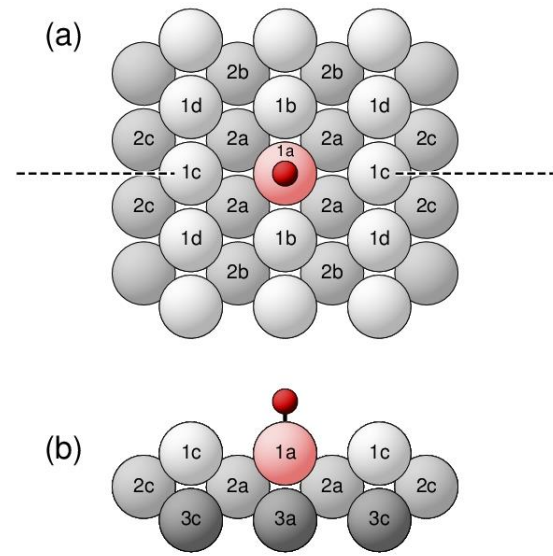


Fig. A.10. fcc(1 1 0) upper top



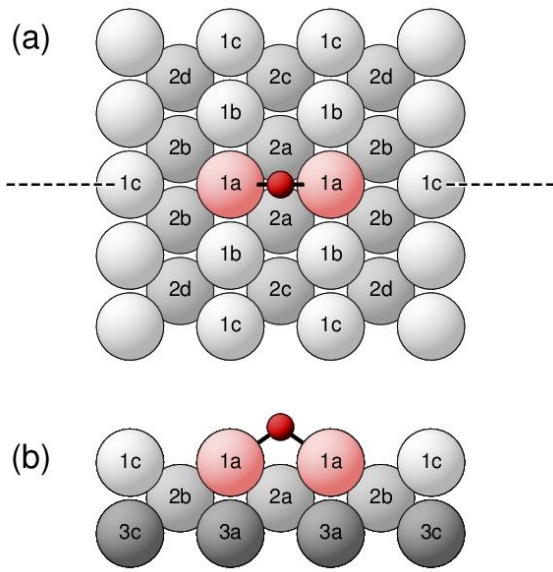


Fig. A.11. fcc(1 1 0) long-bridge

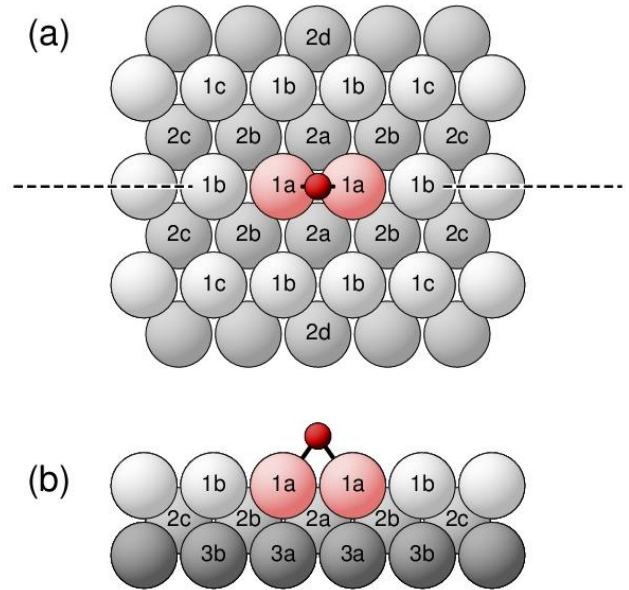


Fig. A.12. fcc(1 1 0) short-bridge

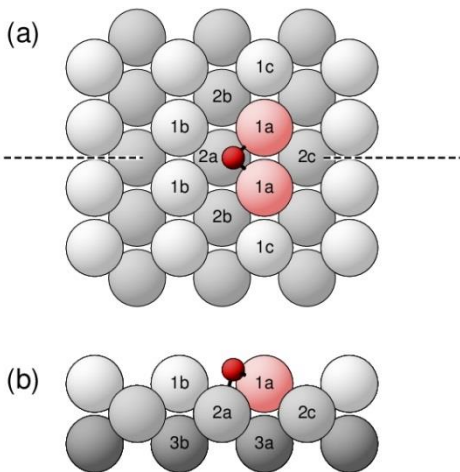


Fig. A.13. fcc(1 1 0) 3-fold hollow

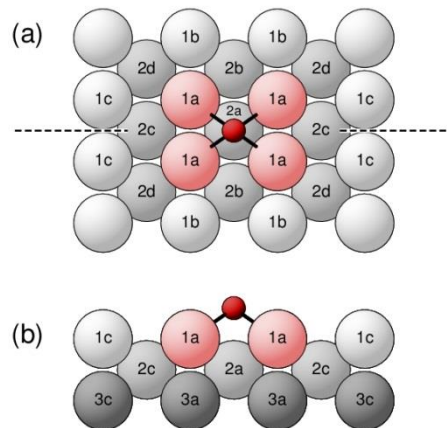


Fig. A.14. fcc(1 1 0) central 4-fold hollow

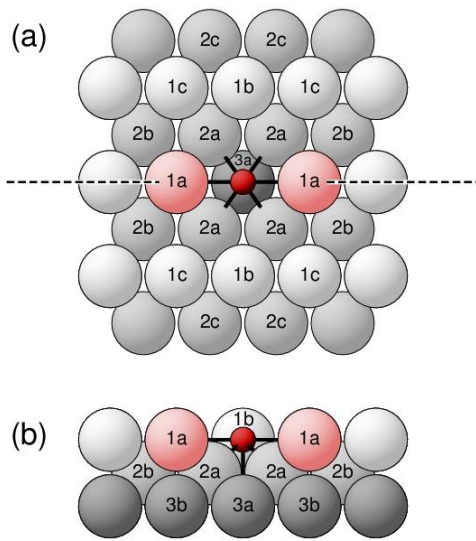


Fig. A.15. fcc(1 1 0) upper substitutional

## A.2 Body-centered cubic (bcc) surface sites

Details of the sketches are explained in the beginning of Appendix A.

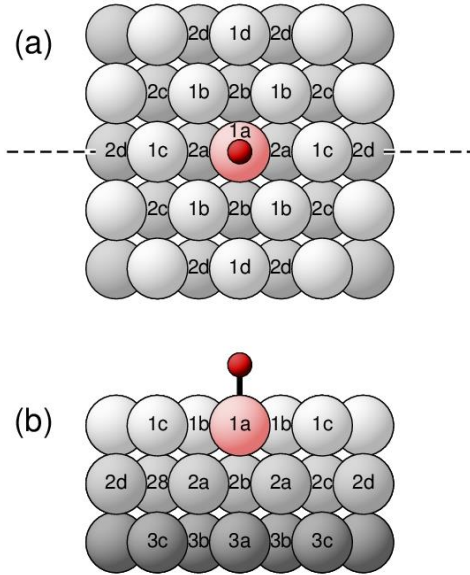


Fig. A.16. bcc(1 1 0) top

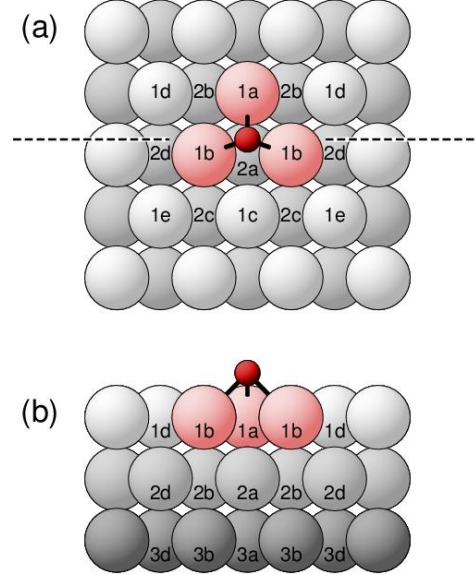


Fig. A.17. bcc(1 1 0) 3-fold hollow

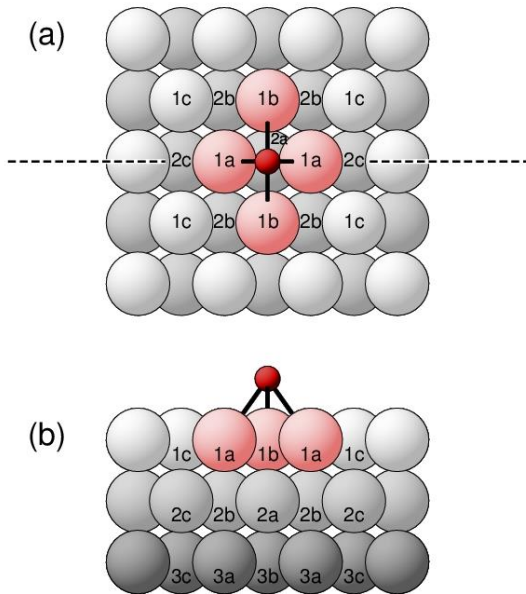


Fig. A.18. bcc(1 1 0) central hollow

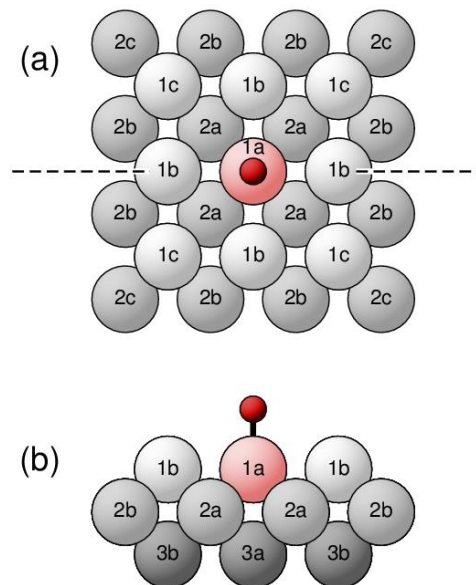


Fig. A.19. bcc(1 0 0) top

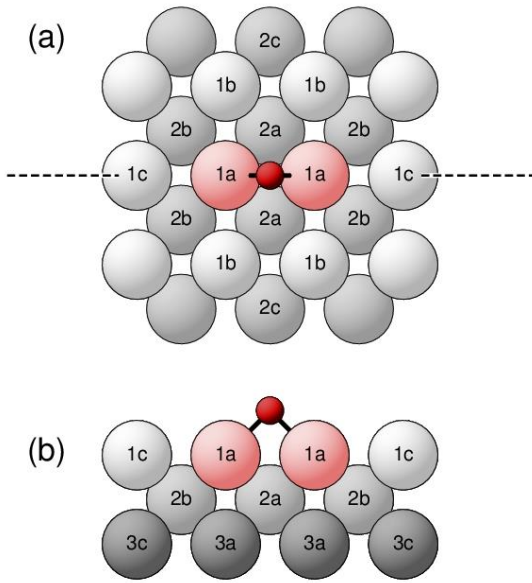


Fig. A.20. bcc(1 0 0) bridge

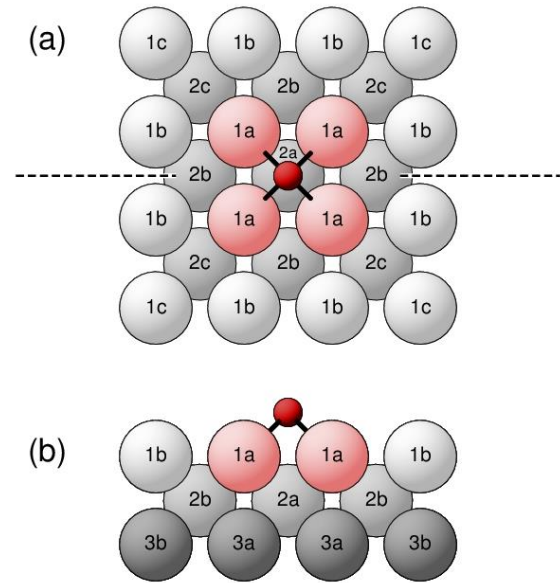


Fig. A.21. bcc(1 0 0) 4-fold hollow

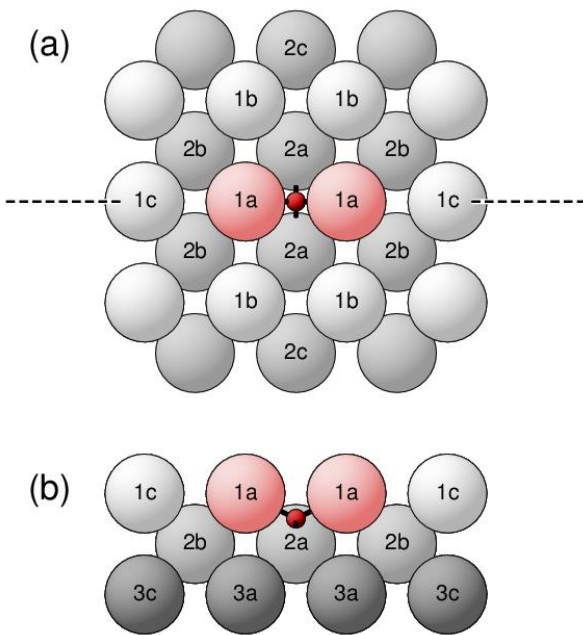


Fig. A.22. bcc(1 0 0) 4-fold interstitial

### A.3 Hexagonal close-packed (hcp) surface sites

Details of the sketches are explained in the beginning of Appendix A.

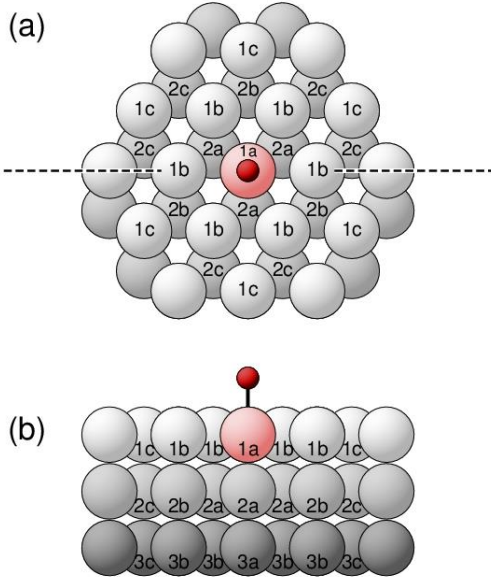


Fig. A.23. hcp(0 0 0 1) top

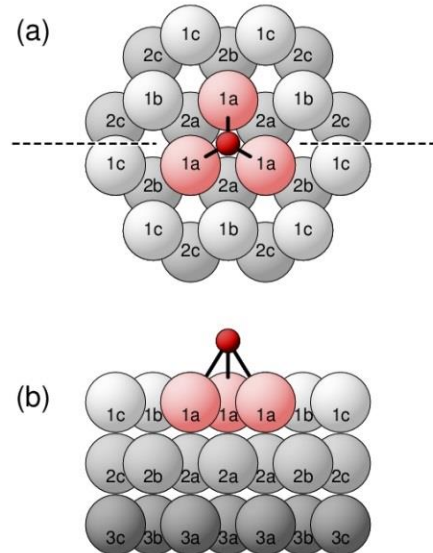


Fig. A.24. hcp(0 0 0 1) fcc-hollow

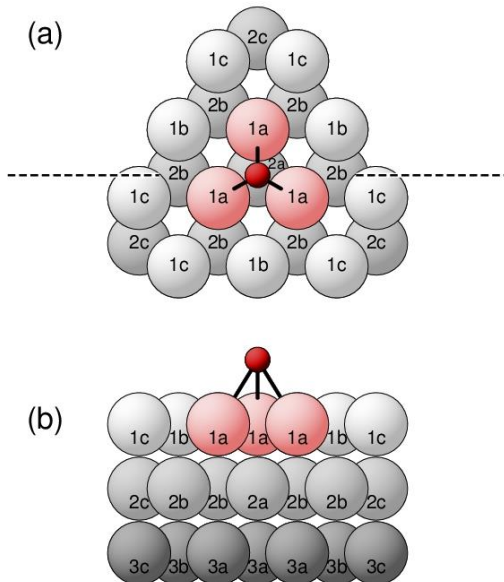


Fig. A.25. hcp(0 0 0 1) hcp-hollow

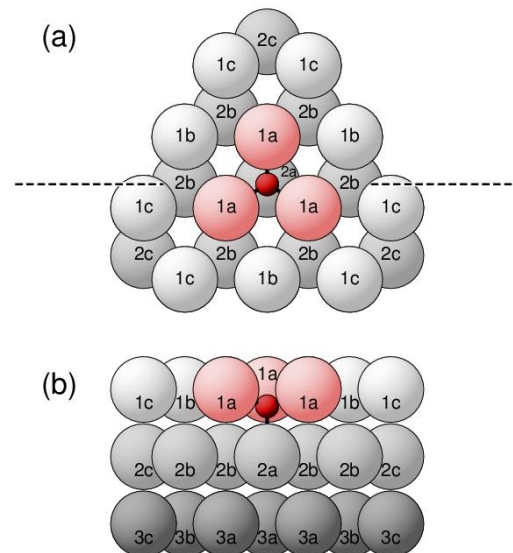


Fig. A.26. hcp(0 0 0 1) tetrahedral interstitial

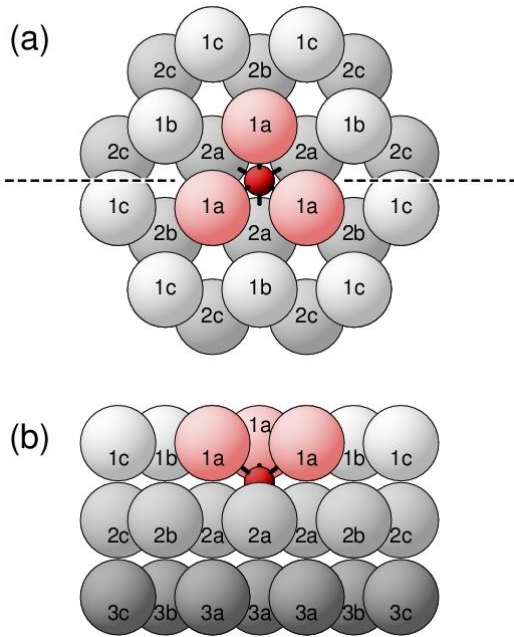


Fig. A.27. hcp(0 0 0 1) octahedral interstitial

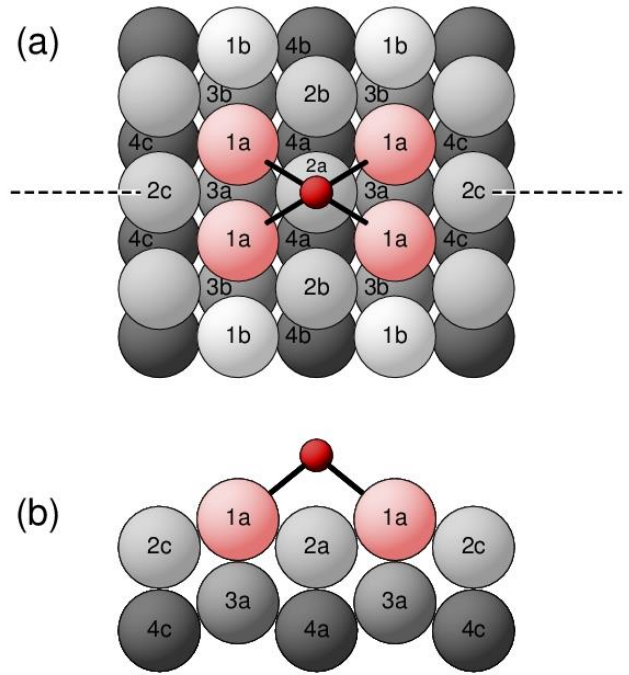


Fig. A.28. hcp(1 0 -1 0) 4-fold center

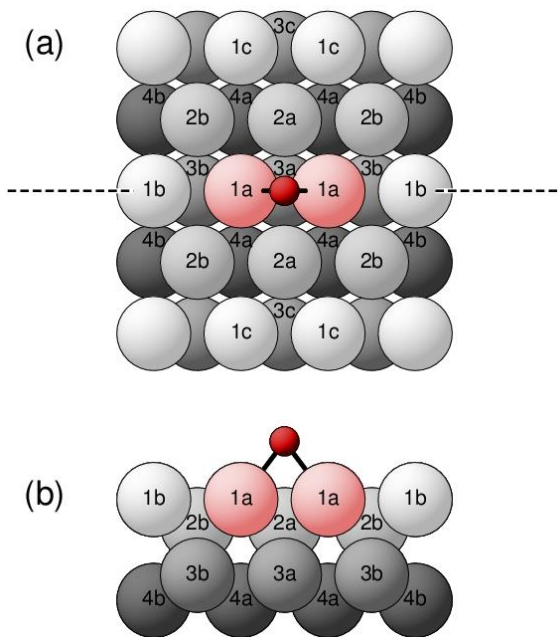


Fig. A.29. hcp(1 0 -1 0) short-bridge

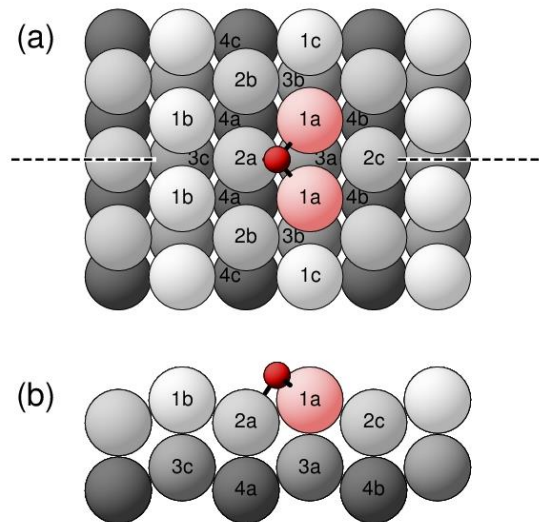


Fig. A.30. hcp(1 0 -1 0) 3-fold hollow

#### A.4 Diamond surface sites

Details of the sketches are explained in the beginning of Appendix A.

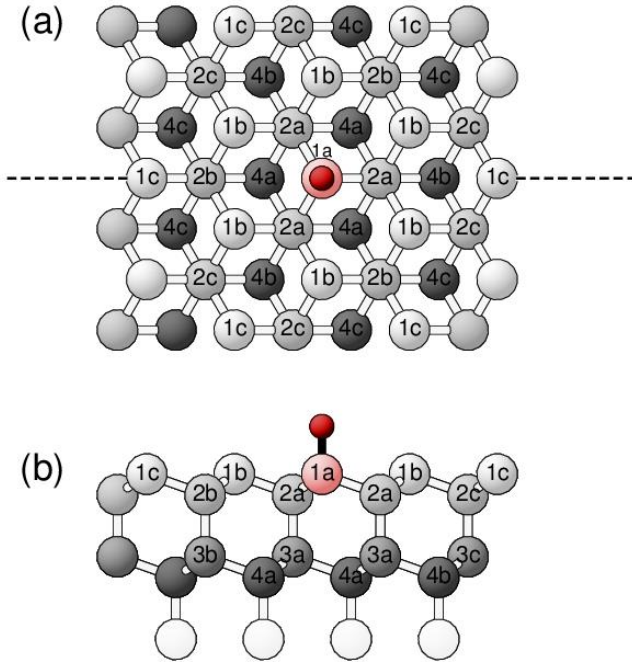


Fig. A.31. Diamond(1 1 1) top

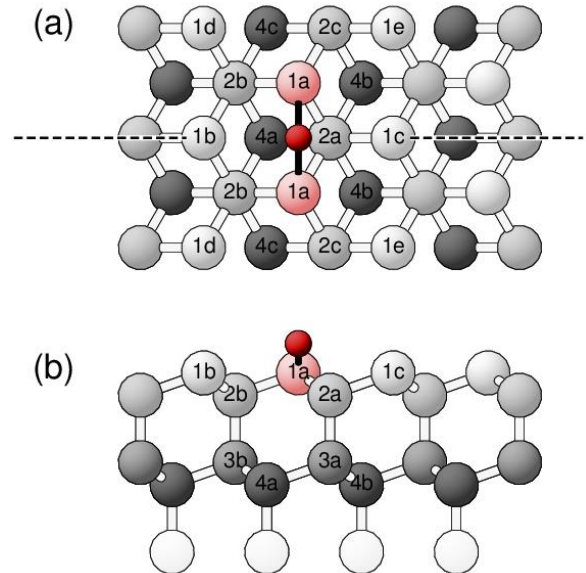


Fig. A.32. Diamond(1 1 1) bridge

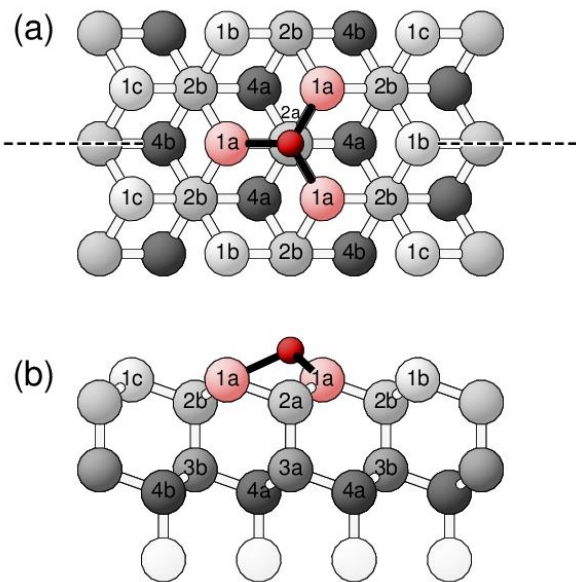


Fig. A.33. Diamond(1 1 1) T4

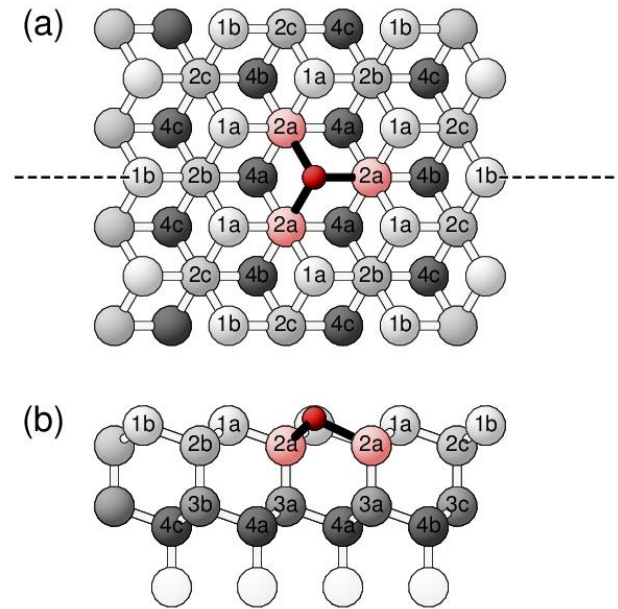


Fig. A.34. Diamond(1 1 1) substitutional top

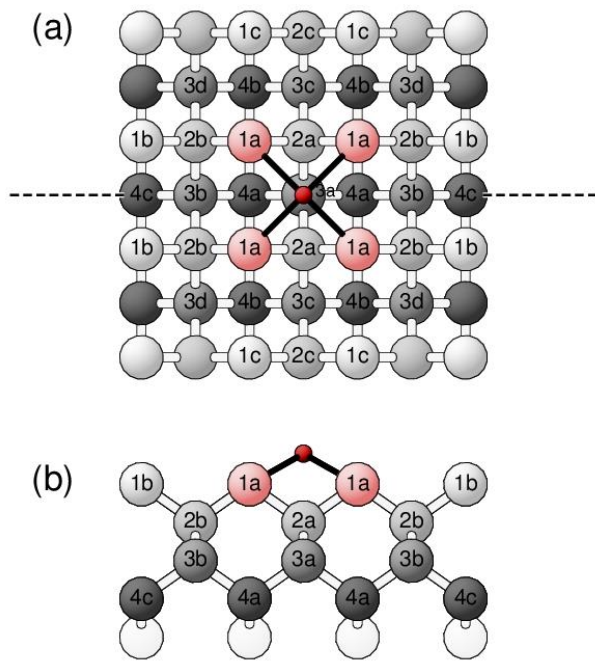


Fig. A.35. Diamond(1 0 0) 4-fold center

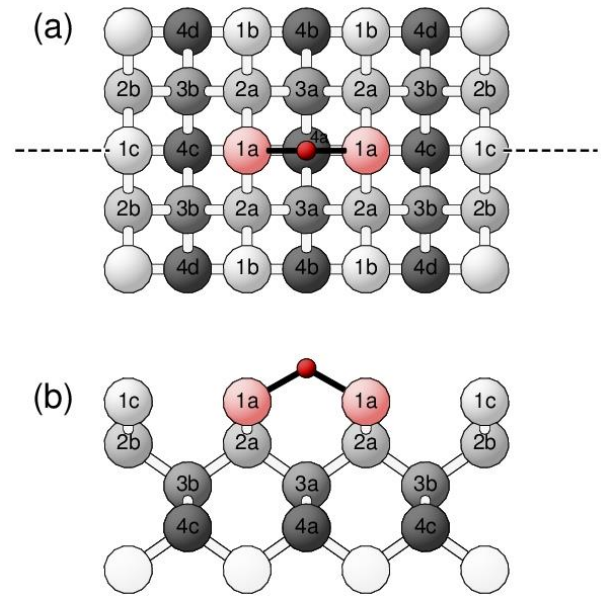


Fig. A.36. Diamond(1 0 0) continuation bridge





## B Parameter Tables of Crystals

This appendix lists the most common lattice types and corresponding lattice parameters of elemental crystals at standard temperature and pressure.

Table B.1. Lattices of elemental single crystals. The Bravais lattice types are abbreviated as listed at the bottom of the table.

Element	Lattice	Element	Lattice	Element	Lattice	Element	Lattice
1 H	hex	26 Fe	bcc	51 Sb	rhl	76 Os	hex
2 He	hex	27 Co	hex	52 Te	hex	77 Ir	fcc
3 Li	bcc	28 Ni	fcc	53 I	ort	78 Pt	fcc
4 Be	hex	29 Cu	fcc	54 Xe	fcc	79 Au	fcc
5 B	tet	30 Zn	hex	55 Cs	bcc	80 Hg	rhl
6 C	dia	31 Ga	ort	56 Ba	bcc	81 Tl	hex
7 N	hex	32 Ge	dia	57 La	hex	82 Pb	fcc
8 O	mcl	33 As	rhl	58 Ce	fcc	83 Bi	rhl
9 F	mcl	34 Se	hex	59 Pr	hex	84 Po	cub
10 Ne	fcc	35 Br	ort	60 Nd	hex	85 At	--
11 Na	bcc	36 Kr	fcc	61 Pm	--	86 Rn	(fcc)
12 Mg	hex	37 Rb	bcc	62 Sm	rhl	87 Fr	(bcc)
13 Al	fcc	38 Sr	fcc	63 Eu	bcc	88 Ra	--
14 Si	dia	39 Y	hex	64 Gd	hex	89 Ac	fcc
15 P	tcl	40 Zr	hex	65 Tb	hex	90 Th	fcc
16 S	ort	41 Nb	bcc	66 Dy	hex	91 Pa	tet
17 Cl	ort	42 Mo	bcc	67 Ho	hex	92 U	ort
18 Ar	fcc	43 Tc	hex	68 Er	hex	93 Np	ort
19 K	bcc	44 Ru	hex	69 Tm	hex	94 Pu	mcl
20 Ca	fcc	45 Rh	fcc	70 Yb	fcc	95 Am	--
21 Sc	hex	46 Pd	fcc	71 Lu	hex	96 Cm	--
22 Ti	hex	47 Ag	fcc	72 Hf	hex	97 Bk	--
23 V	bcc	48 Cd	hex	73 Ta	bcc	98 Cf	--
24 Cr	bcc	49 In	tet	74 W	bcc	99 Es	--
25 Mn	cub	50 Sn	tet	75 Re	hex	100 Fm	--

bcc = body-centered cubic

hex = hexagonal

tcl = triclinic

cub = cubic

mcl = monoclinic

tet = tetragonal

dia = diamond

ort = orthorhombic

fcc = face-centered cubic

rhl = rhombohedral

Table B.2. Lattice constants of face- and body-centered cubic single crystals. The lattice definitions are given in Cartesian coordinates at the bottom of the table.

(a) Face-centered cubic (fcc)

Element	$a$ [Å]
10 Ne	4.43
13 Al	4.05
18 Ar	5.26
20 Ca	5.58
28 Ni	3.52
29 Cu	3.61
36 Kr	5.72
38 Sr	6.08
45 Rh	3.80
46 Pd	3.89
47 Ag	4.09

Element	$a$ [Å]
54 Xe	6.20
58 Ce	5.16
70 Yb	5.49
77 Ir	3.84
78 Pt	3.92
79 Au	4.08
82 Pb	4.95
86 Rn	---
89 Ac	5.31
90 Th	5.08

$$\underline{\mathbf{R}}_1^{\text{fcc}} = a/2 (0, 1, 1) \quad \underline{\mathbf{R}}_2^{\text{fcc}} = a/2 (1, 0, 1) \quad \underline{\mathbf{R}}_3^{\text{fcc}} = a/2 (1, 1, 0)$$

(b) Body-centered cubic (bcc)

Element	$a$ [Å]
3 Li	3.49
11 Na	4.23
19 K	5.23
23 V	3.02
24 Cr	2.88
26 Fe	2.87
37 Rb	5.59
41 Nb	3.30

Element	$a$ [Å]
42 Mo	3.15
55 Cs	6.05
56 Ba	5.02
63 Eu	4.61
73 Ta	3.31
74 W	3.16
87 Fr	---

$$\underline{\mathbf{R}}_1^{\text{bcc}} = a/2 (-1, 1, 1) \quad \underline{\mathbf{R}}_2^{\text{bcc}} = a/2 (1, -1, 1) \quad \underline{\mathbf{R}}_3^{\text{bcc}} = a/2 (1, 1, -1)$$

Table B.3. Lattice constants of hexagonal single crystals. The lattice definition is given in Cartesian coordinates at the bottom of the table. Lattice constant ratios  $c/a$  may be compared with the ideal value  $(c/a)^{\text{hcp}} = \sqrt{8/3} = 1.63299$  for a hexagonal close-packed (hcp) crystal. Note that some the crystals may contain several atoms in the primitive unit cell, two atoms for hcp crystals with lattice basis vectors given at the bottom.

Element	$a$ [Å]	$c/a$
1 H	3.75	1.731
2 He	3.57	1.633
4 Be	2.29	1.567
7 N	4.039	1.651
12 Mg	3.21	1.624
21 Sc	3.31	1.594
22 Ti	2.95	1.588
27 Co	2.51	1.622
30 Zn	2.66	1.856
34 Se	4.36	1.136
39 Y	3.65	1.571
40 Zr	3.23	1.593
43 Tc	2.74(?)	1.604(?)
44 Ru	2.70	1.584
48 Cd	2.98	1.886

Element	$a$ [Å]	$c/a$
52 Te	4.45	1.330
57 La	3.75	1.619
59 Pr	3.67	1.614
60 Nd	3.66	1.614
64 Gd	3.64	1.588
65 Tb	3.60	1.581
66 Dy	3.59	1.573
67 Ho	3.58	1.570
68 Er	3.56	1.570
69 Tm	3.54	1.570
71 Lu	3.51	1.585
72 Hf	3.20	1.582
75 Re	2.76	1.615
76 Os	2.74	1.579
81 Tl	3.46	1.599

$$\begin{aligned} \underline{\mathbf{R}}_1^{\text{hex}} &= a(1, 0, 0) & \underline{\mathbf{R}}_2^{\text{hex}} &= a(-1/2, \sqrt{3}/2, 0) & \underline{\mathbf{R}}_3^{\text{hex}} &= a(0, 0, c/a) \\ \underline{\mathbf{r}}_1^{\text{hcp}} &= a(0, 0, 0) & \underline{\mathbf{r}}_2^{\text{hcp}} &= a(1/2, 1/\sqrt{12}, \sqrt{(2/3)}) \end{aligned}$$

## C Mathematics of the Wood Notation

This appendix gives further mathematical details of the Wood notation [150] introduced in Sec. 6.3 to denote the structure of reconstructed single crystal surfaces as well as of adsorbate layers [94]. As explained in Sec. 6.3 the formal definition of the Wood notation reads

$$\text{Sub}(h k l) - \kappa(\gamma_1 \times \gamma_2)R\alpha \quad \text{for reconstructed surfaces} \quad (\text{C.1a})$$

and

$$\text{Sub}(h k l) + \kappa(\gamma_1 \times \gamma_2)R\alpha - \eta \text{Ovl} \quad \text{for adsorbate surfaces} \quad (\text{C.1b})$$

where, for the sake of simplicity and because of the rare occurrence, we ignore possible substrate reconstruction in the presence of an adsorbate treated by notation (6.4).

### C.1 Basic Formalism and Examples

The periodicity information of the Wood notation given in (C.1) may be expressed alternatively by a more general  $2 \times 2$  matrix transformation according to (5.3). Surface-adapted lattice vectors  $\underline{R}_1$  and  $\underline{R}_2$  of the substrate, forming an angle  $\omega$ , can be represented by orthonormal unit vectors  $\underline{e}_1$  and  $\underline{e}_2$  and written in matrix notation as

$$\begin{pmatrix} \underline{R}_1 \\ \underline{R}_2 \end{pmatrix} = \begin{pmatrix} R_1 & 0 \\ R_2 \cos(\omega) & R_2 \sin(\omega) \end{pmatrix} \begin{pmatrix} \underline{e}_1 \\ \underline{e}_2 \end{pmatrix} \quad (\text{C.2})$$

This relation can be inverted to yield

$$\begin{pmatrix} \underline{e}_1 \\ \underline{e}_2 \end{pmatrix} = \frac{1}{\sin(\omega)} \begin{pmatrix} \frac{1}{R_1} \sin(\omega) & 0 \\ -\frac{1}{R_1} \cos(\omega) & \frac{1}{R_2} \end{pmatrix} \begin{pmatrix} \underline{R}_1 \\ \underline{R}_2 \end{pmatrix} \quad (\text{C.3})$$

Rotating the orthonormal vector set  $\underline{e}_1, \underline{e}_2$  anti-clockwise by an angle  $\alpha$  corresponds to a transformation

$$\begin{pmatrix} \underline{e}_1 \\ \underline{e}_2 \end{pmatrix} \rightarrow \begin{pmatrix} \underline{e}_1' \\ \underline{e}_2' \end{pmatrix} = \begin{pmatrix} \cos(\alpha) & \sin(\alpha) \\ -\sin(\alpha) & \cos(\alpha) \end{pmatrix} \begin{pmatrix} \underline{e}_1 \\ \underline{e}_2 \end{pmatrix} \quad (\text{C.4})$$

Therefore, rotating the two lattice vectors  $\underline{\mathbf{R}}_1$  and  $\underline{\mathbf{R}}_2$  anti-clockwise by an angle  $\alpha$  and scaling each by a factor  $\gamma_1$  and  $\gamma_2$ , respectively, leads to transformed overlayer lattice vectors  $\underline{\mathbf{R}}_1'$  and  $\underline{\mathbf{R}}_2'$ , given by

$$\begin{aligned}
\begin{pmatrix} \underline{\mathbf{R}}_1' \\ \underline{\mathbf{R}}_2' \end{pmatrix} &= \begin{pmatrix} \gamma_1 \mathbf{R}_1 & 0 \\ \gamma_2 \mathbf{R}_2 \cos(\omega) & \gamma_2 \mathbf{R}_2 \sin(\omega) \end{pmatrix} \begin{pmatrix} \underline{\mathbf{e}}_1' \\ \underline{\mathbf{e}}_2' \end{pmatrix} = \\
&= \begin{pmatrix} \gamma_1 \mathbf{R}_1 & 0 \\ \gamma_2 \mathbf{R}_2 \cos(\omega) & \gamma_2 \mathbf{R}_2 \sin(\omega) \end{pmatrix} \begin{pmatrix} \cos(\alpha) & \sin(\alpha) \\ -\sin(\alpha) & \cos(\alpha) \end{pmatrix} \begin{pmatrix} \underline{\mathbf{e}}_1 \\ \underline{\mathbf{e}}_2 \end{pmatrix} = \\
&= \begin{pmatrix} \gamma_1 \mathbf{R}_1 & 0 \\ \gamma_2 \mathbf{R}_2 \cos(\omega) & \gamma_2 \mathbf{R}_2 \sin(\omega) \end{pmatrix} \begin{pmatrix} \cos(\alpha) & \sin(\alpha) \\ -\sin(\alpha) & \cos(\alpha) \end{pmatrix} \frac{1}{\sin(\omega)} \begin{pmatrix} \mathbf{R}_1^{-1} \sin(\omega) & 0 \\ -\mathbf{R}_1^{-1} \cos(\omega) & \mathbf{R}_2^{-1} \end{pmatrix} \begin{pmatrix} \underline{\mathbf{R}}_1 \\ \underline{\mathbf{R}}_2 \end{pmatrix} = \\
&= \frac{1}{\sin(\omega)} \begin{pmatrix} \gamma_1 \mathbf{R}_1 \cos(\alpha) & \gamma_1 \mathbf{R}_1 \sin(\alpha) \\ \gamma_2 \mathbf{R}_2 \cos(\omega + \alpha) & \gamma_2 \mathbf{R}_2 \sin(\omega + \alpha) \end{pmatrix} \begin{pmatrix} \mathbf{R}_1^{-1} \sin(\omega) & 0 \\ -\mathbf{R}_1^{-1} \cos(\omega) & \mathbf{R}_2^{-1} \end{pmatrix} \begin{pmatrix} \underline{\mathbf{R}}_1 \\ \underline{\mathbf{R}}_2 \end{pmatrix} = \\
&= \frac{1}{\sin(\omega)} \begin{pmatrix} \gamma_1 \sin(\omega - \alpha) & \gamma_1 q^{-1} \sin(\alpha) \\ -\gamma_2 q \sin(\alpha) & \gamma_2 \sin(\omega + \alpha) \end{pmatrix} \begin{pmatrix} \underline{\mathbf{R}}_1 \\ \underline{\mathbf{R}}_2 \end{pmatrix} = \underline{\underline{\mathbf{M}}}_p \begin{pmatrix} \underline{\mathbf{R}}_1 \\ \underline{\mathbf{R}}_2 \end{pmatrix}, \quad q = \frac{\mathbf{R}_2}{\mathbf{R}_1} \quad (\text{C.5})
\end{aligned}$$

This proves representation (6.6a) for the transformation matrix  $\underline{\underline{\mathbf{M}}}_p$ , which connects the substrate lattice vectors  $\underline{\mathbf{R}}_1$  and  $\underline{\mathbf{R}}_2$  with those,  $\underline{\mathbf{R}}_1'$  and  $\underline{\mathbf{R}}_2'$ , of the overlayer in the case of **primitive** overlayers denoted by ‘... -  $\mathbf{p}(\gamma_1 \times \gamma_2) \mathbf{R} \alpha$  - ...’. It should be noted that matrix  $\underline{\underline{\mathbf{M}}}_p$  appearing in (C.5) is identical to the transformation matrix (5.16), describing rotational overlayers for scaling factors  $\gamma_1 = \gamma_2 = 1$ .

Corresponding lattice vectors  $\underline{\mathbf{R}}_1''$  and  $\underline{\mathbf{R}}_2''$  of centered overlayers with respect to  $\underline{\mathbf{R}}_1'$  and  $\underline{\mathbf{R}}_2'$  of the primitive overlayers are described by

$$\underline{\mathbf{R}}_1'' = (\underline{\mathbf{R}}_1' + \underline{\mathbf{R}}_2') / 2, \quad \underline{\mathbf{R}}_2'' = (-\underline{\mathbf{R}}_1' + \underline{\mathbf{R}}_2') / 2 \quad (\text{C.6})$$

which yields a transformation

$$\begin{pmatrix} \underline{\mathbf{R}}_1'' \\ \underline{\mathbf{R}}_2'' \end{pmatrix} = \frac{1}{2} \begin{pmatrix} 1 & 1 \\ -1 & 1 \end{pmatrix} \begin{pmatrix} \underline{\mathbf{R}}_1' \\ \underline{\mathbf{R}}_2' \end{pmatrix} = \frac{1}{2} \begin{pmatrix} 1 & 1 \\ -1 & 1 \end{pmatrix} \cdot \underline{\underline{\mathbf{M}}}_p \begin{pmatrix} \underline{\mathbf{R}}_1 \\ \underline{\mathbf{R}}_2 \end{pmatrix} = \underline{\underline{\mathbf{M}}}_c \begin{pmatrix} \underline{\mathbf{R}}_1 \\ \underline{\mathbf{R}}_2 \end{pmatrix} \quad (\text{C.7})$$

and, using (C.5), results in

$$\underline{\underline{\mathbf{M}}}_c = \frac{1}{2 \sin(\omega)} \begin{pmatrix} \gamma_1 \sin(\omega - \alpha) - \gamma_2 q \sin(\alpha) & \gamma_1 q^{-1} \sin(\alpha) + \gamma_2 \sin(\omega + \alpha) \\ -\gamma_1 \sin(\omega - \alpha) - \gamma_2 q \sin(\alpha) & -\gamma_1 q^{-1} \sin(\alpha) + \gamma_2 \sin(\omega + \alpha) \end{pmatrix} \quad (\text{C.8})$$

This proves relation (6.6b) for the transformation matrix  $\underline{\underline{M}}_c$ , connecting the substrate lattice vectors  $\underline{R}_1$  and  $\underline{R}_2$  with those,  $\underline{R}_1''$  and  $\underline{R}_2''$ , of the overlayer in the case of **centered** overlayers denoted by '... -  $\mathbf{c}(\gamma_1 \times \gamma_2)\mathbf{R}\alpha$  - ...'.

In the following, we discuss special cases of primitive overlayers, described by transformation matrices  $\underline{\underline{M}}_p$  of (C.5), where  $q$  is the ratio of the lengths of the periodicity vectors  $\underline{R}_1$  and  $\underline{R}_2$ , i.e.

$$q = R_2 / R_1 \quad (\text{C.9})$$

- a) For **primitive rectangular** substrate lattices the periodicity vectors  $\underline{R}_1$  and  $\underline{R}_2$  are orthogonal ( $\omega = 90^\circ$ ) which yields for  $p(\gamma_1 \times \gamma_2)\mathbf{R}\alpha$

$$\underline{\underline{M}}_p = \begin{pmatrix} m_{11} & m_{12} \\ m_{21} & m_{22} \end{pmatrix} = \begin{pmatrix} \gamma_1 \cos(\alpha) & \gamma_1 q^{-1} \sin(\alpha) \\ -\gamma_2 q \sin(\alpha) & \gamma_2 \cos(\alpha) \end{pmatrix} \quad (\text{C.10})$$

Here **commensurate** overlayers are subject to **integer-valued** elements  $m_{ij}$  where

$$\gamma_1 \cos(\alpha) = m_{11} \quad \gamma_1 q^{-1} \sin(\alpha) = m_{12} \quad (\text{C.11a, b})$$

$$\gamma_2 q \sin(\alpha) = -m_{21} \quad \gamma_2 \cos(\alpha) = m_{22} \quad (\text{C.11c, d})$$

Simple examples are

- Rotation angle  $\alpha = 0^\circ$  and integer  $\gamma_i = n_i$  leading to  $\mathbf{p}(\mathbf{n}_1 \times \mathbf{n}_2)\mathbf{R}0^\circ$  or  $(\mathbf{n}_1 \times \mathbf{n}_2)$  with

$$\underline{\underline{M}}_p = \begin{pmatrix} n_1 & 0 \\ 0 & n_2 \end{pmatrix} \quad (\text{C.12})$$

- Rotation angle  $\alpha = 90^\circ$  and  $\gamma_1 = n_1 q$ ,  $\gamma_2 = n_2/q$ ,  $n_1, n_2$  integer, leading to  $\mathbf{p}(\gamma_1 \times \gamma_2)\mathbf{R}90^\circ$  with

$$\underline{\underline{M}}_p = \begin{pmatrix} 0 & n_1 \\ -n_2 & 0 \end{pmatrix} \quad (\text{C.13})$$

Other combinations of  $\gamma_1, \gamma_2$ , and  $\alpha$  lead in many cases to **incommensurate** overlayers.

- b) For **centered rectangular** substrate lattices the periodicity vectors  $\underline{R}_1$  and  $\underline{R}_2$  are of equal length ( $q = 1$ ) and angle  $\omega$  differs from  $60^\circ, 90^\circ$ , and  $120^\circ$  which yields

$$\underline{\underline{M}}_p = \begin{pmatrix} m_{11} & m_{12} \\ m_{21} & m_{22} \end{pmatrix} = \frac{1}{\sin(\omega)} \begin{pmatrix} \gamma_1 \sin(\omega - \alpha) & \gamma_1 \sin(\alpha) \\ -\gamma_2 \sin(\alpha) & \gamma_2 \sin(\omega + \alpha) \end{pmatrix} \quad (\text{C.14})$$

Here **commensurate** overlayers are subject to **integer-valued** elements  $m_{ij}$  where

$$\gamma_1 \sin(\omega - \alpha) = m_{11} \sin(\omega) \quad \gamma_1 \sin(\alpha) = m_{12} \sin(\omega) \quad (\text{C.15a, b})$$

$$\gamma_2 \sin(\alpha) = -m_{21} \sin(\omega) \quad \gamma_2 \sin(\omega + \alpha) = m_{22} \sin(\omega) \quad (\text{C.15c, d})$$

This means in particular that

$$\gamma_1 \cos(\alpha) = m_{11} + m_{12} \cos(\omega) \quad \text{and} \quad \gamma_2 \cos(\alpha) = m_{22} + m_{21} \cos(\omega) \quad (\text{C.16})$$

A simple example is

- Rotation angle  $\alpha = 0^\circ$  and integer  $\gamma_i = n_i$  leading to  $\mathbf{p}(\mathbf{n}_1 \times \mathbf{n}_2)$  or  $(\mathbf{n}_1 \times \mathbf{n}_2)$  with

$$\underline{\underline{\mathbf{M}}}_p = \begin{pmatrix} n_1 & 0 \\ 0 & n_2 \end{pmatrix} \quad (\text{C.17})$$

Other combinations of  $\gamma_1, \gamma_2$ , and  $\alpha$  lead in many cases to **incommensurate** overlayers.

- c) For **square** substrate lattices the periodicity vectors  $\underline{\mathbf{R}}_1$  and  $\underline{\mathbf{R}}_2$  are orthogonal ( $\omega = 90^\circ$ ) and of equal length ( $q = 1$ ) which yields

$$\underline{\underline{\mathbf{M}}}_p = \begin{pmatrix} m_{11} & m_{12} \\ m_{21} & m_{22} \end{pmatrix} = \begin{pmatrix} \gamma_1 \cos(\alpha) & \gamma_1 \sin(\alpha) \\ -\gamma_2 \sin(\alpha) & \gamma_2 \cos(\alpha) \end{pmatrix} \quad (\text{C.18})$$

Here **commensurate** overlayers are subject to **integer-valued** elements  $m_{ij}$  where

$$\gamma_1 \cos(\alpha) = m_{11} \quad \gamma_1 \sin(\alpha) = m_{12} \quad (\text{C.19a, b})$$

$$\gamma_2 \sin(\alpha) = -m_{21} \quad \gamma_2 \cos(\alpha) = m_{22} \quad (\text{C.19c, d})$$

Simple examples are

- Rotation angle  $\alpha = 0^\circ$  and integer  $\gamma_i = n_i$  leading to  $\mathbf{p}(\mathbf{n}_1 \times \mathbf{n}_2)$  or  $(\mathbf{n}_1 \times \mathbf{n}_2)$  with

$$\underline{\underline{\mathbf{M}}}_p = \begin{pmatrix} n_1 & 0 \\ 0 & n_2 \end{pmatrix} \quad (\text{C.20})$$

- Rotation angle  $\alpha = 90^\circ$  and integer  $\gamma_i = n_i$ , leading to  $\mathbf{p}(\mathbf{n}_1 \times \mathbf{n}_2)\mathbf{R}90^\circ$  with

$$\underline{\underline{\mathbf{M}}}_p = \begin{pmatrix} 0 & n_1 \\ -n_2 & 0 \end{pmatrix} \quad (\text{C.21})$$



- Rotation angles  $-90^\circ < \alpha < 90^\circ$ ,  $\alpha \neq 0^\circ$ , with

$$\cos(\alpha) = m / (m^2 + n^2)^{1/2}, \quad \sin(\alpha) = n / (m^2 + n^2)^{1/2}$$

$$\gamma_1 = a (m^2 + n^2)^{1/2}, \quad \gamma_2 = b (m^2 + n^2)^{1/2}, \quad a, b > 0 \text{ integer}$$

$$m, n > 0 \text{ integer}, \quad \gcd(m, n) = 1$$

leading to  $\mathbf{p}(\gamma_1 \times \gamma_2) \mathbf{R}\alpha$  with

$$\underline{\underline{\mathbf{M}}}_p = \begin{pmatrix} a m & a n \\ -b n & b m \end{pmatrix} \quad (\text{C.22})$$

Other combinations of  $\gamma_1$ ,  $\gamma_2$ , and  $\alpha$  lead in many cases to **incommensurate** overlayers.

- d) For **hexagonal** substrate lattices in **acute** representation ( $\omega = 60^\circ$ ) the periodicity vectors  $\underline{\mathbf{R}}_1$  and  $\underline{\mathbf{R}}_2$  are of equal length ( $q = 1$ ) which yields

$$\underline{\underline{\mathbf{M}}}_p = \begin{pmatrix} m_{11} & m_{12} \\ m_{21} & m_{22} \end{pmatrix} = \frac{2}{\sqrt{3}} \begin{pmatrix} \gamma_1 \sin(60^\circ - \alpha) & \gamma_1 \sin(\alpha) \\ -\gamma_2 \sin(\alpha) & \gamma_2 \sin(60^\circ + \alpha) \end{pmatrix} \quad (\text{C.23})$$

Here **commensurate** overlayers are subject to **integer-valued** elements  $m_{ij}$  where

$$\gamma_1 \sin(60^\circ - \alpha) = c m_{11} \quad \gamma_1 \sin(\alpha) = c m_{12} \quad (\text{C.24a, b})$$

$$\gamma_2 \sin(\alpha) = -c m_{21} \quad \gamma_2 \sin(60^\circ + \alpha) = c m_{22}, \quad c = \sqrt{3}/2 \quad (\text{C.24c, d})$$

This means in particular that

$$\gamma_1 \cos(\alpha) = m_{11} + (m_{12}/2) \quad \text{and} \quad \gamma_2 \cos(\alpha) = m_{22} + (m_{21}/2) \quad (\text{C.25})$$

Simple examples are

- Rotation angle  $\alpha = 0^\circ$  and integer  $\gamma_i = n_i$  leading to  $\mathbf{p}(\mathbf{n}_1 \times \mathbf{n}_2)$  or  $(\mathbf{n}_1 \times \mathbf{n}_2)$  with

$$\underline{\underline{\mathbf{M}}}_p = \begin{pmatrix} n_1 & 0 \\ 0 & n_2 \end{pmatrix} \quad (\text{C.26})$$

- Rotation angle  $\alpha = 60^\circ$  and integer  $\gamma_i = n_i$  leading to  $\mathbf{p}(\mathbf{n}_1 \times \mathbf{n}_2) \mathbf{R}60^\circ$  with

$$\underline{\underline{\mathbf{M}}}_p = \begin{pmatrix} 0 & n_1 \\ -n_2 & n_2 \end{pmatrix} \quad (\text{C.27})$$

- Rotation angle  $\alpha = 120^\circ$  and integer  $\gamma_i = n_i$  leading to  $\mathbf{p}(n_1 \times n_2)\mathbf{R}120^\circ$  with

$$\underline{\underline{\mathbf{M}}}_p = \begin{pmatrix} -n_1 & n_1 \\ -n_2 & 0 \end{pmatrix} \quad (\text{C.28})$$

- Assuming  $\gamma_i = n_i (a^2 + a b + b^2)^{1/2}$ ,

$$\cos(\alpha) = (a + 1/2 b) / (a^2 + a b + b^2)^{1/2}$$

with  $a, b, c$ , and  $p_i$  integer, leading to  $\mathbf{p}(\gamma_1 \times \gamma_2)\mathbf{R}\alpha$  with

$$\underline{\underline{\mathbf{M}}}_p = \begin{pmatrix} n_1 a & n_1 b \\ -n_2 b & n_2 (a + b) \end{pmatrix} \quad (\text{C.29})$$

This includes cases of

$$- a = b = 1, n_1 = n_2 = 1, \underline{\underline{\mathbf{M}}}_p = \begin{pmatrix} 1 & 1 \\ -1 & 2 \end{pmatrix} : \mathbf{p}(\sqrt{3} \times \sqrt{3})\mathbf{R}30^\circ$$

$$- a = 2, b = 1, n_1 = n_2 = 1, \underline{\underline{\mathbf{M}}}_p = \begin{pmatrix} 2 & 1 \\ -1 & 3 \end{pmatrix} : \mathbf{p}(\sqrt{7} \times \sqrt{7})\mathbf{R}19.1^\circ$$

$$- a = 3, b = 1, n_1 = n_2 = 1, \underline{\underline{\mathbf{M}}}_p = \begin{pmatrix} 3 & 1 \\ -1 & 4 \end{pmatrix} : \mathbf{p}(\sqrt{13} \times \sqrt{13})\mathbf{R}13.1^\circ$$

Other combinations of  $\gamma_1, \gamma_2$ , and  $\alpha$  lead in many cases to **incommensurate** overlayers.

- e) For **hexagonal** substrate lattices in **obtuse** representation ( $\omega = 120^\circ$ ) the periodicity vectors  $\underline{\mathbf{R}}_1$  and  $\underline{\mathbf{R}}_2$  are of equal length ( $q = 1$ ) which results in

$$\underline{\underline{\mathbf{M}}}_p = \begin{pmatrix} m_{11} & m_{12} \\ m_{21} & m_{22} \end{pmatrix} = \frac{2}{\sqrt{3}} \begin{pmatrix} \gamma_1 \sin(60^\circ + \alpha) & \gamma_1 \sin(\alpha) \\ -\gamma_2 \sin(\alpha) & \gamma_2 \sin(60^\circ - \alpha) \end{pmatrix} \quad (\text{C.30})$$

Here **commensurate** overlayers are subject to **integer-valued** elements  $m_{ij}$  where

$$\gamma_1 \sin(60^\circ + \alpha) = c m_{11} \quad \gamma_1 \sin(\alpha) = c m_{12} \quad (\text{C.31a, b})$$

$$\gamma_2 \sin(\alpha) = -c m_{21} \quad \gamma_2 \sin(60^\circ - \alpha) = c m_{22}, \quad c = \sqrt{3}/2 \quad (\text{C.31c, d})$$

This means in particular that

$$\gamma_1 \cos(\alpha) = m_{11} - 1/2 m_{12} \quad \text{and} \quad \gamma_2 \cos(\alpha) = m_{22} - 1/2 m_{21} \quad (\text{C.32})$$

Simple examples are

- Rotation angle  $\alpha = 0^\circ$  and integer  $\gamma_i = n_i$  leading to  $\mathbf{p}(\mathbf{n}_1 \times \mathbf{n}_2)$  or  $(\mathbf{n}_1 \times \mathbf{n}_2)$  with

$$\underline{\underline{\mathbf{M}}}_p = \begin{pmatrix} n_1 & 0 \\ 0 & n_2 \end{pmatrix} \quad (\text{C.33})$$

- Rotation angle  $\alpha = 120^\circ$  and integer  $\gamma_i = n_i$  leading to  $\mathbf{p}(\mathbf{n}_1 \times \mathbf{n}_2)\mathbf{R}120^\circ$  with

$$\underline{\underline{\mathbf{M}}}_p = \begin{pmatrix} 0 & n_1 \\ -n_2 & -n_2 \end{pmatrix} \quad (\text{C.34})$$

- Rotation angle  $\alpha = 240^\circ$  and integer  $\gamma_i = n_i$  leading to  $\mathbf{p}(\mathbf{n}_1 \times \mathbf{n}_2)\mathbf{R}240^\circ$  with

$$\underline{\underline{\mathbf{M}}}_p = \begin{pmatrix} -n_1 & -n_1 \\ n_2 & 0 \end{pmatrix} \quad (\text{C.35})$$

- Assuming  $\gamma_i = n_i (a^2 - a b + b^2)^{1/2}$ ,

$$\cos(\alpha) = (a + 1/2 b) / (a^2 - a b + b^2)^{1/2}$$

with  $a, b, c$ , and  $p_i$  integer, leading to

$\mathbf{p}(\gamma_1 \times \gamma_2)\mathbf{R}\alpha$  with

$$\underline{\underline{\mathbf{M}}}_p = \begin{pmatrix} n_1 a & n_1 b \\ -n_2 b & n_2 (a - b) \end{pmatrix} \quad (\text{C.36})$$

This includes cases of

$$- a = 2, b = 1, n_1 = n_2 = 1, \underline{\underline{\mathbf{M}}}_p = \begin{pmatrix} 2 & 1 \\ -1 & 1 \end{pmatrix} : \mathbf{p}(\sqrt{3} \times \sqrt{3})\mathbf{R}30^\circ$$

$$- a = 3, b = 1, n_1 = n_2 = 1, \underline{\underline{\mathbf{M}}}_p = \begin{pmatrix} 3 & 1 \\ -1 & 2 \end{pmatrix} : \mathbf{p}(\sqrt{7} \times \sqrt{7})\mathbf{R}19.1^\circ$$

$$- a = 4, b = 1, n_1 = n_2 = 1, \underline{\underline{\mathbf{M}}}_p = \begin{pmatrix} 4 & 1 \\ -1 & 3 \end{pmatrix} : \mathbf{p}(\sqrt{13} \times \sqrt{13})\mathbf{R}13.1^\circ$$

Other combinations of  $\gamma_1, \gamma_2$ , and  $\alpha$  lead in many cases to incommensurate overlayers.

## C.2 Wood-Representability

Lattice structures given by Wood notation (6.2) and (C.1) make it always possible to construct corresponding  $2 \times 2$  transformations matrices  $\underline{\underline{M}}_{p,c}$  according to (C.5) and (C.8). However, not all  $2 \times 2$  matrices refer to transformations which can be characterized by a Wood notation. The mathematical reason behind it is that  $2 \times 2$  matrices are determined by four parameters, the matrix elements  $m_{ij}$ , allowing four degrees of freedom whereas the Wood notation allows only three, given by the two stretch parameters,  $\gamma_1$  and  $\gamma_2$ , and the rotation angle  $\alpha$ . The fourth degree of freedom does not appear because the Wood notation assumes that the angle  $\omega$  between the lattice vectors  $\underline{R}_1'$  and  $\underline{R}_2'$  of the overlayer agrees with that between the lattice vectors  $\underline{R}_1$  and  $\underline{R}_2$  of the substrate surface. This constraint can be used to select all  $2 \times 2$  matrices which correspond to transformations in Wood notation and will be called **Wood representable** in the following.

In a general lattice transformation according to (5.3)

$$\begin{pmatrix} \underline{R}_1' \\ \underline{R}_2' \end{pmatrix} = \begin{pmatrix} m_{11} & m_{12} \\ m_{21} & m_{22} \end{pmatrix} \cdot \begin{pmatrix} \underline{R}_1 \\ \underline{R}_2 \end{pmatrix} = \underline{\underline{M}} \cdot \begin{pmatrix} \underline{R}_1 \\ \underline{R}_2 \end{pmatrix} \quad (\text{C.37})$$

the area of the periodicity cell of the overlayer, given by  $F' = |\underline{R}_1' \times \underline{R}_2'|$ , can be written as

$$F' = |\underline{R}_1' \times \underline{R}_2'| = R_1' R_2' \sin(\omega') = \det(\underline{\underline{M}}) |\underline{R}_1 \times \underline{R}_2| = \det(\underline{\underline{M}}) R_1 R_2 \sin(\omega) \quad (\text{C.38})$$

where  $\omega$  and  $\omega'$  are the angles formed by vectors  $\underline{R}_1$  and  $\underline{R}_2$  and by  $\underline{R}_1'$  and  $\underline{R}_2'$ , respectively. If transformation (C.37) allows a **primitive Wood notation** then angles  $\omega$  and  $\omega'$  must be equal. Thus, (C.38) leads to

$$\det(\underline{\underline{M}})^2 = \left( \frac{R_1' R_2'}{R_1 R_2} \right)^2 = (m_{11} m_{22} - m_{12} m_{21})^2 \quad (\text{C.39})$$

and hence with

$$\left( \frac{R_1'}{R_1} \right)^2 = m_{11}^2 + m_{12}^2 q^2 + 2m_{11} m_{12} q \cos(\omega) \quad , \quad q = \frac{R_2}{R_1} \quad (\text{C.40})$$

$$\left( \frac{R_2'}{R_2} \right)^2 = m_{21}^2 q^{-2} + m_{22}^2 + 2m_{21} m_{22} q^{-1} \cos(\omega) \quad (\text{C.41})$$

relation (C.39) yields

$$\begin{aligned} (m_{11} m_{22} - m_{12} m_{21})^2 = & \left\{ m_{11}^2 + m_{12}^2 q^2 + 2 m_{11} m_{12} q \cos(\omega) \right\} \cdot \\ & \cdot \left\{ m_{21}^2 q^{-2} + m_{22}^2 + 2 m_{21} m_{22} q^{-1} \cos(\omega) \right\} \end{aligned} \quad (\text{C.42})$$

Relation (C.42) is the **mathematical constraint** for matrices  $\underline{\mathbf{M}}$  to be Wood-representable yielding transformations according to the **primitive** Wood notation, denoted as  $p(\gamma_1 \times \gamma_2)R\alpha$  where

$$\gamma_1 = \frac{R_1'}{R_1} = \sqrt{m_{11}^2 + m_{12}^2 q^2 + 2 m_{11} m_{12} q \cos(\omega)} \quad , \quad q = \frac{R_2}{R_1} \quad (\text{C.43a})$$

$$\gamma_2 = \frac{R_2'}{R_2} = \sqrt{m_{21}^2 q^{-2} + m_{22}^2 + 2 m_{21} m_{22} q^{-1} \cos(\omega)} \quad (\text{C.43b})$$

$$\cos(\alpha) = \frac{R_1' R_1}{R_1' R_1} = (m_{11} + m_{12} q \cos(\omega)) \gamma_1^{-1} = (m_{22} + m_{21} q^{-1} \cos(\omega)) \gamma_2^{-1} \quad (\text{C.43c})$$

These relations depend, apart from all matrix elements  $m_{ij}$ , on the geometry specifications of the substrate lattice given by  $q$  and  $\omega$  which distinguishes between Bravais lattice types.

- a) For **primitive rectangular** substrate lattices,  $q \neq 1$  and  $\omega = 90^\circ$ , Wood-representable matrices  $\underline{\mathbf{M}}$  according to (C.42) are subject to

$$m_{11} m_{21} + q^2 m_{12} m_{22} = 0 \quad (\text{C.44})$$

yielding

$$\begin{aligned} \gamma_1 = \sqrt{m_{11}^2 + m_{12}^2 q^2} \quad , \quad \gamma_2 = \sqrt{m_{21}^2 q^{-2} + m_{22}^2} \\ \cos(\alpha) = m_{11} \gamma_1^{-1} = m_{22} \gamma_2^{-1} \end{aligned} \quad (\text{C.45})$$

- b) For **centered rectangular** substrate lattices,  $q = 1$  and  $\omega \neq 60^\circ, 90^\circ, 120^\circ$ , Wood-representable matrices  $\underline{\mathbf{M}}$  according to (C.42) are subject to

$$\begin{aligned} (m_{11} m_{22} - m_{12} m_{21})^2 = & \left\{ m_{11}^2 + m_{12}^2 + 2 m_{11} m_{12} \cos(\omega) \right\} \cdot \\ & \cdot \left\{ m_{21}^2 + m_{22}^2 + 2 m_{21} m_{22} \cos(\omega) \right\} \end{aligned} \quad (\text{C.46})$$

yielding

$$\begin{aligned} \gamma_i = \sqrt{m_{i1}^2 + m_{i2}^2 + 2 m_{i1} m_{i2} \cos(\omega)} \quad , \quad i=1,2 \\ \cos(\alpha) = (m_{11} + m_{12} \cos(\omega)) \gamma_1^{-1} = (m_{22} + m_{21} \cos(\omega)) \gamma_2^{-1} \end{aligned} \quad (\text{C.47})$$

- c) For **square** substrate lattices,  $q = 1$  and  $\omega = 90^\circ$ , Wood-representable matrices  $\underline{\underline{M}}$  according to (C.42) are subject to

$$m_{11}m_{21} + m_{12}m_{22} = 0 \quad (\text{C.48})$$

yielding

$$\gamma_i = \sqrt{m_{i1}^2 + m_{i2}^2} \quad , \quad i=1,2 \quad , \quad \cos(\alpha) = m_{11}\gamma_1^{-1} = m_{22}\gamma_2^{-1} \quad (\text{C.49})$$

- d) For **hexagonal** substrate lattices in **acute** representation,  $q = 1$  and  $\omega = 60$ , Wood-representable matrices  $\underline{\underline{M}}$  according to (C.42) are subject to

$$(m_{11}m_{22} - m_{12}m_{21})^2 = \{m_{11}^2 + m_{12}^2 + m_{11}m_{12}\} \{m_{21}^2 + m_{22}^2 + m_{21}m_{22}\} \quad (\text{C.50})$$

yielding

$$\gamma_i = \sqrt{m_{i1}^2 + m_{i2}^2 + m_{i1}m_{i2}} \quad , \quad i=1,2$$

$$\cos(\alpha) = \left(m_{11} + \frac{1}{2}m_{12}\right)\gamma_1^{-1} = \left(m_{22} + \frac{1}{2}m_{21}\right)\gamma_2^{-1} \quad (\text{C.51})$$

- e) For **hexagonal** substrate lattices in **obtuse** representation,  $q = 1$  and  $\omega = 120$ , Wood-representable matrices  $\underline{\underline{M}}$  according to (C.42) are subject to

$$(m_{11}m_{22} - m_{12}m_{21})^2 = \{m_{11}^2 + m_{12}^2 - m_{11}m_{12}\} \{m_{21}^2 + m_{22}^2 - m_{21}m_{22}\} \quad (\text{C.52})$$

yielding

$$\gamma_i = \sqrt{m_{i1}^2 + m_{i2}^2 - m_{i1}m_{i2}} \quad , \quad i=1,2$$

$$\cos(\alpha) = \left(m_{11} - \frac{1}{2}m_{12}\right)\gamma_1^{-1} = \left(m_{22} - \frac{1}{2}m_{21}\right)\gamma_2^{-1} \quad (\text{C.53})$$

If transformation (C.37) allows a **centered Wood notation**, described as  $c(\gamma_1 \times \gamma_2)R\alpha$ , then its transformation matrix  $\underline{\underline{M}}_c$  can be written as the product of a simple transformation matrix  $\underline{\underline{T}}$  and matrix  $\underline{\underline{M}}_p$  which provides the corresponding transformation according to a primitive Wood notation,  $p(\gamma_1 \times \gamma_2)R\alpha$ , i.e.

$$\underline{\underline{M}}_c = \underline{\underline{T}} \underline{\underline{M}}_p \quad , \quad \underline{\underline{M}}_p = \underline{\underline{T}}^{-1} \underline{\underline{M}}_c \quad (\text{C.54})$$

where

$$\underline{\underline{\mathbf{T}}} = \frac{1}{2} \begin{pmatrix} 1 & 1 \\ -1 & 1 \end{pmatrix}, \quad \frac{1}{2} \begin{pmatrix} -1 & 1 \\ -1 & -1 \end{pmatrix}, \quad \frac{1}{2} \begin{pmatrix} -1 & -1 \\ 1 & -1 \end{pmatrix}, \quad \frac{1}{2} \begin{pmatrix} 1 & -1 \\ 1 & 1 \end{pmatrix} \quad (\text{C.55})$$

$$\underline{\underline{\mathbf{T}}}^{-1} = \begin{pmatrix} 1 & -1 \\ 1 & 1 \end{pmatrix}, \quad \begin{pmatrix} -1 & -1 \\ 1 & -1 \end{pmatrix}, \quad \begin{pmatrix} -1 & 1 \\ -1 & -1 \end{pmatrix}, \quad \begin{pmatrix} 1 & 1 \\ -1 & 1 \end{pmatrix} \quad (\text{C.56})$$

Therefore, testing a matrix  $\underline{\underline{\mathbf{M}}}_c$  for Wood-representability according to the centered Wood notation can be achieved by first determining the corresponding matrix  $\underline{\underline{\mathbf{M}}}_p$  using (C.54), (C.55), (C.56) followed by testing  $\underline{\underline{\mathbf{M}}}_p$  applying the criteria given in (C.42) and (C.44) to (C.53).

**Combining Wood-representable transformations.** Lattice transformation defined in Wood notation (6.2) or (6.4) and their corresponding  $2 \times 2$  matrices  $\underline{\underline{\mathbf{M}}}_{p,c}$  according to (C.5) and (C.8) can be combined to yield other lattice transformations. Here we restrict the discussion to the **primitive Wood notation**  $p(\gamma_1 \times \gamma_2)R\alpha$  and  $2 \times 2$  matrices  $\underline{\underline{\mathbf{M}}}_p$  given by (C.5).

Applying two Wood-representable transformations,  $p(\gamma_1' \times \gamma_2')R\alpha'$  and  $p(\gamma_1 \times \gamma_2)R\alpha$  in sequence corresponds to transformations

$$\begin{pmatrix} \underline{\underline{\mathbf{R}}}_1' \\ \underline{\underline{\mathbf{R}}}_2' \end{pmatrix} = \frac{1}{\sin(\omega)} \begin{pmatrix} \gamma_1 \sin(\omega - \alpha) & \gamma_1 q^{-1} \sin(\alpha) \\ -\gamma_2 q \sin(\alpha) & \gamma_2 \sin(\omega + \alpha) \end{pmatrix} \begin{pmatrix} \underline{\underline{\mathbf{R}}}_1 \\ \underline{\underline{\mathbf{R}}}_2 \end{pmatrix}, \quad q = \frac{\mathbf{R}_2}{\mathbf{R}_1} \quad (\text{C.57})$$

followed by

$$\begin{pmatrix} \underline{\underline{\mathbf{R}}}_1'' \\ \underline{\underline{\mathbf{R}}}_2'' \end{pmatrix} = \frac{1}{\sin(\omega)} \begin{pmatrix} \gamma_1' \sin(\omega - \alpha') & \gamma_1' q'^{-1} \sin(\alpha') \\ -\gamma_2' q' \sin(\alpha') & \gamma_2' \sin(\omega + \alpha') \end{pmatrix} \begin{pmatrix} \underline{\underline{\mathbf{R}}}_1' \\ \underline{\underline{\mathbf{R}}}_2' \end{pmatrix}, \quad q' = \frac{\mathbf{R}_2'}{\mathbf{R}_1'} = \frac{\gamma_2}{\gamma_1} q \quad (\text{C.58})$$

such that after some basic calculus

$$\begin{pmatrix} \underline{\underline{\mathbf{R}}}_1'' \\ \underline{\underline{\mathbf{R}}}_2'' \end{pmatrix} = \frac{1}{\sin(\omega)} \begin{pmatrix} \gamma_1' \gamma_1 \sin(\omega - \alpha - \alpha') & \gamma_1' \gamma_1 q'^{-1} \sin(\alpha + \alpha') \\ -\gamma_2' \gamma_2 q' \sin(\alpha + \alpha') & \gamma_2' \gamma_2 \sin(\omega + \alpha + \alpha') \end{pmatrix} \begin{pmatrix} \underline{\underline{\mathbf{R}}}_1 \\ \underline{\underline{\mathbf{R}}}_2 \end{pmatrix} \quad (\text{C.59})$$

which is a Wood-representable transformation given by

$$p(\gamma_1' \times \gamma_2')R\alpha' * p(\gamma_1 \times \gamma_2)R\alpha = p(\gamma_1' \gamma_1 \times \gamma_2' \gamma_2)R(\alpha' + \alpha) \quad (\text{C.60})$$

Thus, the application of two Wood-representable transformations yields again a Wood-representable transformation. In addition, swapping the sequence of application of the two transformations yields the same final transformation. Therefore, the order in which the two transformations are applied does not affect the final result.

Next, for every Wood-representable transformation one can construct an inverse transformation. Considering  $\underline{\underline{M}}_p$  defined by (C.5) we find

$$\det(\underline{\underline{M}}_p) = \gamma_1 \gamma_2 \quad (\text{C.61})$$

and hence

$$\begin{aligned} \underline{\underline{M}}_p^{-1} &= \frac{1}{\gamma_1 \gamma_2 \sin(\omega)} \begin{pmatrix} \gamma_2 \sin(\omega + \alpha) & -\gamma_1 q^{-1} \sin(\alpha) \\ \gamma_2 q \sin(\alpha) & \gamma_1 \sin(\omega - \alpha) \end{pmatrix} = \\ &= \frac{1}{\sin(\omega)} \begin{pmatrix} \gamma_1^{-1} \sin(\omega - (-\alpha)) & \gamma_2^{-1} q^{-1} \sin(-\alpha) \\ -\gamma_1^{-1} q \sin(-\alpha) & \gamma_2^{-1} \sin(\omega + (-\alpha)) \end{pmatrix} \end{aligned} \quad (\text{C.62})$$

which is again a Wood-representable matrix of a transformation referring to  $p(\gamma_1^{-1} \times \gamma_2^{-1})\mathbf{R}(-\alpha)$  such that together with (C.60)

$$p(\gamma_1 \times \gamma_2)\mathbf{R}\alpha * p(\gamma_1^{-1} \times \gamma_2^{-1})\mathbf{R}(-\alpha) = p(1 \times 1) \quad (\text{C.63})$$

where  $p(1 \times 1)$  with  $\underline{\underline{M}}_p = \underline{\underline{1}}$  can be considered the Wood-representable unit transformation. Altogether, the set of all Wood-representable transformations described as  $p(\gamma_1 \times \gamma_2)\mathbf{R}\alpha$  and applied to a given Bravais lattice form an (infinite) Abelian group.



## D Mathematics of the Minkowski Reduction

This appendix discusses mathematical details of the Minkowski reduction used to obtain **symmetrically appropriate** lattice vectors  $\underline{R}_{o1}$  and  $\underline{R}_{o2}$  from initial lattice vectors  $\underline{R}_1$  and  $\underline{R}_2$ , see Sec. 3.3.

Let us assume that  $\underline{R}_1$  and  $\underline{R}_2$  are lattice vectors of a two-dimensional lattice with lengths  $R_1$  and  $R_2$ . Then vector  $\underline{r}$  inside the plane spanned  $R_1$  and  $R_2$  and by defined by

$$\underline{r} = \underline{R}_2 - x \underline{R}_1 \quad (\text{D.1})$$

has a squared length

$$r^2 = |\underline{r}|^2 = R_2^2 + x^2 R_1^2 - 2 x (\underline{R}_1 \cdot \underline{R}_2) \quad (\text{D.2})$$

which, by varying  $x$ , reaches its minimum for

$$x = x_{\min} = (\underline{R}_1 \cdot \underline{R}_2) / R_1^2 \quad (\text{D.3})$$

The resulting smallest vector  $\underline{r} = \underline{r}_{\min}$  with

$$\underline{r}_{\min} = \underline{R}_2 - x_{\min} \underline{R}_1 = \underline{R}_2 - ((\underline{R}_1 \cdot \underline{R}_2) / R_1^2) \underline{R}_1 \quad (\text{D.4})$$

is perpendicular to  $\underline{R}_1$ , since

$$(\underline{R}_1 \cdot \underline{r}_{\min}) = (\underline{R}_1 \cdot \underline{R}_2) - ((\underline{R}_1 \cdot \underline{R}_2) / R_1^2) (\underline{R}_1 \cdot \underline{R}_1) = 0 \quad (\text{D.5})$$

However, in general  $\underline{r}_{\min}$  will not be a lattice vector itself. The lattice vector  $\underline{R}_2'$  represented by (D.1), nearest to  $\underline{r}_{\min}$  in length, is given by

$$\underline{R}_2' = \underline{R}_2 - \{x_{\min}\} \underline{R}_1 \quad (\text{D.6})$$

where function  $\{x\}$  denotes the integer nearest to a real number  $x$  as introduced in Appendix E.1.

Then for the length square  $|\underline{R}_2'|^2$  we obtain

$$\begin{aligned} |\underline{R}_2'|^2 &= R_2^2 + \{x_{\min}\}^2 R_1^2 - 2 \{x_{\min}\} (\underline{R}_1 \cdot \underline{R}_2) \\ &= R_2^2 - \{x_{\min}\} (2 x_{\min} - \{x_{\min}\}) R_1^2 = R_2^2 - p(x_{\min}) R_1^2 \end{aligned} \quad (\text{D.7})$$

where the mixing factor

$$p(x) = \{x\} (2x - \{x\}) \quad (\text{D.8})$$

is symmetric in  $x$  and assumes only positive values as discussed in Appendix E.1, i.e.

$$p(-x) = p(x) \geq 0 \quad (\text{D.9})$$

Thus, the reduction  $\underline{\mathbf{R}}_2 \rightarrow \underline{\mathbf{R}}_2'$  yields according to (D.7)

$$|\underline{\mathbf{R}}_2'|^2 \leq \underline{\mathbf{R}}_2^2 \quad (\text{D.10})$$

which proves that it can only decrease the length of vector  $\underline{\mathbf{R}}_2$  or leaves its length unchanged. The latter means that

$$\{x_{\min}\} = 0 \quad \text{or} \quad -1/2 \leq x_{\min} < 1/2 \quad (\text{D.11})$$

and, together with (D.3), leads to

$$-\underline{\mathbf{R}}_1^2 \leq 2(\underline{\mathbf{R}}_1 \cdot \underline{\mathbf{R}}_2) < \underline{\mathbf{R}}_1^2 \quad (\text{D.12})$$

In addition, transformation (D.6) will always lead to a vector  $\underline{\mathbf{R}}_2'$  of finite length, i.e.  $|\underline{\mathbf{R}}_2'| > 0$  since  $\underline{\mathbf{R}}_1$  and  $\underline{\mathbf{R}}_2$  are assumed to be linearly independent. A reduction analogous to (D.1) can be applied to reduce the length of  $\underline{\mathbf{R}}_1$ , yielding

$$\underline{\mathbf{R}}_1' = \underline{\mathbf{R}}_1 - \{x_{\min}'\} \underline{\mathbf{R}}_2, \quad \text{with} \quad x_{\min}' = (\underline{\mathbf{R}}_1 \cdot \underline{\mathbf{R}}_2) / \underline{\mathbf{R}}_2^2 \quad (\text{D.13})$$

where the reduction can only decrease the length of vector  $\underline{\mathbf{R}}_1$  or leaves its length unchanged. The latter results in

$$-\underline{\mathbf{R}}_2^2 \leq 2(\underline{\mathbf{R}}_1 \cdot \underline{\mathbf{R}}_2) < \underline{\mathbf{R}}_2^2 \quad (\text{D.14})$$

Relations (D.6), (D.12), (D.13), and (D.14) form the basis of an **iterative** algorithm, the **Min-kowski reduction**, which can be used to determine a lattice vector set  $\underline{\mathbf{R}}_{o1}, \underline{\mathbf{R}}_{o2}$  with vectors that are the smallest in length. We consider an iterative transformation starting with

$$(k=0) \quad \underline{\mathbf{R}}_1^{(k)} = \underline{\mathbf{R}}_1, \quad \underline{\mathbf{R}}_2^{(k)} = \underline{\mathbf{R}}_2 \quad (\text{D.15})$$

where each iteration step contains two reductions. First, vector  $\underline{\mathbf{R}}_2^{(k)}$  is reduced according to (D.6) which can be written as a linear transformation  $(\underline{\mathbf{R}}_1^{(k)}, \underline{\mathbf{R}}_2^{(k)}) \rightarrow (\underline{\mathbf{R}}_1^{(k)}, \underline{\mathbf{R}}_2^{(k+1)})$  with

$$\begin{pmatrix} \underline{\mathbf{R}}_1^{(k)} \\ \underline{\mathbf{R}}_2^{(k+1)} \end{pmatrix} = \begin{pmatrix} 1 & 0 \\ -\{x_k\} & 1 \end{pmatrix} \cdot \begin{pmatrix} \underline{\mathbf{R}}_1^{(k)} \\ \underline{\mathbf{R}}_2^{(k)} \end{pmatrix}, \quad x_k = (\underline{\mathbf{R}}_1^{(k)} \cdot \underline{\mathbf{R}}_2^{(k)}) / (\underline{\mathbf{R}}_1^{(k)})^2 \quad (\text{D.16})$$

Then vector  $\underline{\mathbf{R}}_1^{(k)}$  is reduced according to (D.13) which can be written as a linear transformation  $(\underline{\mathbf{R}}_1^{(k)}, \underline{\mathbf{R}}_2^{(k+1)}) \rightarrow (\underline{\mathbf{R}}_1^{(k+1)}, \underline{\mathbf{R}}_2^{(k+1)})$  with

$$\begin{pmatrix} \underline{\mathbf{R}}_1^{(k+1)} \\ \underline{\mathbf{R}}_2^{(k+1)} \end{pmatrix} = \begin{pmatrix} 1 & -\{x_k'\} \\ 0 & 1 \end{pmatrix} \cdot \begin{pmatrix} \underline{\mathbf{R}}_1^{(k)} \\ \underline{\mathbf{R}}_2^{(k+1)} \end{pmatrix}, \quad x_k' = (\underline{\mathbf{R}}_1^{(k)} \cdot \underline{\mathbf{R}}_2^{(k+1)}) / (\underline{\mathbf{R}}_2^{(k+1)})^2 \quad (\text{D.17})$$

Since the transformation matrices in (D.16), (D.17) are integer-valued and their inverse matrices

$$\begin{pmatrix} 1 & 0 \\ -\{x_k\} & 1 \end{pmatrix}^{-1} = \begin{pmatrix} 1 & 0 \\ \{x_k\} & 1 \end{pmatrix}, \quad \begin{pmatrix} 1 & -\{x_k'\} \\ 0 & 1 \end{pmatrix}^{-1} = \begin{pmatrix} 1 & \{x_k'\} \\ 0 & 1 \end{pmatrix} \quad (\text{D.18})$$

exist and are also integer-valued, the reduced lattice vectors  $\underline{R}_1^{(k+1)}$  and  $\underline{R}_2^{(k+1)}$  of (D.17) provide the same lattice description as  $\underline{R}_1^{(k)}$  and  $\underline{R}_2^{(k)}$ . However, the vector lengths of  $\underline{R}_1^{(k+1)}$  and  $\underline{R}_2^{(k+1)}$  are equal or smaller compared with those of  $\underline{R}_1^{(k)}$  and  $\underline{R}_2^{(k)}$ .

Since the two vector lengths  $R_1^{(k+1)}$  and  $R_2^{(k+1)}$  have both a finite lower bound, the continued reductions (D.16), (D.17) will, after  $N$  iteration steps, converge to a final vector set

$$\underline{R}_{o1} = \underline{R}_1^{(N)}, \quad \underline{R}_{o2} = \underline{R}_2^{(N)} \quad (\text{D.19})$$

which cannot be reduced further. This means in particular that the transformation matrices in (D.16), (D.17) will become unit matrices resulting in

$$\{x_N\} = \{x_N'\} = 0 \quad (\text{D.20})$$

which, according to (D.11), (D.16), and (D.17), leads to

$$-R_{o1}^2 \leq 2(\underline{R}_{o1} \cdot \underline{R}_{o2}) < R_{o1}^2 \quad (\text{D.21a})$$

$$-R_{o2}^2 \leq 2(\underline{R}_{o1} \cdot \underline{R}_{o2}) < R_{o2}^2 \quad (\text{D.21b})$$

or finally to

$$-\min(R_{o1}^2, R_{o2}^2) \leq 2(\underline{R}_{o1} \cdot \underline{R}_{o2}) < \min(R_{o1}^2, R_{o2}^2) \quad (\text{D.22})$$

Relation (D.22) forms the **basic condition** for **Minkowski-reduced** (MR) lattice vectors, see also (3.16).

Assuming  $\underline{R}_{o1}$  and  $\underline{R}_{o2}$  to form MR lattice vectors according to (D.22), the squared distance  $d^2$  of any lattice vector in this lattice can be written as

$$d^2 = (n_1 \underline{R}_{o1} + n_2 \underline{R}_{o2})^2 = n_1^2 R_{o1}^2 + n_2^2 R_{o2}^2 + 2 n_1 n_2 (\underline{R}_{o1} \cdot \underline{R}_{o2}) \quad (\text{D.23})$$

If  $n_1 \cdot n_2 \geq 0$  and  $(\underline{R}_{o1} \cdot \underline{R}_{o2}) \geq 0$  or if  $n_1 \cdot n_2 < 0$  and  $(\underline{R}_{o1} \cdot \underline{R}_{o2}) \leq 0$  this leads together with (D.22) to

$$d^2 \geq (n_1^2 + n_2^2) \min(R_{o1}^2, R_{o2}^2) \geq \min(R_{o1}^2, R_{o2}^2) \quad (\text{D.24})$$

If, on the other hand,  $n_1 \cdot n_2 < 0$  and  $(\underline{R}_{o1} \cdot \underline{R}_{o2}) \geq 0$  or if  $n_1 \cdot n_2 > 0$  and  $(\underline{R}_{o1} \cdot \underline{R}_{o2}) \leq 0$  and we obtain

$$\begin{aligned}
d^2 &= n_1^2 R_{o1}^2 + n_2^2 R_{o2}^2 - 2 |n_1| |n_2| |(\underline{R}_{o1} \cdot \underline{R}_{o2})| \\
&\geq (n_1^2 + n_2^2 - |n_1| |n_2|) \min (R_{o1}^2, R_{o2}^2) \\
&\geq 1/2 ( (|n_1| - |n_2|)^2 + n_1^2 + n_2^2 ) \min (R_{o1}^2, R_{o2}^2) \\
&\geq \min (R_{o1}^2, R_{o2}^2)
\end{aligned} \tag{D.25}$$

This proves that at least one of the two lattice vectors  $\underline{R}_{o1}$  and  $\underline{R}_{o2}$  connects lattice points of smallest distance in the lattice.

If vectors  $\underline{R}_{o1}$  and  $\underline{R}_{o2}$  span an angle  $\gamma$  then (D.22) can be written as

$$- \min(q, 1/q) \leq 2 \cos (\gamma) < \min(q, 1/q) , \quad q = R_{o2} / R_{o1} \tag{D.26}$$

which leads to absolute limits

$$-1/2 \leq \cos (\gamma) < 1/2 \qquad 60^\circ < \gamma \leq 120^\circ \tag{D.27}$$

Thus, Minkowski-reduced lattice vectors can span only angles  $\gamma$  between  $60^\circ$  and  $120^\circ$ .

Analogues of the Minkowski reduction to bulk lattices have been proposed [42], [43], [49] where for acute lattice representations the reduced lattice vectors  $\underline{R}_{o1}$ ,  $\underline{R}_{o2}$ ,  $\underline{R}_{o3}$  are found to obey

$$- \min ( R_{oi}^2, R_{oj}^2 ) \leq 2 ( \underline{R}_{oi} \cdot \underline{R}_{oj} ) < \min ( R_{oi}^2, R_{oj}^2 ) \quad i, j = 1, 2, 3, \quad i \neq j \tag{D.28}$$

Then the squared distance  $d^2$  of any lattice vector in this lattice can be written as

$$\begin{aligned}
d^2 &= (n_1 \underline{R}_{o1} + n_2 \underline{R}_{o2} + n_3 \underline{R}_{o3})^2 = \\
&= n_1^2 R_{o1}^2 + n_2^2 R_{o2}^2 + n_3^2 R_{o3}^2 + 2 n_1 n_2 s_{12} + 2 n_1 n_3 s_{13} + 2 n_2 n_3 s_{23}
\end{aligned} \tag{D.29}$$

with

$$s_{ij} = \underline{R}_{oi} \cdot \underline{R}_{oj} > 0 , \quad i, j = 1, 2, 3, \quad i \neq j \text{ (acute representation)} \tag{D.30}$$

Relation (D.29) together with (D.28) yields for  $n_1 \geq 0$ ,  $n_2 \geq 0$ , and  $n_3 \geq 0$  or for  $n_1 < 0$ ,  $n_2 < 0$ , and  $n_3 < 0$

$$d^2 \geq n_1^2 R_{o1}^2 + n_2^2 R_{o2}^2 + n_3^2 R_{o3}^2 \geq (n_1^2 + n_2^2 + n_3^2) s^2 \geq s^2 \tag{D.31}$$

with

$$s^2 = \min ( R_{o1}^2, R_{o2}^2, R_{o3}^2 ) \tag{D.32}$$

For  $n_1 \geq 0$ ,  $n_2 \geq 0$ , and  $n_3 < 0$  or for  $n_1 < 0$ ,  $n_2 < 0$ , and  $n_3 \geq 0$  relation (D.29) together with (D.28) yields

$$\begin{aligned}
d^2 &= n_1^2 R_{o1}^2 + n_2^2 R_{o2}^2 + n_3^2 R_{o3}^2 + 2 |n_1| |n_2| s_{12} - 2 |n_1| |n_3| s_{13} - 2 |n_2| |n_3| s_{23} \\
&\geq \frac{1}{2} ( (|n_1| - |n_3|)^2 + n_1^2 + n_3^2 ) \min (R_{o1}^2, R_{o3}^2) + \\
&\quad + \frac{1}{2} ( (|n_2| - |n_3|)^2 + n_2^2 + n_3^2 ) \min (R_{o2}^2, R_{o3}^2) \\
&\geq \frac{1}{2} [ (|n_1| - |n_3|)^2 + n_1^2 + n_3^2 + (|n_2| - |n_3|)^2 + n_2^2 + n_3^2 ] s^2 \\
&\geq s^2
\end{aligned} \tag{D.33}$$

For all other combinations of positive and negative mixing factors  $n_i$ ,  $i = 1, 2, 3$ , proofs analogous to (D.33) yield the same result such that, altogether, we obtain

$$d^2 \geq \min ( R_{o1}^2, R_{o2}^2, R_{o3}^2 ) \tag{D.34}$$

which shows that for acute lattice representations relation (D.28) guarantees that the reduced lattice vector set contains the lattice vector of smallest length.

## E Details of Number Theory

In different sections of this book number theoretical methods are applied and functions used. This appendix discusses only some basic details. Further information and additional proofs may be obtained from the mathematical literature [204], [205], [206].

### E.1 Basic Definitions and Functions

The present definitions deal with the most basic functions and their properties which are necessary for the number theoretical algorithms discussed in Secs. E.2 to E.5.

The **integer truncation function**  $f(x) = [x]$  (written with square brackets) is defined for real numbers  $x$  as the largest integer  $n$  with  $n \leq x$ . Thus, if

$$n = [x] \quad \text{then} \quad n \leq x < (n+1) \quad (\text{E.1})$$

Examples are

$$[1.98] = 1, [5] = 5, [4.5] = 4, [-0.6] = -1, [-3.5] = -4, [-7.3] = -8$$

**Note** that in some textbooks the integer truncation function for negative  $x$  is defined as

$$x < 0 : [x] = -[-x] \quad (\text{E.2})$$

which would yield  $[-0.6] = 0$ ,  $[-3.5] = -3$ ,  $[-7.3] = -7$ , leading to a negative integer value increased by 1 compared to the present definition.

The **nearest integer function**  $g(x) = \{x\}$  (written with curly brackets) is defined for real numbers  $x$  as the integer  $n$  nearest to  $x$ , where values  $x = m + 1/2$ ,  $m$  integer, are defined as

$\{x\} = m + 1$ . Thus, the nearest integer function can be expressed by the integer truncation function given by (E.1) as

$$g(x) = \{x\} = [x + 1/2] \quad (\text{E.3})$$

Examples are

$$\{1.98\} = 2, \{5\} = 5, \{2.5\} = 3, \{-0.6\} = -1, \{-3.5\} = -3, \{-7.3\} = -7$$

The **modulo function**  $\text{mod}(n, m) = n \mid m$  is defined for positive integers  $m, n$  as the (integer) remainder of an integer division of  $n$  by  $m$ , i.e. by

$$\text{mod}(n, m) = n \mid m = n - [n/m] m \quad (\text{E.4})$$

This definition includes cases where  $0 < n < m$  yielding

$$n \mid m = n \quad \text{for } 0 \leq n < m \quad (\text{E.5})$$

Examples are

$$8 \mid 3 = 2, \quad 19 \mid 7 = 5, \quad 5 \mid 6 = 5, \quad 64 \mid 8 = 0, \quad 181 \mid 9 = 1, \quad 9 \mid 12 = 9$$

The **greatest common divisor**  $\text{gcd}(m, n)$  of two integers  $m, n$  is defined as the largest (positive) integer factor (divisor) that is common to both numbers, i.e. if

$$m = c p, \quad n = c q \quad \text{with integer } c > 0, p, q \quad (\text{E.6})$$

and  $c$  is the largest of all factors, then

$$\text{gcd}(m, n) = \text{gcd}(n, m) = c \quad (\text{E.7})$$

If either  $m$  or  $n$  (or both) are **negative** integers, then we set

$$\text{gcd}(m, n) = \text{gcd}(|m|, |n|) = c \quad (\text{E.8})$$

which yields always **positive** values for  $\text{gcd}(m, n)$ . Further, if

- the two integers  $m, n$  are **equal** then

$$\text{gcd}(m, n) = m \quad (\text{E.9})$$

- two different integers  $m, n$  do not contain a common factor  $> 1$  then

$$\text{gcd}(m, n) = 1 \quad (\text{E.10})$$

and the integers are called **coprime**.

- one of two integers  $m, n$  equals **zero**, for example  $n = 0$ , then we define

$$\text{gcd}(m, 0) = \text{gcd}(0, m) = m \quad (\text{E.11})$$

- $m, n$  are integers and  $m$  is a **multiple** of  $n$  then

$$\text{gcd}(m, n) = \text{gcd}(n, m) = n \quad (\text{E.12})$$

- $m, n$  are integers then

$$\text{gcd}(m^2, n^2) = \text{gcd}(m, n)^2 \quad (\text{E.13})$$

- $m, n$  are integers with  $a = \text{gcd}(m, n)$ , then

$$\text{gcd}(m, m+n) = a \text{gcd}(m/a, (m+n)/a) \quad (\text{E.14})$$

The greatest common divisor function can be **generalized** to more than two integers by a recursive procedure, where

$$\begin{aligned} \gcd(n_1, n_2, \dots, n_N) &= \gcd(n_1, \gcd(n_2, \dots, n_N)) = \\ &= \gcd(n_1, \gcd(n_2, \gcd(n_3, \dots, n_N))) = \\ &= \gcd(n_1, \gcd(n_2, \gcd(n_3, \gcd(\dots, \gcd(n_{N-1}, n_N))\dots)) \end{aligned} \quad (\text{E.15})$$

Examples are

$$\begin{aligned} \gcd(87, 9) &= 3, \quad \gcd(147, 49) = 49, \quad \gcd(122, 11) = 1, \quad \gcd(18, 192) = 6 \\ \gcd(18, 192, 333) &= 3 \end{aligned}$$

In the discussion of the Minkowski reduction of Appendix D, the nearest integer function appears in a **composite** function  $\mathbf{p(x)}$  for real-valued  $x$ , see (D.7), (D.8), which is defined by

$$p(x) = \{x\} (2x - \{x\}) \quad (\text{E.16})$$

The definition (E.3) of the nearest integer function  $\{x\}$  yields

$$\{x\} = n, \quad n \text{ integer} \quad \text{for} \quad n - 1/2 \leq x < n + 1/2 \quad (\text{E.17})$$

Thus we can write function  $p(x)$  as a linear function

$$p(x) = n(2x - n) \quad \text{for} \quad n - 1/2 \leq x < n + 1/2 \quad (\text{E.18})$$

At the boundary  $x_b = n + 1/2$  between the intervals  $[n - 1/2, n + 1/2)$  and  $[n + 1/2, n + 3/2)$  function  $p(x)$  yields values

$$\begin{aligned} \text{from the left :} \quad & p(x_{b-}) = n(2x - n) = n(n + 1) \\ \text{from the right :} \quad & p(x_{b+}) = (n + 1)(2x - n - 1) = n(n + 1) \end{aligned} \quad (\text{E.19})$$

which shows that  $p(x)$  is a **continuous** function. Further, if  $x \neq n + 1/2$  then

$$\{x\} = n \quad \text{implies} \quad \{-x\} = -n \quad (\text{E.20})$$

resulting in

$$p(-x) = p(x) \quad (\text{E.21})$$

For  $x = n + 1/2$  we obtain

$$\{x\} = n + 1 \quad \text{and, hence,} \quad \{-x\} = -n - 1 + 1 = -n \quad (\text{E.22})$$

and thus

$$p(-x) = (-n - 1)(-n) = n(n + 1) = p(x) \quad (\text{E.23})$$



This shows that function  $p(x)$  is **symmetric** with respect to  $x$ . Finally, relation (E.18) shows that  $p(x)$  varies linearly with  $x$  inside the interval  $[n - 1/2, n + 1/2)$  where

$$p(n - 1/2) = n(n - 1) \leq p(x) \leq p(n + 1/2) = n(n + 1) \quad (\text{E.24})$$

Altogether,  $p(x)$  has been proven to assume always **positive** values, see also Fig. E.1. Further,  $p(x)$  is close to parabolic shape which is clear from the fact that the parabolic function  $f(x) = x^2 - 1/4$  coincides with  $p(x)$  at all points  $x = n + 1/2$ .

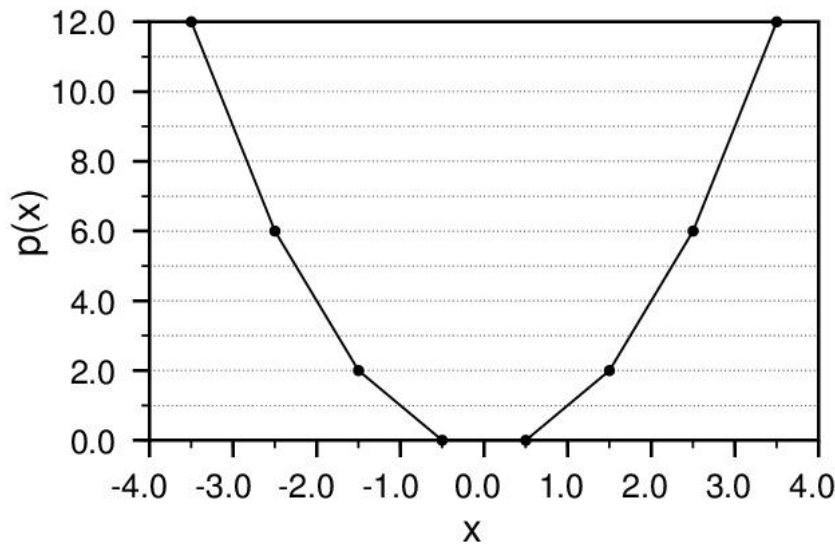


Fig. E.1 Graph of function  $p(x)$  inside the interval  $[-3.5, +3.5]$ .

The **least common multiple**  $\text{lcm}(m, n)$  of two integers  $m, n$  is defined as the smallest integer which contains both numbers as factors, i.e. if

$$m = a p, \quad n = b p \quad \text{where} \quad p = \text{gcd}(m, n) \quad (\text{E.25})$$

then

$$\text{lcm}(m, n) = a b p = m n / \text{gcd}(m, n) \quad (\text{E.26})$$

Further, if

- two integers  $m, n$  are equal, then

$$\text{lcm}(m, n) = m \quad (\text{E.27})$$

- two different integers  $m, n$  are coprime, then

$$\text{lcm}(m, n) = m n \quad (\text{E.28})$$

- one of two integers  $m, n$  equals zero then  $\text{lcm}(m, n)$  is undefined
- one of two integers  $m, n$  equals 1, then

$$\text{lcm}(m, 1) = \text{gcd}(1, m) = m \quad (\text{E.29})$$

Analogous to the greatest common divisor, the least common multiple function can be generalized to more than two integers by a recursive procedure, where

$$\begin{aligned} \text{lcm}(n_1, n_2, \dots, n_N) &= \text{lcm}(n_1, \text{lcm}(n_2, \dots, n_N)) = \\ &= \text{lcm}(n_1, \text{lcm}(n_2, \text{lcm}(n_3, \dots, n_N))) = \\ &= \text{lcm}(n_1, \text{lcm}(n_2, \text{lcm}(n_3, \text{lcm}(\dots, \text{lcm}(n_{N-1}, n_N))\dots)) \end{aligned} \quad (\text{E.30})$$

Examples are

$$\text{lcm}(87, 9) = 261, \text{lcm}(147, 49) = 147, \text{lcm}(122, 11) = 1342$$

$$\text{lcm}(18, 81, 6) = 162.$$

The **partitioning** of multiple-atom-height step regions into subterraces A and B separated by single-height steps, discussed in Sec. 4.3, can be phrased mathematically as the problem to subdivide the positive integer  $w$  into  $h$  integers  $w_i < w$  where  $w_i$  are of smallest variation. (In (4.13)  $n_s$  corresponds to  $h$  and  $n_t$  to  $w$ .) This is equivalent to approximating a linear function  $f(x) = (h/w)x$  with integer  $h$  and  $w$  by a step function  $g(x) = [(h/w)x]$  where  $w_i, i = 1, h$  refers to the intervals of constant  $g(x)$  as sketched in Fig. E.2 for  $w = 18, h = 5$ .

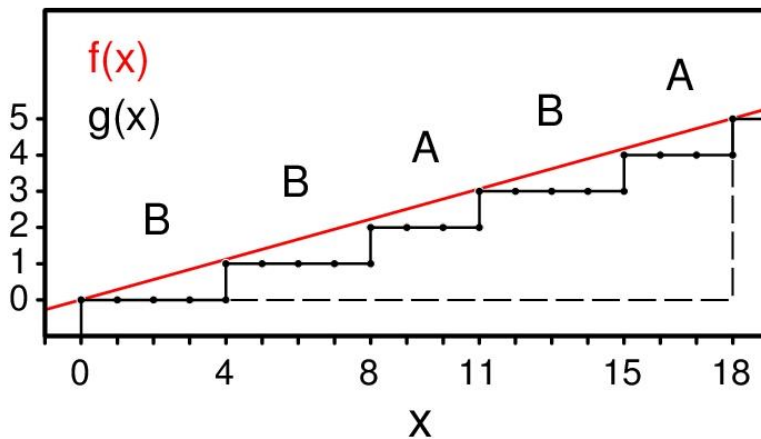


Fig. E.2 Graph of linear function  $f(x)$  (red) and step function  $g(x)$  (black) for  $x$  inside  $[0, 18]$ , see text. The short and long steps are labeled A and B, respectively.

First, we note that

$$w = p h + r, \quad p = [w/h] \quad \text{with } 0 \leq r < h \quad (\text{E.31})$$

which suggests a partitioning of number  $w$  into two kinds,  $(h-r)$  numbers **A** of size  $w_i = p$  and  $r$  numbers **B** of size  $w_i = (p+1)$ . This guarantees that the sum of all  $w_i$  equals  $w$  and, in addition, that the variation between the different  $w_i$  is smallest. If  $w$  is an integer multiple of  $h$ , then  $r = 0$  in (E.31) and there are only type **A** numbers. Otherwise, there are type **A** and type **B** numbers which differ by 1.

While the number of different  $w_i$  values is clear the sequence of type **A** and **B** numbers is not regular and can be obtained from

$$w_i = \left[ \left( \frac{w}{h} \right) i \right] - \left[ \left( \frac{w}{h} \right) (i-1) \right] = p + \Delta p_i, \quad i=1, h \quad (\text{E.32})$$

where

$$\Delta p_i = \left[ \left( \frac{r}{h} \right) i \right] - \left[ \left( \frac{r}{h} \right) (i-1) \right] \quad (\text{E.33})$$

for  $0 \leq r < h$  can only equal 0 or 1 distinguishing between type **A** and type **B** numbers. Here (E.33) yields for the first number  $\Delta p_1 = [r/h] = 0$  such that  $w_1 = p$  (type **A** number) and for the last number  $\Delta p_h = [r] - [r - r/h] = 1$  such that  $w_h = (p+1)$  (type **B** number). However, the intermediate numbers  $w_i$ ,  $1 < i < h$ , alternate between  $p$  and  $p+1$  in an irregular way. As an example, the combination  $w = 18$ ,  $h = 5$ ,  $p = 3$ ,  $r = 3$  yields the sequence **BBABA** shown in Fig. E.2.

## E.2 Euclid's Algorithm

There is a simple number theoretical method to find the **greatest common divisor**  $\text{gcd}(a, b)$  of two integers  $a, b$ , see Appendix E.1, usually referred to as Euclid's algorithm and discussed in this appendix.

First, we note that we can restrict ourselves to **positive** integers  $a, b$  using definition (E.8) for negative integers. Second, for  $a = b$  the greatest common divisor  $\text{gcd}(a, b)$  is equal to the arguments, i.e.

$$\text{gcd}(a, a) = a \quad (\text{E.34})$$

which does not require further evaluation. Further,  $\gcd(a, 0) = a$  and  $\gcd(a, 1) = 1$  do not merit any consideration. In the more general case of  $b > a > 0$  the greatest common divisor  $c = \gcd(a, b)$  implies that

$$a = c p, \quad b = c q \quad \text{with integer } p, q, c > 0 \quad (\text{E.35})$$

Thus, we obtain for the auxiliary parameter  $b'$

$$b' = b \mid a = b - [b/a] a = (q - [q/p] p) c = c q' \quad (\text{E.36})$$

(Definitions of the modulo and the integer truncation function are given in Appendix E.1.) Hence, parameter  $b'$  contains  $c = \gcd(a, b)$  as a factor and, on the other hand, must be smaller than  $a$ , according to the definition of the modulo function. As a result,

$$\gcd(a, b) = \gcd(a, b') \quad \text{where} \quad b > a > b' \geq 0 \quad (\text{E.37})$$

If  $b' = 0$  then  $b$  is a multiple of  $a$ , and according to (E.12),  $\gcd(a, b) = a$ . Otherwise, the reduction can be continued by reducing parameter  $a$  to yield  $a'$  analogous to (E.36) which yields an even smaller pair of numbers  $a', b'$  with the greatest common divisor being equal to that of the initial pair. Further reductions will eventually lead to one of the two numbers assuming the value zero with the other to yield  $\gcd(a, b)$ . This **finishes** the algorithm usually attributed to the Greek mathematician **Euclid**. Its computational procedure can be formally described by the **iteration**

$$\begin{array}{llll} a_0 = a > 0, & b_0 = b > 0, & k = 0 & \\ \text{if } (a_0 = b_0) \text{ then} & \gcd(a, b) = a_0 & \text{finish} & \\ (*) & a_{k+1} = a_k - [a_k/b_k] b_k, & b_{k+1} = b_k - [b_k/a_k] a_k & \\ & \text{if } (a_{k+1} = 0) \text{ then} & \gcd(a, b) = b_{k+1} & \text{finish} \\ & \text{if } (b_{k+1} = 0) \text{ then} & \gcd(a, b) = a_{k+1} & \text{finish} \\ & k = k + 1 & \text{goto } (*) & (\text{E.38}) \end{array}$$

For example finding  $\gcd(333, 90)$  with this algorithm reads

$$(a, b) = (333, 90) \rightarrow (63, 90) \rightarrow (63, 27) \rightarrow (9, 27) \rightarrow (9, 0)$$

and hence  $\gcd(333, 90) = 9$ .

Euclid's algorithm can be used recursively to find the greatest common divisor of a set of integers  $n_1, n_2, \dots, n_N$  according to definition (E.15).

### E.3 Linear Diophantine Equations

In Sec. 3.2 it was shown that netplane-adapted lattice vectors can be obtained by matrix transformations, see (3.11), (3.12), (3.13), where corresponding matrix elements result from solutions of **inhomogenous linear** Diophantine equations in **two** variables, i.e. equations of the type

$$a x + b y = c \quad (\text{E.39})$$

with given integer constants  $a$ ,  $b$ ,  $c$  and unknown integer variables  $x$  and  $y$  to be determined. This appendix discusses an iterative method to find solutions of (E.39), where the method is closely connected with **Euclid's algorithm** of Appendix E.2.

First, we can restrict ourselves to positive constants  $a$ ,  $b$ , and  $c$ , since equation (E.39) can always written with positive constants by changing the corresponding signs of the solutions  $x$ ,  $y$ , for example

$$a < 0, b > 0, \text{ and } c \geq 0 \text{ leads to } |a|(-x) + b y = c \quad (\text{E.40a})$$

$$a < 0, b < 0, \text{ and } c \geq 0 \text{ leads to } |a|(-x) + |b|(-y) = c \quad (\text{E.40b})$$

$$a > 0, b > 0, \text{ and } c < 0 \text{ leads to } |a|(-x) + |b|(-y) = |c| \quad (\text{E.40c})$$

For  $c = 0$  and finite  $a$ ,  $b$  equation (E.39) becomes a **homogeneous** linear Diophantine equation which possesses an infinite number of integer solutions  $x_o$ ,  $y_o$  given by

$$x_o = p (b / g) , \quad y_o = -p (a / g) \quad p \text{ integer} , \quad g = \text{gcd}(a, b) \quad (\text{E.41})$$

Thus, any particular integer solution  $x_p$ ,  $y_p$  of the corresponding **inhomogeneous** equation (E.39) with  $c \neq 0$  can be used to construct an **infinite** set of solutions,  $x_p + x_o$ ,  $y_p + y_o$  by adding those of the homogeneous equation, given by (E.41), since

$$a (x_p + x_o) + b (y_p + y_o) = a x_p + b y_p = c \quad (\text{E.42})$$

In the following we will discuss an algorithm to find a **particular** integer solution  $x$ ,  $y$  of equation (E.39) where we can restrict ourselves to solutions for  $c = 1$ . A solution of (E.39) for  $c \neq 1$  can be easily obtained from that for  $c = 1$  by scaling, since equation

$$a x + b y = 1 \quad (\text{E.43})$$

can be transformed to

$$a x' + b y' = c \quad \text{with} \quad x' = c x , \quad y' = c y \quad (\text{E.44})$$

Constants  $a$  and  $b$  of equation (E.43) must be coprime, i.e. constrained to

$$\gcd(a, b) = 1 \quad (\text{E.45})$$

Otherwise, equation (E.43) has no solution. As an example

$$117x + 18y = 9(13x + 2y) = 1 \quad (\text{E.46})$$

has no integer solution  $x, y$  since the right hand side of (E.46) is not a multiple of 9.

In order to determine a particular solution of equation (E.43) we consider a transformation

$$\begin{pmatrix} x' \\ y' \end{pmatrix} = \begin{pmatrix} 1 & [b/a] \\ [a/b] & 1 \end{pmatrix} \cdot \begin{pmatrix} x \\ y \end{pmatrix} = \underline{\underline{\mathbf{T}}} \cdot \begin{pmatrix} x \\ y \end{pmatrix}, \quad \underline{\underline{\mathbf{T}}} = \begin{pmatrix} 1 & [b/a] \\ [a/b] & 1 \end{pmatrix} \quad (\text{E.47})$$

and, thus,

$$\begin{pmatrix} x \\ y \end{pmatrix} = \underline{\underline{\mathbf{T}}}^{-1} \cdot \begin{pmatrix} x' \\ y' \end{pmatrix} = \begin{pmatrix} 1 & -[b/a] \\ -[a/b] & 1 \end{pmatrix} \cdot \begin{pmatrix} x' \\ y' \end{pmatrix} \quad (\text{E.48})$$

where for  $a \neq b$  either  $[b/a]$  or  $[a/b]$  must equal zero. This transforms equation (E.43) into

$$\begin{aligned} ax + by &= a(x' - [b/a]y') + b(y' - [a/b]x') \\ &= (a - [a/b]b)x' + (b - [b/a]a)y' = a'x' + b'y' = 1 \end{aligned} \quad (\text{E.49})$$

yielding a modified Diophantine equation of the same structure as (E.43) but with changed constants  $a', b'$  where

$$\begin{pmatrix} a' \\ b' \end{pmatrix} = \begin{pmatrix} 1 & -[a/b] \\ -[b/a] & 1 \end{pmatrix} \cdot \begin{pmatrix} a \\ b \end{pmatrix} \quad (\text{E.50})$$

These relations are analogous to the reduction step (E.36) of Euclid's algorithm for finding the greatest common divisor of  $a$  and  $b$ , which suggests to apply the same iterative procedure to finding solutions of equation (E.43).

Thus, in analogy to transformations (E.47), (E.48) we consider an iterative sequence of transformations starting with

$$(k=0) \quad a_k = a, \quad b_k = b, \quad x_k = x, \quad y_k = y \quad (\text{E.51})$$

and given by

$$\begin{pmatrix} x_{k+1} \\ y_{k+1} \end{pmatrix} = \begin{pmatrix} 1 & [b_k/a_k] \\ [a_k/b_k] & 1 \end{pmatrix} \cdot \begin{pmatrix} x_k \\ y_k \end{pmatrix} = \underline{\underline{T}}_k \cdot \begin{pmatrix} x_k \\ y_k \end{pmatrix} \quad (\text{E.52})$$

This transforms equation

$$a_k x_k + b_k y_k = 1 \quad (\text{E.53})$$

into

$$a_{k+1} x_{k+1} + b_{k+1} y_{k+1} = 1 \quad (\text{E.54})$$

where the coefficients  $a_k$  and  $b_k$  transform to  $a_{k+1}$  and  $b_{k+1}$  according to

$$\begin{pmatrix} a_{k+1} \\ b_{k+1} \end{pmatrix} = \begin{pmatrix} 1 & -[a_k/b_k] \\ -[b_k/a_k] & 1 \end{pmatrix} \cdot \begin{pmatrix} a_k \\ b_k \end{pmatrix} = \underline{\underline{T}}_k^{-1} \cdot \begin{pmatrix} a_k \\ b_k \end{pmatrix} \quad (\text{E.55})$$

This transformation can be continued iteratively, where coefficients  $a_k$  and  $b_k$  become successively smaller as a result of reduction (E.55), i.e.

$$0 \leq a_{k+1} \leq a_k \quad \text{and} \quad 0 \leq b_{k+1} \leq b_k \quad (\text{E.56a})$$

while according to Euclid's algorithm

$$\gcd(a_{k+1}, b_{k+1}) = \gcd(a_k, b_k) = 1 \quad (\text{E.56b})$$

The iteration finishes when one of the coefficients  $a_{k+1}$  or  $b_{k+1}$  becomes zero which happens after a finite number of steps since the iteration deals with integers. Assuming that for  $k+1 = N$  coefficient  $a_{k+1}$  vanishes we obtain from (E.53) together with (E.45)

$$a_N x_N + b_N y_N = b_N y_N = \gcd(a, b) y_N = y_N = 1 \quad (\text{E.57})$$

Setting  $x_N = y_N = 1$  we can iterate backwards using relation

$$\begin{pmatrix} x_k \\ y_k \end{pmatrix} = \begin{pmatrix} 1 & -[b_k/a_k] \\ -[a_k/b_k] & 1 \end{pmatrix} \cdot \begin{pmatrix} x_{k+1} \\ y_{k+1} \end{pmatrix} = \underline{\underline{T}}_k^{-1} \cdot \begin{pmatrix} x_{k+1} \\ y_{k+1} \end{pmatrix} \quad (\text{E.58})$$

to find the solution of the initial equation (E.43) according to

$$\begin{aligned} \begin{pmatrix} x \\ y \end{pmatrix} &= \begin{pmatrix} x_0 \\ y_0 \end{pmatrix} = \underline{\underline{T}}_0^{-1} \cdot \begin{pmatrix} x_1 \\ y_1 \end{pmatrix} = \underline{\underline{T}}_0^{-1} \cdot \underline{\underline{T}}_1^{-1} \cdot \begin{pmatrix} x_2 \\ y_2 \end{pmatrix} = \dots = \\ &= \left( \underline{\underline{T}}_0^{-1} \cdot \underline{\underline{T}}_1^{-1} \cdot \dots \cdot \underline{\underline{T}}_{N-1}^{-1} \right) \cdot \begin{pmatrix} x_N \\ y_N \end{pmatrix} = \left( \underline{\underline{T}}_0^{-1} \cdot \underline{\underline{T}}_1^{-1} \cdot \dots \cdot \underline{\underline{T}}_{N-1}^{-1} \right) \cdot \begin{pmatrix} 1 \\ 1 \end{pmatrix} \end{aligned} \quad (\text{E.59})$$

If for  $k+1 = N$  coefficient  $b_{k+1}$  vanishes we can apply the same reasoning as before and obtain the same iterative solution (E.59). Altogether, the iteration defined by (E.55), (E.57), (E.58) with starting values (E.51) allows the iterative calculation of a particular solution of the linear Diophantine equation (E.43), where the iteration requires only a finite number of steps.

#### Solutions of linear Diophantine equations with $n > 2$ variables

$$a_1 x_1 + a_2 x_2 + \dots + a_n x_n = 1 \quad (\text{E.60})$$

can be formally reduced to the  $n = 2$  problem by rewriting (E.60) as

$$a_1 x_1 + a_2 x_2 = 1 - a_3 x_3 - \dots - a_n x_n = C \quad (\text{E.61})$$

where setting  $x_3, \dots, x_n$  equal to an appropriate combination of integers defines an auxiliary constant  $C$ . Then the above described procedure yields a particular solution  $x_1, x_2$  of (E.61) which, together with the predefined values  $x_3, \dots, x_n$ , results in a particular solution of (E.60). Analogous to the constraint (E.45), integer solutions of equation (E.60) impose a constraint on the greatest common divisor of all coefficients  $a_1, a_2, \dots, a_n$ , where

$$\text{gcd}(a_1, a_2, \dots, a_n) = 1 \quad (\text{E.62})$$

## E.4 Quadratic Diophantine Equations

There is an extensive literature on quadratic Diophantine equations [204], [205] which will not be reviewed in this appendix. Here we focus only on solutions of **specific** equations which arise in connection with **neighbor shells** in crystals with high symmetry and **overlayer reconstruction** at single crystal surfaces.

(a) **Diophantine equations** of the type

$$\mathbf{n}_1^2 + \mathbf{n}_2^2 + \mathbf{n}_3^2 = \mathbf{N} \ , \quad \mathbf{n}_i, \mathbf{N} \text{ integer} \ , \quad \mathbf{N} \geq 0 \quad (\text{E.63})$$

appear in connection with neighbor shells discussed in Sec. 2.6. These equations do not have solutions for every value of parameter  $N$ , which can be proven using an octal representation of integers. Here a positive integer  $a$  is written as

$$a = (8p + r) \quad p, r \text{ integer with } 0 \leq r < 8 \quad (\text{E.64})$$



and, hence, the square of an integer can be represented as

$$a^2 = 8(8p^2 + 2pr) + r^2 \quad (\text{E.65})$$

Thus, using the definition of the modulo function  $a | b$  of Appendix E.1, this yields

$$a^2 | 8 = r^2 | 8 \quad (\text{E.66})$$

where the following table lists all possible values of  $r^2 | 8$ .

$\mathbf{r = (a   8)}$	$\mathbf{(r^2   8)}$
0	0
1	1
2	4
3	1
4	0
5	1
6	4
7	1

(E.67)

As a result,  $(r^2 | 8)$  allows only three values, 0, 1, and 4. Further, the sum of three squares can be written in octal representation ( $n_i = 8p_i + r_i$ ) as

$$n_1^2 + n_2^2 + n_3^2 = 64(p_1^2 + p_2^2 + p_3^2) + 16(p_1r_1 + p_2r_2 + p_3r_3) + (r_1^2 + r_2^2 + r_3^2)$$

and hence

$$(n_1^2 + n_2^2 + n_3^2) | 8 = (r_1^2 + r_2^2 + r_3^2) | 8 \quad (\text{E.68})$$

with possible values according to (E.67) in canonical order

$\mathbf{r_i^2, r_j^2, r_k^2}$	$\mathbf{(r_1^2 + r_2^2 + r_3^2)   8}$
0, 0, 0	0
0, 0, 1	1
0, 0, 4	4
0, 1, 1	2
0, 1, 4	5
0, 4, 4	0
1, 1, 1	3
1, 1, 4	6
1, 4, 4	1
4, 4, 4	4

(E.69)

This shows that

$$(n_1^2 + n_2^2 + n_3^2) | 8 \neq 7 \quad \text{or} \quad n_1^2 + n_2^2 + n_3^2 \neq 8q + 7, \quad q \text{ integer} \quad (\text{E.70})$$

Next we note that if all numbers  $n_i$  in (E.63) are even numbers, then their squares are multiples of 4 and, as a consequence,  $N$  in (E.63) must be a multiple of 4. Thus, we can write

$$n_1^2 + n_2^2 + n_3^2 = (2m_1)^2 + (2m_2)^2 + (2m_3)^2 = N = 4M \quad (\text{E.71})$$

which can be reduced to

$$m_1^2 + m_2^2 + m_3^2 = M \quad (\text{E.72})$$

Therefore, if equation (E.72) has no solutions for  $M = (8q + 7)$  then (E.71) has no solutions equal to  $4(8q + 7)$ . This can be continued to yield the final result that equation (E.63) does not have solutions for

$$N = 4^p (8q + 7), \quad p, q \text{ integer} \quad (\text{E.73})$$

For  $N$  values different from those given by (E.73) solutions of equation (E.63) can be determined by trial-and-error since values  $n_i$ ,  $i = 1, 2, 3$ , are restricted to a finite number of integers  $|n_i| \leq [\sqrt{N}]$ . For any given solution  $(n_1, n_2, n_3)$  the sets of triplets  $(\pm n_1, \pm n_2, \pm n_3)$  and  $(\pm n_1', \pm n_2', \pm n_3')$  with  $n_i'$  denoting permutations of  $n_i$  offer other solutions counted by the symmetry degeneracy  $m_{\text{sym}}$  where  $m_{\text{sym}} = 6, 8, 12, 24, 48$  depending on the actual values of  $n_i$ . Thus, equation (E.63) has always multiple solutions for  $N > 1$ . In addition, this equation can have solutions  $(n_1, n_2, n_3)$  and  $(n_1', n_2', n_3')$  where the absolute values of the numbers  $n_i$  and  $n_i'$  differ beyond simple permutations. An example are  $(1, 3, 4)$  and  $(1, 0, 5)$  yielding  $N = 26$ . These solutions are counted by the accidental degeneracy  $m_{\text{acc}}$ . While  $m_{\text{sym}}$  for each solution  $(n_1, n_2, n_3)$  is limited to a maximum of  $m_{\text{sym}} = 48$  values of  $m_{\text{acc}}$  have no upper bound. As an illustration, equation (E.63) for  $N = 972221$  yields  $m_{\text{acc}} = 521$  where for 520 different solutions  $m_{\text{sym}} = 48$  and for one solution  $m_{\text{sym}} = 12$  amounting, altogether, to 24972 different solutions.

It may be mentioned in passing that **Diophantine equations** of the type

$$\mathbf{n}_1^2 + \mathbf{n}_2^2 + \mathbf{n}_3^2 + \mathbf{n}_4^2 = \mathbf{N}, \quad n_i, N \text{ integer} \quad (\text{E.74})$$

have (multiple) solutions for any value of  $N \geq 0$  which is known as Langange's theorem [206].

(b) **Diophantine equations** of the type

$$\mathbf{n_1^2 + n_2^2 = N^2}, \quad \mathbf{n_1, n_2, N \text{ integer}} \quad (\text{E.75})$$

appear in connection with rotationally reconstructed overlayers at single crystal surfaces with **square** geometry discussed in detail in Sec. 5.2. Equation (E.75) is the integer version of the well known Pythagorean equation defining so-called **Pythagorean triplets**  $(N, n_1, n_2)$ . These numbers can be constructed by the generalized **Euclid formula**. Setting

$$\mathbf{n_1 = k(2mn)}, \quad \mathbf{n_2 = k(m^2 - n^2)}, \quad \mathbf{k, m, n \text{ integer}} \quad \text{with} \quad \mathbf{m > n} \quad (\text{E.76})$$

and letting  $m, n, k$  assume all possible values yields

$$\mathbf{N = \sqrt{(n_1^2 + n_2^2)} = k(m^2 + n^2)} \quad (\text{E.77})$$

It can be shown that (E.76) generates all possible Pythagorean triplets. Setting  $k = 1$  in (E.76) yields so-called **primitive triplets**, which are defined by  $\text{gcd}(m, n) = 1$  with either odd  $m$  and even  $n$  or vice versa. In this case the representation of  $(n_1, n_2, N)$  by  $m, n$  is **unique**, i.e. there are no other values  $m, n$  which yield the same triplet  $(n_1, n_2, N)$ . Further, (E.76) shows that there are infinitely many Pythagorean triplets. In addition, the numbers  $n_1, n_2$  must always be different (if the trivial cases  $n_1 = 0$  and/or  $n_2 = 0$  are excluded), since no square number can be represented by  $(2N^2)$ .

The following table lists the 10 smallest primitive Pythagorean triplets  $(N, n_1, n_2)$  with  $n_1 > n_2 > 0$ .

	<b>(N, n<sub>1</sub>, n<sub>2</sub>)</b>
1	(5, 4, 3)
2	(13, 12, 5)
3	(17, 15, 8)
4	(25, 24, 7)
5	(29, 21, 20)
6	(37, 35, 12)
7	(39, 36, 15)
8	(41, 40, 9)
9	(51, 45, 24)
10	(53, 45, 28)

(c) **Diophantine equations** of the type

$$\mathbf{m}^2 + \mathbf{m} \mathbf{n} + \mathbf{n}^2 = \mathbf{N}^2, \quad \mathbf{m}, \mathbf{n}, \mathbf{N} \text{ integer} \quad (\text{E.78})$$

appear in connection with rotationally reconstructed overlayers at single crystal surfaces with **hexagonal** geometry, see Sec. 6.4. If the hexagonal surface is described (in Cartesian coordinates) by lattice vectors in acute representation, i.e. by

$$\underline{\mathbf{R}}_1 = a(1, 0), \quad \underline{\mathbf{R}}_2 = a(1/2, \sqrt{3}/2) \quad (\text{E.79})$$

then rotated overlayer lattice vectors  $\underline{\mathbf{R}}_1'$ ,  $\underline{\mathbf{R}}_2'$  must be of equal length compared with those of  $\underline{\mathbf{R}}_1$ ,  $\underline{\mathbf{R}}_2$ . Assuming a coincidence lattice overlayer, see Sec. 5.2, where

$$\begin{pmatrix} \underline{\mathbf{R}}_1' \\ \underline{\mathbf{R}}_2' \end{pmatrix} = \frac{1}{\mathbf{N}} \begin{pmatrix} \mathbf{m}_{11} & \mathbf{m}_{12} \\ \mathbf{m}_{21} & \mathbf{m}_{22} \end{pmatrix} \cdot \begin{pmatrix} \underline{\mathbf{R}}_1 \\ \underline{\mathbf{R}}_2 \end{pmatrix}, \quad \mathbf{m}_{ij}, \mathbf{N} \text{ integer} \quad (\text{E.80})$$

we obtain for the vector lengths with (E.79)

$$\begin{aligned} \mathbf{N}^2 |\underline{\mathbf{R}}_i'|^2 &= |\mathbf{m}_{i1} \underline{\mathbf{R}}_1 + \mathbf{m}_{i2} \underline{\mathbf{R}}_2|^2 = a^2 (\mathbf{m}_{i1}^2 + \mathbf{m}_{i1} \mathbf{m}_{i2} + \mathbf{m}_{i2}^2) \\ &= \mathbf{N}^2 |\underline{\mathbf{R}}_i|^2 = a^2 \mathbf{N}^2 \end{aligned} \quad (\text{E.81})$$

where setting

$$\mathbf{m}_{i1} = \mathbf{m}, \quad \mathbf{m}_{i2} = \mathbf{n} \quad (\text{E.82})$$

leads to Diophantine equations of the type (E.78). These equations are quadratic and of the elliptic type with multiple solutions for all values  $\mathbf{N}$ . We note that

- for integer  $\mathbf{N} \neq 0$  there are always six trivial solutions,

$$(\mathbf{m}, \mathbf{n}) = \pm(\mathbf{N}, 0), \quad = \pm(0, \mathbf{N}), \quad = \pm(\mathbf{N}, -\mathbf{N}) \quad (\text{E.83})$$

- if  $\mathbf{m}_o \neq 0$ ,  $\mathbf{n}_o \neq 0$  are solutions of equation (E.78) then

- $\mathbf{m}_o, \mathbf{n}_o$  must be different in value, since, assuming  $\mathbf{m}_o = \mathbf{n}_o$ , equation (E.78) would read  $3 \mathbf{n}_o^2 = \mathbf{N}^2$  which cannot be solved for integers  $\mathbf{n}_o, \mathbf{N}$ .

- there are altogether 12 different solutions

$$\begin{aligned} (\mathbf{m}, \mathbf{n}) &= \pm(\mathbf{m}_o, \mathbf{n}_o), \quad = \pm(\mathbf{m}_o, -\mathbf{m}_o - \mathbf{n}_o), \quad = \pm(\mathbf{m}_o + \mathbf{n}_o, -\mathbf{m}_o) \\ &= \pm(\mathbf{n}_o, \mathbf{m}_o), \quad = \pm(\mathbf{n}_o, -\mathbf{m}_o - \mathbf{n}_o), \quad = \pm(\mathbf{m}_o + \mathbf{n}_o, -\mathbf{n}_o) \end{aligned} \quad (\text{E.84})$$

- equation (E.78) can also be written as

$$m = -\frac{n}{2} \pm \sqrt{N^2 - \frac{3}{4}n^2} \quad \text{or} \quad n = -\frac{m}{2} \pm \sqrt{N^2 - \frac{3}{4}m^2} \quad (\text{E.85})$$

This restricts the range of integer solutions (m, n) to

$$\sqrt{N^2 - \frac{3}{4}m^2} \geq 0, \quad \sqrt{N^2 - \frac{3}{4}n^2} \geq 0 \quad \rightarrow \quad |m|, |n| \leq \left[ \frac{2}{\sqrt{3}} N \right] \quad (\text{E.86})$$

and offers a trial-and-error method to determine solutions (m, n) for given  $N > 0$ . Letting integer n run from  $-\lceil (2/\sqrt{3}) N \rceil$  to  $\lceil (2/\sqrt{3}) N \rceil$  and checking the validity of equation (E.85) for integers m yields corresponding solutions.

The following table lists the 10 smallest triplets (N, m, n) with  $m > n > 0$  ( $\text{gcd}(m, n) = 1$ )

	(N, m, n)
1	(7, 5, 3)
2	(13, 8, 7)
3	(19, 16, 5)
4	(31, 24, 11)
5	(37, 33, 7)
6	(43, 35, 13)
7	(49, 39, 16)
8	(61, 56, 9)
9	(67, 45, 32)
10	(73, 63, 17)

(d) **Diophantine equations** of the type

$$m^2 + 2n^2 = N^2, \quad m, n, N \text{ integer} \quad (\text{E.87})$$

appear in connection with rotationally reconstructed overlayers at single crystal surfaces with **rectangular** geometry, see Sec. 6.4. If the rectangular surface is described (in Cartesian coordinates) by lattice vectors

$$\underline{R}_1 = a(1, 0), \quad \underline{R}_2 = a(0, \sqrt{2}) \quad (\text{E.88})$$

then each of the two rotated overlayer lattice vectors  $\underline{R}_i'$  must be of equal length compared with that of  $\underline{R}_i$ . Assuming a coincidence lattice overlayer, see Sec. 5.2, with lattice vectors defined by (E.80),

we obtain for the vector lengths together with (E.88)

$$N^2 |\underline{R}_1'|^2 = |m_{11} \underline{R}_1 + m_{12} \underline{R}_2|^2 = a^2 (m_{11}^2 + 2m_{12}^2) = N^2 |\underline{R}_1|^2 = a^2 N^2 \quad (\text{E.89})$$

The orthogonality of  $\underline{R}_1'$ ,  $\underline{R}_2'$  and the vector ratio  $R_2'/R_1' = \sqrt{2}$  of the rotated lattice is guaranteed by setting  $m_{21} = -2 m_{12}$  and  $m_{22} = m_{11}$ . Further, setting

$$m_{11} = m, \quad m_{12} = n \quad (\text{E.90})$$

leads to Diophantine equations of the type (E.87) which are quadratic and of the elliptic type. Equation (E.87) can also be written as

$$m = \pm \sqrt{N^2 - 2n^2} \quad (\text{E.91})$$

which restricts the range of integer solutions  $(m, n)$  to

$$\sqrt{N^2 - 2n^2} \geq 0 \quad \rightarrow \quad |n| \leq \left[ \frac{1}{\sqrt{2}} N \right] \quad (\text{E.92})$$

Thus, solutions can be obtained by trial-and-error methods analogous to those, used for hexagonal surfaces described above. Letting integer  $n$  run from  $-[(1/\sqrt{2}) N]$  to  $[(1/\sqrt{2}) N]$  and checking the validity equation (E.91) for integers  $m$  yields corresponding solutions.

The following table lists solution triplets  $(N, m, n)$  for the 10 smallest  $N$  values ( $\text{gcd}(m, n) = 1$ )

	<b>(N, m, n)</b>
1	(3, 1, 2)
2	(9, 7, 4)
3	(11, 7, 6)
4	(17, 1, 12)
5	(19, 17, 6)
6	(27, 23, 10)
7	(33, 17, 20)
8	(33, 31, 8)
9	(41, 23, 24)
10	(43, 7, 30)

(e) **Diophantine equations** of the type

$$\mathbf{a m}^2 = \mathbf{b n}^2, \quad \mathbf{a, b, m, n \text{ integer}} \quad (\text{E.93})$$

appear in connection with symmetry constraints of nanotubes, see Sec. 8.2. This equation can also be written as

$$\mathbf{m} = \mathbf{p n} \quad \text{with } \mathbf{p} = \sqrt{\mathbf{b/a}}, \quad \mathbf{a, b, m, n \text{ integer}} \quad (\text{E.94})$$

Thus, for (E.94) to have integer solutions parameter  $p$  must be a rational number which is only possible if  $(b/a)$  equals the square of a rational number, i.e. if

$$\mathbf{b/a} = (\mathbf{w/v})^2 = \mathbf{w}^2/\mathbf{v}^2, \quad \mathbf{w, v \text{ integer}} \quad (\text{E.95})$$

Inserting (E.95) into the initial equation (E.93) yields

$$\mathbf{v m} = \pm \mathbf{w n} \quad \text{with integer solutions } \mathbf{m} = \mathbf{q w}, \quad \mathbf{n} = \mathbf{q v}, \quad \mathbf{q \text{ integer}} \quad (\text{E.96})$$

Constraint (E.95) means, in particular, that the Diophantine equation

$$3 \mathbf{m}^2 = \mathbf{n}^2, \quad \mathbf{m, n \text{ integer}} \quad (\text{E.97})$$

has no solutions. This is the mathematical basis of proving that ideal substrate surfaces with a square lattice, like fcc(1 0 0) or bcc(1 0 0), cannot have commensurate overlayers with a hexagonal lattice. Likewise, the Diophantine equation

$$3 \mathbf{m}^2 = 2 \mathbf{n}^2, \quad \mathbf{m, n \text{ integer}} \quad (\text{E.98})$$

has no solutions which is essential for proving that primitive rectangular substrate surfaces described by fcc(1 1 0) cannot have commensurate overlayers with a hexagonal lattice.

## E.5 Number Theory and $2 \times 2$ Matrices

This appendix discusses a few number theoretical details connected with two-dimensional matrices whose elements are integer or fractional numbers.

The **transposed** matrix  $\underline{\underline{M}}^+$  and the **inverted** matrix  $\underline{\underline{M}}^{-1}$  of an integer-valued  $2 \times 2$  matrix  $\underline{\underline{M}}$  are given by

$$\underline{\underline{M}} = \begin{pmatrix} \mathbf{m}_{11} & \mathbf{m}_{12} \\ \mathbf{m}_{21} & \mathbf{m}_{22} \end{pmatrix}, \quad \underline{\underline{M}}^+ = \begin{pmatrix} \mathbf{m}_{11} & \mathbf{m}_{21} \\ \mathbf{m}_{12} & \mathbf{m}_{22} \end{pmatrix}, \quad \underline{\underline{M}}^{-1} = \frac{1}{\Delta} \begin{pmatrix} \mathbf{m}_{22} & -\mathbf{m}_{12} \\ -\mathbf{m}_{21} & \mathbf{m}_{11} \end{pmatrix} \quad (\text{E.99})$$

where

$$\Delta = \det(\underline{\underline{M}}) = m_{11} m_{22} - m_{12} m_{21} \quad (\text{E.100})$$

is the **determinant** of matrix  $\underline{\underline{M}}$ . The determinant  $\Delta$  and matrix  $\underline{\underline{M}}^+$  are integer-valued while matrix  $\underline{\underline{M}}^{-1}$  is fractional except for  $\Delta = 1$ . However, the product  $(\Delta \underline{\underline{M}}^{-1})$  is always integer-valued.

There is an infinite set of integer-valued  $2 \times 2$  matrices  $\underline{\underline{M}}$  whose inverse matrix is integer, i.e. where

$$\Delta = \det(\underline{\underline{M}}) = m_{11} m_{22} - m_{12} m_{21} = 1 \quad (\text{E.101})$$

This means in particular that  $m_{i1}$  and  $m_{i2}$  as well as  $m_{1i}$  and  $m_{2i}$ ,  $i = 1, 2$  must be coprime to yield a solution of (E.101), i.e.

$$\text{gcd}(m_{i1}, m_{i2}) = \text{gcd}(m_{1i}, m_{2i}) = 1, \quad i = 1, 2 \quad (\text{E.102})$$

Matrices  $\underline{\underline{M}}$  can be obtained by selecting one of the four pairs of coprime integer elements  $(m_{i1}, m_{i2})$  or  $(m_{1i}, m_{2i})$ . Then equation (E.101) can be understood as a linear Diophantine equation for the complementing matrix elements  $(m_{j1}, m_{j2})$  or  $(m_{1j}, m_{2j})$  for which an infinite set of solution can be evaluated following the procedure based on Euclid's algorithm as discussed in Sec. E.3. As an example, the infinite set of matrices with predefined  $m_{11} = 1, m_{12} = 2$  is given by

$$\underline{\underline{M}} = \begin{pmatrix} 1 & 2 \\ p & 2p+1 \end{pmatrix}, \quad p \text{ integer} \quad (\text{E.103})$$

If  $\underline{\underline{A}}$  is a real-valued  $2 \times 2$  matrix then its **integer approximant**  $\{\underline{\underline{A}}\}$  is defined by an integer-valued  $2 \times 2$  matrix

$$\underline{\underline{A}} = \begin{pmatrix} a_{11} & a_{12} \\ a_{21} & a_{22} \end{pmatrix} \Rightarrow \{\underline{\underline{A}}\} = \begin{pmatrix} \{a_{11}\} & \{a_{21}\} \\ \{a_{12}\} & \{a_{22}\} \end{pmatrix} \quad (\text{E.104})$$

where  $\{a_{ij}\}$  denotes the integer nearest to  $a_{ij}$ , see Appendix E.1. As an example, the rotation matrix

$$\underline{\underline{A}} = \begin{pmatrix} \cos \alpha & \sin \alpha \\ -\sin \alpha & \cos \alpha \end{pmatrix} \stackrel{\text{def.}}{=} (\cos \alpha, \sin \alpha \mid -\sin \alpha, \cos \alpha) \quad (\text{E.105})$$

with  $\det(\underline{\underline{A}}) = 1$  has as integer approximants  $\{\underline{\underline{A}}\}$  with their determinants  $\det(\{\underline{\underline{A}}\})$  for ranges of angles  $\alpha$  given in the following table.

$\alpha$	$\{\underline{\underline{A}}\}, \det(\{\underline{\underline{A}}\})$	$\alpha$	$\{\underline{\underline{A}}\}, \det(\{\underline{\underline{A}}\})$
----------	--	----------	--



$[0^\circ, 30^\circ]$	$(1, 0   0, 1), 1$	$[210^\circ, 240^\circ]$	$(-1, -1   1, -1), 2$
$[30^\circ, 60^\circ]$	$(1, 1   -1, 1), 2$	$(240^\circ, 300^\circ)$	$(0, -1   1, 0), 1$
$(60^\circ, 120^\circ)$	$(0, 1   -1, 0), 1$	$[300^\circ, 330^\circ]$	$(1, -1   1, 1), 2$
$[120^\circ, 150^\circ]$	$(-1, 1   -1, -1), 2$	$(330^\circ, 360^\circ)$	$(1, 0   0, 1), 1$
$(150^\circ, 210^\circ)$	$(-1, 0   0, -1), 1$		

(E.106)

In connection with reducing cell sizes of commensurate lattices of HOC overlayer structures discussed in Sec. 6.4 the **reduction** of two  $2 \times 2$  **integer matrices** to yield a coprime pair is of interest.

The starting point are two integer matrices  $\underline{\underline{A}}$  and  $\underline{\underline{B}}$  where  $\underline{\underline{B}}$  is diagonal, i. e.

$$\underline{\underline{A}} = \begin{pmatrix} a_{11} & a_{12} \\ a_{21} & a_{22} \end{pmatrix}, \quad \underline{\underline{B}} = \begin{pmatrix} b_1 & 0 \\ 0 & b_2 \end{pmatrix}, \quad a_{ij}, b_i \text{ integer} \quad (\text{E.107})$$

These matrices form a **coprime pair** if their determinants are coprime, i.e. if

$$g = \gcd(|\det(\underline{\underline{A}})|, |\det(\underline{\underline{B}})|) = 1 \quad (\text{E.108})$$

For  $g > 1$  we consider a pair of reduced integer matrices  $\underline{\underline{A}}'$  and  $\underline{\underline{B}}'$  resulting from a joint integer-valued reduction matrix  $\underline{\underline{T}}$  with

$$\underline{\underline{A}}' = \underline{\underline{T}}^{-1} \underline{\underline{A}}, \quad \underline{\underline{B}}' = \underline{\underline{T}}^{-1} \underline{\underline{B}} \quad (\text{E.109})$$

This yields for the determinants

$$\det(\underline{\underline{A}}) = \det(\underline{\underline{T}}) \det(\underline{\underline{A}}'), \quad \det(\underline{\underline{B}}) = \det(\underline{\underline{T}}) \det(\underline{\underline{B}}') \quad (\text{E.110})$$

Thus, the integer  $\det(\underline{\underline{T}})$  must be a common divisor of both integers  $\det(\underline{\underline{A}})$  and  $\det(\underline{\underline{B}})$  with an upper limit given by

$$|\det(\underline{\underline{T}})| \leq g \quad (\text{E.111})$$

For  $\det(\underline{\underline{T}}) = g$  we obtain

$$|\det(\underline{\underline{A}})| = g |\det(\underline{\underline{A}}')|, \quad |\det(\underline{\underline{B}})| = g |\det(\underline{\underline{B}}')| \quad (\text{E.112})$$

and hence with (E.108)

$$\gcd(|\det(\underline{\underline{A}}')|, |\det(\underline{\underline{B}}')|) = 1/g \gcd(|\det(\underline{\underline{A}})|, |\det(\underline{\underline{B}})|) = 1 \quad (\text{E.113})$$

Thus, the reduced matrices  $\underline{\underline{A}}'$  and  $\underline{\underline{B}}'$  form a coprime pair which can be evaluated by a simple **trial-and-error** procedure. From

$$\underline{\underline{A}}' = \underline{\underline{T}}^{-1} \underline{\underline{A}} = \underline{\underline{B}}' \underline{\underline{B}}'^{-1} \underline{\underline{A}} \quad (\text{E.114})$$

together with (E.107) we obtain for the matrix elements

$$\begin{pmatrix} a_{11}' & a_{12}' \\ a_{21}' & a_{22}' \end{pmatrix} = \begin{pmatrix} \frac{a_{11}}{b_1} b_{11}' + \frac{a_{21}}{b_2} b_{12}' & \frac{a_{12}}{b_1} b_{11}' + \frac{a_{22}}{b_2} b_{12}' \\ \frac{a_{11}}{b_1} b_{21}' + \frac{a_{21}}{b_2} b_{22}' & \frac{a_{12}}{b_1} b_{21}' + \frac{a_{22}}{b_2} b_{22}' \end{pmatrix}, \quad (\text{E.115})$$

which yields four Diophantine equations

$$a_{ij}' = \frac{a_{1j}}{b_1} b_{i1}' + \frac{a_{2j}}{b_2} b_{i2}', \quad i, j = 1, 2 \quad (\text{E.116})$$

transforming between integers  $a_{ij}'$  and  $b_{ij}'$  with integers  $b_i$  and  $a_{ij}$  being determined by the initial matrices  $\underline{\underline{A}}$  and  $\underline{\underline{B}}$ . The search for solutions of (E.116), and, thus for matrices  $\underline{\underline{A}}'$  and  $\underline{\underline{B}}'$ , can be restricted to element values

$$0 \leq b_{ij}' < b_j, \quad j = 1, 2 \quad (\text{E.117})$$

since for larger or smaller values  $b_{ij}'' = b_{ij}' + n_j b_j$  equations (E.116) read

$$\begin{aligned} a_{ij}'' &= \frac{a_{1j}}{b_1} b_{i1}'' + \frac{a_{2j}}{b_2} b_{i2}'' = \frac{a_{1j}}{b_1} b_{i1}' + \frac{a_{2j}}{b_2} b_{i2}' + n_1 a_{1j} + n_2 a_{2j} \\ &= a_{ij}' + n_1 a_{1j} + n_2 a_{2j} \end{aligned} \quad (\text{E.118})$$

such that according to (E.118) the complete set of solutions, yielding matrix elements of  $\underline{\underline{A}}'$ , can be determined from those inside the region (E.117) by additive corrections involving only elements  $a_{ij}$  of the initial matrix  $\underline{\underline{A}}$ . Thus, the search procedure can be performed by inserting the  $b_1 b_2$  different integers combinations  $(b_{i1}', b_{i2}')$  into (E.116) and checking for integer-valued  $a_{ij}'$ . The resulting matrices  $\underline{\underline{A}}'$  and  $\underline{\underline{B}}'$  can then be tested for

$$\text{gcd}(|\det(\underline{\underline{A}}')|, |\det(\underline{\underline{B}}')|) = 1 \quad (\text{E.119})$$

where the validity yields a coprime pair of reduced matrices  $\underline{\underline{A}}'$  and  $\underline{\underline{B}}'$ .

As an example, we consider the transformation (6.17) discussed in Sec. 6.4 where

$$\underline{\underline{\mathbf{M}}} = \frac{1}{13} \begin{pmatrix} 14 & -5 \\ 5 & 14 \end{pmatrix} = \underline{\underline{\mathbf{B}}}^{-1} \underline{\underline{\mathbf{A}}} \quad , \quad \underline{\underline{\mathbf{A}}} = \begin{pmatrix} 14 & -5 \\ 5 & 14 \end{pmatrix}, \quad \underline{\underline{\mathbf{B}}} = \begin{pmatrix} 13 & 0 \\ 0 & 13 \end{pmatrix}, \quad g=13$$

which leads to Diophantine equations according to (E.116)

$$a_{i1}' = \frac{a_{11}}{b_1} b_{i1}' + \frac{a_{21}}{b_2} b_{i2}' = \frac{14}{13} b_{i1}' + \frac{5}{13} b_{i2}'$$

$$a_{i2}' = \frac{a_{12}}{b_1} b_{i1}' + \frac{a_{22}}{b_2} b_{i2}' = \frac{-5}{13} b_{i1}' + \frac{14}{13} b_{i2}'$$

with solutions

$$\mathbf{A}' = \begin{pmatrix} 4 & 1 \\ -1 & 4 \end{pmatrix}, \quad \underline{\underline{\mathbf{B}}}' = \begin{pmatrix} 3 & 2 \\ -2 & 3 \end{pmatrix}$$

and

$$\gcd(|\det(\underline{\underline{\mathbf{A}}}'|), |\det(\underline{\underline{\mathbf{B}}}'|) ) = \gcd(17, 13) = 1$$

## F Details of Vector Calculus and Linear Algebra

This appendix discusses a few mathematical details connected with vector calculus, which are needed in several places of the book.

In three dimensions, a **vector**  $\underline{\mathbf{R}}$  is defined by its Cartesian components  $x_i$  along the x-, y-, and z-axis as

$$\underline{\mathbf{R}} = (x_1, x_2, x_3) \quad \text{with its length } R = |\underline{\mathbf{R}}| = \sqrt{(x_1^2 + x_2^2 + x_3^2)} \quad (\text{F.1})$$

The **scalar product** between two vectors  $\underline{\mathbf{R}}$ ,  $\underline{\mathbf{R}'}$  is a real number given by

$$\underline{\mathbf{R}} \underline{\mathbf{R}'} = x_1 x_1' + x_2 x_2' + x_3 x_3' = \underline{\mathbf{R}'} \underline{\mathbf{R}} = R R' \cos(\gamma) \quad (\text{F.2})$$

with  $\gamma$  defining the angle between the two vectors.

The **vector product**,  $\underline{\mathbf{R}} \times \underline{\mathbf{R}'}$  is a vector given in Cartesian coordinates by

$$\underline{\mathbf{R}} \times \underline{\mathbf{R}'} = (x_2 x_3' - x_3 x_2', x_3 x_1' - x_1 x_3', x_1 x_2' - x_2 x_1') = -(\underline{\mathbf{R}'} \times \underline{\mathbf{R}}) \quad (\text{F.3})$$

with its length

$$\begin{aligned} |\underline{\mathbf{R}} \times \underline{\mathbf{R}'}| &= \sqrt{\{(x_2 x_3' - x_3 x_2')^2 + (x_3 x_1' - x_1 x_3')^2 + (x_1 x_2' - x_2 x_1')^2\}} = \\ &= R R' \sin(\gamma) \end{aligned} \quad (\text{F.4})$$

where  $\gamma$  defines the angle between the two vectors.

The **volume product**  $(\underline{\mathbf{R}} \times \underline{\mathbf{R}'}) \underline{\mathbf{R}''}$  is a real number given by

$$\begin{aligned} (\underline{\mathbf{R}} \times \underline{\mathbf{R}'}) \underline{\mathbf{R}''} &= \det \begin{pmatrix} x_1 & x_2 & x_3 \\ x_1' & x_2' & x_3' \\ x_1'' & x_2'' & x_3'' \end{pmatrix} = (\underline{\mathbf{R}'} \times \underline{\mathbf{R}''}) \underline{\mathbf{R}} = (\underline{\mathbf{R}''} \times \underline{\mathbf{R}}) \underline{\mathbf{R}'} = \\ &= (x_2 x_3' - x_3 x_2') x_1'' + (x_3 x_1' - x_1 x_3') x_2'' + (x_1 x_2' - x_2 x_1') x_3'' \end{aligned} \quad (\text{F.5})$$

Consider a **linear transformation** between lattice vectors  $\underline{\mathbf{R}}_1, \underline{\mathbf{R}}_2, \underline{\mathbf{R}}_3$  and  $\underline{\mathbf{R}}_1', \underline{\mathbf{R}}_2', \underline{\mathbf{R}}_3'$ , where

$$\begin{pmatrix} \underline{\mathbf{R}}_1' \\ \underline{\mathbf{R}}_2' \\ \underline{\mathbf{R}}_3' \end{pmatrix} = \begin{pmatrix} t_{11} & t_{12} & t_{13} \\ t_{21} & t_{22} & t_{23} \\ t_{31} & t_{32} & t_{33} \end{pmatrix} \cdot \begin{pmatrix} \underline{\mathbf{R}}_1 \\ \underline{\mathbf{R}}_2 \\ \underline{\mathbf{R}}_3 \end{pmatrix} = \underline{\mathbf{T}} \cdot \begin{pmatrix} \underline{\mathbf{R}}_1 \\ \underline{\mathbf{R}}_2 \\ \underline{\mathbf{R}}_3 \end{pmatrix} \quad (\text{F.6})$$

Then products of transformed vectors  $\underline{\mathbf{R}}_i', \underline{\mathbf{R}}_j'$  can be expressed by those of the initial vectors  $\underline{\mathbf{R}}_i, \underline{\mathbf{R}}_j$  where

- **Scalar products,  $\underline{R}_i' \underline{R}_j'$ , yield**

$$\begin{aligned}\underline{R}_i' \underline{R}_j' &= (t_{i1} \underline{R}_1 + t_{i2} \underline{R}_2 + t_{i3} \underline{R}_3) (t_{j1} \underline{R}_1 + t_{j2} \underline{R}_2 + t_{j3} \underline{R}_3) \\ &= t_{i1} t_{j1} |\underline{R}_1|^2 + t_{i2} t_{j2} |\underline{R}_2|^2 + t_{i3} t_{j3} |\underline{R}_3|^2 + (t_{i1} t_{j2} + t_{i2} t_{j1}) \underline{R}_1 \underline{R}_2 + \\ &\quad + (t_{i1} t_{j3} + t_{i3} t_{j1}) \underline{R}_1 \underline{R}_3 + (t_{i2} t_{j3} + t_{i3} t_{j2}) \underline{R}_2 \underline{R}_3\end{aligned}\quad (\text{F.7})$$

- **Vector products,  $\underline{R}_i' \times \underline{R}_j'$ , yield**

$$\begin{aligned}\underline{R}_i' \times \underline{R}_j' &= (t_{i1} \underline{R}_1 + t_{i2} \underline{R}_2 + t_{i3} \underline{R}_3) \times (t_{j1} \underline{R}_1 + t_{j2} \underline{R}_2 + t_{j3} \underline{R}_3) \\ &= + (t_{i1} t_{j2} - t_{i2} t_{j1}) (\underline{R}_1 \times \underline{R}_2) + (t_{i1} t_{j3} - t_{i3} t_{j1}) (\underline{R}_1 \times \underline{R}_3) + \\ &\quad + (t_{i2} t_{j3} - t_{i3} t_{j2}) (\underline{R}_2 \times \underline{R}_3)\end{aligned}\quad (\text{F.8})$$

- **Volume products  $(\underline{R}_1' \times \underline{R}_2') \underline{R}_3'$  yield**

$$\begin{aligned}(\underline{R}_1' \times \underline{R}_2') \underline{R}_3' &= \\ &= [ (t_{11} \underline{R}_1 + t_{12} \underline{R}_2 + t_{13} \underline{R}_3) \times (t_{21} \underline{R}_1 + t_{22} \underline{R}_2 + t_{23} \underline{R}_3) ] \underline{R}_3' \\ &= (t_{11} t_{22} - t_{12} t_{21}) (\underline{R}_1 \times \underline{R}_2) \underline{R}_3' + (t_{11} t_{23} - t_{13} t_{21}) (\underline{R}_1 \times \underline{R}_3) \underline{R}_3' + \\ &\quad + (t_{12} t_{23} - t_{13} t_{22}) (\underline{R}_2 \times \underline{R}_3) \underline{R}_3' \\ &= t_{33} (t_{11} t_{22} - t_{12} t_{21}) (\underline{R}_1 \times \underline{R}_2) \underline{R}_3 + t_{32} (t_{11} t_{23} - t_{13} t_{21}) (\underline{R}_1 \times \underline{R}_3) \underline{R}_2 + \\ &\quad + t_{31} (t_{12} t_{23} - t_{13} t_{22}) (\underline{R}_2 \times \underline{R}_3) \underline{R}_1 \\ &= \det(\underline{T}) (\underline{R}_1 \times \underline{R}_2) \underline{R}_3\end{aligned}\quad (\text{F.9})$$

Consider **reciprocal lattice vectors**, defined in Sec. 2.5 and given by

$$\begin{aligned}\underline{G}_1 &= \beta (\underline{R}_2 \times \underline{R}_3), \quad \underline{G}_2 = \beta (\underline{R}_3 \times \underline{R}_1), \quad \underline{G}_3 = \beta (\underline{R}_1 \times \underline{R}_2) \\ \beta &= 2\pi / [(\underline{R}_1 \times \underline{R}_2) \underline{R}_3]\end{aligned}\quad (\text{F.10})$$

and **reciprocal of the reciprocal** lattice vectors given by

$$\begin{aligned}\underline{H}_1 &= \gamma (\underline{G}_2 \times \underline{G}_3), \quad \underline{H}_2 = \gamma (\underline{G}_3 \times \underline{G}_1), \quad \underline{H}_3 = \gamma (\underline{G}_1 \times \underline{G}_2) \\ \gamma &= 2\pi / [(\underline{G}_1 \times \underline{G}_2) \underline{G}_3]\end{aligned}\quad (\text{F.11})$$

Then, using relation

$$(\underline{a} \times \underline{b}) \times \underline{c} = (\underline{a} \underline{c}) \underline{b} - (\underline{b} \underline{c}) \underline{a}\quad (\text{F.12})$$

from basic vector calculus, we obtain

$$\underline{H}_1 = \gamma (\underline{G}_2 \times \underline{G}_3) = \gamma \beta^2 [ (\underline{R}_3 \times \underline{R}_1) \times (\underline{R}_1 \times \underline{R}_2) ] = \gamma \beta^2 (2\pi/\beta) \underline{R}_1 = \underline{R}_1\quad (\text{F.13})$$

since according to (2.99)

$$2\pi \gamma \beta = (2\pi)^3 / [ (\underline{\mathbf{G}}_1 \times \underline{\mathbf{G}}_2) \underline{\mathbf{G}}_3 \cdot (\underline{\mathbf{R}}_1 \times \underline{\mathbf{R}}_2) \underline{\mathbf{R}}_3 ] = 1 \quad (\text{F.14})$$

Likewise, we obtain

$$\underline{\mathbf{H}}_2 = \gamma (\underline{\mathbf{G}}_3 \times \underline{\mathbf{G}}_1) = \gamma \beta^2 [ (\underline{\mathbf{R}}_1 \times \underline{\mathbf{R}}_2) \times (\underline{\mathbf{R}}_2 \times \underline{\mathbf{R}}_3) ] = \gamma \beta^2 (2\pi/\beta) \underline{\mathbf{R}}_2 = \underline{\mathbf{R}}_2 \quad (\text{F.15})$$

$$\underline{\mathbf{H}}_3 = \gamma (\underline{\mathbf{G}}_1 \times \underline{\mathbf{G}}_2) = \gamma \beta^2 [ (\underline{\mathbf{R}}_2 \times \underline{\mathbf{R}}_3) \times (\underline{\mathbf{R}}_3 \times \underline{\mathbf{R}}_1) ] = \gamma \beta^2 (2\pi/\beta) \underline{\mathbf{R}}_3 = \underline{\mathbf{R}}_3 \quad (\text{F.16})$$

As a result, the reciprocal of the reciprocal lattice **agrees** with the initial lattice.

Further, the **vector relation**

$$[(\underline{\mathbf{a}} \times \underline{\mathbf{b}}) \underline{\mathbf{c}}] [(\underline{\mathbf{a}}' \times \underline{\mathbf{b}}') \underline{\mathbf{c}}'] = \det \begin{pmatrix} \underline{\mathbf{a}} \underline{\mathbf{a}}' & \underline{\mathbf{a}} \underline{\mathbf{b}}' & \underline{\mathbf{a}} \underline{\mathbf{c}}' \\ \underline{\mathbf{b}} \underline{\mathbf{a}}' & \underline{\mathbf{b}} \underline{\mathbf{b}}' & \underline{\mathbf{b}} \underline{\mathbf{c}}' \\ \underline{\mathbf{c}} \underline{\mathbf{a}}' & \underline{\mathbf{c}} \underline{\mathbf{b}}' & \underline{\mathbf{c}} \underline{\mathbf{c}}' \end{pmatrix} \quad (\text{F.17})$$

together with the orthogonality relation (2.96) for lattice and reciprocal lattice vectors, i.e.

$$\underline{\mathbf{G}}_i \underline{\mathbf{R}}_j = 2\pi \delta_{ij}; \quad i, j = 1, 2, 3 \quad (\text{F.18})$$

yields

$$\begin{aligned} [(\underline{\mathbf{G}}_1 \times \underline{\mathbf{G}}_2) \underline{\mathbf{G}}_3] [(\underline{\mathbf{R}}_1 \times \underline{\mathbf{R}}_2) \underline{\mathbf{R}}_3] &= \det \begin{pmatrix} \underline{\mathbf{G}}_1 \underline{\mathbf{R}}_1 & \underline{\mathbf{G}}_1 \underline{\mathbf{R}}_2 & \underline{\mathbf{G}}_1 \underline{\mathbf{R}}_3 \\ \underline{\mathbf{G}}_2 \underline{\mathbf{R}}_1 & \underline{\mathbf{G}}_2 \underline{\mathbf{R}}_2 & \underline{\mathbf{G}}_2 \underline{\mathbf{R}}_3 \\ \underline{\mathbf{G}}_3 \underline{\mathbf{R}}_1 & \underline{\mathbf{G}}_3 \underline{\mathbf{R}}_2 & \underline{\mathbf{G}}_3 \underline{\mathbf{R}}_3 \end{pmatrix} = \\ &= \det \begin{pmatrix} 2\pi & 0 & 0 \\ 0 & 2\pi & 0 \\ 0 & 0 & 2\pi \end{pmatrix} = (2\pi)^3 \end{aligned} \quad (\text{F.19})$$

This gives another proof of relation (2.98).

The **vector relation**

$$(\underline{\mathbf{a}} \underline{\mathbf{m}}) ((\underline{\mathbf{b}} \times \underline{\mathbf{c}}) \underline{\mathbf{m}}) + (\underline{\mathbf{b}} \underline{\mathbf{m}}) ((\underline{\mathbf{c}} \times \underline{\mathbf{a}}) \underline{\mathbf{m}}) + (\underline{\mathbf{c}} \underline{\mathbf{m}}) ((\underline{\mathbf{a}} \times \underline{\mathbf{b}}) \underline{\mathbf{m}}) = m^2 ((\underline{\mathbf{a}} \times \underline{\mathbf{b}}) \underline{\mathbf{c}}) \quad (\text{F.20})$$

can be used in connection with mirror symmetry operations. If the lattice vectors  $\underline{\mathbf{R}}_1, \underline{\mathbf{R}}_2, \underline{\mathbf{R}}_3$  are subject to a mirror plane operation

$$\underline{\mathbf{R}}_i \rightarrow \underline{\mathbf{R}}_i' = \underline{\mathbf{R}}_i - 2 (\underline{\mathbf{R}}_i \underline{\mathbf{m}}) \underline{\mathbf{m}}, \quad i = 1, 2, 3, \quad m^2 = 1 \quad (\text{F.21})$$

then

$$\begin{aligned}
(\underline{\mathbf{R}}_1' \times \underline{\mathbf{R}}_2') \underline{\mathbf{R}}_3' &= ([\underline{\mathbf{R}}_1 - 2(\underline{\mathbf{R}}_1 \underline{\mathbf{m}}) \underline{\mathbf{m}}] \times [\underline{\mathbf{R}}_2 - 2(\underline{\mathbf{R}}_2 \underline{\mathbf{m}}) \underline{\mathbf{m}}]) [\underline{\mathbf{R}}_3 - 2(\underline{\mathbf{R}}_3 \underline{\mathbf{m}}) \underline{\mathbf{m}}] = \\
&= ((\underline{\mathbf{R}}_1 \times \underline{\mathbf{R}}_2) - 2(\underline{\mathbf{R}}_1 \underline{\mathbf{m}}) (\underline{\mathbf{m}} \times \underline{\mathbf{R}}_2) - 2(\underline{\mathbf{R}}_2 \underline{\mathbf{m}}) (\underline{\mathbf{R}}_1 \times \underline{\mathbf{m}})) [\underline{\mathbf{R}}_3 - 2(\underline{\mathbf{R}}_3 \underline{\mathbf{m}}) \underline{\mathbf{m}}] = \\
&= (\underline{\mathbf{R}}_1 \times \underline{\mathbf{R}}_2) \underline{\mathbf{R}}_3 - 2(\underline{\mathbf{R}}_3 \underline{\mathbf{m}}) (\underline{\mathbf{R}}_1 \times \underline{\mathbf{R}}_2) \underline{\mathbf{m}} - \\
&\quad - 2(\underline{\mathbf{R}}_1 \underline{\mathbf{m}}) (\underline{\mathbf{m}} \times \underline{\mathbf{R}}_2) \underline{\mathbf{R}}_3 - 2(\underline{\mathbf{R}}_2 \underline{\mathbf{m}}) (\underline{\mathbf{R}}_1 \times \underline{\mathbf{m}}) \underline{\mathbf{R}}_3 = \\
&= (\underline{\mathbf{R}}_1 \times \underline{\mathbf{R}}_2) \underline{\mathbf{R}}_3 - 2 [ (\underline{\mathbf{R}}_1 \underline{\mathbf{m}}) (\underline{\mathbf{R}}_2 \times \underline{\mathbf{R}}_3) \underline{\mathbf{m}} + \\
&\quad + (\underline{\mathbf{R}}_2 \underline{\mathbf{m}}) (\underline{\mathbf{R}}_3 \times \underline{\mathbf{R}}_1) \underline{\mathbf{m}} + (\underline{\mathbf{R}}_3 \underline{\mathbf{m}}) (\underline{\mathbf{R}}_1 \times \underline{\mathbf{R}}_2) \underline{\mathbf{m}} ] \quad (\text{F.22})
\end{aligned}$$

and applying (F.20) to the expression in square brackets yields

$$(\underline{\mathbf{R}}_1' \times \underline{\mathbf{R}}_2') \underline{\mathbf{R}}_3' = (\underline{\mathbf{R}}_1 \times \underline{\mathbf{R}}_2) \underline{\mathbf{R}}_3 - 2 m^2 [(\underline{\mathbf{R}}_1 \times \underline{\mathbf{R}}_2) \underline{\mathbf{R}}_3] = -(\underline{\mathbf{R}}_1 \times \underline{\mathbf{R}}_2) \underline{\mathbf{R}}_3 \quad (\text{F.23})$$

The changed sign in (F.23) shows that mirror operations change the handedness of the coordinate system. However, the corresponding cell volume remains unchanged since

$$V_{el}' = |(\underline{\mathbf{R}}_1' \times \underline{\mathbf{R}}_2') \underline{\mathbf{R}}_3'| = |-(\underline{\mathbf{R}}_1 \times \underline{\mathbf{R}}_2) \underline{\mathbf{R}}_3| = V_{el} \quad (\text{F.24})$$

## G Details of Fourier Theory

Fourier theory plays major role in the approximation of functions in many fields of science and engineering. As a result, there is a vast amount of literature available at all mathematical levels, see for example Refs. [207], [208]. In this appendix we will discuss only a few simple issues dealing with spatially periodic functions which are relevant for topics treated in this book. For further details we refer to the existing literature.

In the following we consider continuous functions  $f(\underline{\mathbf{r}})$  where  $\underline{\mathbf{r}}$  is a three-dimensional coordinate in real space. In the harmonic analysis (**Fourier analysis**) functions  $f(\underline{\mathbf{r}})$  are approximated by weighted superpositions of harmonic functions  $h_{\underline{\mathbf{G}}}(\underline{\mathbf{r}})$ . These **harmonic functions** are of given periodicity defined by a wave vector  $\underline{\mathbf{G}}$  in three-dimensional reciprocal space (whose dimensions are [length<sup>-1</sup>]) and can be written as

$$h_{\underline{\mathbf{G}}}^c(\underline{\mathbf{r}}) = \cos(\underline{\mathbf{G}} \cdot \underline{\mathbf{r}}) \quad \text{and} \quad h_{\underline{\mathbf{G}}}^s(\underline{\mathbf{r}}) = \sin(\underline{\mathbf{G}} \cdot \underline{\mathbf{r}}) \quad (\text{G.1})$$

where the direction of periodicity is given by that of wave vector  $\underline{\mathbf{G}}$  and the periodicity length  $L$  is determined by

$$L = 2\pi / |\underline{\mathbf{G}}| \quad (\text{G.2})$$

The combined set of sine and cosine functions in (G.1) can be written more elegantly using complex variables and the definition of a complex valued exponential  $\exp(i x)$  where according to Euler's Formula complex harmonic functions are given by

$$h_{\underline{\mathbf{G}}}(\underline{\mathbf{r}}) = h_{\underline{\mathbf{G}}}^c(\underline{\mathbf{r}}) + i h_{\underline{\mathbf{G}}}^s(\underline{\mathbf{r}}) = \cos(\underline{\mathbf{G}} \cdot \underline{\mathbf{r}}) + i \sin(\underline{\mathbf{G}} \cdot \underline{\mathbf{r}}) = \exp(i \underline{\mathbf{G}} \cdot \underline{\mathbf{r}}) \quad (\text{G.3})$$

( $i$  being the imaginary unit number) which will be used in the following.

The approximation of a continuous function  $f(\underline{\mathbf{r}})$  by a weighted superposition of harmonic functions  $h_{\underline{\mathbf{G}}}(\underline{\mathbf{r}})$  must include in general an infinite set of superposition functions for all wave vectors  $\underline{\mathbf{G}}$  where the approximation function  $f_{\text{app}}(\underline{\mathbf{r}})$  is written as an integral

$$f_{\text{app}}(\underline{\mathbf{r}}) = \iiint c_{\underline{\mathbf{G}}} \exp(i \underline{\mathbf{G}} \cdot \underline{\mathbf{r}}) d^3 \underline{\mathbf{G}} \quad (\text{G.4})$$

with the integration extending over the full three-dimensional reciprocal space. It can be shown mathematically that the approximation function  $f_{\text{app}}(\underline{\mathbf{r}})$  reproduces the exact function  $f(\underline{\mathbf{r}})$  if the expansion coefficients  $c_{\underline{\mathbf{G}}}$  are chosen as

$$c_{\underline{\mathbf{G}}} = \iiint f(\underline{\mathbf{r}}) \exp(-i \underline{\mathbf{G}} \cdot \underline{\mathbf{r}}) d^3 \underline{\mathbf{r}} \quad (\text{G.5})$$

Thus, expansion (G.4) together with (G.5) can be used to represent the continuous function  $f(\underline{\mathbf{r}})$ .



If the continuous function  $f(\underline{r})$  is periodic in three different directions described by a three-dimensional lattice with lattice vectors  $\underline{R}_{01}, \underline{R}_{02}, \underline{R}_{03}$ , i.e.

$$f(\underline{r} + \underline{R}) = f(\underline{r}) \quad \text{with} \quad \underline{R} = n_1 \underline{R}_{01} + n_2 \underline{R}_{02} + n_3 \underline{R}_{03}, \quad n_i \text{ integer} \quad (\text{G.6})$$

then the Fourier expansion given by integrals (G.4), (G.5) reduces to a discrete sum of harmonic functions where the converged expansion is

$$f(\underline{r}) = \sum_{k_1, k_2, k_3} c_{\underline{G}} \exp(i \underline{G} \underline{r}) \quad \text{with} \quad \underline{G} = k_1 \underline{G}_{01} + k_2 \underline{G}_{02} + k_3 \underline{G}_{03}, \quad k_i \text{ integer} \quad (\text{G.7})$$

Here the (infinite) summation extends over all vectors  $\underline{G}$  of the reciprocal lattice  $\underline{G}_{01}, \underline{G}_{02}, \underline{G}_{03}$  defined in Sec. 2.5. The expansion coefficients  $c_{\underline{G}}$  of the exact function  $f(\underline{r})$  are then given by

$$c_{\underline{G}} = \frac{1}{V_{\text{el}}} \iiint_{V_{\text{el}}} f(\underline{r}) \exp(-i \underline{G} \underline{r}) d^3 r \quad (\text{G.8})$$

where the three-dimensional integration is carried out over the elementary cell  $V_{\text{el}}$  spanned by  $\underline{R}_{01}, \underline{R}_{02}, \underline{R}_{03}$  of the real space lattice. Relation (G.8) can be derived from (G.7) by integration

$$\iiint_{V_{\text{el}}} f(\underline{r}) \exp(-i \underline{G}' \underline{r}) d^3 r = \sum_{k_1, k_2, k_3} c_{\underline{G}} \iiint_{V_{\text{el}}} \exp(i [\underline{G} - \underline{G}'] \underline{r}) d^3 r = c_{\underline{G}'} V_{\text{el}} \quad (\text{G.9})$$

where

$$\iiint_{V_{\text{el}}} \exp(i [\underline{G} - \underline{G}'] \underline{r}) d^3 r = V_{\text{el}} \quad \text{if} \quad \underline{G}' = \underline{G}, \quad \text{and} \quad = 0 \quad \text{if} \quad \underline{G}' \neq \underline{G} \quad (\text{G.10})$$

has been applied.

According to the orthogonality theorem (2.96) of real and reciprocal space lattice vectors we obtain

$$\begin{aligned} \underline{G} \underline{R} &= (k_1 \underline{G}_{01} + k_2 \underline{G}_{02} + k_3 \underline{G}_{03}) (n_1 \underline{R}_{01} + n_2 \underline{R}_{02} + n_3 \underline{R}_{03}) = \\ &= 2\pi (k_1 n_1 + k_2 n_2 + k_3 n_3) = 2\pi N, \quad N \text{ integer} \end{aligned} \quad (\text{G.11})$$

and thus

$$\exp(i \underline{G} \underline{r}) = \exp(i 2\pi N) = 1 \quad (\text{G.12})$$

which guarantees the periodicity of the expansion since

$$f(\underline{r} + \underline{R}) = \sum_{\underline{G}} c_{\underline{G}} \exp(i \underline{G}(\underline{r} + \underline{R})) = \sum_{\underline{G}} c_{\underline{G}} \exp(i \underline{G} \underline{r}) \exp(i \underline{G} \underline{R}) = f(\underline{r}) \quad (\text{G.13})$$

Next we consider the case where function  $f(\underline{r})$  in three-dimensional space is periodic in two different directions, described by a two-dimensional lattice with lattice vectors  $\underline{R}_{01}$  and  $\underline{R}_{02}$ , and de-

depends on a third coordinate  $\underline{r}_3$  perpendicular to  $\underline{R}_{o1}$  and  $\underline{R}_{o2}$  in a non-periodic fashion. Here we write the three-dimensional coordinate vector  $\underline{r}$  as a sum of a projected vector  $\underline{r}_{12}$  parallel to  $\underline{R}_{o1}$  and  $\underline{R}_{o2}$  and the third vector  $\underline{r}_3$  i.e.  $\underline{r} = \underline{r}_{12} + \underline{r}_3$ . Then the periodicity constraint reads

$$f(\underline{r}_{12} + \underline{R} + \underline{r}_3) = f(\underline{r}_{12} + \underline{r}_3) \quad \text{with} \quad \underline{R} = n_1 \underline{R}_{o1} + n_2 \underline{R}_{o2}, \quad n_i \text{ integer} \quad (\text{G.14})$$

and the Fourier expansion given by integrals (G.4), (G.5) reduces to a discrete sum of harmonic functions where the converged expansion is

$$f(\underline{r}) = \sum_{k_1, k_2} c_{\underline{G}}(\underline{r}_3) \exp(i \underline{G} \underline{r}_{12}) \quad \text{with} \quad \underline{G} = k_1 \underline{G}_{o1} + k_2 \underline{G}_{o2}, \quad k_i \text{ integer} \quad . \quad (\text{G.15})$$

Here the (infinite) summation extends over all vectors  $\underline{G}$  of the two-dimensional reciprocal lattice defined by vectors  $\underline{G}_{o1}$  and  $\underline{G}_{o2}$  where the latter can be derived from the orthogonality theorem

$$\underline{G}_{oi} \underline{R}_{oj} = 2\pi \text{ if } i=j, \text{ and } = 0 \text{ if } i \neq j, \quad i, j = 1, 2 \quad (\text{G.16})$$

yielding

$$\underline{G}_{o1} = \gamma_1 \left( \underline{R}_{o1} - \frac{(\underline{R}_{o1} \underline{R}_{o2})}{R_{o2}^2} \underline{R}_{o2} \right), \quad \gamma_1 = 2\pi \frac{R_{o2}^2}{(R_{o1}^2 R_{o2}^2 - (\underline{R}_{o1} \underline{R}_{o2})^2)} \quad (\text{G.17a})$$

$$\underline{G}_{o2} = \gamma_2 \left( \underline{R}_{o2} - \frac{(\underline{R}_{o1} \underline{R}_{o2})}{R_{o1}^2} \underline{R}_{o1} \right), \quad \gamma_2 = 2\pi \frac{R_{o1}^2}{(R_{o1}^2 R_{o2}^2 - (\underline{R}_{o1} \underline{R}_{o2})^2)} \quad (\text{G.17b})$$

The dependence of  $f(\underline{r})$  on the third coordinate  $\underline{r}_3$  in expansion (G.15) is expressed by all expansion coefficients  $c_{\underline{G}}$  being functions of  $\underline{r}_3$  rather than scalar constants where

$$c_{\underline{G}}(\underline{r}_3) = \frac{1}{A_{el}} \iint_{A_{el}} f(\underline{r}_{12}, \underline{r}_3) \exp(-i \underline{G} \underline{r}_{12}) d^2 \underline{r}_{12} \quad (\text{G.18})$$

and the two-dimensional integration is carried out over the area  $A_{el}$  of the elementary cell spanned by the lattice vectors  $\underline{R}_{o1}$  and  $\underline{R}_{o2}$  of the real space lattice such that the integration does not affect the third coordinate  $\underline{r}_3$ .

## H List of Surface Web Sites

This appendix lists a few web sites which are relevant for surface crystallography.

- **Surface Structure Information, different program codes**  
<http://www.icts.hkbu.edu.hk/surfstructinfo/>
- **The ICSOS Web Site**  
<http://www3.lut.fi/projectsites/icsos/>
- **The Nanotube Site**  
<http://www.pa.msu.edu/cmp/csc/nanotube.html>
- **NIST SSD, Surface Structure Database V. 5 (Windows XP/7+)**  
 NIST has discontinued the distribution of SSD, see oSSD (database, V. 5)  
<http://www.fhi-berlin.mpg.de/KHsoftware/ssdin5/index.html> (SSD structure input, SURVIS visualizer, V. 5)
- **open SSD (oSSD) , based on NIST SSD V. 5 (Windows XP/7+)**  
<http://www.fhi-berlin.mpg.de/KHsoftware/oSSD/index.html>  
 oSSD is identical in its content and handling to NIST SSD V. 5 and available as open source database.
- **SURFACE EXPLORER, surface visualization (WWW)**  
<http://surfexp.fhi-berlin.mpg.de>
- **LEEDpat4, LEED symmetry pattern simulator (Windows XP/7+)**  
<http://www.fhi-berlin.mpg.de/KHsoftware/LEEDpat/index.html>
- **SARCH, LATUSE, PLOT3D, surface visualization and analysis (DOS, outdated)**  
<http://www.fhi-berlin.mpg.de/KHsoftware/SLP/index.html>
- **BALSAC, surface visualization, and analysis (Windows XP/7+, Linux)**  
<http://www.fhi-berlin.mpg.de/KHsoftware/Balsac/balpam.html> (pamphlet)  
<http://www.fhi-berlin.mpg.de/KHsoftware/Balsac/index.html> (program download)  
<http://www.fhi-berlin.mpg.de/KHsoftware/Balsac/Balsac4.pdf> (Balsac manual, V. 4.00)  
<http://www.fhi-berlin.mpg.de/KHsoftware/Balsac/pictures.html> (Balsac picture gallery)

The Linux version of Balsac (latest version 2.16) is obsolete and will not be developed further.

- **ANA-ROD, analysis by surface X-Ray diffraction**  
[http://www.esrf.eu/computing/scientific/joint\\_projects/ANA-ROD/index.html](http://www.esrf.eu/computing/scientific/joint_projects/ANA-ROD/index.html)

## I List of Surface Structures

This appendix lists all examples of measured clean and adsorbate covered surfaces used to illustrate structural details in this book. Each example, given in Wood notation, is quoted by its figure number, by its literature reference, and by its SSD database reference 'n.m'. Here n.m refers to the entry number of the corresponding surface structure in the Surface Structure Database (NIST Version 5 or oSSD), see Sec. 7.2. For more extended structure compilations consult the references in Sec. 7.2.

Wood notation	Figure	Ref.	SSD entry
Ag(1 1 0) + (2 × 1) - O	6.45	[172]	-
Ag(1 1 0) + (2 × 1) - O	6.13	[140]	47.8.4
Ag(1 1 1) + Xe(incomm.)	6.6	[128]	47.54.1
Al(1 1 1) + (1 × 1) - O	6.39	[168]	13.8.19
Au(1 0 0) - hex	5.8	[112]	79.80
Au(1 1 1) - ( $\sqrt{3} \times 22$ )rect	5.6	[111]	
Cu(1 0 0) + c(2 × 2) - Cl	6.19	[131]	29.17.7
Cu(1 1 0) + c(2 × 2) - Mn	6.17	[146]	29.25.8
Cu(1 1 0) + (2 × 3) - 4N	6.18	[148]	29.7.10
Cu(1 1 1) + (4 × 4) - C60	6.3	[126]	-
Cu(1 1 1) + ( $\sqrt{3} \times \sqrt{3}$ )R30° - In	5.13	[121]	-
Cu(1 1 1) + (disordered) - C2H2	6.11	[138]	29.6.1.6
Cu(1 1 1) + (disordered) - NH3	6.1, 6.46	[124]	29.7.1.3
Ni(1 0 0) + c(2 × 2) - CO	6.8	[130]	28.6.8.8
Ni(1 1 0) + c(2 × 2) - CN	6.42	[170]	28.6.7.2
Ni(1 1 0) + p2mg(2 × 1) - 2CO	6.2	[125]	28.6.8.45
Ni(1 1 1) + c(4 × 2) - 2NO	6.21	[137]	28.7.8.8
Ni(1 1 1) + (1.155 × 1.155)R2.2° - Ag	6.26	[154]	-
Pb(1 1 1) + ( $\sqrt{403/7} \times \sqrt{403/7}$ )R22.8° - C60	6.25	[151]	-
Pd(1 1 1) + ( $\sqrt{3} \times \sqrt{3}$ )R30° - CO	6.20	[136]	46.6.8.13

Pt(1 1 0) - (1 × 2)	5.2	[106]	78.77
Pt(1 1 0) + c(2 × 2) - Br	6.14	[106]	78.35.1
Pt(1 1 1) + c(4 × 2) - 2CO	6.40	[144]	78.6.8.4
Rh(1 1 0) + (1 × 3) - H	6.44	[171]	45.1.5
Rh(1 1 0) + p2mg(2 × 1) - 2O	6.37	[167]	45.8.7
Ru(0 0 0 1) + (0.92 × 0.92) - Gra(phene)	6.5	[127]	-
Si(1 0 0) - (2 × 1)	5.4	[107]	14.203
Si(1 0 0) - c(4 × 2)	5.4	[108]	14.182b
Si(1 1 1) - (7 × 7)	5.5	[110]	14.132
W(1 0 0) - c(2 × 2)	5.3	[22]	74.14
W(1 1 0) + (2 × 1) - O	6.16	[143]	74.8.1

---

**REFERENCES**

- [1] J.C. Slater, "Symmetry and Energy Bands in Crystals", Dover Publications, New York, 1972.
- [2] N.W. Ashcroft and N.D. Mermin, "Solid State Physics", Holt-Saunders Int., New York, 1976.
- [3] F. Garcia-Moliner and F. Flores, *J. Phys. C: Solid State Phys.* 9 (1976) 1609.
- [4] X. Wang, R.Q. Zhang, T.A. Niehaus, and Th. Frauenheim, *J. Phys. Chem. C* 111 (2007) 2394.
- [5] T. Arai and M. Tomitori, *Phys. Rev. Lett.* 93 (2004) 256101.
- [6] R. Rurali and N. Lorente, *Phys. Rev. Lett.* 94 (2005) 026805.
- [7] K. Hermann and M. Witko in "The Chemical Physics of Solid Surfaces", Vol. 9, Oxide Surfaces, D. P. Woodruff (Ed.), Elsevier, Amsterdam, 2001, p. 136.
- [8] C. Rau, C. Liu, A. Schmalzbauer, and G. Xing, *Phys. Rev. Lett.* 57 (1986) 2311.
- [9] A. Biedermann, R. Tscheließnig, M. Schmid, and P. Varga, *Phys. Rev. Lett.* 87 (2001) 086103.
- [10] Y. Takahashi, Y. Gotoh, J. Akimoto, S. Mizuta, K. Tokiwa, and T. Watanabe, *J. Solid State Chem.* 164 (2002) 1.
- [11] G. Ertl, H. Knötzinger, F. Schüth, and J. Weitkamp, "Handbook of Heterogeneous Catalysis", Wiley-VCH, Weinheim, 2008.
- [12] G.A. Somorjai, "Introduction to Surface Chemistry and Catalysis", Wiley-Interscience, New York, 1994.
- [13] N.M. Marković and P.N. Ross Jr., *Surf. Sci. Rep.* 45 (2002) 117.
- [14] G. Cao, "Nanostructures and Nanomaterials: Synthesis, Properties and Applications", Imperial College Press, London, 2004.
- [15] Z. Tang and P. Sheng, "Nano Science and Technology", Taylor and Francis, London, 2003.
- [16] P.J.F. Harris, "Carbon Nanotubes and Related Structures", Cambridge University Press, Cambridge, 1999.
- [17] Y. Kawazoe, T. Kondow, K. Ohno (Eds.), "Clusters and Nanomaterials, Theory and Experiment", Springer, Berlin, 2002.

- [18] F. Langa and J.-F. Nierengarten (Eds.), “Fullerenes: Principles and Applications”, RSC Publishing, Cambridge, 2007.
- [19] A.L. Rogach (Ed.), “Semiconductor Nanocrystal Quantum Dots: Synthesis, Assembly, Spectroscopy and Applications”, Springer, New York, 2008.
- [20] K. Gong, F. Du, Z. Xia, M. Durstock, and L. Dai, *Science* 323 (2009) 760.
- [21] D.D.D. Ma, C.S. Lee, F.C.K. Au, S.Y. Tong, and S.T. Lee, *Science* 299 (2003) 1874.
- [22] P.R. Watson, M.A. Van Hove, and K. Hermann, “NIST Surface Structure Database (SSD), Standard Reference Database 42”, Software Version 5, 2003, available as open SSD (oSSD), see Appendix H for web reference.
- [23] P.R. Watson, M.A. Van Hove, and K. Hermann, “Atlas of Surface Crystallography based on the NIST Surface Structure Database (SSD)”, *J. Phys. Chem. Ref. Data, Monograph Series*, Vol. 5a, b, American Chemical Society, Washington, 1994.
- [24] M.A. Van Hove, K. Hermann, and P.R. Watson, *Acta Cryst. B* 58 (2002) 338.
- [25] J.M. Maclaren, J.B. Pendry, P.J. Rous, D.K. Saldin, G.A. Somorjai, M.A. Van Hove, and D.D. Vvedenski, “Surface Crystallographic Information Service”, Reidel, Dordrecht, 1987 (Update 1992).
- [26] Balsac software by K. Hermann, Fritz-Haber-Institut, Berlin, see Appendix H for web reference.
- [27] SSDIN and Survis software by K. Hermann, Fritz-Haber-Institut, Berlin, see Appendix H for web reference.
- [28] C. Giacovazzo et al., “Fundamentals of Crystallography”, *IUCr Texts on Crystallography* 2, Oxford Science Publishing, 1998.
- [29] H.D. Megaw, “Crystal Structures: A Working Approach”, W.B. Saunders Co., Philadelphia, 1973.
- [30] R.J.D. Tilley, “Crystals and Crystal Structures”, John Wiley Sons, Chichester, 2006.
- [31] R.W.G. Wyckoff, “Crystal Structures” Vol. I-VI, Interscience Pub., New York, 1963.
- [32] G. Burns and A.M. Glazer, “Space Groups for Solid State Scientists”, 2<sup>nd</sup> Ed., Academic Press, New York, 1990.

- [33] “International Tables for Crystallography”, Vol. A, T. Hahn (Ed. 1965, 1983, 1987), Reidel Publishing, Boston.
- [34] D.P. Woodruff and T.A. Delchar, “Modern Techniques of Surface Science”, 2<sup>nd</sup> Ed., Cambridge University Press, Cambridge, 1994.
- [35] H. Ibach, “Physics of Surfaces and Interfaces”, Springer, Berlin, 2006.
- [36] G.A. Somorjai and M.A. Van Hove, “Adsorbed Monolayers on Solid Surfaces”, Vol. 38 of “Structure and Bonding”, Springer, New York, 1979.
- [37] “The Chemical Physics of Solid Surfaces”, Vols. 1-12, D.P. Woodruff (Ed.), Elsevier Science, Amsterdam, 2015.
- [38] A. Zangwill, “Physics at Surfaces”, Cambridge University Press, Cambridge, 1990.
- [39] V.E. Henrich and P.A. Cox, “The Surface Science of Metal Oxides”, Cambridge University Press, Cambridge, 1994.
- [40] M.S. Dresselhaus, G. Dresselhaus, and A. Jorio, “Group Theory, Application to Physics of Condensed Matter“, Springer, Heidelberg, 2008.
- [41] P. Niggli, “Handbuch der Experimentalphysik“ Vol. 7, Part 1, Akad. Verlagsges., Leipzig, 1928.
- [42] A. Santoro and A.D. Mighell, *Acta Cryst. A* 26 (1970) 124.
- [43] B. Gruber, *Acta Cryst. A* 29 (1973) 433.
- [44] L. Merz and K.-H. Ernst, *Surf. Sci.* 604 (2010) 1049.
- [45] J. Huang, G. Zhang, Y. Huang, D. Fang, and D. Zhang, *J. Mag. Mag. Mat.* 299 (2006) 480.
- [46] A. Kellou and H. Aourag, *phys. stat. sol. (b)* 236 (2003) 166.
- [47] M.J. Puska, S. Pöykkö, M. Pesola, and R.M. Nieminen, *Phys. Rev. B* 58 (1998) 1318.
- [48] see e.g. G.P. Srivastava, “Theoretical modelling of semiconductor surfaces: microscopic studies of electrons and phonons”, World Scientific, Singapore, 1999.
- [49] M.J. Buerger, *Z. Kristallogr.* 109 (1957) 42; *ibid.* 113 (1960) 52.
- [50] B.N. Delaunay, *Z. Kristallogr.* 84 (1983) 109.



- [51] E.C. Bain, *Trans. Am. Inst. Min. Metall. Eng.* 70 (1924) 25.
- [52] R.D. Turner and J.C. Inkson, *J. Phys. C: Solid State Phys.* 11 (1978) 3961.
- [53] K.C. Hass, *Phys. Rev. B* 46 (1992) 139.
- [54] C. Quintanar, R. Caballero, and A.M. Köster, *Int. J. Quant. Chem.* 96 (2003) 483.
- [55] R. Fournier, *J. Chem. Phys.* 115 (2001) 2165.
- [56] R.L. Johnson, “Atomic and Molecular Clusters”, Taylor & Francis, London, 2002.
- [57] B.K. Teo and N.J.A. Sloane, *Inorg. Chem.* 24 (1985) 4545.
- [58] G. Wulff, *Z. Kristallogr.* 34 (1901) 449.
- [59] J.W. Gibbs, “The Collected Works”, Longmans-Green Co., New York, 1928.
- [60] C. Herring, *Phys. Rev.* 82 (1951) 87.
- [61] R.L. Dobrushin, R. Kotecky, S.B. Shlosman, “Wulff Construction: A global shape from local interaction”, web manuscript, 1993, see <http://www.cpt.univ-mrs.fr/dobrushin/DKS-book.pdf>.
- [62] International Union of Crystallography Report 1991, *Acta Cryst. A* 48 (1992) 922.
- [63] S. Van Smaalen, “Incommensurate Crystallography”, Oxford University Press, New York, 2009.
- [64] W. Van Aalst, J. Den Hollander, W.J.A.M. Peterse, and P.M. De Wolff, *Acta Cryst. B* 32 (1976) 47.
- [65] A. Arakcheeva, P. Pattison, G. Chapuis, M. Rossell, A. Filaretov, V. Morozov, and G. Van Tendeloo, *Acta Cryst. B* 64 (2008) 160.
- [66] A. Jobst and S. Van Smaalen, *Acta Cryst. B* 58 (2002) 179.
- [67] J. Nuss, S. Pfeiffer, S. Van Smaalen, and M. Jansen, *Acta Cryst. B* 66 (2010) 27.
- [68] D. Shechtman, I. Blech, D. Gratias, and J.W. Cahn, *Phys. Rev. Lett.* 53 (1984) 1951.
- [69] “The Physics of Quasicrystals”, P.J. Steinhardt and S. Ostlund (Eds.), World Scientific, Singapore, 1987.

- [70] “Quasicrystals: The State of the Art”, 2<sup>nd</sup> Ed., D.P. DiVincenzo and P.J. Steinhardt (Eds.), Series on Directions in Condensed Matter Physics, Vol. 16, World Scientific, Singapore, 1999.
- [71] H.-R. Trebin (Ed.), “Quasicrystals, Structure and Physical Properties”, Wiley-VCH, Weinheim, 2003.
- [72] C. Janot, “Quasicrystals: A Primer”, Clarendon Press, Oxford, 1992.
- [73] Z.M. Stadnik, “Physical Properties of Quasicrystals”, Springer, Berlin, 1999.
- [74] B. Suck, M. Schreiber, and P. Haussler (Eds.), “Quasicrystals: An Introduction to Structure, Physical Properties and Applications“, Springer, Berlin, 2002.
- [75] A.I. Goldman, D.J. Sordelet, P.A. Thiel, and J.M. Dubois (Eds.), “New Horizons in Quasicrystals”, World Scientific Press, Singapore, 1997.
- [76] P.A. Thiel, *Annu. Rev. Phys. Chem.* 59 (2008) 129.
- [77] J.M. Dubois, “Useful Quasicrystals”, World Scientific Press, Singapore, 2005.
- [78] M. Senechal, “Quasicrystals and Geometry”, Cambridge University Press, Cambridge, 1995.
- [79] W. Steurer and S. Deloudi, “Crystallography of Quasicrystals: Concepts, Methods and Structures“, Springer, Berlin, 2009.
- [80] R. Penrose, *Bull. Inst. Math. Appl.* 10 (1974) 266.
- [81] A. Yamamoto, *Sci. Technol. Adv. Mater.* 9 (2008) 013001.
- [82] Y. Calvayrac, A. Quivy, M. Bessière, S. Lefebvre, M. Cornier-Quiquandon, and D. Gratias, *J. Phys. France* 51 (1990) 417.
- [83] T. Cai, F. Shi, Z. Shen, M. Gierer, A.I. Goldman, M.J. Kramer, C.J. Jenks, T.A. Lograsso, D.W. Delaney, P.A. Thiel, and M.A. Van Hove, *Surf. Sci.* 495 (2001) 19.
- [84] K. Hermann, *Surf. Rev. Lett.* 4 (1997) 1063.
- [85] H. Minkowski, *Gesammelte Abhandlungen*, Vol. 1, pp. 145, 153, 217; Vol. 2, p. 78, Teubner Verlag, Leipzig, 1911.
- [86] A.M. Bradshaw and N.V. Richardson, *Pure and Appl. Chem.* 68 (1996) 457.
- [87] A.P. Cracknell, *Thin Solid Films* 21 (1974) 107.

- [88] I. Czekaj, K. Hermann, and M. Witko, *Surf. Sci.* 525 (2003) 33.
- [89] J.F. Nicholas, "An Atlas of Models of Crystal Surfaces", Gordon and Breach, New York, 1965. (out of print).
- [90] J.F. Nicholas, in Landolt-Börnstein, New Series, "Physics of Solid Surfaces, Sub-volume a, Structure", Vol. III/24a, Springer, Heidelberg, 1993.
- [91] G.A. Somorjai and M.A. Van Hove, *Prog. Surf. Sci.* 30 (1989) 201.
- [92] D.R. Eisner and T.L. Einstein, *Surf. Sci. Lett.* 286 (1993) L559.
- [93] B. Lang, R.W. Joyner, and G.A. Somorjai, *Surf. Sci.* 30 (1972) 454.
- [94] M.A. Van Hove, W.H. Weinberg, and C.M. Chan, "Low Energy Electron Diffraction", Springer Series in Surface Science, Vol. 6, New York, 1986.
- [95] M.A. Van Hove and G.A. Somorjai, *Surf. Sci.* 92 (1980) 489.
- [96] S.J. Jenkins and S.J. Pratt, *Surf. Sci. Rep.* 62 (2007) 373.
- [97] G.H. Wagnière, "On Chirality and the Universal Asymmetry", Wiley-VCH, Weinheim, 2007.
- [98] J. Potočka and A. Dvořák, *J. Appl. Biomed.* 2 (2004) 95.
- [99] J.D. Horvath and A.J. Gellman, *Topics in Catal.* 25 (2003) 9.
- [100] S. Barlow and R. Raval, *Surf. Sci. Rep.* 50 (2003) 201.
- [101] IUPAC Rules for the Nomenclature of Organic Chemistry, Section E: Stereochemistry, *Pure and Appl. Chem.* 45 (1976) 11.
- [102] D. Muchay, K. Stadnickay, W. Kaminskyz, and A.M. Glazerz, *J. Phys.: Condens. Matter* 9 (1997) 10829.
- [103] C.F. McFadden, P.S. Cremer, and A.J. Gellman, *Langmuir* 12 (1996) 2483.
- [104] D.S. Sholl, A. Asthagiri, and T.D. Power, *J. Chem. Phys. B* 105 (2001) 4771.
- [105] P. Jiang, F. Jona, and P.M. Marcus, *Phys. Rev. B* 35 (1987) 7952.
- [106] V. Blum, L. Hammer, K. Heinz, C. Franchini, J. Redinger, K. Swamy, C. Deisl, and E. Bertel, *Phys. Rev. B* 65 (2002) 165408.
- [107] Y. Wang, M. Shi, and J.W. Rabalais, *Phys. Rev. B* 48 (1993) 1678.

- [108] R.G. Zhao, J.F. Jia, Y.F. Li, and W.S. Yang, Springer Series in Surf. Sci. 24 (1991) 517.
- [109] K. Takayanagi, Y. Tanishiro, M. Takahashi, and S. Takahashi, J. Vac. Sci. Technol. A3 (1985) 1502.
- [110] S.Y. Tong, H. Huang, C.M. Wei, W.E. Packard, F.K. Men, G. Glander, and M.B. Webb, J. Vac. Sci. Technol. A6 (1988) 615.
- [111] M.A. Van Hove, R.J. Koestner, P.C. Stair, J.P. Bibérian, L.L. Kesmodel, I. Bartoš, and G.A. Somorjai, Surf. Sci. 103 (1981) 189.
- [112] B.M. Ocko, D. Gibbs, K.G. Huang, D.M. Zehner, and S.G.J. Mochrie, Phys. Rev. B 44 (1991) 6429.
- [113] E. Bauer, Z. Kristallogr. 110 (1958) 372; *ibid* 110 (1958) 372.
- [114] P. Schmailzl, K. Schmidt, P. Bayer, R. Döll, and K. Heinz, Surf. Sci. 312 (1994) 73.
- [115] D. Schmitz, C. Charton, A. Scholl, C. Carbone, and W. Eberhardt, Phys. Rev. B 59 (1999) 4327.
- [116] R. Koch, J. Phys.: Condens. Matter 6 (1994) 9519.
- [117] J.A. Venables, G.D.T. Spiller, and M. Hanbücken, Rep. Prog. Phys. 47 (1984) 399.
- [118] E. Bauer, H. Poppa, G. Todd, and P.R. Davis, J. Appl. Phys. 48 (1977) 3773.
- [119] M. Hanbücken, H. Neddermeyer, and P. Rupieper, Thin Solid Films 90 (1982) 37.
- [120] see e.g. “The Chemical Physics of Solid Surfaces”, Vol. 10, Surface Alloys and Alloy Surfaces, D.P. Woodruff (Ed.), Elsevier Science, Amsterdam, 2002.
- [121] H. Wider, V. Gimple, W. Evenson, G. Schatz, J. Jaworski, J. Prokop, and M. Marszałek, J. Phys.: Condens. Matter 15 (2003) 1909.
- [122] V.E. Henrich, Surf. Sci. 57 (1976) 385.
- [123] E. Zaremba and W. Kohn, Phys. Rev. B 15 (1977) 1769.
- [124] P. Baumgärtel, R. Lindsay, T. Giessel, O. Schaff, A.M. Bradshaw, and D.P. Woodruff, J. Phys. Chem. B 104 (2000) 3044.
- [125] K.F. Peters, C.J. Walker, P. Steadman, O. Robach, H. Isern, and S. Ferrer, Phys. Rev. Lett. 86 (2001) 5325.

- [126] W.W. Pai, H.T. Jeng, C.-M. Cheng, C.-H. Lin, X. Xiao, A. Zhao, X. Zhang, G. Xu, X.Q. Shi, M.A. Van Hove, C.-S. Hsue, and K.-D. Tsuei, *Phys. Rev. Lett.* 104 (2010) 036103.
- [127] W. Moritz, B. Wang, M.-L. Bocquet, T. Brugger, T. Greber, J. Winterlin, and S. Günther, *Rev. Lett.* 104 (2010) 136102.
- [128] P.I. Cohen, J. Unguris, and M.B. Webb, *Surf. Sci.* 58 (1976) 429.
- [129] E. Charrier and L. Buzer, *Disc. Appl. Math.* 157 (2009) 3473.
- [130] S.Y. Tong, A. Maldonado, C.H. Li, and M.A. Van Hove, *Surf. Sci.* 94 (1980) 73.
- [131] P.H. Citrin, D.R. Hamann, L.F. Mattheiss, and J.E. Rowe, *Phys. Rev. Lett.* 49 (1982) 1712.
- [132] K. Johnson, Q. Ge, S. Titmuss, and D.A. King, *J. Chem. Phys.* 112 (2000) 10460.
- [133] S.A. Lindgren, L. Wallden, J. Rundgren, P. Westrin, and J. Neve, *Phys. Rev. B* 28 (1983) 6707.
- [134] M. Gierer, A. Barbieri, M.A. Van Hove, and G.A. Somorjai, *Surf. Sci.* 391 (1997) 176.
- [135] D.T. Vu Grimsby, Y.K. Wu, and K.A.R. Mitchell, *Surf. Sci.* 232 (1990) 51.
- [136] I. Zasada and M.A. Van Hove, *Surf. Sci.* 457 (2000) L421.
- [137] N. Materer, A. Barbieri, D. Gardin, U. Starke, J.D. Batteas, M.A. Van Hove, and G.A. Somorjai, *Surf. Sci.* 303 (1994) 319.
- [138] S. Bao, K.-M. Schindler, P. Hofmann, V. Fritzsche, A.M. Bradshaw, and D.P. Woodruff, *Surf. Sci.* 291 (1993) 295.
- [139] P. Hofmann, K.-M. Schindler, S. Bao, V. Fritzsche, A.M. Bradshaw, and D.P. Woodruff, *Surf. Sci.* 337 (1995) 169.
- [140] A. Puschmann and J. Haase, *Surf. Sci.* 144 (1984) 559.
- [141] T. Yokoyama, H. Hamamatsu, Y. Kitajima, Y. Takata, S. Yagi, and T. Ohta, *Surf. Sci.* 313 (1994) 197.
- [142] H.D. Shih, F. Jona, D.W. Jepsen, and O.M. Marcus, *Phys. Rev. Lett.* 46 (1981) 731.
- [143] M.A. Van Hove and S.Y. Tong, *Phys. Rev. Lett.* 35 (1975) 1092.

- [144] D.F. Ogletree, M.A. Van Hove, and G.A. Somorjai, *Surf. Sci.* 173 (1986) 351.
- [145] Z.Q. Wu, S.H. Lu, Z.Q. Wang, C.K.C. Lok, J. Quinn, Y.S. Li, D. Tian, F. Jona, and P.M. Marcus, *Phys. Rev. B* 38 (1988) 5363.
- [146] C. Ross, B. Schirmer, M. Wuttig, Y. Gauthier, G. Bihlmayer, and S. Blügel, *Phys. Rev. B* 57 (1998) 2607.
- [147] G. Helgesen, D. Gibbs, A.P. Baddorf, D.M. Zehner, and S.G.J. Mochrie, *Phys. Rev. B* 48 (1993) 15320.
- [148] A.P. Baddorf, D.M. Zehner, G. Helgesen, D. Gibbs, A.R. Sandy, and S.G.J. Mochrie, *Phys. Rev. B* 48 (1993) 9013.
- [149] A. Nishiyama, G. terHost, M. Lohmeier, A.M. Molenbroek, and J.W.M. Frenken, *Surf. Sci.* 321 (1994) 261.
- [150] E.A. Wood, *J. Appl. Phys.* 35 (1964) 1306.
- [151] H.I. Li, K.J. Franke, J.I. Pascual, L.W. Bruch, and R.D. Diehl, *Phys. Rev. B* 80 (2009) 085415.
- [152] A. Tkatchenko, *Phys. Rev. B* 74 (2006) 035428; 75 (2007) 235411.
- [153] T. Brugger, H. Ma, M. Iannuzzi, S. Berner, A. Winkler, J. Hutter, J. Osterwalder, and T. Greber, *Angew. Chem. Int. Ed.* 49 (2010) 6120; *ibid.* 49 (2010) 6256.
- [154] C. Chambon, J. Creuze, A. Coati, M. Sauvage-Simkin, and Y. Garreau, *Phys. Rev. B* 79 (2009) 125412.
- [155] K. Hermann, *J. Phys.: Condensed Matter* 24 (2012) 314210.
- [156] K. Hermann, *J. Phys.: Condensed Matter* (2016), submitted.
- [157] A. B. Preobrajenski, M.-L. Ng, A. S. Vinogradov, and N. Mårtensson, *Phys. Rev. B* 78 (2008) 073401.
- [158] A.T. N'Diaye, J. Coraux, T.N. Plasa, C. Busse, and T. Michely, *New J. Phys.* 10 (2008) 043033.
- [159] E. Loginova, S. Nie, K. Thürmer, N.C. Bartelt, and K.F. McCarty, *Phys. Rev. B* 80 (2009) 085430.
- [160] B. Wang and M.-L. Bocquet, *J. Phys. Chem. Lett.* 2 (2011) 2341.
- [161] L. Gao, J.R. Guest, and N.P. Guisinger, *Nano Lett.* 10 (2010) 3512.

- [162] W. Zhao, S.M. Kozlov, Ol. Höfert, K. Gotterbarm, M.P.A. Lorenz, F. Viñes, C. Papp, A. Görling, H.-P. Steinrück, *J. Phys. Chem. Lett.* 2 (2011) 759.
- [163] P. Zeller and S. Günther, *New J. Phys.* 16 (2014) 083028.
- [164] T.M. Bernhardt, B. Kaiser, and K. Rademann, *Surf. Sci.* 408 (1998) 86.
- [165] J. Xue, J. Sanchez-Yamagishi, D. Bulmash, P. Jacquod, A. Deshpande, K. Watanabe, T. Taniguchi, P. Jarillo-Herrero, and B.J. LeRoy, *Nature Mat.* 10 (2011) 282.
- [166] J. Coraux, A.T. N'Diaye, C. Busse, and T. Micheley, *Nano Lett.* 8 (2008) 565.
- [167] J.D. Batteas, A. Barbieri, E.K. Starkey, M.A. Van Hove, and G.A. Somorjai, *Surf. Sci.* 339 (1995) 142.
- [168] M. Kerkar, D. Fisher, D.P. Woodruff and B. Cowie, *Surf. Sci.* 271 (1992) 45.
- [169] LEEDpat4 software by K. Hermann, see Appendix H for web reference.
- [170] N.A. Booth, R. Davis, D.P. Woodruff, D. Chrysostomou, T. McCabe, D.R. Lloyd, O. Schaff, V. Fernandez, S. Bau, K.-M. Schindler, R. Lindsay, J.T. Hoefl, R. Terborg, P. Baumgärtel, A.M. Bradshaw, *Surf. Sci.* 416 (1998) 448.
- [171] K. Lehnberger, W. Nichtl-Pecher, W. Oed, K. Heinz, and K. Müller, *Surf. Sci.* 217 (1989) 511.
- [172] M. Pascal, C.L. A. Lamont, P. Baumgärtel, R. Terborg, J.T. Hoefl, O. Schaff, M. Polčík, A.M. Bradshaw, R.L. Toomes, and D.P. Woodruff, *Surf. Sci.* 464 (2000) 83.
- [173] C.J. Baddeley and N.V. Richardson in “Scanning Tunneling Microscopy in Surface Science, Nanoscience, and Catalysis”, M. Bowker and P.R. Davis (Eds.), Wiley-VCH, Weinheim, 2010, p. 1.
- [174] R. Raval, *Chem. Soc. Rev.* 38 (2009) 707.
- [175] A.J. Gellman in “Model Systems in Catalysis”, R. Rioux (Ed.), Springer, New York, 2010 p. 75.
- [176] M.-C. Blüm, E. Cavar, M. Pivetta, F. Patthey, and W.-D. Schneider, *Angew. Chem. Int. Ed.* 44 (2005) 5334.
- [177] M. Ortega Lorenzo, S. Haq, T. Bertrams, P. Murray, R. Raval, and C.J. Baddeley, *J. Phys. Chem. B* 103 (1999) 10661.
- [178] A.G. Mark, M. Forster, and R. Raval, *ChemPhysChem* 12 (2011) 1474.

- [179] B. Bhatia and D.S. Sholl, *Angew. Chem. Int. Ed.* 44 (2005) 7761.
- [180] J. Stöhr, "NEXAFS Spectroscopy", Springer Series in Surface Science, Vol. 25, Heidelberg, 1992-2003.
- [181] F.H. Allen, *Acta Cryst. B*, 58 (2002) 380.
- [182] A. Belsky, M. Hellenbrandt, V. Lynn, K. Luksch, and P. Luksch, *Acta Cryst. B*, 58 (2002) 364.
- [183] P.S. White, J.R. Rodgers, and Y. Le Page, *Acta Cryst. B*, 58 (2002) 343.
- [184] H.M. Berman, J. Westbrook, Z. Feng, L. Iype, B. Schneider, and C. Zardecki, *Acta Cryst. D*, 58 (2002) 889.
- [185] H. M. Berman, T. Battistuz, T.N. Bhat, W.F. Bluhm, P.E. Bourne, K. Burkhardt, Z. Feng, G.L. Gilliland, L. Iype, S. Jain, P. Fagan, J. Marvin, D. Padilla, V. Ravichandran, B. Schneider, N. Thanki, H. Weissig, J.D. Westbrook, and C. Zardecki, *Acta Cryst. D*, 58 (2002) 899.
- [186] H. Ohtani, C.-T. Kao, M.A. Van Hove, and G.A. Somorjai, *Prog. in Surf. Sci.* 23 (1986) 155.
- [187] M. A. Van Hove, K. Hermann, and P. R. Watson, in Landolt-Börnstein, New Series, "Physics of Covered Solid Surfaces", Vol. III/42, Springer, Heidelberg, 2002.
- [188] J.V. Barth, *Annu. Rev. Phys. Chem.* 58 (2007) 375.
- [189] J.A.A. Elemans, S. Lei, and S. De Feyter, *Angew. Chem. Int. Ed.* 48 (2009) 7298.
- [190] W. Wang, X. Shi, S. Wang, J. Liu, M.A. Van Hove, P.N. Liu, R.Q. Zhang, and N. Lin, *Phys. Rev. Lett.* 110 (2013) 046802.
- [191] J. Burchardt, M.M. Nielsen, D.L. Adams, E. Lundgren, and J.N. Andersen, *Phys. Rev. B* 50 (1994) 4718.
- [192] C.T. Campbell, *Surf. Sci.* 604 (2010) 877.
- [193] L.D. Marks, *Surf. Sci.* 604 (2010) 878.
- [194] M.A. Van Hove, K. Hermann, P.R. Watson, D.P. Woodruff, S.Y. Tong, R.D. Diehl, K. Heinz, C. Minot, and H. Tochiyara, *Surf. Sci.* 604 (2010) 1544.
- [195] S.R. Hall, F.H. Allen, I.D. Brown, *Acta Cryst.* A 47 (1991) 655; see also <http://www.iucr.org/resources/cif>.



- [196] H.M. Berman, K. Henrick, and H. Nakamura, *Nature Struct. Biol.* 10 (2003) 908; see also <http://www.wwpdb.org/documentation/file-format.php>.
- [197] G. Kresse and J. Furthmüller, *Phys. Rev. B* 54 (1996) 11169. see also <http://www.vasp.at/index.php/documentation>.
- [198] L.V. Radushkevich and V.M. Lukyanovich, *Zurn. Fisic. Chim.* 111 (1952) 24.
- [199] A. Oberlin, M. Endo, and T. Koyama, *J. Cryst. Growth* 32 (1976) 335.
- [200] S. Iijima and T. Ichihashi, *Nature* 363 (1993) 603.
- [201] N. Wang, Y. Cai, and R.Q. Zhang, *Mat. Sci. Engin. R* 60 (2008) 1.
- [202] see e.g. <http://www.pa.msu.edu/cmp/csc/nanotube.html>.
- [203] W. Chen, J. Peng, L. Mai, Q. Zhu, and Q. Xu, *Mat. Lett.* 58 (2004) 2275.
- [204] L.J. Mordell, “Diophantene Equations”, Academic Press, New York, 1969.
- [205] T. Andreescu and D. Andrica, “Quadratic Diophantine Equations”, Springer Monographs in Mathematics, Heidelberg, 2009; ISBN 978-0-387-35156-8.
- [206] G.H. Hary and E.M. Wright, “An Introduction to the Theory of Numbers”, 6<sup>th</sup> Ed., Oxford University Press, Oxford, 2008.
- [207] M. Pinski, “Introduction to Fourier Analysis and Wavelets”, Brooks/Cole, Pacific Grove, 2002.
- [208] L. Grafakos, “Classical Fourier Analysis”, 2<sup>nd</sup> Ed., Graduate Texts in Mathematics, Springer, New York, 2008.

## GLOSSARY AND ABBREVIATIONS

In this section different keywords and abbreviations which are commonly used in the book are briefly explained. The keywords are arranged in three groups

- Bulk crystals and three-dimensional
- Monolayers, Surfaces and two-dimensional
- Miscellaneous

Within each group the order is alphabetic. Bold faced words in the explanatory text are usually also keywords of the glossary.

### Bulk crystals and three-dimensional

- 4-index notation** ..... See **Miller-Bravais indices**.
- achiral** ..... A three-dimensional object is achiral if it can be superimposed onto its mirror image by simple rotation and shifting. Otherwise, it is **chiral**.
- acute representation** ..... Lattice vectors  $\underline{R}_1$ ,  $\underline{R}_2$ ,  $\underline{R}_3$  which form mutual angles  $\alpha, \beta, \gamma \leq 90^\circ$ .
- Bain path** ..... Geometry variation of a continuous phase transition between face- and body-centered cubic crystals. The intermediate lattice type is described as centered tetragonal (**ct**).
- basis** ..... Collection of atom positions inside the three-dimensional (morphological) unit cell of a **crystal** or **monolayer**.
- bcc** ..... Body-centered cubic, also called cubic-I, a lattice type of cubic crystals.
- Bravais lattice** ..... Lattice type defined by specific translational and point symmetry, given by lattice vectors  $\underline{R}_1$ ,  $\underline{R}_2$ ,  $\underline{R}_3$ . Overall, there are 14 three-dimensional Bravais lattices. Additional (point) symmetry properties are described by the corresponding 230 three-dimensional **space groups**.
- Brillouin zone** ..... Compact polyhedral unit cell of the reciprocal lattice corresponding to the **Wigner-Seitz cell** of the real space lattice.
- Buerger cell** ..... Primitive morphological unit cell spanned by lattice vectors  $\underline{R}_1$ ,  $\underline{R}_2$ ,  $\underline{R}_3$  of a three-dimensional lattice where  $\underline{R}_i$  are smallest in length and  $|\underline{R}_1| \leq |\underline{R}_2| \leq |\underline{R}_3|$ .

- BZ** ..... See **Brillouin zone**.
- centering** ..... Augmenting a lattice by additional lattice points (in the centers of morphological unit cells or at their faces). This may lead to a different Bravais lattice type, e.g. centered tetragonal vs. primitive tetragonal.
- chirality** ..... Also referred to as **handedness**. Symmetry property of a three-dimensional object. An object is called **chiral** if it cannot be superimposed onto its mirror image by simple rotation and shifting. Otherwise, it is **achiral**. Crystals are chiral if their symmetry does not include a mirror plane.
- coordination number** ..... Number of nearest neighbor atoms (including all atoms of the **coordination shell**) with respect to a given atom center in a crystal.
- coordination shell** ..... Set of atoms of (about) the smallest distance from a center (usually an atom position, **nearest neighbor shell**) in a crystal.
- crystal** ..... Strictly defined (IUCr) as a material with a discrete sharp diffraction pattern. This includes three-dimensionally periodic arrangements of atoms. Their periodicity is defined by a **lattice**, corresponding symmetry properties by a three-dimensional **space group**, and atom positions inside the morphological unit cell are given by the **basis**. The **two-dimensional** analog is a **monolayer**.
- crystal system** ..... three-dimensional lattice classification resulting in the 14 primitive and centered **Bravais lattices**.
- ct** ..... Centered tetragonal, also called tetragonal-I, a three-dimensional lattice type of crystals.
- cubic Miller Indices** ..... See **Miller Indices** and **sc notation**.
- fcc** ..... Face-centered cubic, also called cubic-F, a three-dimensional lattice type of cubic crystals.
- general lattice vector** ..... Integer-valued linear combination of the three lattice vectors  $\underline{R}_1$ ,  $\underline{R}_2$ ,  $\underline{R}_3$  of a bulk lattice.
- generic Miller Indices** ..... See **Miller Indices**.
- Gibbs-Wulff theorem** ..... Basis of a quasi-continuum model to determine the shape of polyhedral crystalline particles confined by planar sections (**facets**) of  $(h k l)$  oriented monolayers.
- Gra** ..... Short-hand writing for **graphene**, a  $(0 0 0 1)$  oriented monolayer of graphite exhibiting a honeycomb structure.

- graphene** ..... Monolayer of graphite with (0 0 0 1) orientation exhibiting a honeycomb structure. Graphene sheets also exist in nature as flakes or as adsorbed films. This carbon structure is sometimes abbreviated as **Gra**.
- handedness** ..... See **chirality**.
- hcp** ..... Hexagonal close-packed, a three-dimensional crystal structure with hexagonal lattice, a lattice constant ratio  $c/a = \sqrt{8/3}$ , and two atoms in the morphological unit cell. In practice, lattices of hexagonal crystals with ratios  $c/a$  near  $\sqrt{8/3}$  are also called hcp type.
- Hermann-Mauguin** ..... Notation used to define symmetry operations and symmetry groups describing crystals and monolayers. This notation is preferred by crystallographers, see also **Schönflies**.
- hex (hcp)** ..... A hexagonal lattice with a lattice constant ratio  $c/a$  of  $\sqrt{8/3} = 1.63299$ . Lattice of the **hcp** crystal structure.
- incommensurate composite crystal**  
One of three classes of aperiodic bulk systems with specific long-range order and local symmetry. The other types are **modulated structures** and **quasicrystals**.
- ITC** ..... International Tables for Crystallography, general reference for two- and three-dimensional space groups.
- lattice** ..... Definition of periodicity (translational symmetry) in three dimensions by lattice vectors  $\underline{R}_1, \underline{R}_2, \underline{R}_3$ . Additional point symmetry is given by a corresponding three-dimensional **space group**. The two-dimensional equivalent of a lattice is a **net-plane**, of a space group it is a **plane group**. The term **lattice** is also used sometimes to define periodicity in one and two dimensions.
- lattice basis vectors** ..... Position vectors  $\underline{r}_1, \underline{r}_2, \dots, \underline{r}_p$  of all  $p$  atoms in the primitive unit cell of a crystal.
- lattice constants** ..... Scaling parameters  $a, b, c$  of the three lattice vectors  $\underline{R}_1, \underline{R}_2, \underline{R}_3$  of a crystal where  $a = |\underline{R}_1|, b = |\underline{R}_2|, c = |\underline{R}_3|$ .
- lattice vectors** ..... Periodicity vectors  $\underline{R}_1, \underline{R}_2, \underline{R}_3$  of a lattice.
- Miller-Bravais indices** ..... Referring to the **4-index notation**. Integer quadruplets  $(l m n q)$  characterizing orientations of netplanes in hexagonal lattices. The definition is based on the reciprocal (hexagonal) lattice with symmetry considerations. The 4-index notation is equivalent to the common 3-index notation  $(h k l)$  of generic **Miller indices**.

- Miller indices** ..... Integer triplets  $h, k, l$ , such as in  $(h k l)$  and  $[h k l]$  characterizing orientations of netplanes and directions in a lattice, also called **generic Miller indices**. The definition is based on lattice vectors of the **reciprocal lattice**. For centered cubic lattices (fcc, bcc) Miller indices of the simple cubic lattice, also called **simple cubic (sc) Miller indices**, are often used. For hexagonal lattices an alternative **4-index notation**  $(l m n q)$ , also called **Miller-Bravais indices**, is often used.
- modulated structure** ..... One of three classes of aperiodic bulk systems with specific long-range order and local symmetry. The other types are **incommensurate composite crystals** and **quasicrystals**.
- monoatomic crystal** ..... Crystal with one atom in its primitive morphological unit cell.
- morphological unit cell** ..... Also called **unit cell**. Six-faced polyhedron (parallelepiped) spanned by lattice vectors  $\underline{R}_1, \underline{R}_2, \underline{R}_3$  of a three-dimensional lattice. The cell is **primitive** if it is of smallest volume.
- motif** ..... A cluster of atoms recurring in a **crystal**.
- multiplicity** ..... Number of atom members in **neighbor shells**.
- nanotube** ..... Hollow cylindrical cluster of atoms or molecules. A nanotube may be constructed as a rolled up strip of a planar sheet of atomic or molecular components in a periodic arrangement.
- neighbor shell** ..... Set of atoms of (about) the same distance from a center (usually an atom position) in a crystal.
- netplane-adapted lattice** ... Lattice description by lattice vectors  $\underline{R}_1, \underline{R}_2, \underline{R}_3$  where  $\underline{R}_1, \underline{R}_2$  point parallel to a given netplane of the lattice and  $\underline{R}_3$  connects adjacent netplanes.
- n-fold rotation** ..... Rotation by an angle  $\alpha = 360^\circ/n$  about an axis. For lattices with translational symmetry only values  $n = 1, 2, 3, 4, 6$  are allowed.
- non-symmorphic space group**  
Space group whose generating symmetry elements also include those combining point and translational symmetry, such as glide reflection or rototranslation.
- Niggli cell** ..... Primitive morphological unit cell spanned by lattice vectors  $\underline{R}_1, \underline{R}_2, \underline{R}_3$  of a three-dimensional lattice where  $\underline{R}_i$  are smallest in length and  $|\underline{R}_1| \leq |\underline{R}_2| \leq |\underline{R}_3|$ . Additional constraints are applied to make the lattice definition unique.
- obtuse representation** ..... Lattice vectors  $\underline{R}_1, \underline{R}_2, \underline{R}_3$  which form mutual angles  $\alpha, \beta, \gamma \geq 90^\circ$  with at least one angle  $> 90^\circ$ .

- point symmetry group** ..... Collection of three-dimensional point symmetry operations, such as inversion, rotation, mirroring, forming a mathematical group. Crystals are invariant with respect to all operations of a corresponding point symmetry group.
- polyatomic crystal** ..... Crystal with several atoms in its primitive morphological unit cell defined by lattice vectors  $\underline{R}_1, \underline{R}_2, \underline{R}_3$ . The atoms may be of different element type and/or are placed at different positions  $\underline{r}$  inside the cell with  $\underline{r} = x_1 \underline{R}_1 + x_2 \underline{R}_2 + x_3 \underline{R}_3$  and  $0 \leq x_i < 1$ .
- primitive lattice** ..... Crystal lattice with lattice vectors  $\underline{R}_1, \underline{R}_2, \underline{R}_3$  forming the primitive morphological unit cell containing the smallest number of non-equivalent atoms.
- quasicrystal** ..... One of three classes of aperiodic bulk systems with specific long-range order and local symmetry. The latter may not be compatible with allowed symmetries appearing in crystals. The other types are **modulated structures** and **incommensurate composite crystals**.
- reciprocal lattice** ..... Lattice defined by lattice vectors  $\underline{G}_1, \underline{G}_2, \underline{G}_3$  of dimension [inverse length], which are connected with vectors  $\underline{R}_1, \underline{R}_2, \underline{R}_3$  of the real space lattice by orthogonality relations  $(\underline{G}_i \underline{R}_j) = 2\pi \delta_{ij}$ .
- relative coordinates** ..... Representation of lattice basis vectors by linear combinations of lattice vectors rather than by absolute Cartesian coordinates.
- sc** ..... Simple cubic, also called primitive cubic or cubic-P, the basic lattice type of cubic crystals.
- sc notation** ..... See **simple cubic notation**.
- Schönflies** ..... Notation used to define symmetry operations and symmetry groups describing crystals and monolayers. This notation is preferred by physicists, see also **Hermann-Mauguin**.
- shell multiplicity** ..... Number of atoms in **neighbor shells**.
- simple cubic notation** ..... Notation of Miller indices for face- and body-centered cubic lattices referring to the simple cubic lattice.
- single crystal** ..... Perfect crystal with exact three-dimensional periodicity and symmetry.
- space group** ..... Collection of all symmetry properties (translational and point symmetry elements) available for a given crystal with its periodicity described by a Bravais lattice. There are 230 different space groups for (three-dimensional) crystals. The two-dimensional equivalent of a space group is a **plane group**.

- superlattice** ..... Description of a crystal lattice by lattice vectors  $\underline{R}_1$ ,  $\underline{R}_2$ ,  $\underline{R}_3$  (and corresponding unit cells) which are larger than (often integer multiples of) those suggested by the basic periodicity of the crystal.
- symmorphic (space) group**  
Space group whose generating symmetry elements include only true point symmetry operations and true translations, i.e. no combinations, such as glide planes or screw axes.
- unit cell** ..... See **morphological unit cell**.
- Voronoi cell** ..... See **WSC**, **Wigner-Seitz cell**.
- Wigner-Seitz cell** ..... Compact polyhedral unit cell of a real lattice, sometimes called **Voronoi cell**.
- WSC** ..... See **Wigner-Seitz cell**.
- Wulff construction** ..... See **Gibbs-Wulff theorem**.

### Monolayers, Surfaces and two-dimensional

- $2 \times 2$  matrix notation** ..... Notation of the periodicity and orientation of reconstructed surfaces or adsorbate systems.
- achiral surface** ..... Single crystal surface which is symmetric with respect to at least one mirror plane perpendicular to it. Otherwise, the surface is called **chiral**.
- acute representation** ..... Lattice vectors  $\underline{R}_1$  and  $\underline{R}_2$  which form an angle  $\gamma \leq 90^\circ$  (=  $60^\circ$  for hexagonal lattices).
- additivity theorem** ..... Mathematical theorem connecting **Miller indices** of a **stepped** or **kinked surface** with those of its terraces, steps, and kinks.
- basis** ..... Collection of atom positions inside the two-dimensional (morphological) unit cell.
- Bravais lattice** ..... Lattice type defined by specific translational and point symmetry, given by lattice vectors  $\underline{R}_1$  and  $\underline{R}_2$ . Overall, there are 5 two-dimensional Bravais lattices. Additional (point) symmetry properties are described by the corresponding 17 two-dimensional **space groups**.
- centering** ..... Augmenting a netplane by additional lattice points (in the center of the unit cell). This leads to a different Bravais netplane type only for rectangular netplanes.

- chiral surface** ..... Single crystal surface which does not possess symmetry with respect to a mirror plane perpendicular to it. Otherwise, the surface is called **achiral**.
- coincidence (super)lattice**  
Commensurate reconstruction type where a two-dimensional periodicity cell of the overlayer is shared with the substrate layers. However, this cell is larger than the smallest possible unit cell of each of the two separate subsystems. The reconstruction type is also referred to as high-order commensurate (**HOC**) or **scaled commensurate** reconstruction.
- commensurate reconstruction**  
Surface reconstruction where netplanes of the topmost monolayers are commensurate with those of the substrate layers. Corresponding netplane transformations are described by integer-valued  $2 \times 2$  matrices.
- c-rectangular** ..... Centered rectangular, a netplane type of rectangular monolayers.
- crystallographic plane** ..... See **netplane, monolayer**.
- crystal system** ..... Netplane classification resulting in the 5 primitive and centered **Bravais lattices**.
- cut-and-project** ..... A method to create aperiodic linear atom arrangements (**Fibonacci chains**) by projecting a two-dimensional square lattice.
- DAS model** ..... Dimer-atom-stacking-fault model of the reconstructed Si(1 1 1) - (7 × 7) surface.
- domain formation** ..... A substrate surface with symmetry may allow differently oriented overlayers which are energetically equivalent. This can lead to large but finite patches of overlayers - so-called domains - corresponding to the different orientations.
- facet** ..... Finite flat region at a single crystal surface described by Miller indices ( $h_f k_f l_f$ ). The facet orientation does not need to coincide with that of the long-range surface characterized by ( $h k l$ ).
- Fibonacci chain** ..... Aperiodic linear atom arrangement of alternating short and long interatomic distances characterized by self-similarity. Used to simulate 1-dimensional quasicrystals.
- FM growth mode** ..... See **Frank-Van-der-Merwe**.
- Frank-Van-der-Merwe** ..... Growth mode at surfaces referring to **layer-by-layer** growth.



- general lattice vector** ..... Integer-valued linear combination of the two lattice vectors  $\underline{R}_1$  and  $\underline{R}_2$  of a netplane.
- high-Miller-index surface** . See **vicinal surface**.
- high-order commensurate**  
See **coincidence (super)lattice**.
- HOC reconstruction** ..... See **coincidence (super)lattice**.
- incommensurate reconstruction**  
Surface reconstruction where netplanes of the topmost monolayers are not commensurate with those of the corresponding substrate layers. Corresponding netplane transformations are described by  $2 \times 2$  matrices containing irrational elements.
- interference lattice** ..... Lattice structure at adsorbate covered surfaces with quasi-periodic long-range order expressed by one- and two-dimensional **moiré patterns**.
- kinked surface** ..... Crystal surface composed of terraces separated by steps analogous to a **stepped surface**. However, the step lines are broken in a periodic or non-periodic fashion ('stepped steps' or 'kinked steps'). If the kink and step distribution is regular, i.e. periodic at the surface, the kinked surface can be described in its orientation by large Miller indices, see also **vicinal surface**.
- lattice basis vectors** ..... Position vectors  $\underline{r}_1, \underline{r}_2, \dots, \underline{r}_p$  of all  $p$  atoms in the primitive unit cell of a monolayer.
- lattice gas** ..... Amorphous monolayer of atoms derived from an ideal (periodic) monolayer by occupying lattice sites in a random fashion.
- lattice vectors** ..... Periodicity vectors  $\underline{R}_1$  and  $\underline{R}_2$  of a netplane.
- microfacet notation** ..... Formal notation of the structure and orientation of **stepped** and **kinked surfaces**.
- microfaceted surface** ..... A surface structure built of different **facets** that are finite, usually small, in one or two dimensions, and combine to form the global surface.
- Minkowski reduction** ..... Iterative method to determine symmetrically appropriate lattice vectors  $\underline{R}_{o1}$  and  $\underline{R}_{o2}$  of a netplane from an initial set  $\underline{R}_1, \underline{R}_2$ .
- Moiré pattern** ..... Spatial interference pattern originating from superimposing two-dimensionally periodic objects whose periodicity differs only slightly. Simple examples are identical parallel monolayers which are scaled or rotated by a small angle with respect to each other.

- monolayer** ..... **two-dimensionally** periodic arrangement of atoms. Its periodicity is defined by a **netplane**, corresponding symmetry properties by a two-dimensional **plane group**, and atom positions inside the unit cell are given by the **basis**. The **three-dimensional** analog is a **crystal**. The present definition of a monolayer **deviates** from definitions used elsewhere and referring to adsorbate overlayers of a given atom density, one adsorbate per substrate atom or unit cell.
- morphological unit cell** ..... Also called **unit cell**. 4-sided polygon (parallelogram) spanned by lattice vectors  $\underline{R}_1$  and  $\underline{R}_2$  of a two-dimensional netplane. The cell is **primitive** if it is the unit cell of smallest area.
- motif** ..... A cluster of atoms recurring in a **monolayer**.
- netplane** ..... Definition of periodicity (translational symmetry) in two dimensions by vectors  $\underline{R}_1$  and  $\underline{R}_2$ . Additional point symmetry is given by a corresponding two-dimensional **plane group**. The three-dimensional equivalent of a netplane is a **lattice**, of a plane group it is a three-dimensional **space group**. The present definition of a netplane is **stricter** than definitions used elsewhere and referring sometimes to both periodicity and atom basis which defines a **monolayer** in this book.
- n-fold rotation** ..... Rotation by an angle  $\alpha = 360^\circ/n$  about an axis perpendicular to the netplane. For netplanes with translational symmetry only values  $n = 1, 2, 3, 4, 6$  are allowed.
- obtuse representation** ..... Lattice vectors  $\underline{R}_1$  and  $\underline{R}_2$  which form an angle  $\gamma > 90^\circ$  ( $= 120^\circ$  for hexagonal lattices).
- Penrose tiling** ..... Procedure of covering a plane completely without holes or overlaps using tiles of a finite set of different polygons, e.g. rhombi, where the tiling yields an aperiodic pattern.
- plane group** ..... Also referred to as two-dimensional **space group**. Collection of all symmetry properties (translational and point symmetry elements) available for a given monolayer with its periodicity described by a Bravais lattice. There are 17 different space groups for (two-dimensional) monolayers. The three-dimensional equivalent of a plane group is a three-dimensional **space group**.
- point symmetry group** ..... Collection of two-dimensional point symmetry operations, such as inversion, rotation and mirroring, forming a mathematical group. Netplanes are invariant with respect to all operations of the corresponding point symmetry group.

- rolling vector** ..... General lattice vector inside an  $(h k l)$  monolayer used to define a nanotube by rolling a monolayer strip along the vector.
- p-rectangular** ..... Primitive rectangular, also called rectangular, rect. A two-dimensional lattice type of rectangular monolayers.
- scaled commensurate** ..... See **coincidence (super)lattice**.
- SK growth mode** ..... See **Stranski-Krastanov**.
- space group** ..... See **plane group**.
- step notation** ..... Formal notation of the structure and orientation of **stepped surfaces**.
- stepped surface** ..... Crystal surface composed of terraces of monolayers (with orientations defined by **Miller indices**  $(h_t k_t l_t)$ ), separated by steps (with orientations of step sides defined by **Miller indices**  $(h_s k_s l_s)$ ). If the step distribution is regular, i.e. periodic at the surface, the stepped surface can be described in its orientation by large Miller indices, see also **vicinal surface**.
- Stranski-Krastanov** ..... Growth mode at surfaces referring to mixed **layer-by-layer** and **three-dimensional cluster** growth.
- superlattice** ..... Description of a netplane by lattice vectors  $\underline{R}_1$  and  $\underline{R}_2$  (and corresponding unit cells) which are larger than (integer multiples of) those suggested by the basic periodicity of the netplane. At surfaces, superlattices apply to netplanes of surface-adapted lattice vectors  $\underline{R}_1$  and  $\underline{R}_2$  (and corresponding unit cells).
- surface reconstruction** ..... Structural modification of a singly crystal surface where monolayers near the surface are structurally changed. This can yield changed two-dimensional periodicity compared with that of the bulk termination and/or different atom composition and placement.
- surface relaxation** ..... Structural modification of a single crystal surface where whole monolayers near the surface are shifted. Shifts can occur perpendicular and parallel to the surface.
- surface termination** ..... Structure of the topmost atom layers of the surface of a **single crystal**. In particular, for polyatomic crystals, this specifies which atom(s) terminate(s) the bulk structure at the surface.
- unit cell** ..... See **morphological unit cell**.
- vicinal surface** ..... Surface of a single crystal finishing with monolayers whose orientation in the crystal is close to but not identical with those of densest monolayers. Vicinal surfaces are often stepped or

kinked. Their orientations are usually described by large values of **Miller indices** ( $h k l$ ). Thus, vicinal surfaces are often called **High-Miller-index surfaces**.

- Volmer-Weber** ..... Growth mode at surfaces referring to **three-dimensional cluster** growth.
- Voronoi cell** ..... See **Wigner-Seitz cell**.
- VW growth mode** ..... See **Volmer-Weber**.
- Wigner-Seitz cell** ..... Compact polygonal (distorted hexagonal, rectangular, or square) unit cell of a netplane, sometimes called **Voronoi cell**.
- Wood notation** ..... Formal notation of the structure and orientation of reconstructed surfaces or adsorbate systems.
- WSC** ..... See **Wigner-Seitz cell**.

### Miscellaneous

- CIF** ..... Crystallographic Information Framework.
- CSD** ..... Cambridge Structural Database.
- DFT** ..... Density-functional theory, a quantum mechanical method to examine properties of many-electron systems, such as atoms, molecules, and solids with/without surfaces.
- Diophantine equations** ..... Equations using only integers for constants and variables.
- enantiomer** ..... A chiral molecule and its mirror image are enantiomers (enantiomer pairs).
- enantiopure** ..... Gas or liquid of chiral molecules which contain only one type, left- or right-handed.
- Euclid's algorithm** ..... Algorithm to determine the greatest common divisor **gcd**(a, b) of two integers a, b.
- Fibonacci numbers** ..... Infinite series of integers 0, 1, 1, 2, 3, 5, 8, 13 ... defined by element  $a_k$  being the sum of the two previous elements,  $a_{k-1}$ ,  $a_{k-2}$  with  $a_0 = 0$ ,  $a_1 = 1$ .
- gcd** ..... Greatest common divisor of two or more integers.
- golden mean** ..... See **golden ratio**.

- golden ratio** ..... Also referred to as **golden mean**. Mathematical constant  $\phi = (1 + \sqrt{5}) / 2 = 1.618034$ , appearing in **quasicrystal** structures.
- ICSD** ..... Inorganic Crystal Structure Database.
- lcm** ..... Least common multiple of two or more integers.
- LEED** ..... Low-energy electron diffraction, an experimental method for surface structure determination.
- magic numbers** ..... Total number of atoms in a compact atom cluster with closed polygonal shells.
- moiré** ..... French for ‘of wavy watery appearance’.
- NAD** ..... Nucleic Acid Database.
- number theoretical methods**  
Mathematical methods dealing with integer numbers.
- oSSD** ..... Open access version of SSD, see **Surface Structure Database**.
- PDB** ..... Protein Data Bank.
- racemic mixture** ..... Gas or liquid of chiral molecules which contains both types, left- and right-handed, in equal amounts.
- SSD** ..... See **Surface Structure Database**.
- Surface Structure Database**  
Also referred to as **SSD**. Database of experimentally known surface structures. The latest version 5 of SSD has been made public as open access SSD (**oSSD**).

## INDEX

## A

achiral, 458  
 definition, 226, 228  
 surface, 232, 463  
 acute representation  
 2-dim., 463  
 3-dim., 458  
 hexagonal, 31, 58, 130  
 additivity theorem, 463  
 adsorbate layer, 274  
 clusters, 275  
 coverage, 274  
 fully disordered, 274  
 interference lattice, 306  
 anisotropic scaling, 325  
 basic formalism, 307  
 chiral pairs, 325  
 first order, 310  
 Fourier expansion, 308  
 high-order, 312  
 HOC, 316  
 isotropic scaling, 311, 319  
 isotropic scaling + rotation, 319, 320, 322  
 modulation factor, 310, 313  
 non-periodic, 309  
 order matrix, 313  
 periodic, 309  
 rotation, 320  
 shifting, 328  
 stretching, 326  
 warping, 306  
 Wood notation, 317  
 islands, 275  
 lattice gas, 274  
 partially disordered, 275  
 periodic overlayer, 275  
 coincidence lattice, 277  
 commensurate, 276  
 high-order commensurate, 299  
 hexagonal, 303  
**square**, 304  
 high-order commensurate (HOC), 277  
 incommensurate, 92, 279  
 modulation, 278  
 warping, 279  
 adsorbate sites, 280  
 centered rectangular lattice, 287  
 3-fold hollow, 288  
 4-fold hollow, 288  
 top, 288  
 hexagonal lattice, 282  
 2-fold bridge, 284  
 3-fold hollow, 283  
 top, 283  
 high-symmetry sites, 281  
 mixed, 289  
 primitive rectangular lattice, 285

2-fold long bridge, 286  
 2-fold short bridge, 286  
 4-fold hollow, 287  
 top, 285  
 sketches, 382  
 bcc surface, 387  
 diamond surface, 391  
 fcc surface, 382  
 hcp surface, 389  
 zincblende surface, 393  
 square lattice, 281  
 2-fold bridge, 282  
 4-fold hollow, 282  
 top, 281  
 substitutional, 289  
 adsorbates, 274  
 adsorption  
 chiral, 341  
 cooperative, 343, 346  
 enantiopure, 345  
 enantioselective, 341  
 local, 342  
 racemic, 345  
 anti-ferromagnetic ordering, 36

## B

Bain path, 49, 458  
 Balsac, 3, 13, 443  
 basis, 458, 463  
 bcc, 25, 458  
 Bravais lattice (2-dim.), 463  
 centered rectangular, 147, 149, 151, 158, 161, 170  
 hexagonal, 151, 152, 170  
 oblique, 169  
 overview, 171  
 primitive rectangular, 145, 147, 149, 159, 161, 169  
 square, 150, 170  
 Bravais lattice (3-dim.), 52, 53, 458  
 cubic-F, 57, 64  
 cubic-I, 57, 64  
 cubic-P, 57, 64  
 hexagonal-P, 58, 64  
 monoclinic-A, 55  
 monoclinic-B, 55, 64  
 monoclinic-C, 55  
 monoclinic-P, 54, 64  
 orthorhombic-C, 56, 64  
 orthorhombic-F, 56, 64  
 orthorhombic-I, 56, 64  
 orthorhombic-P, 56, 64  
 overview, 60  
 tetragonal-I, 57, 64  
 tetragonal-P, 56, 64  
 triclinic-P, 53, 64  
 trigonal-R (rhombohedral), 59, 64  
 BrCIFCH, 226  
 Brillouin zone (BZ), 458, 459

Buerger cell, 47, 458  
 bulk crystals, 15  
   representation, 19

## C

$C_4O_6H_6$ , 228, 344  
 Cahn-Ingold-Prelog rules, 228  
 carbon nanotube, 370  
   armchair, 370  
   chiral pairs, 371  
   zigzag, 370  
 Cartesian coordinates, 24  
 catalysis, 11  
 centering, 42, 459, 463  
 cesium chloride, 20, 72  
 chemical binding, 10  
 chiral  
   centers, 228  
   definition, 225, 228  
   molecule, 226  
   partner, 229  
   surface, 225, 464  
 chirality, 225, 459  
 CIF, 468  
 classification scheme  
   crystal lattices, 52, 60  
   netplanes, 168, 175, 190  
 clusters, 78  
 coincidence (super)lattice, 464  
 commensurate reconstruction, 464  
 compatibility constraints  
   2-dim., 131, 136, 144, 149, 156  
   3-dim., 52  
 coordinate transformation (2-dim.)  
   glide reflection, 155  
   inversion, 133  
   mirroring (reflection), 141  
   rotation, 135  
 coordination  
   number, 66, 459  
   shell, 66, 459  
 c-rectangular, 464  
 crystal, 459  
   aperiodic, 88, 89  
   decomposition, 20  
   definition, 16, 19  
   growth, 259  
   growth mode, 259  
     3-dim cluster, 261  
     alloying, 263  
     Frank-Van-der-Merwe (FM), 260, 262  
     layer-by-layer, 260  
     mixed layer, cluster, 261  
     Stranski-Krastanov (SK), 261  
     Volmer-Weber (VW), 261, 262  
   hexagonal close-packed (hcp), 31, 193  
   incommensurate, 88  
   incommensurate composite, 90, 92  
   modulated structures, 88  
   periodic, 89

quasicrystal, 88, 93, 95  
    $Al_{65}Cu_{20}Fe_{15}$ , 99  
   dihedral, 97  
   i-AlCuFe, 99  
   icosahedral, 97  
 crystal parameters, 394  
 crystal systems (2-dim.), 168, 464  
   hexagonal, 170  
   oblique, 169  
   overview, 171  
   rectangular, 169  
   square, 170  
 crystal systems (3-dim.), 52, 459  
   cubic, 57  
   hexagonal, 58  
   monoclinic, 54  
   orthorhombic, 55  
   rhombohedral, 59  
   tetragonal, 56  
   triclinic, 53  
   trigonal, 59  
 crystallites, 78, 85  
   quasi-continuum models, 85  
 crystallographic plane, 110, 464  
 CsCl, 72, 236  
 CSD, 468  
 ct, 459  
 cubic Miller Indices, 459  
 cuboctahedral clusters, 81  
 cut-and-project method, 98, 464

## D

DAS model, 249, 464  
 Density-functional theory, 468  
 DFT, 306, 468  
 diamond, 21  
 Diophantine equations, 468  
   linear, 41, 115, 116, 208, 222, 421  
     (in)homogeneous, 421  
     iterative solution, 421  
   quadratic, 68, 71, 74, 424  
      $a m^2 = b n^2$ , 431  
      $m^2 + 2 n^2 = N^2$ , 429  
      $m^2 + m n + n^2 = N^2$ , 428  
      $n_1^2 + n_2^2 + n_3^2 + n_4^2 = N$ , 426  
      $n_1^2 + n_2^2 + n_3^2 = N$ , 424  
      $n_1^2 + n_2^2 = N$ , 427  
 dodecahedral clusters, 84  
 domain formation, 464

## E

**electronic properties**, 10  
 enantiomer, 226, 468  
 enantiopure, 345, 468  
 Euclid formula, 427  
 Euclid's algorithm, 419, 421, 468  
 experimental methods, 355  
   IS, 363

LEED, 355, 362  
 PED, 355, 363  
 SEXAFS, 355, 363  
 table, 355  
 X-ray grazing incidence, 355  
 XSW, 363

## F

facet, 85, 464  
 facetting, 263  
 fcc, 27, 459  
 ferromagnetic ordering, 36  
 Fibonacci  
   chain, 98, 464  
   numbers, 96, 468  
 five-fold symmetry, 95, 99  
 Fourier theory, 64, 249, 440  
   harmonic functions, 440  
 four-index notation, 129, 458, 460  
 Frank-Van-der-Merwe, 464  
 FW growth mode, 464

## G

GaAs, 104, 201  
 gallium arsenite, 104  
 Gallium arsenite, 201  
 gcd, 468  
 generic Miller Indices, 459  
 Gibbs-Wulff theorem, 86, 459  
 glossary  
   bulk and 3-dim., 458  
   miscellaneous, 468  
   surface and 2-dim., 463  
 glossary, abbreviations, 458  
 golden mean, 469  
 golden ratio, 94, 469  
 Gra, 459  
 grains, 85  
 graphene, 370, 460

## H

handedness, 41, 225, 229, 460  
   left-handed, 230  
   right-handed, 22, 230  
 hcp, 31, 460  
 Hermann-Mauguin notation, 51, 53, 136, 176, 460  
 hex(hcp), 460  
 hexagonal close-packed (hcp) crystal, 76  
 hexagonal graphite, 101  
 high-Miller-index surface, 465  
 high-order commensurate (HOC), 465  
 HOC reconstruction, 250, 465

## I

icosahedral  
   clusters, 79

  symmetry, 79  
 ICSD, 469  
 incommensurate composite crystal, 460  
 incommensurate reconstruction, 465  
 intercept factors, 126  
 interference lattice, 465  
 international notation, 51, 53  
 international tables of crystallography (ITC), 51, 176  
 inversion symmetry, 201  
 ITC, 51, 176, 460  
 IUCr crystal definition, 88  
 IUPAC, 258

## K

kinked surface, 465

## L

label, 18  
 Langange's theorem, 426  
 lattice, 460  
   alternative description, 20, 22, 40  
   basis, 19  
   centered, 42  
     A-centered, 45  
     B-centered, 45  
     body centered, 45  
       cubic (bcc), 25, 57, 63, 71, 121  
     C-centered, 45  
     face centered, 45  
       cubic (fcc), 27, 57, 63, 73, 119  
     F-centered, 45  
     I-centered, 45  
   classification, 50  
   definition, 16, 19  
   geometric constraints, 39  
   hexagonal, 30, 124  
   hexagonal sublattice (trigonal), 33  
   linear transformations, 39  
   perovskite, 220  
   reciprocal, 62  
     Bravais lattices, 63  
     double reciprocal lattice, 437  
     lattice vectors, 62  
     orthogonality relations, 62, 308  
     unit cell volume, 62  
   rhombohedral, 32  
   simple cubic (sc), 25, 57, 63, 68, 119  
   symmetrically appropriate vectors, 117  
   symmetry, 50  
   trigonal, 32, 124  
 lattice basis vectors, 18, 110, 111, 460, 465  
 lattice constant, 17, 460  
 lattice gas, 465  
 lattice points, 16  
 lattice vectors, 16, 460, 465  
   acute, 23, 119  
   general, 110, 266, 459, 465  
   netplane-adapted, 115, 368



obtuse, 23, 119  
 reduced, 23  
 lcm, 469  
 LEED, 99, 469  
 LEEDpat, 334, 443  
 linear algebra, 436  
 linear transformation, 436  
 literature references, 446

## M

magic numbers, 79, 80, 81, 469  
 magnetism, 10, 36  
 matrix notation ( $2 \times 2$ ), 257, 463  
 MgO, 12, 111, 198, 236, 264  
 microfacet notation, 216, 465  
 microfaceted surface, 465  
 Miller indices, 109, 461  
 4-index notation, 129  
 additivity theorem  
 kinked surface, 212, 214  
 stepped surface, 208, 209  
 alternative definition, 126, 128  
 cubic lattices, 119  
 decomposition, 208, 221  
 direction, 114  
 direction family, 114  
 family, 114  
 generic, 112  
 large values, 206, 208, 212  
 negative values, 112, 197  
 simple cubic notation, 120, 122, 197  
 trigonal (hexagonal notation), 126  
 Miller-Bravais indices, 126, 129, 460  
 Minkowski reduction, 117, 118, 410, 465  
 basic condition, 411  
 mathematics, 409  
 modulated structure, 461  
 moiré, 469  
 angle, 319  
 factor, 311, 318  
 lattice vectors, 310, 313  
 matrix, 310, 313, 318  
 moirons, 307  
 pattern, 306, 465  
 stripes, 326  
 molecular adsorbates, 290  
 monoatomic crystal, 461  
 monolayer, 109, 110, 466  
 atom density, 113  
 definition, 110, 111  
 distance, 112  
 NaCl(1 2 2), 368  
 morphological unit cell, 18, 47, 111, 132  
 2-dim., 466  
 3-dim., 461  
 motif, 177  
 2-dim., 466  
 3-dim., 461

## N

NaCl, 75, 198, 236, 264  
 NAD, 469  
 nanoparticle, 11, 78, 367  
 nanotube, 367, 461  
 achiral, 376  
 basic definition, 367  
 carbon, 367  
 chiral pairs, 373  
 complex nanotubes, 377  
 coordinate transformation, 369  
 crystallography, 367  
 rolling indices (m, n), 368  
 rolling vector, 368  
 symmetry, 372  
 translational periodicity, 375  
 nanowire, 377  
 neighbor shells, 65, 461  
 complete set, 68  
 Diophantine equations, 424  
 evaluation, 76  
 polyhedral shells, 79  
 shell center, 67  
 shell multiplicity, 66, 67, 461, 462  
 accidental, 69  
 symmetry related, 68, 72, 74  
 total, 69, 72, 74  
 shell radius, 65, 67  
 shell range, 67  
 shell thickness, 67  
 netplane, 109, 466  
 centered, 132, 170  
 definition, 110  
 distance, 112  
 normal direction, 111, 123  
 symmetry, 131  
 netplane symmetry  
 centered rectangular, 182  
 classification, 171  
 hexagonal, 186  
 oblique, 177  
 primitive rectangular, 178  
 square, 184  
 netplane-adapted  
 lattice, 461  
 lattice vectors, 24, 115  
 matrix, 111  
 transformation, 111  
 n-fold rotation, 52, 461, 466  
 Niggli cell, 47, 461  
 non-primitive  
 lattice vectors, 18, 43  
 unit cell, 18  
 non-symmorphic space group, 461  
 number theory, 115, 414, 469  
 basic definitions, 414  
 composite function  $p(x)$ , 416  
 coprime, 415  
 greatest common divisor (gcd), 116, 415, 419  
 least common multiple (lcm), 417

matrices, 431  
 coprime pair, 433  
 integer approximant, 309, 432  
 reduction, 433  
 modulo function, 414  
 nearest integer function, 414  
 truncation function, 414

## O

obtuse representation  
 2-dim., 466  
 3-dim., 461  
 hexagonal, 31, 58, 128

## P

PDB, 469  
 Penrose tiling, 94, 466  
 periodicity cells, 47  
 plane group, 168, 466  
 point symmetry group, 166  
 2-dim., 466  
 3-dim., 462  
 associativity, 166  
 highest, 176  
 inverse element, 166  
 list of groups, 166  
 product, 166  
 subgroup, 167  
 unit element, 166  
 point symmetry operations  
 2-dim., 131  
 3-dim., 51  
 polyatomic crystal, 462  
 p-rectangular, 467  
 primitive  
 lattice, 18, 462  
 lattice vectors, 18  
 unit cell, 18  
 prototiles, 94  
 Pythagorean  
 equation, 256  
 triplets, 427

## Q

quantitative structure determination, 355  
 quasicrystal, 93, 462  
 quasiperiodic crystal, 93

## R

racemic mixture, 345, 469  
 reciprocal lattice, 462  
 references, 446  
 relative coordinates, 18, 462  
 repeated slab geometry, 35, 37  
 rhombohedral graphite, 101  
 rolling vector, 467

rotation  
 2-, 3-, 4-, and 6-fold, 138  
 angles, 136  
 anti-clockwise, 397  
 rutile, 104

## S

sc, 25, 462  
 notation, 120, 122, 462  
 scaled commensurate, 467  
 Schönflies notation, 52, 53, 136, 163, 176, 462  
 self-similarity, 96  
 shell models, 66  
 simple cubic notation, 462  
 single crystal, 462  
 SK growth mode, 467  
 sodium chloride, 75, 198  
 space group (2-dim.), 176, 467  
 non-symmorphic, 168, 176  
 overview, 190  
 simple, 168  
 symmorphic, 168, 176  
 space group (3-dim.), 62, 462  
 SrTiO<sub>3</sub>, 220  
 SSD, 469  
 experimental methods, 362  
 NIST SSD, 281, 292, 357, 358, 364, 443, 444  
 oSSD, 281, 357, 358, 364, 443, 444, 469  
 SSDIN, 13, 443  
 statistical analysis, 359  
 step notation, 210, 467  
 stepped surface, 467  
 Stranski-Krastanov, 467  
 strontium titanate, 220  
 structure, 18  
 structure database  
 critical, 359  
 Crystmet, 357  
 CSD, 357  
 format, 363  
 Balsac, 364  
 CIF, 364  
 PDB, 364  
 requirements, 365  
 SSD, 364  
 Survis, 364  
 XYZ, 364  
 ICSD, 357  
 NAD, 357  
 PDB, 357  
 SCIS, 358  
 supercell, 35  
 superlattice, 35, 463, 467  
 methods, 24  
 surface  
 achiral, 231, 232  
 bcc crystal, 237  
 fcc crystal, 236  
 hexagonal crystal, 239  
 bulk truncation, 197, 245

- chiral, 225, 229
- ideal, 197
- kinked, 205
  - multiple-atom-height, 218
- microfacet notation, 216
- microfacetted, 268
- moiré pattern, 252, 254
- morphology, 205
- orientation, 197
- polyatomic crystal, 219
- real, 244
- step notation, 210
- stepped, 205
  - multiple-atom-height, 206, 211
  - partitioning, 418
  - step edges, 207
  - subterraces, 211
- surface atoms, 202
- symmetry, 331
- termination, 198
- terrace, 205
- vicinal, 205, 210, 214, 468
- surface domain, 331, 337
  - anti-phase, 341
  - glide line, 339
  - mirrored, 338
  - rotational, 337
  - translational, 340
- surface facet
  - angle, 267
  - edge vector, 266
  - negative, 265
  - positive, 265
- surface free energy, 85
- surface reconstruction, 245, 467
  - buckling, 249, 251
  - coincidence lattice, 250, 254
  - commensurate, 246
  - disordered, 245
  - displacive, 247
  - high-order commensurate, 250
  - incommensurate, 253, 257
  - matrix, 246, 250, 253
  - modulation function, 249
  - reconstruction matrix, 246
  - rotational superlattice, 254
  - scaled commensurate, 250
  - superlattice, 245
- surface relaxation, 244, 467
  - inwards/outwards, 244
- surface structure
  - compilations, 357
  - examples
    - Ag(1 1 0) + (2 × 1) - O, 286, 340
    - Ag(1 1 1) + Xe hex disordered, 279
    - Al(1 1 1) + (1 × 1) - O, 333
    - Au(1 0 0) hex disordered, 253
    - Au(1 1 1) - ( $\sqrt{3} \times 22$ )rect, 251, 326
    - Au(1 1 1) + rubrene, 344
    - Co(1 0 -1 5), 239
    - Cu(0 0 1) - ( $2\sqrt{2} \times \sqrt{2}$ )R45° + 2O, 350
    - Cu(1 0 0) + ( $\sqrt{2} \times \sqrt{2}$ )R45° - Cl, 293
    - Cu(1 0 0) + c(2 × 2) - Cl, 282
    - Cu(1 0 0) + c(2 × 2) - Pd, 289
    - Cu(1 1 0) - (1 × 1), 291
    - Cu(1 1 0) - (9 0 | 1 2) - 3(R,R)-TA, 345
    - Cu(1 1 0) - (9 0 | -1 2) - 3(S,S)-TA, 345
    - Cu(1 1 0) + (2 × 1) - CO, 285
    - Cu(1 1 0) + (2 × 3) - 4N, 291
    - Cu(1 1 0) + c(2 × 2) - Mn, 289
    - Cu(1 1 1) - ( $6\sqrt{3} \times 6\sqrt{3}$ )R30° + 2TPyB - 3Cu, 358
    - Cu(1 1 1) + (1 × 1) - NH<sub>3</sub>(disordered), 274
    - Cu(1 1 1) + (2 × 2) - Cs, 283
    - Cu(1 1 1) + (4 × 4) - C60, 277
    - Cu(1 1 1) + (disordered) - C<sub>2</sub>H<sub>2</sub>, 284
    - Cu(1 1 1) + (disordered) - NH<sub>3</sub>, 342
    - Cu(1 1 1) + (R,R)-TA, 344
    - Cu(1 1 1) + (S,S)-TA, 344
    - Cu(1 1 1) + C<sub>4</sub>O<sub>6</sub>H<sub>6</sub>, 344
    - Cu(1 1 1) + R-(NH<sub>3</sub>)<sub>6</sub>, 343
    - Cu(1 1 1) + S-(NH<sub>3</sub>)<sub>6</sub>, 343
    - Cu(8 7 4)<sup>R</sup> + R/S-FAM, 348
    - Cu(-8 -7 -4)<sup>S</sup> + R/S-FAM, 348
    - fcc(15 15 23), 212
    - fcc(3 3 1), 232
    - fcc(3 3 5), 208
    - fcc(37 25 17), 218
    - fcc(5 6 8), 205
    - fcc(6 1 1), 206
    - fcc(7 1 1) facets, 264
    - fcc(7 7 9), 205
    - fcc(*h k l*) crystal sphere, 269
    - Fe(1 1 0) + (2 × 2) - S, 288
    - Fe(1 2 3), 237
    - Fe(-25 -20 -3)<sup>R</sup>, 347
    - Fe(-25 -20 -3)<sup>R</sup> + R-Co<sub>9</sub>, 347
    - Fe(-25 -20 -3)<sup>R</sup> + S-Co<sub>9</sub>, 347
    - Fe(25 20 3)<sup>S</sup>, 347
    - Fe(25 20 3)<sup>S</sup> + R-Co<sub>9</sub>, 347
    - Fe(25 20 3)<sup>S</sup> + S-Co<sub>9</sub>, 347
    - GaAs(1 1 1), 201
    - GaAs(-1 -1 -1), 201
    - Gra + (1 × 1)R3.5° - Gra, 320
    - h-BN + (0.97 × 0.97)R3° - Gra, 320
    - Ir(1 0 0) + (1 × 2) - O, 282
    - Ir(1 1 1) - ( $\sqrt{(124/151)} \times \sqrt{(124/151)}$ )R29.5° - Gra, 314, 322
    - Ir(1 1 1) - (0.9 × 0.9)R29.5° - Gra, 314
    - Ir(1 1 1) + (0.906 × 0.906) - Gra, 329
    - Ir(1 1 1) + (0.906 × 0.906)R5° - Gra, 329
    - Me - ( $\gamma \times \gamma$ ) - Gra, 311
    - MgO(1 1 1) facets, 264
    - MgO(15 11 9), 219
    - NaCl(*h k l*), 198
    - Ni(1 0 0) + c(2 × 2) - CO, 282, 290
    - Ni(1 1 0) + c(2 × 2) - S, 287
    - Ni(1 1 0) + c(2 × 2) - CN, 338, 339
    - Ni(1 1 0) + p2mg(2 × 1) - 2CO, 276, 286, 290, 294
    - Ni(1 1 1) - (1 × 1) - Gra, 312
    - Ni(1 1 1) + (1.155 × 1.155)R2.2° - Ag, 306

Ni(1 1 1) + (1.167 × 1.167)R2.4° - Ag, 306  
 Ni(1 1 1) + (2 × 2) - O, 283  
 Ni(1 1 1) + c(4 × 2) - 2NO, 283, 289  
 Ni(*h k l*), 197  
 Pb(1 1 1) + ( $\sqrt{403}/7 \times \sqrt{403}/7$ )R22.85° - C<sub>60</sub>, 302  
 Pd(1 1 1) + ( $\sqrt{3} \times \sqrt{3}$ )R30° - CO, 283, 293  
 Pt(1 1 0) - (1 × 2) missing row, 246, 292  
 Pt(1 1 0) + c(2 × 2) - Br, 286  
 Pt(1 1 1) + (0.89 × 0.89) - Gra, 311, 319  
 Pt(1 1 1) + c(4 × 2) - 2CO, 289, 337  
 Rh(1 1 0) + (1 × 3) - H, 340  
 Rh(1 1 0) + p2mg(2 × 1) - 2O, 332  
 Rh(1 1 1) + ( $\sqrt{3} \times \sqrt{3}$ )R30° - CO, 283  
 Rh(1 1 1) + (12/13 × 12/13) - B<sub>3</sub>N<sub>3</sub>, 306  
 Ru(0 0 0 1) + (12/13 × 12/13) - Gra, 306  
 Ru(0 0 0 1) + (13 × 13) - C, 279  
 Ru(0 0 0 1) + (23/25 × 23/25) - Gra, 306, 316  
 sc(0 0 1) - (1 × 1) R 36.87°, 255  
 Si(1 0 0) - (2 × 1) symmetric dimer, 248  
 Si(1 0 0) - c(4 × 2) buckled dimer, 248  
 Si(1 1 1) - (7 × 7) DAS model, 249, 291  
 Si(1 1 1) + (1 × 1) - H, 291  
 SrTiO<sub>3</sub>(0 1 8), 220  
 V<sub>2</sub>O<sub>3</sub>(0 0 0 1), 199  
 V<sub>2</sub>O<sub>5</sub>(0 0 1), 200  
 V<sub>2</sub>O<sub>5</sub>(0 1 0), 200  
 W(1 0 0) - c(2 × 2), 247  
 W(1 1 0) + (2 × 1) - O, 288  
 W(2 1 1) microfacetted, 268  
 listing, 444  
 web sites, 443  
 Surface Structure Database (SSD), 13, 469  
 surface symmetry  
   allowed space groups, 334  
 surface termination, 467  
 symmetry group  
   2-dim., 131, 163, 166  
   3-dim., 62  
 symmetry operation (2-dim.)  
   glide reflection, 131, 154, 162  
   identity, 165  
   inversion, 131, 133, 135  
   mirroring (reflection), 131, 141, 153, 164  
   rotation, 131, 135, 140, 163  
 symmetry operation (3-dim.)  
   glide reflection, 52  
   inversion, 51, 227  
   mirroring (reflection), 51, 227  
   rotation, 51, 227  
   rotoinversion, 51  
   rotoreflexion, 51  
   rototranslation (screw operation), 52  
 symmorphic space group, 463

## T

table of contents, 6  
 tartaric acid (TA), 344  
 thin films, 259  
 TiO<sub>2</sub>, 104

titanium dioxide, 104  
 transformation matrix  
   integer approximant, 307  
   supercell, 35  
 translation  
   group, 168  
   operation, 50  
   symmetry, 50

## U

unit cell, 18  
   2-dim., 467  
   3-dim., 463  
   origin, 19  
   primitive, 18, 111

## V

V<sub>2</sub>O<sub>3</sub>, 199  
 V<sub>2</sub>O<sub>5</sub>, 200  
 vanadium pentoxide, 200  
 vanadium sesquioxide, 199  
 vector calculus, 436  
   scalar product, 436, 437  
   vector product, 437  
   volume product, 436, 437  
 vicinal partner, 210, 214  
 Volmer-Weber, 468  
 Voronoi cell, 48  
   2-dim., 468  
   3-dim., 463  
 VW growth mode, 468

## W

web sites, 443  
 Wigner-Seitz cell (WSC)  
   2-dim., 173, 468  
   3-dim., 48, 463  
 Wood notation, 247, 258, 291, 468  
   centered, 406  
   combined transformation, 407  
   definition, 294  
   examples, 295, 399  
   mathematics, 397  
   matrix transformation, 295, 317  
   primitive, 404  
   simplified, 294  
   symmetry information, 294  
   Wood-representable, 404  
 Wulff  
   construction, 86, 88, 463  
   polyhedron, 86

## Y

YBa<sub>2</sub>Cu<sub>3</sub>O<sub>7</sub>, 15, 20

**Z**

zincblende, 104